PREFACE

The 2024 Geophysical Fluid Dynamics Summer Program ran from June 17th to August 23 under the direction of Greg Chini (University of New Hampshire) and Bruce Sutherland (University of Alberta). The theme of the opening lectures, given during the first two weeks, was Multiscale GFD. One of the principal lecturers was Basile Gallet (Université Paris-Saclay, CEA, CNRS). Keith Julien from the University of Colorado, Boulder, was slated to be the other principal lecturer. Tragically, however, he passed away unexpectedly in April 2024. We are extremely grateful to Edgar Knobloch (University of California, Berkeley) who, on short notice, agreed to be the other principal lecturer along with Greg Chini, who gave one of the principal lectures. Edgar opened the lectures with talks on weakly and strongly nonlinear theory for convection with and without rotation. He went on to describe fingering and parametric instabilities. Greg then described the application of the strongly-nonlinear multiscale approach to stably stratified turbulence. Basile gave lectures on turbulence with and without rotation, going on to discuss two dimensional turbulence above topography before describing multiscale methods used to model turbulent transport and near-inertial waves in the ocean. As is now an annual tradition at Walsh Cottage, Keaton Burns (MIT) delivered a "Dedalus tutorial" for the benefit of the fellows and staff.

The fellows this year were:

Paul Curtis, Yale University
Cy David, University of California Los Angeles
Vincent Laroche, University of California Berkeley
Cécile Le Dizes, Institut de Méchanique des Fluides de Toulouse
Matthew McCormack, University of Edinburgh
Camille Moisset, Université Paris-Saclay, CEA
Ishwari Mulkalwar, University of California San Diego
Nicolaos Petropoulos, University of Cambridge
Lulabel Seitz, Brown University
Adhithiya Sivakumar, University of New Hampshire

Besides the Directors, there were twelve long-term visitors including some new faces. Most of them supervised the fellows in research spanning the mathematical, numerical, and experimental and covering topics inspired by physical oceanography, atmospheric science, and stellar interiors. In addition to the long term visitors, Walsh Cottage welcomed a stream of short term visitors, many of whom were past GFD Fellows.

Making sure the summer ran smoothly, Janet Fields and Julie Hildebrandt expertly applied their administrative skills with characteristic kindness and care for fellows and visitors alike. Anders Jensen lent his unique skills and insights to help three of the fellows set up their experiments in the GFD laboratory.

This year's Distinguished Scholar Award was presented to David Goluskin (University of Victoria) for his academic excellence and dedication to the GFD Program and its fellows. The 2024 Sears Public Lecture was given by Brad Marston (Brown University) on "Fluid Earth: Climate Change and Climate Solutions".

The softball tradition was alive and well during the summer, with the fellows winning against MBL to Coach Chini's great excitement! In the closing fellows-versus-staff softball game, Greg shone by hitting the game-winning RBI.

Table of Contents

Principal Lectures

Fellows Reports:

2024 Participants

FELLOWS

Cy David	University of California, Los Angeles
Paul Curtis	Yale University
Nicolaos Petropoulos	Cambridge University
Vincent Laroche	University of California, Berkeley
Cécile Le Dizes	Toulouse Institute of Fluid Mechanics
Adhithiya Sivakumar	University of New Hampshire
Matthew McCormack	University of Edinburgh
Ishwari Mulkalwar	University of California, San Diego
Camille Moisset	CEA
Lulubel Ruiz Seitz	Brown University

STAFF AND VISITORS

Ali Arslan	ETH Zurich
Jonathan Aurnou	University of California Los Angeles
Lois Baker	University of Edinburgh
Benedikt Barthel Sorensen	Massachusetts Institute of Technology
Edoardo Bellincioni	University of Twente
Dante Buhl	University of California, Santa Cruz
Keaton Burns	Massachusetts Institute of Technology
Colm-cille Caulfield	University of Cambridge
Claudia Cenedese	Woods Hole Oceanographic Institution
Gregory Chini	University of New Hampshire
Pulkit Dubey	University of New Hampshire
Kelsey Everard	New York University
Raffaele Ferrari	Massachusetts Institute of Technology
Glenn Flierl	Massachusetts Institute of Technology
Adrian Fraser	University of Colorado
Federico Fuentes	Pontifica Universidad Catolica de Chile
Basile Gallet de Saint Aurin	CEA Saclay
Pascale Garaud	University of California Santa Cruz
Nimrod Gavriel	Weizmann Institute of Science
Renske Gelderloos	Delft University of Technology
Masoumeh Gharaati	University of New Hampshire
Arefe Ghazi Nezami	University of Texas, Austin
David Goluskin	University of Victoria
Karl Helfrich	Woods Hole Oceanographic Institution
Eric Hester	University of California Los Angeles
Christopher Howland	University of Twente
Sander Huisman	University of Twente
Edward Johnson	University College London

Alexis Kaminski	University of California Berkeley
Wanying Kang	Massachusetts Institute of Technology
Rihard Kerswell	University of Cambridge
Edgar Knobloch	University of California, Berkeley
Ching-Yao Lai	Stanford University
Michael Le Bars	Institut de Recherche sur les Phenomenes Hors Équilibre
Daniel Lecoanet	Northwestern University
Adrien Lefauve	University of Cambridge
Samuel Lewin	University of California, Berkeley
Chang Liu	University of Connecticut
Stefan Llewellyn Smith	University of California, San Diego
Yifeng Mao	Scripps Institution of Oceanography
Loren Matilsky	University of California, Santa Cruz
James McElwaine	Durham University
Julie Meunier	CEA Saclay
Colin Meyer	Dartmouth College
M. Nicholas Moore	Colgate University
Ruth Moorman	California Institute of Technolgy
Philip Morrison	University of Texas Austin
Theresa Oehmke	University of New Hampshire
Joseph Pedlosky	Woods Hole Oceanographic Institution
Raymond Pierrehumbert	Oxford Uniersity
Antonello Provenzale	Istituto di Scienze Dell'Atmosfera
Farid Rajkotia-Zaheer	University of Victoria
Pariyam Thadathil Remil Mushthaq	University of New Hampshire
Anubhab Roy	Indian Institute of Technology, Madras
Alban Sauret	University of California, Santa Barbara
Tobias Schneider	EPFL
Nicole Shibley	Princeton University
Andre Souza	Massachusetts Institute of Technology
Bruce Sutherland	University of Alberta
Geoffrey Vallis	University of Exeter
Adrian van Kan	University of California, Berkeley
Kasia Warburton	Dartmouth College
Xing Wei	Bejing Normal University
Baole Wen	New York Institute of Technology
Jack Whitehead	Woods Hole Oceanographic Institution
Beth Wingate	University of Exeter
Da Yang	University of California Davis
Jun-ichi Yano	Centre Natl. de Recherches Meteorologiques
Xiaojue Zhu	Max Planck Institute

2024 Principal Lecturers

Basile Gallet and Edgar Knobloch (*L-R*)

Greg Chini

2024 Geophysical Fluid Dynamics Summer School Participants

First Row (L-R): Basile Gallet, Edgar Knobloch, Nicolaos Petropoulos, Paul Curtis, Lulabel Ruiz Seitz, Vincent Laroche, Camille Moisset, Cécile Le Dizes, Ishwari Mulkawar, Cy David, Matthew McCormack, Adhithiya Sivakumar

Second Row (L-R): Jim Thomas, Bruce Sutherland, Leo Middleton, David Goluskin, Jon Aurnou, Phil Morrison, Steve Tobias, Pascale Garaud, Renske Gelderloos, Remil Mushthaq, Masoumeh Gharaati, Yifeng Mao, Julie Meunier, Chang Liu, _____, Joe Pedlosky

Third Row: Baole Wen, Eric Hester, Greg Chini, Farid Rajkotia-Zaheer, Jack Whitehead, Chris Howland, Adrian Fraser, Daniel Lecoanet, Geoff Vallis, Kasia Warburton, Jezabel Curbelo, Lois Baker, Glenn Flierl, Wanying Kang, Nicole Shibley, Adrian van Kan, Kasturi Shah, Jahru Shi, Keating Burns, Roy Anubhab

Not in photo: Ali Arslan, Benedikt Barthel Sorensen, Colm Caulfield, Claudia Cenedese, Raffaele Ferrari, Federico Fuentes, Nimrod Gavriel, Karl Helfrich, Sander Huisman, Ted Johnson, Alexis Kaminski, Rich Kerswell, Ching-Yao Lai, Michael Le Bars, Adrien Lefauve, Samuel Lewin, Stefan Llewellyn Smith, Loren Matilsky, Jim McElwaine, Colin Meyer, Nick Moore, Ruth Moorman, Theresa Oehmke, Nick Pizzo, Tobias Schneider, Xing Wei, Beth Wingate, Da Yang, Jun-ichi Yano

Lecture Schedule

PRINCIPAL LECTURES

Monday, June 17

Weakly Nonlinear Theory for Convective Instabilities
Edgar Knobloch

Tuesday, June 18

Strongly Nonlinear Theory for Convective Instabilities
Edgar Knobloch

Wednesday, June 19

WHOI Holiday – no lecture

Thursday, June 20

Turbulence and Turbulent Convection, with and without Rotation
Basile Gallet

Reduced Description of Rapidly Rotating Turbulent Convection
Edgar Knobloch

Friday, June 21

Reduced Description of (a) Fingering Instabilities and (b) Parametric Instabilities
Edgar Knobloch

Monday, June 24

Multiscale Modeling of Layered Anisotropic Stratified Turbulence
Greg Chini

Tuesday, June 25

Two-dimensional Turbulence above Topography
Basile Gallet

Wednesday, June 26

Turbulent Transport in the Ocean, Part I: Baroclinic Turbulence
Basile Gallet

Thursday, June 27

Turbulent Transport in the Ocean, Part II: Multiscale Approach
Basile Gallet

Friday, June 28

Near-inertial Waves Interacting with Balanced Flows
Basile Gallet

SEMINARS

Monday, July 1

Multiscaling with the Stars: Regimes of Stratified Turbulence at Low Prandtl Number
Kasturi Shah, University of Cambridge

Tuesday, July 2

Lagrangian Filtering for Wave-Mean Flow Decomposition
Lois Baker, University of Edinburgh

Wednesday, July 3

Non-ideal Bubbly Drag Reduction
Sander Huisman, University of Twente

Thursday, July 4

Holiday - no seminar

Friday, July 5

Internally Heated Convection with Rotation: Bounds and Scaling Laws
Ali Arslan, ETH Zurich

Preferential Flow-Melt Patterning in the Cryosphere
Kasia Warburton, Dartmouth College

Monday, July 8

Revisiting the Solar Tachocline using 3D MHD Simulations
Loren Matilsky, University of California, Santa Cruz

Tuesday, July 9

The Structure of Stratified Mixing in Baroclinically Forced Shear Flows
Adrien Lefauve, University of Cambridge

Wednesday, July 10

Formation and Dynamics of Coherent Structures in Two-dimensional Turbulent Flows
Adrian van Kan, University of California, Berkeley

Thursday, July 11

Everything I Want to Tell you about Coastal Trapped Waves
Renske Gelderloos, Delft University of Technology

Friday, July 12

Single-mode Equations Based Reduced-Order Modeling of (Double Diffusive) Convection
Chang Liu, University of Connecticut

Monday, July 15

Energy Stability in Ducts of Arbitrary Cross Section
Federico Fuentes, Pontifica Universidad Católica de Chile

SEARS PUBLIC LECTURE – Redfield Auditorium

Fluid Earth: Climate Change and Climate Solutions
Brad Marston, Brown University

Tuesday, July 16

On the Contact Line Dynamics of Three-phase Fluids
Eric Hester, UCLA

Wednesday, July 17

Self-aggregation in Rainy-Bénard Convection
Chris Howland, University of Twente

Thursday, July 18

Nonmodal Growth in MHD Shear Flows
Adrian Fraser, University of Colorado

Friday, July 19

Mixing Dynamics on the California Inner Shelf
Alexis Kaminski, UC Berkeley

Monday, July 22

Superrotation in Planetary Atmospheres
Geoffrey Vallis, University of Exeter

Tuesday, July 23

Transitions between Bistable High and Low West Antarctic Ice Shelf Melt Rates
Ruth Moorman, California Institute of Technology

Wednesday, July 24

On the Way to the Limit: Fast Singular Limits and Averaging over Phase in Highly Oscillatory PDEs
Beth Wingate, University of Exeter

Thursday, July 25

Eigenmodes, Adjoints, and the Solar Dynamo
Keaton Burns, Massachusetts Institute of Technology

Friday, July 26

In Search of Stratified Turbulence
Colm-cille Caulfield, University of Cambridge

Monday, July 29

Convection beyond Rayleigh and Bénard
Stefan Llewellyn Smith, University of California, San Diego

Tuesday, July 30

Reversals of the Large-scale Circulation in Thermal Convection
Nick Moore, Colgate University

Wednesday, July 31

What New Models of Stratified Turbulence Tell Us about the Solar Interior
Pascale Garaud, University of California, Santa Cruz

Thursday, August 1

Melting of Cylindrical Laboratory Icebergs
Edoardo Bellincioni, University of Twente

Friday, August 2

Fluid Dynamics of a Mixed Convective/Stably Stratified System
Michael Le Bars, Institut de Recherche sur les Phenomenes Hors Equilibre

Monday, August 5

Heat and Momentum Transport in Icy Moon Oceans
Wanying Kang, Massachusetts Institute of Technology

Tuesday, August 6

Ghost Hunting: Explaining Flow Patterns by Non-Existing Solutions of the Governing Equations
Tobias Schneider, Swiss Federal Institute of Technology, Lausanne

Wednesday, August 7

Exact Planetary Waves and Jet Streams
Nicholas Pizzo, University of Rhode Island

Thursday, August 8

Compositional Convection and the Interior Structure of Sub-Neptune Exoplanets
Raymond Pierrehumbert, University of Oxford

Friday, August 9

Sometimes All You Need is a Little Nudge: Learning Corrections to Long-Time Climate Simulations from Short-Time Training Data
Benedikt Barthel Sorensen, Massachusetts Institute of Technology

FELLOWS' PRESENTATIONS

Monday, August 19

The Dynamics of Stacked Stratified Shear Layers
Adhithiya Sivakumar, University of New Hampshire

Meshes Don't Dance Anymore
Nicolaos Petropoulos, Cambridge University

Tuesday, August 20

Interaction of Microplastics and Settling Sand
Vincent Laroche, University of California, Berkeley

Not Too Spicy: Effects (or not) of Double Diffusion on Kolmogorov Flow
Ishwari Mulkawar, University of California, San Diego

Density Layering in Rotating Stratified Turbulence
Cécile Le Dizes, Toulouse Institute of Fluid Mechanics

Wednesday, August 21

Idealized Models of Moist Convection
Paul Curtis, Yale University

Fast, Singular Limits of the Lagrangian-averaged Navier-Stokes-alpha Model
Lulabel Ruiz Seitz, Brown University

Internal Tides Get Phased by the Equator
Camille Moisset, CEA

Thursday, August 22

Interaction of Internal Gravity Waves with Magnetohydrodynamic Waves
Cy David, University of California, Los Angeles

A Little Goes a Long Way: Dismantling Weakly Nonlinear, Non-normal Dynamical Systems
Matthew McCormack, University of Edinburgh

GFD 2024 Lecture 1: Weakly Nonlinear Theory for Convective Instabilities

Edgar Knobloch; notes by Cy David and Paul Curtis

June 17, 2024

1 Introduction to Asymptotic Methods

The equations governing the dynamics of numerous systems in geophysical fluid dynamics can be written in the form:

$$L_\mu \boldsymbol{u} = N[\boldsymbol{u}] \tag{1}$$

in which L_μ is a locally defined linear differential operator, μ is a parameter, N captures nonlinear terms, and $\boldsymbol{u}$ is the flow velocity. Asymptotic methods can be used to study the behaviour of such a system, allowing one to find approximate solutions to the equations of motions. As we will see, in such an approach, it is necessary to identify and exploit the presence of a small parameter ϵ in the system, which can be achieved in two ways:

- **Explicit small parameter.** In this instance, a small parameter will appear directly in the equations governing the system (e.g., $\epsilon = \mu \ll 1$). Take, for example, the Rossby number: $Ro \equiv U/fL$, where f is the local Coriolis acceleration, which appears in the Navier Stokes equations in a rotating frame after the equations are non-dimensionalised. In the rapid rotation limit, defined as $Ro \ll 1$, one obtains a dominant balance between the pressure gradient force, and Coriolis acceleration terms. The resulting 'geostrophic balance' is a powerful diagnostic when trying to understand behaviour in Earth's atmosphere and oceans. Often, this approach can be applied to study the bulk dynamics of the system, e.g., a description of the interior of the flow.

- **Intrinsic small parameter.** In this case, the small parameter ϵ may correspond to the difference between the system parameter μ (which may be large) and its critical value μ_c, beyond which some instability or flow transition occurs. This approach is often taken in the development of weakly nonlinear theory and the derivation of envelope (i.e., amplitude) equations.

In both cases, the hope is that the asymptotic solution valid in the limit of small parameter also holds when the parameter is small but finite.

1.1 Asymptotic expansions

Consider a simple problem $f(x,\epsilon) = 0$ from which we would like to find the solution $x = x(\epsilon)$, where $\epsilon \ll 1$. The principal step for asymptotic analysis is to expand x in powers of ϵ:

$$x(\epsilon) = x_0 + \epsilon x_1 + \epsilon^2 x_2 + ...$$

such that

$$\left| x(\epsilon) - \sum_{n=0}^{N} \epsilon^n x_n \right| = O(\epsilon^{N+1}) \quad \text{for} \quad N = 0, 1, 2, ...$$

Note that this expansion is not necessarily convergent for finite values of the small parameter ϵ, but the error is always of the next order in ϵ. This is in contrast to a *convergent* expansion for x defined as:

$$\left| x(\epsilon) - \sum_{n=0}^{N} \epsilon^n x_n \right| \to 0 \quad \text{as} \quad N \to \infty$$

with ϵ a small, fixed number. Put simply, if we included arbitrarily more terms in the above expansion, the series solution would approach the correct solution arbitrarily closely. Conversely, an *asymptotic* expansion is defined through:

$$\left| x(\epsilon) - \sum_{n=0}^{N} \epsilon^n x_n \right| \to 0$$

as $\epsilon \to 0$, but critically for a fixed number N of terms in the expansion. Hence, for a finite number of terms in the series, we would expect to converge to the solution asymptotically as $\epsilon \to 0$. Although these expansions typically diverge for finite ϵ, they become better and better as $\epsilon \to 0$.

2 Rayleigh-Bénard Convection

We start our discussion of asymptotics by considering the case of Rayleigh-Bénard convection, a classic example of a forced dissipative system. We consider a fluid layer between two rigid boundaries (in the plane normal to the vertical; see Fig. 1) which is subject to a fixed vertical temperature gradient; i.e., it is heated from below, and cooled from above [3]. Here gravity is such that $\boldsymbol{g} = -g\hat{\boldsymbol{z}}$. In this lecture, we will use asymptotic methods to determine the behaviour of the system as the temperature gradient is increased.

2.1 System equations

We first write the equations of motion for the system in the Boussinesq approximation:

$$\frac{\partial \boldsymbol{u}}{\partial t} + \boldsymbol{u} \cdot \nabla \boldsymbol{u} = -\frac{1}{\rho_0} \nabla P + g\alpha(T - T_0)\hat{\boldsymbol{z}} + \nu \nabla^2 \boldsymbol{u} \tag{2}$$

$$\frac{\partial T}{\partial t} + (\boldsymbol{u} \cdot \nabla) T = \kappa \nabla^2 T \tag{3}$$

$$\nabla \cdot \boldsymbol{u} = 0 \tag{4}$$

Equation (2) is the momentum equation; equation (3) is the heat equation with (isotropic) thermal diffusivity; equation (4) states that the flow is incompressible at leading order in h/h_ρ where h is the layer thickness and h_ρ the density scale height. Here ρ_0 is a reference density; g is the acceleration due to gravity, and appears in the vertical buoyancy term in the momentum equation (2); ν is the kinematic viscosity and κ defines the thermal diffusivity.

We first consider the case of two-dimensional convection in the (x, z) plane. Here, we can define a streamfunction of the flow: $(u, w) \equiv (-\partial_z\psi, \partial_x\psi)$. Taking $\nabla\times$(equation 2) to eliminate the pressure gradient term we obtain:

$$\partial_t\nabla^2\psi + J(\psi, \nabla^2\psi) = g\alpha\partial_x T + \nu\nabla^4\psi \tag{5}$$

$$\partial_t T + J(\psi, T) = \kappa\nabla^2 T, \tag{6}$$

where J defines the Jacobian on two scalar functions: $J(f, g) \equiv \partial_x f\partial_z g - \partial_z f\partial_x g$. There are two equations for the two fields: $\psi(x, z, t)$, $T(x, z, t)$, and thus we have a closed system which is solvable once suitable boundary conditions are specified. We consider impenetrable, stress-free top and bottom boundaries with fixed temperature:

$$w = \partial_x\psi = 0 \text{ at } z = 0, h \tag{7a}$$

$$\partial_z u = -\partial_z^2\psi = 0 \text{ at } z = 0, h \tag{7b}$$

$$T(z = 0) = T_1,\ T(z = h) = T_0, \quad (T_1 > T_0). \tag{7c}$$

For simplicity, we suppose there is no mean horizontal flow, which implies that

$$0 = \int_0^h u\mathrm{d}z = -\int_0^h \partial_z\psi\mathrm{d}z = \psi(z = 0) - \psi(z = h). \tag{8}$$

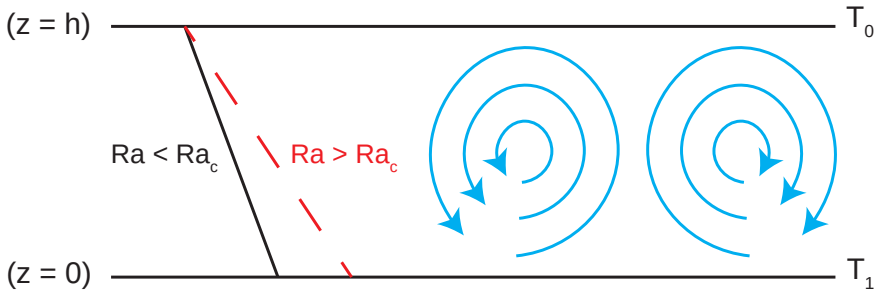

Figure 1: Schematic diagram of the Rayleigh-Bénard system. The two bounding plates are indicated by solid horizontal black lines labeled $z = 0, h$. The oblique black line labeled $Ra < Ra_c$ corresponds to the solution of thermal conduction. Once $Ra > Ra_c$, as indicated by the red dashed line, thermal convection will occur in the fluid layer, as denoted by the blue 'whirls' on the right hand side of the figure. All parameters shown in the figure are equivalent to those described in the text.

Thus, we may set $\psi = 0$ at $z = 0, h$ without loss of generality. Additionally, we note that (5) and (7) imply that

$$\nabla^4 \psi = 0 \text{ at } z = 0, h, \tag{9}$$

and

$$\nabla^2 \psi = 0 \text{ at } z = 0, h. \tag{10}$$

We now non-dimensionalise the system using the thermal diffusivity, κ, introducing nondimensional quantities $(\hat{..})$: time $t = (h^2/\kappa)\hat{t}$, velocity $u = (\kappa/h)\hat{u}$, and $(x, z) = h(\hat{x}, \hat{z})$; finally we non-dimensionalise temperature by the (fixed) absolute temperature difference in the vertical: $T = (T_1 - T_0)\hat{T}$. Here, time has been nondimensionalised by the timescale for thermal diffusion, and velocity by the "thermal diffusion velocity". Inserting these into equations (5)-(6).

$$\partial_t \hat{\nabla}^2 \hat{\psi} + \hat{J}(\hat{\psi}, \hat{\nabla}^2 \hat{\psi}) = \left(\frac{g\alpha \Delta T h^3}{\kappa \nu}\right)\left(\frac{\nu}{\kappa}\right)\frac{\partial \hat{T}}{\partial \hat{x}} + \left(\frac{\nu}{\kappa}\right)\hat{\nabla}^4 \hat{\psi} \tag{11}$$

$$\partial_{\hat{t}} \hat{T} + \hat{J}(\hat{\psi}, \hat{T}) = \hat{\nabla}^2 \hat{T} \tag{12}$$

from which we readily read off the Rayleigh number:

$$Ra = \frac{g\alpha \Delta T h^3}{\kappa \nu} \tag{13}$$

which is a measure of the strength of buoyancy in the fluid compared to the diffusive terms; and the Prandtl number:

$$\sigma = \frac{\nu}{\kappa} \tag{14}$$

which is a measure of the relative effect of momentum to thermal diffusion. In this problem we will take it to be of order unity. Dropping hats, equations (11)-(12) read:

$$\partial_t \nabla^2 \psi + J(\psi, \nabla^2 \psi) = \sigma Ra \partial_x T + \sigma \nabla^4 \psi \tag{15}$$

$$\partial_t T + J(\psi, T) = \nabla^2 T. \tag{16}$$

2.2 Linear theory

An interesting physical problem to solve with the current set up is that of the transition from a state of (thermal) conduction to that of convection. Linear theory allows us to compute the critical Rayleigh number associated with this transition. Physically, increasing Ra through the threshold value could correspond to an increase in T_1 while keeping h and T_0 fixed, as indicated in Fig. 1. We linearize the governing equations by expanding the streamfunction and temperature fields in terms of a small parameter $\epsilon \ll 1$:

$$\psi(x, z, t) = \epsilon \psi_1(x, z, t) + \epsilon^2 \psi_2(x, z, t) + ...$$

$$T(x, z, t) = T_0(z) + \epsilon \theta_1(x, z, t) + ...$$

where the leading order problem is that of pure thermal conduction: $T_0 = 1 - z$ and $\psi_0 = 0$.

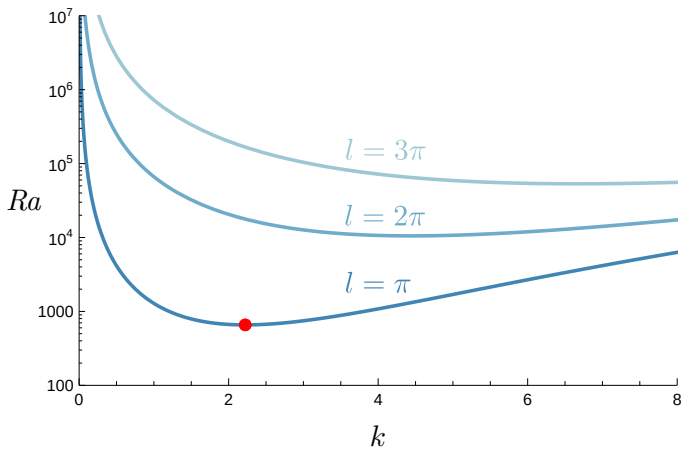

Figure 2: Neutral curves for vertical wavenumbers $l = \pi, 2\pi, 3\pi$. The minimum, $Ra_c = 27\pi^4/4$ at $k_c = \pi/\sqrt{2}$, is indicated with a red point.

It is clear from this expansion that the Jacobian terms in (15) will generate $O(\epsilon^2)$ terms. Hence, to order $O(\epsilon)$ we obtain:

$$\frac{1}{\sigma}\partial_t \nabla^2 \psi_1 = Ra\,\partial_x \theta_1 + \nabla^4 \psi_1 \tag{17}$$

$$\partial_t \theta_1 + \partial_x \psi_1 \partial_z T_0 = \nabla^2 \theta_1. \tag{18}$$

In the second equation, $\partial_z T_0 = -1$. We thus have a system of partial differential equations with constant coefficients, and we may consider simple wave-like solutions: $(\psi, \theta) \sim e^{st} e^{ikx} \sin lz$, in which (k, l) are the horizontal and vertical wavenumber, respectively, and s is the growth rate. Our boundary conditions are stress-free and fixed temperature, which require that $l = n\pi$, $n \in \mathbb{Z}^+$. With this, we obtain the following dispersion relation:

$$\frac{1}{\sigma}s^2 + s(k^2 + l^2) - \frac{Ra\,k^2}{k^2 + l^2} + (k^2 + l^2)^2 = 0. \tag{19}$$

By definition, the condition for exponential growth of solutions (in time) is $s > 0$; when $s = 0$ equation (19) becomes:

$$\frac{Ra\,k^2}{k^2 + l^2} = (k^2 + l^2)^2 \quad \rightarrow \quad Ra = \frac{(k^2 + l^2)^3}{k^2}. \tag{20}$$

The neutral curves given by (20) for $l = \pi, 2\pi, 3\pi, \ldots$ are plotted in Figure 2. Minimizing Ra over the possible wavenumbers $k \in \mathbb{R}$, $l = \pi, 2\pi, 3\pi, \ldots$ yields the critical Rayleigh number and corresponding mode:

$$Ra_c = \frac{27\pi^4}{4}, \quad k_c = \frac{\pi}{\sqrt{2}}, \quad l_c = \pi, \tag{21}$$

which is plotted as a red point in Figure 2.

At $Ra = Ra_c$, there is a bifurcation of the system; i.e., a qualitative difference in the dynamics (conduction vs. convection) is observed.

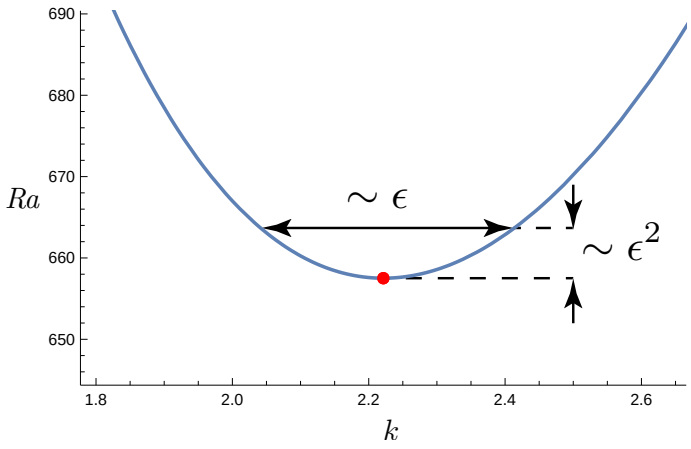

Figure 3: The neutral stability curve is parabolic near $k = k_c$, $Ra = Ra_c$, such that $Ra - Ra_c = O(\epsilon^2)$ for $k - k_c = O(\epsilon)$.

3 Multiscale Description of Weakly Nonlinear Convection

Through linear stability analysis, we found a single most unstable mode $k = k_c$ corresponding to a critical value of the Rayleigh number, $Ra = Ra_c$. When the Rayleigh number exceeds this value slightly ($Ra > Ra_c$), there is instead a band of unstable modes $\{e^{ikx}\}$. Figure 3 shows that the neutral stability curve is parabolic near its minimum such that these modes have wavenumbers with $|k - k_c| = O(\epsilon)$ if $Ra - Ra_c = O(\epsilon^2)$ and $0 < \epsilon \ll 1$.

Thus, the solution, which has the form $e^{i\Delta k x} e^{ik_c x}$, $\Delta k = O(\epsilon)$, is the linear mode with spatial modulation of the amplitude over $O(1/\epsilon)$ scales. Further, we observe from the linear dispersion relation (19) that when the growth rate s is small

$$s \approx \frac{\sigma}{1+\sigma}\left[\frac{Ra\,k^2}{(k^2+l^2)^2} - k^2 - l^2\right] = \frac{\sigma}{1+\sigma}\frac{k^2}{(k^2+l^2)^2}(Ra - Ra_c) = O(\epsilon^2), \tag{22}$$

where (20) is used in the second equality to introduce Ra_c. Hence, the amplitude grows slowly over an $O(1/\epsilon^2)$ timescale. The aim of the following subsection is to derive a model for the slow spatial and temporal behavior of this amplitude.

We begin with the fully nonlinear vorticity and temperature equations:

$$\frac{1}{\sigma}\left[\partial_t \nabla^2 \psi + J(\psi, \nabla^2 \psi)\right] = Ra\,\partial_x \theta + \nabla^4 \psi, \tag{23}$$

$$(\partial_t - \nabla^2)\theta = \partial_x \psi - J(\psi, \theta), \tag{24}$$

on $D = \{(x, z) | x \in \mathbb{R}, 0 \le z \le 1\}$ with stress-free and fixed-temperature boundary conditions:

$$\psi = 0 \text{ and } \theta = 0 \text{ on } \partial D. \tag{25}$$

Taking $(\partial_t - \nabla^2)$(Eqn. 23)$+Ra\partial_x$(Eqn. 24) yields an equation for ψ with θ eliminated from all linear terms:

$$L\psi = N(\psi, \theta), \tag{26}$$

where

$$L = \left(\partial_t - \nabla^2\right)\left(\frac{1}{\sigma}\partial_t - \nabla^2\right)\nabla^2 - Ra\partial_x^2, \tag{27}$$

and

$$N(\psi,\theta) = -Ra\partial_x J(\psi,\theta) - \frac{1}{\sigma}(\partial_t - \nabla^2)J(\psi,\nabla^2\psi). \tag{28}$$

3.1 Multiscale asymptotic approach

The existence of fast and slow scales motivates a multiscale asymptotic approach. We introduce a slow time variable $\tau = \epsilon^2 t$ and slow spatial variable $X = \epsilon x$, such that the solution shows $O(1)$ growth and spatial modulation when $\tau = O(1)$ and $X = O(1)$, respectively. The fields are transformed as $\psi \to \psi(x, X, z, \tau)$, $\theta \to \theta(x, X, z, \tau)$, and the derivative operators as $\partial_t \to \partial_t + \epsilon^2\partial_\tau$, $\partial_x \to \partial_x + \epsilon\partial_X$.

After making these transformations, we will use the asymptotic expansions

$$\psi(x,X,z,\tau) = \epsilon\psi_1(x,X,z,\tau) + \epsilon^2\psi_2(x,X,z,\tau) + O(\epsilon^3), \tag{29a}$$

$$\theta(x,X,z,\tau) = \epsilon\theta_1(x,X,z,\tau) + \epsilon^2\theta_2(x,X,z,\tau) + O(\epsilon^3), \tag{29b}$$

$$Ra = Ra_c + \epsilon R_1 + \epsilon^2 R_2 + O(\epsilon^3), \tag{29c}$$

in Eq. (26) together with Eq. (24). Each equation is treated with following general procedure:

1. Divide Eq. (26) by ϵ and take the limit $\epsilon \to 0$.
2. Group linear terms of the resulting equation. If the system is inhomogeneous, determine the "solvability condition" on the forcing term and solve the resulting equation.
3. To proceed to the next order in ϵ, divide the terms that remain in the full equation by ϵ and return to Step 1.

Step 2 requires the following mathematical machinery from the study of inhomogeneous linear bounary value problems:

Definition 1 (Adjoint) *Let A and B be vector spaces with inner products $\langle\cdot,\cdot\rangle$ and $\langle\!\langle\cdot,\cdot\rangle\!\rangle$, respectively. Given a linear differential operator $L : A \to B$, its adjoint $L^\dagger : B \to A$, is the unique linear operator for which*

$$\langle\!\langle La, b\rangle\!\rangle = \langle a, L^\dagger b\rangle \quad \forall\ a \in A, b \in B. \tag{30}$$

Example 1 *Consider a linear operator $L_0 = \nabla^6 - Ra_c\partial_x^2$ that maps between spaces A, B of differentiable, square-integrable, real-valued functions with inner product*

$$\langle a, \tilde{a}\rangle = \int_0^1 \int_{-\pi/k_c}^{\pi/k_c} a(x,z)\tilde{a}(x,z)\mathrm{d}x\mathrm{d}z, \tag{31}$$

defined on the domain $D = \{(x,z)| -\pi/k_c \le x \le \pi/k_c, 0 \le z \le 1\}$. Suppose that all $a \in A$, $b \in B$ are $2\pi/k_c$-periodic in x and obey the following boundary conditions in z:

$$a = b = 0 \quad at \quad z = 0, 1, \tag{32a}$$

$$\nabla^2 a = \nabla^2 b = 0 \quad at \quad z = 0, 1, \tag{32b}$$

$$\nabla^4 a = \nabla^4 b = 0 \quad at \quad z = 0, 1. \tag{32c}$$

Given these boundary conditions, we can show that L_0 is self-adjoint, that is

$$L_0 = L_0^\dagger \Leftrightarrow \langle L_0 a, b\rangle = \langle a, L_0 b\rangle \quad \forall\ a \in A, b \in B. \tag{33}$$

Beginning with the left hand side,

$$\langle L_0 a, b\rangle = \iint_D (b\nabla^6 a - Ra_c b\partial_x^2 a)\mathrm{d}x\mathrm{d}z. \tag{34}$$

Using the chain rule in reverse, we may write

$$b\nabla^6 a = \boldsymbol{\nabla}\cdot\boldsymbol{S}(a,b) + a\nabla^6 b, \tag{35}$$

where

$$\boldsymbol{S}(a,b) = \boldsymbol{\nabla}(\nabla^4 a)b - (\nabla^4 a)\boldsymbol{\nabla}b + \boldsymbol{\nabla}(\nabla^2 a)\nabla^2 b - \nabla^2 a\boldsymbol{\nabla}(\nabla^2 b) + (\boldsymbol{\nabla}a)\nabla^4 b - a\boldsymbol{\nabla}(\nabla^4 b) \tag{36}$$

and similarly

$$b\partial_x^2 a = \partial_x(b\partial_x a - a\partial_x b) + a\partial_x^2 b. \tag{37}$$

Substituting the identities above into (34) and using the divergence theorem yields

$$\langle L_0 a, b\rangle = (b\partial_x a - a\partial_x b + \boldsymbol{e}_x\cdot\boldsymbol{S})\Big|_{x=-\pi/k_c}^{x=\pi/k_c} + (\boldsymbol{e}_z\cdot\boldsymbol{S})\Big|_{z=0}^{z=1} + \iint_D (a\nabla^6 b - Ra_c a\partial_x^2 b)\mathrm{d}x\mathrm{d}z. \tag{38}$$

The first term above vanishes given the periodicity of a, b in x. The second term vanishes using the boundary conditions in z. Thus,

$$\begin{aligned}\langle L_0 a, b\rangle &= \iint_D (a\nabla^6 b - Ra_c a\partial_x^2 b)\mathrm{d}x\mathrm{d}z \\ &= \langle a, L_0 b\rangle.\end{aligned} \tag{39}$$

Theorem 1 (Fredholm Alternative Theorem) *Given the inhomogeneous linear system $La = f$, the necessary condition for the existence of a solution a is that*

$$\langle b, f\rangle = 0 \quad \forall\ b\ s.t.\ L^\dagger b = 0 \tag{40}$$

(where a and b obey the same boundary conditions that guarantee $\langle\!\langle L^\dagger b, a\rangle\!\rangle = \langle b, La\rangle$). This statement is a "solvability condition" on f. Note that if $b = 0$ is the only solution to the adjoint problem $L^\dagger b = 0$, then the solvability condition is satisfied for any f.

Proof: Using $La = f$, the definition of the adjoint $L^\dagger$, and the requirement that $L^\dagger b = 0$,

$$\begin{aligned}\langle b, f\rangle &= \langle b, La\rangle \\ &= \langle\!\langle L^\dagger b, a\rangle\!\rangle \\ &= \langle\!\langle 0, a\rangle\!\rangle \\ &= 0.\end{aligned}$$

Remark: If the dimension of the nullspace of $L^\dagger$ is $n > 1$, then $L^\dagger b = 0$ has $n > 1$ linearly independent solutions. In this case there are $n > 1$ solvability conditions.

Our final preparatory step before expanding the full equations is to transform and expand the linear operator L and collect powers of ϵ, which shall enable notational brevity in the subsequent steps:

$$L = L_0 + \epsilon L_1 + \epsilon^2 L_2 + O(\epsilon^3), \tag{41}$$

where

$$L_0 = \nabla^6 - Ra_c\partial_x^2, \tag{42a}$$

$$L_1 = 2(3\nabla^4 - Ra_c)\partial_x\partial_X - R_1\partial_x^2, \tag{42b}$$

$$L_2 = -R_2\partial_x^2 - 2R_1\partial_x\partial_X - Ra_c\partial_X^2 - \left(1 + \frac{1}{\sigma}\right)\partial_\tau\nabla^4 + 3\nabla^4\partial_X^2 + 3\nabla^2\left(2\partial_x\partial_X\right)^2. \tag{42c}$$

We now substitute the asymptotic expansions (29) into (26) together with (24) and follow the steps outlined above.

At $O(\epsilon)$:

$$L_0\psi_1 = 0, \tag{43a}$$

$$\nabla^2\theta_1 = -\partial_x\psi_1. \tag{43b}$$

We make the ansatz

$$\psi_1(x, X, z, \tau) = A_1(X, \tau)e^{ikx}\sin lz + A_1^*(X, \tau)e^{-ikx}\sin lz, \tag{44a}$$

$$\theta_1(x, X, z, \tau) = B_1(X, \tau)e^{ikx}\sin lz + B_1^*(X, \tau)e^{-ikx}\sin lz. \tag{44b}$$

Then (43a) yields the same linear dispersion relation (19) found earlier, and we set $k = k_c = \pi/\sqrt{2}$, $l_c = \pi$, corresponding to the most unstable linear mode. The temperature equation (43b) yields the following relationship between $A_1(X, \tau)$ and $B_1(X, \tau)$:

$$B_1(X, \tau) = \frac{ik_c}{k_c^2 + l_c^2}A_1(X, \tau). \tag{45}$$

Determining $A_1(X, \tau)$ requires going to higher order in ϵ.

At $O(\epsilon^2)$:

$$\begin{aligned} L_0\psi_2 + L_1\psi_1 &= -Ra_c\partial_x J(\psi_1, \theta_1) + \frac{1}{\sigma}\nabla^2 J(\psi_1, \nabla^2\psi_1) \\ &= -Ra_c\partial_x(\partial_x\psi_1\partial_z\theta_1 - \partial_x\theta_1\partial_z\psi_1) \\ &\quad + \frac{1}{\sigma}\nabla^2\left(\partial_x\psi_1\partial_z\nabla^2\psi_1 - \partial_z\psi_1\partial_x\nabla^2\psi_1\right), \end{aligned} \tag{46a}$$

$$\begin{aligned} -\nabla^2\theta_2 - 2\partial_x\partial_X\theta_1 &= \partial_x\psi_2 + \partial_X\psi_1 - J(\psi_1, \theta_1) \\ &= \partial_x\psi_2 + \partial_X\psi_1 - (\partial_x\psi_1\partial_z\theta_1 - \partial_x\theta_1\partial_z\psi_1). \end{aligned} \tag{46b}$$

The equation for the streamfunction (46a) may be rewritten as an inhomogeneous linear equation for ψ_2 forced by nonlinearities in lower order terms:

$$L_0\psi_2 = f_2(\psi_1, \theta_1), \tag{47}$$

where

$$f_2(\psi_1, \theta_1) = -L_1\psi_1 - Ra_c\partial_x J(\psi_1, \theta_1) + \frac{1}{\sigma}\nabla^2 J(\psi_1, \nabla^2\psi_1). \tag{48}$$

At this point we refer to the Fredholm Alternative Theorem, which states that an inhomogeneous linear system $Lu = f$ with homogeneous BCs cannot have a unique solution if the adjoint homogeneous problem, $\mathcal{L}^\dagger v = 0$, has a solution other than $v = 0$. If $v \neq 0$ exists, the original inhomogeneous problem only has solutions only if $\langle v, f\rangle = 0$. Since the operator L_0 is self-adjoint (see Example 1), and we know that $L_0 v = 0$ has a nontrivial solution ψ_1, the Fredholm Alternative Theorem requires that

$$\langle v, f_2(\psi_1, \theta_1)\rangle = 0, \tag{49}$$

where v is any eigenfunction of L_0.

Before evaluating this inner product, we substitute in the ansatz (44) for ψ_1 and θ_1 (with $k = k_c$, $l_c = \pi$) into f_2. Since both Jacobians vanish and moreover $3(k_c^2 + \pi^2)^2 - Ra_c = 0$ the expression for f_2 reduces to

$$f_2 = -e^{ik_c x}k_c^2 \sin\pi z R_1 A_1(X,\tau) - e^{-ik_c x}k_c^2 \sin\pi z R_1 A_1^*(X,\tau). \tag{50}$$

The solvability condition (49) is satisfied automatically for all eigenfunctions of L_0 save for $v = e^{\pm ik_c x}\sin\pi z$. Both choices yield

$$R_1 A_1(X,\tau) = 0. \tag{51}$$

Thus, $R_1 = 0$ must hold to permit nontrivial solutions at $O(\epsilon^2)$ and the streamfunction equation at $O(\epsilon^2)$ is simply

$$L_0\psi_2 = 0, \tag{52}$$

which has the same solutions as the $O(\epsilon)$ equation (43a). Therefore, we may set $\psi_2 = 0$ without loss of generality.

Next, we substitute the $O(\epsilon)$ ansatz (44) into the $O(\epsilon^2)$ temperature equation (46b), setting $\psi_2 = 0$:

$$\begin{aligned}\nabla^2\theta_2 = -\sin\pi z\left[e^{ik_c x}\partial_X\left(A_1 + 2ik_c B_1\right) + e^{-ik_c x}\partial_X\left(A_1^* - 2ik_c B_1^*\right)\right] \\ - i\pi k_c \sin 2\pi z(A_1^* B_1 - A_1 B_1^*).\end{aligned} \tag{53}$$

We can simplify this further using the relationship (45) between B_1 and A_1 we found at $O(\epsilon)$:

$$\nabla^2\theta_2 = \left(\frac{k_c^2 - \pi^2}{k_c^2 + \pi^2}\right)\left(\partial_X A_1 e^{ik_c x} - \partial_X A_1^* e^{-ik_c x}\right)\sin\pi z + 2\pi\left(\frac{k_c^2}{k_c^2 + \pi^2}\right)|A_1|^2 \sin 2\pi z. \tag{54}$$

This is a linear inhomogeneous problem, and our procedure tells us to look for a solvability condition that provides a useful constraint on A_1. However, since the only solution of the

adjoint homogeneous problem $\nabla^2 v = 0$ with the prescribed boundary conditions is $v = 0$, the Fredholm Alternative does not constrain the right hand side of (54). We can thus solve (54) to obtain

$$\theta_2 = \frac{\pi^2 - k_c^2}{(\pi^2 + k_c^2)^2}\left(\partial_X A_1 e^{ik_c x} - \partial_X A_1^* e^{-ik_c x}\right)\sin \pi z - \frac{1}{2\pi}\left(\frac{k_c^2}{\pi^2 + k_c^2}\right)|A_1|^2 \sin 2\pi z, \tag{55}$$

but we still have not determined the slow-scale behavior of the amplitude $A_1(X, \tau)$. To do so, we must proceed to the next order in ϵ.

At $O(\epsilon^3)$:

$$\begin{aligned} L_0\psi_3 + L_2\psi_1 =& - Ra_c\partial_x\left[J(\psi_1, \theta_2) + J_X(\psi_1, \theta_1)\right] - Ra_c\partial_X J(\psi_1, \theta_1) \\ &+ \frac{1}{\sigma}\nabla^2\left[J_X(\psi_1, \nabla^2\psi_1) + J(\psi_1, 2\partial_x\partial_X\psi_1)\right] + \frac{2}{\sigma}\partial_x\partial_X J(\psi_1, \nabla^2\psi_1) \\ =& - Ra_c\partial_x\left(\partial_x\psi_1\partial_z\theta_2 + \partial_X\psi_1\partial_z\theta_1 - \partial_x\theta_2\partial_z\psi_1 - \partial_X\theta_1\partial_z\psi_1\right) \\ &+ \frac{1}{\sigma}\nabla^2\left(\partial_x\psi_1 2\partial_z\partial_x\partial_X\psi_1 + \partial_X\psi_1\partial_z\nabla^2\psi_1 - \partial_z\psi_1\partial_X\nabla^2\psi_1 - \partial_z\psi_1 2\partial_x^2\partial_X\psi_1\right) \\ &+ \frac{2}{\sigma}\partial_x\partial_X\left(\partial_x\psi_1\partial_z\nabla^2\psi_1 - \partial_x\nabla^2\psi_1\partial_z\psi_1\right) - Ra_c\partial_X\left(\partial_x\psi_1\partial_z\theta_1 - \partial_x\theta_1\partial_z\psi_1\right), \end{aligned} \tag{56}$$

where we have used $\psi_2 = 0$, $R_1 = 0$, and where $J_X(f, g) = \partial_X f\partial_z g - \partial_z f\partial_X g$. Rearranging shows that (56) is an inhomogeneous linear equation for ψ_3 forced by nonlinearities in lower order terms:

$$L_0\psi_3 = f_3(\psi_1, \theta_1, \theta_2), \tag{57}$$

where

$$\begin{aligned} f_3(\psi_1, \theta_1, \theta_2) =& -L_2\psi_1 - Ra_c\partial_x\left[J(\psi_1, \theta_2) + J_X(\psi_1, \theta_1)\right] - Ra_c\partial_X J(\psi_1, \theta_1) \\ &+ \frac{1}{\sigma}\nabla^2\left[J_X(\psi_1, \nabla^2\psi_1) + J(\psi_1, 2\partial_x\partial_X\psi_1)\right] + \frac{2}{\sigma}\partial_x\partial_X J(\psi_1, \nabla^2\psi_1). \end{aligned} \tag{58}$$

As before, we refer to the Fredholm Alternative Theorem, which requires that

$$\langle v, f_3(\psi_1, \theta_1, \theta_2)\rangle = 0, \tag{59}$$

where v is any eigenfunction $v = e^{\pm ik_c x}\sin \pi z$ of L_0.

Before evaluating this inner product, we substitute the solutions from (44), (55) for ψ_1, θ_1, θ_2 (with $k = k_c$, $l_c = \pi$) into f_3, which yields a "resonant" term (i.e., an eigenfunction of

L_0), its complex conjugate, and "non-resonant" terms:

$$f_3 = e^{ik_c x}\sin\pi z\Big\{ -k_c^2 R_2 A_1 - \frac{k_c^4 Ra_c A_1^2 A_1^* \cos 2\pi z}{k_c^2+\pi^2} + \left(k_c^2+\pi^2\right)^2\left(\frac{1+\sigma}{\sigma}\right)\partial_\tau A_1 \\ + \left[Ra_c - 3\left(k_c^2+\pi^2\right)\left(5k_c^2+\pi^2\right)\right]\partial_X^2 A_1 + 2ik_c R_1 \partial_X A_1\Big\} \\ + e^{-ik_c x}\sin\pi z\Big\{ -k_c^2 R_2 A_1^* - \frac{k_c^4 Ra_c A_1 A_1^{*2} \cos 2\pi z}{k_c^2+\pi^2} + \left(k_c^2+\pi^2\right)^2\left(\frac{1+\sigma}{\sigma}\right)\partial_\tau A_1^* \\ + \left[Ra_c - 3\left(k_c^2+\pi^2\right)\left(5k_c^2+\pi^2\right)\right]\partial_X^2 A_1^* - 2ik_c R_1 \partial_X A_1^*\Big\} \\ - 4\pi k_c^2 \sin\pi z\cos\pi z\left(\frac{Ra_c}{k_c^2+\pi^2}+\frac{4\pi^2}{\sigma}\right)\left(A_1^*\partial_X A_1 + A_1\partial_X A_1^*\right). \tag{60}$$

As before, the solvability condition (59) is satisfied automatically for all eigenfunctions of L_0 save for $v = e^{\pm ik_c x}\sin\pi z$. In both cases evaluating the inner product in (59) yields

$$\left(1+\frac{1}{\sigma}\right)\partial_\tau A_1 = \frac{2R_2}{9\pi^2}A_1 - \frac{\pi^2}{4}|A_1|^2 A_1 + 4\partial_X^2 A_1, \tag{61}$$

where we have used $Ra_c = 27\pi^4/4$, $k_c = \pi/\sqrt{2}$.

Thus, we have obtained a one-dimensional partial differential equation for the amplitude A_1 from the solvability condition (not from the expanded $O(\epsilon^3)$ equations themselves, as one might expect). We may simplify (61) by making the change of variables

$$A_1(X,\tau) = \frac{2\sqrt{2}}{3\pi^2}A(\hat{X},\hat{\tau}), \quad X = 3\sqrt{2}\hat{X}, \quad \tau = \left(\frac{\sigma+1}{\sigma}\right)\frac{9\pi^2}{2}\hat{\tau}, \tag{62}$$

yielding

$$\partial_{\hat{\tau}} A = R_2 A - |A|^2 A + \partial_{\hat{X}}^2 A. \tag{63}$$

Recall that $Ra = Ra_c + \epsilon R_1 + \epsilon^2 R_2 + O(\epsilon^3) = Ra_c + \epsilon^2 R_2 + O(\epsilon^3)$ since we found that $R_1 = 0$. We may choose $\epsilon^2 = Ra - Ra_c$ such that $R_2 = 1$ to get the real Ginzburg-Landau equation (RGLE) [1]

$$\partial_{\hat{\tau}} A = A - |A|^2 A + \partial_{\hat{X}}^2 A, \tag{64}$$

first derived in the context of convection in [2].

3.2 Properties of the real Ginzburg-Landau Equation (RGLE)

3.2.1 Symmetries

The RGLE is invariant under the transformations:

a. $A \longrightarrow Ae^{i\theta}$, θ = constant

b. $A \longrightarrow A^*$

Since $\psi_1(x,X,\tau) = \left[A_1(X,\tau)e^{ik_c x} + A_1^*(X,\tau)e^{-ik_c x}\right]\sin\pi z$, the phase changes (a) are generated by translations $x \longrightarrow x + \theta/k_c$ and the reflections (b) are generated by reflections $x \longrightarrow -x$.

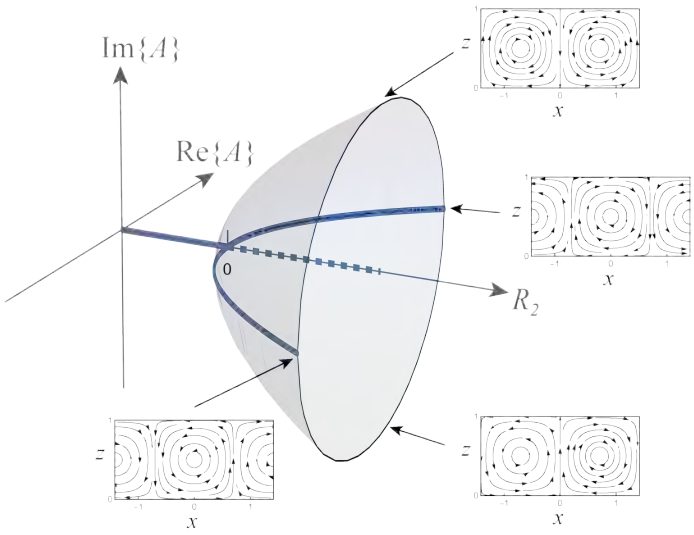

Figure 4: The fixed points of A in the complex plane as R_2 is varied. Solid and dashed lines indicate stable and unstable fixed points, respectively. Inset plots show solution streamlines corresponding to points on the stable surface.

3.2.2 Spatially uniform solutions

For solutions that are uniform over long spatial scales (i.e., $\partial_{\hat{X}} A = 0$),

$$\partial_{\hat{\tau}} A = R_2 A - |A|^2 A, \tag{65}$$

which has fixed points ($\partial_{\hat{\tau}} A = 0$) at

$$A = 0,\ |A| = \sqrt{R_2} \text{ for } R_2 > 0. \tag{66}$$

If $R_2 < 0$ (i.e., $Ra < Ra_c$),

$$\partial_{\hat{\tau}} |A| < 0.$$

If $R_2 > 0$ (i.e., $Ra > Ra_c$),

$$\partial_{\hat{\tau}} |A| > 0 \quad \text{if} \quad |A| < \sqrt{R_2},$$
$$\partial_{\hat{\tau}} |A| < 0 \quad \text{if} \quad |A| > \sqrt{R_2}.$$

Thus, the amplitude undergoes a supercritical pitchfork bifurcation at $R_2 = 0$, beyond which the fixed point $A = 0$ is no longer stable and the solution evolves towards the surface $|A| = \sqrt{R_2}$. The latter is a circle in the complex plane, which exhibits the symmetries (a, b) discussed earlier. Physically, this means that all reflections and translations of the convection rolls along the horizontal direction are possible in a domain with infinite horizontal extent. Figure 4 shows the bifurcation as a "pitchfork of revolution" in the complex plane.

References

[1] V. Ginzburg and L. Landau, *On the theory of superconductivity*, Zhurnal Éksperimental'noĭ i Teoreticheskoĭ Fiziki, 20 (1950), pp. 1064–1082.

[2] A. C. Newell and J. A. Whitehead, *Finite bandwidth, finite amplitude convection*, Journal of Fluid Mechanics, 38 (1969), pp. 279–303.

[3] L. Rayleigh, *On convection currents in a horizontal layer of fluid, when the higher temperature is on the under side*, The London, Edinburgh, and Dublin Philosophical Magazine and Journal of Science, 32 (1916), pp. 529–546.

GFD 2024 Lecture 2: Nonlinear Theory for Convective Instabilities

Edgar Knobloch; notes by Cécile Le Dizes and Vincent Laroche

June 18, 2024

1 Introduction

In Rayleigh–Bénard convection, a horizontal fluid layer of depth h is heated from below and cooled from above, typically under the Boussinesq approximation with fixed temperatures at the plates and either stress-free or no-slip velocity boundary conditions. In this system, the fluid is gravitationally unstable, but not necessarily convectively unstable, as convective motions are slowed by viscous effects and temperature gradients are smoothed by thermal diffusion. The competition between buoyancy and dissipation is quantified by the Rayleigh number

$$Ra = \frac{g\alpha\Delta T h^3}{\nu\kappa}, \tag{1}$$

where ΔT is the difference in temperature between the bottom and top surfaces, h is the layer thickness, α is the thermal expansion coefficient, ν is the fluid kinematic viscosity and κ is the fluid thermal diffusivity.

The study of the linear stability of this system predicts the critical threshold Ra_c above which the conduction state loses stability and convective motions set in, selecting a critical horizontal wavenumber k_c. Linear stability analysis is essential for identifying these thresholds, as well as growth rates, and mode shapes. But it cannot say anything about the amplitude of the motion once the instability develops, nor about how different modes interact. In the study of nonlinear systems, multi-scale analysis plays a central role because it allows us to go beyond the strictly linear regime and obtain a description of how instabilities evolve once they are triggered. Once the threshold is crossed, the amplitudes of the unstable modes grow and nonlinear interactions become unavoidable. The nonlinear terms tend to generate slow modulation of the fast oscillations identified by linear theory, or to couple spatially extended modes through harmonics and resonances.

In this lecture, we study the nonlinear regime and derive amplitude equations for convective oscillatory instabilities that arise when the linear problem yields an oscillatory Hopf bifurcation, such as convection in binary-fluid mixture [5] or under rotation [3]. In these cases, the instability takes the form of oscillating waves, either traveling or standing. We present here two methods to analyse the nonlinear regime in such situations, a multiscale expansion valid for small amplitude motions and an asymptotic analysis valid in the strongly nonlinear regime. In the first part, we assume small nonlinearities and we derive a weakly nonlinear theory for oscillatory instabilities by introducing an intrinsic small parameter ϵ.

This procedure leads to the derivation of amplitude equations, such as the Stuart–Landau or complex Ginzburg–Landau equations, that describe how the envelope of the oscillations evolves with time and space. The second example focuses on fully nonlinear oscillatory convection under strong rotation, where the leading order nonlinearity is of a different nature. Instead of weak envelope modulations, the dominant nonlinear effect is the distortion of the horizontally averaged temperature profile, which feeds back on the convective modes themselves. In this case, the multi-scale procedure leads not to a simple amplitude equation but to a nonlinear eigenvalue problem for the vertical structure of the solution. Traveling and standing waves again emerge, but their existence and properties are controlled by the interplay between rotation and the modified thermal profile rather than by weak nonlinear saturation.

2 Weakly Nonlinear Theory for Wave Instabilities

In this section, we consider a general two-dimensional problem in an unbounded horizontal layer of fluid of height $h = 1$, such as binary-fluid convection [5]. We study the nonlinear evolution of small disturbances near a Hopf bifurcation. At the onset, the system becomes unstable at a critical wavenumber k_c with a nonzero oscillation frequency ω_c. The previous lecture focused on the derivation of amplitude equations (real Ginzburg–Landau) for unstable non-oscillatory modes. Here, we focus on oscillatory instabilities and derive the complex Ginzburg–Landau equations.

2.1 Oscillatory instability without modulation in space

First, we derive the amplitude equations *without* amplitude modulation in space. We look for a constant-amplitude, spatially periodic superposition of left- and right-traveling waves,

$$w(x,z,t) = \Big[\big(A(t)+B(t)\big)e^{ik_c x} + \big(A^*(t)+B^*(t)\big)e^{-ik_c x}\Big] f(z)\,, \tag{2}$$

where w is, for example, the vertical velocity. The function $f(z)$ encodes the vertical structure of the critical mode and may be complex [7]. Here we take $f(z) = \sin(\pi z)$, but the exact form depends on the field being considered. The complex amplitudes A and B represent left and right traveling waves; A^* and B^* denote the complex conjugates.

At the instability threshold k_c, the complex amplitudes satisfy

$$\begin{pmatrix} \dot{A} \\ \dot{B} \end{pmatrix} = \begin{pmatrix} i\omega_c & 0 \\ 0 & -i\omega_c \end{pmatrix} \begin{pmatrix} A \\ B \end{pmatrix}, \tag{3}$$

where the dot operator $\dot{(\,)}$ represents a time derivative. The two carriers then oscillate at $\pm\omega_c$. Moving away from threshold introduces a small real contribution. We parametrize the distance from onset by $\lambda \propto R - R_c$ (with R a control parameter such as the Rayleigh number). The oscillation frequency near onset is given by $\omega = \omega_c + \mathcal{O}(\lambda)$.

The evolution must respect two symmetries. First, the system is translation-invariant since there are no sidewalls and the effect of $x \to x + \frac{\phi_0}{k_c}$ is captured by $(A,B) \to e^{i\phi_0}(A,B)$. Second, the system has reflection symmetry and the effect of $x \to -x$ is captured by

$(A, B) \to (B^*, A^*)$. The most general smooth equivariant vector field at $\lambda = 0$ is then of the form

$$\begin{pmatrix} \dot{A} \\ \dot{B} \end{pmatrix} = \begin{pmatrix} g_1 & g_2 \\ g_2^* & g_1^* \end{pmatrix} \begin{pmatrix} A \\ B \end{pmatrix}, \tag{4}$$

where g_1, g_2 depend only on the invariants $\sigma_1 = |A|^2 + |B|^2$, $\sigma_2 = AB^*$, $\sigma_3 = A^*B$.

Expanding g_1, g_2 in these invariants and using a suitable near-identity nonlinear equivariant coordinate change of the form

$$\begin{pmatrix} \tilde{A} \\ \tilde{B} \end{pmatrix} = \begin{pmatrix} A \\ B \end{pmatrix} + \begin{pmatrix} h_1 & h_2 \\ h_2^* & h_1^* \end{pmatrix} \begin{pmatrix} A \\ B \end{pmatrix}$$

allows us to recast these equations in a simpler form (the *normal form*) that reflects time-translation invariance on time-periodic orbits, viz. invariance under $(\tilde{A}, \tilde{B}) \to (e^{i\phi_1}\tilde{A}, e^{-i\phi_1}\tilde{B})$:

$$\begin{pmatrix} \tilde{A} \\ \tilde{B} \end{pmatrix} = \begin{pmatrix} f(|\tilde{B}|^2, |\tilde{A}|^2 + |\tilde{B}|^2) & 0 \\ 0 & f^*(|\tilde{A}|^2, |\tilde{A}|^2 + |\tilde{B}|^2) \end{pmatrix} \begin{pmatrix} \tilde{A} \\ \tilde{B} \end{pmatrix}. \tag{5}$$

Dropping the tildes, and unfolding the bifurcation by incorporating the small parameter λ, leads to the (truncated) equations

$$\dot{A} = (\lambda + i\omega)A + \left[a|B|^2 + b\left(|A|^2 + |B|^2\right)\right] A, \tag{6}$$

$$\dot{B} = (\lambda - i\omega)B + \left[a^*|A|^2 + b^*\left(|A|^2 + |B|^2\right)\right] B, \tag{7}$$

where $\omega = \omega_c + \mathcal{O}(\lambda)$ and a, b are constant coefficients that can be determined from the equations of motion. These are the amplitude equations in normal form to third order in amplitude.

Writing $A = x_1 e^{i\phi_1}$, $B = x_2 e^{i\phi_2}$ gives

$$\dot{x}_1 = x_1\left[\lambda + a_r x_2^2 + b_r\left(x_1^2 + x_2^2\right)\right] \tag{8}$$

$$\dot{x}_2 = x_2\left[\lambda + a_r x_1^2 + b_r\left(x_1^2 + x_2^2\right)\right] \tag{9}$$

$$\dot{\phi}_1 = \quad \omega + a_i x_2^2 + b_i\left(x_1^2 + x_2^2\right) \tag{10}$$

$$\dot{\phi}_2 = -\omega - a_i x_1^2 - b_i\left(x_1^2 + x_2^2\right), \tag{11}$$

where subscripts r, i denote the real and imaginary parts, respectively. These equations yield four solutions of the form (x_1, x_2): the trivial solution $(0, 0)$, the left-traveling wave $(x, 0)$, the right-traveling wave $(0, x)$, and the standing wave (x, x). The amplitude of these solutions as a function of the bifurcation parameter λ, and their stability properties are summarized in Table 1.

Using the relations in the table, we can construct bifurcation diagrams in the parameter space of a_r and b_r, which are shown in Fig. 1. This figure also describes the competition between traveling and standing waves at small amplitude. Note that at most one nonlinear solution is stable near onset.

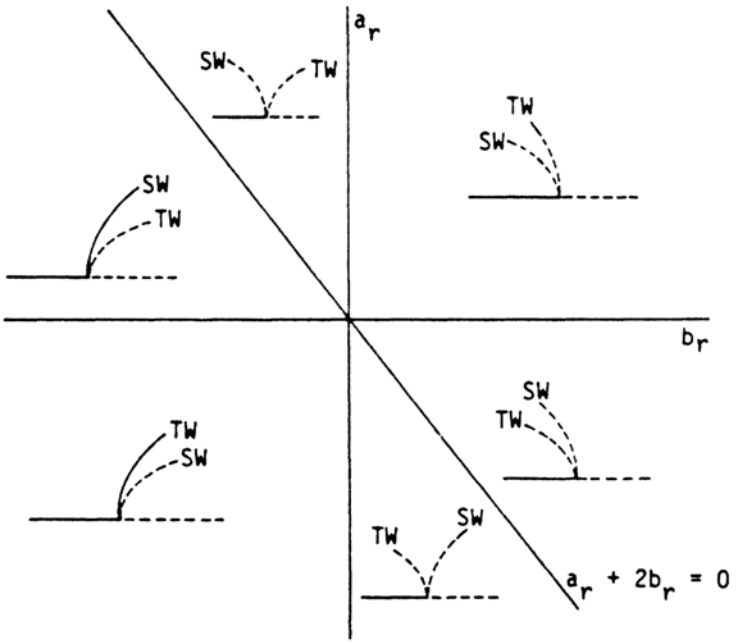

Figure 1: Bifurcations in the a_r-b_r parameter space showing the amplitude $x_1^2 + x_2^2$ as function of λ for standing waves (SW) and traveling waves (TW) [5]. Continuous lines are stable solutions, while dashed lines denote unstable solutions.

Solution	Equation	Eigenvalues	Name
$(0,0)$	$\sim$	λ, λ	trivial
$(x,0)$	$\lambda + b_r x^2 = 0$	$-2\lambda, -\lambda a_r/b_r$	LTW
$(0,x)$	$\lambda + b_r x^2 = 0$	$-2\lambda, -\lambda a_r/b_r$	RTW
(x,x)	$\lambda + (a_r + 2b_r)\, x^2 = 0$	$-2\lambda, -\lambda a_r/(a_r/2 + b_r)$	SW

Table 1: Solution branches.

2.2 Oscillatory instability with modulation in space

We now allow slow spatial modulation of the complex amplitudes. Consider a generic system

$$\mathcal{L}\left(\frac{\partial}{\partial t}, \frac{\partial}{\partial x}, \varepsilon^2\right)\psi = N[\psi]\,,$$

with linear operator $\mathcal{L}$ and nonlinearity N. We introduce the fast, slow and superslow scales

$$x, \quad t, \qquad X_1 = \varepsilon x, \quad T_1 = \varepsilon t, \qquad X_2 = \varepsilon^2 x, \quad T_2 = \varepsilon^2 t, \tag{12}$$

where the slow scales X_1 and T_1 are required to represent advection at the group velocity c_g, and the even slower scales X_2 and T_2 are required by diffusion. We seek a solution of the form

$$\psi(x,t,\varepsilon) = \varepsilon\psi_1 + \varepsilon^2\psi_2 + \mathcal{O}\left(\varepsilon^3\right), \tag{13}$$

where $\psi_j \equiv \psi_j(t, T_1, T_2, x, X_1, X_2)$ is a function of the fast, slow, and superslow scales. Expanding $\mathcal{L}$ about $(\partial_t, \partial_x, 0)$ yields

$$\begin{aligned}\mathcal{L} = \mathcal{L}_0 + \varepsilon\left(\mathcal{L}_1\frac{\partial}{\partial T_1} + \mathcal{L}_2\frac{\partial}{\partial X_1}\right) \\ + \frac{1}{2}\varepsilon^2\left(\mathcal{L}_{11}\frac{\partial^2}{\partial T_1^2} + 2\mathcal{L}_{12}\frac{\partial^2}{\partial T_1 \partial X_1} + \mathcal{L}_{22}\frac{\partial^2}{\partial X_1^2}\right) \\ + \varepsilon^2\left(\mathcal{L}_1\frac{\partial}{\partial T_2} + \mathcal{L}_2\frac{\partial}{\partial X_2} + \mathcal{L}_3\right) + \mathcal{O}\left(\varepsilon^3\right).\end{aligned} \tag{14}$$

At $\mathcal{O}(\varepsilon)$ we recover the linear problem

$$\mathcal{L}_0\left(\frac{\partial}{\partial t}, \frac{\partial}{\partial x}, 0\right)\psi_1 = 0\,. \tag{15}$$

whose plane-wave solutions yield the dispersion relation $\mathcal{L}_0(i\omega, ik, 0) = 0$, i.e., $\omega = \omega(k)$, shown in Fig. 2. The general solution with the critical wavenumber k_c is

$$\psi_1 = A_1(T_1, T_2, X_1, X_2)\, e^{i(k_c x + \omega_c t)} + B_1(T_1, T_2, X_1, X_2)\, e^{i(k_c x - \omega_c t)} + c.c., \tag{16}$$

where A_1 and B_1 are the complex amplitudes of waves propagating to the left and to the right.

At $\mathcal{O}\left(\varepsilon^2\right)$ we obtain

$$\mathcal{L}_0\psi_2 + \left(\mathcal{L}_1\frac{\partial}{\partial T_1} + \mathcal{L}_2\frac{\partial}{\partial X_1}\right)\psi_1 = N\left[\psi_1, \psi_1\right]. \tag{17}$$

The nonlinear quadratic terms on the right force nonresonant mean and second harmonics. The system thus yields the two solvability conditions

$$\left[\mathcal{L}_1\left(i\omega_c, ik_c, 0\right)\frac{\partial}{\partial T_1} + \mathcal{L}_2\left(i\omega_c, ik_c, 0\right)\frac{\partial}{\partial X_1}\right]A_1 = 0 \tag{18}$$

$$\left[\mathcal{L}_1\left(-i\omega_c, ik_c, 0\right)\frac{\partial}{\partial T_1} + \mathcal{L}_2\left(-i\omega_c, ik_c, 0\right)\frac{\partial}{\partial X_1}\right]B_1 = 0 \tag{19}$$

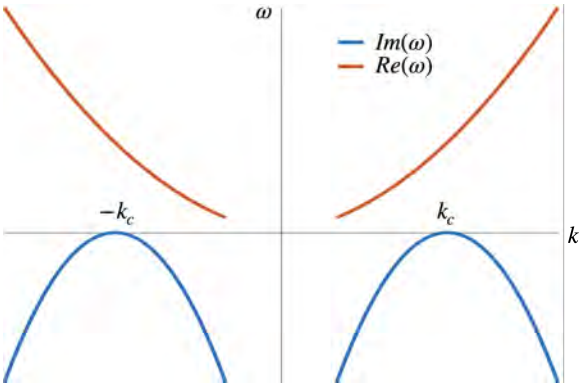

Figure 2: Dispersion relation $\omega = \omega(k)$.

which form a linear hyperbolic system. Differentiating the dispersion relation $\mathcal{L}_0\left(i\omega(k), ik, 0\right) = 0$ with respect to k at $k = k_c$ gives :

$$i\omega'(k_c)\mathcal{L}_1\left(i\omega_c, ik_c, 0\right) + i\mathcal{L}_2\left(i\omega_c, ik_c, 0\right) = 0. \tag{20}$$

As a result, the group velocity can be expressed as :

$$c_g \equiv \omega'(k_c) = -\frac{\mathcal{L}_2\left(i\omega_c, ik_c, 0\right)}{\mathcal{L}_1\left(i\omega_c, ik_c, 0\right)}, \tag{21}$$

and similarly for $-\omega_c$: $c_g = +\mathcal{L}_2\left(-i\omega_c, ik_c, 0\right)/\mathcal{L}_1\left(-i\omega_c, ik_c, 0\right)$,. The solvability conditions thus take the form

$$\partial_{T_1} A_1 - c_g\, \partial_{X_1} A_1 = 0, \tag{22}$$
$$\partial_{T_1} B_1 + c_g\, \partial_{X_1} B_1 = 0, \tag{23}$$

meaning that the envelopes A_1 and B_1 are advected to the right on the T_1 time scale with speeds $\pm c_g$.

Here, there is no saturation at $\mathcal{O}(\epsilon^2)$. This can be resolved by assuming that the group speed is small, $c_g = \mathcal{O}(\epsilon)$, although this can only be achieved by varying a second parameter at the same time as λ. Under this assumption, we obtain at $\mathcal{O}(\epsilon^3)$ the following amplitude equations :

$$\partial_{T_2} A_1 - \frac{c_g}{\epsilon}\partial_{X_1} A_1 = \mu A_1 + a|B_1|^2 A_1 + b\left(|A_1|^2 + |B_1|^2\right) A_1 + \gamma \partial_{X_1}^2 A_1, \tag{24}$$
$$\partial_{T_2} B_1 + \frac{c_g}{\epsilon}\partial_{X_1} B_1 = \mu^* B_1 + a^*|A_1|^2 B_1 + b^*\left(|A_1|^2 + |B_1|^2\right) B_1 + \gamma^* \partial_{X_1}^2 B_1, \tag{25}$$

where $\mu \equiv \lambda + i\omega$, and a, b and γ are complex coefficients. The resulting equations are coupled complex Ginzburg-Landau equations for the envelope functions A_1, B_1. They are local but *nonasymptotic* since when $c_g \neq 0$ at $\lambda = 0$ one cannot take the limit $\epsilon \to 0$: the validity of the equations does not extend all the way to threshold. This fact restricts the applicability of the amplitude equations (24-25).

This problem can be overcome writing the amplitudes A_1, B_1 in the slow co-moving coordinates $X_1^{\pm} = X_1 \pm c_g T_1$ (see [6]). Proceeding to $\mathcal{O}(\varepsilon^3)$ yields evolution equations on the slowest time scale T_2 (we suppress the superscripts on $X_1^{\pm}$ for readability):

$$\partial_{T_2} A_1 - c_g \partial_{X_1^-} A_2 = \mu A_1 + a|B_1|^2 A_1 + b\left(|A_1|^2 + |B_1|^2\right) A_1 + \gamma \partial_{X_1}^2 A_1, \tag{26}$$

$$\partial_{T_2} B_1 + c_g \partial_{X_1^+} B_2 = \mu^* B_1 + a^*|A_1|^2 B_1 + b^*\left(|A_1|^2 + |B_1|^2\right) B_1 + \gamma^* \partial_{X_1}^2 B_1. \tag{27}$$

The solvability conditions for A_2, B_2 are obtained integrating these equations over $X_1^{\pm}$, respectively, which yields asymptotically valid but *nonlocal* evolution equations for the evolution of A_1, B_1 on the superslow time scale T_2 (see equations (13) in [6]).

3 Strongly Nonlinear Rotating Convection

In this section, we consider two-dimensional convection in an unbounded horizontal layer of fluid of height h under strong rotation. At the top and bottom, we consider impermeable ($\boldsymbol{u} \cdot \hat{\boldsymbol{z}} = 0$), stress-free surfaces ($\partial_z u = \partial_z v = 0$) and fixed temperatures ($\theta(z=0) = \theta_0$ and $\theta(z=h) = \theta_1 < \theta_0$). We assume that the fluid is incompressible and that the temperature fluctuations remain small enough to allow the Boussinesq approximation. In addition, rotation is assumed to be antiparallel to gravity, i.e., at the North Pole. The equations governing the problem are then:

$$\boldsymbol{\nabla} \cdot \boldsymbol{u} = 0, \tag{28}$$

$$\boldsymbol{u}_{,t} + (\boldsymbol{u} \cdot \boldsymbol{\nabla})\boldsymbol{u} + 2\boldsymbol{\Omega} \times \boldsymbol{u} = -\frac{1}{\rho_0}\boldsymbol{\nabla} p + \alpha g(\theta - \theta_0)\hat{\boldsymbol{z}} + \nu \nabla^2 \boldsymbol{u}, \tag{29}$$

$$\theta_{,t} + (\boldsymbol{u} \cdot \boldsymbol{\nabla})\theta = \kappa \nabla^2 \theta, \tag{30}$$

where $\boldsymbol{u} = (u, v, w)$ is the velocity vector, θ is the temperature, p is the pressure and $\boldsymbol{\Omega} = \Omega \hat{\boldsymbol{z}}$ is the rotation vector. The constants ν and κ are, respectively, the fluid kinematic viscosity and thermal diffusivity (both in m^2/s), and the constant α is the thermal expansivity. The operator $\boldsymbol{\nabla} = (\partial_x, \partial_y, \partial_z)$ denotes the gradient vector, while commas followed by subscripts denote partial derivatives, e.g., $A_{,t} \equiv \partial A / \partial t$.

Using the streamfunction ψ defined as $(u, w) = (-\partial_z \psi, \partial_x \psi)$ and the following dimensionless quantities

$$\hat{t} = \frac{t\kappa}{h^2} \;;\quad [\hat{x}, \hat{y}, \hat{z}] = \frac{[x, y, z]}{h} \;;\quad \hat{\boldsymbol{u}} = \frac{\boldsymbol{u} h}{\kappa} \;;\quad \hat{\psi} = \frac{\psi}{\kappa} \;;\quad \hat{\theta} = \frac{\theta}{\theta_0 - \theta_1}, \tag{31}$$

we can rewrite the system as follows, dropping the hats for simplicity,

$$\frac{1}{\sigma}[\nabla^2 \psi_t + J(\psi, \nabla^2 \psi)] = R\theta_x - T v_z + \nabla^4 \psi \tag{32}$$

$$\frac{1}{\sigma}[v_t + J(\psi, v)] = T\psi_z + \nabla^2 v \tag{33}$$

$$\theta_t + J(\psi, \theta) = \nabla^2 \theta, \tag{34}$$

where the symbol J is defined by $J(f,g) = f_{,x}Dg - g_{,x}Df$ and $D \equiv \partial_z$. Here σ, R and T are, respectively, the Prandtl number, the Rayleigh number and the square root of the Taylor number, namely,

$$\sigma = \frac{\nu}{\kappa}, \quad R = \frac{g\alpha\Delta T h^3}{\nu\kappa}, \quad T = \frac{2\Omega h^2}{\nu}. \tag{35}$$

The following derivation, as well as most of the figures in this section are taken from [3].

3.1 Linear stability criteria

We analyse the linear stability of the conduction state ($\theta_0(z) = 1 - z, \psi_0 = 0, v_0 = 0$) by adding small perturbations (θ_1, ψ_1, v_1) (see [1]). On substituting in the Boussinesq equations, we can write the following linear equations:

$$\begin{aligned} \frac{1}{\sigma}\nabla^2\psi_{1,t} &= R\theta_{1,x} - Tv_{1,z} + \nabla^4\psi_1 \\ \frac{1}{\sigma}v_{1,t} - \nabla^2 v_1 &= TD\psi_1 \\ \theta_{1,t} + \psi_{1,x}D\theta_0 &= \nabla^2\theta_1 \end{aligned}$$

where $D = \partial_z$.

We look for the onset of instability via a state of purely oscillatory solutions. This means that we look for solutions under the form $f_1(x,t) \sim A(z)\exp(i\Omega t + ik_\perp x)$, with Ω real. With the stress-free and fixed temperature boundary conditions, we can show that for the lowest vertical mode $A(z) = \sin(\pi z)$. We apply the operator $\left(i\frac{\Omega}{\sigma} + k_\perp^2 - D^2\right)\left(i\Omega + k_\perp^2 - D^2\right)$ to the first equation. This leads to :

$$\left(i\Omega + k_\perp^2 + \pi^2\right)\left[\left(i\frac{\Omega}{\sigma} + k_\perp^2 + \pi^2\right)^2\left(k_\perp^2 + \pi^2\right) + \pi^2 T^2\right] = k_\perp^2 R\left(i\frac{\Omega}{\sigma} + k_\perp^2 + \pi^2\right). \tag{36}$$

By separating the real and imaginary parts, we obtain a pair of equations that can be solved for Ω^2:

$$\Omega_0^2 = -\sigma^2\left(k_\perp^2 + \pi^2\right)^2 + \frac{\sigma^2(1-\sigma)}{1+\sigma}\frac{\pi^2}{k_\perp^2 + \pi^2}T^2 \tag{37}$$

and the critical Rayleigh number:

$$R^{(0)} = 2(1+\sigma)\frac{\left(k_\perp^2 + \pi^2\right)^3}{k_\perp^2} + \frac{2\sigma^2}{1+\sigma}\frac{\pi^2}{k_\perp^2}T^2. \tag{38}$$

These equations need to be verified for overstable oscillations to occur with wavenumber $k_\perp$ and a Taylor number of T^2. In particular, for Ω_0 to be real we need to have a Prandtl number $\sigma < 1$. For $\sigma > 1$, overstable oscillations cannot occur, and the conduction state will lose its stability to steady convection.

For $\sigma < 1$ and a given T, overstable oscillations are possible if $k_\perp < k_*$, defined by $\Omega_0^2 = 0$, i.e.,

$$(k_*^2 + \pi^2)^3 = \frac{1-\sigma}{1+\sigma}\pi^2 T^2. \tag{39}$$

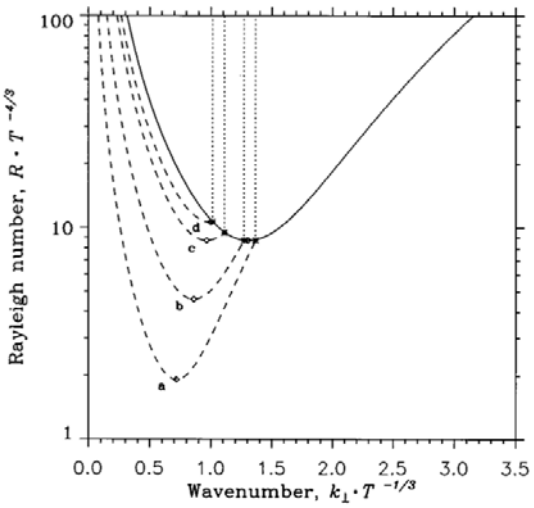

Figure 3: Steady convection (solid line) and overstable oscillations (dashed line) neutral stability curves as a function of the scaled wavenumber $k_\perp.T^{-1/3}$ at (a) $\sigma = 0.2$, (b) $\sigma = 0.4$, (c) $\sigma = \sigma_* \approx 0.677$ and (d) $\sigma = 0.8$. For each σ, nonlinear oscillatory solutions are located between the corresponding dashed and dotted lines.

The marginal stability curves were plotted in Fig. 3. The solid line corresponds to the critical Rayleigh numbers for which steady convection occurs for a given horizontal wavenumber and applies for all Prandtl numbers. The dashed lines are the critical curves for overstable oscillations at different Prandtl numbers ($0 < \sigma < 1$). The two curves intersect at $k_\perp = k_*$, called the Takens-Bogdanov point [2].

Depending on the value of the Prandtl and Taylor numbers, instability will manifest itself as stationary convection or overstable oscillations. For $\sigma \geq \sigma_* \approx 0.677$ (cases c/d), the linear analysis predicts that steady convection destabilizes first, since its critical Rayleigh number is always lower than that for overstable oscillations. This statement applies only at the level of linear onset: nonlinear effects may favor oscillatory states even when the steady mode sets in first, as discussed by [8]. On the other hand, for $\sigma < \sigma_*$ (cases a/b), the linear analysis predicts that instability will manifest itself as overstable oscillations in the limit of large Taylor numbers.

3.2 Asymptotics analysis for the strongly nonlinear problem

In the limit of large Taylor numbers, the critical Rayleigh number is minimised by horizontal wavenumber of scale $k_\perp \propto T^{1/3}$. This leads to :

$$\Omega_0^2 \sim \sigma^2 \left(-k_\perp^4 + \frac{1-\sigma}{1+\sigma}\frac{\pi^2}{k_\perp^2} \right) T^{4/3} \quad \text{and} \quad R^{(0)} = \left(2(1+\sigma)k_\perp^4 + \frac{2\sigma^2}{1+\sigma}\frac{\pi^2}{k_\perp^2} \right) T^{4/3}, \tag{40}$$

where $k_\perp$ now denotes the scaled horizontal wavenumber. Thus, $R^{(0)} \propto T^{4/3}$ and $\Omega_0 \propto T^{2/3}$.

This suggests the scaling :

$$\xi = T^{1/3}x, \quad \tau = T^{2/3}t, \quad R = \hat{R}T^{4/3}, \quad v = \hat{v}T^{1/3}. \tag{41}$$

These scalings are chosen so that in the large Taylor number limit the horizontal scale and frequency of the instability are of order 1 in the new variables. Note that, as a result of the scaling chosen, the velocity $\mathbf{u}$ will be highly anisotropic in the horizontal:

$$\psi(x,z,t) = \psi_0(\xi,z,\tau) + T^{-1/3}\psi_1(\xi,z,\tau) + T^{-2/3}\psi_2(\xi,z,\tau) + ..., \tag{42}$$

$$\hat{v}(x,z,t) = \hat{v}_0(\xi,z,\tau) + T^{-1/3}\hat{v}_1(\xi,z,\tau) + T^{-2/3}\hat{v}_2(\xi,z,\tau) + ..., \tag{43}$$

$$\theta(x,z,t) = \theta_0(\xi,z,\tau) + T^{-1/3}\theta_1(\xi,z,\tau) + T^{-2/3}\theta_2(\xi,z,\tau) + ... \ . \tag{44}$$

The Boussinesq equations (32-34) give at leading orders $\mathcal{O}(T^{5/3})$, $\mathcal{O}(T)$ and $\mathcal{O}(T^{2/3})$, respectively.

$$\theta_{0,\xi} = 0 \quad \Rightarrow \quad \theta_0 = \bar{\theta}_0(z) \tag{45}$$

$$\frac{1}{\sigma} v_{0,\tau} = D\psi_0 + v_{0,\xi\xi}, \tag{46}$$

$$(\partial_\tau - \partial_\xi^2)\theta_0 = 0. \tag{47}$$

At order $\mathcal{O}(T^{4/3})$, equation (32) now gives:

$$\left(\frac{1}{\sigma}\partial_\tau - \partial_\xi^2\right)\psi_{0,\xi\xi} = \hat{R}\theta_{1,\xi} - Dv_0, \tag{48}$$

while equation (34) gives at order $\mathcal{O}(T^{1/3})$:

$$\left(\partial_\tau - \partial_\xi^2\right)\theta_1 = \psi_{0,\xi} D\bar{\theta}_0. \tag{49}$$

Using equations (46) and (48), we can rewrite equation (34) in the form:

$$\left(\partial_\tau - \partial_\xi^2\right) D^2\psi_0 + \left(\partial_\tau - \partial_\xi^2\right)\left(\frac{1}{\sigma}\partial_\tau - \partial_\xi^2\right)^2 \psi_{0,\xi\xi} = -\hat{R}\left(\frac{1}{\sigma}\partial_\tau - \partial_\xi^2\right)\psi_{0,\xi\xi} D\bar{\theta}_0. \tag{50}$$

We look for solutions in the form of left and right-traveling waves with amplitudes that depend on the vertical :

$$\begin{cases} \psi_0 = A(z)\exp\{i\Omega\tau + ik_\perp\xi\} + B(z)\exp\{i\Omega\tau - ik_\perp\xi\} + c.c. \\ v_0 = E(z)\exp\{i\Omega\tau + ik_\perp\xi\} + F(z)\exp\{i\Omega\tau - ik_\perp\xi\} + c.c. \\ \theta_1 = G(z)\exp\{i\Omega\tau + ik_\perp\xi\} + H(z)\exp\{i\Omega\tau - ik_\perp\xi\} + c.c. \end{cases} \tag{51}$$

Substituting in equation (46) leads to:

$$\left(\frac{i\Omega}{\sigma} + k_\perp^2\right) E = DA \ , \quad \left(\frac{i\Omega}{\sigma} + k_\perp^2\right) F = DB \tag{52}$$

and in equation (49), to:

$$\left(i\Omega + k_\perp^2\right) G = -ik_\perp AD\bar{\theta}_0 \ , \quad \left(i\Omega + k_\perp^2\right) H = ik_\perp BD\bar{\theta}_0 \ , \tag{53}$$

i.e., *linear* equations. This is because the Jacobian terms $J(\cdot,\cdot)$ vanish identically. As a result (45) represents a *finite amplitude* solution, and Ω is the (so far unknown) nonlinear frequency.

It remains to obtain an equation for the mean temperature gradient $D\bar{\theta}_0$. Equation (34) at order $\mathcal{O}(T)$ gives:

$$(\partial_\tau - \partial_\xi^2)\theta_2 = D^2\bar{\theta}_0 - D\bar{\theta}_0\psi_{1,\xi} - \psi_{0,\xi}D\theta_1 + D\psi_0\theta_{1,\xi}. \tag{54}$$

By taking the horizontal average of this equation, we keep only the terms without a $e^{2ik_\perp\xi}$ component:

$$\partial_\tau\bar{\theta}_2 = D^2\bar{\theta}_0 - ik_\perp D(AG^* - A^*G - BH^* + B^*H), \tag{55}$$

where $*$ denotes the complex conjugate. Here, the right hand-side is independent of τ. However, the solvability condition tells us that it must be orthogonal to $Ker(\partial_\tau)$ so that $\bar{\theta}_2$ remains bounded as $\tau \to \infty$, thereby preserving the assumed asymptotic ordering in (42-44). This leads to:

$$D^2\bar{\theta}_0 - ik_\perp(AG^* - A^*G - BH^* + B^*H) = 0. \tag{56}$$

Integrating once, we obtain :

$$D\bar{\theta}_0 - ik_\perp(AG^* - A^*G - BH^* + B^*H) = -K \tag{57}$$

with K a constant. Replacing G and H with equations (53) now leads to:

$$D\bar{\theta}_0\left(1 + \frac{2k_\perp^4}{\Omega^2 + k_\perp^4}(|A|^2 + |B|^2)\right) = -K. \tag{58}$$

Since $\int_0^1 D\bar{\theta}_0 dz = \bar{\theta}_0(z=1) - \bar{\theta}_0(z=0) = -1$, we have an expression for K:

$$K^{-1} = \int_0^1 \frac{\Omega^2 + k_\perp^4}{\Omega^2 + k_\perp^4 + 2k_\perp^4(|A|^2 + |B|^2)}dz. \tag{59}$$

Equations (58) and (59) allow us to determine $D\bar{\theta}_0(z)$ in terms of the amplitudes $A(z)$ and $B(z)$ and thus to close the problem. Note that it is not necessary to calculate ψ_1. In the limit of large Taylor numbers, the mean flow associated with a traveling wave is negligible.

The constant K can be identified as the time-averaged Nusselt number $\langle N\rangle$. To see this, we consider the horizontally averaged vertical heat flux

$$N(z,\tau) \equiv -D\overline{\theta} + \overline{w\theta} = -D\bar{\theta}_0 + \overline{\psi_{0\xi}\theta_1} + O\left(T^{-1/3}\right), \tag{60}$$

Replacing $\theta_0, \psi_{0\xi}$ and θ_1 in (60), it follows that $\langle N\rangle = K$. In particular, $\langle N\rangle$ is independent of z.

From equation (50), we can obtain the following two second-order nonlinear coupled equations for the amplitudes A and B:

$$D^2A - k_\perp^2\left(\frac{i\Omega}{\sigma} + k_\perp^2\right)^2 A + \hat{R}k_\perp^2\frac{\left((i\Omega/\sigma) + k_\perp^2\right)\left(-i\Omega + k_\perp^2\right)}{\Omega^2 + k_\perp^4 + 2k_\perp^4(|A|^2 + |B|^2)}KA = 0, \tag{61}$$

$$D^2B - k_\perp^2\left(\frac{i\Omega}{\sigma} + k_\perp^2\right)^2 B + \hat{R}k_\perp^2\frac{\left((i\Omega/\sigma) + k_\perp^2\right)\left(-i\Omega + k_\perp^2\right)}{\Omega^2 + k_\perp^4 + 2k_\perp^4(|A|^2 + |B|^2)}KB = 0. \tag{62}$$

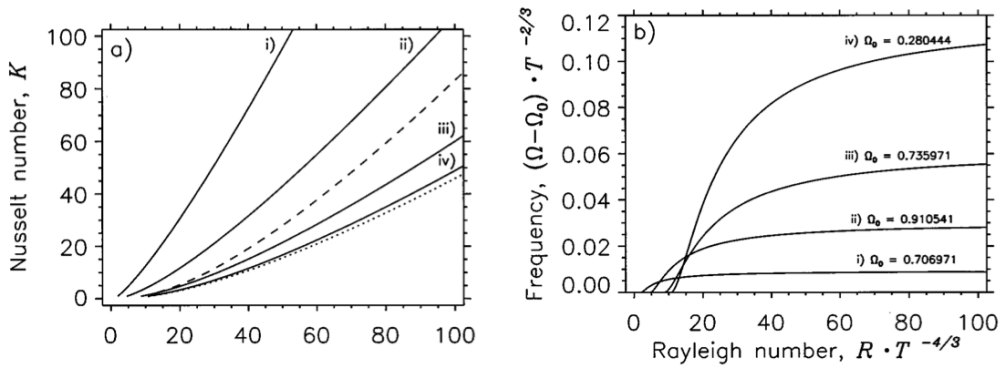

Figure 4: From [3] : (a) Time-averaged Nusselt number K and (b) frequency as functions of the scaled Rayleigh number at the respective critical wavenumber $k_c^{(o,s)}$ for oscillatory (solid) and steady (dashed) solutions for : (i) $\sigma = 0.2$, (ii) $\sigma = 0.4$, (iii) $\sigma \approx 0.68$ and (iv) $\sigma = 0.8$. For comparison, the steady solution at the $k_c^{(o)}$ for $\sigma = 0.8$ is plotted in the dotted line.

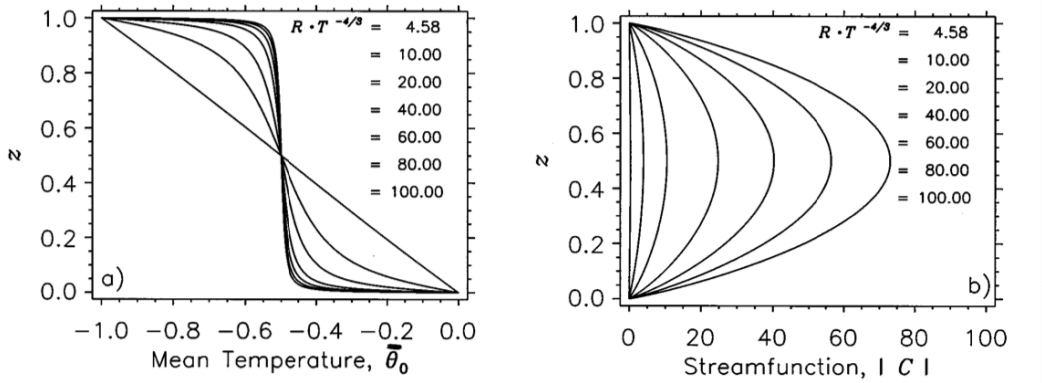

Figure 5: From [3]: Profiles of (a) mean temperature and (b) streamfunction amplitude at various scaled Rayleigh numbers.

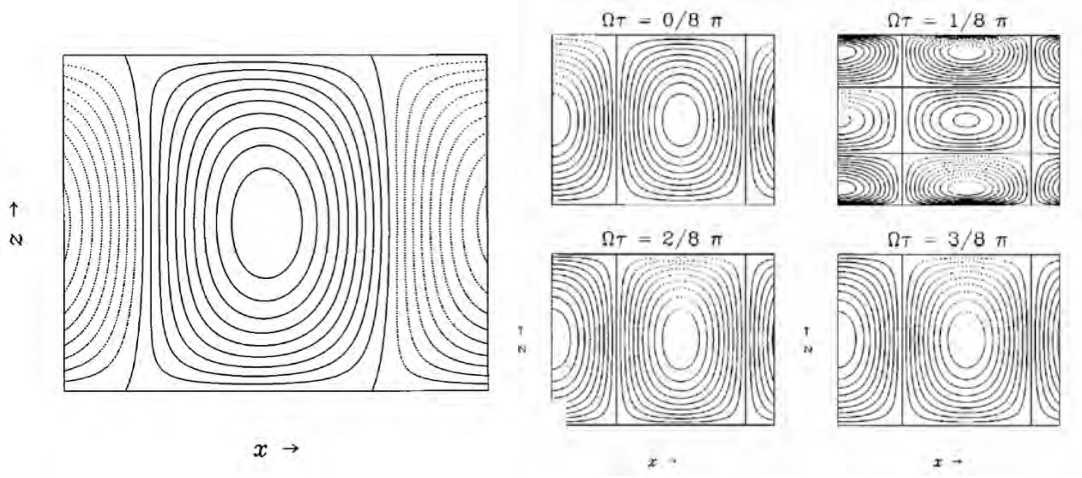

Figure 6: From [3]: Instantaneous streamlines in a left-traveling wave (left) and for a standing wave at four times during half an oscillation period (right). Solid (dotted) contours indicate clockwise (counterclockwise) motion.

We write $A = \frac{C}{\sqrt{1+|c|^2}}$, $B = \frac{cC}{\sqrt{1+|c|^2}}$, which represents traveling ($c = 0$) and standing ($c = 1$) waves as well as modulated waves ($0 < |c| < 1$). In particular, these waves all have the same time-averaged Nusselt number $\langle N \rangle = K$. Equations (61-62) then collapse into a single equation

$$D^2C - k_\perp^2 \left(\frac{i\Omega}{\sigma} + k_\perp^2 \right)^2 C + \hat{R} k_\perp^2 \frac{\left((i\Omega/\sigma) + k_\perp^2 \right) \left(-i\Omega + k_\perp^2 \right)}{\Omega^2 + k_\perp^4 + 2k_\perp^4 |C|^2} KC = 0. \tag{63}$$

with $K^{-1} = \int_0^1 \frac{\Omega^2 + k_\perp^4}{\Omega^2 + k_\perp^4 + 2k_\perp^4 |C|^2} dz$.

This is a complex-valued nonlinear eigenproblem for the vertical structure $C(z)$ with eigenvalues $\hat{R}K$ and Ω. The problem was solved numerically in [3] with impenetrable boundary conditions ($C(0) = C(1) = 0$) using an iterative Newton-Raphson-Kantorovich scheme. The eigenfunction $C(z)$ is then used to calculate K and, hence, the corresponding value of $\hat{R}$.

Fig, (4) shows the resulting $K\left(\hat{R};\ k_c^{(o)}\right)$ and $\Omega\left(\hat{R};\ k_c^{(o)}\right)$ for various Prandtl number σ at the most unstable mode $k_c^{(o)}$. The steady state values $K\left(\hat{R};\ k_c^{(s)}\right)$ for its critical wavenumber are plotted in the dashed line. For sufficiently small Prandtl numbers (cases (i), (ii)), the oscillatory solutions that are the first to set in, transport heat more efficiently than steady convection at its critical wavenumber. For larger σ, this is no longer so. Fig, 4 also shows $K(\hat{R};\ k_c^{(o)})$ for steady convection at the wavenumber preferred for oscillatory convection (dotted line).

Fig, (5) shows $|C(z)|$ and the corresponding mean temperature $\bar{\theta}_0$ for several values of $R \geq R_c^{(o)}$. We can see that the oscillations are responsible for large $\mathcal{O}(1)$ adjustments in the mean temperature profile, and the development of thermal boundary layers as R increases. We illustrate solutions in the form of traveling and standing waves, characterised by $c = 0$ and $|c| = 1$, in Fig. 6 (left and right, respectively).

The above approach generalizes readily to three-dimensional oscillating patterns [4].

References

[1] S. Chandrasekhar, *Hydrodynamic and Hydromagnetic Stability*, Oxford University Press, 1961.

[2] J. Guckenheimer and E. Knobloch, *Nonlinear convection in a rotating layer: Amplitude expansions and normal forms*, Geophysical & Astrophysical Fluid Dynamics, 23 (1983), pp. 247–272.

[3] K. Julien and E. Knobloch, *Fully nonlinear oscillatory convection in a rotating layer*, Phys. Fluids, 9 (1997), pp. 1906–1913.

[4] ——, *Fully nonlinear three-dimensional convection in a rapidly rotating layer*, Phys. Fluids, 11 (1999), pp. 1469–1483.

[5] E. Knobloch, *Oscillatory convection in binary mixtures*, Phys. Rev. A, 34 (1986), pp. 1538–1549.

[6] E. Knobloch and J. de Luca, *Amplitude equations for travelling wave convection*, Nonlinearity, 3 (1990), pp. 975–980.

[7] E. Knobloch and D. Moore, *Linear stability of experimental soret convection*, Phys. Rev. A, 37 (1988), pp. 860–870.

[8] G. Veronis, *Large-amplitude Bénard convection in a rotating fluid*, Journal of Fluid Mechanics, 31 (1968), pp. 113–139.

GFD 2024 Lecture 3: Turbulence, Turbulent Asymptotics and Turbulent Convection

Basile Gallet; notes by Camille Moisset and Matthew McCormack

June 20, 2024

This set of lectures combines standard textbook material with more recent progress in addressing strongly turbulent flows arising in geophysical and astrophysical fluid dynamics. The goal is two-fold: because this is the GFD program, the lectures are motivated by situations of interest arising in geophysical and astrophysical contexts. They aim at designing a minimal model of the (often turbulent) processes at stake. But because this is the GFD program, the goal is also to learn methods in physics and applied mathematics that prove useful to solve these minimal models. Each lecture is thus designed with the goal of illustrating such a method.

To set the stage, we begin with a reminder of basic turbulence dynamics. We do not aim for a comprehensive description. Instead, we wish to highlight the key phenomenology behind the standard scaling arguments entering the description of turbulent flows. We introduce 3D turbulence first before discussing the specificities of 2D turbulence. Once we have basic intuition in turbulence dynamics, we apply these ideas to predict the scaling-laws governing fully turbulent thermal convection, both with and without rotation.

1 3D Turbulence

1.1 Drag force on an object

Turbulence dynamics is perhaps an engineering problem to begin with, sketched in figure 1: an object of size R attached in a wind tunnel is subject to an incoming incompressible flow with uniform velocity $U\mathbf{e}_x$. The fluid has uniform density ρ and kinematic viscosity ν. The fluid exerts a drag force on the object, the time-averaged magnitude of which is denoted by F. We wish to express F in terms of the parameters of the problem.

The five-dimensional parameters of the problem and their respective dimensions are:

$$\begin{array}{ccccc} F\,, & U\,, & R\,, & \rho\,, & \nu\,, \\ MLT^{-2} & LT^{-1} & L\,, & ML^{-3} & L^2T^{-1}\,, \end{array} \tag{1}$$

where M, L, T denote dimensions of mass, length and time, respectively. With five dimensional quantities involving three dimensions, we conclude based on the Buckingham-π theorem that the physical law governing the system involves two independent dimensionless parameters. Choosing the dimensionless parameters $F/(\rho R^2U^2)$ and $Re = UR/\nu$, the physical law takes the form:

$$\frac{F}{\rho R^2U^2} = \mathcal{F}\left(Re = \frac{UR}{\nu}\right)\,, \tag{2}$$

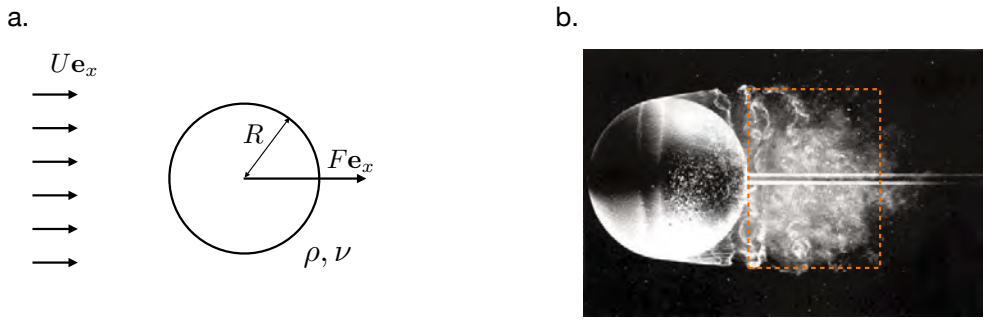

Figure 1: **a.** Schematic of a sphere in a wind tunnel. **b.** Experimental realization (copyright ONERA). We assume that energy dissipation takes place predominantly within a volume of order R^3 within the wake region, represented schematically in dashed orange.

where the function $\mathcal{F}$ is unknown at this stage. Strictly speaking, this is all we can infer from dimensional analysis. However, we are interested in the turbulent regime, which one can think of as the limit $\nu \to 0$ for otherwise constant parameters. If ν is so small, why should it enter the dimensional analysis above? Assuming ν can be forgotten about in the limit $\nu \to 0$, we are left with four dimensional parameters involving three dimensions, hence a single dimensionless quantity according to the Buckingham-π theorem. The physical law reduces to:

$$\frac{F}{\rho R^2 U^2} = \text{const.} \qquad \text{for } Re \to \infty \,, \tag{3}$$

or, equivalently, $\lim_{Re\to\infty} \mathcal{F}(Re) = \text{const.}$. We recover the standard scaling-law for a turbulent drag force, the constant on the right-hand side (rhs) being typically denoted by $C_x/2$ in the engineering literature, with C_x the drag coefficient.

1.2 Anomalous dissipation

Let us estimate the power dissipated by the turbulent flow in figure 1 on time average. In a wind tunnel experiment, this dissipated power equals the mean power required to drive the incoming flow. If, instead, the object is an airplane moving through initially steady fluid, then the dissipated power – the fuel consumption of the airplane – is directly related to the work done by the force F per unit time:

$$P = FU \sim \rho U^3 R^2 \,, \tag{4}$$

valid for $Re \to \infty$. This result should appear as a paradox to the uninitiated reader. Indeed, the estimate (4) does not involve the viscosity ν, even though viscosity is the very process responsible for energy dissipation. For $\nu = 0$ the Navier-Stokes equation reduces to the Euler equation, and, provided the velocity field is smooth, the Euler equation conserves energy. As $\nu \to 0$ in the Navier-Stokes equation, one may thus have expected the dissipated power to smoothly tend to zero. Instead, the wealth of data from wind-tunnel experiments point to the limiting behavior (4) instead, known as **'anomalous dissipation' or 'zeroth law of turbulence': the mean power dissipated by the flow tends to a constant, strictly positive value as the dissipative coefficient (the viscosity) tends to zero for otherwise constant parameters.** The unavoidable conclusion

is that high-Reynolds-number solutions to the Navier-Stokes equation do not resemble smooth solutions to the Euler equation.

To further highlight this point, let us assume that the kinetic energy is dissipated predominantly within the wake region behind the object, inside a volume of order R^3. The mean kinetic energy dissipation rate per unit mass of fluid is denoted by:

$$\epsilon = \nu \left\langle |\boldsymbol{\nabla} \mathbf{u}|^2 \right\rangle_{\mathbf{x},t} , \tag{5}$$

where $\mathbf{u}$ denotes the velocity field and $\langle \cdot \rangle_{\mathbf{x},t}$ denotes a volume average over the wake region together with a time average. Equating the input power (power of the force F acting on the object) with the viscous dissipation inside the wake yields:

$$P \sim \rho R^3 \epsilon \quad \Rightarrow \quad \epsilon \sim \frac{U^3}{R} , \tag{6}$$

where we have inserted (4) to obtain the second estimate. Substituting the definition of ϵ we obtain that the velocity gradients inside the wake diverge as $\nu \to 0$ (for constant U and R),

$$\left\langle |\boldsymbol{\nabla} \mathbf{u}|^2 \right\rangle_{\mathbf{x},t} \sim \frac{U^3}{R\nu} \to \infty \ \text{ as } \nu \to 0 . \tag{7}$$

As announced above, we conclude that the solutions to the Navier-Stokes equation become increasingly rough as $\nu \to 0$ and do not resemble smooth solutions to the Euler equation.[1]

1.3 Turbulent energy cascade

In the 1920s, Lewis F. Richardson proposed the phenomenological picture of an energy cascade to describe the formation of small-scale structures in turbulent flows. The energy cascade is sketched in figure 2, and we discuss it based on the motion of fluid inside a blender. Assuming that the blender has blades of size R spinning at linear velocity U (velocity of the tip of the blades), the motion of the blades inputs a power per unit mass of fluid $\epsilon \sim U^3/R$, see equation (6). This input energy initially takes the form of large vortices of scale comparable to R. However, as a result of the nonlinearities of the Navier-Stokes equation, these vortices break up into smaller vortices, and the smaller vortices again break up into even smaller vortices, etc., the process repeating itself in a self-similar fashion until the vortices are so small that the Reynolds number built on the size ℓ_ν of the smallest vortices is of the order of one. Viscosity then comes into play and damps the fluid motion. In statistically steady state, there is thus a constant **flux of energy** $\epsilon \sim U^3/R$ (per unit mass of fluid) from the larger to the smaller scales of the turbulent flow. Vortices within the so-called **inertial range** of scales $\ell_\nu \ll \ell \ll R$ receive an energy flux ϵ from larger vortices (of size approx. $\sim 2\ell$, say) and transfer an equal energy flux ϵ to smaller vortices (of size approx. $\ell/2$). Such inertial-range flow structures are 'unaware' of the large-scale forcing mechanism and of the small-scale viscosity. Instead, they only 'know' about the energy flux ϵ and their size ℓ. For instance, their typical velocity u_ℓ is obtained from dimensional analysis based on ϵ and ℓ only. We obtain

$$u_\ell \sim (\epsilon \ell)^{1/3} . \tag{8}$$

[1] They may, however, resemble rough solutions to the Euler equation.

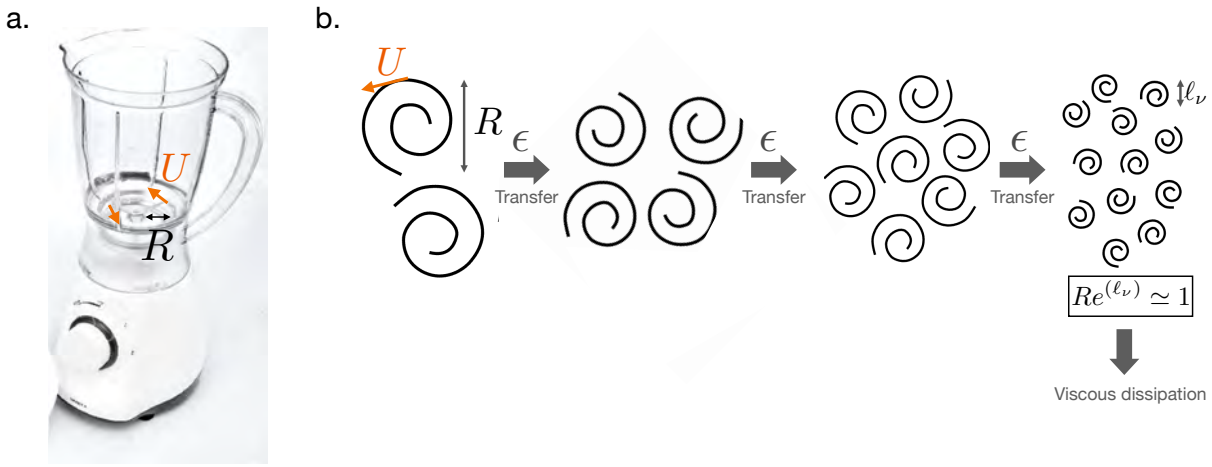

Figure 2: Richardson's turbulent cascade (panel **b**) is a phenomenological model for a high-Reynolds-number flow driven at a scale R with a velocity U, such as the flow in a blender (panel **a**). The motion of the blades inputs a power $\epsilon \sim U^3/R$ per unit mass of fluid. This energy flux ϵ is transferred to smaller and smaller scales until the scales are small enough to be damped viscously.

At the end of the turbulent cascade, the smallest vortices with size ℓ_ν finally dissipate this same energy flux ϵ through viscosity.[2] A scaling expression for ℓ_ν is obtained from dimensional analysis using ϵ and ν, which leads to

$$\ell_\nu \sim \left(\frac{\nu^3}{\epsilon}\right)^{1/4}, \tag{9}$$

known as the Kolmogorov dissipative scale. This is also the scale for which $u_\ell\, \ell/\nu \sim 1$.

To summarize, driving a turbulent flow at scale R with velocity U leads to energy input at a rate of order U^3/R. The forced flow structures are large and completely unaware of the tiny value of the kinematic viscosity. However, the fluid finds a way to dissipate the input energy through the turbulent cascade mechanism: the large flow structures break into smaller and smaller flow structures that induce so much viscous friction that the total input power can be dissipated by the tiny viscosity. In a thought experiment where the viscosity is decreased by a factor of ten, the same power U^3/R is input into the system (that is, the electrical consumption of the blender is independent of the fluid's viscosity). The cascade proceeds down to even smaller flow structures for the input power to be damped by the smaller viscosity, in line with equation (9).

2 2D Turbulence

Although real flows are three-dimensional, flows of geophysical interest come with additional physical ingredients that often make them strongly anisotropic. Global rotation, magnetic field, or simply a very shallow fluid domain tend to favor quasi-two-dimensional motion. A good understanding of 2D turbulence will thus provide useful insight to characterize the various flows of geophysical interest considered in the subsequent lectures.

[2] Of course, in statistically steady state the vortices of all sizes coexist inside the blender at any given instant in time.

Consider an incompressible, two-dimensional, planar flow in the (x, y) plane:

$$\mathbf{u} = \begin{pmatrix} u(x,y,t) \\ v(x,y,t) \\ 0 \end{pmatrix} . \tag{10}$$

The flow being incompressible, $\boldsymbol{\nabla} \cdot \mathbf{u} = 0$, it stems from a streamfunction $\psi(x, y, t)$:[3]

$$\mathbf{u} = -\boldsymbol{\nabla} \times \psi \mathbf{e}_z = \begin{pmatrix} -\psi_y \\ \psi_x \\ 0 \end{pmatrix} . \tag{11}$$

The vorticity is along the vertical direction z only, $\boldsymbol{\nabla} \times \mathbf{u} = \zeta \mathbf{e}_z$, and the vertical vorticity reads $\zeta = \Delta\psi$, where Δ denotes the (horizontal) Laplacian operator. Based on the streamfunction representation (11) the advective nonlinearities are conveniently written using the Jacobian operator J. That is, the advection of some arbitrary field ϕ is written as $\mathbf{u} \cdot \boldsymbol{\nabla}\phi = \psi_x \phi_y - \psi_y \phi_x \equiv J(\psi, \phi)$. In the absence of external forcing, the vertical vorticity equation takes the form:

$$\partial_t \Delta\psi + J(\psi, \Delta\psi) = \nu \Delta^2 \psi \, . \tag{12}$$

An important consequence of the 2D geometry is the absence of a vortex-stretching term in equation (12).

2.1 Conservation of energy and enstrophy

Consider equation (12) in a square domain with periodic boundary conditions, and denote by $\langle \cdot \rangle$ a space average over the domain. Multiplying equation (12) by ψ before averaging over the domain leads to the kinetic energy evolution equation:

$$\frac{\mathrm{d}}{\mathrm{d}t} \frac{\left\langle \mathbf{u}^2 \right\rangle}{2} = -\nu \left\langle (\Delta u)^2 \right\rangle , \tag{13}$$

where we have used $\left\langle |\boldsymbol{\nabla}\psi|^2 \right\rangle = \left\langle \mathbf{u}^2 \right\rangle$ and $\langle \psi J(\psi, \Delta\psi) = 0 \rangle$.[4] The kinetic energy of the flow is thus conserved by the nonlinearities of the equation, and, in the present unforced problem, the kinetic energy decreases as a result of viscosity.

A second conservation equation is obtained by multiplying the Navier-Stokes equation (12) by $\Delta\psi$ before averaging over the domain, which leads to:

$$\frac{\mathrm{d}}{\mathrm{d}t} \frac{\left\langle (\Delta\psi)^2 \right\rangle}{2} = -\nu \left\langle |\boldsymbol{\nabla}\Delta\psi|^2 \right\rangle . \tag{14}$$

On the left-hand side is the time derivative of the enstrophy Z, defined as:

$$Z = \frac{\left\langle \zeta^2 \right\rangle}{2} = \frac{\left\langle (\Delta\psi)^2 \right\rangle}{2} . \tag{15}$$

[3] Beware of the minus sign in this GFD convention.

[4] Here and in the following we make extensive use of the formula $\langle aJ(b,c) \rangle = -\langle bJ(a,c) \rangle$ for any three fields $a(\mathbf{x})$, $b(\mathbf{x})$ and $c(\mathbf{x})$ satisfying the periodic boundary conditions. If any of these two fields are equal, the formula readily gives $\langle aJ(b,c) \rangle = 0$.

Equation (14) shows that Z is conserved by the nonlinearities of the 2D Navier-Stokes equation. In the present unforced problem, enstrophy decreases as a result of viscosity.

Enstrophy conservation is a specific property of 2D turbulence with important consequences for the kinetic energy power integral of the system. Indeed, equation (14) indicates that Z decreases with time as a result of viscous dissipation, such that $0 \leq Z(t) \leq Z(0)$ for any $t \geq 0$. The absolute value of the kinetic energy equation (13) then yields:

$$\left| \frac{\mathrm{d}}{\mathrm{d}t} \frac{\left\langle \mathbf{u}^2 \right\rangle}{2} \right| = 2\nu Z(t) \leq 2\nu Z(0) \to 0 \text{ as } \nu \to 0 \text{ for fixed initial conditions.} \tag{16}$$

We conclude that **there is no anomalous dissipation of kinetic energy in 2D turbulence**. Instead, we have obtained in equation (16) that the instantaneous dissipated power per unit mass $\nu \left\langle |\boldsymbol{\nabla} \mathbf{u}|^2 \right\rangle = 2\nu Z(t)$ tends to zero as $\nu \to 0$.

What happens then to the Richardson's phenomenological picture in 2D turbulence? First, we cannot establish a result similar to (16) for the enstrophy dissipation rate. We expect enstrophy to be transferred to smaller and smaller scales in a turbulent 2D flow, in a cascading process similar to the standard Richardson kinetic energy cascade of 3D turbulence. However, equation (16) forbids a cascade of kinetic energy to small scales, where energy would be dissipated at an anomalous rate. Instead, the following argument shows that kinetic energy is transferred to larger and larger scales in 2D turbulent flows, a process referred to as the **inverse energy cascade**.

2.2 Fjørtoft's argument

The following argument illustrates why energy is transferred to large scales in the freely evolving 2D turbulent flow considered above. Inside a 2D periodic domain, the velocity field can be decomposed into Fourier series in x and y. We thus introduce the energy spectrum $E(k,t)$ defined such that $E(k,t)\mathrm{d}k$ is the kinetic energy contained by the Fourier modes with wavenumber between k and $k + \mathrm{d}k$. The vorticity being a spatial derivative of the velocity field, one readily obtains that $k^2 E(k,t)\mathrm{d}k$ is the enstrophy contained by the Fourier modes with wavenumber between k and $k + \mathrm{d}k$. Integrating over all $k \in \mathbb{R}$ we obtain:

$$\frac{\left\langle \mathbf{u}^2 \right\rangle}{2} = \int_0^\infty E(k,t)\mathrm{d}k \,, \tag{17}$$

$$Z = \int_0^\infty k^2 E(k,t)\mathrm{d}k \,. \tag{18}$$

A typical shape for the energy spectrum is sketched in figure 3. We characterize this spectrum using its centroid $\overline{k}$:

$$\overline{k}(t) = \frac{\int_0^\infty k E(k,t)\mathrm{d}k}{\int_0^\infty E(k,t)\mathrm{d}k} \,, \tag{19}$$

which is a good estimate of the typical energy-containing wavenumber. Additionally, we introduce the typical width δ of the spectrum around this centroid:

$$\delta^2(t) = \frac{\int_0^\infty (k - \overline{k})^2 E(k,t)\mathrm{d}k}{\int_0^\infty E(k,t)\mathrm{d}k} \,. \tag{20}$$

Expanding the square at the numerator yields:

$$\delta^2(t) = \frac{\int_0^\infty k^2 E(k,t)\mathrm{d}k}{\int_0^\infty E(k,t)\mathrm{d}k} - 2\overline{k}\frac{\int_0^\infty kE(k,t)\mathrm{d}k}{\int_0^\infty E(k,t)\mathrm{d}k} + \overline{k}^2 \,, \tag{21}$$

$$= \frac{2Z}{\langle \mathbf{u}^2 \rangle} - 2\overline{k}^2 + \overline{k}^2 = \frac{2Z}{\langle \mathbf{u}^2 \rangle} - \overline{k}^2 \,, \tag{22}$$

which we rewrite as:

$$\overline{k}^2(t) = \frac{2Z}{\langle \mathbf{u}^2 \rangle} - \delta^2(t) \,. \tag{23}$$

We consider an initial condition with a relatively narrow spectrum, as sketched in figure 3 (left). We assume that the viscosity is very small. The Reynolds number based on this initial condition is large and the initial evolution is conservative (and remains conservative until enstrophy has been transferred downscale all the way to the viscous dissipative scale). Z and $\langle \mathbf{u}^2 \rangle$ are independent of time during such conservative evolution and the first term on the rhs of (23) is constant. Now, as a result of the quadratic nonlinearity of the Navier-Stokes equation we expect the generation of harmonics in the spectrum and thus a broadening of $E(k,t)$ with time. In other words, δ^2 increases in time, which using equation (23) implies that $\overline{k}$ decreases in time. We conclude that the energy-containing wavenumber decreases as time evolves, that is, the energy of the flow is contained in larger and larger fluid structures, as sketched in figure 3 (right). In physical space, such inverse transfers are typically associated with mergers of isolated vortices. Such a merger event (i) results in a vortex with a broader vortical core, and (ii) increases the typical inter-vortex distance (comparable to the energy containing scale) by reducing the number of isolated vortices inside the domain.

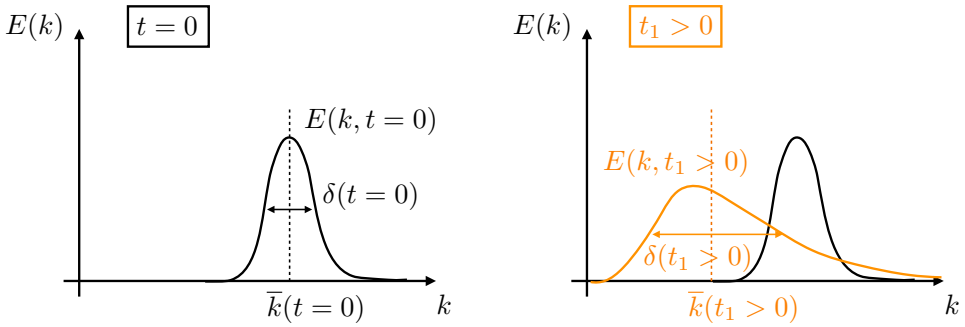

Figure 3: **Fjørtoft's argument.** Left: an initially narrow energy spectrum with centroid wavenumber $\overline{k}(t=0)$ and width $\delta(t=0)$. Right: at some subsequent time $t_1 > 0$ the spectrum has spread as a result of nonlinearity and generation of harmonics. According to equation (23), the centroid wavenumber is then necessarily smaller, $\overline{k}(t_1 > 0) < \overline{k}(t=0)$.

2.3 Summary

To summarize sections 1 and 2 above, turbulent flows transfer invariants to small scales where they are dissipated at an anomalous rate, unless some other conservation law forbids it.

- **3D turbulence:** Energy cascades to small scales. External forcing together with a small viscosity result in anomalous dissipation of energy, at a rate per unit mass of fluid $\epsilon = \nu \left\langle |\boldsymbol{\nabla} \mathbf{u}|^2 \right\rangle \sim U^3/R$ independent of ν. Such anomalous dissipation is sometimes referred to as the zeroth-law of turbulence, an informal but quite general statement of which would be: **large-scale quantities are related in a way that does not involve the tiny molecular viscosity** (which, if applied to the input power P per unit mass, indeed yields $P \sim U^3/R$).
- **2D turbulence:** Energy cascades to large scales because enstrophy conservation forbids a standard 'forward' cascade of energy to small scales. As a consequences, **energy is conserved in the limit** $\nu \to 0$. By contrast, enstrophy cascades to small scales and is damped at an anomalous rate as $\nu \to 0$.

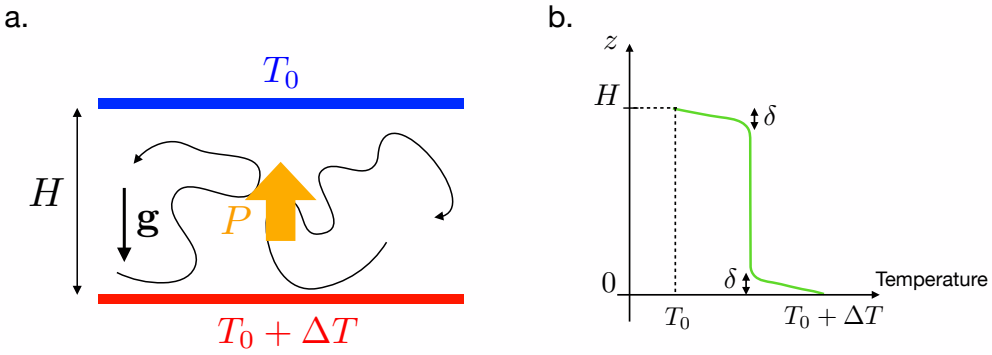

Figure 4: **Rayleigh-Bénard convection. Left:** theoretical setup. **Right:** mean temperature profile in the turbulent regime according to the 'classical theory', see section 3.1. Turbulence homogenizes the temperature in the bulk of the domain. Diffusion of heat across the marginally stable boundary layers at top and bottom throttles the heat flux.

3 Turbulent Convection

Thermal convection is a main driver of geophysical and astrophysical flows. Consider the Earth for instance: convection arises in the outer core, where it induces the geomagnetic field through dynamo action. Above the core is the mantle, where convection drives plate tectonics. Above the mantle is the Ocean, where high-latitude convection drives the downward branch of the meridional overturning circulation. And above the Ocean is the atmosphere, where moist convection leads to cloud formation, with important feedbacks on the global warming of the planet. These natural flows are strongly turbulent, with large Reynolds numbers, beyond what can be achieved in the laboratory of using Direct Numerical Simulations (DNS). The GFD approach thus consists of determining the basic scaling-laws that govern turbulent convection, with the goal of extrapolating these laws to the extreme parameter values of natural flows.

To wit, one typically considers the canonical Rayleigh-Bénard convection setup, sketched in figure 4. A layer of fluid of height H lies between a warm bottom plate maintained at temperature $T_0 + \Delta T$ and a cool top plate maintained at temperature T_0. At the theoretical level, the layer can be considered infinite or periodic in the horizontal directions. The density depends linearly on

temperature T, $\rho = \rho_0[1 - \alpha(T - T_0)]$. Following the traditional Boussinesq approximation, the other coefficients characterizing the fluid's properties are independent of temperature: kinematic viscosity ν, thermal diffusivity κ, thermal expansion coefficient α, specific heat capacity C, etc. One can also show that, for small enough temperature drop ΔT, the density variations need only be included in the expression of the weight of the fluid element [24], while the velocity field can be considered incompressible (divergence-free).

There are two dimensionless control parameters for such Boussinesq RB convection. The Rayleigh number,

$$Ra = \frac{\alpha g \Delta T H^3}{\kappa \nu}\,, \tag{24}$$

characterizes the intensity of the thermal driving as compared to diffusive effects. The Prandtl number,

$$Pr = \frac{\nu}{\kappa}\,, \tag{25}$$

characterizes the relative importance of viscosity and thermal diffusion. To some extent, Pr can be considered constant for a given fluid: $Pr \simeq 7$ for water around room temperature, $Pr \simeq 3 \times 10^{-2}$ for liquid metals, $Pr \ll 1$ in typical astrophysical settings.

For Rayleigh numbers below a critical value Ra_c, the fluid remains motionless and heat is diffused from the bottom to the top plate. The resulting heat flux P from the bottom to the top plate is due entirely to thermal diffusion and equals $\rho_0 C \kappa \Delta T / H$. For $Ra \gg Ra_c$ a vigorous turbulent flow arises inside the convection cell, transporting heat from the bottom to the top plate and therefore enhancing the heat flux P. The heat flux P is a central quantity of the convection system, related to most other global quantities of interest. The heat flux P is directly proportional to the rate of mechanical energy input into the system, which in statistically steady state is balanced by viscous dissipation. The heat flux P is also related to the input of buoyancy variance into the system, the latter being balanced by turbulent mixing. In dimensionless form, the heat flux P is quantified using the Nusselt number, defined as the ratio of P over the diffusive heat flux of the motionless state:

$$Nu = \frac{PH}{\rho_0 C \kappa \Delta T}\,. \tag{26}$$

A significant fraction of the research on thermal convection has been devoted to the determination of the scaling behavior of Nu as a function of Ra and Pr in controlled laboratory experiments and numerical simulations. The goal is to determine the behavior of Nu at asymptotically large Ra, and one typically seeks a power-law of the form $Nu \sim Ra^{\gamma} Pr^{\chi}$. As discussed below, two competing theoretical predictions have been put forward for the values of the exponents γ and χ.

3.1 'Classical' scaling regime

The classical theory is based on the observation that the temperature is almost homogeneous in the interior of high-Ra RB convection, with sharp gradients located within boundary layers adjacent to the top and bottom plates (see figure 3.1b). The interpretation is that the bulk turbulent flow efficiently mixes temperature, hence the isothermal profile in the interior of the domain. However, fluid hardly moves (in the vertical direction) near the top and bottom plates, hence the existence of boundary layers connecting the isothermal interior with the boundary values of the temperature field. Because the fluid hardly moves near the boundaries, heat transfer is dominated by diffusion

in the boundary layers. Assuming that diffusive transfer across the boundary layers throttles the overall heat flux, we estimate P as

$$P \sim \frac{\rho_0 C \kappa \Delta T}{\delta} \tag{27}$$

where δ denotes the thickness of the thermal boundary layer. The boundary layer thickness δ can be deduced from a marginal stability argument initially articulated by Howard [13]: the Rayleigh number based on δ is comparable to the threshold Rayleigh number for thermal convection,

$$Ra^{(\delta)} = \frac{\alpha g \Delta T \delta^3}{\kappa \nu} \simeq Ra_c \,. \tag{28}$$

The rationale is the following: if δ were much thinner than (28), the boundary layer could grow diffusively. However, if δ were greater than the estimate (28), the boundary layer itself would become convectively unstable. The boundary layer would then spontaneously erode and δ would decrease. The conclusion is that, in statistically steady state, the boundary layer thickness δ is given by (28), where Ra_c is a constant number, typically of the order of 10^3. Substituting the estimate (28) for δ into equation (27) yields, after multiplication by $H/(\rho_0 C \kappa \Delta T)$:

$$Nu \sim \frac{H}{\delta} \sim Ra^{1/3} \,, \tag{29}$$

that is, $\gamma = 1/3$ and $\chi = 0$.

3.2 Diffusivity-free or 'ultimate' scaling regime

The competing theoretical prediction, attributed to Spiegel and Kraichnan [23, 22, 15], is based on the zeroth law of turbulence introduced in section 1.2. If the zeroth law holds for turbulent convection, the large-scale quantities characterizing the turbulent flow should be related in a way that does not involve the tiny molecular diffusivities. In the present situation, one thus seeks a scaling relation between P and ΔT that does not involve κ nor ν. Start from the general scaling relation:

$$Nu \sim Ra^{\gamma} Pr^{\chi} \,. \tag{30}$$

Demanding that P and ΔT be related in a way that does not involve ν leads to $\chi = \gamma$, so that:

$$Nu \sim (Ra \times Pr)^{\gamma} \,. \tag{31}$$

Remembering that κ appears at the denominator of Nu, the only way for P and ΔT to be related in a way that does not involve κ is to have the right-hand side of (31) be inversely proportional to κ. We conclude that:

$$Nu \sim \sqrt{Ra \times Pr} \,, \tag{32}$$

that is, $\gamma = \chi = 1/2$. Around Walsh cottage, the scaling relation (32) is often attributed to E.A. Spiegel [23, 22], who is said to have put forward the idea in an astrophysical context without publishing it. In the meantime, his postdoc advisor R.H. Kraichnan published a similar prediction up to logarithmic corrections [15]. Kraichnan's approach consists in arguing that the boundary layers of the classical theory above should become turbulent at sufficiently high Rayleigh number. He assumes that a turbulent velocity boundary layer arises at large Ra, and that this turbulent boundary layer resembles that of standard wall-bounded turbulent flows, with a logarithmic layer

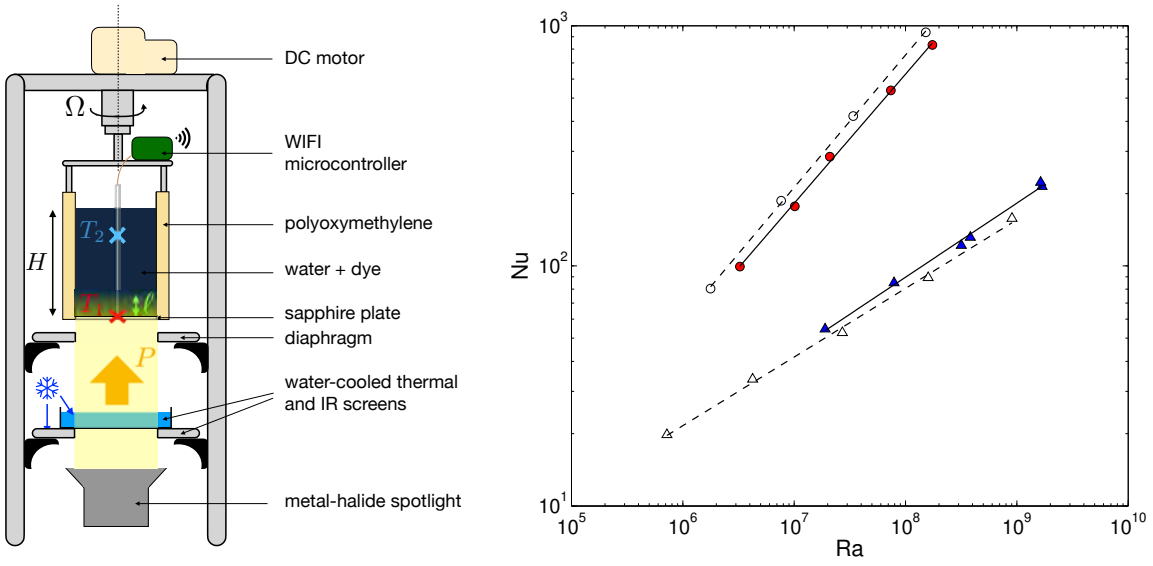

Figure 5: **Radiatively driven convection. Left:** Schematic of the experimental setup, including the motor driving global rotation when studying rotating convection. **Right:** Nusselt number as a function of the Rayleigh number for non-rotating experiments. Filled triangles: Rayleigh-Bénard-like situation with $\ell/H \leq 10^{-4}$. The best-fit exponent is $\gamma = 0.31$, close to a third. Filled circles: $\ell/H = 0.05$. The best-fit exponent is $\gamma = 0.54$, close to a half. Open symbols are DNS.

and a viscous sublayer in the immediate vicinity of the boundary. This structure for the boundary layer leads to the prediction (32) divided by a logarithmic correction in Rayleigh number. In the physics and fluid dynamics community the scaling-law (32) is often referred to as the 'ultimate' scaling regime of convection, possibly because according to Kraichnan the velocity boundary layers should *ultimately* become turbulent as Ra increases. In the astrophysics community, (32) is referred to as the mixing-length scaling-law and is believed to be the relevant scaling-law for the extreme parameter regimes of astrophysical flows.

While the precise value of the exponent γ remains debated for the highest Ra achieved in laboratory experiments, all measured values lie in the range $0.26 \leq \gamma \leq 0.38$ [2, 7, 17, 4, 20, 12, 8], that is, the measured exponent is always strictly less than $1/2$ (restricting attention to smooth top and bottom plates, see below). There is thus a need to get rid of the (laminar or turbulent) boundary layers if one aims at observing $\gamma = 1/2$. This has been attempted experimentally by considering a tall channel connecting a reservoir of hot fluid to a reservoir of cool fluid [9, 5, 18], or by using rough top and bottom plates with the goal of disrupting the boundary layers [6, 19, 21, 27, 28, 21, 26], both approaches showing some degree of success, see Ref. [10] for a discussion. Here, we describe a different experimental approach based on radiative heating, developed within our group at CEA Saclay [16].

3.3 Radiatively driven convection

One way to mitigate the throttling effect of the boundary layers is to input the heat predominantly beyond the latter, directly into the bulk turbulent flow. Lepot et al. [16] put this idea into practice by employing radiative heating in the experimental setup described thereafter and sketched in figure 5.

A cylindrical tank with a transparent bottom plate contains a mixture of water and carbon-black dye. A powerful spotlight shines at the tank from below, and the absorption of light by the dye induces radiative heating. Following Beer-Lambert's law, the light flux decreases exponentially with height z measured from the bottom of the tank, over an e-folding absorption scale ℓ, and so does the internal heat source. The absorption length ℓ is easily tuned through the concentration of the dye. For large dye concentration, the heat source is localized in the immediate vicinity of the bottom plate, with ℓ much smaller than the thickness of the velocity and temperature boundary layers. Such a heat source is similar to an imposed bottom heat flux; we thus expect a throttling effect associated with the presence of the bottom boundary layer, in a similar fashion to Rayleigh-Bénard convection. By contrast, using lower dye concentration, ℓ can be made much thicker than the boundary layers. The heat is then directly input into the bulk turbulent flow, bypassing the high thermal impedance of the boundary layers.

Denoting as P the energy flux radiated by the spotlight in the form of visible light (in units of W.m^{-2}), the governing equation for the temperature $T(x, y, z, t)$ inside the tank becomes [16]:

$$\partial_t T + \mathbf{u} \cdot \boldsymbol{\nabla} T = \kappa \nabla^2 T + \frac{P}{\rho_0 C \ell} e^{-z/\ell} \,, \tag{33}$$

where $\mathbf{u}(x, y, z, t)$ denotes the velocity field and the last term on the rhs is the radiative heat source.

Note that there is no cooling mechanism in this experiment: cooling the fluid through the top surface would necessarily introduce flux-throttling boundary layers. Instead, in the absence of any cooling mechanism and provided the boundaries of the fluid domain are insulating, the system is equivalent to convection heated radiatively and cooled down internally in a uniform fashion throughout the fluid volume. Indeed, averaging equation (33) over space leads to the evolution equation for the spatially averaged temperature $\overline{T}(t)$:

$$\frac{\mathrm{d}\overline{T}}{\mathrm{d}t} = \frac{P}{\rho_0 C H} \left(1 - e^{-H/\ell}\right) \simeq \frac{P}{\rho C H} \,, \tag{34}$$

where H denotes the height of fluid and we have assumed $\ell \ll H$ to obtain the last equality (we have also used the insulated boundary conditions to remove various surface terms). Equation (34) indicates that the mean temperature inside the tank increases linearly with time, because heat is supplied at a constant rate. To investigate the internal temperature structure within the fluid, consider the variable $\theta(x, y, z, t) = T(x, y, z, t) - \overline{T}(t)$, which represents the temperature fluctuations around the spatial average and obeys:

$$\partial_t \theta + \mathbf{u} \cdot \boldsymbol{\nabla} \theta = \kappa \Delta \theta + \frac{P}{\rho_0 C} \left(\frac{e^{-z/\ell}}{\ell} - \frac{1}{H} \right) . \tag{35}$$

In the parentheses is the radiative heat source, together with an effective uniform heat sink that balances the heat source over space average. Secular heating thus induces an effective uniform internal cooling term in equation (35), offering a way to avoid any boundary layer on the cooling side. As for the traditional Boussinesq set of equations, equation (35) is coupled to the incompressible Navier-Stokes equation, the latter including a buoyancy term proportional to θ. Solutions to this set of equations reach a statistically steady state in the long time limit, which one can characterize experimentally by measuring the emergent temperature drop between two probes placed at two different heights (the resulting temperature drop reaches a stationary state according to equation (35)). With the flux and the temperature drop at hand, one has access to the Rayleigh number

and the Nusselt number. In figure 5, the experimental data are shown in the (Ra, Nu) plane for two limiting situations: for large dye concentration, $\ell/H \leq 10^{-4}$, the heat is input radiatively very close to the bottom boundary. As for standard Rayleigh-Bénard convection, the heat needs to diffuse across the lazy bottom boundary layer before entering the turbulent bulk flow, and the measured exponent γ is close to a third. More interestingly, for $\ell/H = 0.05$ the heat is input predominantly into the turbulent bulk flow. The boundary layers are bypassed and an exponent γ close to a half is measured (see Ref. [1] for a more extended dataset).

4 Rapidly Rotating Convection

Global rotation is an important ingredient of various geophysical and astrophysical flows, and we thus investigate how rotation around the vertical axis z impacts the scaling-laws discussed above. Provided the centrifugal acceleration is negligible as compared to gravity, global rotation only enters the problem through the addition of the Coriolis force in the Navier-Stokes equation. As compared to non-rotating convection, the additional dimensional parameter Ω implies the existence of an additional dimensionless control parameter in the problem, and we choose the Ekman number $E = \nu/(2\Omega H^2)$. Because of this additional dimensionless parameter, the physical arguments invoked for non-rotating convection in sections 3.1 and 3.2 are insufficient to determine the scaling-laws of rotating convection. For instance, when seeking a scaling-law for the Nusselt number under the form $Nu \sim Ra^{\gamma} Pr^{\chi} E^{\xi}$, demanding that P and ΔT be related in a way that does not involve κ nor ν (zeroth-law of turbulence) only provides two constraints between the exponents γ, χ and ξ, leaving us with an infinite number of acceptable values.

4.1 'Extrapolation from threshold:' a method to determine the diffusivity-free scaling laws

One way to make progress is to focus on the asymptotic limit of rapid global rotation. This approach was pioneered by Stevenson [25] based on heuristic arguments, before being put on firmer analytical footing by Julien & Knobloch through an asymptotic expansion of the equations in powers of $E^{1/3}$ [14]. As for any asymptotic expansion, one of the most difficult steps is perhaps to infer the scalings of the various fields with the small parameter $E^{1/3}$. In the following, I will describe a method that could be coined 'extrapolation from threshold' to readily obtain the various scaling-laws of the diffusivity-free regime, based on linear stability and the zeroth law of turbulence only.[5] Beyond the sole Nusselt number, we will determine the scaling behavior of the rms flow speed, of the horizontal and vertical scales of the flow, and of the magnitude of the local temperature fluctuations.

The method consists of three steps, detailed in the following subsections:

- Perform a linear stability analysis of the system, before considering the rapidly rotating limit.
- Determine the saturation level based on the dominant nonlinearity.
- Invoke the diffusivity-free argument.

[5] The method is illustrated here for rapidly rotating convection but can be applied to other GFD systems (e.g., magnetoconvection).

4.2 Inferring the scalings in E from linear stability analysis

Consider the simplest setup of rotating thermal convection: Rayleigh-Bénard convection subject to rapid rotation around the vertical axis, with fixed-temperature stress-free boundary conditions at top and bottom. The eigenmodes consist of Fourier modes in all directions and the instability threshold and marginal eigenmode are easily computed, see e.g., the book by Chandrasekhar [3]. In the asymptotic limit of rapid rotation ($E \ll 1$), we obtain the following asymptotic scalings in E for the first unstable mode:

$$\text{Critical Rayleigh number:} \qquad Ra_c \sim E^{-4/3}\,, \tag{36a}$$

$$\text{Growth rate (say at } Ra = 1.1\,Ra_c\text{):} \qquad \sigma \sim \tfrac{\kappa}{H^2} E^{-2/3}\,, \tag{36b}$$

$$\text{Horizontal lengthscale (horizontal wavelength of most unstable mode)}: \qquad \ell^\perp \sim H E^{1/3}\,, \tag{36c}$$

$$\text{Vertical lengthscale (vertical wavelength of most unstable mode)}: \qquad \ell_z \sim H\,, \tag{36d}$$

$$\text{Ratio of temperature fluctuations in the horizontal to velocity fluctuations:} \qquad \theta_{\rm std} \sim \tfrac{\Delta T H}{\kappa} \left\langle \overline{w^2} \right\rangle^{1/2} E^{2/3}\,, \tag{36e}$$

$$\text{Relation between the horizontal and vertical velocity components:} \qquad \left\langle {\mathbf{u}_\perp}^2 \right\rangle \sim \left\langle w^2 \right\rangle\,, \tag{36f}$$

where $\theta_{\rm std}$ denotes the rms temperature fluctuations in the horizontal and in time at a fixed height z (note that these fluctuations do not scale like the overall temperature drop ΔT).

We want to describe the near-threshold regime for asymptotically fast rotation, that is $E \to 0$ for $Ra \sim Ra_c \sim E^{-4/3}$. This corresponds to the distinguished limit:

$$E \to 0 \qquad \text{for fixed} \qquad \widetilde{Ra} = Ra E^{4/3}\,. \tag{37}$$

In this distinguished limit, the various relations (36) can be turned into equals signs, provided a generic function $\mathcal{F}(\widetilde{Ra}, Pr)$ is included on the right-hand side (note that the symbol $\mathcal{F}$ denotes a generic function, which differs between one equation and the next):

$$\frac{\ell^\perp}{H} = E^{1/3} \mathcal{F}(\widetilde{Ra}, Pr)\,, \tag{38a}$$

$$\frac{\ell_z}{H} = \mathcal{F}(\widetilde{Ra}, Pr)\,, \tag{38b}$$

$$\theta_{\rm std} = \frac{\Delta T H}{\kappa} \left\langle w^2 \right\rangle^{1/2} E^{2/3} \mathcal{F}(\widetilde{Ra}, Pr)\,, \tag{38c}$$

$$\left\langle \mathbf{u}_\perp^2 \right\rangle = \left\langle w^2 \right\rangle \mathcal{F}(\widetilde{Ra}, Pr)\,, \tag{38d}$$

$$\sigma = \frac{\kappa}{H^2} E^{-2/3} \mathcal{F}(\widetilde{Ra}, Pr)\,. \tag{38e}$$

At this stage, we do not know the scalings of the various fields $\mathbf{u}_\perp$, w and θ independently.

4.3 Saturation level inferred from dominant nonlinearity

The saturation level of the various fields can be determined based on the dominant nonlinearity. In the present system the nonlinearities are all of advective type: $\mathbf{u}_\perp \cdot \boldsymbol{\nabla}_\perp(\dots)$ and $w\partial_z(\dots)$. Starting from infinitesimal perturbations, the exponential-growth phase proceeds until the advective nonlinearities become comparable to the growthrate. That is, when:

$$\max\{\mathbf{u}_\perp \cdot \boldsymbol{\nabla}_\perp; w\partial_z\} \sim \sigma\,, \tag{39}$$

such that the nonlinear terms can no longer be neglected. Based on the scalings (38) one easily shows that horizontal advection dominates over vertical advection: $\mathbf{u}_\perp \cdot \boldsymbol{\nabla}_\perp \sim w/\ell^\perp \gg w/H \sim w\partial_z$. Equation (39) thus reduces to $\mathbf{u}_\perp/\ell^\perp \sim \sigma$, which yields the saturation level of the flow speed after substituting (38):

$$u_\perp = \frac{\kappa}{H} E^{-1/3}\mathcal{F}(\widetilde{Ra}, Pr)\,. \tag{40}$$

Combining (40) with (38) finally yields the scaling in E of all the dimensionless quantities of interest:

$$Nu = 1 + \frac{\langle w\theta\rangle\, H}{\kappa\Delta T} \sim \frac{H}{\kappa\Delta T} w\,\theta_{\rm std} \sim \frac{H^2}{\kappa^2} u_\perp^2 E^{2/3}\mathcal{F}(\widetilde{Ra}, Pr) = \mathcal{F}(\widetilde{Ra}, Pr) \tag{41a}$$

$$Re = \frac{u_\perp H}{\nu} = \frac{H}{\nu}\frac{\kappa}{H} E^{-1/3}\mathcal{F}(\widetilde{Ra}, Pr) = E^{-1/3}\mathcal{F}(\widetilde{Ra}, Pr) \tag{41b}$$

$$\frac{\theta_{\rm std}}{\Delta T} = \frac{H}{\kappa} u_\perp E^{2/3}\mathcal{F}(\widetilde{Ra}, Pr) = E^{1/3}\mathcal{F}(\widetilde{Ra}, Pr) \tag{41c}$$

$$\frac{\ell^\perp}{H} = E^{1/3}\mathcal{F}(\widetilde{Ra}, Pr)\,. \tag{41d}$$

4.4 Diffusivity-free assumption

By focusing on the rapidly rotating regime, we have crucially simplified the problem: equations (41) involve unknown functions of the two parameters $\widetilde{Ra}$ and Pr only, as opposed to the three parameters $\widetilde{Ra}$, Pr and E initially. As E is made smaller and smaller, equations (41) will remain valid up to higher and higher values of $\widetilde{Ra}$.[6] The leap of faith is then to assume that, for $E \ll 1$, $\widetilde{Ra}$ can be made large enough for a diffusivity-free regime to arise while the relations (41) still hold. The resulting fully turbulent (or 'ultimate') scaling-laws are obtained by demanding that the functions $\mathcal{F}$ in (41a-41d) be such that ν and κ can be crossed out from both sides of the scaling relations.

For instance, assume a power-law dependence in equation (41a), $Nu \sim \widetilde{Ra}^\alpha Pr^\beta$. Remembering that $\widetilde{Ra} = RaE^{4/3} \sim \nu^{1/3}\kappa^{-1}$ and that $Nu \sim \kappa^{-1}$ (for otherwise constant parameters), we equate the powers of κ and ν on both sides of the equation to obtain $\alpha = 3/2$ and $\beta = -1/2$. Substituting $\widetilde{Ra} = RaE^{4/3}$ in the resulting scaling-law finally yields:

$$Nu \sim\ Ra^{3/2}E^2 Pr^{-1/2}\,. \tag{42}$$

[6] The asymptotic expansion of Julien and Knobloch suggests that $\widetilde{Ra}$ must remain $\mathcal{O}(1)$ with respect to their expansion parameter $E^{1/3}$, that is, it must satisfy $\widetilde{Ra} \ll E^{-1/3}$. This allows for large values of $\widetilde{Ra} \gg 1$ provided E is extremely small.

Proceeding in a similar fashion with equations (41b-41d) gives the additional scaling predictions:

$$Re \sim \frac{Ra\,E}{Pr}\,, \tag{43}$$

$$\frac{\theta_{\rm std}}{\Delta T} \sim Ra^{1/2}\,E\,Pr^{-1/2}\,, \tag{44}$$

$$\frac{\ell^{\perp}}{H} \sim Ra^{1/2}\,E\,Pr^{-1/2}\,. \tag{45}$$

The scaling predictions (42-45) correspond to the diffusivity-free regime of rapidly rotating convection, also known as the 'geostrophic turbulence' scaling regime.

4.5 Experimental realization using radiative heating

At the experimental level, the geostrophic turbulence (GT) regime has not been observed using rotating Rayleigh-Bénard convection cells. Indeed, it proves challenging to achieve a strongly turbulent flow in a rapidly rotating regime with negligible centrifugal effects. If the flow is not turbulent enough, boundary layers near the top and bottom plates again throttle the heat flux, as in non-rotating Rayleigh-Bénard convection. Radiative heating again appears as a promising way to bypass the boundary layers and observe the GT regime. Rotating radiatively driven convection experiments were thus performed and indeed led to a clear observation of the GT scaling regime. In such experiments the natural control parameter is the flux-based Rayleigh number $Ra_P = Nu \times Ra$. A convenient way to plot the experimental data consists in introducing a diffusivity-free Nusselt number number $\mathcal{N} = Nu\,E/Pr$ and a diffusivity-free flux-based Rayleigh number $\mathcal{R} = Ra_P E^3/Pr^2$. These two parameters do not involve κ nor ν. If the convective system is indeed in a diffusivity-free regime, we expect the datapoints corresponding to various Ra_P and E to gather onto a single master curve in the $(\mathcal{R},\mathcal{N})$ plane. As shown in figure 6, this is indeed the case. Additionally, using $Ra_P = Nu \times Ra$ the GT scaling-law (42) is easily recast as $\mathcal{N} \sim \mathcal{R}^{3/5}$. The master curve in figure 6 does behave as a power-law in the low-$\mathcal{R}$ rapidly rotating regime, and the exponent of the power-law is in excellent agreement with the prediction 3/5 of the GT regime. A validation of the other scaling predictions of the GT regime using rotating radiatively driven convection is reported in Ref. [11].

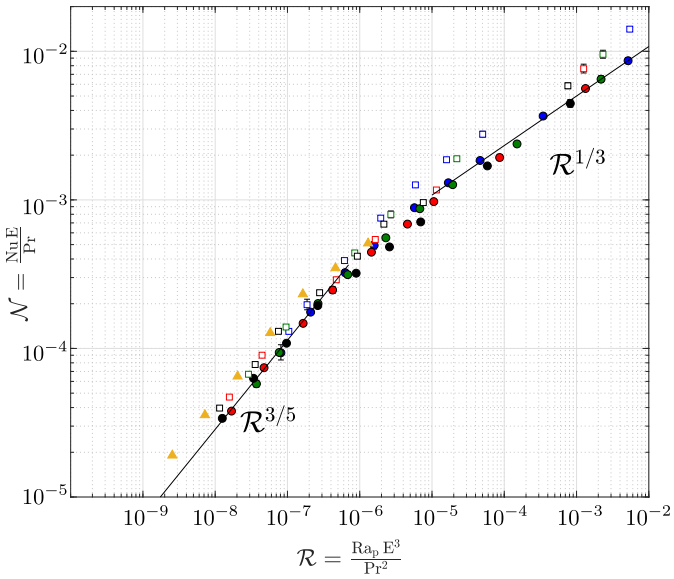

Figure 6: **Rotating radiatively driven convection.** Diffusivity-free Nusselt number $\mathcal{N}$ as a function of the diffusivity-free flux-based Rayleigh number $\mathcal{R}$ for various fluid heights: blue, $H = 10$ cm, $Ra_P \simeq 2.5.10^{10}$; green, $H = 15$ cm, $Ra_P \simeq 1.3.10^{11}$; red, $H = 20$ cm, $Ra_P \simeq 3.5.10^{11}$; black, $H = 25$ cm, $Ra_P \simeq 9.10^{11}$. The dimensionless absorption length is $\ell/H = 0.024$ (filled circles) or $\ell/H = 0.048$ (open squares). The triangles are DNS data for $Ra_P = 10^{12}$, $Pr = 7$, and $\ell/H = 0.048$. In the rapidly rotating regime, entered for $\mathcal{R} \lesssim 3.10^{-7}$, the master curve agrees closely with the geostrophic turbulence scaling prediction $\mathcal{N} \sim \mathcal{R}^{3/5}$, shown as an eye guide.

References

[1] Vincent Bouillaut, Simon Lepot, Sébastien Aumaître, and Basile Gallet. Transition to the ultimate regime in a radiatively driven convection experiment. *Journal of Fluid Mechanics*, 861:R5, feb 2019.

[2] Bernard Castaing, Gemunu Gunaratne, François Heslot, Leo Kadanoff, Albert Libchaber, Stefan Thomae, Xiao-Zhong Wu, Stéphane Zaleski, and Gianluigi Zanetti. Scaling of hard thermal turbulence in rayleigh-bénard convection. *J. Fluid Mech.*, 204:1–30, 1989.

[3] S Chandrasekhar. Hydrodynamic and hydromagnetic stability. January 1961.

[4] X. Chavanne, F. Chillà, B. Chabaud, B. Castaing, and B. Hébral. Turbulent Rayleigh–Bénard convection in gaseous and liquid He. *Physics of Fluids*, 13(5):1300–1320, may 2001.

[5] Murali R Cholemari and Jaywant H Arakeri. Axially homogeneous, zero mean flow buoyancy-driven turbulence in a vertical pipe. *Journal of fluid mechanics*, 621:69–102, 2009.

[6] S. Ciliberto and C. Laroche. Random Roughness of Boundary Increases the Turbulent Convection Scaling Exponent. *Physical Review Letters*, 82(20):3998–4001, may 1999.

[7] S. Cioni, S. Ciliberto, and J. Sommeria. Strongly turbulent rayleigh–bénard convection in mercury: comparison with results at moderate prandtl number. *J. Fluid Mech.*, 335:111–140, 1997.

[8] Charles R. Doering. Absence of Evidence for the Ultimate State of Turbulent Rayleigh-Bénard Convection. *Physical Review Letters*, 124(22):229401, jun 2020.

[9] M. Gibert, H. Pabiou, F. Chillà, and B. Castaing. High-Rayleigh-Number Convection in a Vertical Channel. *Physical Review Letters*, 96(8):084501, feb 2006.

[10] Gabriel Hadjerci, Vincent Bouillaut, Benjamin Miquel, Sébastien Aumaître, and Basile Gallet. Radiatively driven convection: diffusivity-free regimes of geophysical and astrophysical flows in the laboratory. *Comptes-rendus de l'académie des sciences*, 2024.

[11] Gabriel Hadjerci, Vincent Bouillaut, Benjamin Miquel, and Basile Gallet. Rapidly rotating radiatively driven convection: experimental and numerical validation of the 'geostrophic turbulence' scaling predictions. *Journal of Fluid Mechanics*, 998:A9, 2024.

[12] Xiaozhou He, Denis Funfschilling, Holger Nobach, Eberhard Bodenschatz, and Guenter Ahlers. Transition to the Ultimate State of Turbulent Rayleigh-Bénard Convection. *Physical Review Letters*, 108(2):024502, jan 2012.

[13] Louis N. Howard. Heat transport by turbulent convection. *Journal of Fluid Mechanics*, 17(03):405, nov 1963.

[14] Keith Julien, Edgar Knobloch, and Joseph Werne. A New Class of Equations for Rotationally Constrained Flows. *Theoretical and Computational Fluid Dynamics*, 11(3-4):251–261, jun 1998.

[15] Robert H. Kraichnan. Turbulent Thermal Convection at Arbitrary Prandtl Number. *The Physics of Fluids*, 5(11):1374–1389, nov 1962.

[16] Simon Lepot, Sébastien Aumaître, and Basile Gallet. Radiative heating achieves the ultimate regime of thermal convection. *Proceedings of the National Academy of Sciences*, 115(36):8937–8941, sep 2018.

[17] A. Naert, T. Segawa, and M. Sano. High-reynolds-number thermal turbulence in mercury. *Phys. Rev. E*, 56:R1302–R1305, Aug 1997.

[18] Shashikant S Pawar and Jaywant H Arakeri. Two regimes of flux scaling in axially homogeneous turbulent convection in vertical tube. *Physical Review Fluids*, 1(4):042401, 2016.

[19] P.-E. Roche, B. Castaing, B. Chabaud, and B. Hébral. Observation of the 1/2 power law in Rayleigh-Bénard convection. *Physical Review E*, 63(4):045303, mar 2001.

[20] P-E Roche, F Gauthier, R Kaiser, and J Salort. On the triggering of the Ultimate Regime of convection. *New Journal of Physics*, 12(8):085014, aug 2010.

[21] E. Rusaouën, O. Liot, B. Castaing, J. Salort, and F. Chillà. Thermal transfer in Rayleigh–Bénard cell with smooth or rough boundaries. *Journal of Fluid Mechanics*, 837:443–460, feb 2018.

[22] E. A. Spiegel. Convection in Stars I. Basic Boussinesq Convection. *Annual Review of Astronomy and Astrophysics*, 9(1):323–352, sep 1971.

[23] Edward A. Spiegel. A Generalization of the Mixing-Length Theory of Turbulent Convection. *The Astrophysical Journal*, 138:216, jul 1963.

[24] Edward A Spiegel and G Veronis. On the boussinesq approximation for a compressible fluid. *Astrophysical Journal, vol. 131, p. 442*, 131:442, 1960.

[25] David J. Stevenson. Turbulent thermal convection in the presence of rotation and a magnetic field: A heuristic theory. *Geophysical Astrophysical Fluid Dynamics*, 12(1):139–169, jan 1979.

[26] Srikanth Toppaladoddi, Andrew J. Wells, Charles R. Doering, and John S. Wettlaufer. Thermal convection over fractal surfaces. *Journal of Fluid Mechanics*, 907:A12, jan 2021.

[27] Yi-Chao Xie and Ke-Qing Xia. Turbulent thermal convection over rough plates with varying roughness geometries. *Journal of Fluid Mechanics*, 825:573–599, 2017.

[28] Xiaojue Zhu, Richard JAM Stevens, Roberto Verzicco, and Detlef Lohse. Roughness-facilitated local 1/2 scaling does not imply the onset of the ultimate regime of thermal convection. *Physical review letters*, 119(15):154501, 2017.

GFD 2024 Lecture 4: Geostrophic Turbulence and the Formation of Large Scale Structures

Edgar Knobloch; notes by Ishwari Mulkawar and Nicolaos Petropoulos

June 20, 2024

1 The Non-hydrostatic Balanced Geostrophic Equations

1.1 Motivation

The aspect ratio of fluid flows ($= H/L$, or its inverse) often proves to be an important explicit parameter in asymptotic reductions of the full equations. In the classical QG example, we assume $H \ll L$ for rapidly rotating, stably stratified flows and obtain a reduced system that inhibits vertical motion at leading order. We are now interested in studying convective *columnar flows* with strong vertical motion in the rapidly rotating, weakly stratified regime. Examples of this include deep convection in the Labrador Sea and Taylor columns often observed in rotating tank experiments. Dynamically, this regime is described by:

- Rapid rotation: $Ro \ll 1$,
- Thin aspect ratio: $H/L \gg 1$,
- Weakly stratified flows: $Fr = \frac{U}{NL} = \mathcal{O}(1)$

Scales of interest may be set by the conditions at the onset of convective instability but the theory below has broader validity.

1.2 Derivation

1.2.1 Primitive equations

In the following, we consider a Cartesian coordinate system $\boldsymbol{x} = (x, y, z)$ rotating at a constant angular velocity $\boldsymbol{\Omega} = \Omega\hat{\boldsymbol{z}}$ (where $\hat{\boldsymbol{z}}$ is the unit vector in the z direction). The Navier-Stokes equations under the Boussinesq approximation (with characteristic density ρ_0) read

$$\partial_t \boldsymbol{u} + (\boldsymbol{u}\cdot\nabla)\boldsymbol{u} + Ro^{-1}\hat{\boldsymbol{z}}\times\boldsymbol{u} = -\hat{P}\nabla p + \hat{\Gamma}\theta\hat{\boldsymbol{z}} + Re^{-1}\nabla^2\boldsymbol{u}, \quad \nabla\cdot\boldsymbol{u} = 0,$$
$$\partial_t T + (\boldsymbol{u}\cdot\nabla)T = Pe^{-1}\nabla^2 T.$$

These equations have been non-dimensionalized using an arbitrary horizontal length scale L and velocity scale U. They will be prescribed at a later stage. The dimensionless parameters are: the Rossby number $Ro := U/(2\Omega L)$; the Euler number $\hat{P} := \tilde{P}/(\rho_0)U^2$ (the ratio of the a characteristic pressure scale $\tilde{P}$ and the dynamic pressure $\rho_0 U^2$); the buoyancy number $\hat{\Gamma} := -g\alpha\tilde{T}L/U^2$ (here $\tilde{T}$ is a characteristic temperature scale, typically the temperature jump between the top and bottom of the domain); the Reynolds number $Re := UL/\nu$ and the Péclet number $Pe := UL/\kappa = PrRe$ (where $Pr := \nu/\kappa$ is the Prandtl number).

1.2.2 Asymptotic reduction

We consider the limit of fast rotation $Ro \ll 1$ and the dynamics of columnar structures with large aspect ratio $H/L \gg 1$ (where H is the height of the domain). We denote $\epsilon := Ro$ as our small parameter and consider the distinguished limit $L/H = \epsilon$. We assume that the columnar structures can be modulated in the vertical on length scales of order L; these are the processes we want to capture. It is then natural to introduce a large vertical scale $Z = \epsilon z$ and decompose motion as evolving on both the small and large scales:

$$\partial_z \to \partial_z + \epsilon \partial_Z. \tag{1}$$

Time is also split into a fast time t and slow time[1] $T = \epsilon^2 t$:

$$\partial_t \to \partial_t + \epsilon^2 \partial_T. \tag{2}$$

Balances between the Coriolis force, pressure and buoyancy terms in the momentum equation impose $\hat{\Gamma} = \mathcal{O}(\epsilon^{-1})$ and $\hat{P} = \mathcal{O}(\epsilon^{-2})$. Hence, we define

$$\hat{\Gamma} = \epsilon^{-1}\Gamma, \quad \hat{P} = \epsilon^{-2} P. \tag{3}$$

The other constants are assumed order 1. Especially Re, $Pe = \mathcal{O}(1)$ (this will prove to be important in the following). Concerning the fields, we seek solutions of the form:

$$\phi = \phi_0 + \epsilon\phi_1 + \epsilon^2\phi_2 + \cdots. \tag{4}$$

We also denote averages over the fast time and space variables by overbars $\overline{\cdot}$ and split fields into their mean and fluctuation contributions:

$$\phi = \overline{\phi} + \phi'. \tag{5}$$

The momentum and buoyancy equations for the mean quantities are

$$\begin{aligned}
&\epsilon^2 \partial_T \overline{\boldsymbol{u}} + \epsilon \partial_Z \left(\overline{w\boldsymbol{u}}\right) + \epsilon^{-1} \hat{\boldsymbol{z}} \times \overline{\boldsymbol{u}} = \epsilon^{-1} \left(-P\partial_Z \overline{p} + \Gamma \overline{\theta}\right) \hat{\boldsymbol{z}} + \epsilon^2 Re^{-1} \partial_Z^2 \overline{\boldsymbol{u}}, \\
&\epsilon^2 \partial_T \overline{\theta} + \epsilon \partial_Z \left(\overline{w\theta}\right) = \epsilon^2 Pe^{-1} \partial_Z^2 \overline{\theta}, \quad \partial_Z \overline{w} = 0.
\end{aligned}$$

Concerning the fluctuations, we have (with $D_t := \partial_t + \boldsymbol{u} \cdot \nabla$ where $\nabla = (\partial_x, \partial_y, \partial_z)$)

$$\begin{aligned}
&\left(D_t + \epsilon^2 \partial_T + \epsilon w \partial_Z\right) \boldsymbol{u}' + \epsilon w' \partial_Z \overline{\boldsymbol{u}} - \epsilon \partial_Z \left(\overline{w'\boldsymbol{u}'}\right) + \epsilon^{-1} \hat{\boldsymbol{z}} \times \boldsymbol{u}' = -\epsilon^{-2} \left(\nabla p' + \epsilon \partial_Z p' \hat{\boldsymbol{z}}\right) \\
&\qquad\qquad + \epsilon^{-1} \Gamma \theta' \hat{\boldsymbol{z}} + Re^{-1} \left(\nabla + \epsilon \hat{\boldsymbol{z}} \partial_Z\right)^2 \boldsymbol{u}', \\
&\left(D_t + \epsilon^2 \partial_T + \epsilon w \partial_Z\right) \theta' + \epsilon w' \partial_Z \overline{\theta} - \epsilon \partial_Z \left(\overline{w'\theta'}\right) = Pe^{-1} \left(\nabla + \epsilon \hat{z} \partial_Z\right)^2 \theta', \\
&\nabla \cdot \boldsymbol{u}' + \epsilon \partial_Z w' = 0.
\end{aligned}$$

The lowest order balance in the vertical mean momentum equation gives hydrostatic balance:

$$-P\partial_Z \overline{p}_0 + \Gamma \overline{\theta}_0 = 0 \tag{6}$$

[1] This scaling for the slow time seems enigmatic at first sight. However, it can be justified *a posteriori*; we will see that the mean velocity field scales like ϵ at first order and hence, in order to achieve a balance between the advective and viscous terms in the mean momentum equation (a reasonable balance to aim for, at least at the onset of instability — more on this later), time should scale like ϵ^2.

Considering the horizontal components of the leading order (mean) momentum equation give $\overline{u}_0, \overline{v}_0 = 0$. Incompressibility of the mean (leading order) velocity field imposes $\overline{w}_0 = 0$. The leading order balance in the mean buoyancy equation writes

$$\partial_Z(\overline{w_0\theta_0}) = 0 \Rightarrow \overline{w_0\theta_0} = 0 \overset{\overline{w}_0=0}{\Longrightarrow} \overline{w_0'\theta_0'} = 0. \tag{7}$$

Then, one can choose to have $\theta_0' = 0$ or $w_0' = 0$. The choice $w_0' = 0$ leads to the vertical component of the velocity field being (at least) one order smaller than its horizontal components. This is not what we want (see Motivation, section 1.1). Therefore, we consider $\theta_0' = 0$ instead. As a result, the temperature field can be written as:

$$\theta = \overline{\theta}_0 + \epsilon \times [\cdots]. \tag{8}$$

The order $\mathcal{O}(\epsilon^2)$ balance in the mean buoyancy equation is (using $\overline{w}_1 = 0$ — more generally $\overline{w} = 0$ due to the mean incompressibility equation — and $\theta_0' = 0$):

$$\partial_T\overline{\theta}_0 + \partial_Z(\overline{w_0'\theta_1'}) = Pe^{-1}\partial_Z^2\overline{\theta}_0. \tag{9}$$

The order $\mathcal{O}(\epsilon)$ balance in the fluctuation buoyancy equation reads, with $D_t^0 = \partial_t + \boldsymbol{u}_0\cdot\nabla = \partial_t + \boldsymbol{u}_0'\cdot\nabla$ (recall again $\theta_0' = 0$)

$$D_t^0\theta_1' + w_0'\partial_Z\overline{\theta}_0 = Pe^{-1}\nabla^2\theta_1'. \tag{10}$$

The leading order balance in the fluctuation momentum equation is

$$\nabla p_0' = 0 \Rightarrow p_0' = 0. \tag{11}$$

Using this result and $\theta_0' = 0$, the order $\mathcal{O}(\epsilon^{-1})$ balance in the momentum equation gives:

$$\hat{\boldsymbol{z}} \times \boldsymbol{u}_0' = -\nabla p_1' \tag{12}$$

i.e., leading order velocity fluctuations are geostrophically balanced.

The order $\mathcal{O}(1)$ momentum equations are

$$D_t^0\boldsymbol{u}_0' = -\nabla p_2' - \partial_Z p_1'\hat{\boldsymbol{z}} + \Gamma\theta_1'\hat{\boldsymbol{z}} + Re^{-1}\nabla^2\boldsymbol{u}_0'. \tag{13}$$

Incompressibility gives $\nabla\cdot\boldsymbol{u}_0' = 0$ at order $\mathcal{O}(1)$ and $\nabla\cdot\boldsymbol{u}_1' + \partial_Z w_0' = 0$ at order $\mathcal{O}(\epsilon)$.

Using the leading order geostrophic balance (12), we have $\partial_z p_1' = 0$ and $\partial_z u_0' + \partial_y v_0' = 0$. As a result $\partial_z u_0'$, $\partial_z v_0' = 0$ (differentiating (12) with respect to z) and $\partial_z w_0' = 0$ (using the leading-order incompressibility condition $\nabla\cdot\boldsymbol{u}_0' = 0$). Differentiating (10) with respect to z then gives

$$D_t^0\left(\partial_z\theta_1'\right) = Pe^{-1}\nabla^2\left(\partial_z\theta_1'\right). \tag{14}$$

Hence, starting with no fluctuation on the small scales at the lowest order, none will be produced. It therefore seems reasonable to assume $\partial_z\theta_1' = 0$. In other words, we proved the following statement: $\boldsymbol{u}_0'$, p_1' and θ_1' do not vary on the small vertical scale. We will use this result — essentially expressing the Taylor-Proudman constraint[2] — extensively in the following. First, we consider the vertical component of (13)

$$\partial_z p_2' = -D_t^0 w_0' - \partial_Z p_1' + \Gamma\theta_1' + Re^{-1}\nabla^2 w_0'. \tag{15}$$

[2]The Taylor-Proudman theorem states that in a rapidly rotating fluid, streamlines do not vary along the direction of the axis of rotation; the fluid is "stiff" in the direction of Ω.

The left-hand side depends both on the small and large scales whereas the right-hand side depends only on the large ones. As a result, Fredholm's alternative theorem gives the following solvability condition[3]:

$$0 = -D_t^0 w_0' - \partial_Z p_1' + \Gamma\theta_1' + Re^{-1}\nabla^2 w_0'. \tag{16}$$

Cross-differentiating the horizontal components of (13) gives

$$\partial_z w_1' = -D_t^0 \left(\hat{\boldsymbol{z}} \cdot \nabla \times \boldsymbol{u}_0'\right) - \partial_Z w_0' + Re^{-1}\nabla^2 \left(\hat{\boldsymbol{z}} \cdot \nabla \times \boldsymbol{u}_0'\right). \tag{17}$$

To prevent secular growth on small scales in w_1' (the right-hand side of the above depends only on large scale variables), we get the solvability condition

$$0 = -D_t^0 \left(\hat{\boldsymbol{z}} \cdot \nabla \times \boldsymbol{u}_0'\right) - \partial_Z w_0' + Re^{-1}\nabla^2 \left(\hat{\boldsymbol{z}} \cdot \nabla \times \boldsymbol{u}_0'\right). \tag{18}$$

Since the leading order horizontal flow (u_0', v_0') is in geostrophic balance with the pressure gradient $\nabla p_1'$, p_1' can be understood as a streamfunction for the leading order velocity field. Let $\psi := p_1'$ and $\omega := \partial_x^2\psi + \partial_y^2\psi = \hat{\boldsymbol{z}} \cdot (\nabla \times \boldsymbol{u}_0')$ be the vorticity associated with the leading order horizontal flow. Then $\boldsymbol{u}_0' = (-\partial_y\psi, \partial_x\psi, w_0')$ and we get the following set of closed equations:

$$\begin{aligned}
&\partial_t\omega + J[\psi,\omega] - \partial_Z w_0' = Re^{-1}(\partial_x^2\omega + \partial_y^2\omega),\\
&\partial_t w_0' + J[\psi, w_0'] + \partial_Z\psi = \Gamma\theta_1' + Re^{-1}(\partial_x^2 w_0' + \partial_y^2 w_0'),\\
&P\partial_Z\overline{p}_0 = \Gamma\overline{\theta}_0,\\
&\partial_T\overline{\theta}_0 + \partial_Z\left(\overline{w_0'\theta_1'}\right) = Pe^{-1}\partial_Z^2\overline{\theta}_0,\\
&\partial_t\theta_1' + J[\psi,\theta_1'] + w_0'\partial_Z\overline{\theta}_0 = Pe^{-1}(\partial_x^2\theta_1' + \partial_y^2\theta_1').
\end{aligned}$$

Note that we have not specified the scales U and L yet. Our derivation assumed that Re was of order 1. Hence, it seems reasonable to assume the dissipative relationship $U = \nu/L$. The length scale L is also connected to the Rossby number through $L/H = \epsilon = Ro$ (where H is the height of the domain). This is somewhat inconvenient: the Rossby number is an output of (say) an experiment (one has to measure velocities to deduce a Rossby number). It would be more convenient to express the functional dependence between scales in terms of input parameters. We choose the scaling $L/H = Ek^{1/3}$ (where Ek is the Ekman number), corresponding to a known scaling at the onset of rapidly rotating convection [1]. Note that since we are expecting that unbounded growth of unstable modes will be damped by dissipative processes, it seems relevant to look at scales for which $Re = \mathcal{O}(1)$ to describe this phenomenon. All in all, the reduced-order model derived here reads (removing primes and indices)

$$\begin{aligned}
&\partial_t\omega + J[\psi,\omega] - \partial_Z w = \partial_x^2\omega + \partial_y^2\omega,\\
&\partial_t w + J[\psi, w] + \partial_Z\psi = Pr^{-1}RaEk^{4/3}\theta + \partial_x^2 w + \partial_y^2 w,\\
&\partial_T\overline{\theta} + \partial_Z\left(\overline{w\theta}\right) = Pr^{-1}\partial_Z^2\overline{\theta},\\
&\partial_t\theta + J[\psi,\theta] + w\partial_Z\overline{\theta} = Pr^{-1}(\partial_x^2\theta + \partial_y^2\theta).
\end{aligned}$$

Here Ra is the Rayleigh number. These equations correspond to the non-hydrostatic balanced geostrophic equations (NHBGE) [6, 3]. The problem is now fully described by two dimensionless

[3]The null space of ∂_z is the space of all functions independent of z. Then, the solvability condition is that the right-hand side is orthogonal to any z-independent function. But the right-hand side is already z-independent. Hence, it should be 0. This result can also be understood using the following argument. If the right-hand side is *not* 0, then $p_2' \propto z$ and hence is of order $1/\epsilon^2$ for z of order $1/\epsilon^2$, breaking the ordering of the expansions.

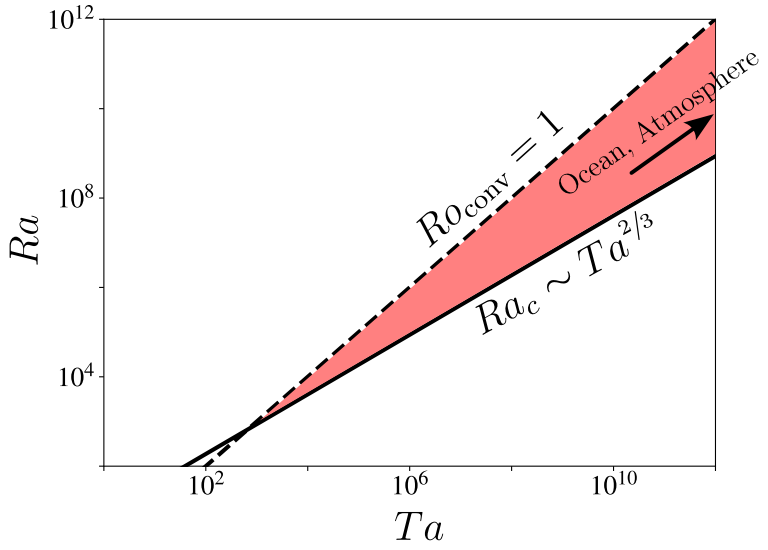

Figure 1: The NHBGE capture the large Ta, low $Ro_{\rm conv}$ regime for Rayleigh-Bénard convection (in red).

numbers: the Prandtl number Pr and the scaled Rayleigh number $\mathcal{R} := RaEk^{4/3}$. The scaled Rayleigh number is consistent with the $Ra \sim Ek^{-4/3}$ scaling at the onset of convection [1]. Note that using the working assumptions $U = \nu/L$ and $L/H = Ek^{1/3}$, the Rossby number associated with the scales of interest scales as $Ek^{1/3}$. Invoking a diffusivity-free argument[4], we can go a bit further and define a 'convective Rossby number' $Ro_{\rm conv} := Ek^{1/3}\mathcal{R}^{1/2}Pr^{-1/2}$. This is an *a priori* measure of the importance of rotation as the Rayleigh number is varied. Figure 1 summarizes the regime of applicability of the NHBGE.

1.3 Comments on the model

The following properties of the NHBGE have important implications.

- The flow is in geostrophic balance at leading order and hence the horizontal divergence of the horizontal leading order flow is 0. However (and on contrary to 'classic' geostrophy), the leading order vertical velocity field is non-zero and more specifically of the same order as the horizontal components of the velocity field (i.e., $u_0' \sim v_0' \sim w_0'$).

- Non-divergent flow at leading order filters out inertia-gravity waves (IGW) in the fast variables. (IGWs need non-stationary, divergent/ageostrophic flow for propagation.)

- NHBGE are fully 3D and fully nonlinear.

- *Conservation laws:* The non-dissipative NHBGE equations conserve the energy E and potential vorticity Π where:

$$E := \frac{1}{2}\int\left[|u_0'|^2 + \frac{\Gamma}{\partial_Z\overline{\theta}}\theta'^2\right]\mathrm{d}x\mathrm{d}y\mathrm{d}Z, \quad \Pi := \omega + \frac{J[w,\theta'] + \partial_Z\theta'}{\partial_Z\overline{\theta}}. \tag{19}$$

[4]More precisely, we write $Ro_{\rm conv} = Ek^{1/3}\mathcal{R}^{\alpha}Pr^{\beta}$, and determine the exponents α and β assuming that the equality is independent of both κ and ν.

- Note that the model is valid in the bulk but not in boundary layers; there are no dissipative terms in the vertical direction to allow for the formation of boundary layers in the case of no-slip boundary conditions, for instance.

- *Surprising symmetry:* The transformation $(x, y) \to (x, -y)$ and $(\psi, w, \overline{\theta}, \theta') \to (-\psi, -w, -\overline{\theta}, \theta')$ leaves the equations unchanged. Hence, at leading order, the model does not present any handedness due to rotation. One needs to go to the next order to break this symmetry and retrieve the expected handedness due to rotation. The idea that strong anisotropy dominates over the chirality introduced by rotation has interesting implications for geophysical and astrophysical problems.

2 Formation of Large-scale Structures

- **Dynamical regimes and large scale structures.** The reduced order model developed in the previous section describes the formation of four dynamical regimes (depending on the value of the reduced Rayleigh number $\mathcal{R}$ and Prandtl number Pr): cellular convection, convective Taylor column, convective plumes and geostrophic turbulence (see figure 2). Qualitatively, these regimes are characterised by elongated columnar structures with more or less vertical structure. Interestingly, these dynamical regimes have been observed in direct numerical simulation of the *primitive* equations, even for values of the Ekman number that were not in the asymptotic regime needed to obtain the NHBG equations.

- **Barotropic/baroclinic decomposition.** Because of the presence of large-scale vertical columnar structures in the four dynamical regimes presented above, it seems natural to decompose solutions of the NHBG equations into barotropic (i.e., independent of the vertical coordinate z) and baroclinic contribution. To this end, we decompose fields into vertical averages and departures from these averages: $\omega = \langle\omega\rangle + \omega'$, $\psi = \langle\psi\rangle + \psi'$. The mean and fluctuation vorticity equations then are

$$\partial_t\langle\omega\rangle + J[\langle\psi\rangle, \langle\omega\rangle] + \langle J[\psi', \omega']\rangle = \nabla_\perp^2\langle\omega\rangle,$$
$$\partial_t\omega' + J[\langle\psi\rangle, \omega'] + J[\psi', \langle\omega\rangle] + J[\psi', \omega'] - \partial_Z w = \nabla_\perp^2\omega'.$$

  The equation for the barotropic contribution is almost identical to the 2D vorticity equation, with the exception of the additional barotropic/baroclinic term $\langle J[\psi', \omega']\rangle$ that acts as a source for the barotropic mode. Without this term, we would expect an inverse energy cascade and a $k_\perp^{-3}$ pile up at large scales (where $k_\perp$ is the horizontal wave-number). This is also the case in the presence of the barotropic/baroclinic term, as shown in [8]. The baroclinic equation corresponds to fully 3D hydrodynamics and exhibits a $k_\perp^{-5/3}$ energy spectrum. These results are summarized in figure 3.

- **Nusselt number.** In steady state, we have

$$\partial_Z\left(\overline{w\theta}\right) = Pr^{-1}\partial_Z^2\overline{\theta}, \quad J[\psi, \theta] + w\partial_Z\overline{\theta} = Pr^{-1}(\partial_x^2\theta + \partial_y^2\theta). \tag{20}$$

  Integrating the first equation gives

$$\overline{w\theta} - Pr^{-1}Nu = Pr^{-1}\partial_Z\overline{\theta}. \tag{21}$$

  Multiplying the second by θ and averaging gives

$$\overline{w\theta}\partial_Z\overline{\theta} = -Pr^{-1}\overline{|\nabla_\perp\theta|^2}. \tag{22}$$

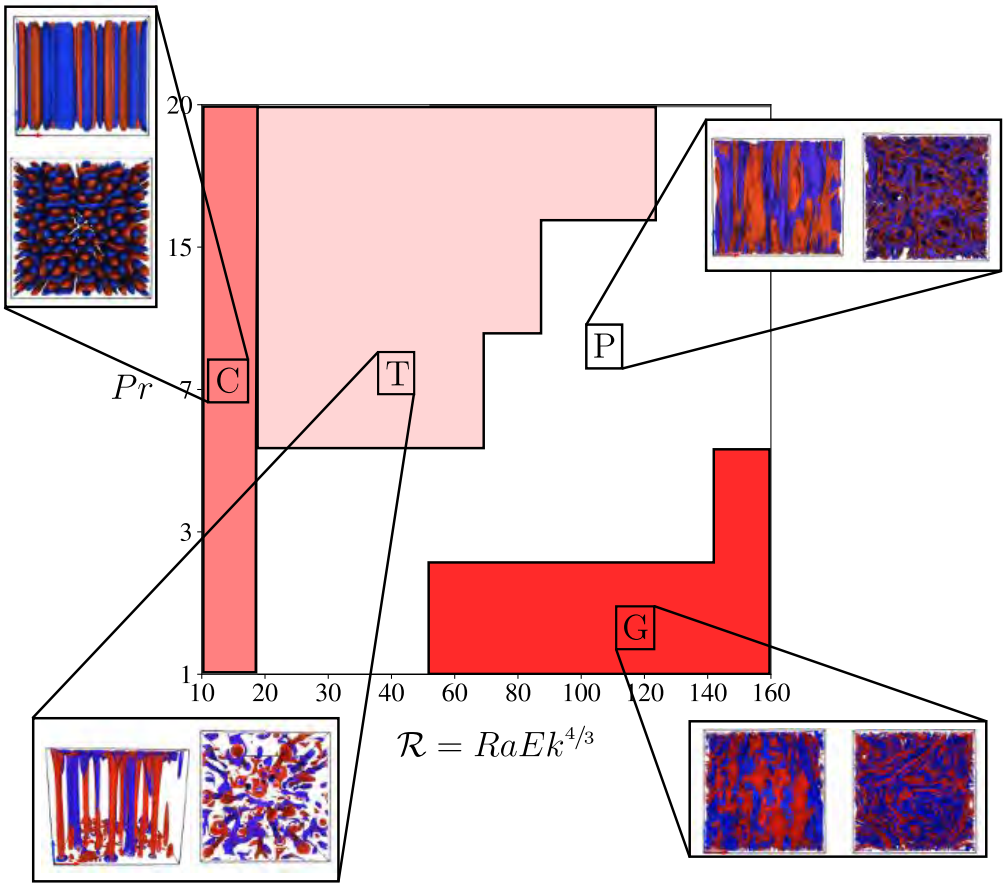

Figure 2: The NHBGE four dynamical regimes, depending on the value of the reduced Rayleigh number $\mathcal{R}$ and Prandtl number Pr: cellular convection (C), convective Taylor columns (T), convective plumes (P), geostrophic turbulence (G). These regimes were observed in direct numerical simulations of the primitive equations at $Ek = 10^{-7}$ with $\mathcal{R} = 11$, $Pr = 1$ for regime C, $\mathcal{R} = 15$, $Pr = 15$ for regime T, $\mathcal{R} = 50$, $Pr = 3$ for regime P and $\mathcal{R} = 90$, $Pr = 1$ for regime G (insets). (Figure adapted from [7]).

Then

$$\left(\partial_Z \overline{\theta}\right)^2 + Nu \partial_Z \overline{\theta} + \overline{|\nabla_\perp \theta|^2} = 0 \Rightarrow \partial_Z \overline{\theta} = \frac{1}{2}\left[-Nu \pm \sqrt{Nu^2 - 4\overline{|\nabla_\perp \theta|^2}}\right]. \tag{23}$$

Here Nu is the Nusselt number, a non-dimensional parameter that measures the heat transport, given by $qH/\rho_0 c_p \kappa \Delta T = -\partial_Z \overline{\theta}|_{Z=0}$. This relation implies that the temperature dissipation rate is bounded by $Nu^2/4$. The negative sign in (23) denotes the (large) temperature gradient in the thermal boundary layer (which is largely conductive) while the positive sign stands for the bulk region (well mixed by the convective instability). The transition between these two regions occurs when $-\partial_Z \overline{\theta} = \overline{w\theta} = Nu/2$, implying equipartition between conduction and convection. This condition determines the extent of the thermal boundary layer.

- **Boundary layer instability and heat transport.** Linear stability analysis around the mean temperature gradients reveals that at large Rayleigh (or large $\mathcal{R}$) numbers, the thermal boundary layer can become unstable even when the convective core is stable (see figure 4). This is in

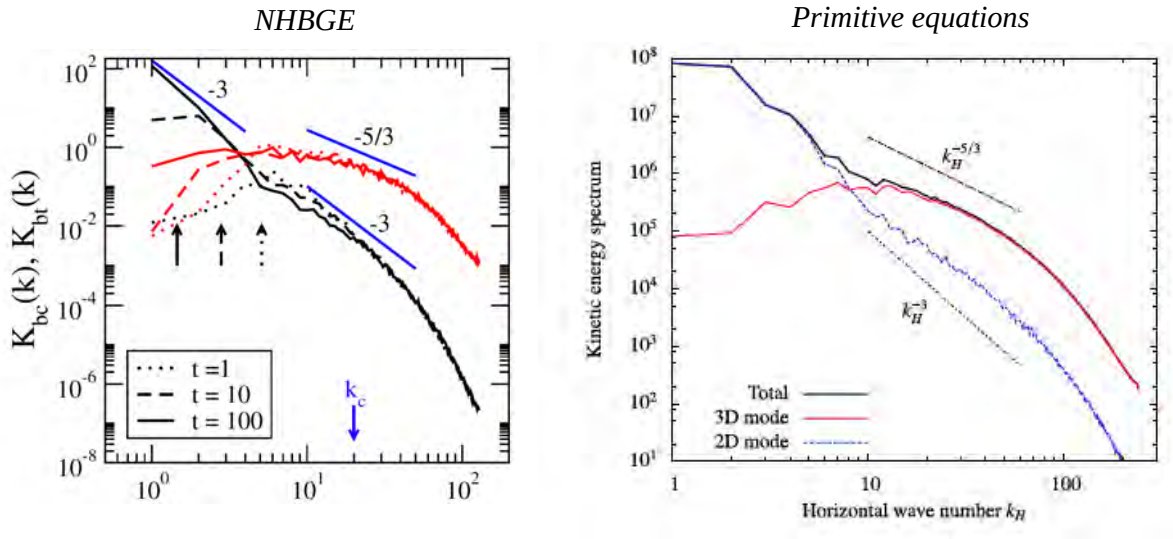

Figure 3: Energy spectra for the NGBGE (left) and primitive equations (right). Here $K_{\rm bc}$ and $K_{\rm bt}$ correspond to the baroclinic and barotropic spectra, respectively. (Figure adapted from [2]).

contrast to nonrotating RB convection, where the core loses stability first and boundary layer instabilities only occur at Rayleigh numbers that are at least an order of magnitude larger than the onset value.

The rapid rotation limit induces stiffness along the axis of rotation, which significantly changes the heat transport properties of low-Rossby number convection from the nonrotating case in the large $\mathcal{R}$ regime. When $Ra \gg Ra_c$, we anticipate a self-similar structure in the thermal boundary layer where all variables scale with some power of $\mathcal{R}$, and thus introduce the scaling

$$\tau = \mathcal{R}^{\hat{\tau}} t, \quad \eta = \mathcal{R}^{\hat{\eta}} Z, \quad \lambda = \mathcal{R}^{\hat{\lambda}} \boldsymbol{x}_\perp, \quad \psi = \mathcal{R}^{\hat{\psi}} \boldsymbol{\Psi},$$
$$\omega = \mathcal{R}^{\hat{\psi}+2\hat{\lambda}} \Omega, \quad w = \mathcal{R}^{\hat{w}} W, \quad \theta = \mathcal{R}^{\hat{\theta}} \Theta, \quad \partial_Z \overline{T} = \mathcal{R}^{\hat{\eta}-\Delta} \partial_\eta \overline{T_\epsilon}.$$

Simulations indicate that all boundary layer variables remain comparable in magnitude even at $\mathcal{R} \gg \mathcal{R}_c$, which gives us the following relations between the exponents

$$\hat{\lambda} = \hat{w} = s, \quad \hat{\eta} = 3s, \quad \hat{\tau} = \hat{\omega} = 2s, \quad \Delta = 1 - s, \quad \hat{\psi} = 0, \quad \hat{\theta} = 3s - 1.$$

Based on our earlier definition of the Nusselt number, this gives

$$Nu \sim \mathcal{R}^{4s-1}. \tag{24}$$

Using numerical simulations to determine s yields $Nu \sim \mathcal{R}^{3/2}$, which implies $s = 5/8$ (see figure 5)[5]. We can also arrive at this result independently using theoretical arguments: we start with the general scaling law for the Nusselt number at large Ra

$$Nu - 1 \sim C(\sigma) Ra^\alpha Ek^\beta. \tag{25}$$

In the nonrotating case, $\beta = 0$, and experimental results indicate $0.28 < \alpha < 0.31$. The mean temperature gradient in the bulk vanishes for large Ra, which implies that the Nusselt

[5]This asymptotic large $\mathcal{R}$ scaling is only valid as long as we are in the geostrophic turbulence regime, i.e., the Prandtl number also needs to be appropriately small.

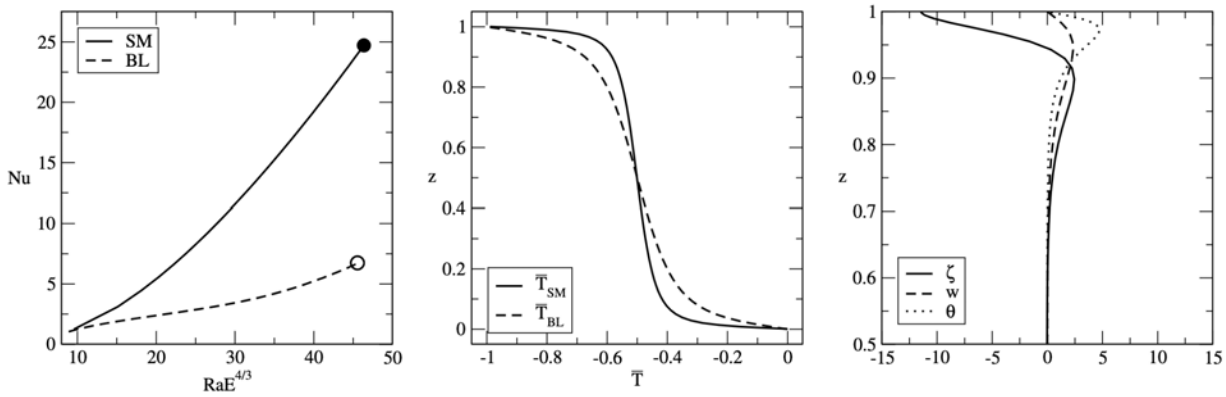

Figure 4: (Left) Nusselt number Nu scaling with $\mathcal{R}$ for single-mode (SM) convection and for the boundary layer (BL). (Middle) Mean temperature profiles for single-mode convection (filled circle) and the boundary layer (open circle) when the BL loses stability. (Right) Boundary layer instability, even where profiles are stable in the core of the flow. Here ζ is the vertical vorticity. (From [7]).

number is determined by the heat flux across the thermal boundary layers, which take up most of the temperature gradient.

For large Rayleigh numbers in the rotating case, we expect Nu to depend only on Ra/Ra_c ($= \mathcal{R}$), i.e., $Nu - 1 \propto \mathcal{R}^\alpha$. Using Kolmogorov-like scaling arguments and assuming that the heat flux is independent of microscopic diffusion coefficients ν and κ, we get

$$Nu - 1 \sim C_1 \sigma^{-1/2} Ra^{3/2} Ek^2, \tag{26}$$

matching with the numerical results from figure 5. The reduced efficiency of the geostrophic turbulence regime ($\alpha = 3/2$) compared to the (larger Pr) convective Taylor column regime ($\alpha \approx 2$) implies that the turbulent interior throttles the heat transport, in contrast to nonrotating RBC where the boundary layers are the bottleneck for transport efficiency. At large $\mathcal{R}$, the mean temperature gradient at midheight *saturates* instead of vanishing as in the nonrotating case. Along with the boundary layer thickness shrinking with $\mathcal{R}$, this leads to the interior taking up most of the temperature gradient, and thus determining the Nusselt number. We have numerical evidence for heat transport in the rapidly rotating case being controlled by the turbulent transport in the interior (see figure 5).

- **Barotropic vortices and jet formation.** The NHBG geostrophic turbulence regime is unstable to the formation of domain-scale barotropic vortices via a strong inverse cascade fed by the baroclinic fluctuations. Increasing the horizontal aspect ratio (going from a square to a rectangular domain) leads to the formation of jet-like structures. In the case of the square domain, the barotropic large scale vortex (see figure 6) transitions to unidirectional depth-invariant jet flows when L_x/L_y is increased.

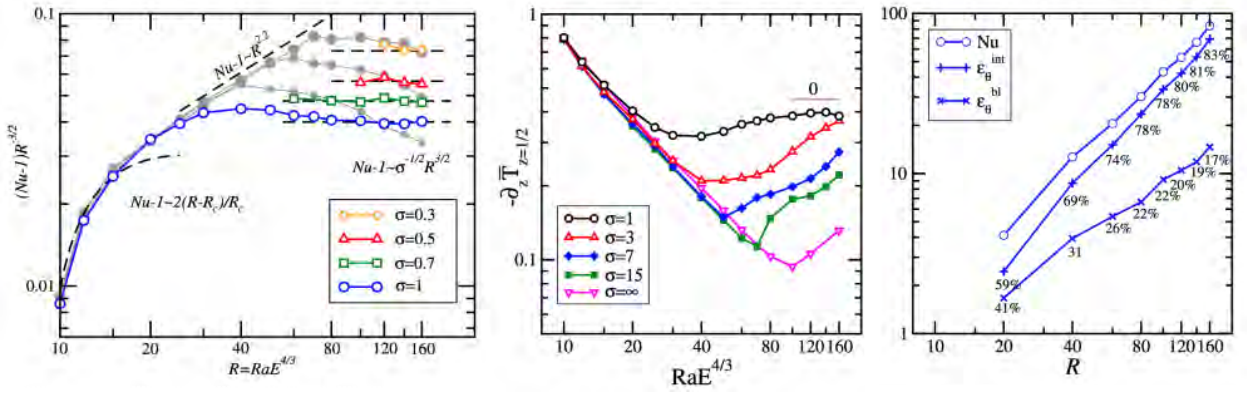

Figure 5: (Left) Simulation results of $Nu-1$ scaling with $\mathcal{R}$. Curves for high $\mathcal{R}$ exhibit the predicted scaling of $\propto \mathcal{R}^{3/2}$ within 6% (from [5]). (Middle) Midheight gradient saturating at large $\mathcal{R}$ for the $Pr = 1$ case (from [7]). (Right) Contributions (in percentage form) to the Nusselt number from the bulk ($\mathcal{E}_\theta^{\text{int}}$) and from the boundary layer ($\mathcal{E}_\theta^{\text{bl}}$). At higher $\mathcal{R}$, a larger contribution comes from the interior indicating that Nu is limited by the ability of the bulk to transport heat (from [5]).

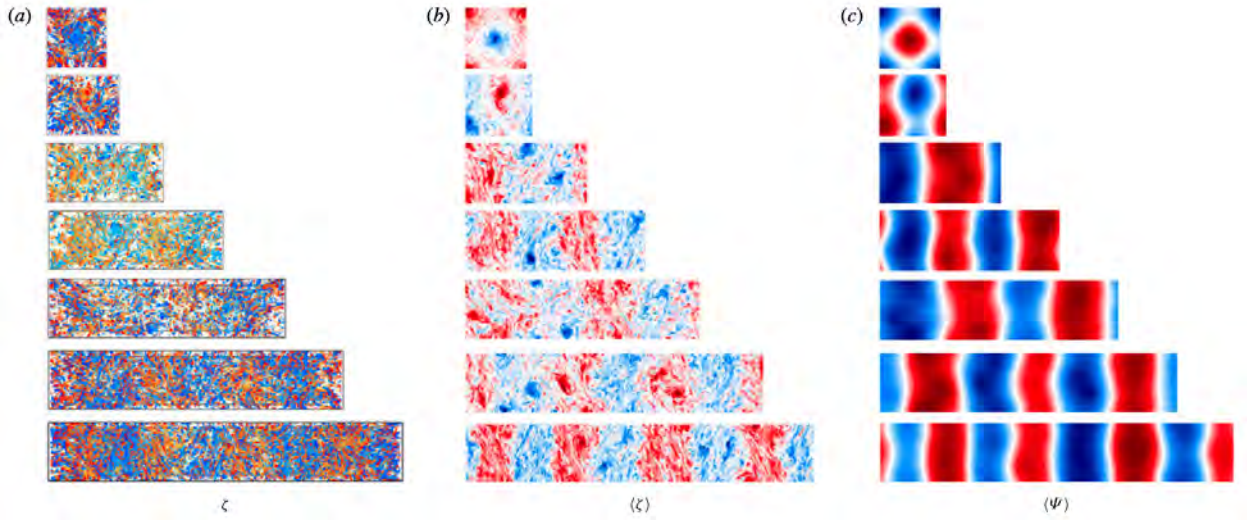

Figure 6: Jet formation is observed in the presence of domain anisotropy. There is a characteristic wavelength associated with the jets. (Figure adapted from [4]).

References

[1] S. Chandrasekhar, *Hydrodynamic and Hydromagnetic Stability*, Clarendon Press, 1968.

[2] B. Favier, L. J. Silvers, and M. R. E. Proctor, *Inverse cascade and symmetry breaking in rapidly rotating [b]oussinesq convection*, Physics of Fluids, 26 (2014), p. 096605.

[3] K. Julien and E. Knobloch, *Reduced models for fluid flows with strong constraints*, Journal of Mathematical Physics, 48 (2007), p. 065405.

[4] K. Julien, E. Knobloch, and M. Plumley, *Impact of domain anisotropy on the inverse cascade in geostrophic turbulent convection*, Journal of Fluid Mechanics, 837 (2018), p. R4.

[5] K. Julien, E. Knobloch, A. M. Rubio, and G. M. Vasil, *Heat transport in low-Rossby-number Rayleigh-Bénard convection*, Phys. Rev. Lett., 109 (2012), p. 254503.

[6] K. Julien, E. Knobloch, and J. Werne, *A new class of equations for rotationally constrained flows*, Theoretical and Computational Fluid Dynamics, 11 (1998), pp. 251–261.

[7] K. Julien, A. M. Rubio, I. Grooms, and E. Knobloch, *Statistical and physical balances in low Rossby number Rayleigh–Bénard convection*, Geophysical & Astrophysical Fluid Dynamics, 106 (2012), pp. 392–428.

[8] L. M. Smith and F. Waleffe, *Transfer of energy to two-dimensional large scales in forced, rotating three-dimensional turbulence*, Physics of Fluids, 11 (1999), pp. 1608–1622.

GFD 2024 Lecture 5: Reduced Description of Fingering and Parametric Instabilities

Edgar Knobloch; notes by Adhithiya Sivakumar and Lulabel Ruiz Seitz

June 19, 2024

Our survey of asymptotic methods and their application to the analysis of fluid flows concludes with the development of reduced models describing (a) the evolution of salt-finger turbulence in the limit where heat diffusion is rapid relative to salinity diffusion, (b) the (strongly nonlinear) saturation of the magnetorotational instability when rotational, wave-crossing, and diffusive timescales are widely separated, and (c) wave-mean flow coupling associated with nearly inviscid Faraday waves.

1 Reduced Description of Fingering Instabilities

In this section, we demonstrate the application of asymptotic (or perturbation) methods to fingering instabilities – so called due to the slender geometry (cf. Figure 1) and primarily unidirectional propagation associated with the resulting patterns. In the first case, we make use of the widely separated timescales that result in the formation of saltwater fingers to derive leading-order reduced equations governing their evolution; and in the second, we exploit the large aspect ratio of fingers in astrophysical accretion disks (formed due to an unstable angular momentum gradient) for the same purpose.

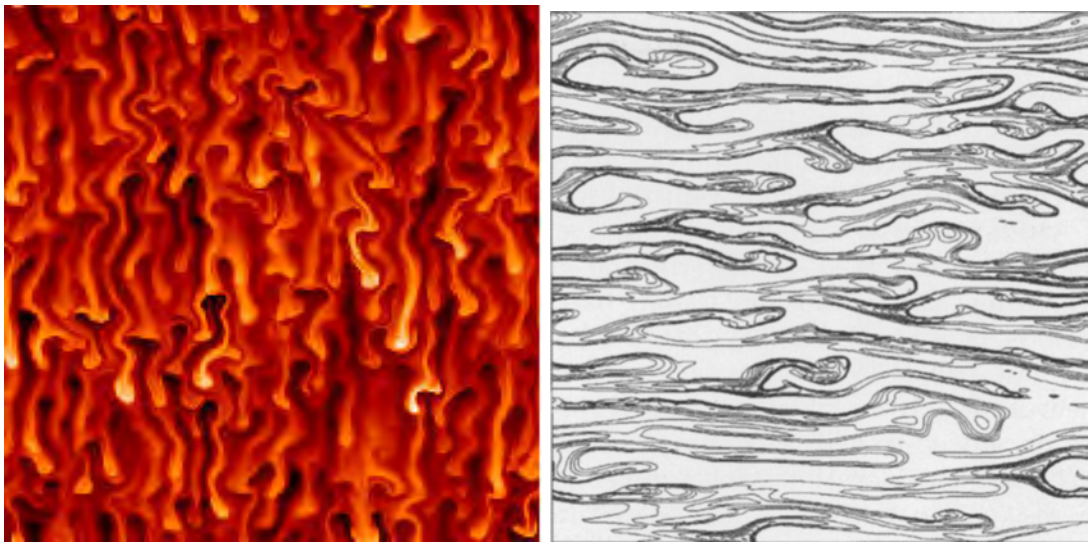

Figure 1: **Left:** DNS snapshot showing salt fingers in a strongly stratified environment. Image sourced from Ref. [14]. **Right:** Evolution of the magnetorotational instability, as shown in Ref. [6]. The horizontal axis represents the radial direction and the vertical axis the poloidal.

1.1 Salt-finger turbulence

Salt fingering is a distinct mode of double-diffusive convection that develops when a warm, saline water layer overlies a cooler, fresher one such that the overall configuration has a stable stratification of density. The density depends on two diffusing scalars which exert opposing effects: temperature reduces density while salinity increases it. More pertinently, one of these scalars diffuses faster than the other: thermal diffusivity is nearly two orders of magnitude larger than saline diffusivity. As thermal energy leaks downward through the interface, the upper layer is stripped of buoyancy while the lower layer gains it. Gravity seizes on this transient imbalance, driving salt-rich parcels at the top to sink and salt-poor parcels at the bottom to rise. The exchange generates plumes which sharpen into tall, slender tendrils – salt fingers – that convey salt downward and fresh water upward. This much is describable via heuristics. A more precise description of the instability and resulting dynamics requires analysis of the governing equations.

1.1.1 Mathematical formulation

A simple model that exhibits salt-fingering is the 2D Boussinesq system, summarized below.

$$\nabla \cdot \boldsymbol{u} = 0, \tag{1}$$

$$\partial_t \boldsymbol{u} + \boldsymbol{u} \cdot \nabla \boldsymbol{u} = -\rho_0^{-1} \nabla p - \frac{\rho g}{\rho_0} \hat{\boldsymbol{k}} + \nu \nabla^2 \boldsymbol{u}, \tag{2}$$

$$\partial_t T + \boldsymbol{u}.\nabla T = \kappa_T \nabla^2 T, \tag{3}$$

$$\partial_t S + \boldsymbol{u}.\nabla S = \kappa_S \nabla^2 S, \tag{4}$$

$$\rho\left(T, S\right) = \rho_0 \left[1 + \alpha_S \left(S - S_0\right) - \alpha_T (T - T_0)\right]. \tag{5}$$

Here $\boldsymbol{u} \equiv (u, w)^T$ is the incompressible Eulerian velocity field; T and S are the temperature and salinity fields, which both modify the density field ρ in accordance with equation (5). T_0 and S_0 are reference values of temperature and salinity, and the reference density $\rho_0 = \rho\left(T_0, S_0\right)$. The positive constants α_S and α_T determine the magnitude of density variation in response to salinity and temperature variation, while κ_S and κ_T determine the diffusivity of salinity and temperature. Finally, g is the acceleration due to gravity and ν is the molecular kinematic viscosity. All fields are functions of the spatial coordinates $\boldsymbol{x} \equiv (x, z)^T$ and time t, and the spatial domain is a plane of infinite extent.

The incompressibility constraint (1) makes $\boldsymbol{u}$ expressible in terms of a streamfunction $\psi = \psi\left(\boldsymbol{x}, t\right)$ such that $\boldsymbol{u} \equiv \nabla \times \psi \hat{\boldsymbol{j}}$ and allows the momentum equation (2) to be recast as an equation for the evolution of the out-of-plane vorticity $\nabla \times \boldsymbol{u} = -\nabla^2 \psi$. Moreover, the temperature and salinity fields may be decomposed into background profiles and departures from them (θ, s):

$$T\left(\boldsymbol{x}, t\right) \equiv \beta_T z + \theta\left(\boldsymbol{x}, t\right), \tag{6}$$

$$S\left(\boldsymbol{x}, t\right) \equiv \beta_S z + s\left(\boldsymbol{x}, t\right). \tag{7}$$

Here β_T and β_S are positive constants that produce the desired configuration: a stabilizing background temperature profile and a destabilizing salinity profile – in other words, warm, salty water over cold, fresh water. The configuration is statically stable provided the background density has a negative vertical gradient, i.e.,

$$\alpha_S \beta_S - \alpha_T \beta_T < 0. \tag{8}$$

This condition can be recast in terms of the density ratio $R_\rho \equiv \alpha_T\beta_T/\alpha_S\beta_S$ as $R_\rho > 1$. The modifications detailed above, when applied to the system (1)-(5), result in

$$\partial_t\nabla^2\psi + J\left[\psi,\nabla^2\psi\right] = g\left(\alpha_T\partial_x\theta - \alpha_S\partial_x s\right) + \nu\nabla^4\psi, \tag{9}$$

$$\partial_t\theta + J\left[\psi,\theta\right] + \beta_T\partial_x\psi = \kappa_T\nabla^2\theta, \tag{10}$$

$$\partial_t s + J\left[\psi, s\right] + \beta_S\partial_x\psi = \kappa_S\nabla^2 s, \tag{11}$$

$$\tag{12}$$

where $J\left[A,B\right] \equiv \partial_x A\partial_z B - \partial_x B\partial_z A$. These equations describing the evolution of perturbations (ψ,θ,s) to the stationary background configuration $(0,\beta_T z,\beta_S z)$.

1.1.2 Preliminary scaling

Following the discussion in Chapter 1 of Ref. [15] we can develop an expression

$$d = \left(\frac{\nu\kappa_T}{g\alpha_T\beta_T}\right)^{1/4}$$

for the natural salt-finger width d. Certain scaling assumptions are made – namely that in steady state, there exists a balance between the horizontal density gradient and vorticity diffusion in (9), and that salinity and temperature have comparable effects on the density anomaly. Scaling distances with d allows us to define natural temperature and salinity scales

$$\theta \sim \beta_T d,$$
$$s \sim \beta_S d.$$

Time can be rendered dimensionless using the salinity diffusion timescale d^2/κ_S and thus velocities using κ_S/d. Applying these scales to the equations (9)-(11) produces the dimensionless equations

$$\frac{\tau}{Pr}\left(\partial_t\nabla^2\psi + J\left[\psi,\nabla^2\psi\right]\right) = \frac{1}{\tau}\partial_x\theta - \frac{1}{R_\rho\tau}\partial_x s + \nabla^4\psi, \tag{13}$$

$$\partial_t\theta + J\left[\psi,\theta\right] + \partial_x\psi = \tau^{-1}\nabla^2\theta, \tag{14}$$

$$\partial_t s + J\left[\psi, s\right] + \partial_x\psi = \nabla^2 s, \tag{15}$$

where the Prandtl number $Pr \equiv \nu/\kappa_T$ and the diffusivity ratio (or inverse Lewis number) $\tau \equiv \kappa_S/\kappa_T$. Note that we may also formulate these equations in terms of the Schmidt number $Sc \equiv Pr\,\tau^{-1}$ instead of Pr or τ.

1.1.3 Linear heory

First, we add infinitesimal perturbations to the trivial solution of the system (13)-(15). This justifies neglecting quadratic nonlinearities. The normal mode ansatz $\phi(\boldsymbol{x},t) \equiv \hat{\phi}\exp\left(\lambda t + i\boldsymbol{k}\cdot\boldsymbol{x}\right) + \text{c.c.}$, where $\boldsymbol{k} \equiv (k,m)^T \in \mathbb{R}^2$, can then be applied to the linearized system, yielding

$$-\lambda\frac{\tau}{Pr}\left|\boldsymbol{k}\right|^2\hat{\psi} = ik\left(\frac{1}{\tau}\hat{\theta} - \frac{1}{R_\rho\tau}\hat{s}\right) + \left|\boldsymbol{k}\right|^4\hat{\psi}, \tag{16}$$

$$\lambda\hat{\theta} + ik\hat{\psi} = -\tau^{-1}\left|\boldsymbol{k}\right|^2\hat{\theta}, \tag{17}$$

$$\lambda\hat{s} + ik\hat{\psi} = -\left|\boldsymbol{k}\right|^2\hat{s}. \tag{18}$$

For specified $\boldsymbol{k}$, this is a linear eigenvalue problem in $\lambda \in \mathbb{C}$ with three possible solutions. The real part of λ represents the growth rate of the associated eigenfunction and the imaginary part represents its oscillation frequency. The characteristic polynomial for λ is cubic:

$$\lambda^3 + \lambda^2 |\boldsymbol{k}|^2 \left[1 + \frac{1}{\tau} + \frac{Pr}{\tau}\right] + \lambda \left[\frac{|\boldsymbol{k}|^4}{\tau}\left(1 + Pr + \frac{Pr}{\tau}\right) + \frac{k^2}{|\boldsymbol{k}|^2}\frac{Pr}{\tau^2}\left(1 - \frac{1}{R_\rho}\right)\right] + \frac{Pr}{\tau^2}\left[|\boldsymbol{k}|^6 + k^2\left(1 - \frac{1}{\tau R_\rho}\right)\right] = 0. \quad (19)$$

The equation above is invariant under the transformation

$$\lambda' = a\lambda, \quad \left|\boldsymbol{k'}\right|^2 = a\,|\boldsymbol{k}|^2, \quad k'^2 = a^3 k^2,$$

for some positive constant a. Choosing $a = |\boldsymbol{k}|\,/k \geq 1$ above yields the result

$$\left|\boldsymbol{k'}\right|^2 = k'^2 \implies m' = 0.$$

Thus, any wave-vector $\boldsymbol{k}$ can be mapped onto another wave-vector representing a vertically uniform *elevator* mode. This means that we may let $m = 0$ in (18) without loss of generality. Further, the eigenvalue λ of the untransformed problem obeys

$$\lambda = \lambda'/a \leq \lambda' \text{ for } a \geq 1,$$

with equality attained only when $a = 1$, or, equivalently, $m = 0$. Thus, the elevator mode growth rate is larger than that of other modes. Taking $m = 0$ in (19) produces

$$\lambda^3 + \lambda^2 k^2 \left[1 + \frac{1}{\tau} + \frac{Pr}{\tau}\right] + \lambda \left[\frac{k^4}{\tau}\left(1 + Pr + \frac{Pr}{\tau}\right) + \frac{Pr}{\tau^2}\left(1 - \frac{1}{R_\rho}\right)\right] + \frac{Pr\,k^2}{\tau^2}\left[k^4 + 1 - \frac{1}{\tau R_\rho}\right] = 0. \quad (20)$$

Given that the salt-fingering instability is expected to be stationary – i.e., it has $\Im(\lambda) = 0$, we may develop an instability criterion by setting $\lambda = 0$ in equation (20). This yields the relation

$$\frac{1}{\tau R_\rho} - 1 = k^4, \quad (21)$$

which has roots $k \in \mathbb{R}$ provided the left-hand side is positive, i.e.,

$$R_\rho < \tau^{-1}. \quad (22)$$

The pure salt-fingering regime is therefore characterized by

$$1 < R_\rho < \tau^{-1}. \quad (23)$$

1.1.4 Asymptotic reduction in the small diffusivity ratio limit

Motivated by the fact that in the ocean, the diffusivity ratio $\tau = O\,(0.01)$, we analyze the governing equations (13)-(15) in the limit $\tau \ll 1$, or equivalently, $\kappa_S \ll \kappa_T$ – where heat diffuses much more rapidly than salinity. Two approximations are developed, distinguished by the scaling of the Schmidt number (Sc) with τ:

1. $\mathbf{Sc} = \mathbf{O(1)}$, which requires small $Pr = O(\tau)$, as is seen in many astrophysical systems. This results in a modified Rayleigh-Bénard system with salinity-driven instability and a rapidly diffusing temperature.

2. $\mathbf{Sc} \gg \mathbf{1}$, which requires $Pr \gg \tau$, as in oceanic thermohaline flows. Here $\kappa_S \ll \nu$, meaning that we expect momentum/vorticity to diffuse almost instantaneously on the long salinity diffusion timescale. The reduced system has this property, and is referred to as the inertia-free salt convection model.

The specification of a distinguished limit requires a scaling law for R_ρ as $\tau \to 0$. We take $R_\rho = O\left(\tau^{-1}\right)$, a hypothesis appropriate for astrophysical, oceanographic, and experimental measurements [19]. The parameter

$$\frac{1}{R_\rho \tau} \equiv Ra$$

therefore remains $O(1)$ as $\tau \to 0$. The rapid diffusion of heat makes temperature fluctuations small, so $\theta \mapsto \tau\theta$ as $\tau \to 0$. Salinity fluctuations remain finite in this limit, but the transformation $s \mapsto Ra^{-1}s$ is applied for convenience. Note that the rescaled temperature and salinity are $O(1)$ quantities in the small diffusivity ratio limit. The rescaled governing equations are given below:

$$Sc^{-1}\left(\partial_t \nabla^2\psi + J\left[\psi, \nabla^2\psi\right]\right) = \partial_x\theta - \partial_x s + \nabla^4\psi, \tag{24}$$

$$\tau\left(\partial_t\theta + J\left[\psi,\theta\right]\right) + \partial_x\psi = \nabla^2\theta, \tag{25}$$

$$\partial_t s + J\left[\psi, s\right] + Ra\partial_x\psi = \nabla^2 s. \tag{26}$$

Modified Rayleigh-Bénard Convection (mRBC) Model: When applied to the equations (24)-(26), the first distinguished limit $\tau \to 0$, $Sc = O(1)$, $Ra = O(1)$ produces at leading order in τ:

$$Sc^{-1}\left(\partial_t \nabla^2\psi + J\left[\psi, \nabla^2\psi\right]\right) = \partial_x\theta - \partial_x s + \nabla^4\psi, \tag{27}$$

$$\partial_x\psi = \nabla^2\theta, \tag{28}$$

$$\partial_t s + J\left[\psi, s\right] + Ra\partial_x\psi = \nabla^2 s. \tag{29}$$

Note the slaving of the temperature anomaly to the vertical velocity. This tends to be a robust feature of systems operating on multiple timescales: fast processes are slaved to slow processes over the slow timescale. Under appropriate boundary conditions, e.g., doubly periodic BCs, the Laplacian operator in equation (28) can be inverted, enabling the system (27)-(29) to be rewritten as

$$Sc^{-1}\left(\partial_t \nabla^2\psi + J\left[\psi, \nabla^2\psi\right]\right) = -\partial_x s + \left(\nabla^4 + \nabla^{-2}\partial_{xx}\right)\psi, \tag{30}$$

$$\partial_t s + J\left[\psi, s\right] + Ra\partial_x\psi = \nabla^2 s. \tag{31}$$

This is the mRBC model. The salient feature of this model is the formal similarity to the Rayleigh-Bénard convection (RBC) model, apart from the presence of large-scale thermal dissipation (manifested in the inverse Laplacian) in addition to small-scale molecular dissipation of vorticity. This enables the mRBC system (30)-(31) to select an intrinsic length scale, like the primitive salt-fingering equations (24)-(26), and unlike the equations governing RBC.

Inertia-Free Salt Convection (IFSC) Model: Taking the limit $Sc \to \infty$ in the mRBC equations (30)-(31) yields the IFSC model

$$\left(\nabla^6 + \partial_{xx}\right)\psi = \partial_x \nabla^2 s, \tag{32}$$

$$\partial_t s + J\left[\psi, s\right] + Ra\partial_x \psi = \nabla^2 s \tag{33}$$

at leading order. The system (32)-(33) is first order in time – featuring a prognostic equation (33) for the evolution of salinity on its diffusive timescale coupled with a diagnostic equation for the streamfunction (32) – and is dependent only on a single parameter Ra. It is thus the simplest derivable model for salt-finger convection [19]. The ∇^6 and ∂_{xx} terms are dominant on different horizontal scales and may thus give rise to dynamics on multiple spatial scales.

1.1.5 Overview of results

Ref. [19] documents stability analyses and numerical simulations of the IFSC model. That the model preserves primary and secondary linear instabilities present in the primitive equations, even in large domains is verified. It captures the three stages – finger dominance, finger disruption, and saturation – that lead to a statistically steady state. However, the oft-observed salinity staircases are not captured by the IFSC model, which may be associated with the inherent filtration of gravity waves. Ref. [18] documents the validation and analysis of the mRBC model. It is demonstrated that this model evolves towards a structure consisting of horizontal jets that disrupt salt-finger turbulence. Understanding of the jet-formation mechanism is achieved using further-reduced models: a quasilinear approximation of the mRBC system and a single-mode reduction. These issues are explored in Refs. [12] and [5].

1.2 Magneto-rotational instability

> The classical problem with accretion disks is that they do of course accrete.
>
> Balbus [3]

Accretion disks are flat, rapidly rotating structures formed by diffuse interstellar or intergalactic matter orbiting around and spiraling onto a massive central body. The inward spiraling of matter in accretion disks requires not only the loss of gravitational potential energy but also of *angular momentum*. Further, since the total angular momentum of the disk is conserved, the loss of angular momentum from matter falling into the gravitational center must be compensated by a gain in angular momentum towards the periphery of the disk, i.e., angular momentum must be transported outwards. One might imagine that some form of turbulence might aid the redistribution of angular momentum, but how exactly this turbulence might be driven was a matter of some debate. That the angular momentum of an accretion disk increases radially outward (making it centrifugally stable) rules out the possibility of a purely hydrodynamic instability mechanism. The addition of a weak, poloidal (meridional) magnetic field, however, can drive a magnetorotational instability (MRI) which is now thought to play a central role in this process [3].

A simple physical picture of the instability mechanism may be obtained by analogy with two masses in orbit around a third massive object. These masses occupy different radial positions relative to the central object, are connected by a weak spring, and the inner mass has a larger angular velocity (but lower angular momentum) than the outer mass. The disparate angular momenta of the masses produce a torque on the spring, whose restoring torque is such that the inner mass

loses angular momentum, which the outer mass gains. The inner mass thus moves closer to the gravitational center, and the outer mass moves further away, increasing the tension on the spring, and "the process runs away" [3]. The instability thus grows by feeding on the shearing of matter in the accretion disk and takes the form of thin sheets (fingers) of lower and higher angular momentum moving alternately inward and outward in the radial direction [10].

1.2.1 Classical formulation and linear theory

The instability may be studied within a magnetohydrodynamic (MHD) framework. Equations governing the motion of electrically conducting, non-magnetic fluids, e.g., liquid metals and plasmas, are given below.

$$\partial_t \boldsymbol{u} + \boldsymbol{u}\cdot\nabla\boldsymbol{u} = -\frac{1}{\rho}\nabla p + \nu\nabla^2\boldsymbol{u} - \frac{1}{2\mu_0\rho}\nabla B^2 + \frac{1}{\mu_0\rho}\boldsymbol{B}\cdot\nabla\boldsymbol{B}, \tag{34}$$

$$\partial_t \boldsymbol{B} + \boldsymbol{u}\cdot\nabla\boldsymbol{B} = \boldsymbol{B}\cdot\nabla\boldsymbol{u} + \eta\nabla^2\boldsymbol{B}, \quad \nabla\cdot\boldsymbol{u} = 0, \quad \nabla\cdot\boldsymbol{B} = 0. \tag{35}$$

We have here, in addition to the variables introduced previously, the solenoidal magnetic field $\boldsymbol{B}(\boldsymbol{x},t)$, its magnitude $B \equiv ||\boldsymbol{B}||_2$ (where $||\cdot||_2$ refers to the vector two-norm), the vacuum permeability μ_0, and the magnetic diffusivity η. The other variables retain their definitions apart from the stipulation that they are now three-dimensional, unless otherwise specified. The MRI is studied most easily in the limit of a non-diffusive flow, the equations for which are obtained by taking $\nu = \eta = 0$ in the equations (34)-(35). The ideal equations thus obtained have axisymmetric exact solutions of the form

$$\boldsymbol{u}_0 = (0, V(r), 0)^T, \quad \boldsymbol{B}_0 = (0, B_\phi(r), B_z(r))^T,$$

in cylindrical polar coordinates (r,ϕ,z), with $r \in [r_i, r_o]$. Following Ref. [9], infinitesimal perturbations to this state are written $\boldsymbol{u} = (u,v,w)^T$, $\boldsymbol{b} = (a,b,c)^T$ with each of the perturbation fields of the form $f(r,\phi,z,t) \equiv f(r)\exp[i(nz+\omega t)]$. Linearizing the ideal MHD equations yields an eigenvalue problem for the frequency $\omega \in \mathbb{C}$,

$$\frac{d}{dr}\left[\left(\omega^2 - n^2V_z^2\right)\left(\frac{du}{dr} + \frac{u}{r}\right)\right] - n^2\left[\omega^2 - n^2V_z^2 + r\frac{d}{dr}\left(\frac{V_\phi^2}{r^2} - \frac{V^2}{r^2}\right)\right]u = -\frac{4n^2\left(nV_\phi V_z + \omega V\right)^2}{r^2\left(\omega^2 - n^2V_z^2\right)}u, \tag{36}$$

where

$$V_\phi \equiv B_\phi/\sqrt{\mu_0\rho}, \text{ and } V_z \equiv B_z/\sqrt{\mu_0\rho}$$

are the Alfvén speeds associated with the imposed azimuthal and vertical magnetic fields, and $-\Im[\omega]$ represents the linear growth rate of the perturbation. Eigenfunctions may either be localized at the radial boundaries (and thus depend strongly on boundary conditions) or may extend across the disk (and only have a weak dependence on boundary conditions). MRI eigenfunctions are an example of the latter. Below, we briefly outline solutions to equation (36) in two different cases.

Case I, Standard MRI: Here, we impose the condition $u(r_i) = u(r_o) = 0$, and take $V_z =$ constant $\neq 0$, $V_\phi = 0$ above. Multiplying equation (36) by u^* – the complex conjugate of u – and integrating by parts, we get

$$\left(\omega^2 - n^2V_z^2\right)^2 = \frac{n^2}{D}\int_{r_i}^{r_o}\left[\frac{\omega^2}{r^2}\frac{d}{dr}r^2V^2 - r^2n^2V_z^2\frac{d}{dr}\left(\frac{V^2}{r^2}\right)\right]|u|^2\,dr, \tag{37}$$

where

$$D \equiv \int_{r_i}^{r_o} \left[r \left| \frac{du}{dr} \right|^2 + \frac{|u|^2}{r} + n^2 r \, |u|^2 \right] dr > 0.$$

Equation (37) is quadratic in ω^2 and has the form

$$\omega^4 - \omega^2 n^2 \left(2V_z^2 + \mathcal{G}_1 \right) + n^4 \left(V_z^4 + V_z^2 \mathcal{G}_2 \right) = 0,$$

where $\omega^2 n^2 \mathcal{G}_1$ is the first term on the right-hand side of (37) and $-n^4 V_z^2 \mathcal{G}_2$ is the second. It can be seen that its discriminant

$$\Delta_q \equiv \mathcal{G}_1^2 + \frac{16 V_z^2}{D} \int_{r_i}^{r_o} \frac{|u|^2 \, V^2}{r} \, dr > 0,$$

and thus $\omega^2 \in \mathbb{R}$. It follows that a magnetized disk is linearly stable provided $\omega^2 > 0$. Thus, for a hydrodynamically stable disk, i.e., one in which

$$\frac{d}{dr} \left(V^2 r^2 \right) > 0,$$

a sufficient condition for the stability of the previously defined basic state is

$$n^2 \left(2V_z^2 + \mathcal{G}_1 \right) \pm \sqrt{\Delta_q} > 0 \implies \frac{d}{dr} \left(\frac{V^2}{r^2} \right) > 0$$

for all $r \in (r_i, r_o)$, i.e., for hydrodynamic stability the angular momentum must increase outwards. This provides a *necessary* condition for instability:

$$\frac{d}{dr} \left(\frac{V^2}{r^2} \right) < 0$$

at some $r \in (r_i, r_o)$, i.e., the angular velocity must decrease outwards. Keplerian accretion disks, for instance, being thin and lacking self-gravity, spin in a gravity field that is predominantly set by the central mass. The angular velocity is given by Kepler's laws of orbital motion, i.e., $V(r) \sim 1/\sqrt{r}$, which can be shown to simultaneously satisfy the conditions for both hydrodynamic stability and MRI.

Case II, helical MRI: Differential rotation accross an accretion disk always generates an azimuthal magnetic field from an imposed vertical magnetic field, hence we repeat the analysis performed above but take $V_z = \text{constant} \neq 0$, $V_\phi \neq 0$. This results in the identity

$$\frac{d}{dr} \left(r \frac{du}{dr} \right) - \frac{u}{r} - n^2 r u$$
$$= \frac{n^2}{\left(\omega^2 - n^2 V_z^2 \right)^2} \left[r^2 \frac{d}{dr} \left(\frac{V_\phi^2 - V^2}{r^2} \right) \left(\omega^2 - n^2 V_z^2 \right) - \frac{4}{r} \left(n V_\phi V_z + \omega V \right)^2 \right] u. \quad (38)$$

Here, exponentially growing perturbations are only possible if (Ref. [9])

$$\int_{r_i}^{r_o} \frac{1}{r} V_\phi V_z \, |u|^2 \, dr = 0,$$

i.e., V_ϕ or V_z (or both) need to change sign at some point across the accretion disk. If not, the instability takes the form of growing axisymmetric waves with a preferred direction of propagation in the vertical direction. This is a consequence of fact that the product $V_\phi V_z \neq 0$ determines the sign of the magnetic field helicity – and thus robs the problem of its invariance (relative to the previous case) under the reflection $z \to -z$.

1.2.2 Saturation of the MRI

Astrophysical applications require estimation of the amplitude at which the MRI saturates in an accretion disk, which in turn enables estimation of the efficiency of angular momentum transport. Sufficient numerical dissipation is known to result in saturation of the MRI [1], however, dissipative processes are generally weaker (though non-negligible) than required in accretion disks [8]. In the astrophysical context, the MRI is believed to saturate by generating turbulence, which enhances dissipation and quenches the instability. Here, the background shear is maintained by the gravitational field of the central object and accretion disk turbulence is too weak to perturb it. This, however, is not the case in experimental studies of the MRI – where the radial boundaries can support pressure gradients that arise due to background shear modification. We explore MRI saturation in this regime using an asymptotic model that leverages the small vertical scale associated with the instability in order to explore its evolution far from threshold (i.e., in the strongly nonlinear regime).

The Shearing Sheet Approximation: Consider a straight channel for which dimensional co-ordinates[1] $\boldsymbol{x}^* = (x^*, y^*, z^*)^T$ are defined such that

$$\boldsymbol{x}^* \in [-L/2, L/2] \times \mathbb{R}^2.$$

This channel is filled with an electrically conducting incompressible fluid and rotates about the vertical axis z^* with constant angular velocity Ω_0^*. A linear shear flow $\boldsymbol{U}_0^* = (0, \sigma^* x^*, 0)^T$, with $\sigma^* < 0$, is maintained in the channel. This could be because of lateral boundaries that slide in the y^* direction with speeds $\pm 0.5\sigma^* L$ or, in the astrophysical context, a result of the shearing box approximation – where a small patch of accretion disk is studied via a local expansion of the shear profile $\Omega^*(r^*)$ about a point r_0^* – with

$$\sigma^* \equiv \left.\frac{d\Omega^*}{d\ln r^*}\right|_{r^*=r_0^*}.$$

Further, imagine that a constant magnetic field $\boldsymbol{B}_0^* = \left(0, B_\phi^*, B_z^*\right)^T$ is present. To proceed, we write down (dimensionless) equations for y^*-independent (i.e., axisymmetric) perturbations $\boldsymbol{u} \equiv (u, v, w)^T \equiv (-\psi_z, v, \psi_x)$, $\boldsymbol{b} \equiv (a, b, c)^T \equiv (-\phi_z, b, \phi_x)$ about the previously defined basic state:

$$\nabla^2\psi_t + 2\Omega v_z + J\left[\psi, \nabla^2\psi\right] = v_A^2\nabla^2\phi_z + v_A^2 J\left[\nabla^2\phi, \phi\right] + \nu\nabla^4\psi, \tag{39}$$

$$v_t - (2\Omega + \sigma)\,\psi_z + J\left[\psi, v\right] = v_A^2 b_z + v_A^2 J\left[b, \phi\right] + \nu\nabla^2 v, \tag{40}$$

$$\phi_t + J\left[\psi, \phi\right] = \psi_z + \eta\nabla^2\phi, \tag{41}$$

$$b_t + J\left[\psi, b\right] = v_z - \sigma\phi_z - J\left[v, \phi\right] + \eta\nabla^2 b. \tag{42}$$

Here

$$v_A \equiv B_z^*/U^*\sqrt{\mu_0\rho}$$

is proportional to the Alfvén speed associated with the imposed vertical (poloidal) magnetic field, and

$$\Omega \equiv \Omega_0^* L/U^*, \quad \sigma \equiv \sigma^* L/U^*, \quad \nu \equiv \nu^*/U^* L, \quad \eta \equiv \eta^*/U^* L,$$

are the dimensionless rotation rate, background shear, kinematic viscosity and ohmic diffusivity, and $J[A, B] \equiv \partial_x A\partial_z B - \partial_z A\partial_x B$. These, and all other variables are non-dimensionalized using

[1] Henceforth, all starred quantities are to be considered dimensional.

the channel width L and an as-yet-undefined velocity scale U^*. Note that the equations (39)-(42) contain no trace of the imposed toroidal (azimuthal) magnetic field B^*_ϕ, making this a two-dimensional three-component (2D-3C) model in which the velocity and magnetic fields are solenoidal in the xz-plane. This reduction is not realistic in an annulus, as previously indicated.

Asymptotic Theory: We identify three timescales: the rotation timescale, the Alfvén crossing timescale, and a dissipative timescale. The first is taken to be $O(\delta)$ relative to the second, which is itself taken to be $O(\varepsilon)$ relative to the third, where $\varepsilon, \delta \ll 1$. Next, we choose the velocity scale $U^* \equiv B^*_z/\sqrt{\mu_0 \rho} \equiv v^*_A$. A series of implications follows:

$$\begin{aligned} v_A &= 1, \\ (\eta, \nu) = (\eta^*, \nu^*)/v^*_A L &= \frac{(\eta^*, \nu^*)/L^2}{v^*_A/L} = O(\varepsilon), \\ (\Omega, \sigma) = (\Omega^*_0, \sigma^*)\, L/v^*_A &= \frac{(\Omega^*_0, \sigma^*)}{v^*_A/L} = O\left(\delta^{-1}\right). \end{aligned}$$

It is thus convenient to transform $(\Omega, \sigma) \to \delta^{-1}(\Omega, \sigma)$ and $(\eta, \nu) \to \varepsilon(\eta, \nu)$. Two distinguished limits are useful to consider: when $\varepsilon = o(\delta)$ as $\delta \to 0$, the instability saturates by modifying the background shear, but does so diffusively when $\varepsilon = O(\delta)$. To see this one must first identify the appropriate scales. Since the MRI is expected to take the form of long, thin fingers propagating in the radial (x) direction, we expect vertical derivatives to be large $\left(\partial_z \to \delta^{-1}\partial_z\right)$. Rapid rotation and consequent shear means that time derivatives are also expected to be large $\left(\partial_t \to \delta^{-1}\partial_t\right)$. Finally, the radial length of the fingers motivates the multi-scale transformation $\left(\partial_x \to \delta^{-1}\partial_x + \partial_X\right)$, where we have introduced the 'slow' length-scale $X \equiv \delta x$ to capture radial modulations to averaged quantities and also retained the 'fast' length-scale x. Rapid shearing by the azimuthal flow also suggests $(\psi, \phi) \to \varepsilon^{1/2}\delta^{1/2}(\psi, \phi)$ and $(v, b) \to \delta^{-1}(v, b)$.

Next, we decompose all fields into mean and fluctuating components, defined for a generic field f as the transformation

$$f(x, X, z, t) \to \overline{f}(X) + f'(x, X, z, t), \text{ with } \overline{\overline{f}} = \overline{f} \text{ and } \overline{f'} = 0,$$

where the overbar denotes an average over (x, z, t). Averaging equations (40)-(41) eliminates all (x, z, t) (i.e., fast) derivatives, yielding the mean azimuthal equations

$$\varepsilon^{1/2}\delta^{1/2}\overline{J_X[\psi, v]} = \varepsilon^{1/2}\delta^{1/2}v^2_A\overline{J_X[\phi, b]} + \varepsilon\delta\nu\overline{v}_{XX}, \tag{43}$$

$$\varepsilon^{1/2}\delta^{1/2}\overline{J_X[\psi, b]} = \varepsilon^{1/2}\delta^{1/2}v^2_A\overline{J_X[\phi, v]} + \varepsilon\delta\nu\overline{b}_{XX}, \tag{44}$$

where $J_X[A, B] \equiv \partial_X A\partial_z B - \partial_z A\partial_X B$. Note that the $J_x[A, B]$ terms can be written $\partial_x(A\partial_z B) - \partial_z(A\partial_x B)$, and can thus be shown to vanish upon averaging. The fluctuating equations are obtained by subtracting the mean equations from their counterparts in (39)-(42):

$$\begin{aligned} &\overline{\nabla}^2\psi'_t + (\varepsilon\delta)^{-1/2}\,2\Omega v'_z + (\varepsilon/\delta)^{1/2}J_x\left[\overline{\psi, \nabla^2\psi}\right] \\ &\qquad = v^2_A\overline{\nabla}^2\phi'_z + (\varepsilon/\delta)^{1/2}v^2_A J_x\left[\overline{\phi, \nabla^2\phi}\right] + (\varepsilon/\delta)\nu\overline{\nabla}^4\psi' + O\left((\varepsilon\delta)^{1/2}, \delta\right), \end{aligned} \tag{45}$$

$$\begin{aligned} &v'_t - (\varepsilon\delta)^{1/2}(2\Omega + \sigma)\,\psi'_z + (\varepsilon/\delta)^{1/2}\left(J_x[\psi, v] + \delta\left(J_X[\psi, v] - \overline{J_X[\psi, v]}\right)\right) \\ &\qquad = v^2_A b'_z + (\varepsilon/\delta)^{1/2}\,v^2_A\left(J_x[\phi, b] + \delta\left(J_X[\phi, b] - \overline{J_X[\phi, b]}\right)\right) + (\varepsilon/\delta)\,\nu\overline{\nabla}^2 v', \end{aligned} \tag{46}$$

$$\phi'_t + (\varepsilon/\delta)^{1/2} J_x[\psi,\phi] = \psi'_z + (\varepsilon/\delta)\,\eta\overline{\nabla}^2\phi' + O\left((\varepsilon\delta)^{1/2},\delta\right), \tag{47}$$

$$\begin{aligned} b'_t + (\varepsilon\delta)^{1/2}\sigma\phi'_z + (\varepsilon/\delta)^{1/2}\left(J_x[\psi,b] + \delta\left(J_X[\psi,b] - \overline{J_X[\psi,b]}\right)\right) \\ = v'_z + (\varepsilon/\delta)^{1/2} v_A^2\left(J_x[\phi,v] + \delta\left(J_X[\phi,v] - \overline{J_X[\phi,v]}\right)\right) + (\varepsilon/\delta)\,\eta\overline{\nabla}^2 b', \end{aligned} \tag{48}$$

where $J_x[A,B] \equiv \partial_x A\partial_z B - \partial_z A\partial_x B$ and $\overline{\nabla} \equiv (\partial_x, 0, \partial_z)^T$. We now posit the expansion

$$f(x,X,z,t;\varepsilon,\delta) = \sum_{i=0}^{\infty}\sum_{j=0}^{\infty}\varepsilon^{i/2}\delta^{j/2} f_{ij}(x,X,z,t)$$

and analyze equations (43)-(48) order by order. At $O\left(\delta^{-1/2}\right)$, we get, from equation (45), that $v'_{10,z} = 0$. Using this in equations (46) and (48) at $O\left(\varepsilon^{1/2}\right)$ allows us to conclude that $b'_{10} = v'_{10} = 0$. Next, from equations (46) and (48) at $O\left(\delta^{j/2}\right)$, $j > 0$, we get the relations

$$\begin{aligned} v'_{0j,t} &= v_A^2 b'_{0j,z}, \\ b'_{0j,t} &= v'_{0j,z}. \end{aligned}$$

These are self-contained linear PDEs representing Alfvén waves propagating in the vertical direction. Non-trivial balances occur at $O(1)$ in equations (45) and (47) and at $O\left(\varepsilon^{1/2}\delta^{1/2}\right)$ in equations (46) and (48). The resulting reduced equations are

$$\begin{aligned} \overline{\nabla}^2\psi'_{00,t} + 2\Omega v'_{11,z} + (\varepsilon/\delta)^{1/2} J_x\left[\overline{\psi'_{00},\nabla}^2\psi'_{00}\right] \\ = v_A^2\overline{\nabla}^2\phi'_{00,z} + (\varepsilon/\delta)^{1/2} v_A^2 J_x\left[\phi'_{00},\overline{\nabla}^2\phi'_{00}\right] + (\varepsilon/\delta)\nu\overline{\nabla}^4\psi'_{00}, \end{aligned} \tag{49}$$

$$\begin{aligned} v'_{11,t} - (2\Omega + \sigma + \overline{v}_{00,X})\,\psi'_{00,z} + (\varepsilon/\delta)^{1/2} J_x\left[\psi'_{00}, v'_{11}\right] \\ = v_A^2\left(b'_{11,z} + (\varepsilon/\delta)^{1/2} J_x\left[\phi'_{00}, b'_{11}\right] - \overline{b}_{00,X}\phi'_{00,z}\right) + (\varepsilon/\delta)\,\nu\overline{\nabla}^2 v'_{11}, \end{aligned} \tag{50}$$

$$\phi'_{00,t} + (\varepsilon/\delta)^{1/2} J_x\left[\phi'_{00},\psi'_{00}\right] = \psi'_{00,z} + (\varepsilon/\delta)\,\eta\overline{\nabla}^2\phi'_{00}, \tag{51}$$

$$\begin{aligned} b'_{11,t} + (\varepsilon/\delta)^{1/2} J_x\left[\psi'_{00}, b'_{11}\right] - \overline{b}_{00,X}\psi'_{00,z} \\ = v'_{11,z} - (\sigma + \overline{v}_{00,X})\,\phi'_{00,z} + (\varepsilon/\delta)^{1/2} v_A^2 J_x\left[\phi'_{00}, v'_{11}\right] + (\varepsilon/\delta)\,\eta\overline{\nabla}^2 b'_{11}. \end{aligned} \tag{52}$$

These equations are stated incorrectly in [9]but the correct equations are given in [7]).

The above formulation, with small parameters ε and δ still present in the leading order equations, shows that the nonlinear and dissipative terms become subdominant when $\varepsilon = o(\delta)$ but are not so when $\varepsilon = O(\delta)$, and captures the feedback of the large-scale quantities $\overline{v}_{00,X}$ and $\overline{b}_{00,X}$ onto small-scale fluctuations. Examination of the mean equations (43)-(44) at $O(\varepsilon\delta)$ shows us that these quantities are locked to fluctuating quantities with

$$\begin{aligned} \nu\overline{v}_{00,XX} &= -\left(\overline{\psi'_{00,z}v'_{11}} - v_A^2\overline{\phi'_{00,z}b'_{11}}\right)_X, \\ \eta\overline{b}_{00,XX} &= -\left(\overline{\psi'_{00,z}b'_{11}} - \overline{\phi'_{00,z}v'_{11}}\right)_X, \end{aligned}$$

the integration of which yields

$$\begin{aligned}\nu\bar{v}_{00,X} &= -\left(\overline{\psi'_{00,z}v'_{11}} - v_A^2\overline{\phi'_{00,z}b'_{11}}\right),\\ \eta\bar{b}_{00,X} &= -\left(\overline{\psi'_{00,z}b'_{11}} - \overline{\phi'_{00,z}v'_{11}}\right) + C,\end{aligned} \tag{53}$$

where the constant C is determined by a radial force balance across the channel upon saturation of the instability [10]. The relations (53) indicate how the stresses induced by the MRI feed back onto the mean and thus allow us to close the system (49)-(52).

1.2.3 Overview of results

Refs. [9, 10] document semi-analytical and numerical solutions to the above reduced model. When $\varepsilon = O(\delta)$, dissipation directly leads to saturation of the MRI on the dissipative timescale. In contrast, when $\varepsilon = o(\delta)$, dissipation is subdominant and the MRI saturates via modification of the background shear on a rotational timescale. The saturated state in the latter case can be predicted analytically and is shown to agree with simulations initialized with multiple modes or with small random perturbations, provided one uses the vertical wavenumber corresponding to the final coarsened state.

2 Wave-Mean Flow Coupling in Nearly Inviscid Faraday Waves

Faraday waves, i.e., gravity-capillary waves formed on the free surface of a fluid due to vertical oscillation of its enclosure, are an example of a parametric instability. That is, they are excited by a time-varying parameter (in this case the time-periodic oscillations of the container) that finds resonance with the natural frequency of the system. These waves are well-studied, but the theory surrounding them is incomplete (particularly in geometries with large aspect ratio) if the effects of viscosity (however weak) are not accounted for. This is because oscillatory viscous boundary layers can drive a mean "streaming" flow in the fluid interior which couples non-trivially with the Faraday waves. Our objective is to develop an asymptotic theory for the coupled evolution of Faraday waves and the resultant streaming flow leveraging the smallness of the viscosity and inverse aspect ratio. Before that, however, it might be useful to illustrate viscous (boundary layer) effects on water waves in a simpler setting.

2.1 Prelude: Stokes drift in nearly inviscid water waves

In this section, we derive expressions for the Stokes drift associated with a surface wave in both inviscid and viscous cases. Considering both versions of this problem illustrates the dangers of ignoring viscosity entirely, motivating why we will not do so when analyzing *nearly* inviscid Faraday waves.

Stokes drift velocity arises from the fact that, in general, the Eulerian and Lagrangian descriptions of the mean flow are not equivalent. Formally, Stokes drift $\boldsymbol{u}_S$ can be defined as

$$\boldsymbol{u}_S \equiv \langle \boldsymbol{u}_L \rangle - \langle \boldsymbol{u}_E \rangle, \tag{54}$$

where $\boldsymbol{u}_L$ denotes the Lagrangian mean velocity, *i.e.*, the mean velocity that would be felt by an individual particle (or parcel) as its evolution is tracked, and $\boldsymbol{u}_E$ denotes the Eulerian mean velocity, *i.e.*, the mean velocity with respect to a fixed spatial reference point, and the brackets denote the time average (in particular, one could consider the time average over a wave period) [2].

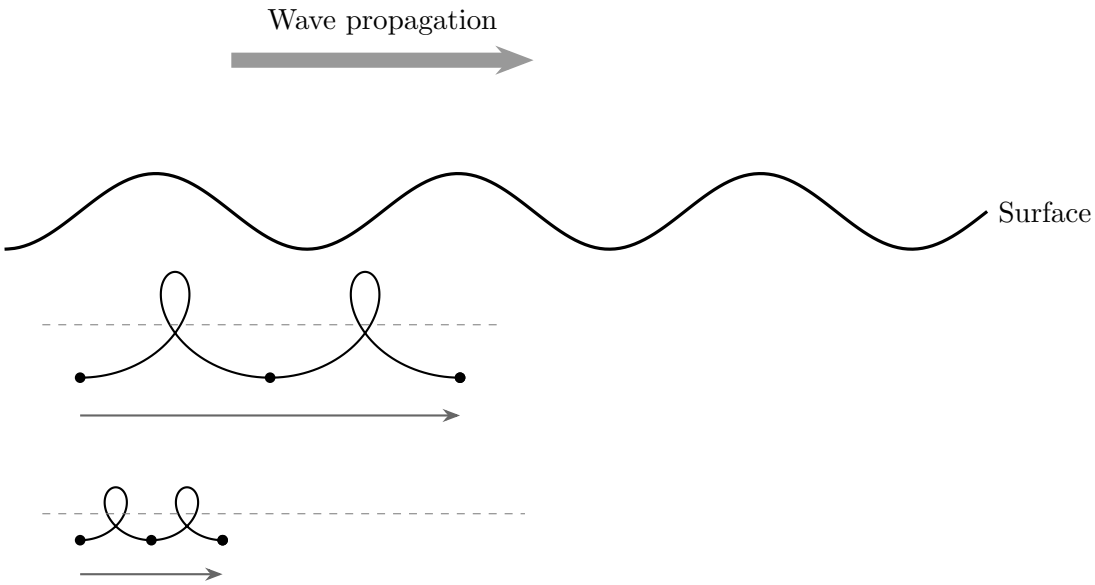

Figure 2: Schematic diagram of Stokes drift. The black line outlines a wave at the surface, propagating in the direction of the arrow. The thin black lines underneath the surface mark the paths of a particles starting at different vertical positions with respect to the surface, and the dots along those lines represent the positions after a wave period. The dashed grey lines indicate how the drift is purely in the horizontal; there is no vertical drift.

To illustrate the existence of Stokes drift, consider a situation in which there is a wave propagating on the surface of a fluid. For an idealized, sinusoidal wave the horizontal average over a wave period at any fixed spatial location will clearly be zero. However, if we were to instead consider the velocity a particle experiences and take the average, we would get a different result. The particle would move faster in the direction of wave propagation when it is near the wave crest and slower (or even slightly backward) when it is in the wave trough. The orbital path of the particle is then not exactly closed, and will consequently not yield a zero (horizontal) average. This results in a net displacement, or drift, in the direction of wave propagation after each wave period, as shown in Figure 2. This figure also shows how in this scenario, there would be smaller Stokes drift for particles starting deeper in the fluid because the influence of the surface wave is weaker at greater depths. As shown in Figure 2, the particle does not change its mean vertical position *relative to the surface*. For instance, a particle starting at the surface would always stay at the surface.

We can see how Stokes drift arises mathematically in the following manner [11]. Note that in the following derivation we are really deriving an expression for the *Lagrangian drift*, *i.e.*, the mean velocity a particle experiences, but this ends up being equal to the Stokes drift because the Eulerian mean is zero (see (54)). We will use Cartesian coordinates, with the x-axis oriented along the unperturbed free surface of the fluid, and the y-axis directed vertically upwards.

If a flow is irrotational and incompressible, we can express the Eulerian velocity $\boldsymbol{u}_E$ in terms of a potential, so that $\boldsymbol{u}_E = (\phi_x, \phi_y)$ and $\nabla^2\phi = 0$. Let η denote the free surface deflection and p denote the excess pressure due to the presence of surface tension. By calculating the curvature at a given point on the surface, one can then find that

$$p = p_0 - T\eta_{xx}(1+\eta_x^2)^{-3/2}, \tag{55}$$

where T is the surface tension. Let ρ denote the fluid density and g denote the acceleration due

to gravity. Then the flow is subject to one boundary condition at the bottom and two at the free surface, respectively:

$$\phi_y = 0 \qquad \text{at } y = -h, \tag{56a}$$

$$\eta_t + \phi_x \eta_x = \phi_y \qquad \text{at } y = \eta, \tag{56b}$$

$$\phi_t + \frac{|\boldsymbol{u}_E|^2}{2} + \frac{p}{\rho} + g\eta = 0 \qquad \text{at } y = \eta. \tag{56c}$$

Since we are first considering the case where the fluid is *strictly* inviscid, the fluid remains irrotational if it is initially irrotational.

Consider a particle starting at the position $\boldsymbol{x} = \boldsymbol{a}$ at time $t = 0$, where particle positions are described in terms of the two-dimensional spatial vector $\boldsymbol{x} = (x, y)$. As in (54) let $\boldsymbol{u}_L(\boldsymbol{x}, t)$ denote the Lagrangian velocity field. At time t, the particle's position is then given by

$$\boldsymbol{x} = \boldsymbol{a} + \int_0^t \boldsymbol{u}_L(\boldsymbol{a}, s)\, ds.$$

To second order[2], the Lagrangian velocity is related to the Eulerian velocity by

$$\boldsymbol{u}_L(\boldsymbol{a}, t) = \boldsymbol{u}_E(\boldsymbol{a}, t) + \left(\int_0^t \boldsymbol{u}_E(\boldsymbol{a}, s)\, ds \right) \cdot \nabla_{\boldsymbol{a}} \boldsymbol{u}_E(\boldsymbol{a}, t). \tag{57}$$

In particular, suppose the wave is a progressive sinusoidal wave of small amplitude A. Then

$$\eta = A\cos(kx - \omega t) + O(A^2)$$

and

$$\phi = \frac{\eta_t \cosh k(y+h)}{k \sinh kh} + O(A^2).$$

Now suppose A is constant in space. We compute, where $\boldsymbol{u}_E = (u, v)$,

$$u = \phi_x = \left[-\left(\frac{\cosh k(y+h)}{k \sinh kh} \right) \omega A \sin(kx - \omega t) \right]_x = -\left(\frac{\cosh k(y+h)}{k \sinh kh} \right) \omega A k \cos(kx - \omega t),$$

$$v = \phi_y = \left[-\left(\frac{\cosh k(y+h)}{k \sinh kh} \right) \omega A \sin(kx - \omega t) \right]_y = -\omega A k \sin(kx - \omega t) \left(\frac{\sinh k(y+h)}{k \sinh kh} \right).$$

Thus, the time-averaged Eulerian velocity $\langle \boldsymbol{u}_E \rangle$ vanishes to second order. On the other hand, we can calculate the time-averaged Lagrangian drift. To this end, we compute the terms in (57),

$$\nabla_{\boldsymbol{a}} \boldsymbol{u}(\boldsymbol{a}, t) = \begin{bmatrix} -\left(\frac{\cosh k(y+h)}{\sinh kh} \right) \omega A k \sin(kx - \omega t) \\ -\omega A k \sin(kx - \omega t) \left(\frac{\cosh k(y+h)}{\sinh kh} \right) \end{bmatrix}$$

and

$$\int_0^t \boldsymbol{u}(\boldsymbol{a}, s)\, ds = \begin{bmatrix} -\left(\frac{\cosh k(y+h)}{\sinh kh} \right) A(\sin(kx - \omega t) - \sin(kx)) \\ -\left(\frac{\sinh k(y+h)}{\sinh kh} \right) \omega A(-\cos(kx - \omega t) + \cos(kx)) \end{bmatrix}.$$

[2]Following the convention that the first term in the Taylor expansion, i.e., the constant term, is the "first-order" term.

Substituting into (57) and applying the double-angle identity for cosh, we obtain the time-averaged $\boldsymbol{u}_L$,

$$\langle \boldsymbol{u}_L \rangle = \left(\frac{\omega k A^2 \cosh 2k(y+h)}{2 \sinh^2 kh}, 0 \right). \tag{58}$$

Since the Eulerian mean velocity is zero, we can also identify this quantity with the Stokes drift $\boldsymbol{u}_S$. Notice here that there is no Stokes drift in the vertical (here, y) direction.

We now contrast this with the case of small but nonzero viscosity, so the fluid is not *strictly* inviscid. In this case the above is not correct, as the description of the velocity field in terms of the potential does not hold, and the boundary conditions are incorrect.

Let $\beta = (\omega/2\nu)^{1/2}$. If there is sufficiently small viscosity, $\beta h \gg 1$ and $\beta k^{-1} \gg 1$, then the inviscid solution applies outside of the two thin oscillatory viscous boundary layers, along the top and bottom, respectively, of thickness $O(\beta^{-1})$. In other words, when the viscosity is sufficiently small, the inviscid solution applies in most of the domain. Now we consider the flow inside the boundary layers. In the bottom boundary layer, decompose

$$\boldsymbol{u}_E = \nabla \phi + \boldsymbol{u}'_E,$$

where $\boldsymbol{u}'_E = (u', v')$. At leading order, $\boldsymbol{u}'_E$ satisfies the vorticity equation

$$\frac{\partial \Omega}{\partial t} = \nu \left(\frac{\partial^2 \Omega}{\partial x^2} + \frac{\partial^2 \Omega}{\partial y^2} \right), \quad \Omega = \nabla \times \boldsymbol{u}'_E,$$

with boundary conditions at the bottom

$$\begin{cases} u' &= -\phi_x \\ v' &= 0 \end{cases} \qquad \text{at } y = -h$$

and

$$u' = 0 \text{ for } \beta(y+h) \gg 1.$$

An explicit solution can be obtained for u' and v',

$$\begin{aligned} u' &= -\omega A \operatorname{cosech}(kh) e^{-\beta(y+h)} \cos(kx - \omega t + \beta(y+h)) \\ v' &= -\int_{-h}^{y} \frac{\partial u'(x, \tilde{y}, t)}{\partial x} \, d\tilde{y}. \end{aligned}$$

The time-averaged Reynolds stress in the oscillatory boundary layer can then be computed as (to second order in A)

$$\langle u'v' \rangle = \frac{\omega^2 A^2 k}{4\beta \sinh^2 kh} (2(\beta(y+h) \sin \beta(y+h) + \cos \beta(y+h)) e^{-\beta(y+h)} - e^{-2\beta(y+h)} - 1). \tag{59}$$

The Reynolds stress induces a mean flow $(U'(y), 0)$ (so $U'(y)$ is the time-averaged Eulerian velocity), as can be seen from the mean momentum equation

$$\nu \frac{\partial^2 U'}{\partial y^2} = \frac{\partial \langle u'v' \rangle}{\partial y}.$$

Letting $\langle u'v' \rangle_\infty$ represent the Reynolds stress just outside of the boundary layer, we have

$$\nu \frac{\partial U'}{\partial y} = \langle u'v' \rangle - \langle u'v' \rangle_\infty. \tag{60}$$

Now we consider $\beta(y+h) \to \infty$, *i.e.*, the situation in which y is outside the boundary layer at $y = -h$. We need to match the inner boundary layer solution to the $y + h \to 0$ limit of the outer (bulk) solution. This boundary layer is very thin for small ν, so we can set $\beta(y+h) = 0$ in (58). Letting $\beta(y+h) \to \infty$ in (59) yields

$$\langle u'v' \rangle_\infty = -\frac{\omega^2 k A^2}{4\beta \sinh^2 kh}.$$

Since $U'(-h) = 0$, (60) implies that

$$\lim_{y\to\infty} U'(y) = \frac{3\omega k A^2}{4\sinh^2 kh},$$

valid when $\beta(y+h) \ll 1$. This is a finite limit (at second order) and does not feature any dependence on ν. The impact of this Eulerian mean flow needs to be added to the Stokes drift computed in the inviscid case, (58). The net Lagrangian drift for $\beta h \gg 1$ and $\beta/k \gg 1$ is thus

$$\langle \boldsymbol{u}_L \rangle_\infty = \left(\frac{5\omega^2 k A^2}{4\sinh^2 kh}, 0 \right).$$

We have thus seen that the computed Stokes drift (to second order) is different when we consider the effects of viscosity, which we must do, as there is an $O(1)$ impact even when viscosity is very small. We will now apply this insight to analyze Faraday waves, going beyond the traditional potential theory description as used in Ref. [4].

2.2 Nearly inviscid Faraday waves

Faraday waves (or "Faraday patterns") are nonlinear standing waves that appear in liquids which are in vibrating, enclosed containers. They can easily be observed in a laboratory setting: put liquid in a petri dish on a loudspeaker, play a sound, and the fluid in the dish will form patterns depending on the frequency of the sound being played. There are many different structures that may be obtained, especially in the case of multi-frequency forcing, but in the simplest case Faraday waves are the manifestation of a subharmonic instability, that is, the observed waves have half the frequency of the container vibration.

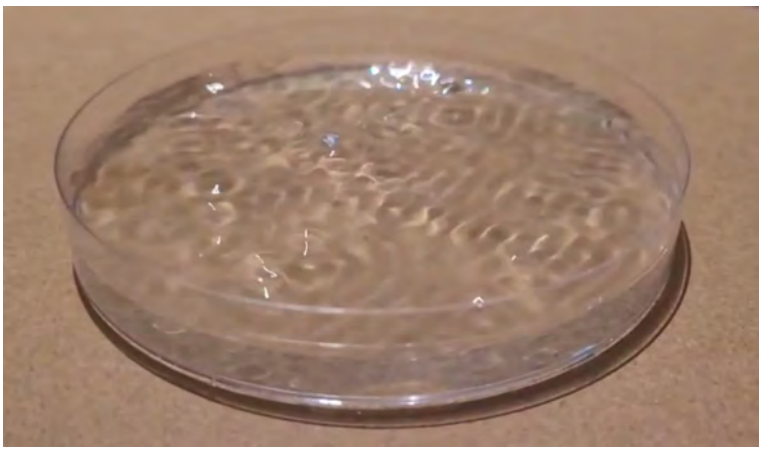

Figure 3: Faraday waves in a petri dish.[17] For more interesting Faraday patterns, see this link.

2.2.1 Dispersion relation for viscous water waves: two types of modes

To see how Faraday waves arise mathematically, we consider viscous water waves. Since we are not neglecting viscosity altogether, it is not guaranteed that a flow, which is initially irrotational, stays irrotational, and we are therefore not guaranteed a potential description for the velocity field for all time. Instead, one must use a streamfunction, which is one reason why it is simpler to consider the strictly inviscid case.

We follow [13]. The dimensionless equations for gravity-capillary waves in a layer of fluid with (undisturbed) depth h that is viscous and incompressible are

$$\boldsymbol{u}_t + \boldsymbol{u}\cdot\nabla\boldsymbol{u} = -\nabla p + C\nabla^2\boldsymbol{u}, \tag{61}$$

$$\nabla\cdot\boldsymbol{u} = 0, \tag{62}$$

where C is a dimensionless constant measuring the viscous effects. Note that we no longer specify the subscript of E for an Eulerian velocity, and unless otherwise specified, it can be assumed a given velocity is Eulerian. The constant C can be prescribed, depending on the scale adopted for time. A natural choice is [13]

$$C \equiv \nu(gh^3)^{-1/2} \ll 1, \tag{63}$$

where ν is the kinematic viscosity. At the bottom (in the non-dimensional variables, this is at $y=-1$) we impose the boundary condition $\boldsymbol{u}=\boldsymbol{0}$. In the non-dimensionalization, all lengths are in units of h and time in units of $\sqrt{h/g}$. At the free surface $y=\eta(x,t)$, we have the kinematic boundary condition

$$\eta_t + u\eta_x = v$$

as before. The mean of the free surface is then at $y=0$. Define the (dimensionless) *inverse Bond number*

$$B^{-1} = \frac{T}{\rho g h^2}, \tag{64}$$

which measures the importance of surface tension T versus the importance of gravity. There are two additional boundary conditions at the free surface:

$$\begin{cases} 2C\left(\frac{u_x\eta_x^2 - \eta_x(u_y+v_x)+v_y}{1+\eta_x^2}\right) = p - \eta + T\frac{\partial}{\partial x}\left(\frac{\eta_x}{\sqrt{1+\eta_x^2}}\right) \\ (u_y+v_x)(1-\eta_x^2) + 2\eta_x(v_y-u_x) = 0. \end{cases} \qquad \text{at } y=\eta(x,t). \tag{65}$$

Now we linearize about the state $(u,v,p,\eta)=(0,0,0,0)$,

$$(u,v,p,\eta) = (u_k(y), v_k(y), p_k(y), \eta_k)\exp(ikx+st), \tag{66}$$

where

$$su_k = -ikp_k + C(u_{kyy} - k^2u_k), \tag{67}$$

$$sv_k = -p_{ky} + C(v_{kyy} - k^2v_k), \tag{68}$$

$$iku_k + v_{ky} = 0, \tag{69}$$

subject to the conditions

$$u_k(-1) = v_k(-1) = 0. \tag{70}$$

In (67)-(69), the subscript of k denotes the functions u_k, etc. whereas the subscript y denotes a derivative of such a function with respect to y. Lastly,

$$s\eta_k = v_k(0), \quad 2Cv_{ky}(0) = p_k(0) - (1+k^2T)\eta_k, \quad u_{ky}(0) + ikv_k(0) = 0, \tag{71}$$

and $\eta_0 = 0$ due to mass continuity.

Suppose $k \neq 0$. Then (67)-(69) can be written as a fourth-order eigenvalue problem for $v_k(y)$. The solution of this eigenvalue problem is of the form

$$v_k(y) = a\cosh ky + b\sinh ky + c\cosh qy + d\sinh qy,$$

where $q^2 \equiv (s/C) + k^2$.

By additionally imposing the boundary conditions (70) and (71), we can now obtain the dispersion relation, which is more conveniently written in terms of the new variable q. It is given by:

$$\begin{aligned} k(1+Tk^2)(q\cosh q\sinh k - k\cosh k\sinh q) =& C^2(4k^2q(k^2+q^2) + (k^4+6k^2q^2+q^4)k\sinh k\sinh q \\ &- (5k^4+2k^2q^2+q^4)q\cosh k\cosh q). \end{aligned} \tag{72}$$

We need to solve (72) for s (recall this is the frequency in (66), which appears also in (72) via the definition of q) in order to understand the different modes. To that end, we solve (72) for $q = q(k; C, T)$, from which we can find s via the relation $s = C(q^2 - k^2)$.

The special case $k = 0$ is particularly simple. The solutions are of the form

$$(u_0, v_0, p_0, \eta_0) \propto \left(\cos\left(\left(n+\frac{1}{2}\right)\pi y\right), 0, 0, 0\right),$$

$n = 0, 1, 2, ...$, with $s = -C(n+\frac{1}{2})^2\pi^2$. Notice that $s < 0$. These are pure hydrodynamic modes and decay viscously.

Next we turn to the asymptotic behavior of the solutions s to (72) in the limiting case $C \ll 1$. There are three different regimes depending on the magnitude of the wavenumber k but we only discuss the case $k = O(1)$.

In this case, the wavelength is of the order of the depth of the fluid layer. For these general values of k ($k \neq 0$), the dispersion relation has two solution types: gravity-capillary modes and viscous modes.

Gravity-Capillary Modes: The gravity-capillary modes, also called **nearly inviscid modes** or **surface modes**, are associated with solutions of the form

$$s = \pm i\sqrt{k(1+Tk^2)\tanh k} - \frac{(k(1+Tk^2)\tanh k)^{1/4}}{\sinh 2k}k\left(\frac{1\pm i}{\sqrt{2}}\right)\sqrt{C} - k^2\left(2 + \frac{5+3\tanh^2 k}{16\sinh^2 k}\right)C + ..., \tag{73}$$

where $q_r \sim C^{-1/2} \gg 1$, $q_r > 0$. Linear Faraday waves are given by the frequencies in the first term of (73) with a decay due to viscous dissipation in the boundary layer (real parts of remaining terms of (73)). This decay comes in already at order $\sqrt{C}$ (also at higher orders if one expands further). The modes associated with these frequencies oscillate with $O(1)$ dimensionless frequency and their decay rate is proportional $\sqrt{C}$.

Viscous Modes: There is another class of solutions to (72). The **viscous modes**, also called **hydrodynamic modes**, have $|q| = O(1)$. At leading order, these are given by

$$q\cosh q\sinh k = k\cosh k\sinh q$$

, which has infinitely many solutions of the form $q = i\zeta_n(k)$, $n = 1, 2, ...$, where $\zeta_n(k)$ are monotonically decreasing functions of k and satisfy

$$\lim_{k\to\infty} \zeta_n(k) = n\pi, \qquad \text{where } n\pi \le \zeta_n(k) \le \left(n + \frac{1}{2}\right)\pi,$$
$$\lim_{k\to 0} \zeta_n(k) = \zeta_n(0), \qquad \text{where } \zeta_n(0) = \tan\zeta_n(0).$$

Then solution s (which is the decay rate) is given by

$$s = -C(k^2 + \zeta_n(k)) + ...$$

which shows that the viscous modes decay more slowly than the gravity-capillary modes, given that C is small. More specifically, the viscous modes decay on a timescale determined by C rather than $\sqrt{C}$. This indicates the viscous modes are actually the slowest modes of the system. In a consistent theory, the fast modes are necessarily controlled by the slow modes, and so these viscous modes must be considered.

2.2.2 Multiscale analysis of the viscous fluid equations

With this timescale separation in mind, we can now perform a multiscale analysis for the viscous fluid equations. Considering small viscosity, there are three regions in the physical domain: two oscillatory boundary layers with thickness $O(C_g^{1/2})$ and the remaining part of the domain (referred to as the "bulk" in Ref. [11]). We omit the details of the derivation, which may be found in Ref. [16], and instead present the main steps.

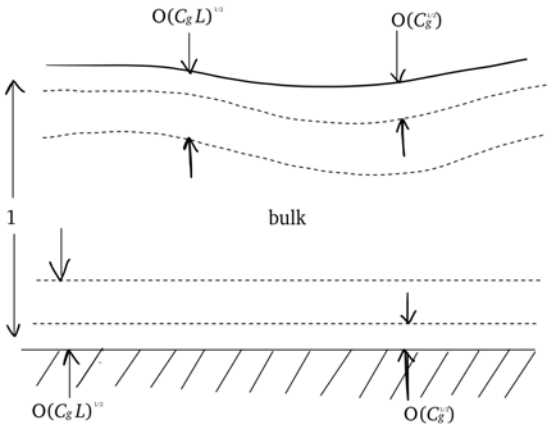

Figure 4: Problem set-up, reproduced based on [16].

Setup: We consider a model of Faraday waves in annular containers. Accordingly, we consider a two-dimensional, laterally unbounded fluid layer which is above a horizontal plate being vibrated vertically with frequency 2ω and a sufficiently small amplitude. We use a Cartesian coordinate system, where the x-axis is oriented to be along the unperturbed free surface and y is oriented vertically upward. We non-dimensionalize space with the unperturbed depth h and time with the *gravity-capillary time* $(g/h + T/(\rho h^3))^{-1/2}$. Non-dimensionalizing with respect to the gravity-capillary time is useful because in the resulting equations, we have the option to take either the limit $T \to 0$ or $g \to 0$, enabling analysis of both effects.

Governing Equations: Let ψ be a streamfunction such that $(u, v) = (-\psi_y, \psi_x)$. Let Ω denote the vorticity and η the free surface deflection, as before. Recall the definition of the capillary number, given in (63), and of the *Bond number*

$$B \equiv \frac{\rho g h^2}{T}. \tag{74}$$

In the non-dimensionalized governing equations, two parameters will arise naturally: the *capillary-gravity number*

$$C_g \equiv \frac{C}{(1+B)^{1/2}} \tag{75}$$

and the *gravity-capillary balance parameter*

$$S \equiv \frac{1}{1+B}. \tag{76}$$

Notice from the definitions of B and S that $0 \leq S \leq 1$. The extreme values of S, $S = 0$ and $S = 1$, correspond to the purely gravitational ($T = 0$) and purely capillary ($g = 0$) cases, respectively. The non-dimensionalized governing equations are

$$\psi_{xx} + \psi_{yy} = \Omega, \tag{77}$$

$$\Omega_t - \psi_y \Omega_x + \psi_x \Omega_y = C_g(\Omega_{xx} + \Omega_{yy}). \tag{78}$$

Equation (77) is simply the vorticity in terms of the Laplacian of ψ, and (78) is the vorticity equation. We additionally impose two boundary conditions at $y = \eta$:

$$\eta_t - \psi_x - \psi_y \eta_x = (\psi_{yy} - \psi_{xx})(1 - \eta_x^2) - 4\eta_x \psi_{xy} = 0 \tag{79a}$$

$$\begin{aligned}(1-S)\eta_x - S\left(\frac{\eta_x}{\sqrt{1+\eta_x^2}}\right)_{xx} - \psi_{yt} + \psi_{xt}\eta_x - (\psi_x + \psi_y\eta_x)\Omega + \frac{1}{2}(\psi_x^2 + \psi_y^2)_x + \frac{1}{2}(\psi_x^2 + \psi_y^2)_y \eta_x \\ = 4\mu\omega^2 \cos(2\omega t)\eta_x - C_g(3\psi_{xxy} + \psi_{yyy} - (\psi_{xxx} + \psi_{xyy})\eta_x) \\ + 2C_g\left(\left(\frac{2\psi_{xy}\eta_x^2 + (\psi_{xx} - \psi_{yy})\eta_x}{1+\eta_x^2}\right)_x + \frac{(\psi_{xxy} - \psi_{yyy})\eta_x^2 - \psi_{xyy}(1-\eta_x^2)\eta_x}{1+\eta_x^2}\right).\end{aligned} \tag{79b}$$

Here, μ is a nondimensional measure of the amplitude of the vibrations applied to the system. As this is a free surface problem, η would need to be calculated.

On the other hand, the bottom boundary condition is given at $y = -1$:

$$\int_0^L \Omega_y \, \mathrm{d}x = \psi = \psi_y = 0 \tag{80}$$

and ψ and η are both taken to be periodic in x with spatial period L (which is the non-dimensional length of the annulus). Lastly, η must satisfy the volume conservation condition

$$\int_0^L \eta \, \mathrm{d}x = 0. \tag{81}$$

The first boundary condition in (79a) ensures that the pressure is periodic in x.

Asymptotic Expansion: We assume that the viscosity is small so that $C_g \ll 1$. We also assume that there are two well-separated scales: in space, $x \sim 1$ vs. $x \gg 1$, and in time, $t \sim 1$ vs. $t \gg 1$. We saw in the previous section that in the case of small viscosity, there are two different types of modes that arise: the nearly inviscid modes and the viscous modes. Although the viscous modes do not significantly deform the free-surface at leading order, as discussed previously, they cannot be neglected. However, we can at least assume that the relevant viscous modes are concentrated around a discrete set of wavenumbers (see Ref. [16] for more details). It is this assumption that allows us to decompose the streamfunction in the bulk and the free surface deflection into three parts:

1. Two counter-propagating wavetrains, with amplitudes A and B, respectively, slowly modulated in space and time about wavenumbers $\pm k$ and response frequency ω,
2. A mean flow that has a weak time dependence but can have a strong spatial dependence, and
3. The remaining component, which is referred to as "nonresonant."

Equations for η, ψ and Ω can then be written according to this separation. Using boundary conditions that are derived via an asymptotic expansion with small parameter ϵ chosen to be the order of magnitude of the complex amplitudes of the counterpropagating wavetrains (i.e., $|A| \sim |B| \sim \epsilon$), equations for the mean quantities η^m, ψ^m, and Ω^m and for the perturbation quantities η^+, ψ^+, and Ω^+ can be obtained. A solvability condition must be imposed on these quantities, and this leads to the evolution equations for the amplitudes A and B.

We look at the spectrum of the unforced problem, linearized around $\psi = \eta = 0$. The normal modes are then of the form

$$(\psi, \eta) = (\Psi, \hat{\eta}) e^{\lambda t + ikx}.$$

The nearly inviscid modes obey the dispersion relation

$$\lambda = i\omega - (1+i)\alpha_1 C_g^{1/2} - \alpha_2 C_g + O(C_g^{3/2}) \tag{82}$$

$$\omega = (1 - S + Sk^2) k \tanh k)^{1/2}, \quad \alpha_1 = \frac{k(\omega/2)^{1/2}}{\sinh(2k)}, \quad \alpha_2 = \left(2 + \frac{5 + 3\tanh^2 k}{16 \sinh^2 k}\right) k^2 \tag{83}$$

From the dispersion relation, the damping rate δ can be approximated,

$$\delta \equiv -\mathrm{Re}(\lambda) = \alpha_1 C_g^{1/2} + \alpha_2 C_g.$$

The viscous modes on the other hand follow the dispersion relation

$$\lambda = -C_g(k^2 + q_n(k)^2) + O(C_g^2)$$

where q_n denotes the nth root of $q \tanh k = k \tan q$, $k > 0$.

Resulting Equations: The evolution equations for A and B are

$$\begin{aligned} A_t - v_g A_x = {} & i\alpha A_{xx} - (\delta + \mathrm{id})A + i(\alpha_3 |A|^2 - \alpha_4 |B|^2)A + i\alpha_5 \mu \overline{B} \\ & + i\alpha_6 \int_{-1}^{0} \frac{2\omega k \cosh(2k(y+1))}{\sinh^2 k} \langle \psi_y^m \rangle^x \mathrm{d}y \; A + i\alpha_7 \langle \eta^m \rangle^x A + \text{ higher order terms}, \end{aligned} \tag{84a}$$

$$\begin{aligned} B_t + v_g B_x = {} & i\alpha B_{xx} - (\delta + \mathrm{id})B + i(\alpha_3 |B|^2 - \alpha_4 |A|^2)B + i\alpha_5 \mu \overline{A} \\ & - i\alpha_6 \int_{-1}^{0} \frac{2\omega k \cosh(2k(y+1))}{\sinh^2 k} \langle \psi_y^m \rangle^x \mathrm{d}y \; B + i\alpha_7 \langle \eta^m \rangle^x B + \text{ higher order terms}, \end{aligned} \tag{84b}$$

$$A(x+L,t) \equiv A(x,t), \quad B(x+L,t) \equiv B(x,t).$$

Here, $\alpha = -\frac{1}{2}\omega''(k)$ and may be found via (82) and (83). The group velocity v_g can also be calculated from (82), as $v_g = \omega'(k)$. The remaining coefficients $\alpha_3, ..., \alpha_7$ are calculated from the solvability condition, and depend on $\omega = \omega(k)$, k and S (see Ref. [16] for the full definitions). The small parameter $\mu \ll 1$ denotes the nondimensional vibration amplitude. The aspect ratio of the system, $L \gg 1$, is in units of the layer depth. Note that it was also assumed that

$$1 \ll L \ll \frac{v_g}{\delta + |d| + \mu},$$

where δ is the damping rate as before and d is the detuning of the surface waves. Lastly, the mean value $\langle\cdot\rangle^x$ is defined

$$\langle G(x,y,t)\rangle^x = (2\ell)^{-1}\int_{x-\ell}^{x+\ell} G(z,y,t)\,\mathrm{d}z \text{ with } 1 \ll \ell \ll L.$$

Notice that the first seven terms of the equations (84a)-(84b) represent inertia, propagation at the group velocity, dispersion, damping, detuning, cubic nonlinearity, and parametric forcing. The last two terms express the coupling with the mean flow in the bulk. These terms are conservative, implying that the mean flow does not extract energy from the system, at least at leading order. The mean flow variables in the bulk, which depend weakly on time but strongly on the spatial variables x and y, evolve according to the equations

$$\psi^m_{xx} + \psi^m_{yy} = \Omega^m$$
$$\Omega^m_t - [\psi^m_y + (|A|^2 - |B|^2)g(y)]\Omega^m_x + \psi^m_x\Omega^m_y = C_g(\Omega^m_{xx} + \Omega^m_{yy})$$

subject to the top boundary conditions, at $y = 0$,

$$\psi^m_x - \eta^m_t = \beta_1(|B|^2 - |A|^2)_x \tag{85a}$$
$$\psi^m_{yy} = \beta_2(|A|^2 - |B|^2) \tag{85b}$$
$$(1-S)\eta^m_x - S\eta^m_{xxx} - \psi^m_{yt} + C_h(\psi^m_{yyy} + 3\psi^m_{xxy}) = -\beta_3(|A|^2 + |B|^2)_x \tag{85c}$$

and the bottom boundary conditions, at $y = -1$,

$$\int_0^L \Omega^m_y\,\mathrm{d}x = \psi^m = 0 \tag{86}$$
$$\psi^m_y = -\beta_4(iA\overline{B}e^{2ikx} + \text{ c.c. } + |B|^2 - |A|^2). \tag{87}$$

These boundary conditions are determined by matching the boundary layer solutions at the top and bottom to the bulk solution just as done in Section 2.1. In particular the Reynolds stress in the bottom boundary drives a horizontal mean flow ψ^m_y at $y = -1$ while a similar analysis at the upper stress-free boundary shows that this boundary layer imposes a mean velocity gradient ψ^m_{yy} at $y = 0$ (Eq. (85b)), with additional contributions from the presence of large scale spatial modulation (Eqs. (85a,c)). Finally, the mean fields satisfy the periodicity conditions

$$\psi^m(x+L,y,t) \equiv \psi^m(x,y,t) \quad \text{ and } \quad \eta^m(x+L,t) \equiv \eta^m(x,t)$$

together with the volume constraint

$$\int_0^L \eta^m(x,t)\,\mathrm{d}x = 0.$$

Together, these equations are referred to as the **general coupled amplitude-mean-flow (GCAMF) equations**.

Differences Between the GCAMF and the Governing Equations: The GCAMF equations describe the bulk dynamics, outside of asymptotically thin boundary layers at the top and bottom, in the weakly nonlinear regime. The right-hand sides of the boundary conditions (85a) and (85c) provide a normal forcing mechanism. The right-hand sides of the boundary conditions (85b) and (86) provide shear forcing mechanisms via a tangential stress at the free surface and a tangential velocity at the bottom boundary. The presence of these forcing terms is important as they capture the effect of the primary viscous boundary layers on the bulk. These forcing terms are one of the essential ways the GCAMF equations differ from the exact equations at the outset of the analysis. The other key difference is in two simplifications: (1) fast oscillations associated with surface waves are filtered out in the GCAMF, and (2) the boundary conditions are applied at $y = 0$ which is the *unperturbed* location of the free surface.

3 Concluding Remarks

We have outlined the application of asymptotic methods to derive reduced descriptions of complex, nonlinear phenomena by exploiting scale disparities and small parameters. In salt-fingering turbulence, it was the disparity between the heat and salinity diffusion timescales, whereas in accretion disk turbulence (driven by the magnetorotational instability) it was the disparity between the characteristic vertical and horizontal length scales of the fingers, and in nearly inviscid Faraday waves, it was the small amplitude of the waves together with the low value of the viscosity (and the large aspect ratio of the domain). Fingering instabilities exemplify a characteristic feature of systems with timescale disparities – rapidly varying fields often lock onto slowly evolving ones, presenting opportunities for model reduction. Nearly inviscid Faraday waves illustrate the non-trivial effects that slow modes may have over long periods of time.

References

[1] D. J. Acheson, *Hydromagnetic wavelike instabilities in a rapidly rotating stratified fluid*, Journal of Fluid Mechanics, 61 (1973), pp. 609–624.

[2] D. G. Andrews and M. E. McIntyre, *An exact theory of nonlinear waves on a Lagrangian-mean flow*, Journal of fluid Mechanics, 89 (1978), pp. 609–646.

[3] S. A. Balbus, *Enhanced angular momentum transport in accretion disks*, Annual Review of Astronomy and Astrophysics, 41 (2003), pp. 555–597.

[4] T. B. Benjamin and F. J. Ursell, *The stability of the plane free surface of a liquid in vertical periodic motion*, Proceedings of the Royal Society of London. Series A. Mathematical and Physical Sciences, 225 (1954), pp. 505–515.

[5] A. Fraser, A. van Kan, E. Knobloch, K. Julien, and C. Liu, *Spontaneous generation of helical flows by salt fingers*, Journal of Fluid Mechanics, 1020 (2025), p. R1.

[6] J. F. Hawley and S. A. Balbus, *A Powerful Local Shear Instability in Weakly Magnetized Disks. III. Long-Term Evolution in a Shearing Sheet*, The Astrophysical Journal, 400 (1992), p. 595.

[7] B. Jamroz, K. Julien, and E. Knobloch, *An asymptotically exact reduced PDE model for the magnetorotational instability: Derivation and numerical simulations*, Physica Scripta, 2008 (2008), p. 014027.

[8] K. Julien and E. Knobloch, *Reduced models for fluid flows with strong constraints*, Journal of Mathematical Physics, 48 (2007), p. 065405.

[9] ——, *Magnetorotational instability: Recent developments*, Philosophical Transactions: Mathematical, Physical and Engineering Sciences, 368 (2010), pp. 1607–1633.

[10] E. Knobloch and K. Julien, *Saturation of the magnetorotational instability*, Physics of Fluids, 17 (2005), p. 094106.

[11] E. Knobloch and J. M. Vega, *Nearly inviscid Faraday waves*, in Geometry, Mechanics, and Dynamics, P. Newton, P. Holmes, and A. Weinstein, eds., Springer, New York, NY, 2002, pp. 181–222.

[12] C. Liu, K. Julien, and E. Knobloch, *Staircase solutions and stability in vertically confined salt-finger convection*, Journal of Fluid Mechanics, 952 (2022), p. A4.

[13] C. Martel and E. Knobloch, *Damping of nearly inviscid water waves*, Physical Review E, 56 (1997), p. 5544.

[14] W. Merryfield, *Saltfingers in stable stratification*.

[15] T. Radko, *Double-Diffusive Convection*, Cambridge University Press, New York, UNITED STATES, 2013.

[16] J. M. Vega, E. Knobloch, and C. Martel, *Nearly inviscid Faraday waves in annular containers of moderately large aspect ratio*, Physica D: Nonlinear Phenomena, 154 (2001), pp. 313–336.

[17] Wikimedia Commons, *Faraday waves observed in water vibrating at a frequency of about 50 hz.*, 2007. File: FaradayWaves.jpg.

[18] J.-H. Xie, K. Julien, and E. Knobloch, *Jet formation in salt-finger convection: A modified Rayleigh–Bénard problem*, Journal of Fluid Mechanics, 858 (2019), pp. 228–263.

[19] J.-H. Xie, B. Miquel, K. Julien, and E. Knobloch, *A reduced model for salt-finger convection in the small diffusivity ratio limit*, Fluids, 2 (2017), p. 6.

GFD 2024 Lecture 6: Multiscale Modeling of Layered Anisotropic Stratified Turbulence (LAST)

Greg Chini; notes by Paul Curtis and Cy David

June 24, 2024

1 Introduction

This lecture continues to develop the theme of utilizing asymptotic methods for studying turbulence in constrained flows. While earlier lectures in this series have discussed rotationally or magnetically influenced systems, the focus of this lecture is on turbulent flows constrained by stable stratification, i.e., the increase of background density with depth.

Stratified turbulence is an essential ingredient in closing the oceanic overturning circulation (e.g., [6]), although it occurs on scales too small to be resolved in global circulation models. Overcoming this issue via parameterization requires an understanding of the fundamental properties of stratified turbulence.

2 Layered Anisotropic Stratified Turbulence (LAST)

Strongly stratified turbulence dominates atmospheric and oceanic flows on horizontal scales L less than the scale of rotationally constrained (quasi-geostrophic) flows and larger than the Ozmidov scale,

$$L_O = \left(\frac{\mathcal{E}}{N^3}\right)^{1/2}, \tag{1}$$

below which buoyancy forces are unimportant [7]. Here, $\mathcal{E}$ denotes the turbulent kinetic energy (TKE) dissipation rate, and N is the Brunt–Väisälä frequency, which characterizes the free oscillation of a parcel of fluid within a stably-stratified layer and is given by

$$N = \sqrt{-\frac{g}{\rho_0}\frac{\mathrm{d}\overline{\rho}}{\mathrm{d}z}}, \tag{2}$$

where g is the acceleration due to gravity, ρ_0 is the mean density, and $\overline{\rho}(z)$ is the background density profile as a function of height z.

Far from boundaries and for fixed Prandtl number $Pr \equiv \nu/\kappa$, where ν is the kinematic viscosity and κ is the thermal diffusivity of the fluid, two parameters control stratified turbulent flows: the Reynolds number

$$Re \equiv \frac{UL}{\nu} \tag{3}$$

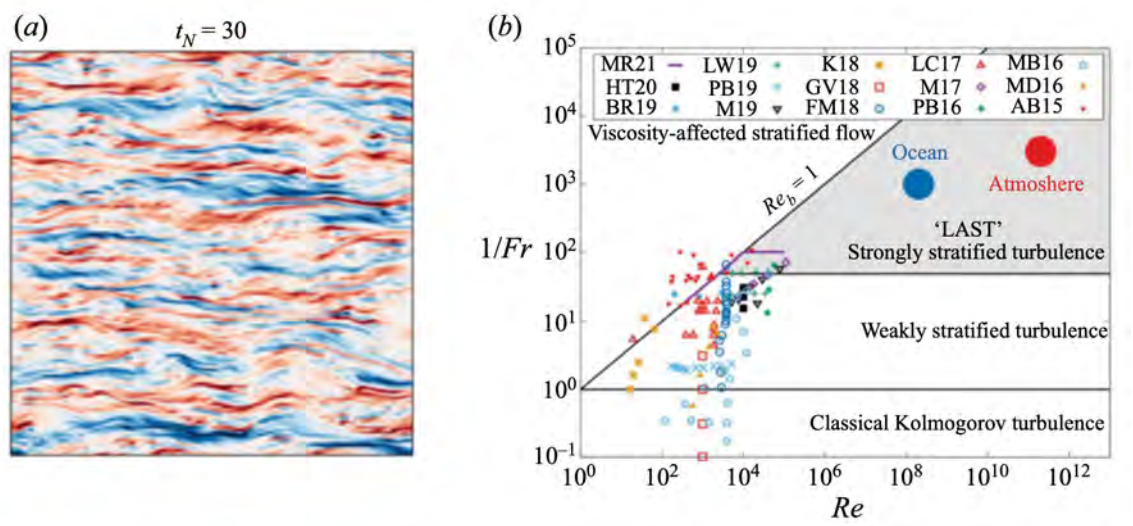

Figure 1: (a). Snapshot of the out-of-plane vorticity field from a direct numerical simulation (DNS) in the LAST regime, illustrating the characteristic anisotropic horizontal layering. (b) Regime diagram indicating the location of the LAST regime in the space of Re and Fr^{-1}. Reproduced from [7].

and the Froude number

$$Fr \equiv \frac{N^{-1}}{L/U}, \tag{4}$$

which may be interpreted as the ratio of the buoyancy period to the horizontal advection time of the large-scale,layer-like flow with characteristic speed U. An alternative interpretation of the Froude number may be obtained by assuming that $\mathcal{E} \sim U^3/L$, from which it follows that

$$Fr \equiv \frac{U}{NL} = \frac{\left(\sqrt{\frac{U^3}{LN^3}}\right)^{2/3}}{L^{2/3}} \sim \left(\frac{\sqrt{\mathcal{E}/N^3}}{L}\right)^{2/3} \sim \left(\frac{L_O}{L}\right)^{2/3}. \tag{5}$$

Hence, strongly-stratified flows ($Fr \ll 1$) exhibit a wide range of scales, with $L_O \ll L$.

Such flows may exhibit an additional inertial range $\in (L_K, L_O)$, where L_K is the Kolmogorov microscale

$$L_K = \left(\frac{\nu^3}{\mathcal{E}}\right)^{1/4}. \tag{6}$$

Assuming again that $\mathcal{E} \sim U^3/L$, the width of this inertial range is characterized by the *buoyancy* Reynolds number

$$Re_b \equiv ReFr^2 = \left(\frac{UL}{\nu}\right)\left(\frac{U^2}{N^2L^2}\right) = \left[\left(\frac{U^3}{LN^3}\right)^{1/2}\left(\frac{\nu^3}{U^3/L}\right)^{-1/4}\right]^{4/3}$$
$$\sim \left[\left(\frac{\mathcal{E}}{N^3}\right)^{1/2}\left(\frac{\nu^3}{\mathcal{E}}\right)^{-1/4}\right]^{4/3} \sim \left(\frac{L_O}{L_K}\right)^{4/3}. \tag{7}$$

Stratified turbulence in the ocean and atmosphere is characterised by $Re_b > 1$ and $Fr \ll 1$, a regime termed "layered anisotropic stratified turbulence" (LAST) following [8]. Figure 1b highlights the LAST regime in the space of Re and $1/Fr$.

The LAST regime is distinguished from weakly-stratified turbulence by the presence of

1. Anisotropic layers with horizontal scales L that are much greater than their vertical extent h ($h \ll L$), as suggested in figure 1a;

2. Spectrally non-local energy transfers that compete with an anisotropic (hydrostratic) energy cascade [1];

3. Self-organization such that the horizontally-averaged flow is approximately marginally stable to linear instabilities [15].

For inviscid two-dimensional (2D) disturbance to (vertically) stratified parallel shear flows, these instabilities are governed by the Taylor–Goldstein eigenvalue problem:

$$\hat{w}_{zz} - \left[k^2 + \frac{\overline{u}_{zz}}{\overline{u} - c} - \frac{\overline{B}_z}{(\overline{u} - c)^2}\right]\hat{w} = 0, \tag{8}$$

where the z subscript denotes ordinary differentiation with respect to z;

$$w' = \hat{w}(z)e^{ik(x-ct)} + \text{complex conjugate} \tag{9}$$

is the vertical velocity perturbation with (real) horizontal wavenumber k and complex phase speed c; and here

$$\overline{B}_z = -\frac{g}{\rho_0}\overline{\rho}_z = N^2(z) \tag{10}$$

is the background buoyancy gradient, while $\overline{u}(z)$ is the background parallel flow profile.

The unstable modes include Kelvin-Helmholtz, Holmboe, and Taylor-Caulfield modes. Though the *sufficient* conditions for these instabilities may vary, a *necessary* condition for instability (of the background flow) may be found by making the transformation $\hat{w} = (\overline{u} - c)^{1/2}\phi$ in (8) and taking the inner product with ϕ^*, yielding

$$\mathrm{Im}\{c\}\int\left(|\phi_z|^2 + \frac{\overline{B}_z - \frac{1}{4}\overline{u}_z^2}{|\overline{u} - c|^2}|\phi|^2 + k^2|\phi|^2\right)dz = 0. \tag{11}$$

Growth of the perturbations can occur ($\mathrm{Im}\{c\} \neq 0$) only if

$$\overline{B}_z - \frac{1}{4}\overline{u}_z^2 < 0 \tag{12}$$

somewhere in the flow. Defining the gradient Richardson number

$$Ri_g = \overline{B}_z/\overline{u}_z^2 = N^2/\overline{u}_z^2, \tag{13}$$

the necessary condition for instability is that

$$Ri_g < 1/4 \tag{14}$$

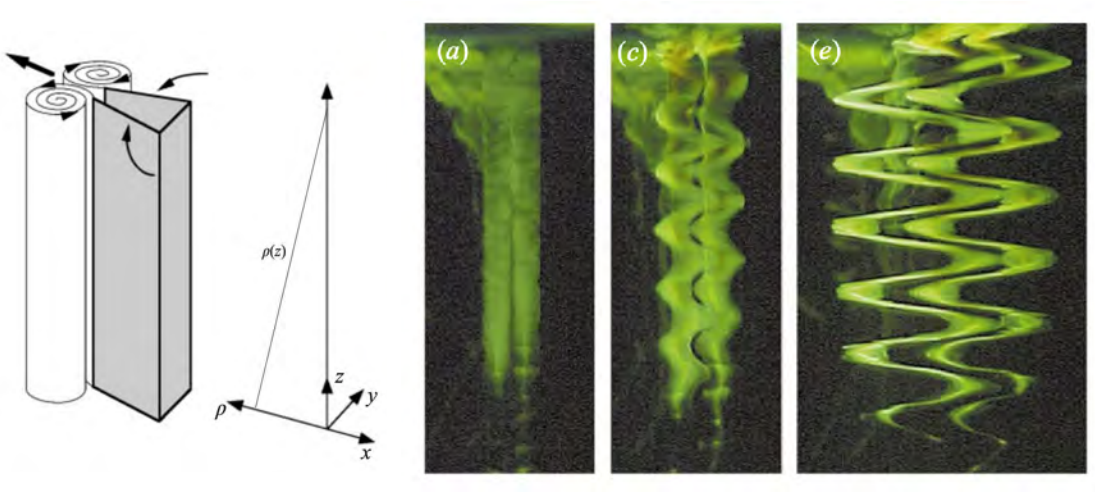

Figure 2: Schematic of the columnar vortex dipole generated by the closing of flaps in the experiment performed by [2]. Laboratory visualizations of the zigzag instability using fluorescein dye. Figure adapted from [2].

somewhere in the flow, a result known as the Miles–Howard theorem. Interestingly, flows in the LAST regime appear to self-organize such that the turbulent mean $Ri_g \lesssim 1/4$ [15].

The instabilities discussed thus far are applicable to a unidirectional background parallel shear flow. A different type of instability, which can arise when the background flow is instead a vertical columnar vortex pair, has been studied in the context of layer formation seen in strongly stratified turbulence [2, 3]. Sinusoidal undulations of the columnar vortex pair with height tend to grow unstably and slice the column into a set of "pancake" vortices. Figure 2 shows laboratory visualizations of this "zigzag" instability and the formation of vertically-layered vortices.

Connecting this physical picture to the actual mechanism(s) of layer formation in the LAST regime requires investigations at extreme values of Re and Fr. The corresponding range of scales that must be resolved makes geophysically-relevant parameter values currently inaccessible to direct numerical simulations (DNS).

An alternative approach, laid out by [7] and validated by [10], relies on an asymptotic reduction of the full Boussinesq equations.

3 Single-Scale Asymptotic Reduction

We first describe a single-scale asymptotic reduction. Consider a (non-rotating) Boussinesq flow with an imposed linear background buoyancy profile $b_B(z)$ such that the total buoyancy

$$\begin{aligned} b_{\text{total}} &= \frac{-(\rho_{\text{total}} - \rho_0)}{\rho_0} g \\ &= b_B(z) + b. \end{aligned} \tag{15}$$

Let $\boldsymbol{g} = -g\boldsymbol{e_z}$, $\boldsymbol{x}_\perp = x\boldsymbol{e_x} + y\boldsymbol{e_y}$, where x and y are horizontal coordinates, and $\boldsymbol{u}_\perp = u\boldsymbol{e_x} + v\boldsymbol{e_y} = \boldsymbol{u} - w\boldsymbol{e_z}$ is the horizontal velocity field. In the following, we scale horizontal

coordinates $\boldsymbol{x}_\perp$ by L, height z by h, horizontal velocity $\boldsymbol{u}_\perp$ by U, pressure p by $\rho_0 U^2$, and time t by L/U. Buoyancy b is scaled by U^2/h to allow for a balance with the vertical pressure gradient. The vertical velocity w is scaled by $W = Fr^2 UL/h = U^3/(N^2 Lh) \sim \mathcal{E}/(N^2 h)$, where $N^2 h$ is a buoyancy anomaly (cf. [14]). With this choice, W is the vertical velocity scale at which the work done against the vertical buoyancy gradient balances the TKE:

$$WN^2 h \sim \mathcal{E}. \tag{16}$$

The resulting dimensionless equations are

$$\boldsymbol{\nabla}_\perp \cdot \boldsymbol{u}_\perp + \left(\frac{Fr^2}{\alpha^2}\right) \partial_z w = 0, \tag{17a}$$

$$\partial_t \boldsymbol{u}_\perp + (\boldsymbol{u}_\perp \cdot \boldsymbol{\nabla}_\perp)\boldsymbol{u}_\perp + \left(\frac{Fr^2}{\alpha^2}\right) w \partial_z \boldsymbol{u}_\perp = -\boldsymbol{\nabla}_\perp p + \boldsymbol{f}_\perp + D[\boldsymbol{u}_\perp], \tag{17b}$$

$$Fr^2 \left[\partial_t w + (\boldsymbol{u}_\perp \cdot \boldsymbol{\nabla}_\perp) w + \left(\frac{Fr^2}{\alpha^2}\right) w \partial_z w\right] = -\partial_z p + b + Fr^2 D[w], \tag{17c}$$

$$\partial_t b + (\boldsymbol{u}_\perp \cdot \boldsymbol{\nabla}_\perp) b + \left(\frac{Fr^2}{\alpha^2}\right) w \partial_z b = -w + \frac{1}{Pr} D[b], \tag{17d}$$

where the Laplacian diffusion operator D is given by

$$D = \frac{1}{Re}\left[\nabla_\perp^2 + \frac{1}{\alpha^2}\partial_z^2\right], \tag{18}$$

$\alpha = h/L$ is the aspect ratio of layered structures, and $\boldsymbol{f}_\perp$ is a (large-scale) horizontal body force incorporated to drive the flow.

As $Fr \to 0$, two distinct asymptotic reductions of system (17) can be envisaged.

1. Following [11], consider $Fr/\alpha \to 0$.

   All vertical advection terms in equations (17) vanish, and the continuity equation reduces to $\boldsymbol{\nabla}_\perp \cdot \boldsymbol{u}_\perp = 0$. The resulting system captures layer-wise 2D flow, for which an upscale transfer of energy (inverse cascade) may be expected, contradicting what is known about strongly-stratified turbulence. Thus, this limit system is not appropriate.

2. Following [4, 5], set $\alpha = Fr$ as $Fr \to 0$ with Pr and $Re_b \equiv ReFr^2$ fixed.

   The Boussinesq equations (17) then reduce to the "hydrostratic primitive equations":

$$\boldsymbol{\nabla}_\perp \cdot \boldsymbol{u}_\perp + \partial_z w = 0, \tag{19a}$$

$$\partial_t \boldsymbol{u}_\perp + (\boldsymbol{u}_\perp \cdot \boldsymbol{\nabla}_\perp)\boldsymbol{u}_\perp + w \partial_z \boldsymbol{u}_\perp = -\boldsymbol{\nabla}_\perp p + \boldsymbol{f}_\perp + \frac{1}{Re_b}\partial_z^2 \boldsymbol{u}_\perp, \tag{19b}$$

$$0 = -\partial_z p + b, \tag{19c}$$

$$\partial_t b + (\boldsymbol{u}_\perp \cdot \boldsymbol{\nabla}_\perp) b + w \partial_z b = -w + \frac{1}{PrRe_b}\partial_z^2 b, \tag{19d}$$

   which filter out isotropic turbulence while permitting fully 3D flow.

Although the second limit system is an improvement over the first, the hydrostatic primitive equations (19) cannot capture small-scale isotropic and non-hydrostatic dynamics, e.g., associated with stratified shear instabilities. Instead of modeling these processes phenomenologically, [7] proceed more formally using a multiscale asymptotic reduction.

4 Multiscale Asymptotic Reduction

4.1 Multiscale problem formulation

Multiple scales asymptotic analysis can be employed to systematically incorporate small scale ('fast') dynamical behaviour. Treating the aspect ratio $\alpha = h/L$ as a small parameter, we introduce a fast (dimensionless) spatial variable $\chi = x/\alpha$ and a corresponding fast (dimensionless) time variable $\tau = t/\alpha$. In dimensional terms (where $\tilde{x}$ and $\tilde{t}$ are dimensional variables), we see that

- χ measures horizontal variability in units of h, i.e., commensurate with the layer thickness: $x = \tilde{x}/L \to x/\alpha = \chi = (\tilde{x}/L)\cdot(L/h) = \tilde{x}/h$;
- τ measures temporal variability in units of h/U, i.e., commensurate with the vertical shearing timescale: $t = \tilde{t}U/L \to \tau = t/\alpha = (\tilde{t}U/L)\cdot(L/h) = \tilde{t}U/h$. Moreover, in the asymptotic analysis that follows, $\alpha = Fr$; thus, $h/U = N^{-1}$; i.e., τ equivalently measures variability on the buoyancy timescale.

Spatiotemporal derivative operators transform as $\partial_x \to \partial_x + \alpha^{-1}\partial_\chi$ and $\partial_t \to \partial_t + \alpha^{-1}\partial_\tau$, while, e.g., the x-component of the velocity transforms as $u(x,z,t;Fr) \to u(\chi,x,z,\tau,t;Fr)$ and analogously for other dependent fields. In our analysis, we further decompose these fields into fast and slow components respectively denoted with an overbar and a prime:

$$u = \overline{u}(x,z,t;Fr) + u'(\chi,x,z,\tau,t;Fr), \tag{20}$$

where

$$\overline{(\cdot)} \equiv \frac{1}{\Delta\tau\Delta\chi}\int_{\chi}^{\chi+\Delta\chi}\int_{\tau}^{\tau+\Delta\tau} d\chi d\tau(\cdot)$$

defines an average over the fast time and fast spatial coordinates, and $\overline{u'} = 0$. (Here, $\Delta\tau$ and $\Delta\chi$ are suitable fast-averaging periods.)

For brevity of exposition, we restrict attention to 2D dynamics in the x–z plane; the generalization of the derivation of the multiscale reduced model to 3D dynamics is straightforward. We first identify a physically relevant and mathematically consistent distinguished limit in which $Re \to \infty$ while $Fr \to 0$ and $\alpha \to 0$ such that $\alpha = Fr$ and the buoyancy Reynolds number $Re_b \equiv ReFr^2$ remains (asymptotically) fixed and $\mathcal{O}(1)$. Next, we posit the following asymptotic expansions for the various (total) fields:

$$[u,w,p,b] = [u_0,w_0,p_0,b_0] + Fr^a[u_1,w_1,p_1,b_1] + Fr^{2a}[u_2,w_2,p_2,b_2] + \mathcal{O}(Fr^{3a}). \tag{21}$$

Here, it is important to note that, for consistency in the indexing of the expansion, the vertical velocity w has been scaled by U and not by αU and, as in Section 3, the buoyancy b has been scaled by U^2/h. The *a priori* unspecified exponent a is determined from the following considerations. First, the leading-order incompressibility condition for the presumed *isotropic* fluctuations requires $w' = \mathcal{O}(u')$. Secondly, the dominant "Reynolds stress" divergence feedback from the fluctuations should balance the time-tendency and nonlinear advection of the large-scale horizontal velocity. As evident in the subsequent derivation, these considerations imply $a = 1/2$. In particular, while the mean fields $\overline{u} \sim \overline{u}_0$ and $\overline{b} \sim \overline{b}_0$,

the corresponding fluctuation fields $u' \sim Fr^{1/2} u'_1$ and $b' \sim Fr^{1/2} b'_1$; i.e., these fluctuations are small compared to their respective means. It is this ordering that leads to a systematic *generalized quasilinear* (GQL) reduction. In contrast, it will be shown that $\overline{w} \sim Fr\,\overline{w}_2$, as already evident from the single-scale asymptotic reduction described in Section 3. Since $w' \sim Fr^{1/2} w'_1$, a key deduction is that, in stratified turbulence, vertical velocities are larger for motions with small horizontal scales than they are for motions with large horizontal scales. This prediction accords with available DNS results [12, 10].

We begin by writing the exact equations of motion (17) in 2D using the multiscale derivative operators:

$$(\partial_x + Fr^{-1}\partial_\chi)u + Fr^{-1}\partial_z w = 0, \tag{22a}$$

$$(\partial_t + Fr^{-1}\partial_\tau)u + u(\partial_x + Fr^{-1}\partial_\chi)u + Fr^{-1} w\partial_z u = -(\partial_x + Fr^{-1}\partial_\chi)p + f + D[u], \tag{22b}$$

$$(\partial_t + Fr^{-1}\partial_\tau)w + u(\partial_x + Fr^{-1}\partial_\chi)w + Fr^{-1} w\partial_z w = Fr^{-1}\partial_z p + Fr^{-1} b + D[w], \tag{22c}$$

$$(\partial_t + Fr^{-1}\partial_\tau)b + u(\partial_x + Fr^{-1}\partial_\chi)b + Fr^{-1} w(\partial_z b + 1) = Pr^{-1} D[b], \tag{22d}$$

where the Laplacian diffusion operator

$$D \;\equiv\; \frac{1}{Re_b}\left[(\partial_\chi + Fr\partial_x)^2 + \partial_z^2\right] \;=\; \frac{1}{Re_b}\left[\left(\partial_\chi^2 + \partial_z^2\right) + 2Fr\partial_x\partial_\chi + Fr^2\partial_x^2\right].$$

4.2 Multiscale reduced model of stratified turbulence

In this section, we summarize the multiscale asymptotic reduction of the non-rotating Boussinesq equations in the limit of strong stratification and large Reynolds number. The result is a multiscale reduced model of strongly stratified turbulence, which, as noted above, will be shown to have a GQL form. We first parse the equations into two sets, one governing the mean and one governing the fluctuation fields. We then use the asymptotic expansions (21) to determine the leading-order equations. In the following, numbered equations correspond to key results, while un-numbered equations provide critical methodological steps.

1. **The Continuity Equation.**

   Substituting the decomposition (20) into the continuity equation (22a) and performing a fast average yields the following mean and perturbation equations:

   $$\partial_x \overline{u} + Fr^{-1}\partial_z \overline{w} = 0, \tag{23}$$

   $$\partial_x u' + Fr^{-1}(\partial_\chi u' + \partial_z w') = 0. \tag{24}$$

   The balance in equation (23) implies that $\overline{w} \sim \mathcal{O}(Fr)$ (and, hence, $\bar{w}_0 = \bar{w}_1 = 0$). At leading order, equation (24) implies that $w' \sim \mathcal{O}(u')$, consistent with the expectation that isotropic flow structures can arise on small scales. Substituting the asymptotic expansions into equation (23) then yields

   $$\partial_x(\overline{u}_0 + Fr^{1/2}\overline{u}_1 + Fr\overline{u}_2 + ...) + Fr^{-1}\partial_z(\overline{w}_0 + Fr^{1/2}\overline{w}_1 + Fr\overline{w}_2 + ...) = 0.$$

   The leading order balance $[\mathcal{O}(Fr^0)]$ for the mean continuity equation is

   $$\partial_x \overline{u}_0 + \partial_z \overline{w}_2 = 0. \tag{25}$$

Similarly, for the perturbation continuity equation (24), we obtain

$$\partial_x \left(Fr^{1/2} u_1' + ... \right) + \frac{1}{Fr} \left[\partial_\chi (Fr^{1/2} u_1' + Fr u_2' + ...) + \partial_z (Fr^{1/2} w_1' + Fr w_2' + ...) \right] = 0,$$

recalling the perturbations to the velocity field are $\mathcal{O}(Fr^{1/2})$. Here, the leading order balance arises at $\mathcal{O}(Fr^{-1/2})$:

$$\partial_\chi u_1' + \partial_z w_1' = 0. \tag{26}$$

Thus, to leading order, variability in the fluctuation fields occurs on commensurate horizontal and vertical scales, corresponding to small-scale isotropic structures in the flow. In contrast, large-scale horizontal divergences in the horizontal mean flow are balanced by vertical divergences of a much smaller vertical flow, consistent with a layering of the mean large-scale flow.

2. **The Horizontal and Vertical Momentum Equations.**

Considering next the horizontal momentum equation, we proceed by first using the exact continuity equation (22a) to re-express equation (22b) in conservative form, then substitute the Reynolds decomposition (20), noting, e.g., $\overline{uu} = \overline{u}\,\overline{u} + \overline{u'u'}$, and finally fast average to obtain

$$\begin{aligned} \partial_t \overline{u} + \partial_x \left(\overline{u}\,\overline{u} \right) + \frac{1}{Fr} \partial_z \left(\overline{u}\,\overline{w} \right) &= -\partial_x \overline{p} + \overline{f} + \frac{1}{Re_b} \left(\partial_z^2 + Fr^2 \partial_x^2 \right) \overline{u} \\ &\quad - \partial_x \left(\overline{u'u'} \right) - \frac{1}{Fr} \partial_z \left(\overline{u'w'} \right), \end{aligned} \tag{27}$$

where the forcing is assumed to be strictly large scale (i.e., $f = \overline{f} := \overline{f}_0$, and $f' = 0$). Recalling $\overline{w} = \mathcal{O}(Fr)$ and that $w' = \mathcal{O}(u')$, a physically meaningful dominant balance as $Fr \to 0$ can be obtained by requiring the leading-order fluctuation fields to be $O(Fr^{1/2})$; i.e., by requiring the expansion exponent $a = 1/2$, as noted previously. Validation of this crucial scaling has recently been provided via the DNS of [10]. Substituting the expansion (21) into (27),

$$\begin{aligned} &\partial_t \left(\overline{u}_0 + Fr^{1/2} \overline{u}_1 + ... \right) + \partial_x \left[(\overline{u}_0 + Fr^{1/2} \overline{u}_1 + ...)(\overline{u}_0 + Fr^{1/2} \overline{u}_1 + ...) \right] \\ &+ \frac{1}{Fr} \partial_z \left[(\overline{u}_0 + Fr^{1/2} \overline{u}_1 + ...)(Fr \overline{w}_2 + Fr^{3/2} \overline{w}_3 + ...) \right] = \partial_x \left(\overline{p}_0 + Fr^{1/2} \overline{p}_1 + ... \right) + \overline{f}_0 \\ &\frac{1}{Re_b} \partial_z^2 \left(\overline{u}_0 + Fr^{1/2} \overline{u}_1 + ... \right) - \partial_x \left[\overline{(Fr^{1/2} u_1' + Fr u_2' + ...)(Fr^{1/2} u_1' + Fr u_2' + ...)} \right] \\ &\qquad - \frac{1}{Fr} \partial_z \left[\overline{(Fr^{1/2} u_1' + Fr u_2' + ...)(Fr^{1/2} w_1' + Fr w_2' + ...)} \right], \end{aligned}$$

yields, at $\mathcal{O}(1)$,

$$\partial_t \overline{u}_0 + \partial_x \left(\overline{u}_0 \overline{u}_0 \right) + \partial_z (\overline{u}_0 \overline{w}_2) = -\partial_x \overline{p}_0 + \overline{f}_0 + \frac{1}{Re_b} \partial_z^2 \overline{u}_0 - \partial_z (\overline{u_1' w_1'}). \tag{28}$$

The horizontal component of the fluctuation dynamics is obtained by subtracting the exact horizontal momentum mean equation (27) from the exact full equation (22b).

Substituting the asymptotic expansions for the various fields then yields

$$\begin{aligned}
&\partial_t\left(Fr^{1/2}u_1'+...\right)+\frac{1}{Fr}\partial_\tau\left(Fr^{1/2}u_1'+Fru_2'+...\right)+\left(Fr^{1/2}u_1'+...\right)\partial_x\left(Fr^{1/2}u_1'+...\right)\\
&+\left(\overline{u}_0+Fr^{1/2}\overline{u}_1+...\right)\partial_x\left(Fr^{1/2}u_1'+Fru_2'+...\right)+\left(Fr^{1/2}u_1'+Fru_2'+...\right)\partial_x\left(\overline{u}_0+Fr^{1/2}\overline{u}_1+...\right)\\
&\quad+\frac{1}{Fr}\left[\left(\overline{u}_0+Fr^{1/2}\overline{u}_1+Fr\overline{u}_2+...\right)+\left(Fr^{1/2}u_1'+\ldots\right)\right]\partial_\chi\left(Fr^{1/2}u_1'+...\right)\\
&\quad+\frac{1}{Fr}\left(Fr\overline{w}_2+Fr^{1/2}w_1'+Frw_2'\right)\partial_z\left(Fr^{1/2}u_1'+Fru_2'+...\right)\\
&+\frac{1}{Fr}\left(Fr^{1/2}w_1'+Frw_2'+...\right)\partial_z\left(\overline{u}_0+Fr^{1/2}\overline{u}_1+...\right)=-\partial_x\left(Fr^{1/2}p_1'+Frp_2'+...\right)\\
&-\frac{1}{Fr}\partial_\chi\left(Fr^{1/2}p_1'+Frp_2'+...\right)+\frac{1}{Re_b}\left[\partial_\chi^2+\partial_z^2+2Fr\partial_\chi\partial_x+Fr^2\partial_x^2\right]\left(Fr^{1/2}u_1'+Fru_2'+...\right)\\
&\quad+\partial_x\left[\overline{\left(Fr^{1/2}u_1'+...\right)\left(Fr^{1/2}u_1'+...\right)}\right]+\frac{1}{Fr}\partial_z\left[\overline{\left(Fr^{1/2}w_1'+...\right)\left(Fr^{1/2}u_1'+...\right)}\right].
\end{aligned}$$

The leading-order dynamics arises at $\mathcal{O}(Fr^{-1/2})$:

$$\partial_\tau u_1'+\overline{u}_0\partial_\chi u_1'+w_1'\partial_z\overline{u}_0\;=\;-\partial_\chi p_1'. \tag{29}$$

The detailed analysis used to simplify the vertical momentum equation is similar to that used for the horizontal momentum equation, although the resulting leading-order mean equation,

$$0=-\partial_z\overline{p}_0+\overline{b}_0, \tag{30}$$

is hydrostatic owing to the relative smallness of $\overline{w}$. In contrast, the leading-order equation for the vertical velocity fluctuations,

$$\partial_\tau w_1'+\overline{u}_0\partial_\chi w_1'\;=\;-\partial_z p_1'+b_1', \tag{31}$$

more closely resembles the corresponding equation for the horizontal component of the fluctuating velocity field (apart from the absence of a $w'\partial_z\overline{w}$ term and the inclusion of a fluctuation buoyancy term).

3. **The Buoyancy Equation.**

Derivation of the reduced mean and fluctuation buoyancy equations closely parallels the reduction of the mean and fluctuation horizontal momentum equations. Accordingly, only the resulting leading-order equations are documented here. Specifically, the mean equation is given by

$$\partial_t\overline{b}_0+\overline{u}_0\partial_x\overline{b}_0+\overline{w}_2(\partial_z\overline{b}_0+1)=\frac{1}{PrRe_b}\partial_z^2\overline{b}_0, \tag{32}$$

while the fluctuation equation reduces to

$$\partial_\tau b_1'+\overline{u}_0\partial_\chi b_1'+w_1'(\partial_z\overline{b}_0+1)\;=\;0. \tag{33}$$

It is straightforward to extend the derivation given above to 3D scenarios having two fast horizontal coordinates $\boldsymbol{\chi} = (\chi, \zeta)$ and two slow horizontal coordinates $\mathbf{x} = (x, y)$, where $\zeta = y/Fr$ The only restriction is that the fast-time average of the fast-streamwise mean fields should vanish; i.e., the extension excludes scenarios in which slow dynamics occur on fast 'spanwise' scales. With this caveat, the resulting asymptotically-reduced multiscale model of strongly stratified turbulence is summarized below.[1]

Mean Field Equations

$$\partial_t \overline{\mathbf{u}}_0 + (\overline{\mathbf{u}}_0 \cdot \nabla_{\mathbf{x}})\overline{\mathbf{u}}_0 + \overline{w}_2 \partial_z \overline{\mathbf{u}}_0 = -\nabla_{\mathbf{x}} \overline{p}_0 - \partial_z(\overline{w_1' \mathbf{u}_1'}) + \frac{1}{Re_b}\partial_z^2 \overline{\mathbf{u}}_0 + \bar{\mathbf{f}}_0 \tag{34a}$$

$$0 = -\partial_z \overline{p}_0 + \bar{b}_0 \tag{34b}$$

$$\nabla_{\mathbf{x}} \cdot \overline{\mathbf{u}}_0 + \partial_z \overline{w}_2 = 0 \tag{34c}$$

$$\partial_t \bar{b}_0 + (\overline{\mathbf{u}}_0 \cdot \nabla_{\mathbf{x}})\bar{b}_0 + \overline{w}_2 \left(\partial_z \bar{b}_0 + 1\right) = -\partial_z(\overline{w_1' b_1'}) + \frac{1}{PrRe_b}\partial_z^2 \bar{b}_0 \tag{34d}$$

Fluctuation Equations

$$(\partial_\tau + \overline{\mathbf{u}}_0 \cdot \nabla_{\boldsymbol{\chi}})\mathbf{u}_1' + w_1' \partial_z \overline{\mathbf{u}}_0 = -\nabla_{\boldsymbol{\chi}} p_1' \tag{35a}$$

$$(\partial_\tau + \overline{\mathbf{u}}_0 \cdot \nabla_{\boldsymbol{\chi}})w_1' = -\partial_z p_1' + b_1' \tag{35b}$$

$$\nabla_{\boldsymbol{\chi}} \cdot \mathbf{u}_1' + \partial_z w_1' = 0 \tag{35c}$$

$$(\partial_\tau + \overline{\mathbf{u}}_0 \cdot \nabla_{\boldsymbol{\chi}})b_1' + w_1' \left(\partial_z \bar{b}_0 + 1\right) = 0 \tag{35d}$$

Crucially, equation (35b) confirms that vertical motions at small scales are non-hydrostatic. Moreover, equations (35a) and (35d) indicate that small-scale fluctuations can be amplified via interactions with vertical gradients in the leading-order mean fields $\overline{\mathbf{u}}_0$ and $\bar{b}_0$.

4.3 Structure of the reduced equations

Equations (34a)–(34d) are precisely the *hydrostatic* primitive equations (19) obtained from the single-scale reduction (Section 3), but here self-consistently augmented with the vertical divergences of the leading horizontal-momentum and buoyancy fluxes arising from the fast dynamics. Inspection of equations (35a)–(35d) confirms that the fast fluctuations dynamics are non-hydrostatic, formally inviscid (since $Re \to \infty$ as $Fr \to 0$ in the distinguished limit considered), and linear about the mean fields. Thus, taken together, the mean and fluctuation equations comprise a quasilinear (QL) system. More precisely, the retention of the slow x variation of the mean fields implies that the reduction is of generalized quasilinear (GQL) form. Note that the (G)QL reduction is often invoked as a useful but ultimately *ad hoc* approximation; one virtue of the present analysis is to show the formal asymptotic validity of the (G)QL approximation for strongly stratified shear flows at large Reynolds number.

[1] In these equations, it is implicit that all vectors lie in the plane perpendicular to the vertical; e.g., $\mathbf{u} \equiv (u, v)$.

Two strategies can be employed to numerically simulate the multiscale reduced equations. Firstly, a strict QL *initial-value* problem can be obtained by reinterpreting the averaging as a strict horizontal average (only), i.e., suppressing the slow x and slow y coordinate dependencies, and formally replacing $\partial_t = (1/Fr)\partial_\tau$ so that the resulting system of $\boldsymbol{\chi}$-mean and fluctuation equations can be co-evolved on a single (fast) time scale. Of course, this strategy has the undesirable feature of rendering the equation set numerically stiff, as the small parameter Fr is reintroduced into the system. An alternative strategy, which respects the multi-time-scale character of the reduced system, involves treating the fluctuation system as an *eigenvalue* problem. Unlike more standard 'wave/mean-flow interaction' models, here it is crucial to recognize that, with the mean fields locally frozen in fast time, the fluctuation fields can undergo exponential growth; that is, modal instabilities can arise as the fluctuations 'feed' off of vertical gradients of the mean horizontal velocity and buoyancy fields. Indeed, when treated as an eigensystem, the fluctuation equations (35a)–(35d) can be reduced exactly to the Taylor–Goldstein (TG) equation (8) discussed in Section 2. Thus, by inspection, the fluctuation subsystem admits all of the stratified shear instabilities admitted by the TG equation.

The new algorithm then couples the fast dynamics, treated as an eigenvalue problem, with a slow initial-value problem for the mean fields. As discussed in the next section, temporal scale separation can be maintained for this slow–fast (G)QL system only by ensuring at each slow time instant that the mean fields are marginally stable with respect to the fast fluctuations. Otherwise, the fluctuations can grow exponentially on the fast time scale, with the mean fields locally frozen in fast time, thereby breaking the 'asymptoticness' of the posited expansion. Before describing this novel algorithm, we note that, in practice, the formally non-diffusive fluctuation dynamics must be regularized once the fast subsystem is treated as an eigenvalue rather than initial-value problem. One approach, followed here, is simply to reincorporate formally small Laplacian diffusion terms (in the fast coordinates) on the grounds that, should critical layers arise, vertical gradients would become sufficiently large to require inclusion of these terms. Another possibility should be acknowledged, however; namely, that nonlinearity may become significant within the thin critical layers, providing a mechanism by which strong fluctuation–fluctuation nonlinearity (beyond the reach of the QL reduction) could arise even in the given distinguished limit.

5 Integration of Slow–Fast QL Models with Fast Instabilities

For QL systems with fast instabilities (rather than fast waves), the reduced ($Fr \to 0$) two time-scale system is problematic. If the slow field is fixed locally in time while the fast field advanced, the latter can become unbounded. As shown in [13], this issue may be resolved using a new asymptotic formalism for slow–fast QL systems subject to fast instabilities that

1. exploits *emergent* marginal stability; and
2. algebraically slaves the amplitude of fluctuations to the mean fields.

As an example of emergent marginal stability, consider the following slow–fast QL system of ordinary differential equations (ODEs), with slow time t, in the limit the parameter $Fr \to 0$:

$$\frac{\mathrm{d}U}{\mathrm{d}t} = 4(1+\sin t) - U - b^2, \qquad \frac{\mathrm{d}b}{\mathrm{d}t} = \frac{1}{Fr}Ub. \tag{36}$$

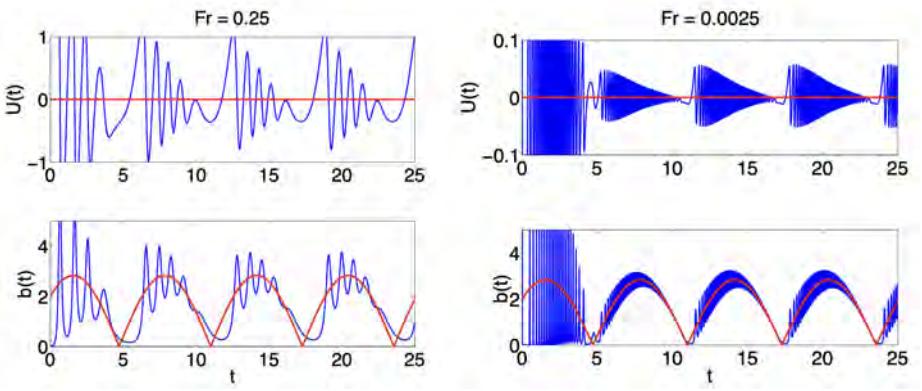

Figure 3: Numerical integration of the ODE system (36) for two values of Fr. The red lines show the leading asymptotic approximations (37) as $Fr \to 0$, confirming that, in this limit, the slow variable U is maintained in a state of *emergent* marginal stability.

As shown in figure 3, there is an initial transient after which the system evidently tunes itself so that the "mean" variable U is statistically marginally stable. (Note that here the dominant, slow part of U—shown by the red curve—plays the role of an eigenvalue.) It is straightforward to obtain an asymptotic reduction of this system of ODEs that algebraically links the fast variable b to the slow variable U such that the leading-order approximation to U is marginally stable. To wit,

$$U \sim 0 + FrU_1(t) + ... \tag{37a}$$

$$b \sim 2\sqrt{1+\sin t} + ... \tag{37b}$$

Although $\mathrm{d}b/\mathrm{d}t \neq 0$, asymptotic consistency is maintained since $|\mathrm{d}b/\mathrm{d}t| \ll 1/Fr$ as $Fr \to 0$.

This approach can be extended to partial differential equations (PDEs). As an example, consider the coupled evolution of a slow field U and fast field η subject to z- and (slow) time-varying forcing F:

$$\partial_t U = F(z,t) - U - \eta^2, \tag{38a}$$

$$\epsilon\partial_t \eta = U\eta + \partial_z^2\eta - \epsilon\eta^3. \tag{38b}$$

To analyze the limit in which the small parameter $\epsilon \to 0$, two time variables $T = t$ and $\tau = t/\epsilon$ are introduced such that $\partial_t \to \partial_T + \epsilon^{-1}\partial_\tau$. After expanding the fields as $(u,\eta) \sim (u_0,\eta_0) + \epsilon(u_1,\eta_1) + ...$, the leading-order reduction of the PDE system (38) becomes

$$\partial_T \overline{u}_0 = F - \overline{u}_0 - \overline{\eta_0^2}, \tag{39a}$$

$$\partial_\tau \eta_0 = L\eta_0, \tag{39b}$$

where the linear differential operator

$$L = \partial_z^2 + \overline{u}_0(z,T) \tag{40}$$

and $\overline{(\,\cdot\,)}$ denotes a fast time average; i.e.,

$$\overline{(\,\cdot\,)} = \lim_{\tau_*\to\infty} \frac{1}{\tau_*}\int_0^{\tau_*} (\,\cdot\,)d\tau. \tag{41}$$

Letting

$$\eta_0 = A\hat{\eta}_0(z)e^{\sigma\tau}, \tag{42}$$

equation (38b) is transformed into the eigenvalue problem

$$[L - \sigma I]\hat{\eta}_0 = 0, \tag{43}$$

where the operator on the left-hand side (LHS) can vary in slow time T. Taking a cue from the analysis of the slow–fast ODE system, we insist that the (real) eigenvalue σ remain bounded above by zero (i.e., corresponding to a mean state of marginally stability) to maintain temporal scale separation. We use this requirement as a constraint on the otherwise indeterminate amplitude A by first forming an equation for the slow-time evolution of σ. Differentiating (43) gives

$$(\partial_T L)\hat{\eta}_0 + L\partial_T\hat{\eta}_0 = \frac{\mathrm{d}\sigma}{\mathrm{d}T}\hat{\eta}_0 + \sigma\partial_T\hat{\eta}_0. \tag{44}$$

Rearranging yields

$$[L - \sigma I]\partial_T\hat{\eta}_0 = \frac{\mathrm{d}\sigma}{\mathrm{d}T}\hat{\eta}_0 - (\partial_T L)\hat{\eta}_0. \tag{45}$$

Since the operator on the LHS has a nontrivial kernel, the Fredholm Alternative Theorem requires that the right-hand side must satisfy a solvability condition. As the operator is self-adjoint, we may take the inner product [$\langle f, g\rangle = \int fg\mathrm{d}z$ for functions f, g] with $\hat{\eta}_0$:

$$\left\langle \frac{\mathrm{d}\sigma}{\mathrm{d}T}\hat{\eta}_0 - (\partial_T L)\hat{\eta}_0, \hat{\eta}_0 \right\rangle = 0. \tag{46}$$

Rearranging and normalizing such that $\langle\hat{\eta}_0, \hat{\eta}_0\rangle = 1$ yields

$$\frac{d\sigma}{dT} = \langle(\partial_T L)\hat{\eta}_0, \hat{\eta}_0\rangle. \tag{47}$$

Using equations (40) and (39a), we obtain

$$\partial_T L = F - \overline{u}_0 - \overline{\eta_0^2}. \tag{48}$$

Collecting these results, the slow evolution of the fast eigenvalue σ can be expressed as

$$\frac{d\sigma}{dT} = \alpha - \beta A^2, \tag{49}$$

where, when $\sigma = 0$,

$$\alpha = \int_0^{l_z} (F - \overline{u}_0)\hat{\eta}_0^2\mathrm{d}z, \tag{50a}$$

$$\beta = \int_0^{l_z} \hat{\eta}_0^4\mathrm{d}z. \tag{50b}$$

The following algorithm then ensures the amplitude A is self-consistently tuned to maintain the slow dynamics in a state of marginally stability provided the 'forcing' functional α is driving the mean field toward instability:

- If $\sigma < 0$, $A = 0$;
- If $\sigma = 0$ and $\alpha > 0$, set $A = \sqrt{\alpha/\beta}$ such that $d\sigma/dT = 0$.

This formalism has been extended to two space dimensions by [9], who also predict the slow evolution of the marginal k, and implemented in strongly stratified Kolmogorov flow by [7].

References

[1] P. Augier, P. Billant, and J.-M. Chomaz, *Stratified turbulence forced with columnar dipoles: numerical study*, Journal of Fluid Mechanics, 769 (2015), pp. 403–443.

[2] P. Billant and J.-M. Chomaz, *Experimental evidence for a new instability of a vertical columnar vortex pair in a strongly stratified fluid*, Journal of Fluid Mechanics, 418 (2000), pp. 167–188.

[3] ——, *Theoretical analysis of the zigzag instability of a vertical columnar vortex pair in a strongly stratified fluid*, Journal of Fluid Mechanics, 419 (2000), pp. 29–63.

[4] ——, *Self-similarity of strongly stratified inviscid flows*, Physics of Fluids, 13 (2001), pp. 1645–1651.

[5] G. Brethouwer, P. Billant, E. Lindborg, and J.-M. Chomaz, *Scaling analysis and simulation of strongly stratified turbulent flows*, Journal of Fluid Mechanics, 585 (2007), pp. 343–368.

[6] P. Cessi, *The global overturning circulation*, Annual Review of Marine Science, 11 (2019), pp. 249–270.

[7] G. P. Chini, G. Michel, K. Julien, C. B. Rocha, and C.-c. P. Caulfield, *Exploiting self-organized criticality in strongly stratified turbulence*, Journal of Fluid Mechanics, 933:A22 (2022).

[8] M. Falder, N. J. White, and C. P. Caulfield, *Seismic imaging of rapid onset of stratified turbulence in the South Atlantic Ocean*, Journal of Physical Oceanography, 46 (2016), pp. 1023–1044.

[9] A. Ferraro, G. P. Chini, and T. M. Schneider, *Following marginal stability manifolds in quasilinear dynamical reductions of multiscale flows in two space dimensions*, Physical Review E, 111 (2025), p. 025105.

[10] P. Garaud, G. P. Chini, L. Cope, K. Shah, and C.-c. P. Caulfield, *Numerical validation of scaling laws for stratified turbulence*, Journal of Fluid Mechanics, 991:R1 (2024).

[11] D. K. Lilly, *Stratified turbulence and the mesoscale variability of the atmosphere*, Journal of the Atmospheric Sciences, 40 (1983), pp. 749–761.

[12] A. Maffioli and P. Davidson, *Dynamics of stratified turbulence decaying from a high buoyancy Reynolds number*, Journal of Fluid Mechanics, 786 (2016), pp. 210–233.

[13] G. Michel and G. Chini, *Multiple scales analysis of slow–fast quasilinear systems*, Proceedings of the Royal Society A, 475 (2019), p. 20180630.

[14] T. R. Osborn, *Estimates of the local rate of vertical diffusion from dissipation measurements*, Journal of Physical Oceanography, 10 (1980), pp. 83–89.

[15] H. Salehipour, W. R. Peltier, and C. P. Caulfield, *Self-organized criticality of turbulence in strongly stratified mixing layers*, Journal of Fluid Mechanics, 856 (2018), pp. 228–256.

GFD 2024 Lecture 7: Two-dimensional Turbulence Above Topography

Basile Gallet; notes by Vincent Laroche and Cécile Le Dizes

June 25, 2024

With the goal of discussing ocean turbulence, we build upon the simple 2D Navier-Stokes model considered in the Lecture 3, adding physical ingredients of oceanic relevance. The first such ingredient is ocean bathymetry, whose influence is illustrated in figure 1. We show the geostrophic flow inferred from satellite altimetry (OSCAR surface currents) together with ocean bathymetry. While the flow displays various eddies and appears rather turbulent, one can notice some correlation between the direction of the flow and the bottom topography. Indeed, in figure 1a we observe that the flow somewhat follows the main trenches and topographic mounts. Figure 1b shows the Lofoten basin, a topographic depression at the center of which lives a persistent anticyclone. Why is it that the flow inferred from surface altimetry contains information about topographic variations several kilometers below? The main physical reason is rapid planetary rotation: the Taylor-Proudman theorem suggests that the flow tends to organize into vertically coherent columnar structures that communicate the topographic variations all the way to the surface. A first motivation for the present lecture is to derive a simple asymptotic model that captures this phenomenon.

A second motivation is perhaps at a more fundamental level. Topography can be thought of as external 'disorder' that disrupts the natural tendency for 2D flows to self-organize into large-scale coherent structures. In a similar fashion to statistical physics, one would like to be able to predict the influence of the disorder onto the end state of the 2D flow: does topography affect the natural tendency for freely-evolving 2D flows to form a large scale 'condensate' at the domain scale? How to predict the strength of the resulting condensate as a function of the strength and structure of the topographic disorder? More generally, can one determine a **large-scale organizing principle** that would allow for predictions of the end state? Historically, two such principles have been designed over the last 50 years. The statistical mechanics of two-dimensional flows assumes that the system is fully conservative and makes predictions based on the conservation of the many invariants of the system [11, 7, 9, 10, 2]. By contrast, the **selective decay principle** assumes that, even when the viscosity is made very small, some invariants decay as a result of turbulent transfers to small scales and anomalous dissipation [5, 13, 8, 3]. In this lecture we will focus on the selective decay principle, because numerical simulations show that enstrophy indeed robustly decays regardless of the small value of the (hyper)viscosity [12]. A limitation of such variational approaches, however, is that they apply to unforced systems in the limit where the small-scale viscosity tends to zero. As discussed in the first lecture, the system then conserves energy. However, in most situations of interest energy is input by some external forcing mechanism and removed by some combination of viscosity and large-scale friction. How to adapt the selective decay principle to such a forced-dissipative system?This will be the topic of the last section, where we will provide a large-scale organizing principle for (weakly) forced-dissipative systems.

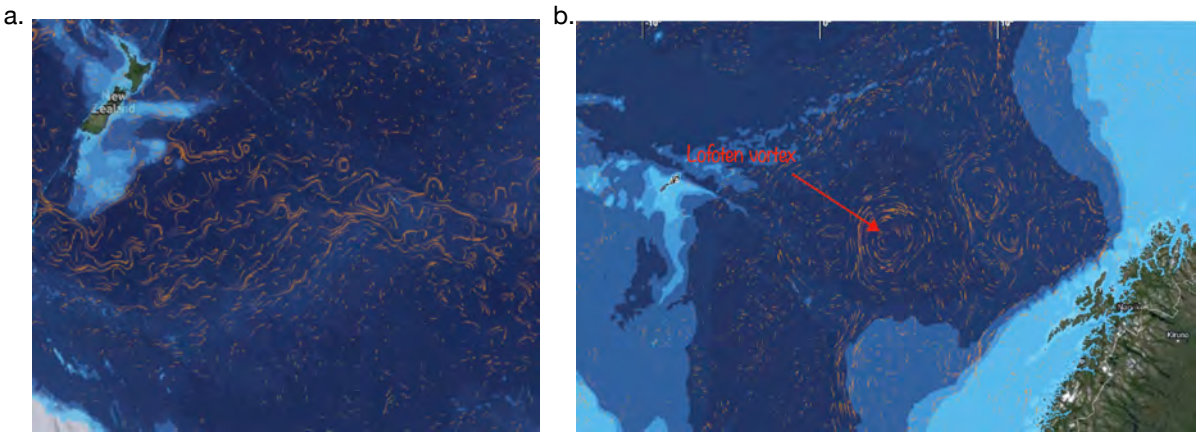

Figure 1: OSCAR surface currents (orange) superposed onto the ocean bathymetry (blue, the darker the deeper). **a.** Southern Ocean East of New Zealand. **b.** Lofoten basin off the coast of Norway.

Let us start with the derivation of what is arguably the simplest model to study the influence of bottom topography on the dynamics of a rapidly rotating flow: the single-layer quasi-geostrophic model.

1 Derivation of the Single-layer Quasi-geostrophic Model

1.1 Rotating shallow-water equations

With ocean dynamics in mind, we consider a shallow layer of fluid in a frame rotating around the vertical axis at a rate $f/2$, as sketched in figure 2. The mean-zero irregular bathymetry of the ocean floor is denoted by $h(x, y)$. We denote the vertical coordinate by z, with $z = 0$ at the average depth of the ocean floor. The fluid surface lies at $z = H(x, y, t)$, the mean fluid height being at $z = H_0$. Above the fluid, the atmosphere has uniform pressure P_0. The total thickness of the fluid layer is

$$\mathcal{H}(x, y, t) = H(x, y, t) + h(x, y)\,. \tag{1}$$

Within the shallow-water approximation, the horizontal velocity field is vertically invariant, with horizontal components $\mathbf{u}_\perp = [u(x, y, t), v(x, y, t)]$. The pressure field $P(x, y, z, t)$ satisfies hydrostatic balance. Denoting as g the acceleration of gravity and ρ the uniform fluid density:

$$0 = -\partial_z P/\rho - g\,, \tag{2}$$

which we integrate into:

$$P = -\rho g[z - H(x, y, t)] + P_0\,. \tag{3}$$

The rotating shallow-water equations then read:

$$\partial_t \mathbf{u}_\perp + (\mathbf{u}_\perp \cdot \boldsymbol{\nabla})\mathbf{u}_\perp + f\mathbf{e}_z \times \mathbf{u}_\perp = -g\boldsymbol{\nabla} H\,, \tag{4}$$

$$\partial_t \mathcal{H} + \boldsymbol{\nabla} \cdot (\mathcal{H}\mathbf{u}_\perp) = 0\,, \tag{5}$$

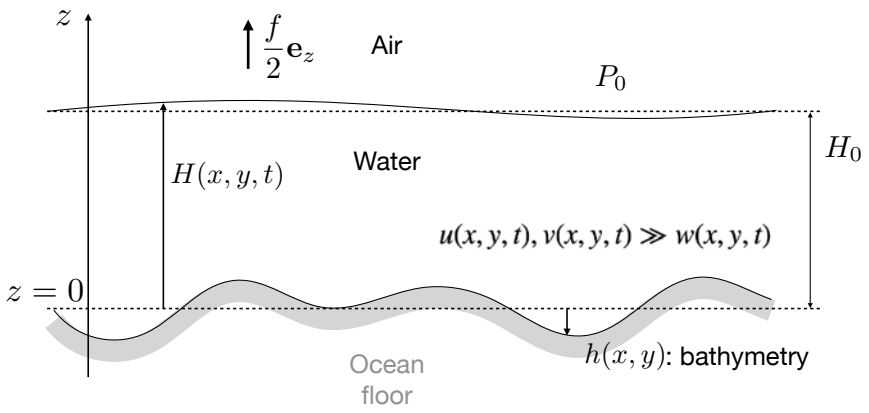

Figure 2: **Single-layer shallow-water model.** A shallow layer of fluid is subject to gravity $\mathbf{g}$ in a frame rotating at a rate $f/2$ around the vertical axis z. The mean-zero bathymetry of the ocean floor is denoted by $h(x,y)$. The free surface lies at $z = H(x,y,t)$, with $z = 0$ denoting the average depth of the ocean floor. H_0 denotes the average thickness of the layer at rest. The atmospheric pressure above the fluid layer is uniform and equal to P_0.

where $\boldsymbol{\nabla} = (\partial_x, \partial_y)$. Cross-differentiation of equation (4) yields the governing equation for the vertical vorticity $\zeta = \partial_x v - \partial_y u$:

$$\partial_t \zeta + \mathbf{u}_\perp \cdot \boldsymbol{\nabla}\zeta + (f+\zeta)\boldsymbol{\nabla}\cdot\mathbf{u}_\perp = 0\,. \tag{6}$$

We non-dimensionalize the set of equations (4-6) using the timescale f^{-1} and the lengthscale H_0 (in all three directions):

$$\mathbf{x} = H_0\tilde{x}\,, \qquad t = \tilde{t}/f\,, \qquad \mathbf{u}_\perp = H_0 f\tilde{\mathbf{u}_\perp}\,, \tag{7}$$

$$\mathcal{H} = H_0\tilde{\mathcal{H}}\,, \qquad H = H_0\tilde{H}\,, \qquad h = H_0\tilde{h}\,. \tag{8}$$

Dropping the tildes for brevity, the dimensionless equations read:

$$\partial_t \mathbf{u}_\perp + (\mathbf{u}_\perp\cdot\boldsymbol{\nabla})\mathbf{u}_\perp + \mathbf{e}_z\times\mathbf{u}_\perp = -Bu^2\,\boldsymbol{\nabla}H \tag{9}$$

$$\partial_t \mathcal{H} + \mathbf{u}_\perp\cdot\boldsymbol{\nabla}\mathcal{H} = -\mathcal{H}\boldsymbol{\nabla}\cdot\mathbf{u}_\perp\,, \tag{10}$$

$$\partial_t \zeta + \mathbf{u}_\perp\cdot\boldsymbol{\nabla}\zeta = -(1+\zeta)\boldsymbol{\nabla}\cdot\mathbf{u}_\perp\,, \tag{11}$$

where we have isolated the total (Lagrangian) derivatives of $\mathcal{H}$ and ζ on the left-hand sides, using $\boldsymbol{\nabla}\cdot(\mathcal{H}\mathbf{u}_\perp) = \mathbf{u}_\perp\cdot\boldsymbol{\nabla}\mathcal{H} + \mathcal{H}\boldsymbol{\nabla}\cdot\mathbf{u}_\perp$ for equation (10). In equation (9), Bu denotes a Burger number, defined as :

$$Bu = \sqrt{\frac{g}{f^2 H_0}}\,. \tag{12}$$

1.2 Conservation of potential vorticity

Quasi-geostrophy greatly simplifies the description of the system: as opposed to the three evolution equations (9-11), we will end up with a single evolution equation for a scalar quantity – the potential

vorticity (PV) – that encodes the full evolution of the system. For the present shallow-water system, PV is defined as $Q(x,y,t) = (f+\zeta)/\mathcal{H}$ in dimensional form, its dimensionless counterpart being $\tilde{Q} = (1+\tilde{\zeta})/\tilde{\mathcal{H}}$. Dropping the tildes again, the Lagrangian derivative of the dimensionless PV is:

$$(\partial_t + \mathbf{u}_\perp \cdot \boldsymbol{\nabla})Q = \frac{(\partial_t + \mathbf{u}_\perp \cdot \boldsymbol{\nabla})\zeta}{\mathcal{H}} - \frac{1+\zeta}{\mathcal{H}^2}(\partial_t + \mathbf{u}_\perp \cdot \boldsymbol{\nabla})\mathcal{H} \tag{13}$$

$$= \frac{-(1+\zeta)\boldsymbol{\nabla}\cdot\mathbf{u}_\perp}{\mathcal{H}} + \frac{(1+\zeta)\mathcal{H}(\boldsymbol{\nabla}\cdot\mathbf{u}_\perp)}{\mathcal{H}^2} = 0\,, \tag{14}$$

where we have substituted the expressions (10) and (11) of the Lagrangian derivatives of $\mathcal{H}$ and ζ to obtain the second line. We conclude from the computation above that **potential vorticity is a material invariant, conserved along flow trajectories in the absence of forcing and dissipation.**

1.3 Asymptotic expansion

We are interested in the rapidly rotating, strongly stratified (strong gravity) regime where the dynamics are governed by quasi-geostrophy. We thus focus on the following range of parameters:

- Rapid rotation: small Rossby number $\frac{\mathbf{u}_\perp}{fH_0}$, that is $\tilde{\mathbf{u}_\perp} \ll 1$.
- Strong stratification (strong gravity): $Bu \gg 1$.
- Weak topography: $h \ll H_0$, that is $\tilde{h} \ll 1$.
- Even weaker fluctuations of the height of the free surface, also known as the 'rigid-lid' regime.

Introducing a bookkeeping parameter $\epsilon \ll 1$, we posit the following expansions for the various dimensionless fields:

$$\tilde{\mathbf{u}_\perp} = \epsilon\,\mathbf{u}_1(x,y,T) + \epsilon^2\,\mathbf{u}_2(x,y,T) + \mathcal{O}(\epsilon^3)\,, \tag{15}$$

$$\tilde{\zeta} = \epsilon\,\zeta_1(x,y,T) + \epsilon^2\,\zeta_2(x,y,T) + \mathcal{O}(\epsilon^3)\,, \tag{16}$$

$$\tilde{h} = \epsilon\,h_1(x,y)\,, \tag{17}$$

$$\tilde{H} = 1 + \epsilon^2\,H_2(x,y,T) + \mathcal{O}(\epsilon^3)\,, \tag{18}$$

$$\tilde{\mathcal{H}} = 1 + \epsilon\,h_1(x,y) + \epsilon^2\,H_2(x,y,T) + \mathcal{O}(\epsilon^3)\,, \tag{19}$$

where we have introduced the slow time variable $T = \epsilon\,t$.[1] Finally, we assume a large Burger number:

$$Bu^2 = 1/\epsilon\,. \tag{20}$$

To $\mathcal{O}(\epsilon)$, equation (9) reduces to geostrophic balance:

$$\mathbf{e}_z \times \mathbf{u}_1 = -\boldsymbol{\nabla} H_2\,, \tag{21}$$

a consequence being that $\mathbf{u}_1$ is divergence-free. Introducing the streamfunction $\psi(x,y,T)$ such that $\mathbf{u}_1 = -\boldsymbol{\nabla}\times(\psi\mathbf{e}_z)$ leads to:

$$\psi = H_2 \qquad \text{and} \qquad \zeta_1 = \Delta\psi = \Delta H_2\,, \tag{22}$$

[1] Note that this is not a multiple-scale expansion but simply a rescaling of the time variable, with $\partial_t = \epsilon\partial_T$.

where $\Delta = \partial_{xx} + \partial_{yy}$. Now, expanding the expression of the (dimensionless) PV $\tilde{Q}$ yields:

$$\tilde{Q} = \frac{1+\tilde{\zeta}}{\tilde{\mathcal{H}}} = \frac{1+\epsilon\,\Delta\psi}{1+\epsilon\,h_1} + \mathcal{O}(\epsilon^2) = 1 + \epsilon\,Q_1 + \mathcal{O}(\epsilon^2)\,, \text{ where } Q_1 = \Delta\psi - h_1\,. \tag{23}$$

To $\mathcal{O}(\epsilon^2)$, the PV conservation equation becomes:

$$\partial_T Q_1 + \mathbf{u}_1 \cdot \boldsymbol{\nabla} Q_1 = 0\,, \tag{24}$$

where the advective term can be written as $\mathbf{u}_1 \cdot \boldsymbol{\nabla} Q_1 = J(\psi, Q_1)$. Equation (24) together with the definition of Q_1 in (23) can be recast under the dimensional form:

$$\partial_t q + J(\psi, q) = 0\,, \tag{25}$$

$$q = \Delta\psi + \eta(x,y)\,, \tag{26}$$

where the quasi-geostrophic PV q consists of the relative vorticity $\Delta\psi$ and the 'topographic potential vorticity' $\eta(x,y) = -f\,h(x,y)/H_0$. The set of equations (25-26) fully determines the evolution of the system in the quasi-geostrophic regime.[2] One easily checks that in the absence of topography, $\eta = 0$, equations (25-26) reduce to the standard 2D Euler equation.

In the following we will consider both the unforced, undamped system (25-26), but also the following forced-dissipative version:

$$\partial_t q + J(\psi, q) = \mathcal{F}(x,y) - \kappa\Delta\psi - \nu\Delta^3\psi\,, \tag{27}$$

$$q = \Delta\psi + \eta(x,y)\,. \tag{28}$$

On the right-hand side of equation (27) is a steady forcing term $\mathcal{F}(x,y)$, together with a linear damping term $-\kappa\Delta\psi$ and a hyperviscous term $-\nu\Delta^3\psi$ to damp small-scale structures. In the ocean context, $\mathcal{F}(x,y)$ stems from the curl of a wind stress applied on the ocean surface, while $-\kappa\Delta\psi$ stems from Ekman friction on the ocean floor.

2 Selective Decay

2.1 Invariants of the conservative system

We first consider the conservative system (25-26) (that is, $\mathcal{F} = 0$, $\kappa = 0$, $\nu = 0$) inside a square domain $\mathcal{D}$ with periodic boundary conditions. We denote by $\langle\cdot\rangle$ a space average inside this domain. Multiplying equation (25) with ψ before averaging over space leads to:

$$\langle\psi\partial_t\Delta\psi\rangle + \langle\psi J(\psi, q)\rangle = 0 \tag{29}$$

The second term on the left-hand side vanishes (based on properties of J discussed in the previous lecture). Performing an integration by parts in space for the first term, using the periodic boundary conditions, finally yields:

$$\frac{\mathrm{d}}{\mathrm{d}t}\left\langle|\boldsymbol{\nabla}\psi|^2\right\rangle = 0\,. \tag{30}$$

[2]Indeed, starting from the knowledge of $q(x,y,t)$, one can invert (26) to obtain $\psi(x,y,t)$, before time-stepping (25) to obtain $q(x,y,t+dt)$, and so on.

We obtain that **the kinetic energy $E = \langle \mathbf{u}^2 \rangle$ is conserved**, where we omit the 1/2 prefactor in the standard definition of the kinetic energy to alleviate the algebra in the next sections. Now multiply equation (25) with q before averaging over space to get:

$$\frac{\mathrm{d}}{\mathrm{d}t} \langle q^2 \rangle = 0 \,, \tag{31}$$

where we have used $\langle qJ(\psi, q) \rangle = 0$. We conclude that **the (potential) enstrophy $\mathcal{Q} = \langle q^2 \rangle$ is conserved** in the absence of forcing and dissipation.[3]

Two-dimensional turbulence above topography thus possesses two quadratic invariants, just like standard (flat-bottom) 2D turbulence. Based on our understanding of standard 2D turbulence, we expect $\mathcal{Q}$ to be transferred to smaller and smaller scales, while E should be transferred to larger scales. If some tiny hyperviscosity ν is retained in the problem, we expect $\mathcal{Q}$ to be robustly damped (anomalous dissipation), while we expect E to be conserved to an excellent approximation. Based on this intuition, Bretherton and Haidvogel [3] proposed in 1976 to apply the selective decay principle to this system:

Selective decay principle: the end state of the system is obtained by minimizing Q while conserving the initial value of E.

2.2 The variational problem

To minimize the enstrophy $\mathcal{Q}$ while conserving the initial value of the energy E we consider the following functional:

$$\mathcal{L}\{\psi\} = \iint_{\mathcal{D}} q^2 \mathrm{d}x\mathrm{d}y + \mu \iint_{\mathcal{D}} \mathbf{u}^2 \mathrm{d}x\mathrm{d}y = \iint_{\mathcal{D}} q^2 + \mu(\boldsymbol{\nabla}\psi)^2 \mathrm{d}x\mathrm{d}y \,, \tag{32}$$

where μ is a Lagrange multiplier ensuring the energy constraint. For a small variation $\delta\psi$ of the streamfunction, the variation of $\mathcal{L}$ reads:

$$\delta\mathcal{L} = \iint_{\mathcal{D}} 2q\delta q + 2\mu(\boldsymbol{\nabla}\psi) \cdot \boldsymbol{\nabla}\delta\psi \mathrm{d}x\mathrm{d}y \,, \tag{33}$$

$$= \iint_{\mathcal{D}} 2q\delta q - 2\mu\psi\Delta(\delta\psi) \mathrm{d}x\mathrm{d}y \,, \tag{34}$$

$$= \iint_{\mathcal{D}} 2q\delta q - 2\mu\psi\delta(\Delta\psi) \mathrm{d}x\mathrm{d}y \,, \tag{35}$$

$$= 2 \iint_{\mathcal{D}} (q - \mu\psi)\, \delta q \, \mathrm{d}x\mathrm{d}y \,, \tag{36}$$

where we have perfomed an integration by parts using the periodic boundary conditions. Extremalizing $\mathcal{L}$ requires $\delta\mathcal{L}$ to vanish for any small variation δq, which implies that the parenthesis in (36) must vanish. We finally obtain:

$$q = \Delta\psi + \eta = \mu\psi \,. \tag{37}$$

[3] In fact, the space average of any function of q is conserved. When the system is truncated at some finite large wavenumber, however, the truncated system only conserves the quadratic invariants E and $\mathcal{Q}$. We focus on E and $\mathcal{Q}$ in the following, discarding the other invariants.

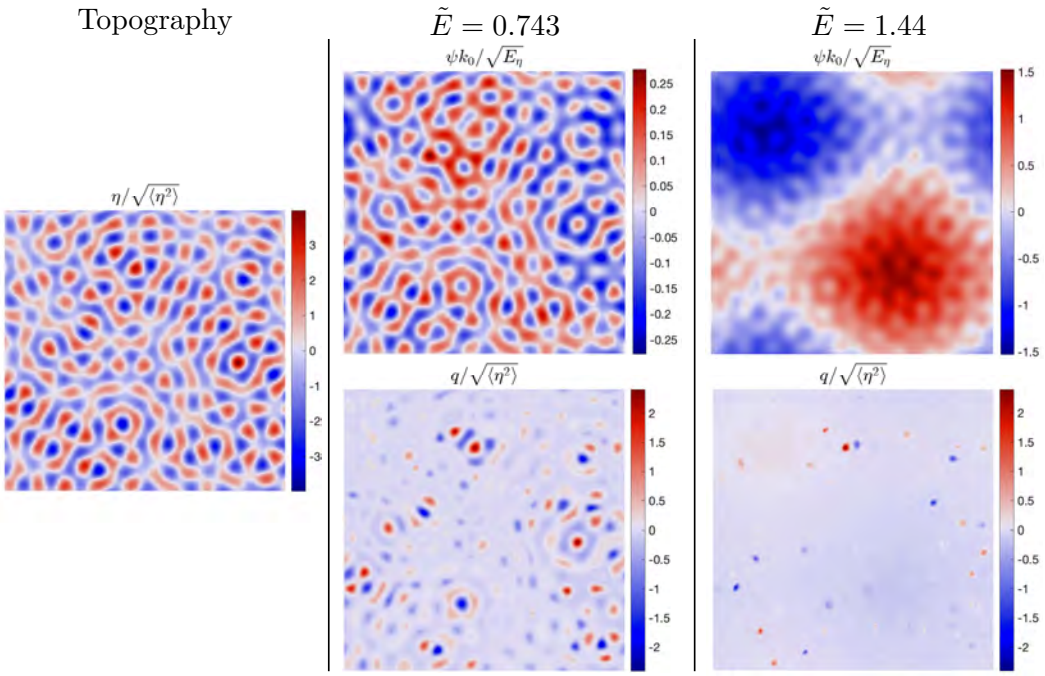

Figure 3: For the topography shown on the left-hand panel, a numerical run initialized with energy $\tilde{E} = 0.743$ displays no condensation (center column), whereas a run initialized with $\tilde{E} = 1.44$ settles in a condensed state in the long-time limit (right-hand column).

Remark 1: Fields satisfying (37) correspond either to extrema of $\mathcal{Q}$ or to saddle points. The extrema can be either local or global.

Remark 2: Once (37) has been solved for ψ, the value of the Lagrange multiplier μ is obtained from the value of the initial energy using the constraint $E = \langle|\boldsymbol{\nabla}\psi|^2\rangle$.

Remark 3: An appealing aspect of selective decay is that any solution to (37) is a steady solution to (25). Indeed, using $q = \mu\psi$ we have $J(\psi, q) = \mu J(\psi, \psi) = 0$.

Remark 4: Additionally, if the state obtained by solving (37) corresponds to the minimum of $\mathcal{Q}$ then it is stable [1]. Indeed, any departure from this minimum of $\mathcal{Q}$ would increase $\mathcal{Q}$. This cannot happen spontaneously, however, because $\mathcal{Q}$ can only decrease as a result of the dynamics (for $\mathcal{F} = 0$, $\kappa = 0$ and very small ν).

3 Solutions to the Variational Problem: Transition to Condensation

For simplicity, we consider monoscale topography in the following, such that $\Delta\eta = -k_\eta^2\,\eta(x, y)$, where k_η denotes the wavenumber of the topography. Denoting as k_0 the gravest wavenumber within the square domain ($k_0 = 2\pi/\text{sidelength}$), we restrict attention to topography at smaller scale than the domain size, $k_\eta > k_0$, with a strict inequality (although there is no need for scale separation, that is, we do not demand $k_\eta \gg k_0$).

3.1 The Betherton-Haidvogel branch of solutions

Seeking a solution to the variational problem (37) at the scale k_η of the topography, one can substitute $\Delta\psi = -k_\eta^2\,\psi(x,y)$ into (37) to obtain:

$$\psi(x,y) = \frac{\eta(x,y)}{\mu + k_\eta^2}\,. \tag{38}$$

We refer to this solution as the **'Bretherton-Haidvogel' (BH) branch of solutions** to the variational problem. The energy of the BH solution (38) is:

$$E = \left\langle |\boldsymbol{\nabla}\psi|^2 \right\rangle = -\left\langle \psi\Delta\psi \right\rangle = k_\eta^2 \left\langle \psi^2 \right\rangle = \frac{k_\eta^2}{(\mu + k_\eta^2)^2} \left\langle \eta^2 \right\rangle\,, \tag{39}$$

while the enstrophy is:

$$\mathcal{Q} = \left\langle q^2 \right\rangle = \mu^2 \left\langle \psi^2 \right\rangle = \frac{\mu^2}{(\mu + k_\eta^2)^2} \left\langle \eta^2 \right\rangle\,. \tag{40}$$

As discussed above, equation (39) can be inverted to express the Lagrange multiplier μ in terms of the (conserved) initial energy E. The resulting μ can be substituted into (40) to express the enstrophy $\mathcal{Q}$ in terms of the initial energy E on the BH branch of solutions. We leave these steps as an exercise for the motivated reader, the result being:

$$\frac{\mathcal{Q}}{\langle \eta^2 \rangle} = \left(\sqrt{\tilde{E}} - 1\right)^2\,. \tag{41}$$

where we have introduced the dimensionless energy $\tilde{E} = Ek_\eta^2/\left\langle \eta^2 \right\rangle$. Expression (41) for $\mathcal{Q}$ vs E on the BH branch is shown in figure 4 (right).

3.2 The condensed branch of solutions

We are about to show that the BH branch considered above does not always correspond to the absolute minimum of the enstrophy $\mathcal{Q}$. Indeed, there are other solutions to the variational problem (37), as seen by recasting (37) as:

$$\Delta\psi - \mu\psi = -\eta\,. \tag{42}$$

When computing the BH branch above, we have implicitly assumed that the operator acting on ψ on the left-hand side of (42) is invertible. However, this is not necessarily the case. Consider for instance $\mu = -k_0^2$. Equation (42) becomes:

$$\Delta\psi + k_0^2\psi = -\eta\,. \tag{43}$$

The solution consists of the sum of a particular solution and a solution to the homogeneous equation $\Delta\psi + k_0^2\psi = 0$. We seek a particular solution at scale k_η, which we denote by ψ_η. Using $\Delta\psi_\eta = -k_\eta^2\psi_\eta$, we obtain:

$$\psi_\eta = \frac{\eta(x,y)}{k_\eta^2 - k_0^2}\,. \tag{44}$$

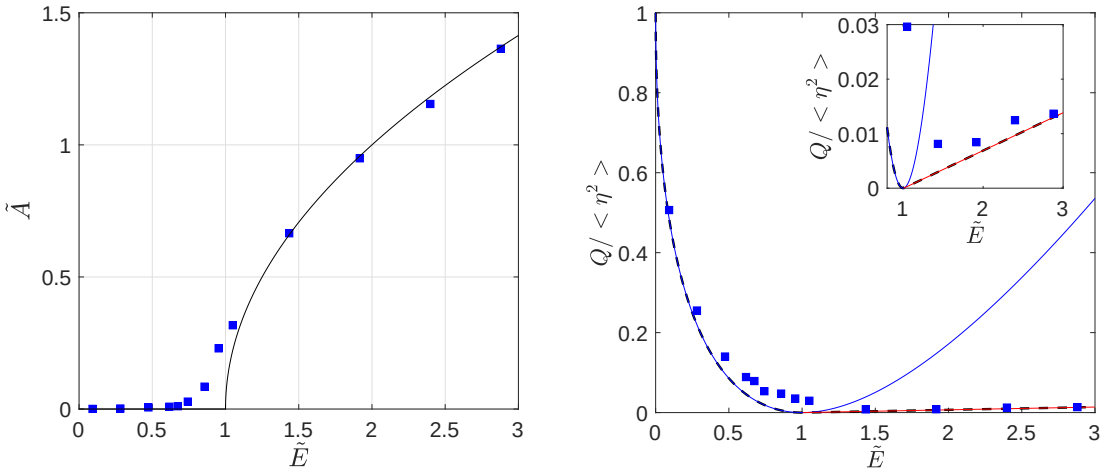

Figure 4: **Left:** Amplitude $\tilde{A}$ of the condensate as a function of the (conserved) energy of the initial condition $\tilde{E}$. The theory predicts the existence of a condensed branch for $\tilde{E} > 1$ in the scale separation limit. The data points agree well with the prediction (48), shown as a solid line. **Right:** Enstrophy $\mathcal{Q}$ in the (quasi-)stationary state as a function of the (conserved) energy $\tilde{E}$ of the initial condition. Also shown are the results of the minimization: BH branch in blue and condensed branch in red, for $k_\eta/k_0 = 12$. The absolute minimum (over the branches) is shown as a black dashed line. The inset is a zoom on the data for $\tilde{E} \geq 1$.

The solution to the homogeneous solution is written as $A\,\psi_0(x,y)$, where $A \geq 0$ is an amplitude and $\psi_0(x,y)$ is a normalized harmonic function at the gravest wavenumber k_0 of the domain. That is, $\psi_0(x,y)$ satisfies $\Delta\psi_0 = -k_0^2\,\psi_0$, and we further demand that ψ_0 satisfy the normalization condition $\langle\psi_0^2\rangle = 1$.

Adding the particular solution to the solution of the homogeneous equation finally leads to:

$$\psi = A\,\psi_0(x,y) + \psi_\eta(x,y)\,. \tag{45}$$

We refer to (45) as the **'condensed' branch of solutions** to the variational problem. Indeed, (45) consists of a flow ψ_η at the topographic scale, together with a 'condensed' flow at the scale of the domain, with spatial structure ψ_0 and amplitude A. The amplitude A is determined by writing the energy associated with the streamfunction (45):

$$E = \langle|\boldsymbol{\nabla}\psi|^2\rangle = A^2k_0^2 + k_\eta^2\,\langle\psi_\eta^2\rangle\,, \tag{46}$$

$$\Rightarrow A^2k_0^2 = E - \frac{k_\eta^2\,\langle\eta^2\rangle}{(k_\eta^2 - k_0^2)^2}\,. \tag{47}$$

Although not a necessary assumption, the algebra is made even simpler by focusing on the limit of scale separation, $k_\eta \gg k_0$, which we consider in the following. The expression of the dimensionless amplitude of the condensate then reduces to:

$$\tilde{A} = \sqrt{\tilde{E} - 1}\,, \qquad \text{where } \tilde{A} = \frac{Ak_\eta k_0}{\sqrt{\langle\eta^2\rangle}}\,. \tag{48}$$

One immediately observes that expression (48) is valid only for $\tilde{E} \geq 1$. There are no condensed solutions for $\tilde{E} < 1$.

One can also compute the enstrophy associated with the condensed branch of solutions (45), before substituting the expression of A above to express $\mathcal{Q}$ as a function of E. We leave these steps as an exercise for the interested reader, the result being:

$$\frac{\mathcal{Q}}{\langle \eta^2 \rangle} = \frac{k_0^2}{k_\eta^2}(\tilde{E} - 1)\,, \tag{49}$$

valid for $k_\eta \gg k_0$ and $\tilde{E} \geq 1$. We plot expression (49) in figure 4 (right) for comparison with the BH branch. The prefactor k_0^2/k_η^2 in (49) is an asymptotically small quantity in the limit $k_\eta \gg k_0$ considered here, and $\mathcal{Q}$ is thus much smaller on the condensed branch of solutions than on the BH branch.

We conclude that, for $E \geq 1$, there are (at least) two branches of solutions to the variational problem. The enstrophy on the condensed branch of solutions is smaller than the enstrophy on the BH branch. Based on the selective decay principle, we thus expect the system to end up in a condensed state. For $E < 1$ there is a single branch of solutions and we expect the system to be on the BH branch of solutions. This is summarized in figure 4 (left), where we plot the amplitude of the condensate as a function of the energy of the initial condition. **We predict a continuous transition to condensation** as the initial energy exceeds a threshold value $\langle \eta^2 \rangle / k_\eta^2$, the amplitude of the condensate above threshold being given by expression (48).

We compare the predictions to numerical simulations in figures 3 and 4. We consider random approximately monoscale topography around wavenumber $k_\eta/k_0 = 12$ (see Ref. [4] for details). There is no forcing nor friction, and we employ very small hyperviscosity. Enstrophy robustly decreases in such simulations, while energy is conserved to a very good approximation. In figure 3 we show snapshots obtained at the end time of two simulations differing in the value of the initial energy. The streamfunction ψ agrees qualitatively with the theory: the simulation with $\tilde{E} < 1$ displays no large-scale condensation, whereas the simulation with $\tilde{E} > 1$ displays a strong large-scale condensate. By contrast, in line with previous studies the PV q exhibits strong isolated vortices that are not predicted by enstrophy minimization [14, 12, 6]. When condensation arises, however, these vortices appear to be rather sparsely distributed above the faint background PV structure of the condensed branch, given by (37) with $\mu = -k_0^2$. There is thus hope for large-scale condensation to be quantitatively predicted by enstrophy minimization despite the emergence of the isolated vortices.

To characterize the condensation transition quantitatively, we extract from the DNS the amplitude A (rms value of the streamfunction restricted to the gravest Fourier modes only). In figure 4 we show the resulting dimensionless condensate amplitude $\tilde{A}$ as a function of the dimensionless initial energy $\tilde{E}$. The numerical data are in very good agreement with the theoretical prediction from enstrophy minimization. There is some departure from the theoretical prediction in the immediate vicinity of the bifurcation threshold only, as a consequence of the isolated vortices pinned to the topography.

In figure 4, we also plot the equilibrated enstrophy $\mathcal{Q}$ extracted from the DNS. Above the transition $\mathcal{Q}$ is significantly lower than the enstrophy of the BH branch, because the latter is not the absolute minimizer. Instead, the equilibrated $\mathcal{Q}$ lies close to the prediction of the condensed branch. It is slightly greater than this absolute minimum as a result of the extra isolated vortices. Once again, this slight departure from the absolute minimum of $\mathcal{Q}$ has only a modest impact on

the value of the condensate amplitude A, which closely follows the theoretical prediction.

4 Forced Dissipative System

As discussed at the outset, selective decay deals with unforced systems in the limit of weak small-scale damping. Most flows of interest, however, are forced and dissipative. How to adapt selective decay to such an out-of-equilibrium situation? Progress can be made by considering weak forcing and dissipation. While the energy-conserving system has a continuum of solutions indexed by the initial energy, we show in the following that weak forcing and dissipation select a single member out of this continuum of solutions to the energy-conserving problem, leading to quantitative predictions for the strength of the condensate.

4.1 Selection of minimum-enstrophy states

Consider equation (27) with weak forcing and friction:

$$\partial_t q + J(\psi, q) = \epsilon[\mathcal{F}^{(1)}(x,y,t) - \kappa^{(1)}\Delta\psi]\,, \tag{50}$$

$$q = \Delta\psi + \eta \tag{51}$$

where $\epsilon \ll 1$ is a small parameter and we omit the hyperviscous term (assumed to be even smaller) for brevity. Expand the fields in powers of ϵ:

$$q(x,y,t) = q^{(0)}(x,y,T) + \epsilon q^{(1)}(x,y,T) + \dots\,, \tag{52}$$

$$\psi(x,y,t) = \psi^{(0)}(x,y,T) + \epsilon\psi^{(1)}(x,y,T) + \dots\,, \tag{53}$$

where we have introduced the slow time variable $T = \epsilon t$, that is, $\partial_t \to \partial_t + \epsilon\partial_T$.

Collecting terms of order $\mathcal{O}(\epsilon^0)$ leads to:

$$\partial_t q^{(0)} + J(\psi^{(0)}, q^{(0)}) = 0\,, \qquad q^{(0)} = \Delta\psi^{(0)} + \eta\,. \tag{54}$$

This is the set of equations discussed in the previous section. We consider a solution to these equations that lies on the condensed branch, allowing the amplitude of the condensate to vary slowly in time:

$$\psi^{(0)}(x,y,T) = \psi_\eta(x,y) + A(T)\,\psi_0(x,y)\,. \tag{55}$$

Following the standard method of mutiple-scale expansion, the slow evolution equation for the amplitude $A(T)$ can be obtained from a solvability condition at next order. An alternate and more enlightening way of obtaining this amplitude equation consists of writing the energy evolution equation to lowest order. Upon multiplying equation(27) with ψ before averaging over x and y, one obtains the evolution equation for the energy:

$$\frac{\mathrm{d}}{\mathrm{d}T}\frac{\left\langle|\boldsymbol{\nabla}\psi|^2\right\rangle}{2} = -\left\langle\mathcal{F}\psi\right\rangle - \kappa\left\langle|\boldsymbol{\nabla}\psi|^2\right\rangle\,, \tag{56}$$

where, in line with selective decay, the hyperviscous term does not contribute to energy dissipation and has been omitted. Using the lowest-order streamfunction (55), we estimate the various terms

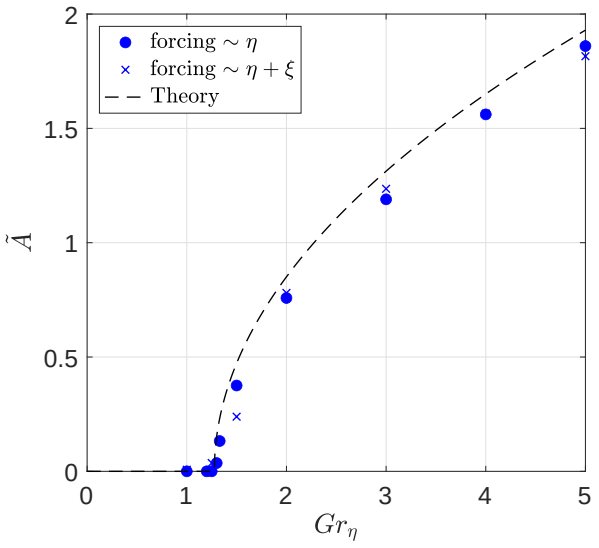

Figure 5: **Topographic-scale forcing.** Condensate amplitude as a function of the forcing expressed in terms of the Grashof number. When small hyperviscosity is retained the theoretical prediction becomes $\tilde{A} = \sqrt{Gr_\eta - 1 - \nu k_\eta^4/\kappa}$, shown as a dashed line using $\nu k_\eta^4/\kappa = 0.28$. DNS data points for these parameter values are in good agreement with this theoretical prediction.

of equation (56) to lowest order ϵ, considering for brevity the scale separation limit $\tilde{k}_\eta \gg 1$:

$$\frac{\mathrm{d}}{\mathrm{d}T}\frac{\langle|\boldsymbol{\nabla}\psi|^2\rangle}{2} = \epsilon\,\frac{k_0^2}{2}\frac{\mathrm{d}(A^2)}{\mathrm{d}T} + \mathcal{O}(\epsilon^2)\,, \tag{57}$$

$$\langle\mathcal{F}\psi\rangle = \epsilon\left[A(T)\left\langle\mathcal{F}^{(1)}\psi_0\right\rangle + \frac{\langle\mathcal{F}^{(1)}\eta\rangle}{k_\eta^2}\right] + \mathcal{O}(\epsilon^2)\,, \tag{58}$$

$$\kappa\left\langle|\boldsymbol{\nabla}\psi|^2\right\rangle = \epsilon\,\kappa^{(1)}\left[A^2k_0^2 + \frac{\langle\eta^2\rangle}{k_\eta^2}\right] + \mathcal{O}(\epsilon^2)\,. \tag{59}$$

Keeping these dominant contributions only, equation (56) leads to the following evolution equation for the dimensionless amplitude $\tilde{A}$ of the condensate, recast in terms of the non-expanded variables:

$$\frac{1}{2\kappa}\frac{\mathrm{d}}{\mathrm{d}t}\left(\tilde{A}^2\right) \;=\; Gr_\eta + Gr_0\,\tilde{A} - 1 - \tilde{A}^2\,, \tag{60}$$

where the forcing enters the equation through a domain-scale Grashof number Gr_0 and a topographic-scale Grashof number Gr_η, defined as:

$$Gr_0 = -\frac{\langle\mathcal{F}\psi_0\rangle}{k_0\kappa\sqrt{E_\eta}} \qquad \text{and} \qquad Gr_\eta = -\frac{\langle\mathcal{F}\eta\rangle}{\kappa\,\langle\eta^2\rangle}\,. \tag{61}$$

4.2 Topographic-scale forcing

We first consider the (arguably somewhat academic) situation of a small-scale forcing correlated with the topography and uncorrelated with the domain-scale condensate, that is $Gr_0 = 0$ and

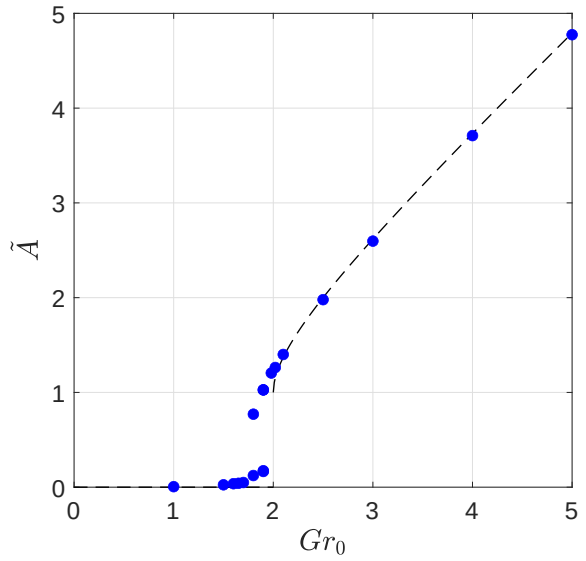

Figure 6: **Domain-scale forcing.** Condensate amplitude as a function of the large-scale forcing amplitude expressed in terms of Gr_0. The DNS data points are in good agreement with the theoretical prediction A_+ in (63) associated with the selection of minimum-enstrophy solutions (dashed line).

$Gr_\eta \neq 0$. Seeking steady solutions to the amplitude equation (60) leads to $0 = Gr_\eta - 1 - \tilde{A}^2$, with solution:

$$\tilde{A} = \sqrt{Gr_\eta - 1}\,, \tag{62}$$

valid for $Gr_\eta \geq 1$. For $Gr_\eta < 1$ we find $\tilde{A}^2 < 0$; this is an indication that the ansatz (55) is incorrect and that the system lies on the BH branch instead, with $\tilde{A} = 0$. **We thus predict a continuous transition to condensation as the topographic-scale Grashof number exceeds one.** In figure 5, we plot a slightly modified version of this prediction where an $\mathcal{O}(\epsilon)$ hyperviscosity is retained in the computation, the consequence being that the threshold value of Gr_η shifts from 1 to $1+\nu k_\eta^4/\kappa$ (see Ref. [4] for details). We compare the prediction to numerical simulations of the forced-dissipative system with forcing that is either directly proportional to $\eta(x,y)$, or proportional to $\eta(x,y)+\xi(x,y)$, where $\xi(x,y)$ is a random field with the same statistics as $\eta(x,y)$ but corresponding to another realization. Both forcing protocols lead to data points that fall close to the theoretical prediction, illustrating the predictive skill of the present approach.

4.3 Domain-scale forcing

We now consider the more geophysically relevant situation of large-scale forcing at the scale of the domain: $Gr_0 \neq 0$ and $Gr_\eta = 0$. Seeking steady solutions to the amplitude equation (60), we obtain:

$$\tilde{A}_\pm = \frac{Gr_0 \pm \sqrt{Gr_0^2 - 4}}{2}\,, \tag{63}$$

valid for $Gr_0 \geq 2$ only (for $Gr_0 < 2$ the system lies on the BH branch). Closer investigation indicates that the branch $\tilde{A}_-$ is unstable. We thus expect a discontinuous transition to condensation as Gr_0 exceeds 2. We plot the predicted bifurcation curve in figure 6, together with data points from numerical simulations performed with a forcing proportional to $\cos(k_0 y)$ (see Ref. [4] for details). Once again, the agreement with the theory is excellent at finite distance from the instability threshold, with slight discrepancies near threshold. In particular, the amplitude of the condensate is very well captured by the upper-branch $\tilde{A}_+$ for $Gr_0 \geq 2$. We observe only a very narrow region of bistability, possibly because the uncondensed BH branch has other directions of instability, besides direct condensation following equation (60). Additionally, the region of stability of the condensed branch extends somewhat below $Gr_0 = 2$, down to $Gr_0 \simeq 1.8$. This 10% correction in threshold value may be a consequence of the extra vortices pinned to the topography. As for the previous case considered above, we conclude that the amplitude of the condensate is accurately predicted by the theory, except in the immediate vicinity of the instability threshold where the pinned vortices impact the dynamics of the system.

References

[1] Vladimir Igorevich Arnol'd. *Mathematical methods of classical mechanics*. Springer Science & Business Media, 1978.

[2] Freddy Bouchet and Antoine Venaille. Statistical mechanics of two-dimensional and geophysical flows. *Physics reports*, 515(5):227–295, 2012.

[3] Francis P Bretherton and Dale B Haidvogel. Two-dimensional turbulence above topography. *Journal of Fluid Mechanics*, 78(1):129–154, 1976.

[4] Basile Gallet. Two-dimensional turbulence above topography: condensation transition and selection of minimum enstrophy solutions. *Journal of Fluid Mechanics*, 988:A13, 2024.

[5] Martin David Kruskal and RM Kulsrud. Equilibrium of a magnetically confined plasma in a toroid. *The Physics of Fluids*, 1(4):265–274, 1958.

[6] JH LaCasce, A Palóczy, and M Trodahl. Vortices over bathymetry. *Journal of Fluid Mechanics*, 979:A32, 2024.

[7] Jonathan Miller. Statistical mechanics of euler equations in two dimensions. *Physical review letters*, 65(17):2137, 1990.

[8] David Montgomery, Leaf Turner, and George Vahala. Three-dimensional magnetohydrodynamic turbulence in cylindrical geometry. *The Physics of Fluids*, 21(5):757–764, 1978.

[9] Raoul Robert. A maximum-entropy principle for two-dimensional perfect fluid dynamics. *Journal of Statistical Physics*, 65:531–553, 1991.

[10] Raoul Robert and Joel Sommeria. Statistical equilibrium states for two-dimensional flows. *Journal of Fluid Mechanics*, 229:291–310, 1991.

[11] Rick Salmon, Greg Holloway, and Myrl C Hendershott. The equilibrium statistical mechanics of simple quasi-geostrophic models. *Journal of Fluid Mechanics*, 75(4):691–703, 1976.

[12] Lia Siegelman and William R Young. Two-dimensional turbulence above topography: Vortices and potential vorticity homogenization. *Proceedings of the National Academy of Sciences*, 120(44):e2308018120, 2023.

[13] J Brian Taylor. Relaxation of toroidal plasma and generation of reverse magnetic fields. *Physical Review Letters*, 33(19):1139, 1974.

[14] Bowen Zhao, Emma Chieusse-Gérard, and Glenn Flierl. Influence of bottom topography on vortex stability. *Journal of Physical Oceanography*, 49(12):3199–3219, 2019.

GFD 2024 Lecture 8: Baroclinic Instability and Ocean Mesoscale Turbulence

Basile Gallet; notes by Ishwari Mulkawar, Nicolaos Petropoulos,
Camille Moisset and Matthew McCormack

June 26, 2024

The external fluid layers of planets and their satellites are subject to meridionally dependent heating due to incoming radiation from a distant star, or intrinsic heat fluxes emanating from the planetary interior. On a rocky planet without an atmosphere, such a heat source would induce a strong difference in surface temperature between the equator and the poles. The presence of an atmosphere and/or an ocean strongly mitigates that temperature difference: the meridional temperature gradient induces turbulence in these external fluid layers through a process called baroclinic instability. The resulting 'baroclinic turbulence' greatly enhances heat transport from the equator to the poles, thereby reducing the emergent meridional temperature gradient. Predicting the equilibrated meridional temperature profile of these external fluid layers is arguably one of the central questions that a theory of climate should address. We provide two illustrations of baroclinic turbulence in figure 1: panels a and b correspond to the near-surface layer of Jupiter, while panel c corresponds to the Southern Ocean, where turbulent eddies result from the baroclinic instability of the Antarctic Circumpolar Current flowing around Antarctica.

The images in figure 1 show that the equilibrated state of baroclinic turbulence consists of a turbulent flow whose energy-containing scale is small compared to the size of the planet or ocean basin, which is also the extent of the large-scale heating pattern: scale separation spontaneously arises in this problem, opening an avenue for describing the turbulent heat transport in terms of a diffusive closure. A diffusive closure relates the turbulent heat flux to the meridional temperature gradient through a diffusivity coefficient that encodes the macroscopic transport induced by the small-scale erratic turbulent motion. The situation is analogous to the textbook examples of molecular diffusion, where a macroscopic downgradient flux of heat or particles is induced by molecular agitation at microscopic scale. In both cases the role of theory is to express the diffusion coefficient in terms of external parameters [2, 7]. That scale separation spontaneously arises in a fully turbulent flow is more the exception than the rule, and the reader accustomed to the standard textbook examples of turbulent flows – Couette flow, Rayleigh-Bénard convection, etc. – which all lack scale separation, ought to be skeptical about the use of a diffusive closure. That reader would be right in the sense that the diffusive closure is valid only when applied at scales larger than the energy containing scale, but this is precisely what a parameterization of turbulence in coarse atmosphere and/or ocean models intends to do: the diffusive closure is to be used as a parameterization of tur-bulent transport in a coarse model that cannot resolve the turbulent eddies that populate baroclinic turbulence.

With the goal of keeping the description as simple as possible, we build upon the model of the previous lecture and complexify it by considering two shallow layers of fluid sitting on top of one

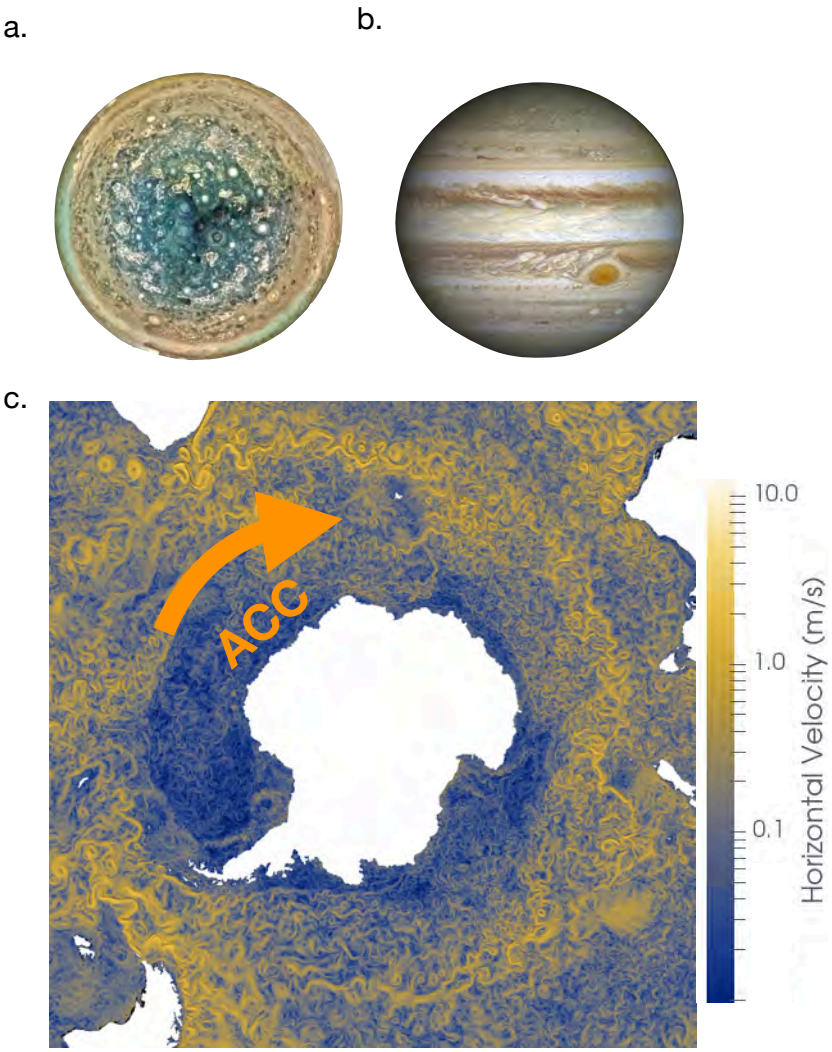

Figure 1: Baroclinic turbulence in planetary atmospheres and oceans. South pole (**a**) and sideview (**b**) of Jupiter (composite image from NASA Juno mission). **c:** Magnitude of the horizontal velocity 20 meters below the surface from a numerical simulation of the Southern Ocean run at 2.5-km resolution by the ICON-N group [8], illustrating baroclinic instability of the Antarctic Circumpolar Current (ACC).

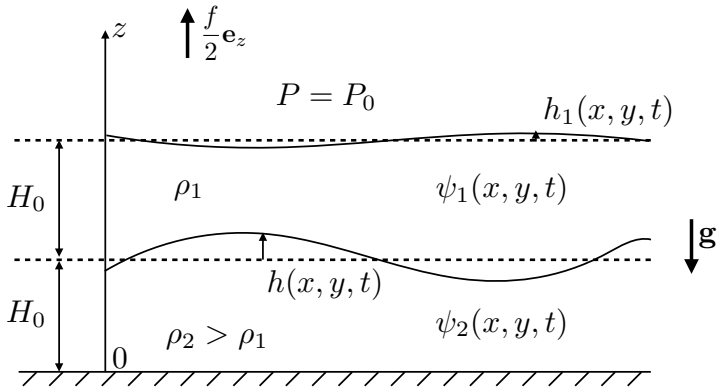

Figure 2: Schematic of the 2LQG model. The fluctuations $h_1(x,y,t)$ of the position of the free surface are much smaller than the fluctuations $h(x,y,t)$ of the position of the interface between the two layers.

another, within the QG regime: this is the two-layer quasi-geostrophic (2LQG) model [10, 9, 12]. As compared to a single-layer model, including a second fluid layer allows for a description of density variations within a fluid column. New equilibria arise through thermal-wind balance (section 1) and these new equilibria are subject to new instability mechanisms, such as baroclinic instability (section 2). The derivation of the multi-scale model for turbulent heat transport proceeds in two steps: we first derive a scaling theory for the turbulent transport arising in a homogeneous model (section 3), before implementing the resulting effective diffusivity in an inhomogeneous model with large-scale forcing (section 4).

1 The Two-layer Quasi-geostrophic (2LQG) Model

We consider the system sketched in figure 2. A shallow fluid layer of density ρ_1 lies above a shallow fluid layer of density $\rho_2 > \rho_1$, in a frame rotating around the vertical axis at a rate $f/2$. For simplicity, we consider the following regime:

- No dependence of the Coriolis parameter with latitude: we work on the f plane (as opposed to the β plane).[1]
- Equal depth at rest for the two layers, denoted by H_0.
- Rigid-lid approximation: the mean-zero fluctuations $h_1(x,y,t)$ of the height of the free surface are much smaller than the mean-zero fluctuations $h(x,y,t)$ of the position of the interface between the two layers.

[1] Mostly for simplicity, although the f plane may be a reasonable first approximation to describe baroclinic turbulence in the Southern Ocean.

1.1 Conservation of QGPV within each layer

We consider a QG regime similar to the one derived in the previous lecture for the single-layer model. Namely, the vertically invariant horizontal flow within each layer obeys geostrophic balance to lowest order, with a streamfunction $\psi_1(x,y,t)$ in the upper layer and $\psi_2(x,y,t)$ in the lower layer. A QGPV conservation equation holds within each layer (same derivation as in the previous lecture). The QGPV is the sum of a relative vorticity term $\Delta\psi_{1;2}$ and a topographic PV term $\eta_{1;2}(x,y,t)$ proportional to the local departure of the thickness of the layer from its rest value: $-h(x,y,t)$ in layer 1 and $+h(x,y,t)$ in layer 2, making use of the rigid-lid approximation $h_1 \ll h$. Including the prefactor f/H_0 from the previous lecture yields $\eta_1(x,y,t) = f\,h(x,y,t)/H_0$ for the upper layer and $\eta_2(x,y,t) = -f\,h(x,y,t)/H_0$ for the lower layer. The QGPV conservation equation within each layer finally reads:

$$q_1 = \Delta\psi_1 + \frac{f}{H_0}h(x,y,t)\,, \qquad \partial_t q_1 + J(\psi_1, q_1) = 0\,, \tag{1}$$

$$q_2 = \Delta\psi_2 - \frac{f}{H_0}h(x,y,t)\,, \qquad \partial_t q_2 + J(\psi_2, q_2) = 0\,. \tag{2}$$

The equations are not closed at this stage, as we need to relate the position $h(x,y,t)$ of the interface to the streamfunctions $\psi_{1;2}$.

1.2 Relating the position of the interface to the streamfunctions

We relate the position of the interface to the streamfunctions based on hydrostatic and geostrophic balance. When invoking hydrostatic balance, it is safer to keep track of the small fluctuations $h_1(x,y,t) \ll h(x,y,t)$ in the position of the free surface. Measuring the vertical coordinate z upwards from the flat ocean floor, the interface lies at $z = H_0 + h(x,y,t)$, while the top free surface lies at $z = 2H_0 + h_1(x,y,t)$. We denote by P_0 the uniform atmospheric pressure above the upper layer, $P_1(x,y,z,t)$ the pressure field in the upper layer and $P_2(x,y,z,t)$ the pressure field in the lower layer. Hydrostatic balance in the upper layer leads to:

$$0 = -\partial_z P_1 - \rho_1 g \Rightarrow P_1 = -\rho_1 g(z - 2H_0 - h_1) + P_0\,. \tag{3}$$

Hydrostatic balance in the lower layer leads to:

$$0 = -\partial_z P_2 - \rho_2 g \Rightarrow P_2 = -\rho_2 g(z - H_0 - h) + \mathcal{C}(x,y,t)\,, \tag{4}$$

where the integration constant $\mathcal{C}(x,y,t)$ is obtained by demanding that $P_1 = P_2$ at the interface $z = H_0 + h$. We finally obtain:

$$P_2 = -\rho_2 g(z - H_0 - h) + P_0 - \rho_1 g(h - h_1 - H_0)\,. \tag{5}$$

The pressure field within each layer decomposes into a horizontally invariant z-dependent part $A_{1;2} + B_{1;2}z$, plus a mean-zero horizontally varying z-independent part $\tilde{p}_{1;2}(x,y,t)$. Using this decomposition, geostrophic balance within each layer reads $\psi_{1;2} = \tilde{p}_{1;2}(x,y,t)/(\rho_{1;2}\,f)$, that is:

$$\psi_1 = \frac{g h_1}{f}\,, \tag{6}$$

$$\psi_2 = \frac{\rho_1 g h_1 + g(\rho_2 - \rho_1)h}{\rho_2 f}\,. \tag{7}$$

We focus on the situation where there is only a slight density difference between the two layers: $\rho_2 - \rho_1 \ll \rho_1$. Then, to lowest order, ρ_2 can be replaced with ρ_1 at the denominator of (7), leading to:

$$\psi_2 \simeq \frac{gh_1}{f} + g\frac{\rho_2 - \rho_1}{\rho_1} h \,. \tag{8}$$

Subtracting (6) from (8) finally leads to the desired relation between h and the two streamfunctions:

$$h = \frac{f}{g'}(\psi_2 - \psi_1) \,, \tag{9}$$

where we have introduced the reduced gravity $g' = g(\rho_2 - \rho_1)/\rho_1 \ll g$.[2]

Substituting expression (9) for $h(x, y, t)$ into equations (1-2) finally leads to the 2LQG system:

$$q_1 = \Delta\psi_1 + \frac{\psi_2 - \psi_1}{2\lambda^2} \,, \qquad \partial_t q_1 + J(\psi_1, q_1) = 0 \,, \tag{10}$$

$$q_2 = \Delta\psi_2 - \frac{\psi_2 - \psi_1}{2\lambda^2} \,, \qquad \partial_t q_2 + J(\psi_2, q_2) = 0 \,, \tag{11}$$

where we have introduced the Rossby deformation radius $\lambda = \sqrt{g'H_0}/(\sqrt{2}f)$, a characteristic length-scale set by the relative importance of density stratification over global rotation.

1.3 Barotropic-baroclinic decomposition

Instead of using streamfunctions associated with each layer, it proves insightful to decompose the flow into a vertical average (over the two layers) and the remaining z-dependent part. That is, we introduce the fields $\psi(x, y, t)$ and $\tau(x, y, t)$, defined as:

$$\psi = \frac{\psi_1 + \psi_2}{2} \,, \tag{12}$$

$$\tau = \frac{\psi_1 - \psi_2}{2} \,. \tag{13}$$

ψ is referred to as the 'barotropic streamfunction'.[3] It is the vertically averaged streamfunction, which is also the streamfunction of the vertically averaged flow. τ is called the 'baroclinic streamfunction', but in the present context we will refer to τ as the temperature field. Indeed, consider the situation where the density stratification is entirely due to temperature, the uniform temperature of the upper-layer fluid being warmer than the uniform temperature of the lower-layer fluid. As illustrated, e.g., in figure 3a, the vertically averaged temperature of a fluid column then depends only the position of the interface. If the interface is locally deeper, there is more warm fluid inside the water column and the vertically averaged temperature is higher. Conversely, if the interface is locally shallower there is locally more cool fluid in the water column and the vertically averaged temperature is lower. Now, notice using equation (9) that τ is directly proportional to $-h$: a fluid column with larger τ is warmer on vertical average, and **$\tau(x, y, t)$ is a direct proxy for the vertically averaged temperature of the local fluid column. We thus refer to τ as the temperature field, even though τ has units of a streamfunction.**

[2] Equation (6) can be recast as $h_1 = f\psi_1/g$. Assuming that ψ_1, ψ_2, and $\psi_2 - \psi_1$ are comparable, using (9) we obtain that $h_1/h \sim (\rho_2 - \rho_1)/\rho_1 \ll 1$, which justifies the rigid-lid approximation a posteriori.

[3] Often, in physical oceanography, barotropic simply means 'z-invariant', while baroclinic means 'z-dependent'.

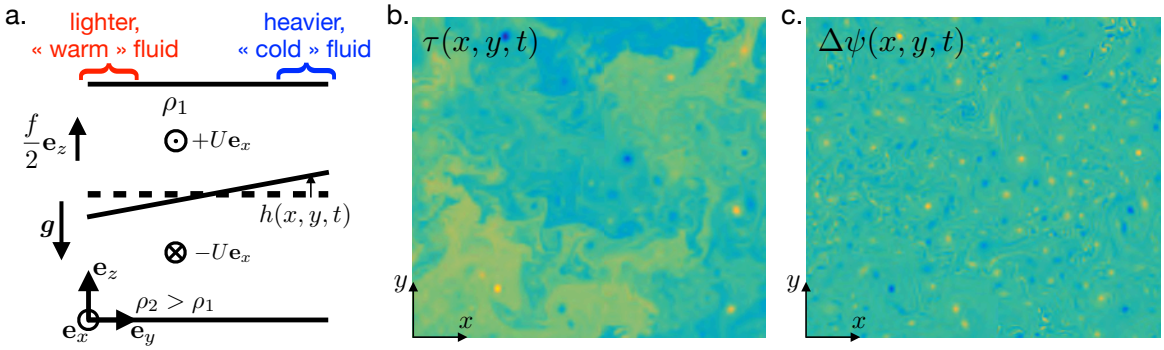

Figure 3: **Homogeneous model for a local patch of ocean or atmosphere. a.** Base state of the model. The uniform meridional temperature gradient corresponds to a tilted interface in the 2LQG framework. It is associated with a vertically sheared zonal flow through thermal-wind balance. This base state is subject to baroclinic instability, the ensuing baroclinic turbulence being illustrated in the low-drag regime in panels **b** (temperature) and **c** (barotropic vorticity).

1.4 Thermal-wind balance

Consider a local patch of ocean or atmosphere at mid-latitudes in the Northern hemisphere. We wish to describe this patch of fluid using a local Cartesian 2LQG model, with x the zonal coordinate, y along latitude, pointing northward, and z along the local vertical. Because the poles are cooler, $\partial_y \tau < 0$, and because the patch of ocean is small we consider a uniform latitudinal temperature gradient, which we denote by $U = -\partial_y \tau$. Based on equation (9) the uniform gradient of τ corresponds to a sloping interface between the two fluid layers, as sketched in figure 3a. But based on the definition (13) of τ, the uniform gradient also corresponds to a vertically sheared zonal flow:

$$U = -\partial_y \tau = \frac{\partial_y \psi_2 - \partial_y \psi_1}{2} = \frac{U_1 - U_2}{2}\,, \tag{14}$$

where U_1 and U_2 correspond to uniform zonal flows in the upper and lower layers, respectively. Equation (14) is referred to as **thermal-wind balance: the meridional temperature gradient necessarily coexists with a vertically sheared zonal flow.** Physically, the latitudinal pressure gradient associated with the tilted interface has opposite signs in the two layers (the interface would like to relax to a flat position) and can only be balanced by the Coriolis force inside each layer, hence the opposite zonal flows in the two layers. Figure 3a corresponds to a situation where the vertically averaged velocity vanishes.[4] Another possibility is for the zonal flow to vanish in the lower layer, for instance as a result of strong bottom friction on the ocean floor or on the ground below the atmosphere. One then has $U_2 = 0$, and using equation (14), $U_1 = 2U$. This simple model explains why the latitudinal temperature gradient in the atmosphere is associated with a strong eastward jet stream, and why a similar latitudinal temperature gradient in the Southern Ocean is associated with the Antarctic Circumpolar Current.

[4] or has been removed by switching to a comoving frame.

2 Baroclinic Instability

The lowest energy state of the two-layer system corresponds to motionless layers separated by a flat interface. As compared to this lowest energy state, the thermal-wind state sketched in figure 3a has available potential energy associated with the tilt of the interface. While this thermal-wind state is a valid solution to the equations, it turns out to be an unstable one. Indeed, we are about to introduce the baroclinic instability mechanism, through which the system taps into the potential energy reservoir to induce fluid motion and heat transport. In a model of finite extent, such heat transport acts to flatten the interface between the two layers.[5]

To wit, perform the sum and difference of equations (10) and (11) to recast the evolution equations in terms of $\psi(x,y,t)$ and $\tau(x,y,t)$:

$$\partial_t(\Delta\psi) + J(\psi,\Delta\psi) + J(\tau,\Delta\tau) = 0\,, \tag{15}$$

$$\partial_t\left(\Delta\tau - \frac{\tau}{\lambda^2}\right) + J\left(\psi,\Delta\tau - \frac{\tau}{\lambda^2}\right) + J(\tau,\Delta\psi) = 0\,. \tag{16}$$

Decompose the temperature field into a uniform background meridional gradient $-Uy$, plus an arbitrary departure $\tilde{\tau}(x,y,t)$:

$$\tau = -Uy + \tilde{\tau}(x,y,t)\,. \tag{17}$$

Inserting this decomposition into (15-16) yields:

$$\partial_t(\Delta\psi) + J(\psi,\Delta\psi) + J(\tilde{\tau},\Delta\tilde{\tau}) + U\partial_x(\Delta\tilde{\tau}) = 0\,, \tag{18}$$

$$\partial_t\left(\Delta\tilde{\tau} - \frac{\tilde{\tau}}{\lambda^2}\right) + J\left(\psi,\Delta\tilde{\tau} - \frac{\tilde{\tau}}{\lambda^2}\right) + J(\tilde{\tau},\Delta\psi) + U\partial_x\left(\Delta\psi + \frac{\psi}{\lambda^2}\right) = 0\,. \tag{19}$$

2.1 Linear instability

Let us focus first on the linear stability of the system by considering infinitesimal perturbations ψ and $\tilde{\tau}$. Linearizing the equations leads to:

$$\partial_t(\Delta\psi) + U\partial_x(\Delta\tilde{\tau}) = 0\,, \tag{20}$$

$$\partial_t\left(\Delta\tilde{\tau} - \frac{\tilde{\tau}}{\lambda^2}\right) + U\partial_x\left(\Delta\psi + \frac{\psi}{\lambda^2}\right) = 0\,. \tag{21}$$

Seeking solutions under the form:

$$\begin{pmatrix}\psi(x,y,t)\\ \tilde{\tau}(x,y,t)\end{pmatrix} = \begin{pmatrix}\hat{\psi}\\ \hat{\tau}\end{pmatrix} e^{i\mathbf{k}\cdot\mathbf{x}+\sigma t} \tag{22}$$

leads to a 2×2 system in $\hat{\psi}$ and $\hat{\tau}$, the determinant of which must vanish for non-trivial solutions to exist. This leads to a dispersion relation providing the acceptable values of the growth rate:

$$\tilde{\sigma}^2 = \tilde{k}_x^2\,\frac{1-\tilde{k}^2}{1+\tilde{k}^2}\,, \tag{23}$$

[5] In the following doubly-periodic model, however, the tilt of the interface is prescribed and the flow cannot feed back onto it.

where the dimensionless growth rate and wavevector are defined as $\tilde{\sigma} = \sigma\lambda/U$ and $\tilde{\mathbf{k}} = \mathbf{k}\lambda = (\tilde{k}_x, \tilde{k}_y)$. Expression (23) immediately shows that there are many values of $\tilde{\mathbf{k}}$ associated with a positive growth rate σ: **the system is linearly unstable, this instability being known as 'baroclinic instability'.** As an exercise, the interested reader can maximize (23) over wavevector $\mathbf{k}$ to check that the most unstable wavenumber corresponds to $\tilde{k}_y = 0$ and $\tilde{k}_x = \sqrt{\sqrt{2}-1}$. **The most unstable (dimensional) wavelength is thus of the order of the Rossby deformation radius λ.**

2.2 Equilibrated state: baroclinic turbulence

Following the exponential growth of perturbations in the linear regime, we expect a fully nonlinear regime where the flow is turbulent. To numerically investigate such baroclinic turbulence, we consider the governing equations (18) and (19) inside a doubly periodic domain $(x, y) \in [0, 2\pi L]^2$, with the addition of dissipative terms:

- We include hyperviscous terms in both equations to damp the small-scale vorticity filaments.
- We expect the turbulent 2D flow to display some form of inverse energy cascade, towards large scale. We thus include a large-scale drag term to damp kinetic energy at the end of this cascade.

For simplicity, we include a drag term in the governing equation for the barotropic flow only. We consider both the case of a linear drag force, proportional to the barotropic velocity, and the case of a quadratic drag force, proportional to the squared barotropic velocity. Taking the curl of this force yields the contribution to the barotropic vorticity equation. Equations (18) and (19) are thus supplemented with the following terms on the right-hand side:

$$\partial_t(\Delta\psi) + J(\psi, \Delta\psi) + J(\tilde{\tau}, \Delta\tilde{\tau}) + U\partial_x(\Delta\tilde{\tau}) = -\nu\Delta^5\psi + \text{drag}\,, \tag{24}$$

$$\partial_t\left(\Delta\tilde{\tau} - \frac{\tilde{\tau}}{\lambda^2}\right) + J\left(\psi, \Delta\tilde{\tau} - \frac{\tilde{\tau}}{\lambda^2}\right) + J(\tilde{\tau}, \Delta\psi) + U\partial_x\left(\Delta\psi + \frac{\psi}{\lambda^2}\right) = -\nu\Delta^4\left(\Delta\tilde{\tau} - \frac{\tilde{\tau}}{\lambda^2}\right)\,, \tag{25}$$

where ν denotes hyperviscosity and the drag term reads:

$$\text{drag} = \begin{cases} -\kappa\Delta\psi & \text{for linear drag} \\ -\frac{\mu}{2}\left[\partial_x(|\boldsymbol{\nabla}\psi|\partial_x\psi) + \partial_y(|\boldsymbol{\nabla}\psi|\partial_y\psi)\right] & \text{for quadratic drag} \end{cases} \tag{26}$$

with κ the linear drag coefficient and μ the quadratic drag coefficient. The motivation for linear friction is that it naturally arises as a consequence of a laminar Ekman boundary layer near a flat bottom boundary. The flow may not be laminar at the bottom of the Ocean, however, and the Ocean floor is certainly not smooth. In this context, quadratic friction may be a better model for the turbulent drag force on the 3D roughness elements of the Ocean floor (as discussed in the first lecture). In the following, for brevity we drop the tilde on τ, but the reader should remember that τ now denotes the departure from the uniform background temperature gradient.

In figure 3b,c, we show snapshots in the equilibrated state of a simulation with weak hyperviscosity and friction. The barotropic vorticity $\Delta\psi$ displays strong isolated coherent vortices with weak fluctuations in between. By contrast, the temperature field displays strong fluctuations between the vortices.

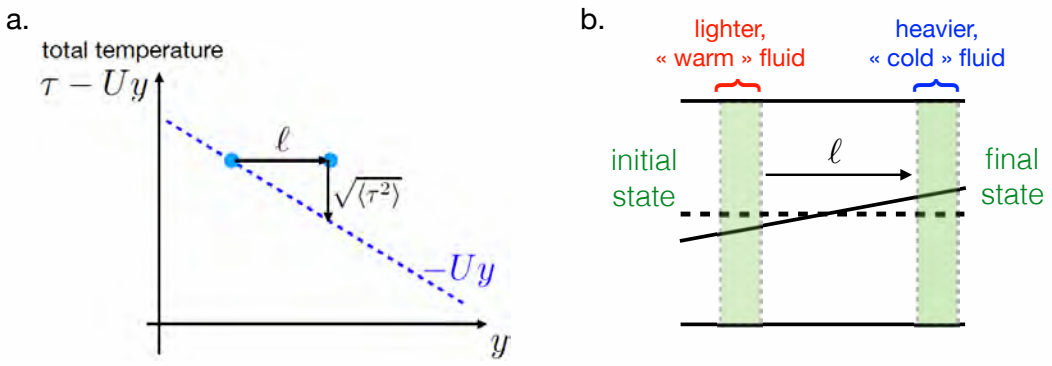

Figure 4: **a.** The mixing length ℓ can be thought of as the typical mean free path over which a fluid element travels carrying its initial background temperature, before interacting with the environment, thereby relaxing to the new local background temperature. **b**. A fluid column initially at rest 'freely falls' in the meridional direction over a distance ℓ, transforming potential energy into kinetic energy. The final velocity is given by (35).

2.3 Quantities of interest

Denoting as $\langle\cdot\rangle$ a space and time average, our main goal is to determine the eddy-induced meridional heat flux $\langle\psi_x\tau\rangle$, or equivalently the diffusivity $D = \langle\psi_x\tau\rangle/U$ connecting this heat flux to the background temperature gradient $-U$. As will be illustrated in section 4, the heat diffusivity D is the key quantity to parameterize the turbulent transport in a coarse-grained model. We thus focus primarily on D in the following.

When the domain is large enough, the energy-containing scale is much smaller than the domain size, which becomes irrelevant. Similarly, the heat flux is independent of the hyperviscosity ν when the latter is small enough. We thus seek D as a function of the relevant dimensional parameters U, λ, and the friction coefficient κ or μ. **In dimensionless form, we seek the dimensionless diffusivity $D_* = D/(U\lambda)$ as a function of the dimensionless drag coefficient $\kappa_* = \kappa\lambda/U$ or $\mu_* = \mu\lambda$ (for linear and quadratic drag, respectively).**

A related quantity of interest is the mixing length $\ell = \sqrt{\langle\tau^2\rangle}/U$. As illustrated schematically in figure 4a, ℓ is the typical distance – or mean free path – traveled by a fluid element carrying its background temperature before it is mixed with the environment and relaxes to the local background temperature. It follows that the typical temperature fluctuations around the background gradient are of the order of $U\ell$. The dimensionless mixing length $\ell_* = \ell/\lambda$ is again a function of κ_* or μ_*, depending on the form of the drag.

Thompson & Young ran simulations of the present model with linear drag and report a somewhat surprising observation [11]: the numerical data for both D_* and ℓ_* seem to lie onto a curve of the form $\exp(\text{const.}/\kappa_*)$. This empirical observation points to an extreme sensitivity of the heat transport and mixing-length on bottom drag, stronger than the typical power-law relations observed in most turbulent scaling regimes (see e.g. Lecture 3). More recently, Chang & Held revisited this problem, considering quadratic bottom drag instead of linear drag [1]. They report power-law behaviors for the diffusivity and the mixing-length: $D_* \sim \mu_*^{-1.24}$ and $\ell_* \sim \mu_*^{-0.58}$. These scaling exponents depart from the values predicted based on standard inverse cascade phenomenology, the predictions being $D_* \sim \mu_*^{-2}$ and $\ell_* \sim \mu_*^{-1}$ (see Ref. [1] for details). The conclusion is that standard inverse cascade

arguments do not apply to baroclinic turbulence. In the following section we introduce an alternate scaling theory that predicts both the exponential dependence of D_* and ℓ_* on inverse linear drag coefficient, and the correct power-law exponents for quadratic drag.

3 A Scaling Theory for the Turbulent Transport

The derivation of a scaling theory hinges on a combination of exact relations on the one hand, and plausible physical arguments on the other hand. We start with the former, more rigorous arguments of the theory, before discussing the more hand-wavy arguments.

3.1 An exact relation: the energy power integral

Let us derive the evolution equation for the mechanical energy in the system, considering the case of linear drag. Multiply equation (24) with ψ before averaging over the domain (denoted by $\langle\cdot\rangle_{\mathbf{x}}$). After a few integrations by parts using the periodic boundary conditions, this leads to:

$$\frac{\mathrm{d}}{\mathrm{d}t}\frac{\left\langle|\boldsymbol{\nabla}\psi|^2\right\rangle_{\mathbf{x}}}{2} = \langle\psi J(\tau,\Delta\tau)\rangle_{\mathbf{x}} + U\,\langle\psi\partial_x(\Delta\tau)\rangle_{\mathbf{x}} - \kappa\left\langle|\boldsymbol{\nabla}\psi|^2\right\rangle_{\mathbf{x}}\,, \tag{27}$$

where we omit the hyperviscous term, whose contribution vanishes in 2D as $\nu \to 0$. Multiplying equation (25) with τ before averaging over the domain and neglecting the hyperviscous contribution leads to:

$$\frac{\mathrm{d}}{\mathrm{d}t}\left(\frac{\left\langle|\boldsymbol{\nabla}\tau|^2\right\rangle_{\mathbf{x}}}{2} + \frac{\left\langle\tau^2\right\rangle_{\mathbf{x}}}{2\lambda^2}\right) = \frac{U}{\lambda^2}\,\langle\psi_x\tau\rangle_{\mathbf{x}} - U\,\langle\psi\partial_x(\Delta\tau)\rangle_{\mathbf{x}} - \langle\psi J(\tau,\Delta\tau)\rangle_{\mathbf{x}}\,. \tag{28}$$

The evolution equation for the mechanical energy in the system is obtained by adding equations (27) and (28):

$$\frac{\mathrm{d}}{\mathrm{d}t}\left(\underbrace{\frac{\left\langle|\boldsymbol{\nabla}\psi|^2\right\rangle_{\mathbf{x}}}{2}}_{\text{barotropic KE}} + \underbrace{\frac{\left\langle|\boldsymbol{\nabla}\tau|^2\right\rangle_{\mathbf{x}}}{2}}_{\text{baroclinic KE}} + \underbrace{\frac{\left\langle\tau^2\right\rangle_{\mathbf{x}}}{2\lambda^2}}_{\text{potential energy}}\right) = \underbrace{\frac{U}{\lambda^2}\,\langle\psi_x\tau\rangle_{\mathbf{x}}}_{\text{power released by instability}} - \underbrace{\kappa\left\langle|\boldsymbol{\nabla}\psi|^2\right\rangle_{\mathbf{x}}}_{\text{frictional dissipation}}\,. \tag{29}$$

Performing a time average leads to the energy power integral. Substituting $\langle\psi_x\tau\rangle = D\,U$, we obtain:

$$\frac{U^2}{\lambda^2}D = \kappa\left\langle\mathbf{u}^2\right\rangle\,, \tag{30}$$

where $\mathbf{u} = -\boldsymbol{\nabla}\times(\psi\mathbf{e}_z)$ denotes the barotropic velocity field. In the case of quadratic drag instead of linear drag, the energy power integral takes the form:

$$\frac{U^2}{\lambda^2}D = \frac{\mu}{2}\left\langle|\mathbf{u}|^3\right\rangle\,. \tag{31}$$

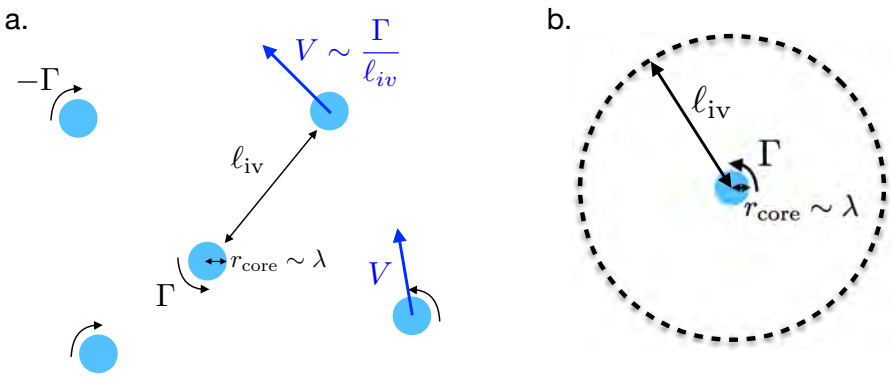

Figure 5: **a.** The barotropic vorticity field is modeled as an ideal gas of identical vortices with circulation $\pm\Gamma$, core radius $r_{\rm core} \sim \lambda$ and typical inter-vortex distance $\ell_{\rm iv}$. **b.** The moments of the barotropic velocity field are estimated by considering a single isolated vortex at the center of a disk-shaped domain or radius $\ell_{\rm iv}$.

3.2 Large-scale dynamics of τ

At scales much greater than λ, the evolution equation for τ can be simplified based on the approximation $\Delta\tau \ll \tau/\lambda^2$ and $\Delta\psi \ll \psi/\lambda^2$:

$$\partial_t \left(\cancel{\Delta\tau} - \frac{\tau}{\lambda^2} \right) + J\left(\psi, \cancel{\Delta\tau} - \frac{\tau}{\lambda^2}\right) + \cancel{J(\tau, \Delta\psi)} + U\partial_x \left(\cancel{\Delta\psi} + \frac{\psi}{\lambda^2} \right) = 0\,, \tag{32}$$

$$\Rightarrow \quad \partial_t \tau + J(\psi, \tau) = U\partial_x \psi\,. \tag{33}$$

This equations shows that, at large scales, τ is simply advected by the barotropic flow. The source of fluctuations of τ on the right-hand side is the distortion of the background temperature gradient $-Uy$ by the barotropic flow.

3.3 Vortex-gas model

The failure of standard cascade arguments to model the present turbulent flow is somewhat puzzling and points to the role of coherent structures in physical space. In figure 3c, we observe that the barotropic vorticity exhibits strong isolated vortices. We embrace this picture and propose a vortex-gas model for the barotropic vorticity, sketched in figure 5a [3, 4]. We consider a dilute gas of identical vortices with vortical cores of radius comparable to the injection scale λ of baroclinic instability, and circulation $\pm\Gamma$. The vortices are separated by a typical inter-vortex distance $\ell_{\rm iv}$, and they wander around as a result of mutual induction, with a typical velocity $V \sim \Gamma/\ell_{\rm iv}$. There are now five dimensional quantities in the model: D, ℓ, $\ell_{\rm iv}$, Γ (or $V \sim \Gamma/\ell_{\rm iv}$) and a drag coefficient κ or μ. To come up with a fully closed scaling theory, in the following we derive four relations between these five quantities.

Transport by a vortex dipole. The first relations are obtained by assuming that the transport properties of the vortex gas are correctly estimated by considering an isolated dipole of counter-rotating vortices. As sketched in figure 6a, according to equation (33) such a dipole induces effective heat sources and sinks that are directly correlated with the meridional velocity component ψ_x. We

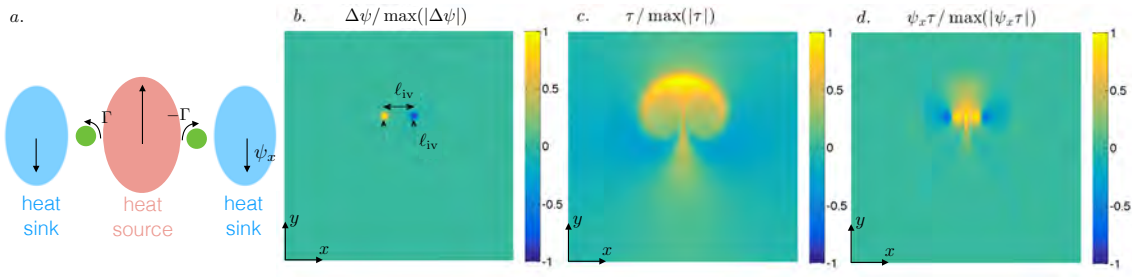

Figure 6: Transport by an idealized vortex dipole. **a.** Through the distortion of the background gradient, a vortex dipole induces temperature fluctuations that are directly correlated to the meridional velocity. Simulating equation (33) for the velocity field of a self-translating vortex dipole leads to the following vorticity (**b**), temperature (**c**) and heat flux (**d**) maps at the end time of the simulation.

thus expect a positive heat flux $\langle\psi_x\tau\rangle_{\mathbf{x}}$. As time evolves, the vortex dipole sketched in figure 6a would translate along y as a result of mutual induction. We expect the dipole to translate over a typical distance $\ell_{\rm iv}$, before the vortices pair up with other neighbors within the vortex gas. With this idealized picture in mind, we carried out simulations of the large-scale τ equation (33) for the velocity field of a self-propagating vortex dipole, stopping the simulation when the vortices have propagated over a distance $\ell_{\rm iv}$ (after which we assume that the vortices would pair up with other neighbors within the gas). At the end time of the simulation (illustrated in figure 6b,c,d), we compute the space averaged heat flux and the rms temperature fluctuations over an area of several $\ell_{\rm iv}^2$ around the dipole. Repeating this experiment for various values of $\ell_{\rm iv}$ allows us to obtain the (perhaps obvious from a dimensional point of view) scaling relations for the mixing-length and diffusivity associated with dipolar transport:

$$\ell \sim \ell_{\rm iv}\,, \qquad D \sim \Gamma \sim \ell V\,. \tag{34}$$

Slantwise free fall. The second scaling argument is an equivalent of the standard 'free-fall' velocity estimate for standard upright thermal convection. We consider baroclinic instability as some form of 'slantwise convection' and we adopt the 'kinetic theory' view of the vortex gas sketched in figure 4b. We consider a fluid element in the inter-vortex region, initially at rest. The free evolution of this fluid element consists of an acceleration in the meridional direction, the fluid particle transforming potential energy into kinetic energy. Such slantwise free-fall motion takes place over a typical distance ℓ – the 'mean free path' of the turbulent motion – after which the particle interacts – or 'collides' – with neighboring fluid elements. At the end of the slantwise free-fall motion, the typical velocity of the fluid element V is obtained by equating the final barotropic kinetic energy V^2 with the drop in available potential energy associated with a displacement by a distance ℓ in latitude, $U^2\ell^2/\lambda^2$. This leads to the velocity estimate:

$$V \sim \frac{U\ell}{\lambda}\,. \tag{35}$$

Using equation (34), this relation can be recast into the useful relation:

$$D_* \sim \ell_*^2\,. \tag{36}$$

Energy power integral. The last relation is based on an estimate of frictional dissipation within the vortex gas. To estimate the moments of the velocity field $\langle \mathbf{u}^2 \rangle$ and $\langle |\mathbf{u}|^3 \rangle$ entering the power integral (30) or (31), we consider the idealized situation of an isolated vortex located at the center of a disk-shaped domain of radius $\ell \sim \ell_{\rm iv}$, see figure 5b. Using polar coordinates, the velocity field is azimuthal, with magnitude $\Gamma/(2\pi r)$ outside the vortex core. The moments of the velocity field are thus estimated as:

$$\langle \mathbf{u}^2 \rangle \sim \frac{1}{\pi \ell^2} \int_\lambda^\ell \frac{\Gamma^2}{4\pi^2 r^2} 2\pi r \mathrm{d}r \sim V^2 \log \ell_* \,, \tag{37}$$

$$\langle |\mathbf{u}|^3 \rangle \sim \frac{1}{\pi \ell^2} \int_\lambda^\ell \frac{\Gamma^3}{8\pi^3 r^3} 2\pi r \mathrm{d}r \sim V^3 \, \ell_* \,. \tag{38}$$

Focusing on linear drag first, substituting (37) into the power integral (30) yields, using (34) and (35):

$$D \frac{U^2}{\lambda^2} \sim \kappa V^2 \log \ell_* \sim \kappa \frac{U^2 \ell^2}{\lambda^2} \log \ell_* \sim \kappa U^2 \ell_*^2 \log \ell_* \sim \kappa U^2 D_* \log \ell_* \tag{39}$$

$$\Rightarrow \quad \log \ell_* \sim \frac{1}{\kappa_*} \tag{40}$$

$$\Rightarrow \quad \ell_* = c_1 e^{c_2/(2\kappa_*)} \,, \tag{41}$$

where the $(c_i)_{i\in\mathbb{N}}$ are dimensionless constants and the factor 2 in front of κ_* in (41) is arbitrary. Substitution into (36) yields:

$$D_* = c_3 e^{c_2/\kappa_*} \,. \tag{42}$$

For quadratic drag, substituting (38) into the power integral (31) yields, using (34) and (35):

$$D \frac{U^2}{\lambda^2} \sim \mu V^3 \ell_* \mu U^3 \ell_*^4 \sim \mu U^3 D_*^2 \tag{43}$$

$$\Rightarrow \quad D_* \sim \frac{1}{\mu_*} \,, \tag{44}$$

and using (36) once again:

$$\ell_* \sim \frac{1}{\sqrt{\mu_*}} \,. \tag{45}$$

To summarize, we have obtained the following scaling dependence of ℓ_* and D_* on the dimensionless drag coefficient:

$$\text{linear drag:} \qquad \ell_* = c_1 e^{c_2/(2\kappa_*)} \qquad\qquad D_* = c_3 e^{c_2/\kappa_*} \,, \tag{46}$$

$$\text{quadratic drag:} \qquad \ell_* = \frac{c_4}{\sqrt{\mu_*}} \qquad\qquad D_* = \frac{c_5}{\mu_*} \,. \tag{47}$$

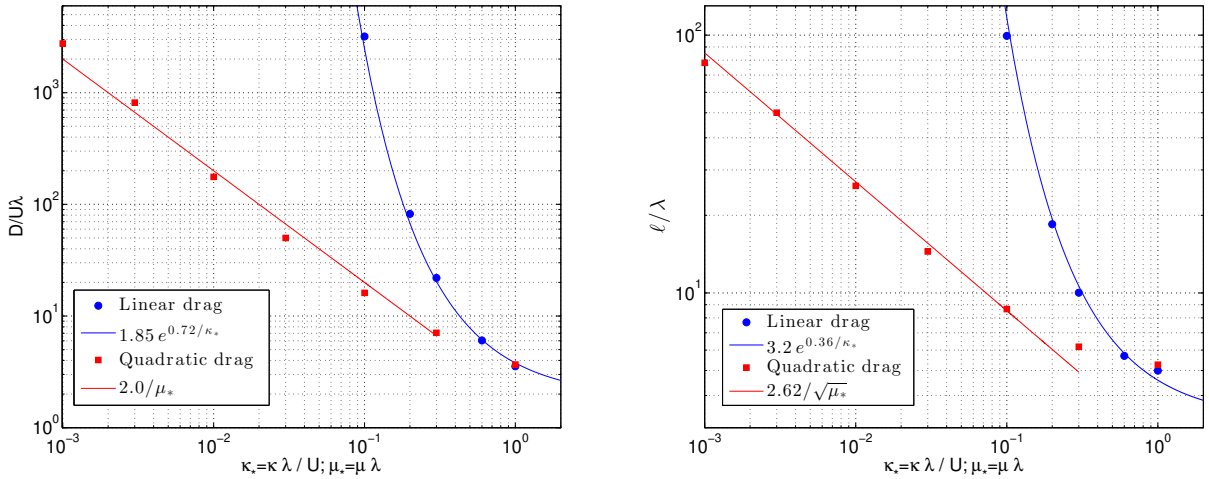

Figure 7: Dimensionless diffusivity (left) and mixing-length (right) as functions of the dimensionless drag coefficient for both linear and quadratic drag. The solid lines are the predictions (46) and (47) of the vortex-gas scaling theory.

The same vortex-gas scaling theory thus provides theoretical footing for Thompson & Young's empirical observation that the diffusivity is exponentially sensitive to the inverse linear drag coefficient, and for Chang & Held's empirical scaling exponents for D_* and ℓ_* versus μ_*. In figure 7, we provide numerical data on ℓ_* and D_* as functions of κ_* or μ_*.[6] The numerical data are in excellent agreement with the predictions (46) and (47) of the vortex-gas scaling theory.[7]

4 Forcing at the Planetary Scale: Multiscale Approach

We now illustrate the implementation of the eddy diffusivity derived in the previous section into a model forced at the large planetary scale. We will show how the expression of the diffusivity computed using a local model with prescribed background temperature gradient holds in the more general situation where turbulence feeds back onto the temperature profile.

4.1 Latitudinally varying external heat source

Our starting point is a 2LQG system without base state, in Cartesian geometry for simplicity. We consider linear drag, but the procedure readily carries over to quadratic drag. **The system is forced by a weak heat flux that depends slowly on the 'latitude' coordinate y:**

$$\partial_t(\Delta\psi) + J(\psi,\Delta\psi) + J(\tau,\Delta\tau) = -\kappa\Delta\psi\,, \tag{48}$$

$$\partial_t\left(\Delta\tau - \frac{\tau}{\lambda^2}\right) + J\left(\psi,\Delta\tau - \frac{\tau}{\lambda^2}\right) + J(\tau,\Delta\psi) = -Q(y)\,, \tag{49}$$

[6] The numerical simulations employ a friction term in the lower layer only, but this does not affect the scaling predictions of the vortex-gas model.

[7] Some slight discrepancy may be visible for D_* at very low quadratic drag μ_*. A recent study indicates that this due to the vortex cores becoming larger than λ for very small drag (see Refs. [5, 6] for refined predictions that capture the very low μ_* regime).

where we omit the hyperdiffusive terms for brevity. The external heat source term on the right-hand side of the temperature equation reads:

$$Q(y) = \frac{\lambda}{L} Q_0 S\left(\frac{y}{L}\right) , \tag{50}$$

where the scale L is much greater than the deformation radius λ. The multiscale approach is based on the small parameter $\epsilon = \lambda/L$. The magnitude of the forcing is quantified by Q_0, and we include an extra prefactor $\epsilon = \lambda/L$ in (50) in anticipation of the scalings below. The latitudinal variations of the forcing are encoded by the dimensionless function S. We non-dimensionalize the equations using the lengthscale λ and the time scale $1/\sqrt{Q_0}$, denoting with a hat the dimensionless variables:

$$\hat{t} = \sqrt{Q_0}\, t\,, \quad \hat{\mathbf{x}} = \frac{\mathbf{x}}{\lambda}\,, \quad \hat{\psi} = \frac{\psi}{\lambda^2\sqrt{Q_0}}\,, \quad \hat{\tau} = \frac{\tau}{\lambda^2\sqrt{Q_0}}\,, \quad \hat{\kappa} = \frac{\kappa}{\sqrt{Q_0}}\,. \tag{51}$$

The dimensionless equations read:

$$\partial_{\hat{t}}(\hat{\Delta}\hat{\psi}) + \hat{J}(\hat{\psi}, \hat{\Delta}\hat{\psi}) + \hat{J}(\hat{\tau}, \hat{\Delta}\hat{\tau}) = -\hat{\kappa}\hat{\Delta}\hat{\psi}\,, \tag{52}$$

$$\partial_{\hat{t}}(\hat{\Delta}\hat{\tau} - \hat{\tau}) + \hat{J}(\hat{\psi}, \hat{\Delta}\hat{\tau} - \hat{\tau}) + \hat{J}(\hat{\tau}, \hat{\Delta}\hat{\psi}) = -\epsilon S(\epsilon\hat{y})\,, \tag{53}$$

where the operators with a hat involve differentiation with respect to the dimensionless variables.

4.2 Multiple-scale expansion

We consider the following slow time and space variables:

- Slow variable along latitude, $Y = \epsilon\hat{y}$. That is, $\partial_{\hat{y}} = \partial_{\tilde{y}} + \epsilon\partial_Y$, where $\tilde{\mathbf{x}} = (\tilde{x}, \tilde{y})$ denotes the standard (fast) variables.
- Slow time variable, $T = \epsilon^2\hat{t}$. That is, $\partial_{\hat{t}} = \partial_{\tilde{t}} + \epsilon^2\partial_T$, where $\tilde{t}$ denotes the standard (fast) time.

Introduce an average $\overline{\cdot}$ over the fast space variables $\tilde{x}$ and $\tilde{y}$. This average can be thought of as an average or coarse-graining over some intermediate scale, much greater than λ but much smaller than L. Decompose the fields into mean and fluctuating parts:

$$\hat{\tau} = \frac{\overline{\tau}(Y,T)}{\epsilon} + \tilde{\tau}(\tilde{\mathbf{x}}, t, Y, T)\,, \qquad \text{with } \overline{\tilde{\tau}} = 0\,, \tag{54}$$

$$\hat{\psi} = \tilde{\psi}(\tilde{\mathbf{x}}, t, Y, T)\,, \qquad \text{with } \overline{\tilde{\psi}} = 0\,. \tag{55}$$

Finally, we assume $\hat{\kappa} = \mathcal{O}(1)$ and $S = \mathcal{O}(1)$.

To obtain the evolution equation for $\overline{\tau}$, we wish to average equation (53) over $\tilde{x}$ and $\tilde{y}$. It proves useful to first recast the advective nonlinear terms in divergence form:

$$\hat{J}(\hat{\psi}, \hat{\Delta}\hat{\tau} - \hat{\tau}) = \hat{\boldsymbol{\nabla}} \cdot \left[-[\hat{\boldsymbol{\nabla}} \times (\hat{\psi}\mathbf{e}_z)]\,(\hat{\Delta}\hat{\tau} - \hat{\tau})\right]\,, \tag{56}$$

$$\hat{J}(\hat{\tau}, \hat{\Delta}\hat{\psi}) = \hat{\boldsymbol{\nabla}} \cdot \left[-[\hat{\boldsymbol{\nabla}} \times (\hat{\tau}\mathbf{e}_z)]\,\hat{\Delta}\hat{\psi}\right]\,. \tag{57}$$

Averaging equation (53) then yields, to order $\mathcal{O}(\epsilon)$:

$$\epsilon^2 \partial_T \left(-\frac{\overline{\tau}}{\epsilon} \right) + \epsilon \partial_Y \left(\overline{\tilde{\psi}_{\tilde{x}} (\tilde{\Delta}\tilde{\tau} - \tilde{\tau})} \right) + \epsilon \partial_Y \underbrace{\left(\overline{\tilde{\tau}_{\tilde{x}} \tilde{\Delta} \tilde{\psi}} \right)}_{= -\overline{\tilde{\psi}_{\tilde{x}} \tilde{\Delta} \tilde{\tau}}} = -\epsilon S(Y) \tag{58}$$

$$\Rightarrow \quad \partial_T \overline{\tau} + \partial_Y \left(\overline{\tilde{\psi}_{\tilde{x}} \tilde{\tau}} \right) = S(Y) \,, \tag{59}$$

where operators with a tilde involve differentiation with respect to the fast variables $\tilde{x}$ and $\tilde{y}$ only (that is, $\tilde{\Delta} = \partial_{\tilde{x}\tilde{x}} + \partial_{\tilde{y}\tilde{y}}$).

The governing equations for $\tilde{\psi}$ and $\tilde{\tau}$ are obtained from equations (52) and (53) at $\mathcal{O}(1)$. The only contributions from $\overline{\tau}$ arise from the substitution $\partial_{\tilde{y}} \hat{\tau} \to \partial_Y \overline{\tau} + \partial_{\tilde{y}} \tilde{\tau}$ in the advective terms. We thus introduce the field $U(Y,T) \equiv -\partial_Y \overline{\tau}$. Equations (52) and (53) at $\mathcal{O}(1)$ read:

$$\partial_{\tilde{t}} \tilde{\Delta} \tilde{\psi} + \tilde{J}(\tilde{\psi}, \tilde{\Delta}\tilde{\psi}) + \tilde{J}(\tilde{\tau}, \Delta\tilde{\tau}) + U \partial_{\tilde{x}} (\tilde{\Delta}\tilde{\tau}) = -\hat{\kappa} \tilde{\Delta} \tilde{\psi} \,, \tag{60}$$

$$\partial_{\tilde{t}} (\tilde{\Delta}\tilde{\tau} - \tilde{\tau}) + \tilde{J}(\tilde{\psi}, \tilde{\Delta}\tilde{\tau} - \tilde{\tau}) + \tilde{J}(\tilde{\tau}, \tilde{\Delta}\tilde{\psi}) + U \partial_{\tilde{x}} (\tilde{\Delta}\tilde{\psi} + \tilde{\psi}) = 0 \,. \tag{61}$$

We stress the fact that $U(Y,T)$ appears only as a 'parameter' in these equations for the evolution of $\tilde{\psi}$ and $\tilde{\tau}$ with respect to the fast time and space variables. That is, we recover the set of equations governing the local homogeneous patch of ocean considered in section 3.

The multiscale model consists of equations (60) and (61) for the fast evolution of the fluctuating fields, together with equation (59) for the slow evolution of the background temperature profile. The determination of the equilibrated temperature profile $\overline{\tau}(Y)$ consists of three steps:

1. 'Solve' equations (60) and (61) to obtain the eddy-induced heat flux $\overline{\tilde{\psi}_{\tilde{x}} \tilde{\tau}}$ in terms of U and $\hat{\kappa}$. Instead of actually solving the equations (likely an impossible task), we will use the quantitative scaling theory introduced in section 3.

2. Substitute the resulting expression for $\overline{\tilde{\psi}_{\tilde{x}} \tilde{\tau}}$ into (59) to get a closed equation for $\overline{\tau}(Y,T)$.

3. Solve for the equilibrated temperature profile $\overline{\tau}(Y)$.

4.3 An example: $S(Y) = \sin Y$

As an example, we consider sinusoidal variations of the external heat source/sink term, $S(Y) = \sin Y$. This large-scale heating/cooling pattern is represented in figure 8a. To avoid confusion, we denote by $U_{\rm dim}$ the dimensional version of the shearing velocity U. From the scaling theory in section 3, we know that:

$$D_* = \frac{D}{U_{\rm dim} \lambda} = c_3 e^{c_2/\kappa_*} \,, \tag{62}$$

where $\kappa_* = \kappa\lambda / U_{\rm dim}$. The dimensional shearing velocity is $U_{\rm dim} = -\lambda \sqrt{Q_0}\, \partial_Y \overline{\tau}$, the dimensional friction coefficient is $\kappa = \sqrt{Q_0} \hat{\kappa}$ and the dimensional eddy-induced heat flux is $\langle \psi_x \tau \rangle = \lambda^3 Q_0 \overline{\tilde{\psi}_{\tilde{x}} \tilde{\tau}}$. Equation (62) thus leads to the following expression for the dimensionless flux:

$$\overline{\tilde{\psi}_{\tilde{x}} \tilde{\tau}} = -c_3 (\partial_Y \overline{\tau}) |\partial_Y \overline{\tau}| e^{c_2 |\partial_Y \overline{\tau}| / \hat{\kappa}} \,. \tag{63}$$

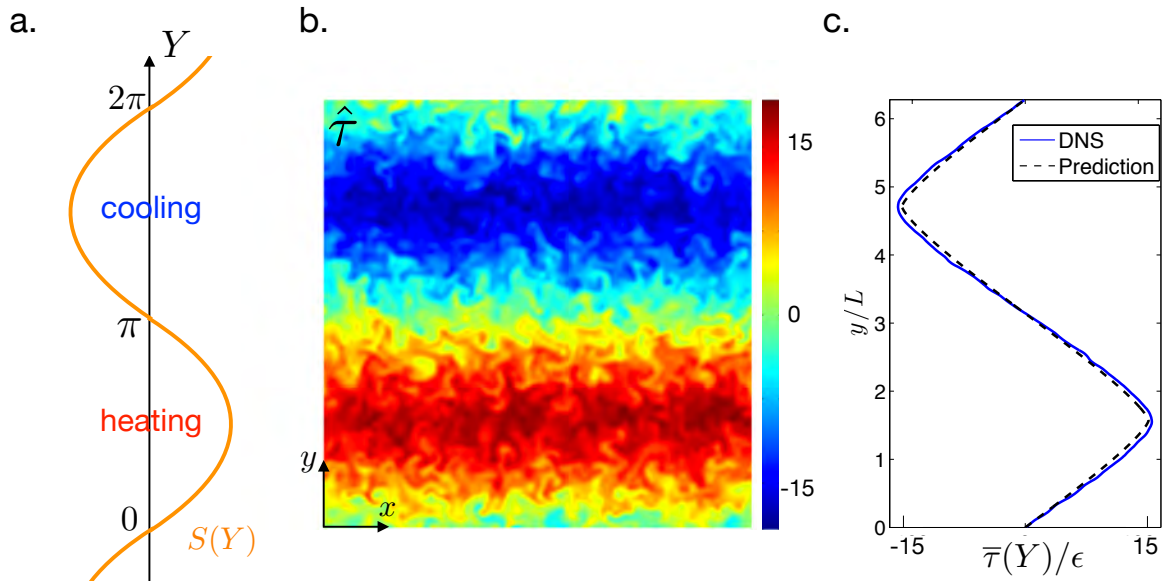

Figure 8: **Numerical solution of the inhomogeneous model. a.** Sinusoidal pattern of the heat source/sink term. **b.** Instantaneous snapshot of the temperature field $\hat{\tau}$ in the statistically steady state of a numerical simulation ($\hat{\kappa} = 0.0707$, $\epsilon = 0.02$). **c.** Corresponding zonally averaged temperature profile (blue) compared to the theoretical prediction (67) from the multiscale model (black dashed).

The steady version of equation (59) with sinusoidal forcing reads:

$$\partial_Y \left(\overline{\tilde{\psi}_{\tilde{x}} \tilde{\tau}} \right) = S(Y) = \sin Y \tag{64}$$

$$\Rightarrow \quad \overline{\tilde{\psi}_{\tilde{x}} \tilde{\tau}} = -\cos Y + \cancel{\text{const.}} \,, \tag{65}$$

where the integration constant is set to zero based on the vanishing Y-average of the eddy-induced heat flux. Substituting expression (63) for the flux yields:

$$c_3 (\partial_Y \overline{\tau}) |\partial_Y \overline{\tau}| e^{c_2 |\partial_Y \overline{\tau}| / \hat{\kappa}} = \cos Y \,. \tag{66}$$

This is an implicit equation for $\partial_Y \overline{\tau}$, which we solve using the Lambert function W,[8] before integrating over Y. We finally obtain:

$$\overline{\tau}(Y) = \frac{2\hat{\kappa}}{c_2} \int_{s=0}^{z=Y} W \left(\frac{c_2}{2\hat{\kappa}\sqrt{c_3}} \sqrt{\cos s} \right) \, \mathrm{d}s \,, \tag{67}$$

valid for $Y \in [-\pi/2; \pi/2]$ (use symmetry and periodicity for other ranges of Y). We stress the fact that there are no adjustable parameters in the prediction (67) once the constants c_2 and c_3 have been determined from the study of the homogeneous model (see section 3).

To test the prediction above, we have integrated the inhomogeneous model (52-53) numerically for a sinusoidal heating/cooling pattern, using $\epsilon = \lambda/L = 0.02$, $\hat{\kappa} = 0.0707$, and very small hyperviscosity. In figure 8b we show an instantaneous snapshot of the temperature field $\hat{\tau}$ in the statistically steady state. We clearly see the large-scale pattern of the forcing, together with erratic smaller-scale fluctuations. The corresponding zonally averaged temperature profile is shown in panel c, together with the prediction (67) computed using the values of c_2 and c_3 deduced from figure 7. We obtain an excellent agreement between the numerical data and the theoretical prediction from the multiscale model.

[8] such that $W(x) \exp[W(x)] = x$.

References

[1] Chiung-Yin Chang and Isaac M. Held. The Control of Surface Friction on the Scales of Baroclinic Eddies in a Homogeneous Quasigeostrophic Two-Layer Model. *Journal of the Atmospheric Sciences*, 76(6):1627–1643, June 2019.

[2] A. Einstein. Über die von der molekularkinetischen Theorie der Wärme geforderte Bewegung von in ruhenden Flüssigkeiten suspendierten Teilchen. *Annalen der Physik*, 4, 1905.

[3] Basile Gallet and Raffaele Ferrari. The vortex gas scaling regime of baroclinic turbulence. *Proceedings of the National Academy of Sciences*, 117(9):4491–4497, March 2020.

[4] Basile Gallet and Raffaele Ferrari. A Quantitative Scaling Theory for Meridional Heat Transport in Planetary Atmospheres and Oceans. *AGU Advances*, 2(3), September 2021.

[5] Gabriel Hadjerci and Basile Gallet. Vortex core radius in baroclinic turbulence: Implications for scaling predictions. *Physical Review Fluids*, 8(9):094501, September 2023.

[6] Gabriel Hadjerci and Basile Gallet. Two-layer baroclinic turbulence with arbitrary layer depths. *Physical Review Fluids*, 9(5):L051802, 2024.

[7] Isaac M. Held. The macroturbulence of the troposphere. *Tellus A*, 51(1):59–70, January 1999.

[8] Peter Korn. Formulation of an unstructured grid model for global ocean dynamics. *Journal of Computational Physics*, 339:525–552, 2017.

[9] Joseph Pedlosky. *Geophysical fluid dynamics*. Springer study edition. Springer, New York, 2003.

[10] Rick Salmon. *Lectures on Geophysical Fluid Dynamics*. Oxford University Press, 1998.

[11] Andrew F. Thompson and William R. Young. Scaling Baroclinic Eddy Fluxes: Vortices and Energy Balance. *Journal of Physical Oceanography*, 36(4):720–738, April 2006.

[12] Geoffrey K. Vallis. *Atmospheric and Oceanic Fluid Dynamics: Fundamentals and Large-Scale Circulation*. Cambridge University Press, 2 edition, June 2017.

GFD 2024 Lecture 9: Near-inertial Waves Interacting with Balanced Flows

Basile Gallet; notes by Lulabel Ruiz Seitz and Adhithiya Sivakumar*

June 27, 2024

We have focused so far on the slow balanced motion arising in rapidly rotating shallow layers of fluid, described through quasi-geostrophic (QG) dynamics. But what if the initial condition is incompatible with geostrophic balance and hydrostatic balance? The short answer is that the resulting flow consists of a combination of balanced flow and waves. The simplest example is perhaps a 3D homogeneous body of fluid subject to rapid rotation around the vertical axis: if the initial condition is incompatible with the Taylor-Proudman theorem, the flow consists of inertial waves interacting with vertically invariant Taylor columns.

The motivation for this lecture is two-fold. The first motivation comes from ocean dynamics: a significant fraction of the ocean kinetic energy takes the form of near-inertial waves interacting with the slower balanced QG flow. The second motivation is at the level of physics or applied mathematics: wave-mean flow interaction is a fascinating topic that bridges seemingly different research areas. In the present context, we will see in section 2 that there is an exact analogy between the evolution of near-inertial waves in a background flow and the dynamics of a quantum particle in an electromagnetic field. While this analogy may seem far-fetched, it has useful practical consequences. In particular, it points to equilibrium statistical mechanics as an efficient way to predict the statistics of the near-inertial wave field, as discussed in section 4.

To introduce inertial oscillations and near-inertial waves, we consider a two-layer system with a shallow upper layer of depth $h(x, y, t)$, described within the rigid-lid approximation (see figure 2). The atmospheric pressure above the layers is uniform. We denote the horizontal velocity inside the upper layer by $\mathbf{u} = [u(x, y, t), v(x, y, t)]$ and the Coriolis parameter as f. Linearizing the shallow-water equations around a state of rest with $\mathbf{u} = \mathbf{0}$ and $h = H_0$, we obtain:

$$\partial_t u - fv = -g'\partial_x h\,, \tag{1}$$

$$\partial_t v + fu = -g'\partial_y h\,, \tag{2}$$

$$\partial_t h + H_0 \boldsymbol{\nabla}\cdot\mathbf{u} = 0\,, \tag{3}$$

where $\boldsymbol{\nabla} = (\partial_x, \partial_y)$ and we have used hydrostatic balance to express the horizontal pressure gradient in terms of the reduced gravity g' and $h(x, y, t)$ (see previous lecture).

Let us first focus on a horizontally homogeneous initial condition. With $\partial_x = \partial_y = 0$, the evolution is governed by:

$$\partial_t u - fv = 0\,, \tag{4}$$

$$\partial_t v + fu = 0\,. \tag{5}$$

*Some of the material presented during the lecture corresponds to the internship work of Alexandre Tlili, who is gratefully acknowledged (see Ref.[4])

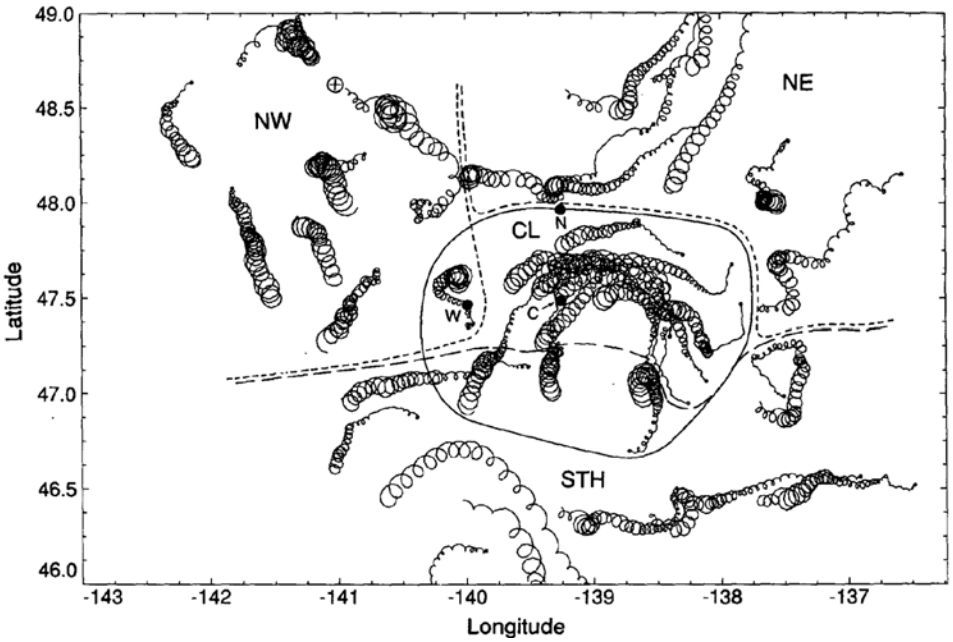

Figure 1: Following a storm, the trajectories of surface drifters consist of circular motion associated with near-inertial waves, together with a drift induced by the background flow. (figure reproduced from d'Asaro et al. [3]).

Introducing the complex velocity field $\mathcal{U} = u + iv$, this set of equations is recast as $\partial_t \mathcal{U} + if\mathcal{U} = 0$, with solution:

$$\mathcal{U} = Me^{-ift}\,, \tag{6}$$

where $M \in \mathbb{C}$ is an integration constant. Shifting the origin of time such that $M \in \mathbb{R}$, one can check that the trajectories corresponding to (6) are:

$$x(t) = x_0 + \frac{M}{f}\sin(ft)\,, \tag{7}$$

$$y(t) = y_0 + \frac{M}{f}\cos(ft)\,. \tag{8}$$

The fluid elements describe circular trajectories, in the clockwise direction in the Northern hemisphere. Such circular motion at the Coriolis frequency is called 'inertial oscillation'. If some dependence on x and y is retained under the form of a single Fourier mode, one obtains the following dispersion relation between the angular frequency ω of the waves and the wavenumber k:

$$\omega^2 = f^2 + g'H_0k^2\,. \tag{9}$$

A natural lengthscale arising in this dispersion relation is the deformation radius based on the depth H_0 of the upper layer, $\lambda_0 = \sqrt{g'H_0}/f$. If the wavenumber k is much smaller than λ_0^{-1}, ω is close to f and the waves are called 'near-inertial waves' (NIW).

In figure 1 we show the trajectories of surface drifters following the impulsive forcing of the ocean surface by an extended atmospheric storm. The trajectories of the drifters consist of circular motion

together with a drift. The circular motion is the signature of NIWs, while the drift corresponds to advection by the background balanced flow.[1]

Near-inertial waves represent a significant fraction of the kinetic energy of the ocean. Within a timescale of several weeks following a storm, NIWs are observed to propagate deeper into the water column, where they can induce mixing as a result of shear instabilities. Such rapid downward propagation is not obvious at the theoretical level. Indeed, atmospheric storms have a large horizontal scale of $\sim 10^3$ km. They drive a NIW field that is quasi-homogeneous in the horizontal directions. In a fully 3D body of fluid, the dispersion relation of inertia-gravity waves is such that the group velocity is perpendicular to the phase velocity: the energy of waves with no horizontal structure (purely vertical wave vector) does not propagate vertically. The solution to this puzzle lies in the interaction between NIWs and the balanced QG flow: the balanced flow shapes the NIW field, which rapidly develops a smaller horizontal scale.[2] Horizontal structure in the NIW field allows for downward propagation of the wave energy. In this lecture we address the following questions:

- In the absence of spatial scale separation between the wave field and the balanced flow, how to describe the interaction between the two?
- Starting from a horizontally homogeneous initial condition induced by an impulsive storm, how to predict the distribution of NIW energy within the quasi-2D balanced flow? Where does the wave kinetic energy localize? What about the wave potential energy?
- How does the NIW field contribute to horizontal transport near the ocean surface? Can we predict the Stokes drift induced by the NIW field?

A solution to the first question above was proposed by Young & Ben Jelloul [5]. They took advantage of the timescale separation between the fast inertial frequency and the slow advection by the balanced flow to derive a reduced equation governing the evolution of the NIW field. We derive a simple version of this equation in section 1. It turns out that the Young-Ben Jelloul (YBJ) equation is also the Schrödinger equation for a charged particle in a steady, 2D electromagnetic field. We introduce this analogy in section 2, focusing first on the 'strong-dispersion' quantum limit (section 3). In the opposite, 'strong-advection' limit, the analogy suggests leveraging the statical mechanics of conservative systems to predict the various statistics of the charged particles, and thus of the NIW field. We describe this approach in section 4, where we derive quantitative predictions for the spatial distribution of the wave kinetic energy, wave potential energy, and Stokes drift.

1 Multiscale Derivation of the YBJ Equation

1.1 Wave dynamics in a shallow upper layer

Consider the system sketched in figure 2. This is the two-layer system mentioned in the introduction, with an infinitely deep lower layer. The base state consists of a steady, vertically invariant background flow $\mathbf{U}(x, y)$ spanning both layers. The background flow is in geostrophic balance with a vertically invariant lateral pressure gradient. It stems from a streamfunction $\psi(x, y)$, that is, $\mathbf{U} = [U(x, y), V(x, y)] = -\boldsymbol{\nabla} \times (\psi\, \mathbf{e}_z)$. There is no deformation of the interface associated with

[1] together with possible Stokes drift.

[2] The β-effect also plays a role in this process, but we will restrict attention to the effect of the balanced flow in this lecture.

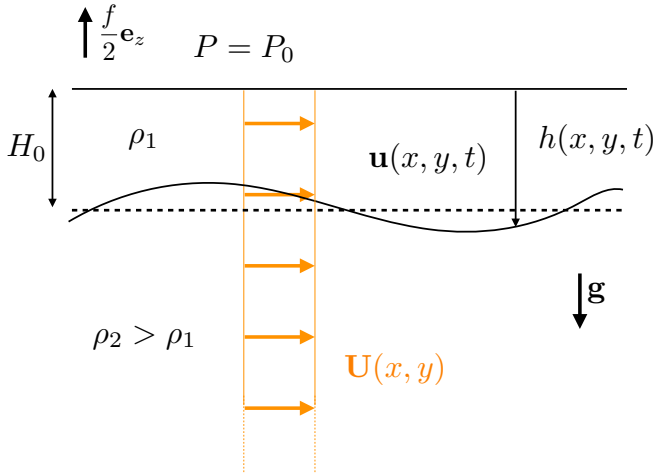

Figure 2: A two-layer model with an infinitely deep lower layer. The base state consists of a vertically invariant steady horizontal flow $\mathbf{U}(x,y)$ spanning both layers, together with a flat interface between the two layers ($\mathbf{U} = \mathbf{0}$ in the introduction section). We consider perturbations $\mathbf{u}(x,y,t)$ to the horizontal velocity in the upper layer only, whose depth is then denoted by $h(x,y,t)$. In line with the rigid-lid approximation, we neglect the fluctuations of the free surface as compared to h.

such a vertically invariant balanced flow. We consider the rotating shallow-water equations in the upper layer, linearized around the background balanced flow:

$$\partial_t u + J(\psi, u) + u\partial_x U + v\partial_y U - fv = -g'\partial_x h\,, \tag{10}$$
$$\partial_t v + J(\psi, v) + u\partial_x V + v\partial_y V + fu = -g'\partial_y h\,, \tag{11}$$
$$\partial_t h + J(\psi, h) + H_0 \boldsymbol{\nabla}\cdot\mathbf{u} = 0\,. \tag{12}$$

We non-dimensionalize the equations using a timescale f^{-1}, a velocity scale $\sqrt{g'H_0}$ and a height scale H_0:

$$t = \frac{\tilde{t}}{f}\,, \quad \mathbf{u} = \sqrt{g'H_0}\,\tilde{\mathbf{u}}\,, \quad \mathbf{x} = \frac{\sqrt{g'H_0}}{f}\tilde{\mathbf{x}}\,, \quad \psi = \frac{g'H_0}{f}\tilde{\psi}\,, \quad h = H_0\tilde{h}\,. \tag{13}$$

Substituting and dropping the tildes for brevity leads to the following dimensionless equations:

$$\partial_t u + J(\psi, u) + u\partial_x U + v\partial_y U - v = -\partial_x h\,, \tag{14}$$
$$\partial_t v + J(\psi, v) + u\partial_x V + v\partial_y V + u = -\partial_y h\,, \tag{15}$$
$$\partial_t h + J(\psi, h) + \boldsymbol{\nabla}\cdot\mathbf{u} = 0\,. \tag{16}$$

Introduce the complex velocity field $\mathcal{U} = u + iv$. Denoting the complex conjugate with a star, the velocity components read:

$$u = \frac{\mathcal{U} + \mathcal{U}^*}{2} \qquad v = \frac{\mathcal{U} - \mathcal{U}^*}{2i}\,. \tag{17}$$

The evolution equation for $\mathcal{U}$ is obtained from the linear combination (14)+i(15) of the equations above:

$$\partial_t\mathcal{U} + i\mathcal{U} + J(\psi,\mathcal{U}) + \frac{i}{2}(\Delta\psi)\mathcal{U} + \mathcal{U}^*\left(-\psi_{xy} - \frac{i}{2}\psi_{yy} + \frac{i}{2}\psi_{xx}\right) = -h_x - ih_y\,, \tag{18}$$

where $\Delta = \partial_{xx} + \partial_{yy}$. This equation is coupled to the evolution equation for h, where u and v are recast in terms of $\mathcal{U}$ and $\mathcal{U}^*$ using (17):

$$\partial_t h + J(\psi, h) = -\partial_x \left(\frac{\mathcal{U} + \mathcal{U}^*}{2} \right) - \partial_y \left(\frac{\mathcal{U} - \mathcal{U}^*}{2i} \right) . \tag{19}$$

1.2 Multiple-scale expansion

We consider weak waves that are slowly modulated in space and time:

$$\psi = \psi_0(X, Y) , \tag{20}$$

$$\mathcal{U} = \epsilon \mathcal{U}_1(X, Y, t, T) + \epsilon^3 \mathcal{U}_3 + \dots , \tag{21}$$

$$h = 1 + \epsilon^2 h_2(X, Y, t, T) + \dots , \tag{22}$$

where we have introduced the slow variables:

$$X = \epsilon x , \qquad Y = \epsilon y , \quad T = \epsilon^2 t . \tag{23}$$

The single bookkeeping parameter $\epsilon \ll 1$ encodes the various scalings considered here. Through equation (23), ϵ can be interpreted as the ratio of the Rossby deformation radius λ_0 over the large horizontal scale of both the background flow and the wave field. As discussed in the introduction, such a large horizontal scale for the wave field indeed corresponds to the NIW regime of the full dispersion relation (9). Based on this large horizontal scale, the Rossby numbers of both the background flow and the wave field are of order ϵ^2, providing another interpretation for ϵ.

We stress the fact that the ansatz (20-22) is really a mutliple-scale expansion in time only, with two time variables t and T. By contrast, the introduction of X and Y is only a mere rescaling of the space variables. In other words:

$$\partial_x = \epsilon \partial_X , \qquad \partial_y = \epsilon \partial_Y , \qquad \partial_t \to \partial_t + \epsilon^2 \partial_T . \tag{24}$$

To order ϵ, equation (18) reads:

$$\partial_t \mathcal{U}_1 + i \mathcal{U}_1 = 0 , \tag{25}$$

with solution:

$$\mathcal{U}_1 = M(X, Y, T) e^{-it} . \tag{26}$$

The lowest-order velocity field above corresponds to near-inertial oscillations with an amplitude M that is slowly modulated over space and time. Our goal is to obtain an evolution equation for M. To order ϵ^3, equation (18) reads:

$$\begin{aligned} \partial_t \mathcal{U}_3 + i \mathcal{U}_3 = & - \partial_T \mathcal{U}_1 - J(\psi_0, \mathcal{U}_1) - \frac{i}{2} (\Delta \psi_0) \mathcal{U}_1 - \mathcal{U}_1^* \left[-\partial_{XY} \psi_0 - \frac{i}{2} \partial_{YY} \psi_0 + \frac{i}{2} \partial_{XX} \psi_0 \right] \\ & - \partial_X h_2 - i \partial_Y h_2 , \end{aligned} \tag{27}$$

The solvability condition demands that there be no resonant terms on the rhs: the amplitude in front of e^{-it} on the rhs must vanish. To write this solvability condition, we first need to determine the resonant part of h_2, denoted by $h_2^{(\mathrm{res})}$. To wit, we consider equation (19) at $\mathcal{O}(\epsilon^2)$:

$$\partial_t h_2 = -\partial_X \left(\frac{\mathcal{U}_1 + \mathcal{U}_1^*}{2} \right) - \partial_Y \left(\frac{\mathcal{U}_1 - \mathcal{U}_1^*}{2i} \right) . \tag{28}$$

On the rhs, only the terms involving $\mathcal{U}_1$ contribute to the resonant part of h_2, while the terms involving $\mathcal{U}_1^*$ are non-resonant. Keeping the contributions from $\mathcal{U}_1$ only leads to:

$$\partial_t h_2^{(\mathrm{res})} = \left[-\frac{1}{2}\partial_X M + \frac{i}{2}\partial_Y M\right] e^{-it} \;\Rightarrow\quad h_2^{(\mathrm{res})} = \left[-\frac{i}{2}\partial_X M - \frac{1}{2}\partial_Y M\right] e^{-it}\,. \tag{29}$$

Denoting with an arrow the amplitude in front of e^{-it} of the resonant contribution from each term on the rhs of equation (27), we obtain:

$$-\partial_T \mathcal{U}_1 \to -\partial_T M\,, \tag{30}$$

$$-J(\psi_0, \mathcal{U}_1) \to -J(\psi_0, M)\,, \tag{31}$$

$$-\frac{i}{2}(\Delta\psi_0)\mathcal{U}_1 \to -\frac{i}{2}(\Delta\psi_0)M\,, \tag{32}$$

$$-\mathcal{U}_1^*[\dots] \to 0\,, \tag{33}$$

$$-\partial_X h_2 - i\partial_Y h_2 \to \frac{i}{2}\Delta M\,. \tag{34}$$

The solvability condition requires that the sum of the terms appearing on the rhs of (30-34) be zero. Recasting this solvability condition in terms of the original fields and variables leads to (the simplest version of) the YBJ equation:

$$\partial_t M + \underbrace{J(\psi, M)}_{\text{advection}} + \underbrace{\frac{i}{2}(\Delta\psi)M}_{\text{refraction}} \underbrace{-\frac{i}{2}\Delta M}_{\text{dispersion}} = 0\,. \tag{35}$$

This equation describes the slow modulation of the complex NIW amplitude as a result of advection by the background flow velocity, refraction by the background flow vorticity, and dispersion.[3]

2 Quantum Analogy

2.1 Charged particle in a static electromagnetic field

Upon multiplication by i, the YBJ equation can be recast as a Schrödinger equation:

$$i\partial_t M = -\frac{1}{2}\Delta M - iJ(\psi, M) + \frac{1}{2}(\Delta\psi)M\,. \tag{36}$$

To interpret this Schrödinger equation, recall the Hamiltonian for a particle of mass m and charge q in a static 2D electromagnetic field:

$$H = \frac{1}{2m}[\mathbf{p} - q\mathbf{A}(x,y)]^2 + qV(x,y)\,, \tag{37}$$

where $V(x,y)$ denotes the electric potential and $\mathbf{A}(x,y)$ denotes the vector potential. We choose the Coulomb gauge, $\boldsymbol{\nabla}\cdot\mathbf{A} = 0$, such that the vector potential itself reads $\mathbf{A}(x,y) = -\boldsymbol{\nabla}\times[\phi(x,y)\,\mathbf{e}_z]$. Denoting the wave function as $\Psi(x,y,t)$, the Schrödinger equation for this particle reads $i\hbar\partial_t\Psi =$

[3] The reader can check that the term $-\frac{i}{2}\Delta M$ corresponds to the first correction in a low-k expansion of the NIW dispersion relation.

$H\{\Psi\}$, where the operator $H\{\cdot\}$ is obtained by substituting $\mathbf{p} = -i\hbar\boldsymbol{\nabla}$ into (37). Expanding the square in (37) we obtain:[4]

$$i\hbar\partial_t\Psi = \frac{1}{2m}[-\hbar^2\Delta\Psi + \underbrace{iq\hbar\boldsymbol{\nabla}\cdot(\mathbf{A}\Psi)}_{iq\hbar\mathbf{A}\cdot\boldsymbol{\nabla}\Psi} + iq\hbar\mathbf{A}\cdot\boldsymbol{\nabla}\Psi + q^2\mathbf{A}^2\Psi] + qV\Psi\,. \tag{38}$$

Choosing units such that $\hbar = 1$, $m = 1$ and $q = 1$,[5] this equation becomes:

$$i\partial_t\Psi = -\frac{1}{2}\Delta\Psi + iJ(\phi,\Psi) + \left(\frac{\mathbf{A}^2}{2} + V\right)\Psi\,. \tag{39}$$

Finally, we consider the situation where the external electric potential is given by:

$$V(x,y) = -\frac{\mathbf{A}^2}{2} - \frac{1}{2}\Delta\phi = -\frac{|\boldsymbol{\nabla}\phi|^2}{2} - \frac{1}{2}\Delta\phi\,. \tag{40}$$

With this choice for the electric potential, the dimensionless Schrödinger equation (39) becomes:

$$i\partial_t\Psi = -\frac{1}{2}\Delta\Psi + iJ(\phi,\Psi) - \frac{1}{2}(\Delta\phi)\Psi\,. \tag{41}$$

This is the YBJ equation (36), where the wavefunction Ψ plays the role of the complex wave amplitude M, and ϕ plays the role of minus the streamfunction ψ. **There is thus an exact analogy between the YBJ equation and the quantum dynamics of a charged particle in a 2D static electromagnetic field.** Table 1 summarizes the analogy between the various quantities of interest. In particular, the vector potential $\mathbf{A}(x,y)$ plays the role of minus the background velocity field $\mathbf{U}(x,y)$, and the vertical magnetic field $B(x,y)\mathbf{e}_z$ is analogous to minus the vorticity $\Delta\psi\mathbf{e}_z$ of the background balanced flow. Parts of the quantum analogy are discussed at various places the literature: early on, YBJ noticed the similarity between the YBJ equation and a Schrödinger equation. Balmforth et al. [1] notice the analogy between the advective term of the YBJ equation and the effect of an external magnetic field on a charged particle, but they deem the potential term unphysical. Danioux, Vanneste and Bülher [2] (DVB in the following) discuss the fact that, in the absence of the advective term, the YBJ equation reduces to the Shrödinger for a charged particle in an electric potential. By contrast, the present version of the analogy includes all the terms of the YBJ equation.

2.2 Conserved quantities

There are two ways of determining the conserved quantities of the YBJ equation: one can directly deduce them from the equation, or one can readily infer them from the quantum analogy. Consider the YBJ equation inside a doubly periodic domain $(x,y) \in \mathcal{D} = [0, 2\pi L]^2$. Multiplying the YBJ equation (35) with M^* before adding the complex conjugate and averaging over the domain $\mathcal{D}$ yields, after a few integrations by parts using the periodic boundary conditions:

$$\frac{\mathrm{d}\mathcal{A}}{\mathrm{d}t} = 0 \qquad \text{where} \qquad \mathcal{A} = \left\langle |M|^2 \right\rangle\,, \tag{42}$$

[4] Beware that the operators inside the square bracket do not commute.

[5] That is, we nondimensionalize the equation using the scales $\hbar = 1$ for action, m for mass and q for electric charge, assuming that the particle is positively charged, $q > 0$.

Quantum particle	YBJ system
wave function $\Psi(x,y,t)$	$M(x,y,t)$
vector potential $\mathbf{A}(x,y)$	$-\mathbf{U}(x,y)$
magnetic field $B(x,y)\mathbf{e}_z$	$-\Delta\psi\mathbf{e}_z$
electric potential $V(x,y)$	$\frac{\Delta\psi}{2} - \frac{\lvert\boldsymbol{\nabla}\psi\rvert^2}{2}$
conserved probability $\int_{\mathcal{D}} \lvert\Psi\rvert^2 \mathrm{d}\mathbf{x}$	conserved wave action $\mathcal{A} = \langle \lvert M\rvert^2 \rangle$
conserved energy $\langle \Psi \lvert H \rvert \Psi \rangle$	conserved wave energy E, see (43).

Table 1: Summary of the analogy between the Schrödinger equation for a charged particle (left) and the YBJ equation (right).

where the angular brackets denote space average over the domain $\mathcal{D}$. The conservation of $\mathcal{A}$ is also readily inferred from the quantum analogy, as $\mathcal{A}$ corresponds to the conserved total probability of finding the particle somewhere inside the domain $\mathcal{D}$. Wave action is defined as the ratio of the wave energy to the wave frequency. In the YBJ context, the mechanical energy of the waves is dominated by the kinetic energy $\langle |M|^2 \rangle$ (omitting the prefactor 1/2), while the frequency is equal to f to lowest order. The conservation of wave action thus reduces to the conservation of the space-averaged kinetic energy of the wave field, $\langle |M|^2 \rangle$.

The conservation of $\mathcal{A}$ is discussed in the original YBJ paper [5]. Eighteen years later, a second independent conserved quantity was uncovered by DVB based on manipulations of the YBJ equation. Once again, this second conserved quantity is easily inferred from the quantum analogy. Indeed, the Hamiltonian being time independent, its expectation value is conserved over time: the mechanical energy of the charged particle is conserved. In the quantum context, this expectation value is $\langle \Psi | H | \Psi \rangle = \int_{\mathcal{D}} \Psi^* H\{\Psi\} \mathrm{d}\mathbf{x}$. For the YBJ system the analog of Ψ^* is M^*, while the analog of $H\{\Psi\}$ is the rhs of (36). The conserved quantity becomes:

$$E = \left\langle M^* \left[-\frac{1}{2}\Delta M - iJ(\psi, M) + \frac{1}{2}(\Delta\psi)M \right] \right\rangle$$
$$= \left\langle \frac{|\boldsymbol{\nabla} M|^2}{2} + \frac{(\Delta\psi)|M|^2}{2} - i\psi J(M, M^*) \right\rangle , \tag{43}$$

where we have performed various integrations by parts using the periodic boundary conditions to obtain the second expression. We refer to (43) as the wave energy. Strictly speaking, the total mechanical energy of the waves consists of a leading-order kinetic energy term, proportional to $\mathcal{A}$, and the weaker contributions gathered in E above. In the present context $\mathcal{A}$ and E are conserved independently. In the absence of background flow, $\psi = 0$, only the term $|\boldsymbol{\nabla} M|^2/2$ remains in (43). This term corresponds to the potential energy of the waves.

2.3 Two limits of interest

At this stage one may reasonably object that we have made an analogy with a system that is even less intuitive than the original system. We argue, however, that the analogy leads to various simple observations. Among our goals is to predict where NIW action gets localized by the background flow. DVB address this question based on a partial quantum analogy: neglecting the advective term in (36), the YBJ equation looks like a Schrödinger equation with a potential proportional to

the vorticity $\Delta\psi$ of the background flow. DVB thus argue that the particles will accumulate in the regions of lowest potential, which correspond to the anticyclones of the background flow. This prediction is backed by numerical data for flows of intermediate strength only, whereas simulations with very weak or very strong background flows exhibit only a weak correlation between wave action and background flow vorticity. The exact quantum analogy somewhat challenges the argument by DVB. Indeed, the full potential (40) consists of half the background flow vorticity, to which is added minus the flow kinetic energy. In the limit of fast background flow, the potential minima correspond to fast-flow regions, as opposed to anticyclones. Finally, one may wonder why the particles would accumulate in potential minima at all. Indeed, while a damped particle ends up in the potential well, a conservative particle accelerates as it reaches the potential minimum, spending very little time in the well.

In the following we thus revisit the problem of predicting the statistics of NIW interacting with a background flow. We quantify the strength of the background flow using the rms magnitude of the dimensionless streamfunction. Recasting ψ as:

$$\psi(x,y) = \psi_{\rm rms}\,\chi(x,y) \;\text{ with }\quad \left\langle \chi^2 \right\rangle = 1\,, \tag{44}$$

the YBJ equation (35) reads:

$$\frac{1}{\psi_{\rm rms}}\partial_t M + J(\chi, M) + \frac{i}{2}(\Delta\chi)M - \frac{i}{2\psi_{\rm rms}}\Delta M = 0\,. \tag{45}$$

In the next sections we consider a homogeneous initial condition $M(x,y,t=0)=1$,[6] with the goal of characterizing the long-time statistics of the NIW field in two limits of interest:

- $\psi_{\rm rms} \ll 1$: this is the 'quantum' or 'strong-dispersion' limit. The flow is weak and the dispersive effects in (45) are strong.
- $\psi_{\rm rms} \gg 1$: this is the limit of 'classical mechanics'. The YBJ equation is analogous to the dynamics of a quantum particle in the small-$\hbar$ limit.

3 The Strong-dispersion, 'Quantum' Limit

In the strong-dispersion limit $\psi_{\rm rms} \ll 1$ the potential reduces to:

$$V(x,y) = -\psi_{\rm rms}^2 \frac{|\boldsymbol{\nabla}\chi|^2}{2} + \frac{\psi_{\rm rms}}{2}\Delta\chi \simeq \frac{\psi_{\rm rms}}{2}\Delta\chi\,. \tag{46}$$

In line with the intuition of DVB, the potential minima then correspond to the anticyclones of the background flow. Following YBJ we introduce the following expansion for the NIW complex amplitude:

$$M = \mathcal{M}(t) + \psi_{\rm rms}\, m(x,y,t) + \mathcal{O}(\psi_{\rm rms}^2), \qquad \text{with } \langle m \rangle = 0\,. \tag{47}$$

In (47) the homogeneous initial condition has evolved into a strong homogeneous part $\mathcal{M}(t)$ of the solution, together with a weaker mean-zero spatial modulation $\psi_{\rm rms}\, m(x,y,t)$ induced by the

[6] The YBJ equation being linear and phase invariant, the uniform initial value of M is irrelevant and can be set to one without loss of generality.

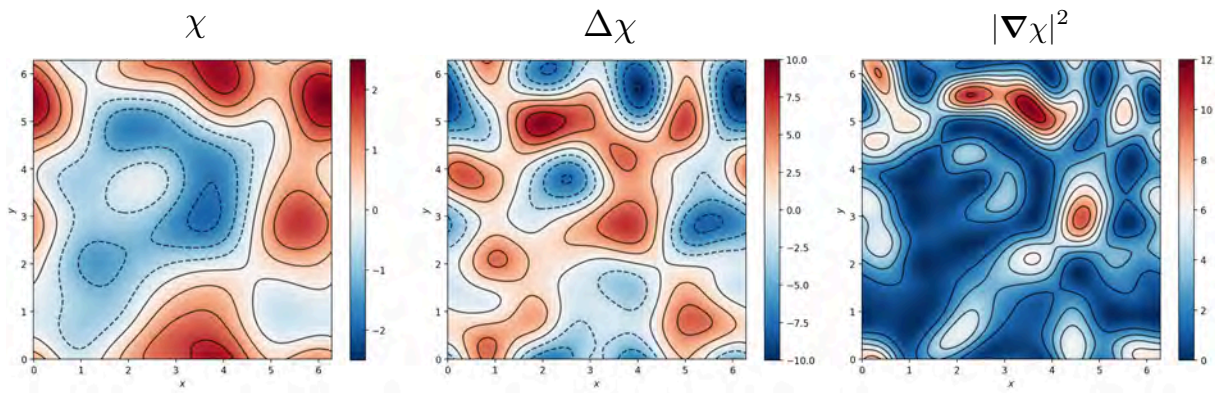

Figure 3: The normalized background flow considered throughout this lecture. From left to right: streamfunction χ, vorticity $\Delta\chi$ and kinetic energy $|\nabla\chi|^2$.

weak background flow. Both $\mathcal{M}$ and m are $\mathcal{O}(1)$ in the expansion above. Averaging equation (45) over space simply leads to $\partial_t\mathcal{M} = 0 + \mathcal{O}(\psi_{\rm rms})$: the spatially homogeneous part of the solution is time-independent to lowest order, and using the initial condition we obtain $\mathcal{M} = 1$. To $\mathcal{O}(1)$, equation (45) then yields:

$$\partial_t m + \frac{i}{2}\Delta\chi - \frac{i}{2}\Delta m = 0\,. \tag{48}$$

The solution to this equation is:

$$m = \chi(x,y) + \tilde{m}(x,y,t)\,, \tag{49}$$

where the term $\tilde{m}(x,y,t)$ oscillates in time with vanishing long-time average. The approximate solution then reads:

$$M \simeq 1 + \psi_{\rm rms}\,\chi(x,y) + \psi_{\rm rms}\tilde{m} = 1 + \psi(x,y) + \psi_{\rm rms}\tilde{m}\,. \tag{50}$$

Denoting time average as $\bar{\cdot}$, the time-averaged distribution of wave action finally reads:

$$\overline{|M|^2}(\mathbf{x}) = 1 + 2\psi(x,y) + \mathcal{O}(\psi_{\rm rms}^2)\,. \tag{51}$$

We conclude that, although the potential minima correspond anticyclonic regions, the distribution of wave kinetic energy (or wave action) is modulated by the streamfunction of the flow, the regions of maximal wave kinetic energy corresponding to the regions of maximal streamfunction. In the particular case of a monoscale flow, where ψ is a harmonic function, the vorticity is directly proportional to $-\psi$: regions of strong ψ indeed correspond to anticyclonic regions, confirming the intuition of DVB. For multiscale flows involving a broad range of scales, however, the streamfunction can differ very much from the vorticity field. Beyond the sole kinetic energy, one may be interested in the distribution of wave potential energy, $\overline{|\nabla M|^2}(\mathbf{x})$, omitting the prefactor 1/2. As opposed to $\overline{|M|^2}(\mathbf{x})$, a quantitative prediction for $\overline{|\nabla M|^2}(\mathbf{x})$ requires computing $\tilde{m}$ above, which goes beyond the scope of the present lecture. Upon arbitrarily neglecting $\tilde{m}$ in (50), however, one expects some level of correlation between the wave potential energy $\overline{|\nabla M|^2}(\mathbf{x})$ and the kinetic energy $|\nabla\psi|^2$ of the background flow.

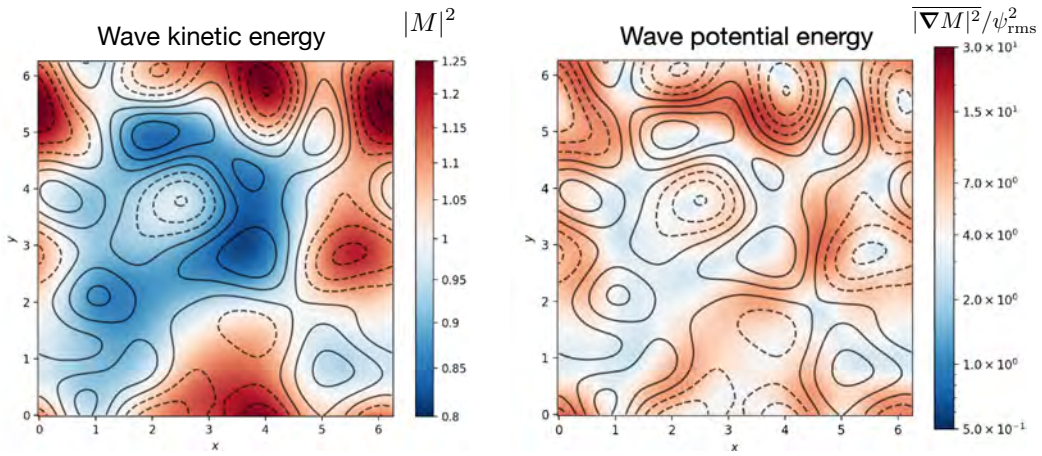

Figure 4: Time averaged NIW kinetic energy (left) and potential energy (right) for a simulation with $\psi_{\rm rms} = 0.05$ (strong-dispersion limit). The structure of the wave kinetic energy is given by that of the streamfunction $\chi(x, y)$, see figure 3. The prefactor agrees quantitatively with the prediction (51). The structure of the wave potential energy is correlated with that of the background flow kinetic energy, although a quantitative prediction would require computing the unsteady term $\tilde{m}$. Contours on both panels correspond to isovorticity lines.

To test these predictions, following DVB we consider a steady flow obtained from a homogeneous isotropic Gaussian random process, with Gaussian correlation function and a correlation length of approximately 1/7 of the domain size. In figure 3, we show the streamfunction χ, the vorticity $\Delta\chi$, and the kinetic energy $|\boldsymbol{\nabla}\chi|^2$ of the background flow considered throughout this lecture.

We consider first a simulation of the YBJ equation with weak background flow, $\psi_{\rm rms} = 0.05$. In figure 4 we show the time-averaged spatial distributions of wave kinetic energy and wave potential energy. One clearly sees that the modulation of wave kinetic energy is given by the streamfunction pattern, as opposed to the vorticity pattern.[7] The strength of the modulation agrees quantitatively with the prediction (51). As far as the wave potential energy is concerned, there is indeed some correlation with the kinetic energy of the background flow (see figure 3). A quantitative prediction would require computing the unsteady term $\tilde{m}$ in (50).

4 The Classical Limit, $\psi_{\rm rms} \gg 1$

In the classical limit, $\psi_{\rm rms} \gg 1$, the potential reduces to:

$$V(x, y) = -\psi_{\rm rms}^2 \frac{|\boldsymbol{\nabla}\chi|^2}{2} + \frac{\psi_{\rm rms}}{2}\Delta\chi \simeq -\psi_{\rm rms}^2 \frac{|\boldsymbol{\nabla}\chi|^2}{2}\,. \tag{52}$$

We thus expect the particles to be attracted to the regions of maximum kinetic energy. $\psi_{\rm rms} \gg 1$ is also the ray-tracing limit, where the trajectories of compact wave packets are determined based on a WKB expansion. We readily infer the resulting ray-tracing equations using the quantum analogy: this is the limit of classical mechanics. A compact wave packet localized at $\mathbf{X}(t)$ corresponds to a

[7] There is, however, some correlation between the two.

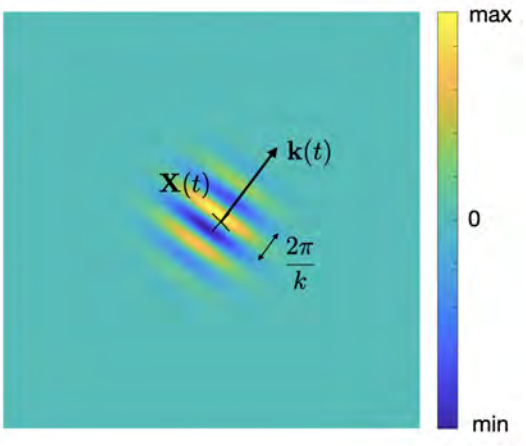

Figure 5: A narrow wave packet with mean position $\mathbf{X}(t)$ and wavevector $\mathbf{k}(t)$ behaves like a charged classical particle in a static 2D electromagnetic field.

charged classical particle subject to a Lorentz force, and Newton's third principle yields:

$$m\ddot{\mathbf{X}} = q(\mathbf{E} + \dot{\mathbf{X}} \times \mathbf{B})\,. \tag{53}$$

where $\mathbf{E} = -\boldsymbol{\nabla} V$, $\mathbf{B} = \boldsymbol{\nabla} \times \mathbf{A}$, and we have explicitly written the mass m and the charge q to highlight the analogy.

As mentioned above, it is far from obvious that the conservative dynamics of such classical particles would lead to accumulation in the potential minima. One should not immediately conclude from (52) that the particles – and thus the NIW kinetic energy – will accumulate in the fast-flow regions. Instead, a better-suited framework to infer the statistics of such classical particles is the statistical mechanics of equilibrium systems, which we recall in the following.

4.1 Ergodic theory and microcanonical ensemble

Instead of Newton's third law, the statistical mechanics of equilibrium system starts from the classical version of the Hamiltonian (37). Setting the mass and charge of the particle to one and denoting as $\mathbf{X}(t)$ and $\mathbf{k}(t)$ the position and momentum of the classical particle, the classical Hamiltonian reads:

$$H(\mathbf{X}, \mathbf{k}) = \frac{1}{2}[\mathbf{k} + \mathbf{U}(\mathbf{X})]^2 + V(\mathbf{X})\,, \tag{54}$$

where we have substituted the expression of the vector potential given in table 1. The potential V is also to be read in table 1. Hamilton's equations for the above-written Hamiltonian govern the evolution of a narrow wave packet located at $\mathbf{X}(t) = [X(t), Y(t)]$ with wavevector $\mathbf{k}(t) = [k_x(t), k_y(t)]$ (see sketch in figure 5):

$$\frac{\mathrm{d}\mathbf{X}}{\mathrm{d}t} = \frac{\partial H}{\partial \mathbf{k}}\,, \qquad \frac{\mathrm{d}\mathbf{k}}{\mathrm{d}t} = -\frac{\partial H}{\partial \mathbf{X}}\,, \tag{55}$$

where the equations are to be understood componentwise. Consider a cloud of initial conditions in the phase space (X, Y, k_x, k_y). Liouville theorem states that, following the Hamiltonian evolution (55), the cloud will deform in phase space conserving its initial volume. In other words,

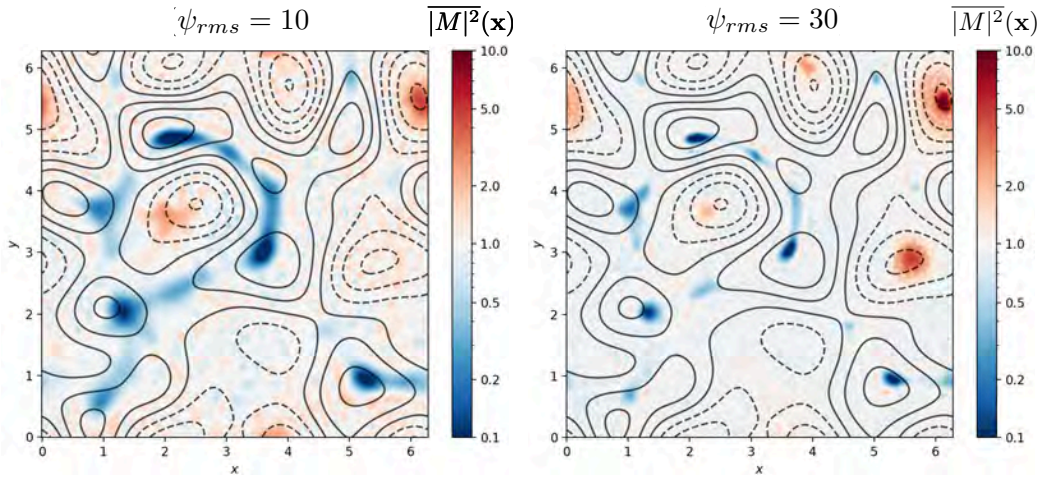

Figure 6: Time-averaged distribution of NIW kinetic energy for numerical simulations with two large values of $\psi_{\rm rms}$. The numerical data agree with the prediction of uniform $\overline{|M|^2}$ over most of the domain. The deficits in kinetic energy near the centers of cyclones are captured by a refined statistical mechanics calculation. By contrast, the excess kinetic energy near the centers of anticyclones results from a local failure of the ergodic assumption.

the volume in phase space is conserved by the dynamics because equations (55) correspond to an incompressible phase-space flow.

Consider now an ensemble of particles with the same initial energy E_0. Because energy is conserved, these particles only have access to the hypersurface $H(\mathbf{X}, \mathbf{k}) = E_0$ in phase space. Like a cloud of dye getting homogenized by a chaotic flow and achieving uniform concentration in the long-time limit, we expect the Hamiltonian phase-space flow (55) to homogenize a cloud of initial conditions with initial energy E_0 over the hypersurface $H(\mathbf{X}, \mathbf{k}) = E_0$. The ergodic assumption thus consists in assuming that, in the long time limit, the probability of finding a particle with position $\mathbf{X}$ and momentum $\mathbf{k}$ is uniform over the hypersurface $H(\mathbf{X}, \mathbf{k}) = E_0$ and zero elsewhere. Introducing a probability density $P(\mathbf{x}, \mathbf{k})$ in phase space such that the $P(\mathbf{x}, \mathbf{k})\mathrm{d}\mathbf{x}\mathrm{d}\mathbf{k}$ is the probability for a particle to be in a phase-space volume $\mathrm{d}\mathbf{x}\mathrm{d}\mathbf{k}$ around the point $(\mathbf{x}, \mathbf{k})$, the ergodic assumption translates into:

$$\mathcal{P}(\mathbf{x}, \mathbf{k}) = \mathcal{C}\, \delta[H(\mathbf{x}, \mathbf{k}) - E_0]\,, \tag{56}$$

where the constant $\mathcal{C}$ is a normalization factor. In the following we assume that the ergodic assumption holds and we replace long-time averages with averages in phase space using the probability density (56).

4.2 Distribution of NIW kinetic energy

As a first illustration, let us determine the spatial distribution of NIW kinetic energy using an average in phase space. The time-averaged NIW kinetic energy at location $\mathbf{x}_0$ is given by $\overline{|M|^2}(\mathbf{x}_0)$. According to table 1, this is also the time-averaged probability of finding the quantum particle at location $\mathbf{x}_0$. And in the classical limit, this is also the time-averaged probability of finding the classical particle at location $\mathbf{x}_0$, regardless of its momentum $\mathbf{k}$. Using the probability density (56),

the probability of finding the classical particle at location $\mathbf{x}_0$, regardless of its momentum $\mathbf{k}$ is given by:

$$\overline{|M|^2}(\mathbf{x}_0) = \int_{\mathbf{x}\in\mathcal{D};\mathbf{k}\in\mathbb{R}^2} \underbrace{\delta(\mathbf{x}-\mathbf{x}_0)}_{\text{particle located at } \mathbf{x}_0} \mathcal{P}(\mathbf{x},\mathbf{k})\,\mathrm{d}\mathbf{x}\mathrm{d}\mathbf{k} \tag{57}$$

$$= \mathcal{C}\int_{\mathbf{x}\in\mathcal{D};\mathbf{k}\in\mathbb{R}^2} \delta(\mathbf{x}-\mathbf{x}_0)\,\delta[H(\mathbf{x},\mathbf{k})-E_0]\,\mathrm{d}\mathbf{x}\mathrm{d}\mathbf{k} \tag{58}$$

$$= \mathcal{C}\int_{\mathbf{k}\in\mathbb{R}^2} \delta[H(\mathbf{x}_0,\mathbf{k})-E_0]\,\mathrm{d}\mathbf{k} \tag{59}$$

$$= \mathcal{C}\int_{\mathbf{k}\in\mathbb{R}^2} \delta\left[\frac{1}{2}(\mathbf{k}+\mathbf{U}(\mathbf{x}_0))^2 + V(\mathbf{x}_0) - E_0\right]\,\mathrm{d}\mathbf{k}\,. \tag{60}$$

Changing the integration variable to $\mathbf{K} = \mathbf{k} + \mathbf{U}(\mathbf{x}_0)$ with norm $K = |\mathbf{K}|$, this integral becomes:

$$\overline{|M|^2}(\mathbf{x}_0) = \mathcal{C}\int_{\mathbf{K}\in\mathbb{R}^2} \delta\left[\frac{1}{2}K^2 + V(\mathbf{x}_0) - E_0\right]\,\mathrm{d}\mathbf{K} \tag{61}$$

$$= \mathcal{C}\int_{K\in\mathbb{R}^+} \delta\left[\frac{1}{2}K^2 + V(\mathbf{x}_0) - E_0\right] 2\pi K\,\mathrm{d}K \tag{62}$$

$$= 2\pi\mathcal{C}\int_{K\in\mathbb{R}^+} \delta\left[\frac{1}{2}K^2 + V(\mathbf{x}_0) - E_0\right]\,\mathrm{d}\left(\frac{K^2}{2}\right) \tag{63}$$

The remaining integral equals one if $V(\mathbf{x}_0) - E_0 < 0$ and zero if $V(\mathbf{x}_0) - E_0 > 0$. That is:

$$\overline{|M|^2}(\mathbf{x}_0) = 2\pi\mathcal{C}\,\mathcal{H}[E_0 - V(\mathbf{x}_0)]\,, \tag{64}$$

where $\mathcal{H}$ denotes the Heavyside function.

The initial energy of the particles is estimated by inserting the initial condition $M(x,y,t=0)=1$ into expression (43) for the energy. Only the term $(\Delta\psi)|M|^2/2$ remains: the local initial energy is of the order of the local vorticity ; it is thus proportional to ψ_{rms}. By contrast, the potential (52) has much greater magnitude, of order ψ_{rms}^2, and it is always negative. We conclude that the initial energy is negligible as compared to the potential $V < 0$ in the limit $\psi_{\mathrm{rms}} \gg 1$ of interest here: $E_0 \simeq 0$. To a good approximation, $\mathcal{H}[E_0 - V(\mathbf{x}_0)] = 1$ almost everywhere, and we thus predict a uniform distribution of NIW kinetic energy, $\overline{|M|^2}(\mathbf{x}_0) = 2\pi\mathcal{C}$. Because of action conservation the space average of $|M|^2$ is conserved and equal to one. We thus obtain:

$$\mathcal{C} = \frac{1}{2\pi}\,, \tag{65}$$

the prediction for the time-averaged spatial distribution of kinetic energy being simply:

$$\overline{|M|^2}(\mathbf{x}) = 1\,. \tag{66}$$

Somewhat surprisingly, based on statistical mechanics we predict a uniform distribution of NIW kinetic energy, despite the spatial structure of the potential (52). In figure 6 we plot $\overline{|M|^2}(\mathbf{x})$ for simulations with large values of ψ_{rms}. We observe indeed an almost uniform background level of NIW kinetic energy. Failures of the statistical mechanics prediction are observed only in regions of two kinds:

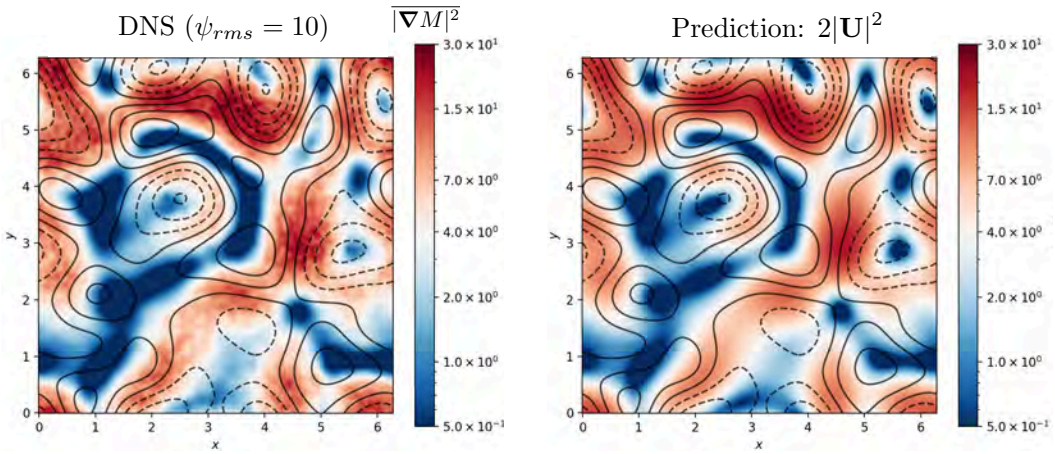

Figure 7: Time-averaged distribution of NIW potential energy from a numerical simulation with $\psi_{\rm rms} = 10$ (left), compared to the theoretical prediction from statistical mechanics (right).

- The particles are absent from the central regions of cyclones. This is because the precise value of E_0 matters near the center of a cyclone. Indeed, the full potential V in table 1 becomes positive there. Few of the particles have sufficient initial energy to get on top of such a potential hill, hence the gap in NIW kinetic energy.[8]

- In line with DVB, there is a concentration of NIW kinetic energy near the centers of anticyclones. The reason is that the ergodic assumption breaks down there. For instance, the motion of a particle in a locally axisymmetric anticyclone conserves both energy and angular momentum, so that the dynamical system (55) is effectively two-dimensional. A 2D autonomous dynamical system cannot lead to chaos and is unable to mix the probability density in phase space. Hence, the loss of ergodicity in such regions. Overall, only a modest fraction of the total kinetic energy remains trapped in the anticyclones in figure 6. For a more realistic 2D background flow of ocean relevance, such as the vortex gases discussed in the previous lectures, a negligible fraction of the kinetic energy gets trapped in anticyclones.

4.3 Distribution of NIW potential energy

As a second illustration of the statistical mechanics approach, we consider the time-averaged spatial distribution of NIW potential energy, $\overline{|\nabla M|^2}(\mathbf{x}_0)$. Remembering that the momentum operator is $-i\hbar\nabla$ in quantum mechanics, the NIW potential energy is analogous to the expectation value of the squared momentum. Alternatively, based on the sketch in figure 5 one estimates $\nabla M \simeq i\mathbf{k}M$ and $|\nabla M|^2 \simeq \mathbf{k}^2|M|^2$. We thus want to compute the averaged squared momentum of the particles that are located at $\mathbf{x}_0$. In phase space this average reads:

$$\overline{|\nabla M|^2}(\mathbf{x}_0) = \int_{\mathbf{x}\in\mathcal{D};\mathbf{k}\in\mathbb{R}^2} \underbrace{k^2}_{\text{squared momentum}} \underbrace{\delta(\mathbf{x}-\mathbf{x}_0)}_{\text{particle located at } \mathbf{x}_0} \mathcal{P}(\mathbf{x},\mathbf{k})\,\mathrm{d}\mathbf{x}\mathrm{d}\mathbf{k}\,. \tag{67}$$

[8] A refined computation taking this effect into account is feasible but goes beyond the scope of the present lecture.

Substituting the probability density (56) with the prefactor (65), before changing integration variable again to $\mathbf{K} = \mathbf{k} + \mathbf{U}(\mathbf{x}_0)$ leads to:

$$\overline{|\boldsymbol{\nabla} M|^2}(\mathbf{x}_0) = \frac{1}{2\pi} \int_{\mathbf{x}\in\mathcal{D};\mathbf{k}\in\mathbb{R}^2} k^2 \delta(\mathbf{x}-\mathbf{x}_0)\delta[H(\mathbf{x},\mathbf{k}) - E_0]\,\mathrm{d}\mathbf{x}\mathrm{d}\mathbf{k} \tag{68}$$

$$= \frac{1}{2\pi} \int_{\mathbf{k}\in\mathbb{R}^2} k^2 \delta[H(\mathbf{x}_0,\mathbf{k}) - E_0]\,\mathrm{d}\mathbf{k} \tag{69}$$

$$= \frac{1}{2\pi} \int_{\mathbf{k}\in\mathbb{R}^2} k^2 \delta\left[\frac{1}{2}(\mathbf{k}+\mathbf{U}(\mathbf{x}_0))^2 + V(\mathbf{x}_0) - E_0\right]\,\mathrm{d}\mathbf{k} \tag{70}$$

$$= \frac{1}{2\pi} \int_{\mathbf{K}\in\mathbb{R}^2} [\mathbf{K}-\mathbf{U}(\mathbf{x}_0)]^2 \delta\left[\frac{1}{2}K^2 + V(\mathbf{x}_0) - E_0\right]\,\mathrm{d}\mathbf{K} \tag{71}$$

$$= \frac{1}{2\pi} \int_{\mathbf{K}\in\mathbb{R}^2} [K^2 - \cancel{2\mathbf{K}\cdot\mathbf{U}(\mathbf{x}_0)} + \mathbf{U}(\mathbf{x}_0)^2]\,\delta\left[\frac{1}{2}K^2 + V(\mathbf{x}_0) - E_0\right]\,\mathrm{d}\mathbf{K}\,, \tag{72}$$

where the crossed-out term above is odd in $\mathbf{K}$, thus leading to a vanishing integral. We finally obtain:

$$\overline{|\boldsymbol{\nabla} M|^2}(\mathbf{x}_0) = \frac{1}{2\pi} \int_{K\in\mathbb{R}^+} [K^2 + \mathbf{U}(\mathbf{x}_0)^2]\,\delta\left[\frac{1}{2}K^2 + V(\mathbf{x}_0) - E_0\right]\,2\pi\,\mathrm{d}\left(\frac{K^2}{2}\right) \tag{73}$$

$$= \int_{K\in\mathbb{R}^+} K^2\,\delta\left[\frac{1}{2}K^2 + V(\mathbf{x}_0) - E_0\right]\,\mathrm{d}\left(\frac{K^2}{2}\right) \tag{74}$$

$$+ \mathbf{U}(\mathbf{x}_0)^2 \int_{K\in\mathbb{R}^+} \delta\left[\frac{1}{2}K^2 + V(\mathbf{x}_0) - E_0\right]\,\mathrm{d}\left(\frac{K^2}{2}\right) \tag{75}$$

$$= 2\underbrace{(E_0 - V(\mathbf{x}_0))}_{\simeq \frac{\mathbf{U}(\mathbf{x}_0)^2}{2}} + \mathbf{U}(\mathbf{x}_0)^2 \underbrace{\mathcal{H}(E_0 - V(\mathbf{x}_0))}_{=1} \tag{76}$$

$$= 2\mathbf{U}(\mathbf{x}_0)^2\,. \tag{77}$$

We conclude that the spatial distribution of NIW potential energy is directly given by the kinetic energy distribution of the background flow, with an accumulation of NIW potential energy in fast-flow regions. In figure 7 we plot $\overline{|\boldsymbol{\nabla} M|^2}(\mathbf{x})$ extracted from simulations of the YBJ equation with large values of ψ_{rms}. The numerical data are in very good agreement with the prediction (77) from statistical mechanics, both the spatial structure and the prefactor being correct.

4.4 Other quantities

The same approach can be applied to various other quantities of interest. For instance, one can predict the time-averaged Stokes drift induced by the NIW field, $\overline{\mathbf{u}_s}(\mathbf{x}) = \overline{(\boldsymbol{\xi}\cdot\boldsymbol{\nabla})\mathbf{u}}$, where the particle displacement is defined as $\partial_t\boldsymbol{\xi} = \mathbf{u}$. We leave this as an exercise for the interested reader. For the normalized initial condition $M(x, y, t = 0) = 1$ (and therefore $\mathcal{A} = 1$) the end result is:

$$\overline{\mathbf{u}_s}(\mathbf{x}) = -\frac{\mathbf{U}(\mathbf{x})}{2}\,. \tag{78}$$

For arbitrary initial action $\mathcal{A}$ the expression (78) is to be multiplied by $\mathcal{A}$. The time-averaged Stokes drift is proportional to the local velocity of the background flow and antiparallel to it.

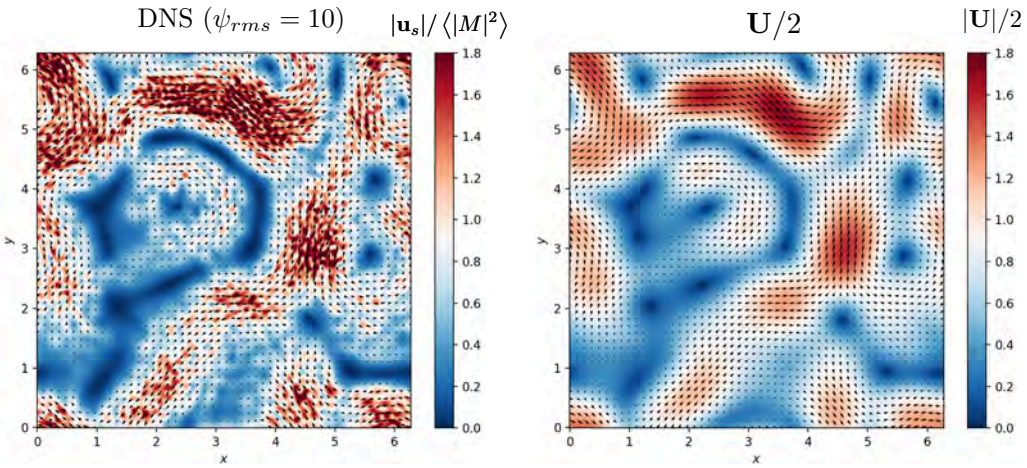

Figure 8: Time-averaged Stokes drift velocity for a numerical simulation with $\psi_{\rm rms} = 10$ (left), compared to the theoretical prediction from statistical mechanics (right).

5 Conclusion

Focusing on the simplest instance of the YBJ model for NIWs interacting with a steady background flow, we have studied how the flow shapes the NIW field. Following the original article by YBJ, the strong-dispersion regime is efficiently studied through an asymptotic expansion in $\psi_{\rm rms} \ll 1$, corresponding to a dimensional streamfunction much weaker than $g'H_0/f$. For instance, the NIW kinetic energy has an almost uniform spatial distribution, together with a small modulation proportional to the streamfunction of the background flow.

The opposite limit is that of strong advection, $\psi_{\rm rms} \gg 1$ (dimensional streamfunction much greater than $g'H_0/f$). Introducing an analogy with the dynamics of a charged particle in an electromagnetic field, we have predicted various statistics of the NIW field using the statistical mechanics of equilibrium systems. We have obtained that the NIW kinetic energy is almost uniformly distributed on average, while the NIW potential energy is spatially distributed following the kinetic energy of the background flow. Finally, the time-averaged Stokes drift induced by the NIW wave field is proportional and antiparallel to the local background flow velocity.

References

[1] NJ Balmforth, Stefan G Llewellyn Smith, and WR Young. Enhanced dispersion of near-inertial waves in an idealized geostrophic flow. *Journal of Marine Research*, 1998.

[2] Eric Danioux, Jacques Vanneste, and Oliver Bühler. On the concentration of near-inertial waves in anticyclones. *Journal of Fluid Mechanics*, 773:R2, 2015.

[3] Eric A D'Asaro, Charles C Eriksen, Murray D Levine, Peter Niiler, Pim Van Meurs, et al. Upper-ocean inertial currents forced by a strong storm. part i: Data and comparisons with linear theory. *Journal of Physical Oceanography*, 25(11):2909–2936, 1995.

[4] Alexandre Tlili and Basile Gallet. Statistics of near-inertial waves over a background flow via quantum and statistical mechanics. *arXiv preprint arXiv:2510.21463*, 2025.

[5] WR Young and Mahdi Ben Jelloul. Propagation of near-inertial oscillations through a geostrophic flow. *Journal of Marine Research*, 1997.

The Dynamics of Stacked Stratified Shear Layers

Adhithiya Sivakumar

August 19, 2024

1 Introduction

Stratified shear flows are unstable to several distinct instabilities. Three canonical examples are the Kelvin–Helmholtz (KH) instability, the Holmboe wave (HW) instability, and the Taylor–Caulfield (TC) instability. The KH instability develops when shear across a density interface is strong enough to roll the interface into billow-like structures [3]. In contrast, the HW instability—first described by Holmboe [10]—arises at higher levels of stratification, producing cusped interfacial waves propagating in opposite directions on a sharp density jump. The TC instability was originally identified by Taylor in his 1915 Adams Prize essay, reported in the paper in which he also presented the derivation of Taylor-Goldstein Equation (TGE) for normal mode analysis of stratified shear flows[8, 16] and subsequently generalised by Caulfield [5] and observed experimentally by Caulfield and co-workers [6]. It emerges when two buoyancy interfaces lie within a single shear layer and is canonically characterized by the formation of stationary elliptical vortices, although its finite-amplitude development and morphology can be sensitive to flow parameters [7].

These instabilities have been documented in the literature [3], usually in the context of an isolated stratified shear layer. However, multiple vertically arrayed stratified shear layers are frequently observed in laboratory experiments and naturally occurring flows [1, 9]. Until recently, the dynamics of closely spaced shear layers received relatively little attention. New studies have begun to explore how instabilities in adjacent shear layers interact, for example, recent work by Liu et al. [12] examined a stacked stratified system susceptible to the KH instability and found, among other things, a novel oscillatory mode unique to the stacked configuration. Such findings motivate the present investigation into stacked Holmboe wave instabilities, which are prevalent when stratification is sufficiently strong to favor HW instabilities over KH instabilities.

In this report, we examine the stability of a three-layer stably stratified fluid with two buoyancy interfaces embedded in two distinct shear layers separated by a quiescent middle layer. Our approach is to first analyze the inviscid limit using piecewise-continuous idealizations of the velocity and buoyancy profiles and classical linear stability theory. This permits analytical insight into the growth of small disturbances and the identification of instability modes. We then introduce diffusive effects (finite viscosity and thermal diffusivity) to investigate how nonzero diffusivity alters the stability characteristics, such as growth rates and instability bands.

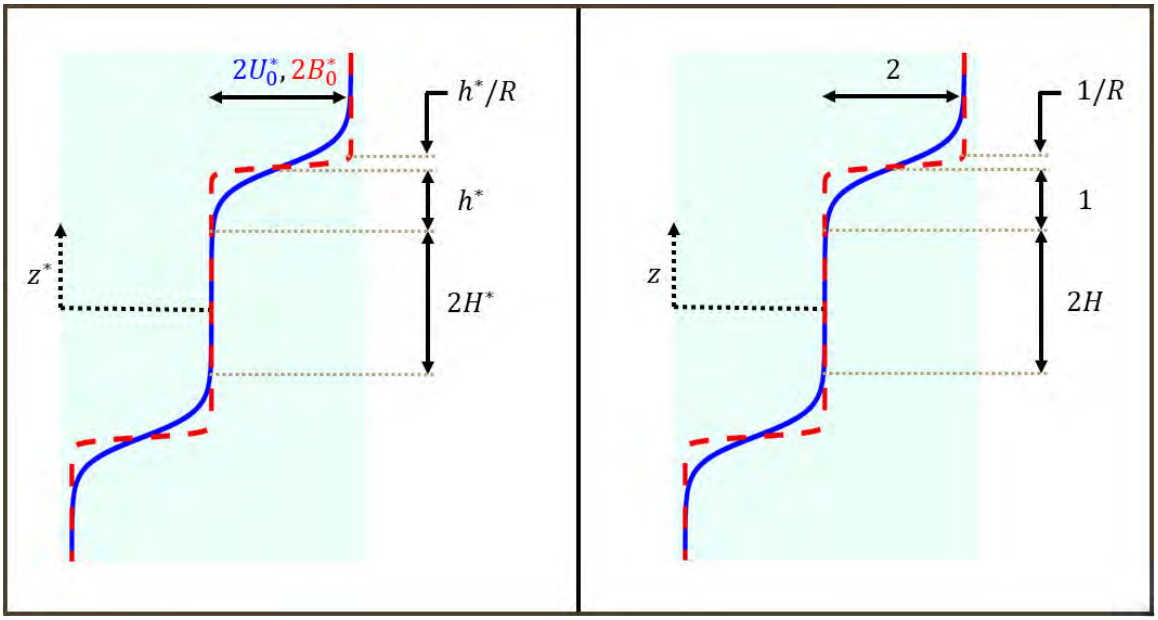

Figure 1: Dimensonal (left) and dimensionless (right) profiles of the background velocity (solid blue curve) and buoyancy (dashed red curve).

Finally, we explore the finite-amplitude evolution of instabilities in this stacked-layer system through direct numerical simulations. These simulations reveal how nonlinear interactions between Holmboe waves on the two interfaces lead to flow features and statistics that differ from those of the classical case described in Refs. [10, 15]. The overall aim of this study is to characterize the dynamics of stacked stratified shear layers across the linear and nonlinear regimes, thereby extending classical single-layer instability theory to more complex, multilayered flow environments.

1.1 Mathematical formulation

We start with the 2D Boussinesq equations, presented here in dimensional form (denoted by asterisks) on the cartesian (x^*-z^*) plane [14],

$$\begin{aligned} \nabla \cdot \boldsymbol{u}^* &= 0, \\ \partial_{t^*} \boldsymbol{u}^* + \boldsymbol{u}^* \cdot \nabla^* \boldsymbol{u}^* &= -\nabla^* \pi^* + b^* \hat{z} + \nu^* \nabla^{*2} \boldsymbol{u}^*, \\ \partial_t b^* + \boldsymbol{u}^* \cdot \nabla^* b^* &= \kappa^* \nabla^{*2} b^*, \end{aligned} \tag{1}$$

where the velocity $\boldsymbol{u}^* \equiv (u^*, w^*)^T$, and $b^* \equiv -g^* \delta\rho^*/\rho^*_{ref}$ is the buoyancy (or negative reduced gravity), π^* is the dynamic pressure, ν^* is the molecular kinematic viscosity and κ^* is the thermal diffusivity. Our initial condition consists of a streamwise flow $U^*(z^*)$ and buoyancy $B^*(z^*)$, given by

$$\begin{aligned} U^*(z^*) &\equiv U_0^* \left[\tanh\left(\frac{z^* - H^* - h^*}{h^*} \right) + \tanh\left(\frac{z^* + H^* + h^*}{h^*} \right) \right], \\ B^*(z^*) &\equiv B_0^* \left[\tanh\left(\frac{z^* - H^* - h^*}{h^*/R} \right) + \tanh\left(\frac{z^* + H^* + h^*}{h^*/R} \right) \right]. \end{aligned}$$

This configuration (see Figure 1, left panel) organizes the domain into two stratified shear layers of thickness $2h^*$ separated by a quiescent region of thickness $2H^*$. Non-dimensionalizing velocities using U_0^*, distances using h^*, and the buoyancy using B_0^* produces the equations

$$\begin{aligned} \nabla \cdot \boldsymbol{u} &= 0, \\ \partial_t \boldsymbol{u} + \boldsymbol{u} \cdot \nabla \boldsymbol{u} &= -\nabla \pi + Ri_0 b \hat{z} + Re^{-1} \nabla^2 \boldsymbol{u}, \\ \partial_t b + \boldsymbol{u} \cdot \nabla b &= (PrRe)^{-1} \nabla^2 b, \end{aligned} \tag{2}$$

and the basic velocity and buoyancy profiles

$$\begin{aligned} U(z) &\equiv \tanh(z - H - 1) + \tanh(z + H + 1), \\ B(z) &\equiv \tanh[R(z - H - 1)] + \tanh[R(z + H + 1)], \end{aligned} \tag{3}$$

where $Ri_0 \equiv B_0^* h^* / U_0^{*2}$ is the bulk Richardson number of the flow, $Pr = \nu^*/\kappa^*$ is the Prandtl number, $Re \equiv U_0^* h^*/\nu^*$ is the Reynolds number, $H \equiv H^*/h^*$ is a dimensionless measure of shear layer separation, and R is the ratio of shear layer thickness to buoyancy layer thickness. Figure 1, right panel, represents these profiles schematically. At the outset, we note two limiting configurations previously examined in the literature, which appear as special cases of ours:

1. When $H \to 0$, the two stratified shear layers merge into a single shear layer which envelops both density interfaces. This configuration was investigated in the work of Caulfield [5].
2. When $H \to \infty$, the two stratified shear layers are too widely separated to realistically influence each other. Each layer is then expected to have purely the dynamics originally elaborated by Holmboe [10].

We next examine the response of this set-up to small-amplitude perturbations using the mechanics of linear stability theory, first in the inviscid case, and next in the viscous case.

2 Inviscid Linear Theory

Taking $Re \to \infty, Pr = O(1)$ in equations 2 and using the variable transformation

$$\begin{aligned} \boldsymbol{u} &\to U(z)\hat{x} + \varepsilon \hat{\boldsymbol{u}}(z) e^{i\alpha(x-ct)}, \\ b &\to B(z) + \varepsilon \hat{b}(z) e^{i\alpha(x-ct)}, \\ \pi &\to \Pi(z) + \varepsilon \hat{\pi}(z) e^{i\alpha(x-ct)}, \end{aligned}$$

(where the base-state pressure $\Pi(z)$ is in hydrostatic balance with the base state buoyancy $B(z)$) produces, at $O(\varepsilon)$ as $\varepsilon \to 0$, the aforementioned Taylor-Goldstein Equation (TGE)

$$w_{zz} + \left[Ri_0 \frac{B_z}{(U-c)^2} - \frac{U_{zz}}{(U-c)} - \alpha^2 \right] w = 0, \tag{4}$$

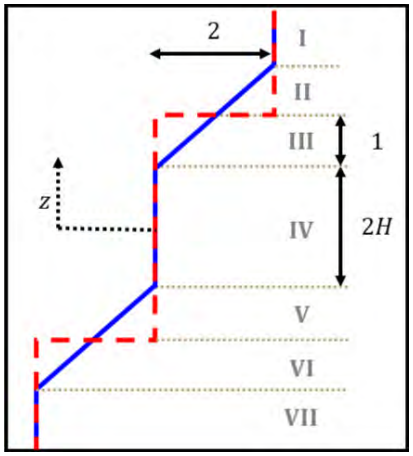

Figure 2: Piecewise approximations to the basic velocity (solid blue lines) and buoyancy (dashed red lines) profiles (3).

where the caret has been dropped for convenience, and which describes the evolution of small vertical velocity perturbations (with real wavenumber α and complex phase speed $c = c_r + ic_i$) to the basic state $(U\hat{x}, B, \Pi)$. Analytical solutions to the TGE may be found by approximating $U(z)$ and $B(z)$ by piecewise linear and constant functions, with linear instabilities corresponding to solutions with non-zero imaginary phase speed c_i and hence growth rate αc_i. Noting that the sharp interfaces implied by such approximations are permitted by the inviscid equations, we use

$$U(z) \equiv \begin{cases} 2, & z \in [H+2, \infty) \\ (z-H), & z \in [H, H+2] \\ 0, & z \in [-H, H] \\ (z+H), & z \in [-H-2, -H] \\ -2, & z \in (-\infty, -H-2] \end{cases}, \quad B(z) \equiv \begin{cases} 2, & z \in (H+1, \infty) \\ 0, & z \in (-H-1, H+1) \\ -2, & z \in (-\infty, -H-1) \end{cases}, \tag{5}$$

which is represented schematically in Figure 2. It also proves convenient to calculate the vertical shear

$$U_z(z) = \begin{cases} 0, & z \in (H+2, \infty) \\ 1, & z \in (H, H+2) \\ 0, & z \in (-H, H) \\ 1, & z \in (-H-2, -H) \\ 0, & z \in (-\infty, -H-2) \end{cases}, \tag{6}$$

The problem, thus reduced, has three parameters (H, Ri_0, α), on which the stability of the basic state (5) depends. Our objective is to investigate the effects of these parameters on the stability of the basic state by solving the TGE (4) with the basic state (5-6) and, further, to summarize state transitions in the $Ri_0 - \alpha$ plane for various values of H. The methods used are well documented in the literature (see Ref. [14], for instance), but some simple calculations will be presented below as examples.

2.1 Isolated interfaces, wave resonances, and the large-α approximation

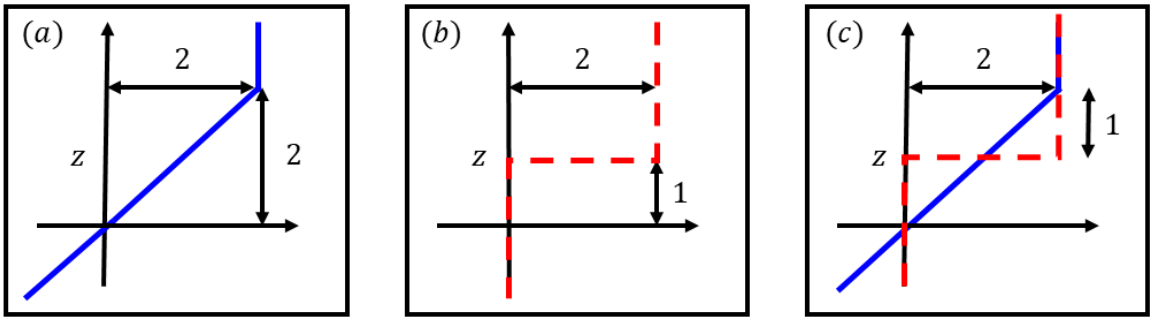

Figure 3: Three simple cases. An isolated shear interface (a), an isolated buoyancy interface (b), and a semi-infinite stratified shear layer (c).

Judging by the jumps in background shear (6) and buoyancy (5), our set-up has four shear interfaces and two buoyancy interfaces. Therefore, we may divide our domain into seven regions (labelled **(I)-(VII)**), separated by six buoyancy or shear interfaces. We label these interfaces using the roman numerals **(i)-(vi)** starting from the top. Table 1 below collects definitions/labels for each region and interface, and indicates for each interface whether it is a shear (S) or a buoyancy (B) interface.

Region	Definition
I	$z \in (H+2, \infty)$
II	$z \in (H+1, H+2)$
III	$z \in (H, H+1)$
IV	$z \in (-H, H)$
V	$z \in (-H-1, -H)$
VI	$z \in (-H-2, -H-1)$
VII	$z \in (-\infty, -H-2)$

Interface	Definition	Type
(i)	$z = H+2$	S
(ii)	$z = H+1$	B
(iii)	$z = H$	S
(iv)	$z = -H$	S
(v))	$z = -(H+1)$	B
(vi)	$z = -(H+2)$	S

Table 1: Division of the fluid domain into regions of continuous shear and buoyancy and labelling of these regions (left), as well as the interfaces which separate them (right). Refer also to Figure 2.

Our strategy is to solve the TGE in each region separately and then to apply continuity conditions across each interface, using the 'Wave-Interaction-Theory' (WIT) (see reviews [3, 14]). Before diving into the heavy algebra of our problem, we describe the WIT methodology and build intuition through three simplified scenarios, illustrated schematically in Figure 3.

2.1.1 An isolated shear interface

First, we consider an isolated shear interface at $z = 2$ with the streamwise velocity held constant at 2 above it and decreasing linearly below it (see Figure 3a). The background velocity is

$$U(z) \equiv \begin{cases} 2, & z \in [2, \infty) \\ z, & z \in (-\infty, 2] \end{cases}, \tag{7}$$

and the TGE reduces to

$$w_{zz} - \left[\frac{U_{zz}}{(U-c)} + \alpha^2\right] w = 0. \tag{8}$$

U_{zz} vanishes everywhere in the domain except at the location of the interface ($z = 2$), and therefore, the TGE further reduces to $w_{zz} - \alpha^2 w = 0$, which has general solutions

$$w_{top} = Ae^{\alpha z} + Be^{-\alpha z}, \text{ and } w_{bot} = Ce^{\alpha z} + De^{-\alpha z},$$

above and below the interface, respectively. The undetermined constants must now be determined by imposing additional constraints on the general solution.

1. First, we require that the solution remain bounded throughout the domain. This requirement (*far-field boundedness*) fails as $|z| \to \infty$ when A and D are non-zero. Therefore, we set $A = D = 0$.

2. Next, we enforce the kinematic boundary condition of *interfacial continuity of* $w(z)$, i.e., $w_{top}(z \to 2_+) = w_{bot}(z \to 2_-)$. This yields the equation $Be^{-2\alpha} = Ce^{2\alpha}$.

3. Finally, we enforce the dynamical boundary condition of *interfacial continuity of* $\pi(z)$, without which the vertical acceleration across the interface would become infinite. Applying the perturbation ansatz defined above to the inviscid horizontal momentum equation produces a formula for the perturbation pressure

$$\pi(z) = \frac{i}{\alpha}\left[(U-c)\, w_z - U_z\, w\right].$$

As above, pressure continuity may be cast as $\pi_{top}(z \to 2_+) = \pi_{bot}(z \to 2_-)$. Substituting into this known values of U and U_z above and below the interface, we obtain a condition on the jump in w_z

$$w_z(z \to 2_+) - w_z(z \to 2_-) = -\frac{w(z=2)}{2-c}.$$

Using here expressions for w_z above and below the interface produces the equation

$$\alpha\left(Be^{-2\alpha} + Ce^{2\alpha}\right) = \frac{Be^{-2\alpha}}{2-c}.$$

4. Eliminating the constants B and C between the equation above and that produced by step 2 results in the dispersion relation

$$c = c_v \equiv 2 - \frac{1}{2\alpha}, \tag{9}$$

which corresponds to a neutrally stable vorticity (or Rayleigh) wave (VW) supported on the shear interface.

The limiting behaviour of c_v as $\alpha \to \infty$, and the exponential structure of the vertical velocity eigenfunctions $w(z)$ imply that short wavelength perturbations (larger values of α) are more highly localized at the interface and propagate with phase speeds closer to the mean flow velocity $U(z)$ at the interface. In contrast, longer wavelength perturbations are less localized and subject to the shear-induced reduction in phase speed $1/(2\alpha)$.

2.1.2 An isolated buoyancy interface

Next, we consider an isolated buoyancy interface at $z = 1$ with the buoyancy held constant at 1 above it and vanishing abruptly below it (see Figure 3b). The background buoyancy is

$$B(z) \equiv \begin{cases} 2, & z \in [1, \infty) \\ 0, & z \in (-\infty, 1] \end{cases}, \tag{10}$$

and the TGE reduces to

$$w_{zz} + \left[Ri_0 \frac{B_z}{(U-c)^2} - \alpha^2\right] w = 0. \tag{11}$$

Repeating the steps above, we derive

$$c = c_b \equiv 1 \pm \sqrt{\frac{Ri_0}{\alpha}}, \tag{12}$$

representing rightward and leftward propagating gravity waves (GW). Like vorticity waves, longer waves have vertical structure that is not localized to the interface, and suffer stratification-dependent modifications to phase speed. The same cannot be said of shorter waves.

2.1.3 A semi-infinite stratified shear layer

A single stratified shear layer may be modelled by superimposing the velocity profile (7) and the buoyancy profile (10). This is shown schematically in Figure 3c. The full TGE 4 applies, and the algorithm detailed above produces the cubic dispersion relation [14]

$$\begin{aligned}(c-1)^3 - (c_v-1)(c-1)^2 - 0.5(c_b-1)^2(c-1) \\ - 0.5(c_b-1)^2\left[1 + (c_v-2)\left(1-e^{-2\alpha}\right)\right] = 0.\end{aligned} \tag{13}$$

Considering, in sequence, the balances between the leading term and the next two terms above shows that these terms codify the isolated effect of vorticity waves and gravity waves, respectively. The constant term encodes wave-wave interactions and is worth pausing over. This term can be rewritten

$$T_3(Ri_0, \alpha) \equiv Ri_0\left(\frac{1}{2\alpha} + \frac{1}{4\alpha^2} - \frac{e^{-2\alpha}}{4\alpha^2}\right).$$

Clearly, the term is significant when $\alpha \ll 1$. That is to say, long wavelength perturbations whose eigenfunctions are not localized around interfaces are susceptible to 'proximity' based wave interaction (hence the name 'Wave-Interaction-Theory') – longer waves enable greater coupling between interfaces, allowing gravity and vorticity waves to 'feel' one another across a finite vertical gap. As one might expect, this term appears to vanish when $\alpha \gg 1$. However, this is true only for certain values of Ri_0. Importantly, when $c_b = c_v$, i.e., when the vorticity and gravity waves have the same phase speed,

$$Ri_0 = \alpha\left(1 - \frac{1}{2\alpha}\right)^2,$$

and $T_3(\alpha \to \infty) = 1/2$. Balancing the leading term and constant term in (13) in this limit yields complex conjugate roots for c, indicating the possibility of strong wave-wave interactions leading to a linear instability even in the large-α limit, where proximity-based effects are expected to be weak.

This phenomenon, known as *wave resonance*, is comprehensively and more rigorously documented in the shear instability literature [3, 4, 14]. Here, we provide an intuitive overview of the conditions that must be met for it to occur. Briefly, wave pairs that are Doppler-shifted by the background shear can support mutual resonant growth, which may lead to a flow instability, provided that:

(a) the waves can attain a position in which the vertical velocity perturbations of one amplify crests and troughs of the other. This is always possible if the fluid in the layer between two interfaces is subject to shear; and:

(b) the waves can maintain this position over time (essentially travelling as one while they amplify each other). This is known as phase locking, and requires that the shear profile be such that the mutual amplification of nearly phase-locked waves acts to reduce the phase difference between them [14]. This occurs if both waves are propagating against the background shear at their height.

Wave resonance provides a powerful interpretive framework for shear flow instabilities. Different classes of resonant wave interactions are associated with different instability mechanisms. VW-VW interactions are associated with the Kelvin-Helmholtz (KH) instability, GW-VW interactions are associated with the Holmboe Wave (HW) instability, and GW-GW interactions are associated with the Taylor-Caulfield (TC) instability. More importantly for our purposes, it can be used to determine approximately the corresponding values of Ri_0 and α for which instabilities occur [5]. We do this by setting the phase speeds of the interacting waves equal to each other and taking the short-wave limit $\alpha \to \infty$. The procedure results, in this case, in the relation $Ri_0 = \alpha - 1$. Figure 4.11 of Ref. [14] shows that the actual stability boundaries are well approximated by this line on the $Ri_0 - \alpha$ plane in the wave resonance limit.

2.1.4 Wave resonances in stacked stratified shear layers

We now return to Figure 2 and enumerate all possible instabilities and the (approximate) $Ri_0 - \alpha$ conditions for their occurrence using the wave resonance framework. We consider each of the interfaces **(i)** – **(vi)** (see Table 1) in isolation and, using the procedure outlined in section 2.1.1, we derive dispersion relations describing the neutrally stable waves supported on each of them.

$$\begin{array}{llll} c^{(\mathbf{i})} & = 2 - (2\alpha)^{-1}\,, & c^{(\mathbf{vi})} & = -2 + (2\alpha)^{-1}\,, \\ c_{\pm}^{(\mathbf{ii})} & = 1 \pm \sqrt{Ri_0\alpha^{-1}}, & c_{\pm}^{(\mathbf{v})} & = -1 \pm \sqrt{Ri_0\alpha^{-1}}, \\ c^{(\mathbf{iii})} & = (2\alpha)^{-1}\,, & c^{(\mathbf{iv})} & = -\,(2\alpha)^{-1}\,. \end{array} \tag{14}$$

As mentioned before, each buoyancy interface supports two internal gravity waves (GW) and each shear interface supports one vorticity wave (VW). As we did in the previous section, we will look for sustainable wave resonances by setting the above dispersion relations equal to each other pairwise, and checking whether criterion (b) for phase-locking is met. For each potential instability, we will also estimate the phase speed using the formula

$$c_{in} \equiv \frac{U_{max} + U_{min}}{2}, \tag{15}$$

from Howard's Semicircle Theorem[11], where U_{max} and U_{min} are extremal values of streamwise velocity taken over the pair of interfaces under consideration.

VW-VW Interactions. The interaction between two vorticity waves gives rise to a KH instability which is stationary relative to the background shear flow. Three such interactions are possible in total, enumerated by counting points where the dispersion curves $c(Ri_0, \alpha)$ intersect. In this case, it can be shown that all three interactions can be sustained by phase locking. In addition to the local KH instabilities in each shear layer (K), there is also a non-local one (K_N) that arises from the interaction of VWs at the top-most and bottom-most interfaces. These results are summarized in table 2 below.

Interaction	**Interaction Condition**	$\|\mathbf{c_{in}}\|$	**Label**
$c^{(\mathbf{i})} = c^{(\mathbf{iii})}$	$\alpha \approx 1/2$	1	K
$c^{(\mathbf{i})} = c^{(\mathbf{vi})}$	$\alpha \approx 1/4$	0	K_N
$c^{(\mathbf{iv})} = c^{(\mathbf{vi})}$	$\alpha \approx 1/2$	1	K

Table 2: Summary of resonant VW-VW interactions. Labels are defined as a useful shorthand for future usage on plots and charts.

GW-VW Interactions. The interaction between a vorticity wave and a gravity wave gives rise to a HW instability which is nonstationary relative to the background shear flow. Eight such interactions are possible in total (counting interactions with right- and left-propagation GWs as one). Only six of these meet criterion (b) above. These may be said to cause three classes of HW instabilities (see Table 3): *Exterior* instabilities (H_E), which arise due to the interaction between a GW and the VW on its 'outside' (i.e., above it at the top shear layer, and below it at the bottom); *interior* instabilities (H_I), which arise from the interaction between a GW and the VW on its 'inside'; and *non-local* instabilities (H_N), which involve the interaction between a GW and the farthest VW from it.

Interaction	**Interaction Condition**	$\|\mathbf{c_{in}}\|$	**Label**
$c^{(\mathbf{i})} = c_+^{(\mathbf{ii})}$	$Ri_0 \approx \alpha - 1$	1.5	H_E
$c^{(\mathbf{iii})} = c_-^{(\mathbf{ii})}$	$Ri_0 \approx \alpha - 1$	0.5	H_I
$c^{(\mathbf{vi})} = c_-^{(\mathbf{ii})}$	$Ri_0 \approx 9\alpha - 3$	0.5	H_N
$c^{(\mathbf{iv})} = c_+^{(\mathbf{v})}$	$Ri_0 \approx \alpha - 1$	0.5	H_I
$c^{(\mathbf{vi})} = c_-^{(\mathbf{v})}$	$Ri_0 \approx \alpha - 1$	1.5	H_E
$c^{(\mathbf{i})} = c_+^{(\mathbf{v})}$	$Ri_0 \approx 9\alpha - 3$	0.5	H_N

Table 3: Summary of resonant GW-VW interactions.

GW-GW Interactions. The interaction between two internal waves gives rise to a TC instability, which is stationary relative to the background shear flow.

Interaction	**Interaction Condition**	$\|\mathbf{c_{in}}\|$	**Label**
$c_-^{(\mathbf{ii})} = c_+^{(\mathbf{v})}$	$Ri_0 \approx \alpha$	0	T

Table 4: Summary of resonant GW-GW interactions.

To recap, our setup admits 3 KH instabilities, 6 HW instabilities, and 1 TC instability; their corresponding Ri0-alpha conditions are shown in Figure 4.

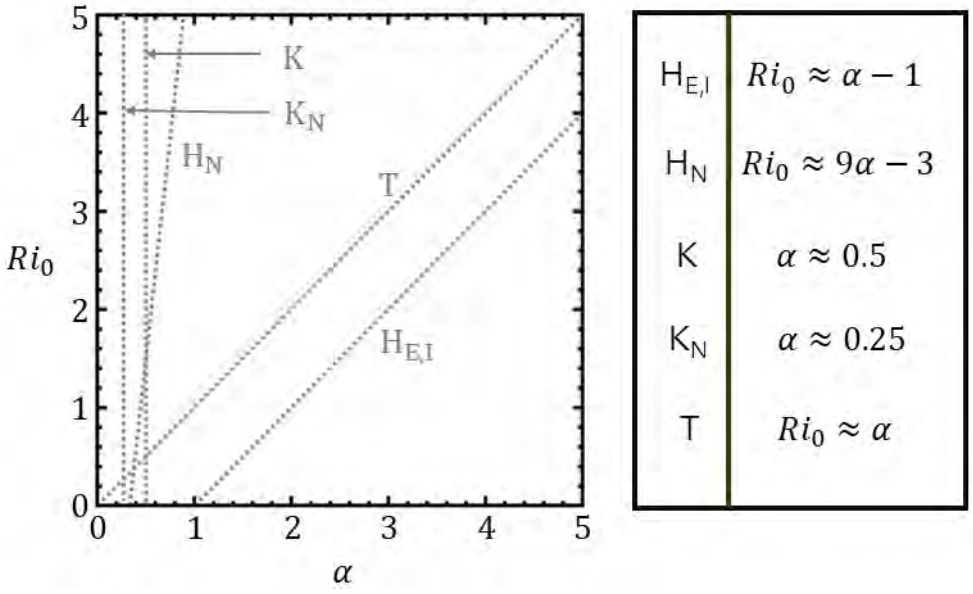

Figure 4: Conditions for sustainable wave-wave resonance on the Ri_0-α plane.

2.2 A dispersion relation for stacked stratified shear layers

The previous section focused on individual pairs of waves. Now we will follow the algorithm outlined in section 2.1.1 to derive a dispersion relation for normal mode perturbations to our basic configuration (5). Away from the interfaces (**i**)-(**vi**), defined in Table 1, we have $B_z = U_{zz} = 0$, which reduces the inviscid TGE (4) to

$$w_{zz} - k^2 w = 0, \tag{16}$$

a general solution to which can be defined inside each region, as summarized in Table 5. The unknown constants A_c–N_c must be determined by enforcing far-field boundedness, interfacial continuity, and interfacial jump conditions.

Region	**w(z)**
I	$A_c e^{\alpha z} + B_c e^{-\alpha z}$
II	$C_c e^{\alpha z} + D_c e^{-\alpha z}$
III	$E_c e^{\alpha z} + F_c e^{-\alpha z}$
IV	$G_c e^{\alpha z} + H_c e^{-\alpha z}$
V	$I_c e^{\alpha z} + J_c e^{-\alpha z}$
VI	$K_c e^{\alpha z} + L_c e^{-\alpha z}$
VII	$M_c e^{\alpha z} + N_c e^{-\alpha z}$

Table 5: General solution to the TGE in each region between two interfaces.

Far-field Boundedness. The function $w(z)$ has to remain bounded as $z \to \pm\infty$, which requires $A_c = N_c = 0$.

Interfacial Continuity of Vertical Velocity. The function $w(z)$ must remain continuous across each interface, which yields the equations in table 6.

Interface	Continuity Condition	Implication
(i)	$w(z \to H + 2_+) = w(z \to H + 2_-)$	$B_c - C_c e^{2\alpha(H+2)} - D_c = 0$
(ii)	$w(z \to H + 1_+) = w(z \to H + 1_-)$	$C_c e^{2\alpha(H+1)} + D_c - E_c e^{2\alpha(H+1)} - F_c = 0$
(iii)	$w(z \to H_+) = w(z \to H_-)$	$E_c e^{2\alpha H} + F_c - G_c e^{2\alpha H} - H_c = 0$
(iv)	$w(z \to -H_+) = w(z \to -H_-)$	$G_c + H_c e^{2\alpha H} - I_c - J_c e^{2\alpha H} = 0$
(v)	$w(z \to -H - 1_+) = w(z \to -H - 1_-)$	$I_c + J_c e^{2\alpha(H+1)} - K_c - L_c e^{2\alpha(H+1)} = 0$
(vi)	$w(z \to -H - 2_+) = w(z \to -H - 2_-)$	$K_c + L_c e^{2\alpha(H+2)} - M_c = 0$

Table 6: Application of continuity conditions at each interface to the general solutions summarized in table 5.

Interfacial Continuity of Pressure. The previous condition allowed for determination of six out of twelve unknowns. We require six more equations for a fully determined system. These are obtained by ensuring that the perturbation pressure remains continuous across each interface, as in section 2.1.1. We note here that the resulting jump condition on w_z can also be derived by integrating the TGE in the vicinity of a discontinuity. For a generic discontinuity at $z = z_j$ and this produces

$$\lim_{\varepsilon\to 0}\int_{z_j-\varepsilon}^{z_j+\varepsilon}\left\{\frac{d}{dz}\left[(U-c)\,w_z - U_z w + Ri_0\frac{B}{U-c}w\right] - Ri_0 B\frac{d}{dz}\left[\frac{w}{U-c}\right] - \alpha^2\,(U-c)\,w\right\}dz = 0,$$

which means that the jump across the interface

$$\lim_{\varepsilon\to 0}\phi(z)\big|_{z_j-\varepsilon}^{z_j+\varepsilon} = [[\phi]]_{z_j} \equiv \left[\left[(U-c)\,w_z - U_z w + Ri_0\frac{B}{U-c}w\right]\right]_{z_j} = 0. \tag{17}$$

Note that the second and third terms in the integral equation above vanish upon taking the limit $\varepsilon \to 0$ since they are continuous. Applying this jump condition to each interface yields a completely determined system of equations, from which a dispersion relation may be derived.

Dispersion Relation. The following substitutions are made for convenience:

$$\mathcal{E} \equiv e^{2\alpha H},\ \mathcal{E}_1 \equiv e^{2\alpha(H+1)},\ \mathcal{E}_2 \equiv e^{2\alpha(H+2)},\ \delta_\pm \equiv \alpha\,(2 \pm c)\,, \beta_\pm \equiv \alpha\,(1 \pm c)^2\,,\ \gamma \equiv \alpha c.$$

Then, we may summarize the results of these calculations as

$$\begin{aligned}
B_c - C_c\mathcal{E}_2 - D_c &= 0,\\
C_c\mathcal{E}_1 + D_c - E_c\mathcal{E}_1 - F_c &= 0,\\
E_c\mathcal{E} + F_c - G_c\mathcal{E} - H_c &= 0,\\
G_c + H_c\mathcal{E} - I_c - J_c\mathcal{E} &= 0,\\
I_c + J_c\mathcal{E}_1 - K_c - L_c\mathcal{E}_1 &= 0,\\
K_c + L_c\mathcal{E}_2 - M_c &= 0,\\
B\delta_- + C_c\mathcal{E}_2\left[\delta_- - 1\right] - D_c\left[\delta_- + 1\right] &= 0,\\
C_c\mathcal{E}_1\left[\beta_- + 2Ri_0\right] - D_c\left[\beta_- - 2Ri_0\right] - E_c\mathcal{E}_1\beta_- + F_c\beta_- &= 0,\\
E_c\mathcal{E}\left[\gamma + 1\right] - F_c\left[\gamma - 1\right] - G_c\mathcal{E}\gamma + H_c\gamma &= 0,\\
G_c\gamma - H_c\mathcal{E}\gamma - I_c\left[\gamma + 1\right] + J_c\mathcal{E}\left[\gamma - 1\right] &= 0,\\
I_c\beta_+ - J_c\mathcal{E}_1\beta_+ - K_c\left[\beta_+ - 2Ri_0\right] + L_c\mathcal{E}_1\left[\beta_+ + 2Ri_0\right] &= 0,\\
K_c\left[\delta_+ + 1\right] - L_c\mathcal{E}_2\left[\delta_+ - 1\right] - M_c\delta_+ &= 0,
\end{aligned} \tag{18}$$

or in matrix-vector notation as $\mathcal{A}\boldsymbol{c} = \boldsymbol{0}$, with $\boldsymbol{c} \equiv (B_c, C_c, \ldots, M_c)^T$ and $\mathcal{A}$ defined as the matrix of coefficients. The existence of non-trivial solutions to equation (18) requires that $\det\mathcal{A} = 0$. This yields a biquartic equation in c

$$\mathbb{P}\left(c\right) \equiv c^8 + A_6c^6 + A_4c^4 + A_2c^2 + A_0 = 0 \tag{19}$$

where A_0, A_2, A_4, and A_6 are functions of (α, Ri_0, H). We will analyze this dispersion relation in various limits.

2.3 Stability at zero separation

When $H = 0$, the basic configuration (5) reduces to a rescaled version of the $R - 1/2$ flow considered by Caulfield with doubled length scales, velocity and density variation [5], i.e.,

$$U(z) \equiv \begin{cases} 2, & z \in [2,\infty) \\ z, & z \in [-2,2] \\ -2, & z \in (-\infty,-2] \end{cases}, \quad B(z) \equiv \begin{cases} 2, & z \in (1,\infty) \\ 0, & z \in (-1,1) \\ -2, & z \in (-\infty,-1) \end{cases},$$

and the dispersion relation (19), upon division by c^2 (note that $A_0(H=0) = 0$), reduces to a bicubic polynomial

$$\mathbb{P}_1\left(c\right) \equiv c^6 + L_4c^4 + L_2c^2 + L_0 = 0. \tag{20}$$

where again L_4, L_2, and L_0 are coefficients depending on α and Ri_0. These correspond to the expressions presented in Ref. [5] after applying the transformation

$$c \equiv \tilde{c}/2, \quad \alpha \equiv \tilde{\alpha}/2$$

and noting that in the present problem, the ratio of density layer depth to shear layer depth (the variable denoted R in Ref. [5]) is fixed at 1/2. By way of verification, we attempt to reproduce some results obtained in Ref. [5].

2.3.1 Oscillatory instability boundaries

Transitions between neutrally stable waves and oscillatory instabilities are associated with the dispersion relation (20) having a pair of double roots[1] ($c = \pm m; m \in \mathbb{R}^+$). Being cubic in c^2, $\mathbb{P}_1(c)$ has a pair of double roots when $\mathbb{P}_1\left(c^2\right)$ has a double root, i.e., if and only if the cubic discriminant

$$\Delta_3(Ri_0, \alpha) \equiv \sum_{n=0}^{5} b_n Ri_0^n = 0, \tag{21}$$

where the coefficients $\{b_n\}$ are defined in Ref. [5]. The discriminant takes the form of a quintic polynomial in Ri for which closed form roots are in general not possible to find. In order to calculate stability boundaries, we find the roots numerically. It transpires that for sufficiently large α, four root branches $Ri_0 = Ri_0(\alpha)$ exist that are real and positive. These demarcate regions of instability on the $Ri_0 - \alpha$ plane. The fifth branch corresponds to negative values of Ri_0, which corresponds to unstable stratification, and so it is ignored. Note that this approach also captures transitions from an oscillatory instability to a stationary instability, which tend to occur for smaller values of α.

2.3.2 Stationary instability boundaries

Transitions marking the onset of stationary instabilities are associated with $c = 0$ being a double root of equation (20). This can happen if $L_0 \equiv A_2(H = 0) = 0$. Being a quadratic polynomial in Ri, L_0 has the roots

$$Ri_{0,\pm} = \frac{\alpha\left[(4\alpha - 1) \pm e^{-4\alpha}\right]}{\left[1 \mp e^{-2\alpha}\right]\left[(4\alpha - 1) + e^{-2\alpha}\right]}, \tag{22}$$

which is identical to the reference up to the transformation defined above. Further, note that upon taking the large-α limit, exponential terms decay faster than algebraic terms grow, leaving behind, at leading order

$$Ri_0 \sim \alpha,$$

which recovers the resonance-approximated stability boundary for the TC instability.

[1] That this has to be the case can be seen by realizing that there are a finite number of dynamics that can occur in the $Ri_0 - \alpha$ plane: neutrally stable waves ($c \in \mathbb{R}$), oscillatory instabilities ($c \in \mathbb{C}, \Re[c] \neq 0$), and stationary instabilities ($c \in \mathbb{C}, \Re[c] = 0$). Any (continuous) transition between neutrally stable waves and an instability requires the creation or destruction of imaginary parts of a complex conjugate pair. At the point of creation or destruction, it follows that the system needs to have two nondistinct real roots which eventually merge/separate into complex conjugate pairs.

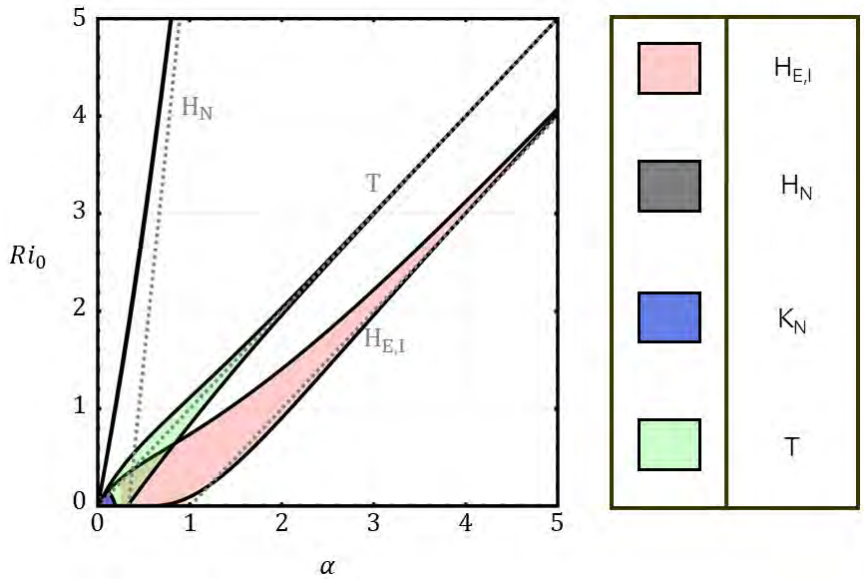

Figure 5: Invisicid stability boundaries (solid black curves) at zero separation. White regions represent neutrally stable waves, coloured regions represent instability. Dashed grey lines are the corresponding resonance approximations, which agree well with the actual stability boundaries at large α, as expected. The instability naming convention developed in section 2.1.4 is used here.

2.3.3 Stability diagram

Positive solutions to the equation (21) and the curves (22) partition the $Ri_0 - \alpha$ plane into regions of stability and various kinds of instability. These curves have been plotted in Figure 5. Solid lines are stability boundaries separating regions where the fastest growing perturbations represent neutrally stable waves (white) from those where the fastest growing perturbations represent various perturbations (coloured). The resonance approximation to each stability boundary has been plotted as a dashed line. These lines, among other things, enable identification of the linear instability mechanism (KHI, HWI, or TCI).

Pink and grey regions in Figure 5 have $\Delta_3 < 0$, meaning that $\mathbb{P}_1(c^2)$ has a complex conjugate pair of roots $c_R \pm ic_I$, and consequently $\mathbb{P}_1(c)$ has 4 roots of the form $\pm\sqrt{c_R \pm ic_I}$ – two complex conjugate pairs, out of which the two with positive c_I correspond to a HW instability. Everywhere else, meanwhile, corresponds to $\Delta_3 > 0$, meaning that $\mathbb{P}_1(c)$ has 6 roots given by $\pm\sqrt{c_{R,1,2,3}}$. These are born from the three real roots $c_{R,1,2,3}$ of $\mathbb{P}_1(c^2)$. In the event that one of these is negative, its square root would give rise to a conjugate imaginary pair, representing a stationary instability (the TC or KH instability). This is what occurs in the regions coloured green (TCI) and blue (KHI).

2.4 Stability at finite separation

We now investigate the effect of finite shear layer separation on the stability properties of the system. To begin, we revisit the dispersion relation (19).

Behaviour	**Criterion**	$\mathbb{P}\left(c^2\right)$ **Roots**
Neutrally Stable Waves	$\Delta_4 > 0$, $P_4 < 0$, and $D_4 < 0$	4 real distinct roots
Stationary Instability	$\Delta_4 < 0$	2 real, 2 imaginary roots
1 Oscillatory Instability	$\Delta_4 < 0$	2 real distinct, 2 c.c. roots
2 Oscillatory Instabilities	$\Delta_4 > 0$, and $P_4 > 0$, or $D_4 > 0$	2 c.c. root pairs

Table 7: Criteria for the segregation of the $Ri_0 - \alpha$ plane based on values of Δ_4 and the root determinants (23). The abbreviation c.c. refers to *complex conjugate*. Note that the criterion $\Delta_4 < 0$ is somewhat non-specific at this stage, being that it could mean either a stationary instability (if the real part of the complex conjugate root pair is zero) or a single oscillatory instability (if it is non-zero).

Being a quartic polynomial, $\mathbb{P}\left(c^2\right)$ has four roots[2], whose positions in the complex plane may be determined by studying the functions

$$\begin{aligned} P_4\left(Ri_0, \alpha, H\right) &= 8A_4 - 3A_6, \\ R_4\left(Ri_0, \alpha, H\right) &= A_6^3 - 8A_2 - 4A_6A_4, \\ \Delta_0\left(Ri_0, \alpha, H\right) &= A_4^2 - 3A_6A_2 + 12A_0, \\ D_4\left(Ri_0, \alpha, H\right) &= 64A_0 - 16A_4^2 + 16A_4A_6^2 - 16A_6A_2 - 3A_6^2, \end{aligned} \tag{23}$$

in addition to the quartic discriminant $\Delta_4\left(Ri_0, \alpha, H\right)$, which happens to be a tenth order polynomial in Ri_0. As before, stability boundaries are identified as values of $(Ri_0, \alpha; H)$ for which $\mathbb{P}\left(c^2\right)$ has a double root, i.e., when $\Delta_4 = 0$, which occurs, for fixed H and α, at ten values of Ri_0. Among them, only those which are positive real numbers are considered stability boundaries. Thus, upon solution of the equation $\Delta_4 = 0$ at a fixed H, the $Ri_0 - \alpha$ plane is segmented into multiple regions. Whether each region supports neutrally stable waves, stationary instabilities, or (one or two) oscillatory instabilities[3] is determined by examination of the values of Δ_4 and the root determinants (23) in that region. The criteria are presented in Table 7 below. Determination of instability type (KHI, interior/exterior HWI, TCI) may be made by reference to the resonance approximation (see Figure 4), or by solving the biquartic equation (19).

2.4.1 Structure of the $\mathbf{Ri_0} - \alpha$ plane, $\mathbf{H = 1}$

We apply the procedures outlined above to equation (19), fixing $H = 1$, an intermediate value chosen with the expectation that the interfaces will be neither so far apart as to exert no influence on each other, nor so close together as to render the resonance approximation results invalid. Stability boundaries are found by solving $\Delta_4 = 0$ numerically for a range of wavenumbers, and perturbation characteristics (growth rate and phase speed) are obtained by solving $\mathbb{P}\left(c^2\right) = 0$. Using these in conjunction with the criteria listed in Table 7 and the resonance approximation results (Figure 4), we produce the stability and growth rate diagrams in Figures 6 and 7.

[2]The square roots of which constitute the eight roots of the biquartic polynomial $\mathbb{P}\left(c\right)$.

[3]The possibility for two oscillatory instabilities arises due to the fact that a quartic polynomial can have two complex conjugate root pairs.

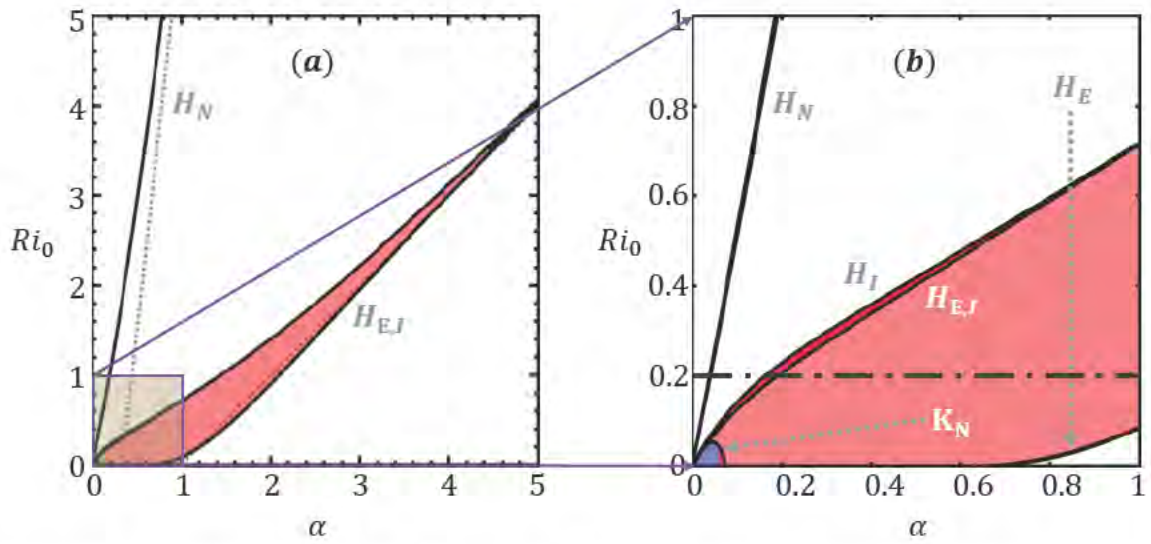

Figure 6: Stability diagram for $H = 1$. **Panel (a),** a plot demarcating regions of linear stability (white) and instability (coloured) in the $Ri_0 - \alpha$ plane. The unstable regions appear to be similar to those in Figure 5, save for the absence of the TC-unstable region, and a vastly reduced KH-unstable region. **Panel (b),** magnification of the former, showing that the HW-unstable region is actually composed of two overlapping 'leaves'. The top (deep red) is unstable only to the interior HWI, the large middle region (pink) is unstable to both interior and exterior HWIs, and a narrow, practically invisible, region at the bottom is unstable only to the exterior HWI. In addition, a small non-local KH-unstable region (blue) is active at small α and Ri_0. The local KH instabilities are absent.

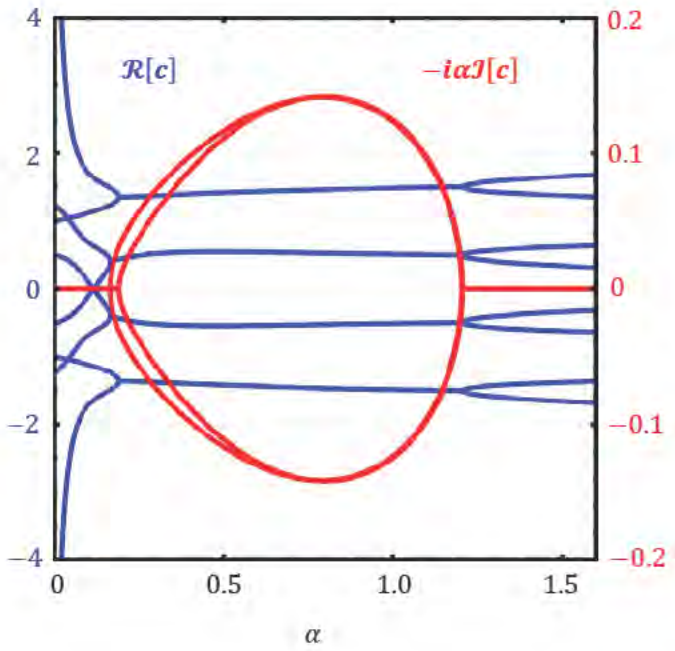

Figure 7: Solutions to the biquartic equation (19), i.e., eigenvalues of the inviscid TGE (4), with $H = 1$ and $Ri_0 = 0.2$ (marked by the dash-dot line in Figure 6). The perturbation growth rate, related to the imaginary part of c, is coloured red and should be read off the right axis. The phase speed is coloured blue and should be read off the left axis. Going from left to right along the abcissa, we see the onset of the interior HWI (identified by its large-α phase speed of 0.5), then the onset of exterior HWI (phase speed 1.5), their coexistence, and finally their suppression.

The stability diagram (Figure 6) provides a high-level overview of our system's response to small perturbations in parameter space. Overall, it looks very much like the zero separation stability diagram (Figure 5), save for a few important departures.

1. Unlike the case when $H = 0$, no region of the $\mathrm{Ri}_0 - \alpha$ plane exhibits TCI-type instability when $H = 1$, or indeed for any nonzero value of H, however small. This is due to the reappearance of the coefficient A_0 in the biquartic dispersion relation (19), which vanishes only when $H = 0$. Recall that stationary instability boundaries were previously identified by locating curves in parameter space along which the characteristic polynomial (20) admitted a double root at $c = 0$. A sufficient condition for this to occur was $L_0\left(Ri_0, \alpha\right) = 0$. For $H \neq 0$, the condition $A_0(\mathrm{Ri}_0, \alpha, H) = 0$ remains sufficient for $\mathbb{P}(c^2)$ to possess such a root. Although A_0, like L_0, is quadratic in Ri_0, its two roots coalesce into a double root given by

$$\mathrm{Ri}_0 = \frac{\alpha\left(1 - e^{4\alpha} + 4\alpha e^{4\alpha}\right)}{\left(e^{2\alpha} - 1\right)\left(1 - e^{2\alpha} + 4\alpha e^{2\alpha}\right)},$$

   which defines a single curve in the $\mathrm{Ri}_0 - \alpha$ plane rather than the bounded region found in the $H = 0$ case. Moreover, the expression above is independent of H, confirming that the TC-unstable region does not re-emerge for any finite value of H.

2. Although at first glance it appears as though no changes have occurred in the HW-unstable region (Figure 6a), closer examination reveals that this region has foliated into two overlapping leaves (see Figure 6b) composed of

   (a) a small lobe which is unstable only to to interior Holmboe waves (coloured deep red in Figure 6b),

   (b) a large middle lobe (coloured pink) which is unstable to both interior and exterior Holmboe waves, and,

   (c) a very narrow lobe (invisible in Figure 6) which is unstable only to exterior Holmboe waves.

   We see how these transitions between the two kinds of HWIs occur by computing eigenvalues of the inviscid TGE (4) at $Ri_0 = 0.2$ (marked by the dash-dot line in Figure 6b, eigenvalues plotted in Figure 7). Very large wavelength (very small α) perturbations excite neutrally stable waves. As perturbation wavelength is decreased, unstable interior Holmboe waves are excited. A further decrease in wavelength prompts the excitation of unstable exterior Holmboe waves, which initially have a lower growth rate than interior waves. However, as wavelength is decreased even further, exterior HW modes grow faster relative to interior HW modes. For very small wavelengths (large α), both interior and exterior HW modes are suppressed, although the former are suppressed earlier (i.e., for larger wavelengths relative to the latter).

In sum, for $H = 1$, the TCI is never excited, and two different types of HWI, distinguished by their large-α phase speeds (or equivalently, by the interfaces which interact to drive them), are seen. The interior HWI is dominant for larger wavelengths than the exterior HWI. We expect these disparities to become more pronounced as $H \to 0$ and the stacked layers exert a greater influence on each other.

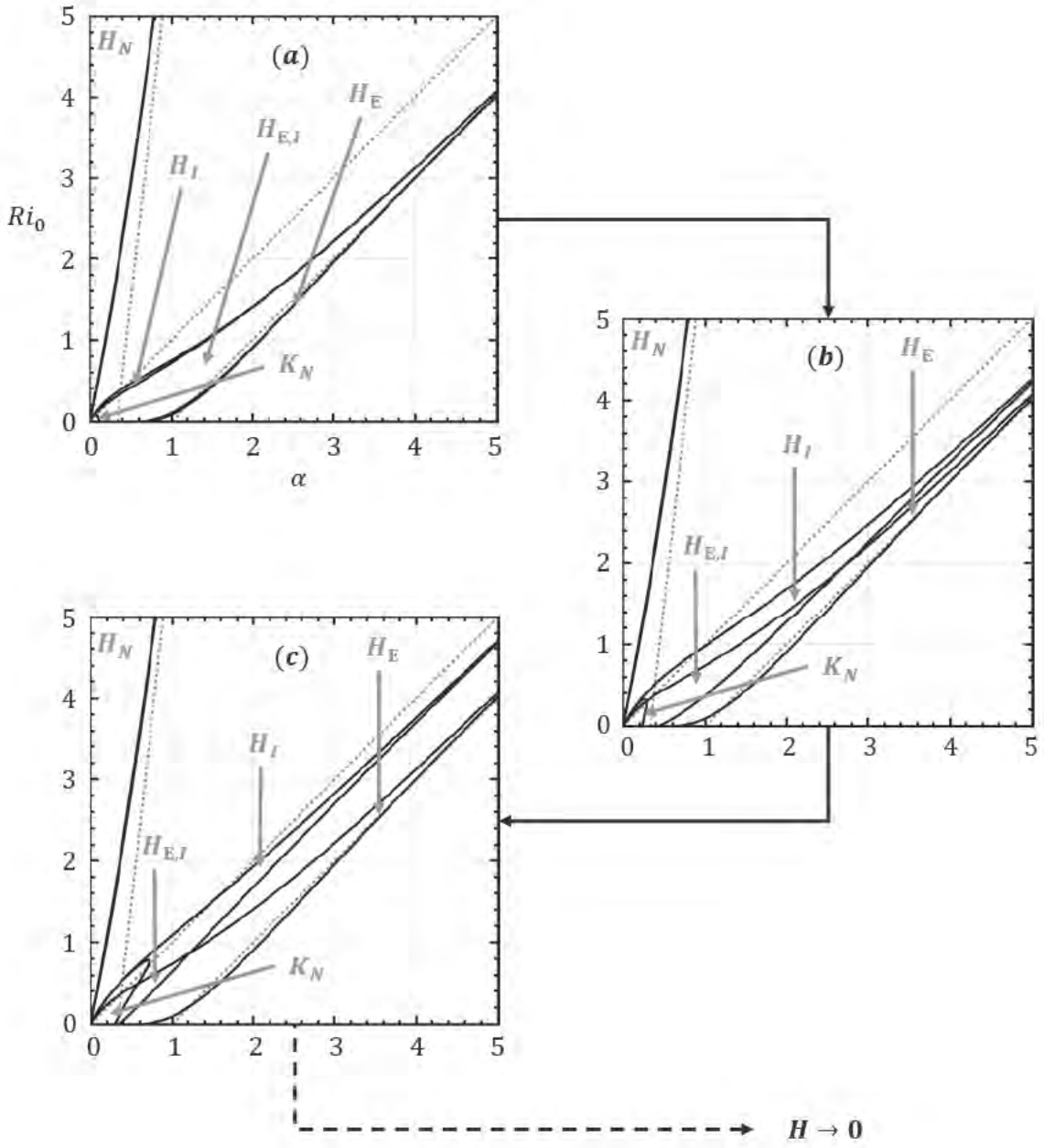

Figure 8: A sequence of three stability diagrams computed with (a) $H = 0.5$, (b) $H = 0.05$, and (c) $H = 0.005$. Each unstable region is labelled by instability type (see section 2.1.4 for the naming convention). Two features are noteworthy. As H decreases, interior and exterior HW-unstable lobes separate, reducing the size of the overlapping region. Further, the non-local KH-unstable region grows in size and seems set to merge with the interior HW-unstable region for very small values of H, thus birthing the TC-unstable region when $H = 0$.

2.4.2 Unstable regions in the zero separation limit

Having identified and demarcated instability regions for $H = 1$ and $H = 0$, we now examine the transition from the former to the latter. Stability diagrams at successively smaller values of H, viz. $H = 0.5$, 0.05, and 0.005, are provided in Figure 8. From these, we may see that as $H \to 0$:

1. The interior and exterior HW-unstable lobes fan out further, as expected, reducing the size of the overlapping region where they are both active.

2. The (non-local) KH-unstable region grows in size, a phenomenon which may be understood by recalling that the associated KH instability occurs due to the interaction of vorticity waves on the top-most and bottom-most shear interfaces. These interfaces are drawn closer in the zero separation limit and, therefore, interact more strongly for a larger range of α and Ri_0. Moreover, for very small values of H, this region appears to merge with the interior HW-unstable region, thus producing the TC-unstable region when $H = 0$.

3. The local KHI do not appear in any of these stability diagrams. Their suppression likely has to do with proximity-based interactions between vorticity waves on the interior shear interface and requires further investigation. At this stage we merely conjecture that they appear only for large H.

2.5 Summary

In this section, we employed piecewise-linear approximations of $U(z)$ and $B(z)$ (5) and solved the inviscid Taylor-Goldstein equation (4) analytically, ultimately obtaining a biquartic characteristic polynomial (19), the roots of which encoded temporal attributes (growth rate, phase speed) of small perturbations to our setup. We then tracked these roots across (Ri_0, α, H) in order to chart the temporal behaviour (decay, exponential growth) of these perturbations in parameter space. Our survey of the inviscid linear problem highlights three new behaviours relative to the zero separation case of Caulfield [5]. First, any finite separation ($H > 0$) cleaves the HW-unstable band into distinct *interior* and *exterior* HW-unstable lobes distinguished by their large-α phase speeds. The interior HWI is dominant for smaller wavenumbers than the exterior HWI, although there always is a range of wavenumbers for which they both coexist (see Figures 6 and 7). Second, once $H > 0$ the constant coefficient A_0 in the dispersion polynomial (19) re-appears, erasing the TC-unstable region altogether. Third, as the vertical gap between stratified shear layers narrows, the interior and exterior HW lobes fan out, and the KH-unstable region swells in size, ultimately fusing with the interior HW lobe and resurrecting the TC instability at zero separation (see Figure 8). These results demonstrate that even modest layer separation reorganizes the instability landscape and changes the character of the classic HW instability.

Going forward, we will incorporate viscosity and diffusivity to determine how finite Re and Pr reshape or modify the inviscid stability diagrams, and perform fully nonlinear DNS to track how interior and exterior HW modes evolve once they have grown to finite amplitude, restricting attention initially to the intermediate values of H, viz. $H = 1, 0.5$.

3 Viscous Linear Theory

We now reintroduce the diffusion of momentum and buoyancy into the governing equations. This necessarily precludes sharp shear and buoyancy interfaces, so we return to the diffuse-interface configuration given by equations (3) and represented schematically in the right panel of Figure 1. The linearization procedure described in the previous section now yields the viscous Taylor-Goldstein Equations

$$\begin{aligned}(\sigma + i\alpha U)\,\nabla^2\hat{w} - i\alpha U_{zz}\hat{w} &= -Ri_0\alpha^2\hat{b} + Re^{-1}\nabla^4\hat{w},\\ (\sigma + i\alpha U)\,\hat{b} + B_z\hat{w} &= (PrRe)^{-1}\,\nabla^2\hat{b},\end{aligned} \tag{24}$$

a generalized eigenvalue problem where $\sigma = -i\alpha c$ is the complex eigenvalue whose *real part* provides the growth rate of the perturbation eigenfunction $\left[\hat{w}(z),\ \hat{b}(z)\right]^T$, and the differential operator ∇ is (re)defined $\nabla \equiv [i\alpha,\ d_z]^T$. We solve this eigenvalue problem numerically using open-source code developed by W.D. Smyth and colleagues [13]. This code utilizes a Fourier-Galerkin discretization and a QR factorization encoded in MATLAB's `eig()` function.

We choose $Re = 10^4$ and $Pr = 1$ to simulate a fluid relatively weakly affected by momentum and buoyancy diffusion, $L_z = 20$ is chosen so that the vertical boundaries are far away from the interfaces, $R = 6$ ensures that the buoyancy interface is much sharper than the shear interface (which is conducive to the HW instability), and finally H takes values of 0.5, 1, and ∞. With these parameters, the number of vertical gridpoints required for the eigenvalues to converge is 1024.

The generalized eigenvalue problem is solved for a range of wavenumbers. At each one, the numerical solution consists of 1024 eigenvalues and as many eigenfunctions, ranked by growth rate. In what follows, we will adopt the convention $\hat{\phi}_{j,2\alpha}$, where $\hat{\phi}\,(z)$ is some eigenfunction and $j \in \mathbb{Z}^+$ is the mode index. Note that the streamwise wavenumber of the perturbation is represented by 2α instead of α so as to avoid decimal points in the subscript. First, results from the $H = \infty$ case will be presented, followed by the $H = 1$ and $H = 0.5$ cases.

3.1 H = ∞, pure Holmboe waves

The $H = \infty$ label represents calculations with a modified basic state consisting of just one stratified shear layer – i.e., the classical HWI setup – intended to validate the solver and, more importantly, provide a comparative baseline for the $H = 0.5$ and $H = 1$ calculations. The modification is implemented by setting $H = 1$ in our basic state (3) and then excising the stratified shear layer at the bottom. This leaves us with a single stratified shear layer whose buoyancy interface is centered at $z = 2$. This is presented schematically in Figure 9a. The other three panels of the figure contain selected results from the stability calculation.

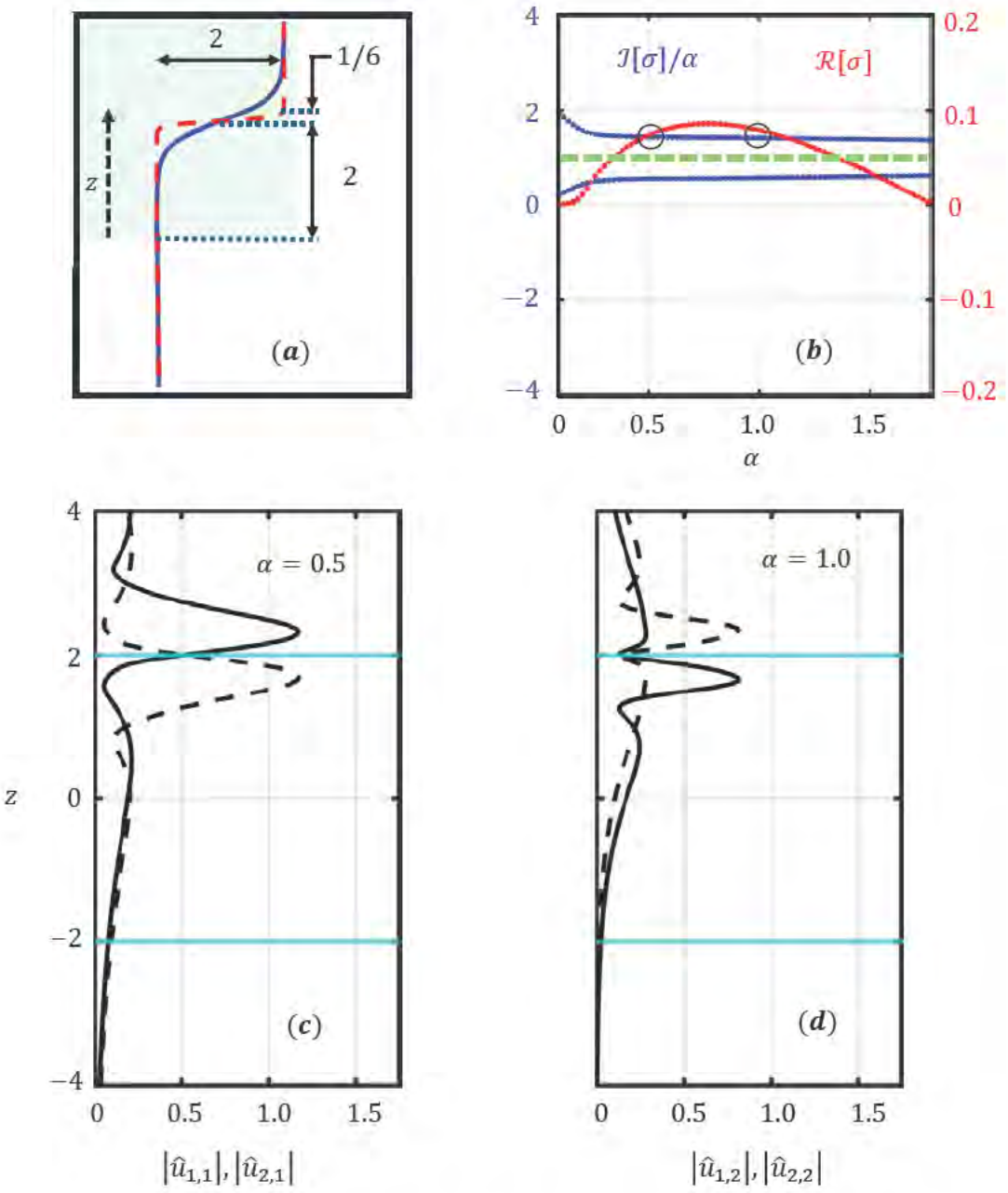

Figure 9: Linear stability results for a single stratified shear layer ($H = \infty$). **Panel (a),** schematic of the basic state $U(z)$, $B(z)$ using the colour convention adopted in Figure 1. **Panel (b),** (complex conjugate) eigenvalues of the top two fastest growing modes computed at $Ri_0 = 0.2$. Blue curves (left axis) represent phase speed, and the two coincident red curves (right axis) represent growth rate. The dashed green line represents the streamwise velocity at the buoyancy interface $z = 2$. The circles mark wavenumbers $\alpha = 0.5$ and $\alpha = 1$, for which streamwise velocity mode amplitudes are plotted in **Panels (c)** and **(d)**, respectively. Note that in this case alone, the different line-types (solid and dashed) are meant only to aid in distinction between the plotted eigenmodes and carry no additional meaning.

Figure 9b contains (complex conjugate) eigenvalues associated with the top two fastest growing modes for $\alpha \in [0, 1.7]$ and $Ri_0 = 0.2$. The blue curves represent their phase speeds, which are measured on the left axis; and the red curves represent their growth rates, which are measured on the right axis. The dashed green line should be read off the left axis and represents the basic state velocity $U = 1$ at the buoyancy interface. The circles mark wavenumbers $\alpha = 0.5$ and $\alpha = 1$ for which growth rates are nearly (though not quite) equal.

The vertical structures of the first two streamwise velocity modes with $\alpha = 0.5$ (i.e., modes $\hat{u}_{1,1}$ and $\hat{u}_{2,1}$, following our naming convention) are plotted in Figure 9c. Similarly modes $\hat{u}_{1,2}$ and $\hat{u}_{2,2}$ are plotted in 9d. Note that in each case, one mode has an amplitude peak below the buoyancy interface ($z = 2$), and the other has a peak above the interface. The former has a large-α phase speed of 0.5, whereas the latter has 1.5. This is the criterion that we previously used to distinguish interior HW modes from exterior HW modes; however, for a single stratified shear layer, the distinction is meaningless since both of these modes have the same growth rate.

3.2 $\mathbf{H \neq \infty}$, stacked Holmboe waves

Solutions to the viscous TGE obtained at $H = 1$ and $H = 0.5$ are characterized in Figure 10. For each H, $Ri_0 - \alpha$ growth rate contours are plotted on the left, and eigenvalues associated with the first six fastest growing modes are plotted on the right. Streamwise velocity eigenfunctions are provided in Figure 11. We outline a few observations below.

1. At least for the parameters considered, there is no evidence for a TC-unstable region.
2. As in the inviscid case, two distinct, disparately growing branches of HWI (interior and exterior) emerge, distinguished by their large-α phase speeds (Figures 11b,d). The disparity in growth rates is more pronounced at smaller values of H.
3. Interior HW modes grow faster at smaller α than exterior HW modes, and the converse is true at larger α, as indicated by the dashed blue separatrices in Figures 10a,c. However, in addition to suppressing growth rates, the reintroduction of diffusion has also broadened both interior and exterior HWI bands, thereby rendering the region of overlap (where both interior and exterior HW modes are growing) larger. Indeed, at $Ri_0 = 0.2$ and $H = 1$ (Figure 11b) there is no α for which only one HW mode is growing, and at $H = 0.5$ (Figure 11d), there is only a very small interval near $\alpha = 0$ where interior HW modes alone grow.
4. The zero phase speed non-local KHI (denoted K_N) is fully suppressed at $H = 1$ but reappears at $H = 0.5$ at very low wavenumber. As in the inviscid case, the local KHI is absent.
5. Finally, as the naming convention suggests, interior HWI streamwise velocity modes have an amplitude peak interior to the buoyancy interface on which they occur. Likewise, the corresponding exterior HWI modes have a peak exterior to their buoyancy interface (see Figure 11).

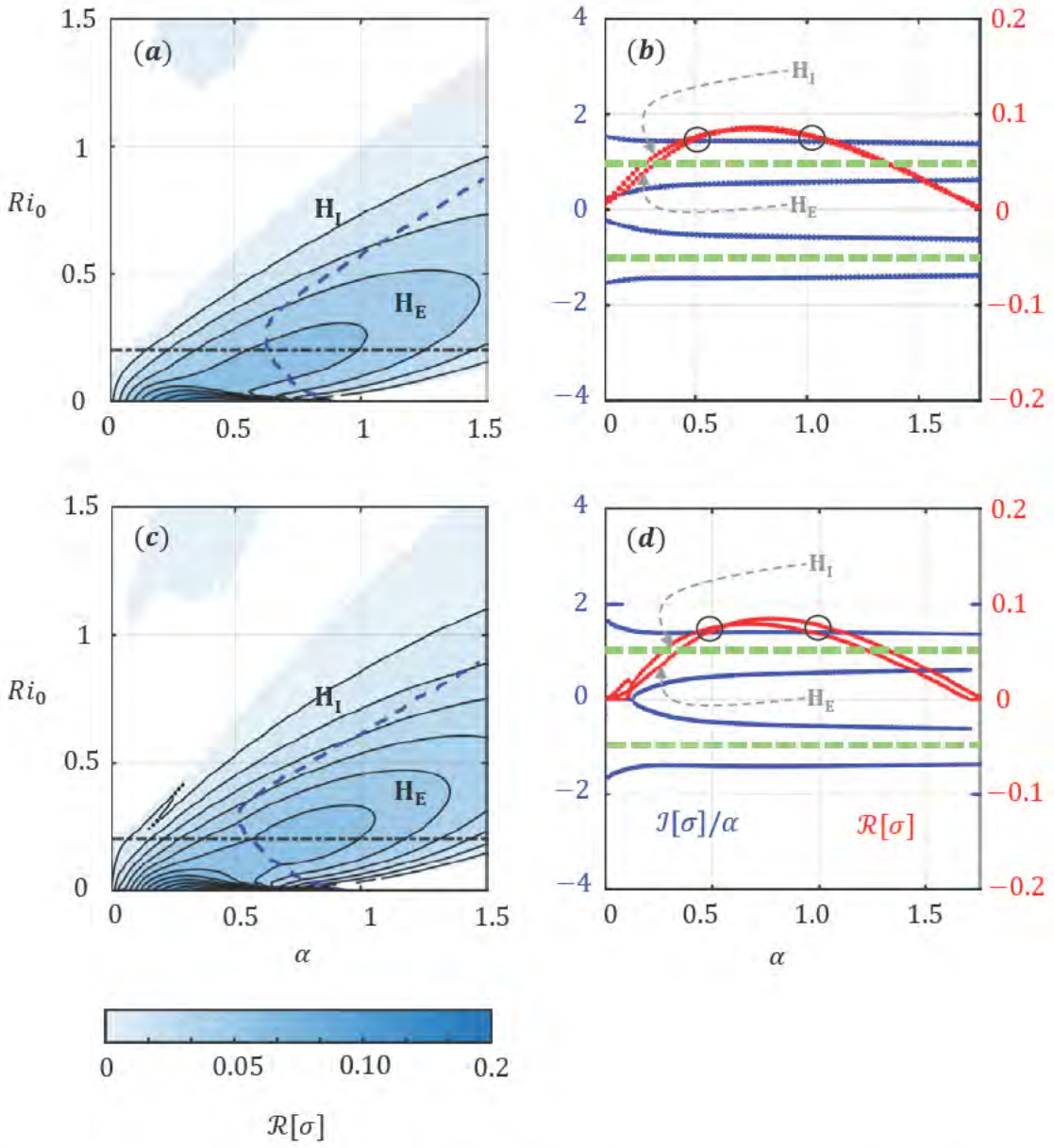

Figure 10: Solutions of the viscous TGE for $H = 1$ (top row) and $H = 0.5$ (bottom row). Growth rate contours in the $Ri_0 - \alpha$ plane are provided in **panels (a)** and **(c)**. The white regions have $\mathcal{R}[\sigma] < 10^{-3}$. The dashed blue curves separate interior HW-dominant regions from exterior HW-dominant ones, and the dash-dotted black line marks $Ri_0 = 0.2$, for which eigenvalues of the top six fastest growing modes have been plotted in **panels (b)** and **(d)**. Colour and annotation conventions for these are the same as in Figure 9b, except that base state speeds at both the top and bottom buoyancy interfaces have been marked by dashed green lines.

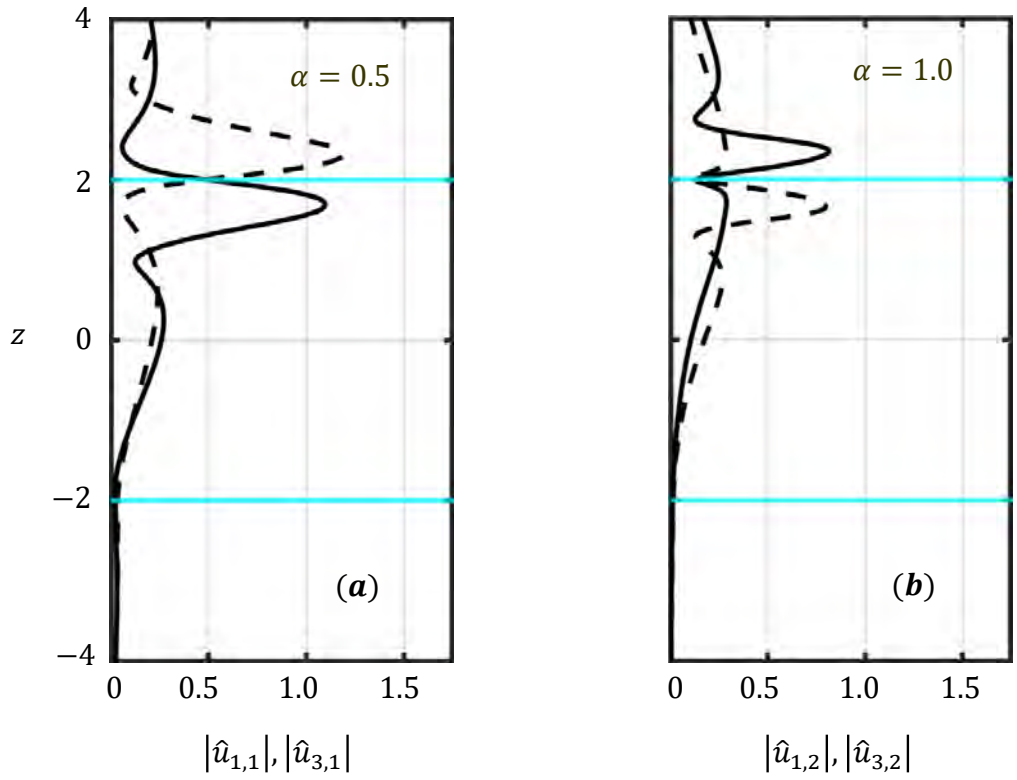

Figure 11: Streamwise velocity mode amplitudes at $H = 1$, and $Ri_0 = 0.2$. The modes in **panel (a)** have wavenumber $\alpha = 0.5$ and those in **panel (b)** have wavenumber $\alpha = 1$, corresponding to the circles in Figure 10b. In each case, interface locations $z = \pm 1$ have been marked with a cyan line, and amplitudes of the first and third ranked eigenmodes – $\hat{u}_{1,2\alpha}$ and $\hat{u}_{3,2\alpha}$ – have been plotted. The second and fourth ranked ones, being reflections of these about $z = 0$, have been omitted. Note that here, the line-type does carry an additional meaning (cf. Figure 9c, d). Solid black curves represent dominant eigenmodes (i.e., those that grow faster) and dashed black curves represent subdominant ones. At $\alpha = 0.5$, the interior HWI is dominant and the exterior HWI is subdominant, whereas the exterior HWI is dominant at $\alpha = 1$.

3.3 Summary

As might be expected, the primary effect of viscosity is to diminish interior and exterior HW mode growth rates and broaden their instability bands in the $Ri_0 - \alpha$ plane. Other features observed from our inviscid linear stability calculations, i.e., the absence of a TC-unstable region, the presence of a KH-unstable region at very small α persist (the latter with similar diffusive modifications). Through our calculations, we have identified perturbation wavenumbers $\alpha = 0.5,\ 1$ for which different types of HW instabilities are dominant and parameter values ($Ri_0 = 0.2$) where they have similar growth rates. These results will inform numerical simulations of the governing equations (2), utilized to study the finite-amplitude evolution of interior and exterior HW instabilities.

4 Finite Amplitude Evolution of Stacked Holmboe Waves

We would now like to understand the evolution of stacked HW instabilities beyond the exponential growth regime (i.e., once they have attained finite amplitude). In particular, we are interested in differences from the pure HW case. Our study consists of six direct numerical simulations of the 2D Boussinesq equations (2). These are summarized in Table 8, below.

Group	**Label**	α_0	**Dominant HWI Type**
Pure HWI **(P)** $H = \infty$	I	0.5	Interior/Exterior
	E	1	Interior/Exterior
Stacked HWI **(SA)** $H = 1$	I	0.5	Interior
	E	1	Exterior
Stacked HWI **(SB)** $H = 0.5$	I	0.5	Interior
	E	1	Exterior

Table 8: Simulation plan for our investigation into the finite-amplitude evolution of stacked Holmboe waves. Group P (pure HW) simulations provide a comparative baseline (i.e., they constitute a control group). The parameter α_0, listed for each simulation in the third column, is the streamwise wavenumber of the initial perturbation. The simulation label reflects the dominant HW type at the wavenumber α_0, except for group P, where, as discussed in section 3.1, there is no growth rate disparity (and hence no meaningful distinction) between the interior and exterior HW mode.

Physical and numerical parameters chosen for our simulations are summarized in Table 9 below.

$\mathbf{Re}$	$\mathbf{Pr}$	$\mathbf{H}$	$\mathbf{R}$	$\mathbf{Ri_0}$	$\boldsymbol{\alpha_0}$	$\mathbf{L_x \times L_z}$	$\mathbf{N_x \times N_z}$
10^4	1	0.5, 1, ∞	6	0.2	0.5, 1	$4\pi \times 20$	512^2

Table 9: Parameter values for DNS of the 2D Boussinesq equations.

All physical parameters remain the same between the previous section and this one. The only addition is $Ri_0 = 0.2$, chosen to leverage the dominance (in terms of growth rate) of different HWI types at two different wavenumbers (0.5 and 1) related by an integer factor (see section 3.2). Recall that despite the difference in dominant HWI types, the excited modes have nearly equal growth rates.

To solve the governing equations, we utilize a pseudospectral method with Fourier-Chebyshev spatial discretization and time-marching using a Semi-Implicit Backward Difference Formula. The computational domain is chosen to be 4π units long in order to accommodate perturbations of wavenumber 0.5 (one wavelength) and 1 (two wavelengths). We use 512 gridpoints in each direction, and our simulations appear to remain resolved up to around 65 time units (as judged by the visual absence of numerical artifacts in simulated primitive variables), which covers a few cycles of the nonlinear regime. Admittedly, the chosen

resolution is not sufficient to resolve fine features that appear late into the simulations. Nevertheless, it was judged to be resource-efficient for the preliminary exploration presented here. This is a limitation of the study in its current stage, and will be addressed as it progresses (see section 5). For now, we note that the discussion in this section covers only the early nonlinear evolution of HW instabilities and that the preliminary results presented here should be subject to verification via higher-resolution computations.

Our discretization enables the implementation of periodic boundary conditions in the streamwise direction and the appropriate Dirichlet boundary conditions in the vertical direction. We use the Dedalus [2] framework to implement our solvers and run simulations on UNH computing clusters Premise and Plasma.

Stacked HW simulations (groups SA and SB) are initialized with the basic state (3) and a small monochromatic perturbation composed of the four fastest growing eigenmodes a single wavenumber α_0. For example, the generic state variable $\phi(x, z, t)$ with basic state $\Phi(z)$ is initialized

$$\phi_{SH}(x, z, 0) = \Phi(z) + 0.01 \sum_{n=1}^{4} \hat{\phi}_{n,2\alpha_0}(z) \exp\left(i \frac{4\pi\alpha_0}{L_x} x\right) + \text{c.c.}, \tag{25}$$

where, in accordance with linear stability results, we consider $\alpha_0 = 1$ and 0.5. To reiterate, in the former case, the dominant mode is an interior HWI, and in the latter case, an exterior HWI. The initial perturbations (25) for groups SA and SB contain the dominant complex conjugate pair (e.g. the interior HW modes for SA-I) as well as the subdominant one (the exterior HW modes). The subdominant HW mode pair is included since, for the parameters chosen, its growth rate is not very small compared to the dominant pair (see Figures 10b, d). In contrast Pure HW simulations (group P) use an initial perturbation composed only of the two fastest growing eigenmodes, i.e.,

$$\phi_{PH}(x, z, 0) = \Phi(z) + 0.01 \sum_{n=1}^{2} \hat{\phi}_{n,2\alpha_0}(z) \exp\left(i \frac{4\pi\alpha_0}{L_x} x\right) + \text{c.c.} \tag{26}$$

The amplitude 0.01 renders the perturbation peak value $O(0.01)$, ensuring that it is small enough for linear theory to apply. In our simulations, we track the volume-averaged perturbation kinetic energy and verify that the growth rate and phase speed of initial perturbations match that predicted by linear theory. Moreover, linear growth appears to hold for 30 – 40 time units. In what follows, we will first cover the linear growth phase of Holmboe waves (pure and stacked) and then describe the early-stage nonlinear evolution of stacked HWIs qualitatively, comparing and contrasting with the pure HWI. In both phases of development, we will attempt to diagnose and quantify the interaction of stacked HWs relative to pure HWs.

4.1 Linear growth and early-time interaction of Holmboe waves

Much of the terminology and diagnostics used in this and subsequent sections comes from the work of Smyth et al. [15]. Our simulations (especially in group P) are qualitatively comparable to the 'moderate stratification simulations' described in Ref. [15]. Holmboe

waves (both pure and stacked) occur in counterpropagating pairs on each side of a buoyancy interface. In our set-up the wave on top of the interface travels rightward, and the wave at the bottom travels leftward. These waves impart onto the central buoyancy interface a sinusoidal deformation (see Figures 12b, e), pushing heavier (less buoyant) fluid above the interface and pulling lighter (more buoyant) fluid below it. This allows us to identify the streamwise position of a Holmboe wave 'crest' at a particular depth with the point at a depth where buoyancy is minimized (if above the interface) or maximized (if below the interface). In other words, buoyancy extrema at a fixed value of z can be used as a proxy for the location of the Holmboe wave crest [15].

Note, however, that the identification of buoyancy extrema with HW crests does not hold

(a) very far from the interface, due to the localization of Holmboe waves, and

(b) beyond the linear growth phase, as nonlinear effects can lead to the destruction of extant buoyancy extrema as well as the creation of new ones that have nothing to do with HW crests.

HWI evolution is characterized by the regular crossing and interaction of waves on either side of the buoyancy interface. At the instant where HW crests have zero horizontal separation, the central buoyancy interface becomes completely flat (see Figures 12c, f) and HW speeds (relative to the mean flow) are maximized [15]. A natural question, at this point, is whether stacking Holmboe waves has any effect whatsoever on their crossing speeds.

Therefore, we track HW crests (i.e., buoyancy extrema) in all our simulations at selected depths on either side of the top buoyancy interface for 30 time units, as shown in Figure 12. Our results confirm that wave speeds (for both pure and stacked Holmboe waves) are minimum when wave crests on either side are far apart, increase as they cross each other, and are maximized at the instant of zero horizontal separation. Stacking effects appear to be slight for the parameters we have chosen; nevertheless, we observe that

1. the maximum absolute speed of Holmboe waves below the interface increases with decreasing H – i.e., it is the same as the maximum absolute speed above the interface when $H = \infty$, very slightly higher when $H = 1$, and even higher when $H = 0.5$.

2. Further, this effect is more pronounced when the interior HW modes are dominant (i.e., for $\alpha_0 = 0.5$), than when they are subdominant ($\alpha_0 = 1$).

In sum, stacking enables cross-layer HW interaction, i.e., interaction between Holmboe waves on different buoyancy interfaces. The effects, though slight, are observed to be stronger on waves below the top buoyancy interface – likely due to proximity with their counterparts atop the bottom buoyancy interface – and on interior HW modes ($\alpha = 0.05$). We now proceed to discuss the nonlinear regime of evolution.

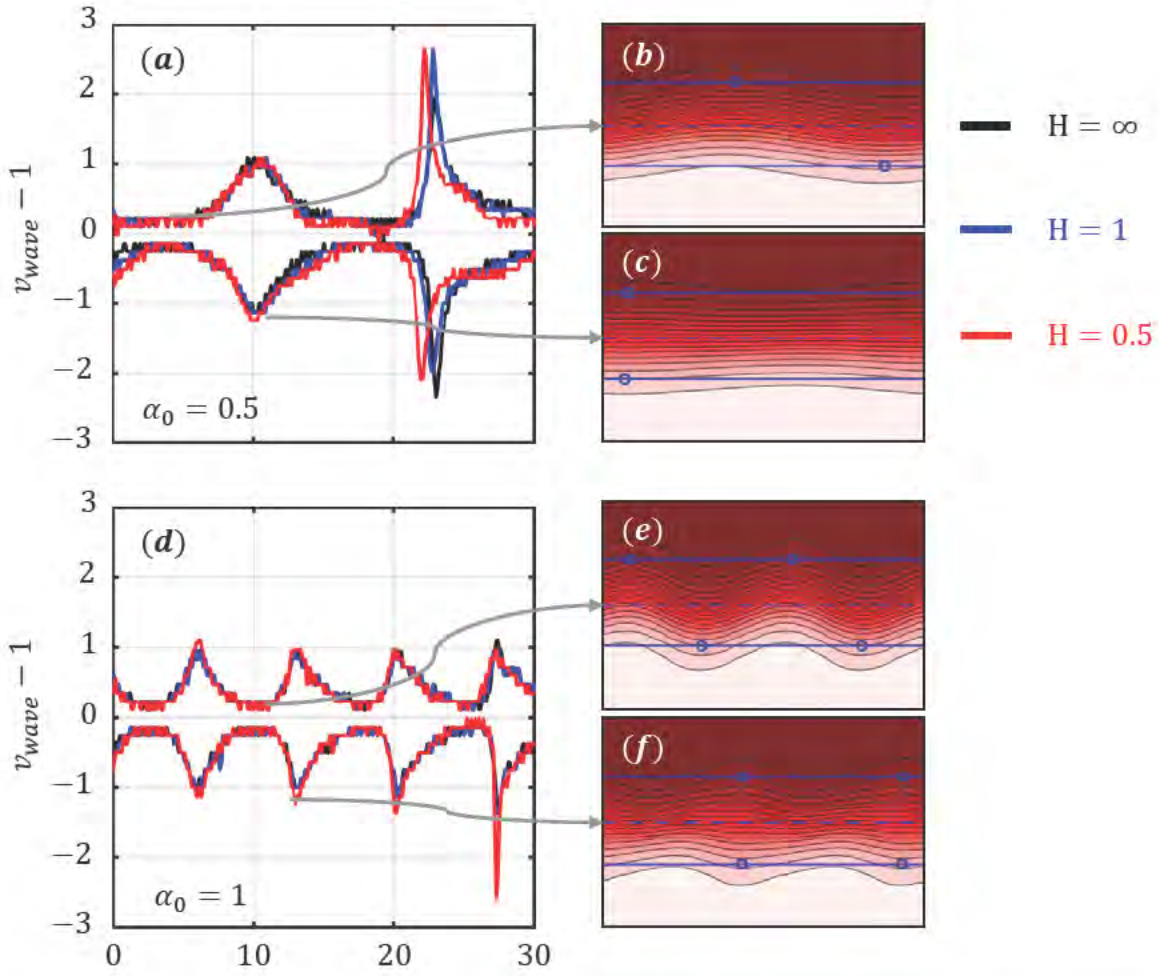

Figure 12: Early time HW speeds relative to the speed of the base flow at the top buoyancy interface. Results from simulations PI, SAI, and SBI are presented in **panels (a) – (c)**; and results from simulations PE, SAE, and SBE are presented in **panels (d) – (f)**. In each of these panels, black is used for group P, blue for group SA, and red for group SB simulations. The curves on top in each panel refer to Holmboe waves above the buoyancy interface, and the curves at the bottom refer to Holmboe waves below it. The smaller panels (b), (c), (e), and (f) contain representative buoyancy contours in the region $[0,\ 4\pi) \times [1.5,\ 2.5]$ for simulations SAI (b, c) and SAE (e, f). These panels also have dashed blue lines indicating the depth of the buoyancy interface ($z = 1$), blue circles marking the positions of HW crests (i.e., buoyancy extrema) at a chosen depth, indicated by solid blue lines. The panels (b,e) show maximally separated HW crests, where wave speeds are at a minimum, and buoyancy contours have a sinusoidal envelope. The panels (c, f), meanwhile, depict crossing HW crests, where wave speeds are maximized, and buoyancy contours have a varicose envelope.

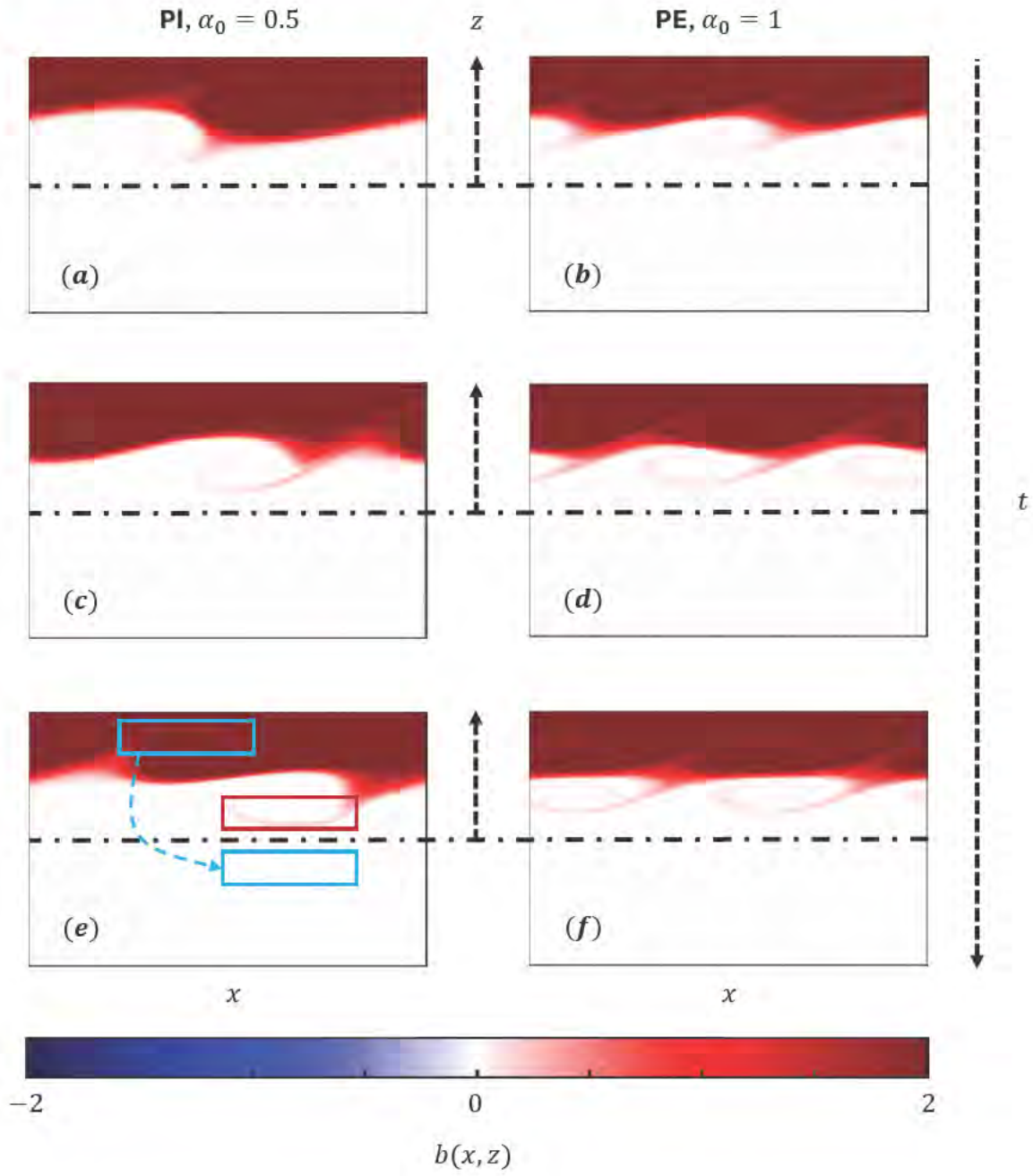

Figure 13: Snapshots of the buoyancy $b\,(x, z)$ from pure HW simulations restricted to $[0, 4\pi) \times [-4, 4]$. The first column – **panels (a), (c), (e)** – contains data from simulation PI (with $\alpha_0 = 0.5$), while the second column – **panels (b), (d), (f)** – contains data from simulation PE (with $\alpha_0 = 1$). The dash-dotted black line marks the centerline $z = 0$. Time increases from top to bottom, and each vertical sequence depicts the crossing of two finite-amplitude Holmboe waves, one on either side of the interface. A plume of stratified fluid is visible on either side of the interface in each simulation. It undergoes significant morphological changes during wave crossing in PI, and to a lesser extent, in PE. The red and blue boxes in panel (e) are to aid comparisons of HW plume length on either side of the interface.

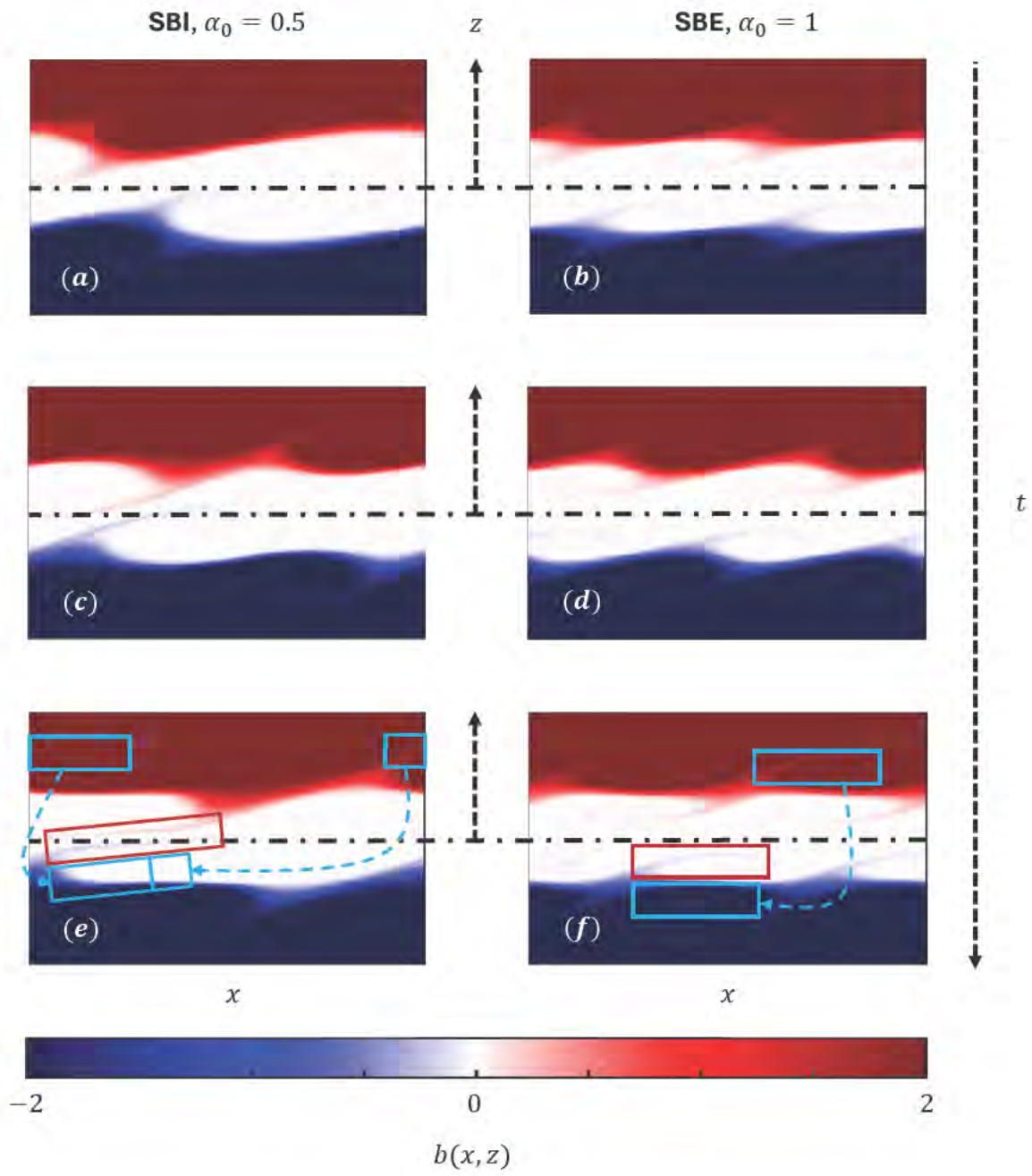

Figure 14: Snapshots of the buoyancy $b(x, z)$ from stacked HW simulations SB restricted to $[0, 4\pi) \times [-4, 4]$. The first column – **panels (a), (c), (e)** – contains data from simulation SBI (with $\alpha_0 = 0.5$), while the second column – **panels (b), (d), (f)** – contains data from simulation SBE (with $\alpha_0 = 1$). The dash-dotted black line marks the centerline $z = 0$. Time increases from top to bottom, and each vertical sequence depicts the crossing of two finite-amplitude stacked Holmboe waves, one on either side of each interface. As we observed in the pure HW simulations, plumes of stratified fluid straddle each interface; and likewise, these undergo greater morphological changes during wave crossing in SBI than in SBE. The red and blue boxes in panels (e) and (f) are to aid comparisons of HW plume length on either side of a buoyancy interface.

4.2 Holmboe wave crossing in the nonlinear regime

A well-known characteristic of HWIs is that component waves have concentrations of clockwise vorticity at their leading (downwind) edges [15]. The strength of these vortices fluctuates as Holmboe waves propagate along the buoyancy interface – attaining a maximum when the waves are far apart (i.e., when wave phase speed is minimized) and decreasing as the waves come closer to each other (and their phase speed increases). These vortices support the sharpening of Holmboe waves in streamwise-localized cusp/ridge-like structures (see Figures 13a, b), and are also responsible for entraining stratified fluid from within the shear layer and ejecting it outward, ultimately forming the thin plumes or fringes that crown travelling wave cusps.

Figure 13 consists of buoyancy field snapshots illustrating a single wave crossing cycle – with HW cusps approaching each other (panels a, b), passing each other (panels c, d), and then reapproaching (panels e, f) – for simulations PI (left) and PE (right). The period covered by these snapshots is approximately from $t = 43$ to $t = 56$. We can see that over the period of time covered by the snapshots, HW cusps become thicker and jut out farther away from the interface; and the plumes lengthen, flatten, and also occupy more space away from the interface. These changes are more pronounced in simulation PI (left panels) than in simulation PE (right panels).

A similar sequence of events is depicted for simulations SBI (left) and SBE (right) in Figure 14. Comparing HW plumes exterior to the buoyancy interfaces to those interior to the buoyancy interfaces between panels (c), (d), (e), and (f), we make two observations:

1. HW plumes interior to their respective interfaces grow flatter and longer as they propagate than plumes exterior to their interfaces. This can be visually seen by comparing the lengths of the red boxes (interior plume) and the blue boxes (exterior plume) in Figures 13e and 14(e, f). This asymmetric morphology has to be a result of cross-layer HW interaction.

2. As before, these changes are more pronounced in simulations where the interior HWI is dominant (SBI, left panels) than in those where the exterior HWI is dominant (SBE, right panels).

These observations hold true for simulation group SA as well (not shown), although the stacking-induced changes in HW plume structure are comparatively muted.

To better quantify and compare stacking-induced effects, we compute streamwise averaged Reynolds stress profiles $\langle u'w' \rangle_x$ for simulations PI, SAI, and SBI. This quantity provides information about the vertical flux of horizontal momentum (through its negative vertical derivative, a positive value of which denotes net upward flux). Results for two instants of time after HW cusps on either side of an interface have crossed each other – when the cusps are (a) closer together, and (b) farther apart – are plotted in Figure 15 below. We see that:

1. When HW cusps are close to each other, the Reynolds stress profiles have peaks of positive magnitude at buoyancy interfaces and similar values in the center of the quiescent region between the two stratified shear layers. This corresponds to a net transport of horizontal momentum into the center of each shear layer. In simulation

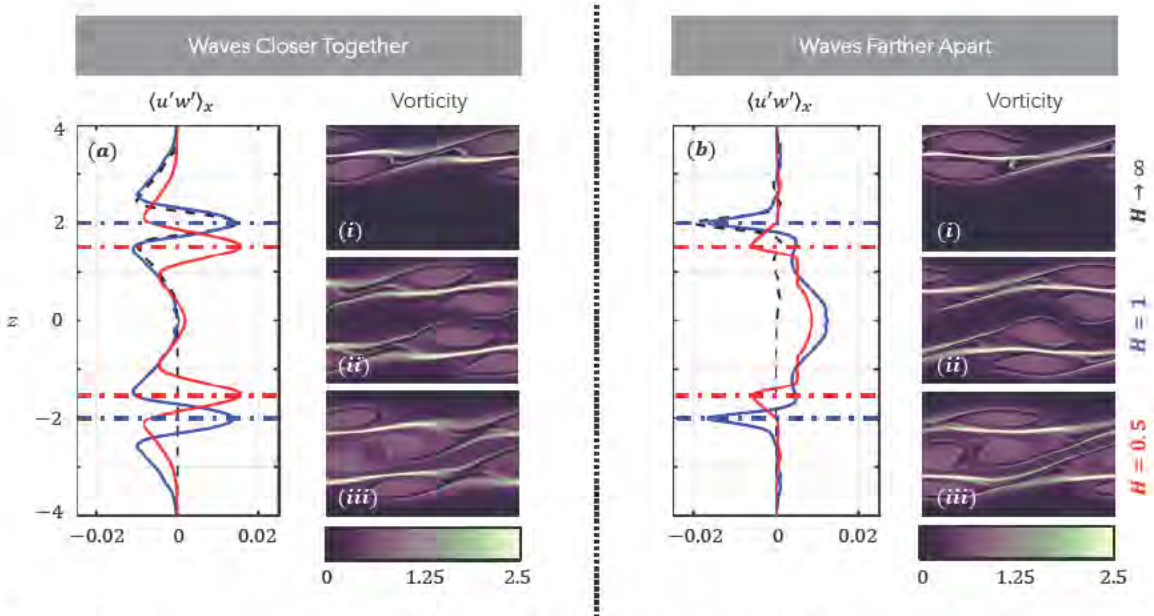

Figure 15: Streamwise averaged Reynolds stress profiles $\langle u'w' \rangle_x$ in simulations PI (dashed black curve), SAI (solid blue curve), and SBI (solid red curve) computed at instants when wave cusps at the buoyancy interface(s) are **(a)** close together and **(b)** far apart. These panels also have dash-dotted lines in black, blue, and red marking the interface position in the corresponding simulation. The sub-panels (i) - (iii) of each panel contain snapshots of out-of-plane vorticity in the region $[0,\ 4\pi) \times [-4,\ 4]$ in the sequence PI (i), SAI (ii), and SBI (iii). These snapshots show the positions of HW cusps and their leading vortices on either side of the buoyancy interface(s).

SBI in particular, there also appears to be a concentration of Reynolds stress at the center of the quiescent region, indicating some transport of horizontal momentum there from the interior edges of the shear layer. The red curve corresponding to simulation SBI displays a visible, albeit slight, difference in Reynolds stress values interior to and exterior to its buoyancy interfaces.

2. When HW cusps are farther apart, the interfacial peaks of Reynolds stress are reversed in magnitude, corresponding to transport of horizontal momentum away from the shear layers. In simulations SAI and SBI, there is a stronger concentration of Reynolds stress at the centerline, the difference in its values between simulations PI, SAI, and SBI is greater, and its cross-interface asymmetry is magnified. Interestingly, the centerline value is greater for SAI than SBI, even though the trend is reversed near the buoyancy interfaces.

Thus, stacking Holmboe waves visibly and quantifiably modifies evolutionary features in the nonlinear regime. Moreover, as one would expect, these modifications are enhanced when the vertical separation between stacked waves is smaller.

4.3 Summary

Our direct numerical simulations confirm and extend the picture developed in the preceding sections on linear theory. Stacking effects are characterized by asymmetries in flow structures and statistics across buoyancy interfaces. We find that these effects are sensitive to the initial perturbation: perturbations composed of interior HWI modes exhibit noticeably stronger asymmetries in HW speeds, plume morphology, and streamwise-averaged Reynolds stress across the buoyancy interface than those composed of exterior HWI modes. Moreover, the separation between stacked stratified shear layers (or stacked Holmboe waves) plays a key role. Reducing the separation half-width from $H = 1$ to $H = 0.5$ amplifies cross-interface asymmetries.

5 Conclusion

In this report, we have studied the dynamics of a stably stratified three-layer fluid system with localized shear around buoyancy interfaces (see Figure 1). This configuration, with its relatively sharp density transitions, is conducive to the growth of Holmboe wave instabilities. Our goals were threefold:

(a) to chart the onset and growth of Holmboe waves from infinitesimal disturbances as a function of stratification strength Ri_0^{-1}, shear layer gap H, and perturbation wavelength $2\pi/\alpha$, using inviscid linear stability theory;

(b) to investigate the effects of finite diffusivity on the stability properties; and

(c) to characterize their finite-amplitude evolution through direct numerical simulations.

Two well-studied configurations emerge as limiting cases of our setup: (i) a two-layer fluid sheared around a single buoyancy interface [10], and (ii) a three-layer fluid with both buoyancy interfaces embedded in a single shear layer [5].

Both limiting cases exhibit Holmboe wave instabilities within a bounded region of the (Ri_0, α) plane. Our setup introduces new dynamics: analytical solutions of the inviscid Taylor-Goldstein equation reveal a splitting of the Holmboe-unstable region into two bands associated with distinct interior and exterior Holmboe wave modes, distinguished by their large-α phase speeds. Moreover, the Taylor-Caulfield instability, present in case (ii), is suppressed.

The reintroduction of diffusive effects broadens interior and exterior Holmboe wave instability bands and lowers growth rates but preserves the differential dominance of interior and exterior Holmboe modes at different wavenumbers. Finally, a suite of direct numerical simulations initialized with either interior or exterior Holmboe wave modes reveals novel effects in the finite-amplitude regime of evolution: stacking induces asymmetries across buoyancy interfaces in Holmboe wave speeds, plume morphology, and Reynolds stresses. These asymmetries are more pronounced for interior Holmboe wave instabilities and are amplified when the shear layers are more closely spaced.

This work is ongoing; therefore, there are several opportunities for refinement. Firstly, it would be useful to identify and draw stability boundaries separating Holmboe wave-unstable

regions from Kelvin-Helmholtz-unstable regions systematically in viscous stability diagrams. This may be accomplished by tracking transitions from zero to finite wavenumbers along the wavenumber axis, thereby clarifying the relative prevalence of each instability type across parameter space. Secondly, a more complete picture of linear instability mechanisms could be obtained by investigating the dependence of interior and exterior stacked Holmboe waves on the Prandtl number. Varying Pr would allow us to assess the role of buoyancy and viscous diffusion separately and to chart changes in instability growth rates and structures. Our direct numerical simulations could also benefit from enhanced spatial resolution, particularly near the buoyancy interfaces, as well as from the adoption of more judicious basis functions in the vertical direction, which may help to better resolve fine-scale features of the flow. Finally, studies of finite-amplitude evolution at a range of Ri_0 and Pr values would be valuable, enabling an assessment of the robustness of stacking-induced asymmetries across different stratification and diffusion regimes. More comprehensive diagnostics of flow structure, energy exchanges, and mixing statistics would complement these efforts and further elucidate the nonlinear dynamics of stacked Holmboe instabilities.

Beyond these immediate refinements, several non-trivial extensions of this work suggest themselves. One natural avenue is the study of stacked Holmboe waves in three spatial dimensions, enabling direct comparison with the recent numerical simulations of Liu et al. [12] on neighboring stratified shear layers, as well as with measurements of turbulent energetics and mixing efficiency from laboratory experiments and field observations. The transition to three dimensions would allow us to explore secondary instabilities, spanwise coherence, and the breakdown of stacked Holmboe modes into turbulence. Other promising avenues include the exploration of asymmetric configurations, in which the buoyancy interface is displaced away from the center of the shear layer, leading to distinct upper and lower Holmboe wave modes, and the consideration of alternative velocity profiles, such as vertically stacked jets. These profiles could support new types of instabilities or modify the competition between interior and exterior Holmboe waves, opening up a broader landscape of layered stratified turbulence.

6 Acknowledgements

I would like to thank my mentors, Colm-cille Caulfield and Alexis Kaminski, for their supportive and insightful guidance on this project. I would also like to thank Greg Chini[4] and Bruce Sutherland[5] for a very well-organized and fantastic GFD experience. Janet Fields and Julie Hildebrandt deserve all the thanks in the world for managing the day-to-day of this program and ensuring everything operated smoothly; as do the other fellows for all the fun discussions, Bachelors in Paradise watch-parties, and assorted memorable experiences (only one of which actually involved Mountain Dew [17]). Lastly, I would like to thank Maison Villatte for existing and having the best chocolate éclairs I have tried so far.

[4]There is a threateningly long list of things I should really thank Greg for, as my doctoral advisor.
[5]Let's Go Oilers!

References

[1] P. Billant and J.-M. Chomaz, *Three-dimensional stability of a vertical columnar vortex pair in a stratified fluid*, Journal of Fluid Mechanics, 419 (2000), pp. 65–91.

[2] K. J. Burns, G. M. Vasil, J. S. Oishi, D. Lecoanet, and B. P. Brown, *Dedalus: A flexible framework for numerical simulations with spectral methods*, Phys. Rev. Res., 2 (2020), p. 023068.

[3] J. R. Carpenter, N. J. Balmforth, and G. A. Lawrence, *Identifying unstable modes in stratified shear layers*, Physics of Fluids, 22 (2010), p. 054104.

[4] J. R. Carpenter, E. W. Tedford, E. Heifetz, and G. A. Lawrence, *Instability in stratified shear flow: Review of a physical interpretation based on interacting waves*, Applied Mechanics Reviews, 64 (2011), p. 060801.

[5] C.-C. P. Caulfield, *Multiple linear instability of layered stratified shear flow*, Journal of Fluid Mechanics, 258 (1994), pp. 255–285.

[6] C. P. Caulfield, W. R. Peltier, S. Yoshida, and M. Ohtani, *An experimental investigation of the instability of a shear-flow with multilayered density stratification*, Phys. Fluids, 7 (1995), pp. 3028–3041.

[7] T. Eaves, *Instability of sheared density interfaces*, Journal of Fluid Mechanics, 860 (2019), pp. 145–171.

[8] S. Goldstein, *On the stability of superposed streams of fluids of different densities*, Proc. Roy. Soc. Lond. A, 132 (1931), pp. 524–548.

[9] J. M. Holford and P. F. Linden, *Turbulent mixing in a stratified fluid*, Dynamics of Atmospheres and Oceans, 30 (1999), pp. 173–198.

[10] J. Holmboe, *On the behavior of symmetric waves in stratified shear layers*, Geofysiske Publikasjoner, 24 (1962), pp. 67–113.

[11] L. N. Howard, *Note on a paper of J. W. Miles*, Journal of Fluid Mechanics, 10 (1961), pp. 509–512.

[12] C.-L. Liu, A. K. Kaminski, and W. D. Smyth, *Turbulence and mixing from neighbouring stratified shear layers*, Journal of Fluid Mechanics, 987 (2024), p. A8.

[13] W. Smyth, J. Moum, and J. Nash, *Narrowband, high-frequency oscillations at the equator. part ii: properties of shear instabilities*, J. Phys. Oceanogr, 41 (2010), pp. 412–428.

[14] W. D. Smyth and J. R. Carpenter, *Instability in Geophysical Flows*, Cambridge University Press, Cambridge, 2019.

[15] W. D. Smyth, G. P. Klaassen, and W. R. Peltier, *Finite amplitude holmboe waves*, Geophysical & Astrophysical Fluid Dynamics, 43 (1988), pp. 181–222.

[16] G. I. Taylor, *Effect of variation in density on the stability of superposed streams of fluid*, Proc. Roy. Soc. Lond. A, 132 (1931), pp. 499–523.

[17] Woods Hole Oceanographic Institution, *Life at gfd*. https://gfd.whoi.edu/gfd-life-at-gfd/, 2025. Accessed: 2025-04-28.

Settling of Porous and Deformable Disks

Nicolaos Petropoulos

August 19, 2024

1 Introduction

The study of the motion of bodies falling in a fluid dates back to Stokes (1851) [13] and Maxwell [11], and has received a lot of interest since then. Indeed, rigid or deformable objects that settle (or rise, depending on their density relative to that of the surrounding fluid) are encountered in a wide range of fields. Of oceanographic and biological relevance, many marine plants and animals rely on the settling of propagules (i.e., any material that functions in propagating an organism to the next stage in its life cycle, such as by dispersal) as their only means of reproduction and dispersal [1]. Similarly, settling rates affect the flux of nutrients, food, and wastes to and from organisms throughout the water column [5]. Settling of marine snow (a continuous shower of mostly organic detritus falling from the upper layers of the water column; see figure 1) is of crucial importance in bringing energy and nutrients from the photic (light-rich) upper ocean to the aphotic regions of the water column. Of topical concern are also microplastics whose path in the world's oceans is still highly uncertain [15].

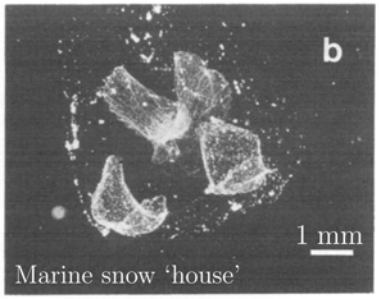

Figure 1: Abandoned filter net or 'house' of an *appendicularian*, a free-swimming invertabrate (from [2]).

Most theoretical, experimental and numerical studies of slowly settling objects have focused on solid particles with simple geometries (such as spheres or disks). The problem is already challenging. In fact, a dimensional analysis reveals that three dimensionless parameters govern the problem of a solid disk settling in a homogeneous fluid: the aspect ratio λ of the disk (characterizing its geometry); the ratio of the object and fluid densities, ρ and ρ_f, respectively (characterising the strength of the buoyancy force driving the motion); the Reynolds number Re (quantifying the importance of inertia over viscous forces). Interestingly, as the Reynolds number increases, the settling motion's characteristics change drastically [7]. At low Re, the settling motion is rectilinear and for intermediate ones, it is oscillatory. For large Re, the motion becomes chaotic. The transition between oscillatory and chaotic motion happens at smaller Reynolds numbers as the product of the density ratio ρ/ρ_f and aspect ratio λ (often referred to as the dimensionless moment of inertia $I^* := \pi\rho\lambda/(64\rho_f)$ of the settling disk) increases. For large enough I^*, the transition disappears and the settling dynamics is characterized by a tumbling motion at all Reynolds

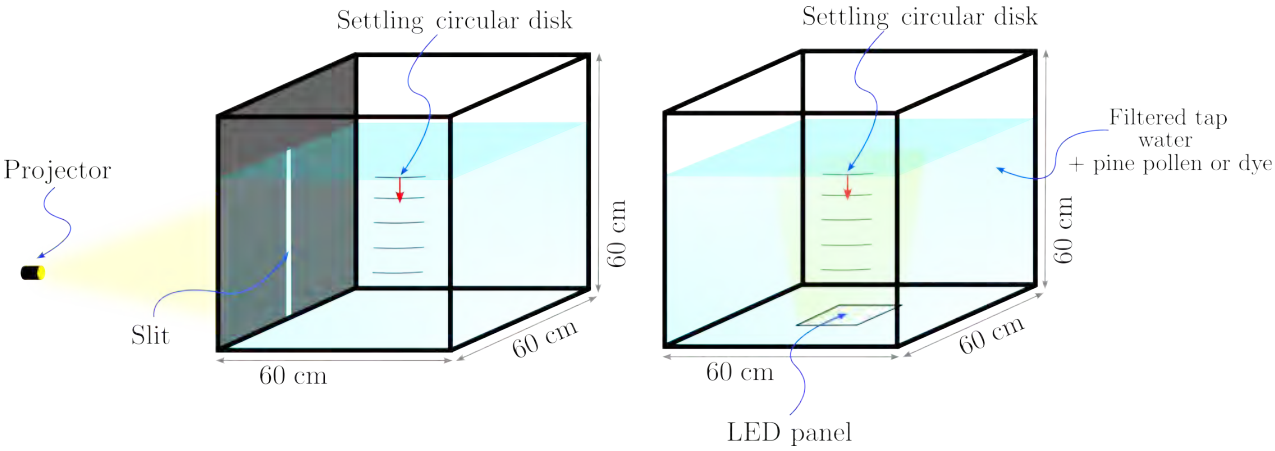

Figure 2: Set-up for the PIV (left) and the settling velocity measurements (right) experiments.

numbers [7]. These intricate transitions are thought to be linked with changes in the structure of the wake behind the settling disk and more precisely the development of a wake instability and vortex shedding as Re increases [16].

The research presented here is ultimately motivated by the desire to understand the settling behaviour of fragile, porous objects like marine snow and biofouled microplastics. However, these objects have wide-ranging and ill-defined geometries and density distributions. Consequently, as a step towards this more complex problem, here we examine the settling of porous (rather than solid) disks. Specifically we examine settling meshes, asking how is their settling and the ambient flow modified when allowing fluid to flow through as well as around the settling object? To answer this question, we experimentally characterize the settling behaviour and wake structure of meshes as the control parameters of the problem are varied.

Microplastic and marine snow aggregates are also flexible (see figure 1). In an attempt to better understand how elastic structures and flow interact to modify the shape of elastic objects settling and consequently their settling trajectories, we present in this work a simple model for the settling dynamics of a filament in a viscous fluid and numerically solve for the stationary shapes of the filament as the ratio of elastic and buoyancy (i.e., driving) forces is varied.

The rest of the report is organised as follows. In section 2 we present the experimental apparatus and techniques used to decipher the settling dynamics and flow structure around and behind a settling mesh; results of these experiments are presented in sections 3.1 and 3.2. In section 4, elasticity is introduced in the problem and a model for the settling dynamics of an elastic filament in a viscous homogeneous fluid is presented. Brief conclusions are drawn in section 5.

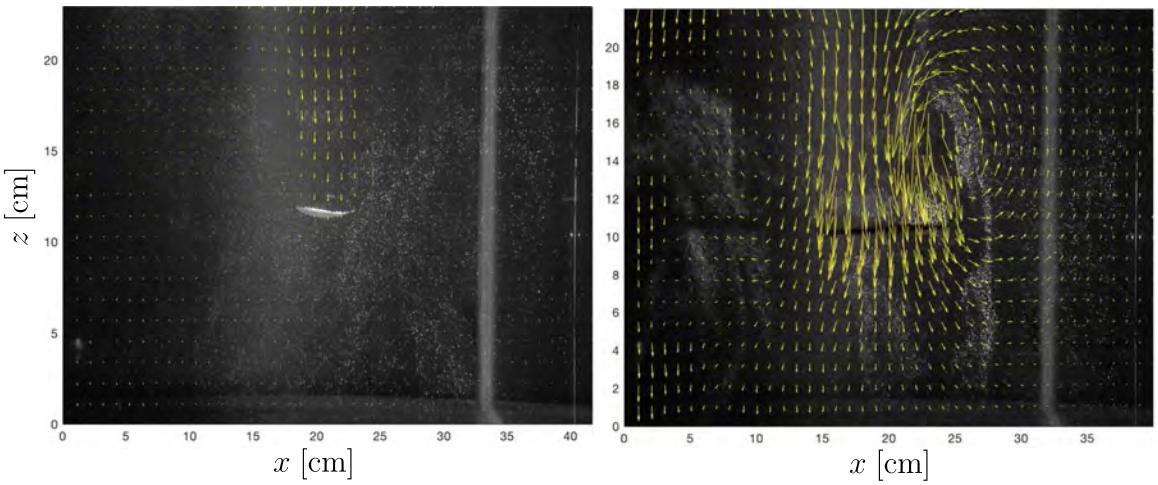

Figure 3: Examples of PIV results. (Left) Plug flow behind mesh 1 with $R = 2.5$ cm. (Right) Wake behind mesh 7 with $R = 5$ cm.

2 Experiment Set-up and Measurement Techniques

All experiments use a 60 cm $\times$ 60 cm $\times$ 60 cm cubic tank filled with filtered tap water (viscosity $\nu = 10^{-6}$ m^2/s). Circular disks (cut out of various meshes) of radius $R = 2.5$ cm or $R = 5$ cm are released individually and their settling dynamics, as well as the flow around, them are analysed. To ensure similar initial conditions throughout the experiments, a release mechanism, made out of two immersed thin plastic plates that can horizontally translate to release the disk carefully disposed on top of them, was used. Note that the tank is assumed to be large enough (compared to the size of the settling disks) so that boundary effects can be neglected.

Two different experimental setups are employed as illustrated in figure 2. In one, an LED panel placed underneath the tank shines upward upon the settling disks and a video of the mesh settling is recorded using a smartphone camera (model Samsung Galaxy S20). This setup was used to measure mesh settling speed and behaviour. In some of these experiments dye was injected in the path of the mesh to observe bulk flow through and around it. In the other set-up used for particle image velocimetry (PIV) measurements of ambient fluid motion, a projector produced a vertical light sheet by shining on a thin (~ 3 mm) slit cut through a black screen placed on one side of the tank. The light sheet illuminated micron-sized particles consisting of store-bought pollen. Videos are recorded using the same camera as in the first setup. We used the PIV package DPIVsoft2010 [12] to calculate (two-dimensional) velocity fields with 40 $\times$ 20 vectors over an area equivalent of 25 cm $\times$ 40 cm.

The disks used in this work are cut from 13 different meshes composed of different materials that have different thicknesses, h (measured using a calliper with 0.1 mm accuracy) and pore geometries (squares, circles, hexagons). The geometry of a single pore is characterised by an equivalent radius r_p (i.e., the radius of the circle of similar area as the one of the pore), as listed in table 1. Note that the area of one pore is estimated using precise (with a 0.1 mm accuracy) measurements of relevant lengths characterising the pore (such

as the length of the size of polygonal pores or the diameter of circular ones). These lengths being typically of order 1 mm, we estimate that the error in approximating r_p is of about 10%.

As another measure of the mesh porosity, we determine the area of the solid part of a mesh, A by taking a snapshot of it on a background of contrasting colour. The image is then binarised (with solid represented by 1 and pore represented by 0; see figure 4). The area A is estimated by counting the number of pixels with value 1, and multiplying by the pixel area. Note that this method provides an approximation of the total area of the mesh; more precisely, the fine-scale porous structure of the fibres (of the polyester meshes, for instance) cannot be properly mapped using this optical technique (the main limitation being due to the resolution of the camera). From the geometric characteristics of a mesh, we construct two dimensionless numbers: the dimensionless area of mesh $A/(\pi R^2)$ (a measure of the mesh porosity) and its aspect ratio h/R. Our meshes allowed us to explore variations of almost an order of magnitude for each of these dimensionless numbers (see figure 5).

The density ρ of the meshes is evaluated using displacement and geometric methods. In the latter case, a mesh thread is extracted and its volume is computed using precise measurements of its thickness and length (using a calliper with an accuracy of 0.1 mm). Its mass is measured using a high-precision scale (precision of 0.001 g). From the density estimates, we computed a third set of dimensionless numbers characterising the meshes, namely the density ratio ρ/ρ_f (with ρ_f the density of water). The 13 meshes used in this work span an order of magnitude in each dimensionless parameter (see figure 5). Note that two of the meshes are buoyant (i.e., $\rho/\rho_f < 1$). In that case, the release mechanism was placed at the bottom of the tank. However, in that case, the release mechanism was perturbing the entire fluid column ahead of the (rising) mesh, polluting velocity measurements. For that reason, we use PIV measurements only for settling meshes (i.e., for which $\rho/\rho_f > 1$).

Note also that some meshes were slightly deformable (see figure 5). We characterise a mesh as 'deformable' when it visibly bent under its own weight when held at one side. No measure of bending moduli or any other relevant measure of 'deformability' was conducted during the summer.

In conclusion, we fully characterised the settling dynamics of 11 meshes, as we will see in the next section. Except for mesh 4 (for which the $A \simeq 1$) that oscillates while settling, all the meshes settle following a straight line.

3 Experimental Results

3.1 Settling velocities

We recorded between 4 and 10 videos for each mesh settling in the quiescent tank. For each video, a vertical line of pixels going through the mesh is extracted for each frame of the video and then stacked together to form a vertical time series from which the settling velocity of the mesh can be estimated from the slope of the line of bright pixels (see figure 6). These estimates are then averaged over settling experiments, for each mesh. We denote the average settling velocity U_s. The experimental results are presented in table 2. Interestingly, the settling velocity does not depend on the radius R. Based on these velocity estimates, three Reynolds numbers based on the mesh radius R, thread thickness h and pore size r_p,

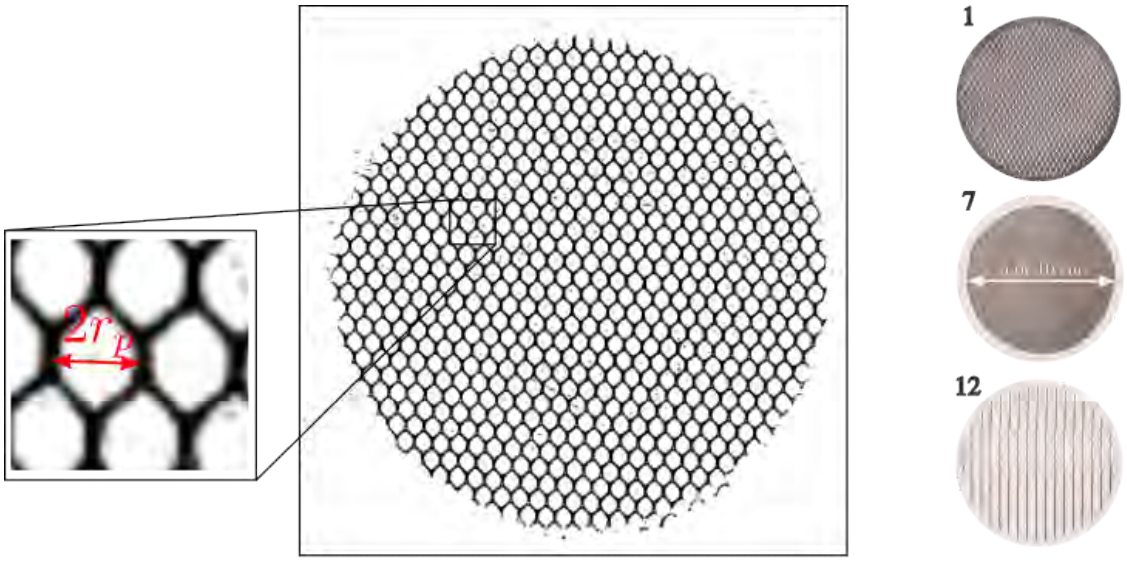

Figure 4: (Left) Geometric characterisation of a mesh (2) and its pores. (Right) Example of meshes. The numbers correspond to the mesh number in table 1.

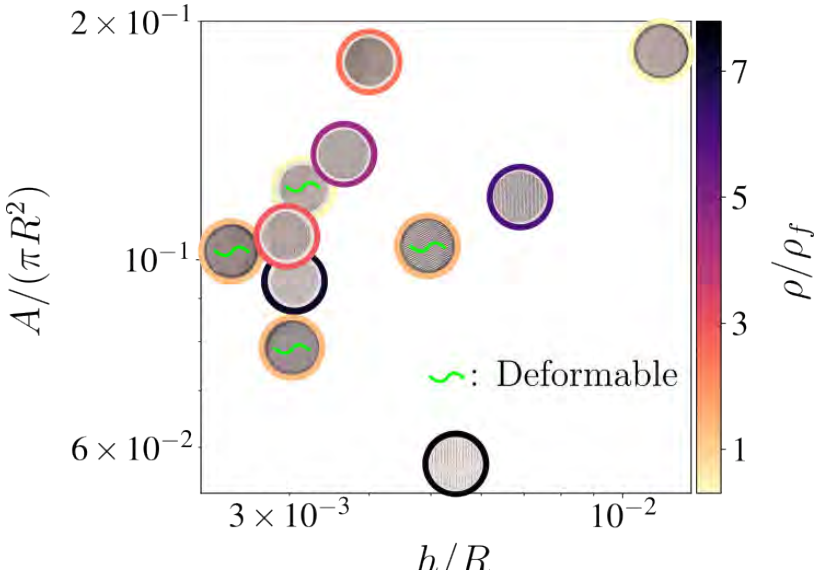

Figure 5: Solid area fraction versus aspect ratio for the meshes used in this work (in log-log scale). The green wiggle denotes a flexible mesh. The shade of the outer circle surrounding each point represents relative density as indicated in the colourbar to the right. Note also that the silk screen (mesh 4), for which $A/(\pi r^2) \simeq 1$ is not presented here.

Mesh	Use	Material	Flexible	Pore	ρ [g/cm^3]	h [mm]	r_p [mm]	$A/(\pi R^2)$
1	Mesh bag	Polyester	yes	hexagon	1.3	0.5	4.6	0.1
2	Mesh bag for balls	Polyester	yes	hexagon	1.3	0.3	3.6	0.08
3	Aquarium bag	Polyester	yes	hexagon	1.3	0.2	1.8	0.1
4	Silk screen	Polyester	yes	-	1.3	0.09	< 0.1	1
5	Window screen	Fiber glass	no	square	3.0	0.5	1.5	0.1
6	Garden drainage	Polyamide	yes	square	0.3	0.3	1.3	0.1
7	Computer screen	PVC	no	circle	1.2	0.4	0.9	0.2
8	Embroidery	Acrylic	no	square	0.7	1.2	2.4	0.2
9	Beehive screen	Steel	no	square	6.2	0.4	1.0	0.1
10	Rodent barrier	Steel	no	square	6.6	0.7	2.6	0.1
11	Window screen	Steel	no	square	7.6	0.3	1.0	0.09
12	Window screen	Steel	no	square	7.6	0.6	5.5	0.06
13	Window screen	Steel	no	square	7.8	0.3	1.2	0.1

Table 1: Properties of meshes used in this work including their density ρ and geometric characteristics: thickness h, pore size r_p and solid fraction $A/(\pi R^2)$.

of the pores are computed:

$$Re := \frac{U_s R}{\nu}, \quad Re_p := \frac{U_s r_p}{\nu}, \quad Re_h := \frac{U_s h}{\nu}. \tag{1}$$

The Reynolds number on the scale of the mesh is of order between 10^3 and 10^4. The Reynolds numbers on the scale of the pores and of the thickness range from 10 to 10^3 (see table 2).

The settling velocity U_s arises as a balance between the buoyancy and hydrodynamic forces acting on the settling meshes. The large values of the Reynolds numbers justify modelling the effect of the hydrodynamic forces as a drag force proportional to U_s^2. Then, the force balance acting on the settling mesh reads

$$Ah(\rho - \rho_f)g = C_D \rho_f A U_s^2, \tag{2}$$

with C_D a drag coefficient that might depend on the particular shape of the pores, threads, etc. This balance gives $U_s \propto \sqrt{\frac{\rho-\rho_f}{\rho_f} gh}$ that is independent of A and R. This theoretical estimate is compared to the experimental measurements in figure 7. Two trends stand out. The settling velocities of the steel mesh — that have circular thread cross-section and square pores — collapse onto the same linear curve, suggesting a similar drag coefficient C_D. Similarly, the plastic ones, with square-ish thread cross-sections and hexagonal pores, collapse onto another linear curve, suggesting another drag coefficient C_D. Note also that these meshes slightly bend as they settle, giving another potential explanation for the relatively lower drag coefficient observed in figure 7 (indeed, we can speculate that a mesh settling with a characteristic Pringles-like shape will settle faster than if straight and orthogonal to the settling velocity, as is the case for settling deformable *filaments* [6]; tangential drag is usually weaker than normal drag).

Most interestingly, whereas the Reynolds number Re is large enough so that a solid full disk of similar dimensions to the meshes used in this work should oscillate as they settle (the transition between a rectilinear and oscillatory descent is thought to happen for $Re \simeq 100$ [7, 16]), none of the meshes considered here oscillate nor tumble while settling.

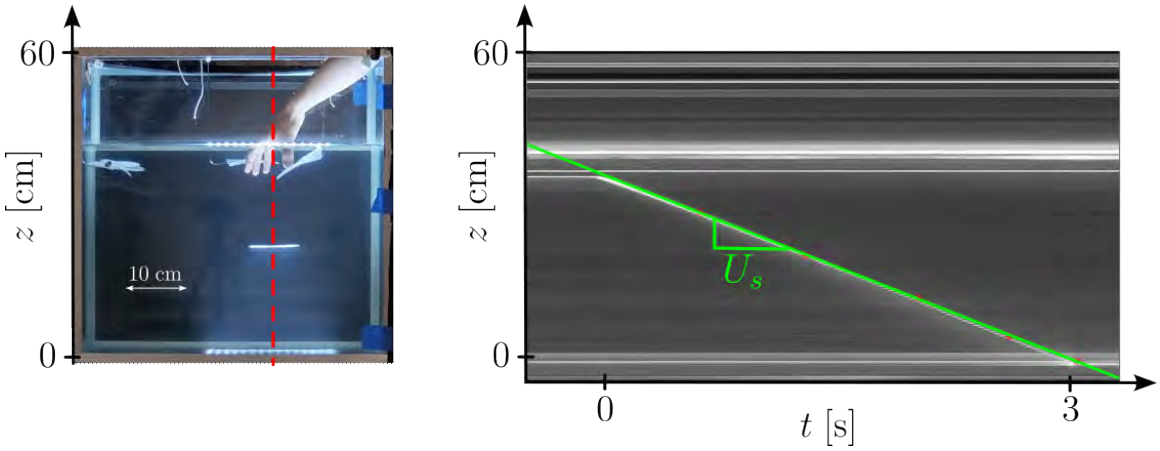

Figure 6: Method to estimate settling velocity. (Left) Snapshot from experiment with settling mesh (11). (Right) Vertical time series constructed by horizontally stacking in time successive vertical lines of pixels passing through the mesh, as indicated by a red line in the left panel. The slope of the green line (passing through the bright pixel of the vertical time series, corresponding to the mesh) corresponds to the settling speed U_s.

	$R = 5\,\text{cm}$			$R = 2.5\,\text{cm}$		
Mesh	U_s [cm/s]	Re	Re_p	U_s [cm/s]	Re	Re_p
1	2.0(± 0.04)	2022	92	2.1(±0.04)	1082	99
2	1.4(± 0.03)	1433	51	1.4(±0.03)	701	50
3	1.2(± 0.02)	1179	21	1.4(±0.03)	686	24
4	0.92(± 0.02)	934	-	0.93(±0.02)	472	-
5	2.5(± 0.05)	2550	38	2.5(±0.05)	1250	37
6	0.75(± 0.01)	762	10	0.74(±0.01)	376	10
7	3.6(± 0.07)	3698	33	4.0(±0.08)	2052	36
8	2.4(± 0.01)	2459	57	2.6(±0.01)	1306	60
9	14.4(± 0.3)	14630	144	15.3(±0.3)	7777	153
10	23.3(± 0.5)	23622	605	23.5(±0.5)	11948	612
11	12.3(± 0.2)	12517	123	12.9(±0.3)	6558	129
12	21.3(± 0.4)	21620	1170	21.5(±0.4)	10937	1184
13	12.6(± 0.3)	12760	151	13.5(±0.3)	6853	162

Table 2: Measured settling velocities for the meshes with $R = 5$ cm and $R = 2.5$ cm, and their associated Reynolds numbers associated with the disk radius R (Re) and the pore size r_p (Re_p).

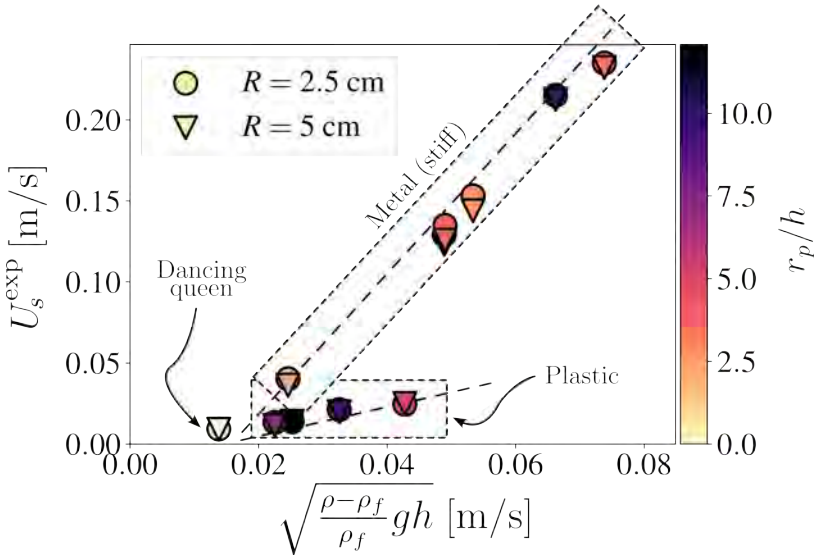

Figure 7: Comparison of the theoretical estimate of the settling velocity based on equation 2 ($\sqrt{gh(\rho-\rho_f)/\rho_f}$) with the experimental data (U_s^{exp}). The slope of the dashed lines gives the inverse of the square root of the effective drag coefficient C_D for the metal and plastic meshes. The 'dancing queen' mesh refers to the silk screen (mesh 4) that is (almost) not porous and that oscillates while settling, as expected for a full solid disk settling in the range of Reynolds numbers (of order 1000; see table 2) considered here.

We hypothesise that flow through the pores of the mesh prevents the vortex formation and wake destabilization that is at the heart of settling disk oscillations. We discuss this hypothesis in the next section.

3.2 Ambient flow structure

In this section, we study the flow structure around, through and behind the settling mesh. First, a blob of dye is released below the initial location of the settling mesh. An example is presented in figure 8. As the mesh settles, the entirety of the dyed fluid goes through the mesh. Second, PIV measurements are performed. These show that fluid in front of the mesh travels through the pores. After a short transient, a plug flow with approximately uniform speed $U_p < U_s$ and depth develops in the wake of the mesh, as shown in figure 9. This, plus flow, is followed by a return flow that replenishes the volume behind the plug (by incompressibility). Importantly, no vortex shedding and wake instabilities are observed.

We now seek to predict the plug flow velocity U_p. The arguments presented here are based on mass conservation. First, we assume that in each pore, the flow is made of a Blasuis boundary layer and an undisturbed plug flow with velocity U_s in a reference frame attached to the settling mesh (see figure 10). Note that order of magnitude estimates assure that the Blasius boundary layer (which is growing as $\sqrt{\nu z/U_s}$) is not interfering with itself in the pore (i.e., $\sqrt{\nu h/U_s}$ is always much smaller than r_p). Then, we have that the mass

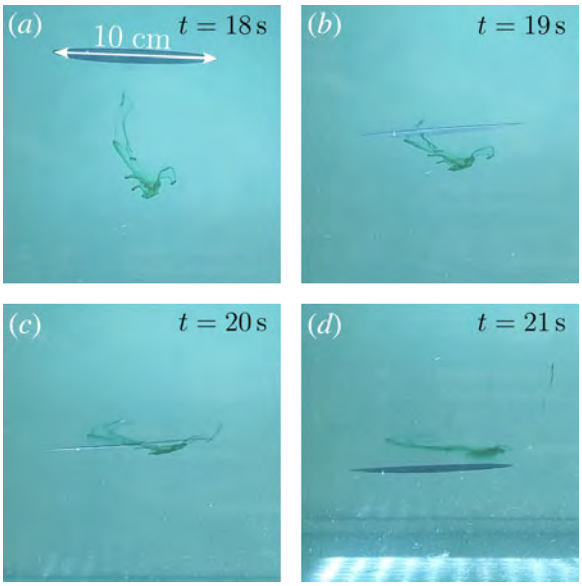

Figure 8: Dye experiments: a blow of dye (food colouring) is released in front of the settling meshes. Mesh 7 is presented here. As the mesh settles, the entirety of the dye goes through the pores of the mesh.

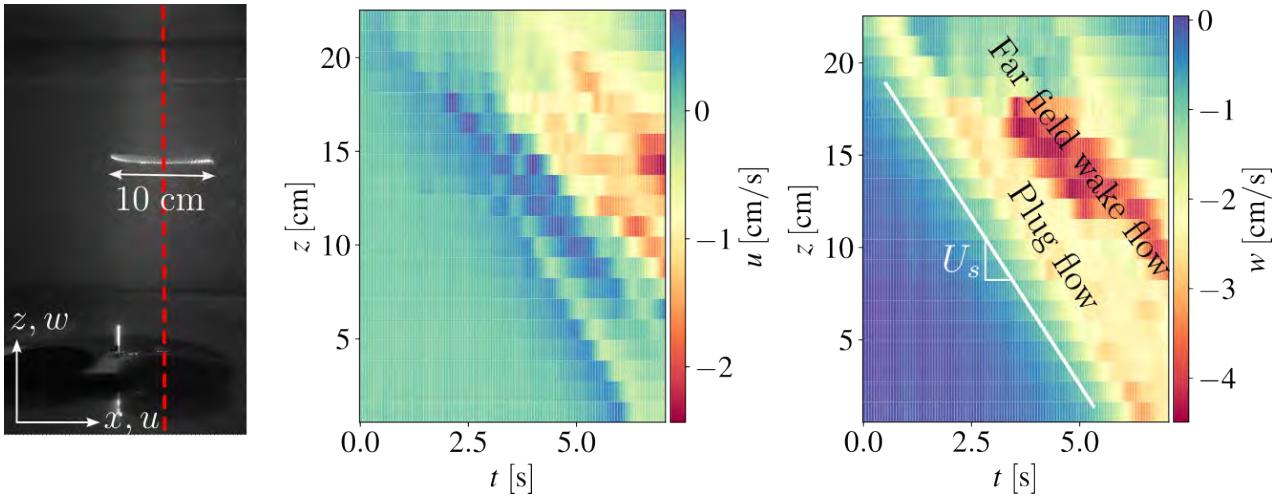

Figure 9: (Left) Snapshot from PIV experiment (mesh 7). (Middle, right) PIV measurement of the horizontal (u; middle) and vertical (w, right) components of the velocity field. The time series is constructed by stacking in time successive velocity measurements along a vertical line passing through the mesh, as indicated by the red line in the leftmost panel. The slope of the white line, separating the quiet fluid ahead of the mesh from the plug flow in its wake, corresponds to the settling speed of the mesh U_s.

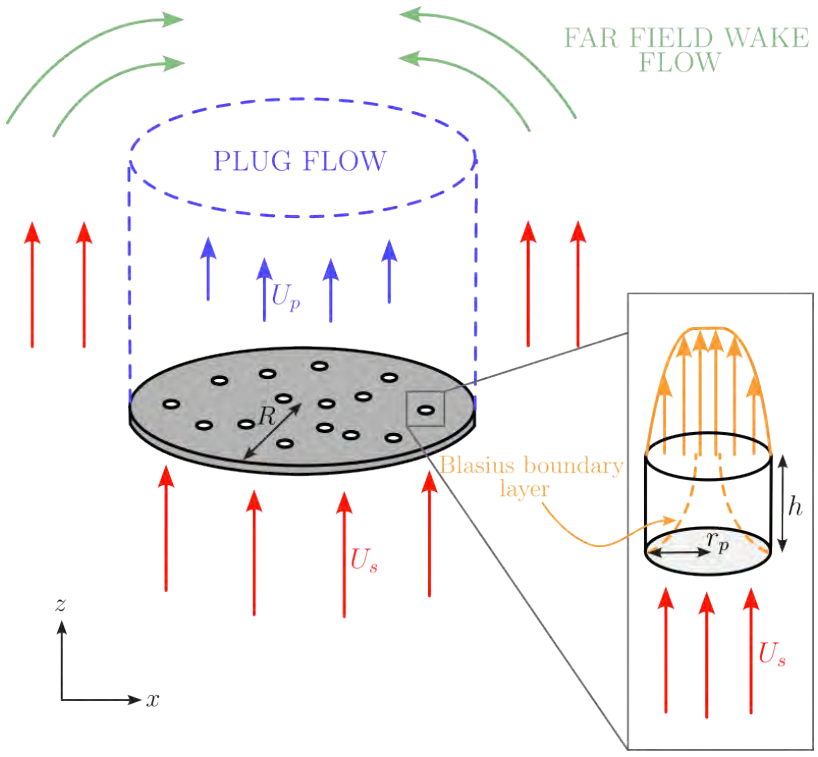

Figure 10: Flow structure in the wake of the settling mesh and assumed flow structure in the pores of the mesh (note that the reference frame is here attached with the mesh).

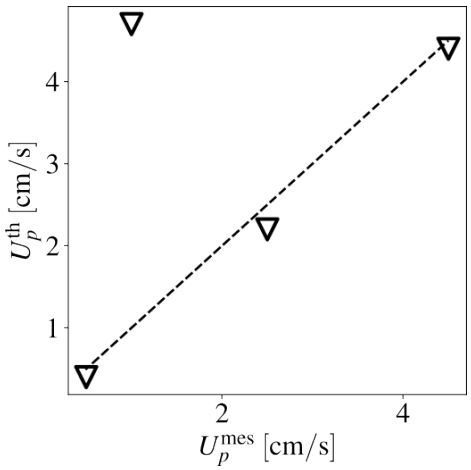

Figure 11: Comparison between the theoretical prediction of U_p (equation (5); U_p^{th}) and experimental measurements U_p^{mes}. The dashed line corresponds to $U_p^{\text{th}} = U_p^{\text{exp}}$.

flux Q_p though one pore is

$$Q_p = \rho \pi r_p^2 U_s \left[1 - C_B Re_p^{-1/2} \left(\frac{h}{r_p} \right)^{1/2} \right]. \tag{3}$$

Here we used the fact that, for a Blasius boundary layer (with velocity profile u), we have

$$\frac{1}{r_p^2} \int \left(1 - \frac{u}{U_s} \right) r \mathrm{d}r = C_B Re_p^{-1/2} \left(\frac{h}{r_p} \right)^{1/2}, \tag{4}$$

where C_B is an order 1 integration constant [4, 14]. Then, using mass conservation in the blue (dashed line) control volume depicted in the schematic figure 10, we get:

$$U_p = U_s \frac{N_p \pi r_p^2}{\pi R^2} \left[1 - C_B Re_p^{-1/2} \left(\frac{h}{r_p} \right)^{1/2} \right] = U_s \left[1 - \frac{A}{\pi R^2} \right] \left[1 - C_B Re_p^{-1/2} \left(\frac{h}{r_p} \right)^{1/2} \right]. \tag{5}$$

Here, N_p is the number of pores in the mesh (and hence $N_p \pi r_p^2 = \pi R^2 - A$). This estimate is compared to experimental measurement in figure 11. Note that the PIV measurements were precise enough only for four experiments. Therefore, we unfortunately cannot conclude anything regarding the validity of our model.

However, the above ideas can potentially be useful in designing a code to simulate a settling mesh without fully resolving the structure of the flow inside the pores of the mesh. More precisely, the object is represented as a field H such that $H = 1$ where the mesh is and $H = 0$ otherwise (with a smooth transition at the object boundary) that is advected at a velocity $\boldsymbol{U}$ that arises from the following force balance on the settling object:

$$M \mathrm{d}_t \boldsymbol{U} = \underbrace{\boldsymbol{F}_h}_{\text{hydrodynamic forces}} + \underbrace{\boldsymbol{F}_b}_{\text{buoyancy forces}}. \tag{6}$$

Here M is the mass of the settling object. The hydrodynamic forces, that arise from the interaction between the surrounding fluid and the complex porous structure of the object, need to be modelled. We consider the formulation (with $\boldsymbol{u}$ the fluid velocity), following ideas from [9]

$$\boldsymbol{F}_h \propto \frac{1}{\tau} H \times (\boldsymbol{u} - \boldsymbol{U}). \tag{7}$$

As a rule of thumb, as the fluid (with velocity $\boldsymbol{u}$) penetrates the porous structure of the settling object it is decelerated by viscous drag to match the velocity of the object over a time-scale τ.

Since the object exerts a force $-\boldsymbol{F}_h$ on the fluid, the (incompressible) velocity field $\boldsymbol{u}$ is a solution of the Navier-Stokes equation

$$\partial_t \boldsymbol{u} + \boldsymbol{u} \cdot \nabla \boldsymbol{u} = -\frac{1}{\rho_f} \nabla p + \nu \Delta \boldsymbol{u} - \frac{1}{\tau} H \times (\boldsymbol{u} - \boldsymbol{U}), \quad \nabla \cdot \boldsymbol{u} = 0, \tag{8}$$

with p the pressure. The closed set of equations (6-8) can now be solved using, for instance, Dedalus.

In the case of the mesh considered here, we can estimate τ in function of the geometric structure of the mesh. Indeed, considering at first one pore and the flow structure described in figure 10, we have, using results from Blasius boundary layer theory (U_e is the mean velocity at the exit of the pore):

$$\tau \simeq \frac{h}{U_s - U_e} = \frac{1}{2C_B} Re_h^{1/2} \frac{r_p}{U_s}. \tag{9}$$

Then considering all the (N_p) pores, we get:

$$\tau \simeq \frac{N_p \pi r_p^2}{\pi R^2} \frac{1}{2C_B} Re_h^{1/2} \frac{r_p}{U_s} = \left(1 - \frac{A}{\pi R^2}\right) \frac{1}{2C_B} Re_h^{1/2} \frac{r_p}{U_s}. \tag{10}$$

This relationship, linking the free parameter τ and the geometric characteristic of the mesh and fluid properties, arises from a set of assumptions concerning the flow geometry inside each pore of the mesh. Comparing simulation and experimental outputs could validate or invalidate these assumptions. We did not have time to run accurate simulations during the summer. Especially, we ran into convergence issues when time-stepping the equations.

4 Settling of Deformable Objects

In the previous sections, we saw how porosity influences the settling dynamics of disks and the structure of their wake. Here we consider another property of settling objects that might influence their settling velocity: deformability. More precisely, we aim to answer the following question: how does the deformability of an object influence its settling velocity? Presumably, a stiff settling disk falling perpendicular to its settling velocity will settle at a lower speed than a deformable one taking a U-shape (everything else being equal), tangential drag being usually smaller than normal drag [3]. It is therefore crucial to understand first how the fluid and the deformable object interact to set the shape of the settling object. In an act of extreme reductionism, we will consider one-dimensional filaments rather than

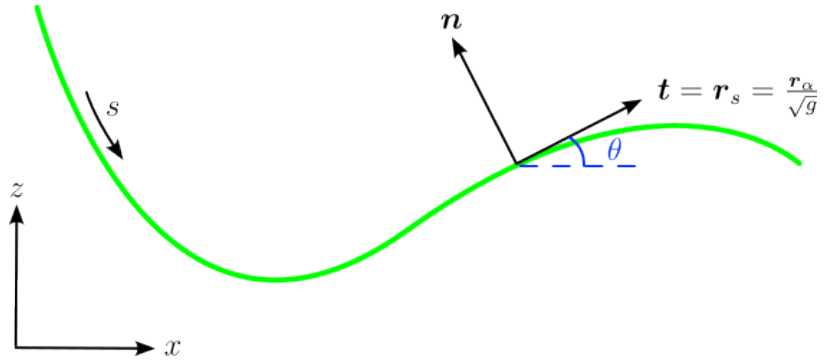

Figure 12: Schematic of a (green) filament

two-dimensional disks. The framework presented here closely follows the one described in [8], adapted to take into account buoyancy forces, the driving force of our problem. Note that porosity is not considered here.

A filament, depicted in figure 12, will be represented as a map $\alpha \in [0,1] \mapsto \boldsymbol{r}(\alpha)$, $\boldsymbol{r}(\alpha)$ being the position of a point labelled α on the filament. We also define s the arclength coordinate along the filament. We denote $\boldsymbol{r}_\alpha := \partial_\alpha \boldsymbol{r}$. Similar notation will be adopted for other partial derivatives. Note also that

$$\partial_s = \frac{1}{\sqrt{g}}\partial_\alpha, \quad g := \boldsymbol{r}_\alpha \cdot \boldsymbol{r}_\alpha, \tag{11}$$

with g the metric. We then define the tangent vector to the filament $\boldsymbol{t} := \partial_s \boldsymbol{r}$. Normal to this vector is the normal vector $\boldsymbol{n}$. Our aim here is to write Newton's force balance on the filament in the coordinate system associated with the tangent and normal vector $\boldsymbol{t}$ and $\boldsymbol{n}$. To this end, we will use a variational approach and hence first need to account for the different forms of energy in the system at hand.

First, the filament is subject to a bending energy that tends to bring the filament to a state of zero curvature. More precisely, the bending energy is assumed to be of the form

$$\mathcal{E}_\mathrm{b} = \frac{A}{2}\int_\alpha \kappa^2 \sqrt{g}\mathrm{d}\alpha. \tag{12}$$

Here, A is the bending modulus and has units energy·length and $\kappa = \partial_s \theta$ is the local curvature of the filament with θ being the tangent angle to the filament (i.e., the angle between the tangent vector $\boldsymbol{t}$ and the horizontal). In terms of calculus of variations, this means that the filament pays a cost of being in a position with non-zero curvature. Second, the filament is subject to the buoyancy force that derives from the following energy:

$$\mathcal{E}_\mathrm{gr} = -\int_\alpha \boldsymbol{\beta} \cdot \boldsymbol{r}\sqrt{g}\mathrm{d}\alpha. \tag{13}$$

Here $\boldsymbol{\beta}\sqrt{g}\mathrm{d}\alpha = \boldsymbol{\beta}\mathrm{d}s$ is the buoyancy force of a piece of size $\mathrm{d}s$ of filament. Third, the filament is assumed inextensible. This constraint will be imposed using a Lagrange multiplier $\Lambda(\alpha)$ (the tension along the filament) and the energy

$$\mathcal{E}_\mathrm{t} = -\int_\alpha \Lambda(\alpha)\sqrt{g}\mathrm{d}\alpha. \tag{14}$$

Finally, the filament has a kinetic energy

$$\mathcal{K} = \frac{1}{2}\int_\alpha \boldsymbol{r}_t^2 \sqrt{g}\mathrm{d}\alpha. \tag{15}$$

Here $\boldsymbol{r}_t$ is the time derivative of $\boldsymbol{r}$.

From the above potential and kinetic energies, one could write a variational version of Newton's force balance from the following minimum action principle:

$$\text{Minimize } \int \mathcal{L}\mathrm{d}t = \int [\mathcal{K} - \mathcal{E}_\mathrm{b} - \mathcal{E}_\mathrm{gr} - \mathcal{E}_\mathrm{t}]\mathrm{d}t. \tag{16}$$

The above is equivalent to the following Euler-Lagrange equation:

$$\frac{\mathrm{d}}{\mathrm{d}t}\frac{\partial \mathcal{K}}{\partial \boldsymbol{r}_t} = \frac{\partial}{\partial \boldsymbol{r}}[\mathcal{E}_\mathrm{b} + \mathcal{E}_\mathrm{gr} + \mathcal{E}_\mathrm{t}]. \tag{17}$$

This is exactly Newton's force balance, with acceleration (inertia) on the left and conservative forces on the right. Here, no interaction between the filament and the surrounding fluid is taken into account. We will *model* this interaction as a drag force deriving from the following Rayleigh dissipation function:

$$\mathcal{R} := \int_\alpha \left[\zeta_\perp(\boldsymbol{r}_t\cdot\boldsymbol{n})^2 + \zeta_\parallel(\boldsymbol{r}_t\cdot\boldsymbol{t})^2\right]\sqrt{g}\mathrm{d}\alpha. \tag{18}$$

Here, $\zeta_\perp$ and $\zeta_\parallel$ are the drag coefficients in the normal and tangential direction, respectively. For simplicity, we consider the slender-body approximation for which $\zeta_\perp = 2\zeta_\parallel$ [3]. Finally, to take into account the non-conservative drag forces, we consider the following variational formulation:

$$\frac{\mathrm{d}}{\mathrm{d}t}\frac{\partial \mathcal{K}}{\partial \boldsymbol{r}_t} = \frac{\partial}{\partial \boldsymbol{r}}[\mathcal{E}_\mathrm{b} + \mathcal{E}_\mathrm{gr} + \mathcal{E}_\mathrm{t}] - \frac{\partial \mathcal{R}}{\partial \boldsymbol{r}_t}. \tag{19}$$

For simplicity, we consider the overdamped limit for which the inertia (left-hand side) can be neglected compared to the over forces, i.e.,

$$\frac{\partial \mathcal{R}}{\partial \boldsymbol{r}_t} = \frac{\partial}{\partial \boldsymbol{r}}[\mathcal{E}_\mathrm{b} + \mathcal{E}_\mathrm{gr} + \mathcal{E}_\mathrm{t}]. \tag{20}$$

Taking the necessary functional derivative involved in the force balance (20) (note that the functionals considered here are written in function of the coordinate α rather that s; α and $\boldsymbol{r}$ are independent variables whereas s and $\boldsymbol{r}$ are not) and projecting into $\boldsymbol{t}$ and $\boldsymbol{n}$ (with $\boldsymbol{r}_t = U\boldsymbol{n} + W\boldsymbol{t}$), we get:

$$U = \zeta_\perp^{-1}\left[A\left(\kappa_{ss} + \frac{1}{2}\kappa^3\right) + \boldsymbol{\beta}\cdot\boldsymbol{n} + (\boldsymbol{\beta}\cdot\boldsymbol{r})\kappa + \Lambda\kappa\right], \tag{21}$$

$$W = 2\zeta_\perp^{-1}\left[-\Lambda_s + \boldsymbol{\beta}\cdot\boldsymbol{t} - \boldsymbol{\beta}\cdot\boldsymbol{t}\right]. \tag{22}$$

The cubic non-linearity arises from the functional derivative of the bending energy $\mathcal{E}_\mathrm{b}$ with respect to $\boldsymbol{r}$. It is usually neglected in the small displacement approximation [10] but is needed when considering large deviations from a flat filament (indeed, if one considers the

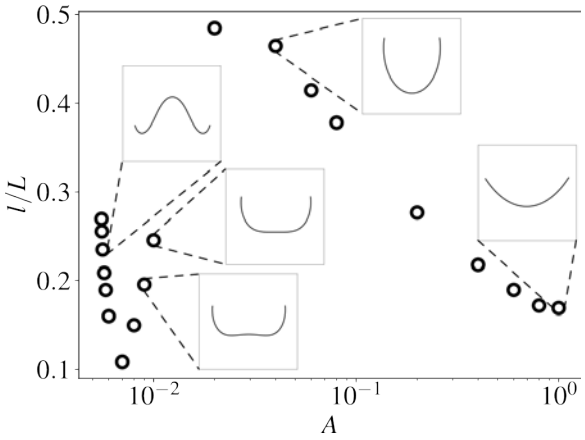

Figure 13: Equilibrium positions of the filament for different values of the dimensionless bending modulus A. Here l/L is the ratio of the distance between the tips of the filaments and the distance between the highest and lowest point of the filament.

extreme case of a filament taking the shape of a circle for which $\kappa_s = 0$ everywhere, the κ^3 term is needed to bring the filament back to its state of minimal energy). The tension ensures that the metric g is time-independent (i.e., that the filament is inextensible). This condition can be written $W_s + \kappa U = 0$, i.e.,

$$\Lambda_{ss} - \frac{1}{2}\left(\Lambda + \boldsymbol{\beta}\cdot\boldsymbol{r}\right)\kappa^2 = \frac{1}{2}(\boldsymbol{\beta}\cdot\boldsymbol{n})\kappa + \frac{A}{2}\left(\kappa_{ss} + \frac{1}{2}\kappa^3\right)\kappa. \tag{23}$$

Note that equations (21-23) are written in both extrinsic ($\boldsymbol{r}$) and intrinsic ($\boldsymbol{t}$ and $\boldsymbol{n}$) coordinates, which is not handy. However, making the change of tension $\Lambda \to \Lambda + \boldsymbol{\beta}\cdot\boldsymbol{r}$, we get the force balance

$$U = \zeta_\perp^{-1}\left[A\left(\kappa_{ss} + \frac{1}{2}\kappa^3\right) + \boldsymbol{\beta}\cdot\boldsymbol{n} + \Lambda\kappa\right], \tag{24}$$

$$W = 2\zeta_\perp^{-1}\left[-\Lambda_s + \boldsymbol{\beta}\cdot\boldsymbol{t}\right], \tag{25}$$

$$\Lambda_{ss} - \frac{1}{2}\Lambda\kappa^2 = \frac{1}{2}(\boldsymbol{\beta}\cdot\boldsymbol{n})\kappa + \frac{A}{2}\left(\kappa_{ss} + \frac{1}{2}\kappa^3\right)\kappa, \tag{26}$$

that is independent of $\boldsymbol{r}$ and hence of any extrinsic reference frame. The above set of equations gives the normal (U) and tangential (W) velocity of the filament in function of its curvature as well as the necessary tension along the filament to ensure inextensibility. The tangent angle evolves in time as $\theta_t = -U_s + \theta_s W$. The boundary conditions are no force and no torque at the tips of the filament, i.e., $\kappa = 0$ and $\kappa_s = 0$ at $s = 0, L$ where L is the total length of the filament.

We now seek stationary solutions to the above set of equations, with $\boldsymbol{r}_t \parallel \hat{\boldsymbol{z}}$, i.e., $U = V\cos(\theta)$ and $W = V\sin(\theta)$ where V is the settling velocity of the filament. For symmetry, we also impose $\theta(s = L/2) = 0$. Then, we need to solve a differential and algebraic nonlinear problem for θ (recall that $\kappa = \theta_s$ by definition), V and Λ. This is numerically extremely challenging and we could not find a way to numerically converge solutions (using

Dedalus) without further simplifications. We eliminate the algebraic part of the problem (i.e., V) assuming that the settling velocity arises from a balance between buoyancy and drag, i.e., $V \simeq \zeta_\perp^{-1}|\boldsymbol{\beta}|$. We also non-dimensionalise the system in the following way:

$$U \to \frac{\beta}{\zeta_\perp} U,\ s \to Ls,\ \kappa \to \frac{1}{L}\kappa,\ \Lambda \to L\beta\Lambda.$$

so that the only control parameter of the problem is the (dimensionless) bending modulus $A/(L^3\beta)$ (denoted A in the subsequent), effectively quantifying the ratio of elastic and buoyancy forces. All in all, we numerically solve the non-linear boundary value problem defined by equations (24) and (26) (the tangential velocity can then be recovered by inextensibility) with no force and no torque boundary conditions for θ and Λ using Dedalus. The results are presented in figure 13 for various dimensionless bending moduli A. As A decreases and the filament becomes more flexible, the filament takes a characteristic U shape. For A even smaller, a W shape develops, as already observed in [6] using a different method (more precisely the authors considered a mass and spring description of the filament).

Finally, we now need to check if our ansatz for the settling velocity V is adequate. To do so, for a given value of the dimensionless bending modulus A we would like to time-step the set of equations (24-26) (with $\theta_t = -U_s + \theta_s W$ and appropriate boundary conditions) starting from the equilibrium configuration of the filament found above (that hopefully is not too far from the actual stationary state of the filament) for the considered value of A and see if this configuration is indeed a stationary one and, if not, analyse the arising stationary state of the simulation, if it exists. This has proven to be an extremely difficult task (and in fact we did not manage to find a satisfactory solution by the end of the summer). Indeed it involves solving a differential, algebraic and non-linear initial value problem for U, W, θ and Λ, a numerically challenging endeavour. First, ensuring that the problem's algebraic constraint is satisfied at each time step is not obvious. Second, because of the cubic non-linearity, small errors in the curvature equation are rapidly amplified, leading to rough (and unphysical) numerical solutions for θ. The (not so satisfying) solution found was to add diffusive terms in the equation defining the time evolution of θ:

$$\theta_t = -U_s + \theta_s W + D\theta_{ss}. \tag{27}$$

This has proven enough to time-step the set of equations defining our problem over long simulation times (we show an example in figure 14). However, the relatively large value of D needed makes it difficult to draw any conclusion regarding the stationary shape of the filament (since the diffusive term tends to smooth θ, leading to a flat filament) and settling velocity V and the hack used here was not enough to answer our initial question and find a relationship between V and A.

5 Conclusion

Here, we summarise the findings (even partial) that arise from our work and suggest avenues for future research.

Even though solid (full) disks settling at a speed such that the associated Reynolds number is of order 100 and above showcase oscillatory or chaotic settling trajectories, meshes

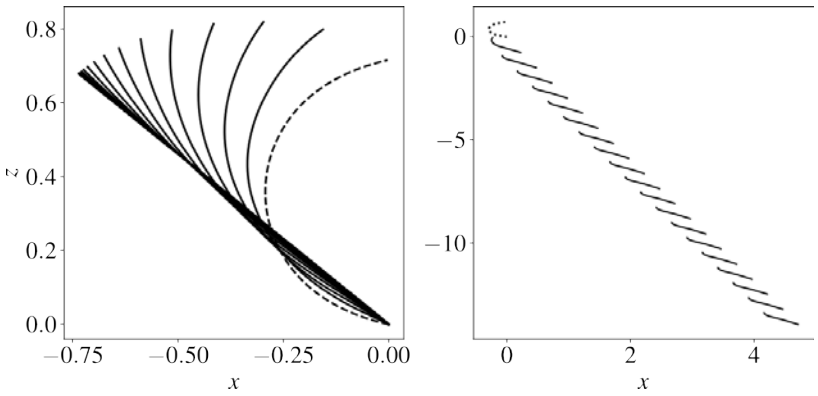

Figure 14: A filament with an initial U-shape (dotted line) unfolds and settles in its reference frame (right) and in the 'laboratory' reference frame (left). Gravity is in the z direction

— for which fluid can flow through their porous structure — settle in a straight line regardless the Reynolds numbers (however this one is defined, based on the mesh thickness, pore size, or object size). The structure of a mesh wake differs from that of a full disk in many ways. Importantly, no vortex shedding and wake instability were observed in our PIV experiments. On the contrary, the wake is a plug flow that follows the mesh at a speed smaller than the mesh settling speed. Using conservation of mass arguments and assuming that the structure of the flow inside each pore making up the mesh was essentially a Blasius boundary layer, we concluded that the ratio of the plug and settling velocities was controlled by the number and geometry of the pores as well as the pore size-based Reynolds number. This theoretical result was verified on an impressive number (three!) of PIV experiments. Further experimental investigation is therefore needed.

The shape of a settling object also influences its settling velocity (drag being a function of the shape). Hence, the complex interaction between a deformable object and the flow around it that constantly changes the shape of the object might have important implications on how an elastic object settles. We developed here a simple model for the settling dynamics of an elastic filament settling under gravity in a low Reynolds number flow. This model is based on an energetic approach and reduces flow-filament interaction to drag forces. Stationary solutions of the model are numerically found. These solutions depend on a single control parameter A (quantifying the ratio of elastic and buoyancy forces) and interesting behaviours arise for relatively small values of A. Indeed, for A small enough, the stationary shape of the settling filament takes the form of a W rather than the classic U. Such a result has already been numerically observed [6], using a bead-spring model. We hope that our model is flexible (no pun intended) and generalisable enough to be extended to two-dimensional objects. The numerical resolution of the model also opens avenues for interesting (but extremely challenging) numerical and theoretical questions such as how to accurately solve a non-linear set of (ordinary or partial) differential and algebraic equations. Finally, is the W stationary shape of physical relevance or a mere theoretical construction?

All in all, we explored how certain aspects of porosity *or* deformability could influence the settling of objects in a quiescent and homogeneous fluid. However, most of the 'objects' of marine biology interest (such as 'marine snow') are both porous *and* flexible. Is there any interesting coupling to expected?

6 Acknowledgements

I would like to thank Bruce Sutherland for proposing this project and supervising me during the Summer School. Thanks are also due to Claudia Cenedese and Jim McElwaine for their helpful support in the lab and Greg Chini for being an awesome programme director and softball coach. I am indebted to Eric Hester, Nick Moore and Keaton Burns for the useful discussions and thoughtful comments during the summer. Thank you to the GFD fellows, staff and visitors for making this summer an unforgettable one.

References

[1] A. Abelson and M. Denny, *Settlement of marine organisms in flow*, Annual Review of Ecology and Systematics, 28 (1997), pp. 317–339.

[2] A. L. Alldredge and M. W. Silver, *Characteristics, dynamics and significance of marine snow*, Progress in oceanography, 20 (1988), pp. 41–82.

[3] G. K. Batchelor, *Slender-body theory for particles of arbitrary cross-section in stokes flow*, Journal of Fluid Mechanics, 44 (1970), pp. 419–440.

[4] H. Blasius, *The boundary layers in fluids with little friction*, no. 1256 in 1, National Advisory Committee for Aeronautics, 1950.

[5] C. Butman, *Larval settlement of soft-sediment invertebrates: the spatial scales of pattern explained by active habitat selection and the emerging role of hydrodynamical processes*, Oceanogr. Mar. Biol, 25 (1987), pp. 113–165.

[6] M. Cosentino Lagomarsino, I. Pagonabarraga, and C. Lowe, *Hydrodynamic induced deformation and orientation of a microscopic elastic filament*, Physical Review Letters, 94 (2005), p. 148104.

[7] S. B. Field, M. Klaus, M. Moore, and F. Nori, *Chaotic dynamics of falling disks*, Nature, 388 (1997), pp. 252–254.

[8] R. E. Goldstein and E. Lauga, *Biological Physics and Fluid Dynamics*, Department of Applied Mathematics and Theoretical Physics, University of Cambridge, 2023.

[9] M. Le Bars and M. G. Worster, *Interfacial conditions between a pure fluid and a porous medium: implications for binary alloy solidification*, Journal of Fluid Mechanics, 550 (2006), pp. 149–173.

[10] B. Marchetti, V. Raspa, A. Lindner, O. Du Roure, L. Bergougnoux, E. Guazzelli, and C. Duprat, *Deformation of a flexible fiber settling in a quiescent viscous fluid*, Physical Review Fluids, 3 (2018), p. 104102.

[11] J. C. Maxwell, *On a particular case of the descent of a heavy body in a resisting medium*, Camb. Dublin Math. J, 9 (1854), pp. 145–148.

[12] P. Meunier and T. Leweke, *Analysis and treatment of errors due to high velocity gradients in particle image velocimetry*, Experiments in fluids, 35 (2003), pp. 408–421.

[13] G. G. Stokes, *On the effect of the internal friction of fluids on the motion of pendulums*, Transactions of the Cambridge Philosophical Society, IX (1851).

[14] O. Tutty, W. Price, and A. Parsons, *Boundary layer flow on a long thin cylinder*, Physics of fluids, 14 (2002), pp. 628–637.

[15] E. Van Sebille, S. Aliani, K. L. Law, N. Maximenko, J. M. Alsina, A. Bagaev, M. Bergmann, B. Chapron, I. Chubarenko, A. Cózar, et al., *The physical oceanography of the transport of floating marine debris*, Environmental Research Letters, 15 (2020), p. 023003.

[16] H. Zhong, C. Lee, Z. Su, S. Chen, M. Zhou, and J. Wu, *Experimental investigation of freely falling thin disks. Part 1. The flow structures and Reynolds number effects on the zigzag motion*, Journal of Fluid Mechanics, 716 (2013), pp. 228–250.

Interaction of Microplastics and Settling Sand

Vincent Laroche

August 20, 2024

1 Introduction

It is estimated that 10 million tonnes of plastic waste enter the world's oceans each year [3]. This comes from a variety of anthropogenic sources including consumer products, industrial runoff, and commercial fishing. Once in the ocean, larger plastic pieces will continuously be broken down to smaller sizes due to mechanical abrasion, exposure to UV radiation, and biological degradation [1], such that approximately 13.5% of oceanic plastic by mass can be classified as microplastic (<1mm) [6].

This plastic poses a grave threat to the environment, as it is typically either made of toxic material itself or covered in a toxic substance. Microplastics, when suspended in the ocean surface layer, are readily consumed by fish, krill, and other animals fundamental to the food chain. In addition to harming these creatures themselves, microplastics can be further passed along to humans where they accumulate in vital organs. This leads to a variety of negative health impacts including metabolic dysfunction, organ failure, neurotoxicity, and infertility [8].

1.1 Physical transport of microplastic

In order to quantify and predict the impact of plastics on the environment and human populations using numerical modeling, a robust physical description of microplastic transport is required, but this is an area that still has significant room for development [11]. Although the majority of plastic waste is buoyant [2], the plastic apparent in the ocean surface layer only accounts for ∼1% of the total estimated oceanic plastic [3], leaving the open question regarding the fate of the remaining 99%. The leading hypothesis is that much of this plastic ends up on the ocean floor, with many studies documenting accumulations of both buoyant and dense plastic in locations off the continental shelf [4]. Because 80% percent of plastic waste originates from land (versus offshore sources), turbidity currents have been suggested as one possible mechanism contributing to these seafloor accumulations of plastic [5]. A turbidity current can occur when suspended sediment, e.g., from a river outlet, creates a density imbalance with the ambient water, leading to the sediment-laden water propagating downslope and along the ocean floor. If plastics are present in the outcoming river water, it is possible that they are carried by the turbidity current and end up on the seafloor as well.

Pohl et al. (2020) explores the potential role of turbidity currents in the transport of microplastic in a laboratory setting [9]. In their setup, dense plastic of two types, elongated

fibers and more spherically shaped fragments, are mixed with sediment and then injected along the floor of a sloped tank. After all particles have settled, the fibers are found in greater concentrations buried among the sediment than the fragments are, suggesting that the fibers are more easily physically pushed downwards by the sediment particles due to their shape. In the present study, we explore a different mechanism (conglomeration, see Figure 1) as a potential factor in deposition of microplastic, specifically in the case of buoyant plastic. By this mechanism, sediment and plastic particles become attached to each other, forming a conglomerate. The sediment has a greater density than the buoyant plastic, causing the overall density of the conglomerate to be negatively buoyant. As such, the formation of these conglomerates can result in deposition of otherwise buoyant plastic. The actual mechanism behind the attachment of one particle to another is not fully understood. Current research suggests that conglomeration is caused by surface charges induced by the presence of water and surfactant [10], but this process is not the focus of the present study.

Conglomeration of buoyant plastic and sediment particles has been previously studied using laboratory experiments [10; 7]. Sutherland et al. (2023) used beaker experiments in which clay, plastic, and surfactant are stirred together in a beaker with water and then allowed to settled undisturbed (Figure 1a). Their results indicated that the clay and surfactant enhanced the deposition of microplastics. The authors of Kriaa et al. (2024) similarly conducted experiments in a beaker, using plastic and glass spheres as sediment (Figure 1b). While they saw conglomerates forming and settling to the bottom, they observed that small disturbances to the beaker would frequently result in conglomerates breaking apart, indicating that the conglomerates are very fragile. They also ran experiments of a turbidity current, which offered a less energetic turbulent event and saw greater plastic deposition.

While the beaker and turbidity current experiments described above provide useful results, we seek to examine the interaction of plastic and sediment in a more controlled experiment for the purpose of constructing a numerical model that describes plastic transport and deposition. We achieve this by allowing settling sand to pass through suspended microplastics in vertical tube experiments, which will be described in Section 3. Here, a key parameter we consider is the relative particle size between sediment and plastic. Work by Sutherland et al. (2023) and Kriaa et al. (2024) fell in a regime where sediment was smaller than plastic; in the present study we highlight a case where this is reversed (Figure 1c). Additionally, while both studies varied surfactant concentration, we do not explore this as an experimental parameter, although it could be an area of future work.

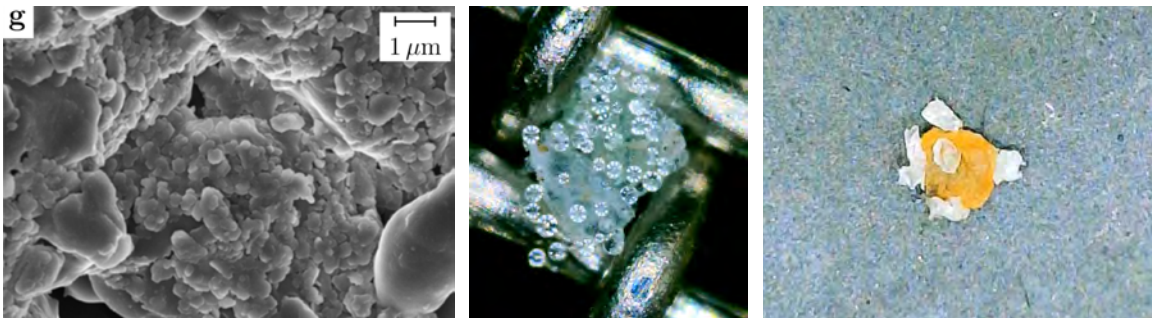

(a) (b) (c)

Figure 1: Examples of conglomerates formed by the adhesion of plastic and sediment. (a) Plastic fragment (mean $d_p = 83$ μm) with microscopic pieces of clay ($d_s < 1$ μm) attached to it [10]. (b) Plastic fragment (mean $d_p = 338$ μm) with glass spheres (mean $d_s = 75$ μm) attached to it [7]. The small ring of eight lights in each sphere are reflections of the microscope LEDs. (c) Sand grain (mean $d_s = 568$ μm) with multiple plastic fragments (mean $d_p = 215$ μm) attached to it.

2 Experimental Theory and Design

2.1 Population dynamics for continuum model

In order to relate a laboratory experiment to a numerical model, first consider standard governing equations for a multi-species model of particles in a continuum flow, defined as

$$\frac{\partial n_p}{\partial t} + \nabla \cdot (\mathbf{u} n_p) = -\alpha n_p n_s + \beta n_s n_c \,, \tag{1}$$

$$\frac{\partial n_s}{\partial t} + \nabla \cdot (\mathbf{u} n_s) = -\alpha n_p n_s + \beta n_s n_c \,, \tag{2}$$

$$\frac{\partial n_c}{\partial t} + \nabla \cdot (\mathbf{u} n_c) = +\alpha n_p n_s - \beta n_s n_c \,, \tag{3}$$

where n_p, n_s, and n_c represent the number density of the three species of particles in our experiments: plastic, sand, and conglomerates. The velocity field of the fluid is $\mathbf{u}$. The first term on the right-hand side ($\alpha n_p n_s$) represents formation rate of conglomerates due to collisions of plastic and sand. This term will depend on the amounts of plastic and sand, as well as some unknown coefficient α. This term is positive in the conglomerate evolution equation and negative in the plastic and sand equations since formation of a conglomerate will remove plastic and sand from their respective populations. Likewise, the second term on the right-hand side ($\beta n_s n_c$) represents destruction rate of conglomerates by collision with sand. As in the first term, this will depend on sand and conglomerate quantity and a coefficient β. While in reality there may be numerous additional terms incorporating the many complex interactions between particles, e.g., plastic colliding with a conglomerate and breaking it apart, plastic colliding with a conglomerate and becoming attached, two conglomerates colliding, etc., but the two terms shown here are sufficient for illustrating the mechanism explored in the present study. Implementing this model requires a closure for the unknown right-hand side terms, in particular the conglomerate production rate term.

2.2 Kinetic theory of particles

To estimate the rate of conglomerate production, we draw upon concepts from the kinetic theory of gases, which describes how gas molecules interact with each other. Although we are not working with gases, we are interested in particle-particle interactions, and we apply the ideas of kinetic theory in order to calculate the number of collisions occurring in the flow.

Consider an individual grain of sand as it travels through the suspended plastic particles as shown in Figure 2. Here, all particles, both sand and plastic, are assumed to be spheres. Plastic particles are stationary, while the sand particle moves with velocity u. The total distance traveled by the sand over an arbitrary time period t is the length ut. As the sand moves through the field of plastic, it "sweeps out" a cylindrical volume in which collisions with plastic will occur. The radius of this cylindrical volume is the combined radius of the two types of particles, $r = r_s + r_p$. Plastic particles whose center point lies within the cylinder will experience a collision with the sand, while those outside the cylinder will not (see annotated plastic particles in Figure 2). Thus, the total number of collisions can be calculated as the volume of the cylinder ($ut\pi\left(r_s + r_p\right)^2$) multiplied by the number of particles per unit volume,

$$n_{\text{collisions}} = ut\pi\left(r_s + r_p\right)^2 n_p\,. \tag{4}$$

The frequency of collision is likewise defined as

$$f_{\text{collisions}} = \frac{n_{\text{collisions}}}{t} = u\pi\left(r_s + r_p\right)^2 n_p\,. \tag{5}$$

Equations (4) and (5) apply to a single sand particle, so to account for all sand particles in the domain the rate of conglomerate production can be estimated by

$$\alpha n_p n_s = n_s f_{\text{collisions}} P\,, \tag{6}$$

where P represents the probability that an individual collision between sand and plastic particles results in the formation of a conglomerate. Note that the relationship between α and P is simply given by $\alpha = u\pi(r_s+r_p)^2 P$. Substituting this result back into Equation (3) yields

$$\frac{\partial n_c}{\partial t} + \nabla\cdot\left(\mathbf{u}n_c\right) = u\pi\left(r_s + r_p\right)^2 n_s n_p P - \beta n_s n_c\,. \tag{7}$$

Equation (7) can then be simplified in various ways. First, we neglect the second right-hand side term representing destruction of conglomerates due to collision with sand, which we expect to be small. We can also integrate over time and volume, leading to an equation for the total, final number of conglomerates,

$$N_{c,\text{final}} = \left(\frac{r_s + r_p}{r_{\text{tube}}}\right)^2 N_s N_p P\,, \tag{8}$$

where the radius of the tube r_{tube} has entered the equation due to volume integration.

In this equation, r_s, r_p, r_{tube}, N_s, and N_p are known quantities. P is unknown and $N_{c,\text{final}}$ will be measured experimentally, which is the primary focus of this project. We will measure $N_{c,\text{final}}$ by assuming that it is equal to the number of plastic particles deposited. In

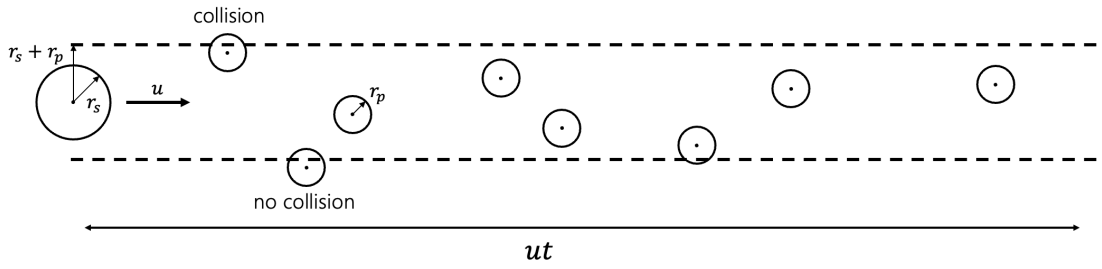

Figure 2: Hypothetical particle path for a single grain of sand traveling through a field of suspended plastic.

other words, we assume that each conglomerate forms as a result of a single plastic particle adhering to a single sand particle, and that if a plastic particle is present at the bottom of our experiment, it is there because it was part of a conglomerate.

Two important nondimensional parameters in this flow are the Stokes number, which describes to what degree a particle follows the flow, and the particle Reynolds number, which compares the particle motion to the effects of viscosity. These are defined as

$$St = \frac{ut}{l}, \qquad Re_p = \frac{ud_p}{\nu},$$

where u is particle velocity, t is a characteristic timescale of particle travel, l is a length scale of the flow, d is the diameter of the particle, and ν is the kinematic viscosity of the fluid. These parameters describe how particles interact with the flow and with each other, and are related to the collision probability P.

3 Vertical Tube Experiments

3.1 Procedure

The experiments described in this study are conducted in a vertical tube, as shown in Figure 3. The tube has an inner diameter of 5 cm, a length of 111 cm, a total volume of $V = 2.18$ L, and is made of hard plastic. First, the tube is aligned vertically and levelled, and a plumber's plug is inserted into the bottom end to seal it. Then it is filled roughly halfway with 1 L of fresh tap water that has been filtered and deaerated. Separately, another 1 L of filtered and deaerated freshwater is mixed in a large beaker with 10 drops (0.5 mL) of Kodak Photo-Flo surfactant (octylphenoxypolyethoxyethanol). Approximately 0.5 g of plastic is then added to the beaker and mixed until homogeneous. The plastic-laden water is poured from the beaker into the tube, with a squeezable wash bottle being used to rinse all plastic from the beaker. Roughly 100 mL of additional water is added until the tube is full. Then sand, typically 100 g, is poured into the tube through a funnel and quickly sinks to the bottom, bringing some plastic with it. The lower half of the tube is recorded with a 4K 60fps camera (iPhone 13 mini) in order to capture the settling sand. A lid is then placed on top of the tube to prevent dust contamination while the experiment is left to rest overnight. This allows sufficient time for any unattached plastic to rise to the water surface and for any conglomerates to settle to the bottom.

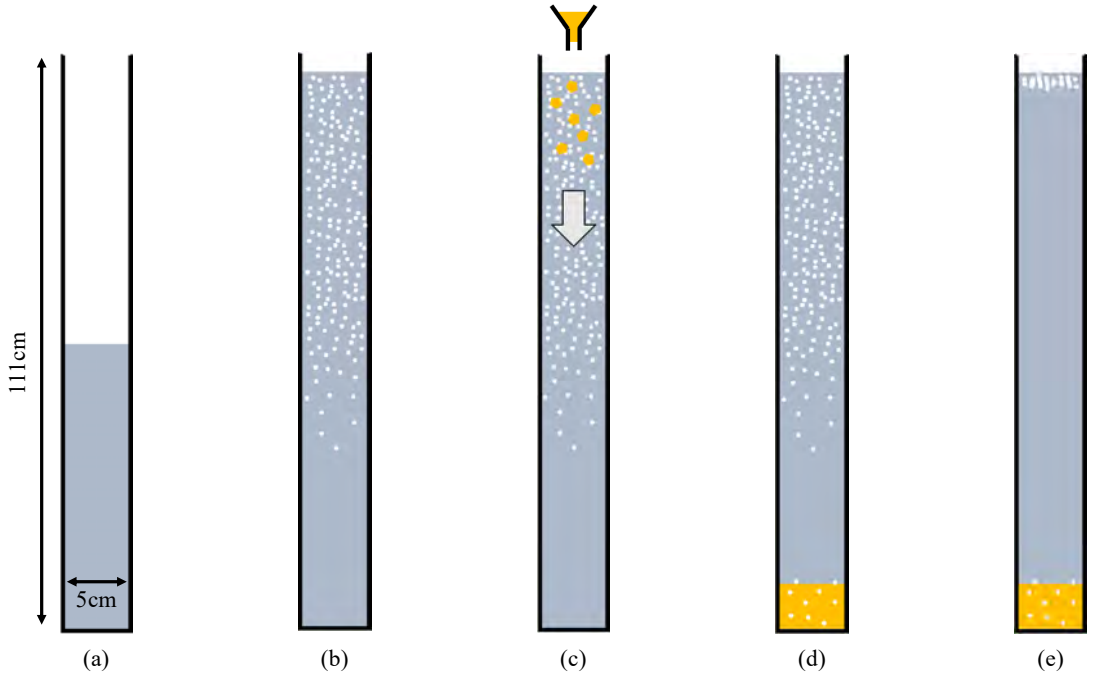

Figure 3: Step-by-step progression of the vertical tube experiments. (a) Tube half-filled with filtered and deaerated freshwater. (b) Upper half of tube filled with plastic-laden water. (c) Sand deposited in tube via funnel. (d) Sand accumulates at bottom of tube having transported some plastic with it. (e) All plastic has risen to top of tube after being left to rest overnight.

3.2 Data collection

Obtaining high-accuracy measurements of the plastic mass, particularly the plastic mass from the bottom of the tube, is the primary goal of the vertical tube experiments. While this is a straightforward objective, the procedure proved to be quite an extensive and delicate process, which we will describe in detail here.

As indicated in Figure 3e, the final state of an experimental run features an accumulation of plastic at the top of the tube and a mixture of sand and plastic at the bottom. In order to access the bottom contents, the rest of the tube must be carefully emptied in such a way that plastic from the top does not contaminate measurements of the bottom plastic. First, the top plastic is skimmed from the water surface and side walls using a combination of a silicone spatula, a plastic 60ml syringe, and a small pump. The plastic is collected on a sheet of filter fabric lining a mesh colander, allowing any water to drain out. Once the water surface is plastic-free, a siphon is used to remove the majority of the remaining water in the tube. This water is likewise deposited in the same filter-colander apparatus, ensuring that any lingering plastic particles are also collected. The tip of the siphon tube is positioned approximately 5cm above the sand level so that the bottom contents remain undisturbed during the siphoning process. All tools used up to this point (spatula, syringe, pump, siphon) are then disassembled and thoroughly rinsed inside-and-out with water that is then deposited in the filter.

Before collecting the bottom contents, a separate filter-colander apparatus is created using a clean sheet of fabric. The plug is removed from the bottom of the tube and the sand and plastic mixture are deposited into the new filter. Remaining sand stuck to the walls is removed and collected using the spatula and a small squeezable wash bottle.

With the tube now completely empty, the final step is to rinse the inner walls of the tube to dislodge any plastic left behind. This plastic is collected in the first filter-colander, which contains the rest of the top plastic.

Both sheets of filter fabric and their contents are then transferred to an oven, where they are dried at 49°C overnight. Once dry, the bottom contents are separated by size using a stack of sieves on a lab vibrator. As we discuss later, we run experiments with various combinations of sizes for the plastic and sand. The sieves are chosen such that there is always one level of separation between the minimum size of the larger particle and the maximum size of the smaller particle. For example, in a case with $d_s = 425{-}710$ μm and $d_p = 180{-}250$ μm (Exp. 7 in Table 1), we use sieves of sizes 425, 250, and 45 μm. In theory, all sand remains in the 425 μm sieve, the 250 μm sieve is left empty, and all plastic works its way down to accumulate in the 45 μm sieve. However, this is not always the case in practice. In our experiments, we see small amounts of sand present among the plastic even after sieving (see Figure 4). This can be attributed to how the sand was initially prepared. We use real sand that was first washed, dried, and sieved on its own in order to sort it into the desired size ranges. The sieving process was repeated a few times when preparing the sand, but it is still possible that the sand wasn't perfectly separated. In the quantities we use in each experiment (most commonly 100 g, or approximately $\sim$400,000 individual grains), it is inevitable that there are a handful of missized particles mixed in.

While the number of sand particles present among the plastic is relatively small, their contribution to the measured mass is non-negligible as they have a much larger density

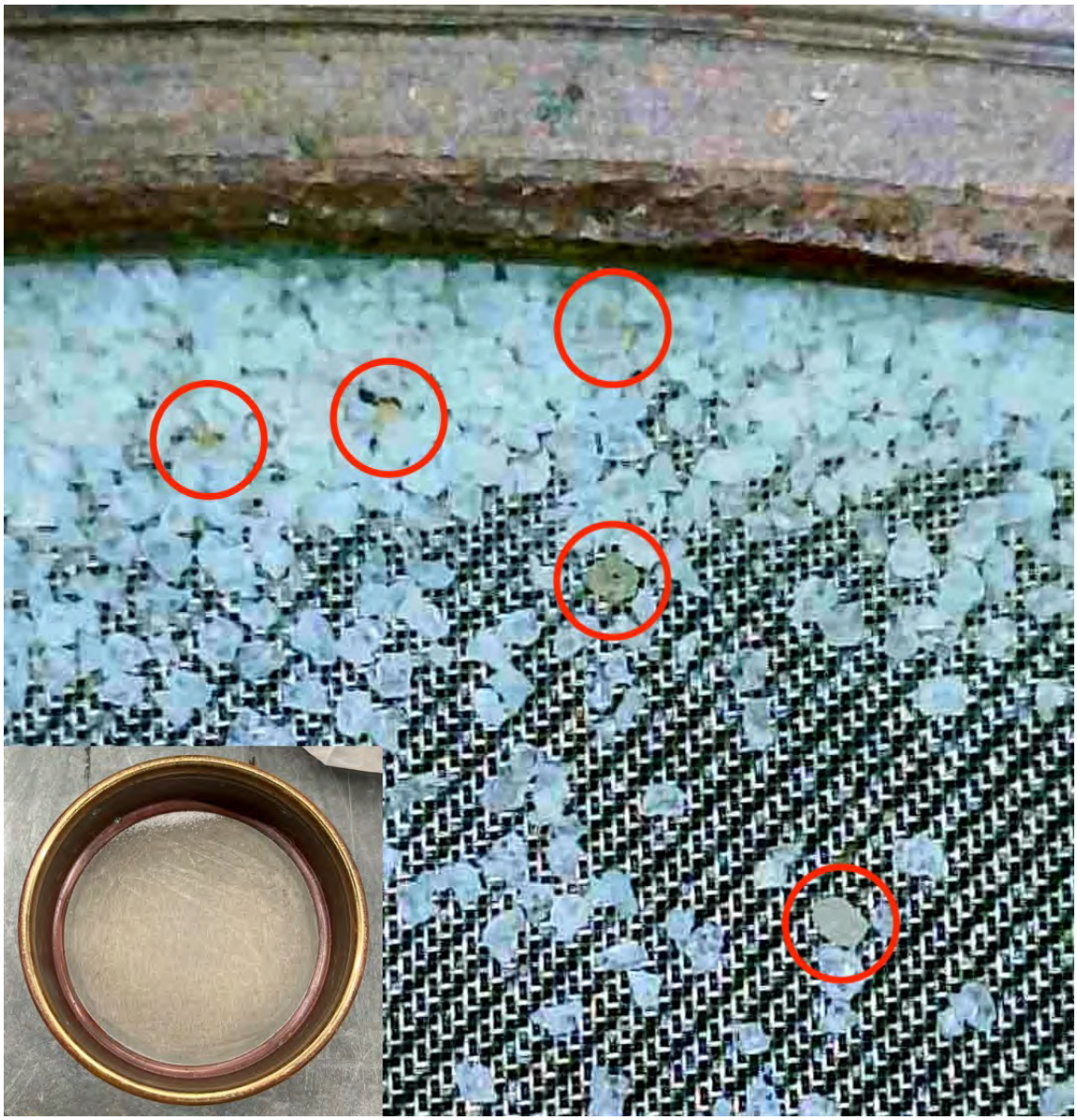

Figure 4: Post-sifting contents of a 45 μm sieve containing plastic with $d_p = 180{-}250$ μm. Note that there are a few similarly sized grains of sand among the plastic, circled in red. The inset in the lower left-hand corner shows the full sieve.

($\rho_s = 2500$ kg/m^3 versus $\rho_p = 930$ kg/m^3). Removing these sand particles poses a challenge because they cannot be separated from the plastic using size. Instead, we use density to separate the two types of particles by placing them back into water. The particles are mixed in a small beaker filled with 100 mL of freshwater and 5 drops (0.25 mL) of surfactant. The few remaining sand particles sink to the bottom of the beaker, allowing the plastic to be skimmed from the top. The extracted plastic is again collected on filter paper, dried in the oven, and finally weighed. The final measurements of plastic present at the bottom of the tube are reported as a percentage of total input plastic mass in Table 1.

In summary, running and collecting data from each experiment took about 5−6 hours to complete, spread out over a minimum of 3 days. Because the plastic needed to remain in the tube overnight in order rise to the surface, only one experiment could be run each day. Coupled with the fact that the experimental apparatus was not finalized until Week 8 of the program, this resulted in a relatively small number of experiments. Our priority was not to have a large amount of inaccurate data, but rather to have the highest quality measurements achievable, with all of the experiments presented in Section 4 having a plastic loss, defined as the percentage of plastic mass *not* recovered post-experiment, of 10% or less.

4 Results and Discussion

The parameters of each vertical tube experiment, including the dependent variable of plastic deposition at the bottom, are shown in Table 1. A typical example of one experiment (Exp. 7) is shown in Figure 5.

The figure shows the lower half of the tube, which is mostly devoid of plastic at first. Some plastic is visible near the midway point of the tube (top of the image in Figure 5), but there is a sizable region of clean water separating the plastic from the bottom. This prevents any accidental deposition of plastic before the experiment begins. Once we begin to add the sand, it takes anywhere from 20−120 seconds for all of it to reach the bottom, depending on funnel diameter, input mass of sand, and sand size. During this time, sand particles collide with plastic and form conglomerates, which deposit at the bottom of the tube. As the sand continues to settle, conglomerates are covered and locked in with the sand. Towards the end of the experiment, all sand has settled, and a few remaining conglomerates become visible in the water column (see Figure 5d). These conglomerates slowly sink and eventually come to rest atop the sand.

4.1 Formation of conglomerates

The first result from the vertical tube experiments is simply the fact that conglomerates *are* forming (see Figure 5e), just as in the previous work by Sutherland et al. (2023) and Kriaa et al. (2024). The figure shows grains of sand, usually tan or dark grey in color, joined with plastic particles, white in color and semi-translucent. In other words, our experiments confirm that conglomeration is indeed a mechanism that actively yields plastic deposition in a sediment-laden flow.

As an aside, the mechanism of physical burial set forth in Pohl et al. (2020) may also play a role here. In one experiment (Exp. 5) not shown here, plastic particles are visibly hit by and jostled around by sand in the flow. It is not clear whether these are

Exp.	Input Plastic [g]	Input Sand [g]	Plastic Diam. [μm]	Sand Diam. [μm]	Funnel Diam. [mm]	Bottom Plastic [%]
1	0.4939	94.0077	215	568	3.94	1.98
2	0.5072	100.1300	215	780	3.94	1.50
3	0.4938	100.1647	100	568	3.94	1.68
4	0.4997	100.0448	925	568	3.94	2.08
5	0.5074	99.1999	568	200	3.94	7.00
6	0.5099	99.8723	215	568	3.94	1.69
7	0.5079	100.0505	215	568	3.94	1.87
8	0.5011	188.6490	215	568	3.94	3.45
9	0.4899	50.1463	215	568	3.94	1.45
10	0.5005	99.9901	215	568	7.69	1.16
11	0.5000	101.6981	215	568	12.91	0.44

Table 1: Vertical tube experiment parameters. Particle diameters are calculated as the average of a range of values.

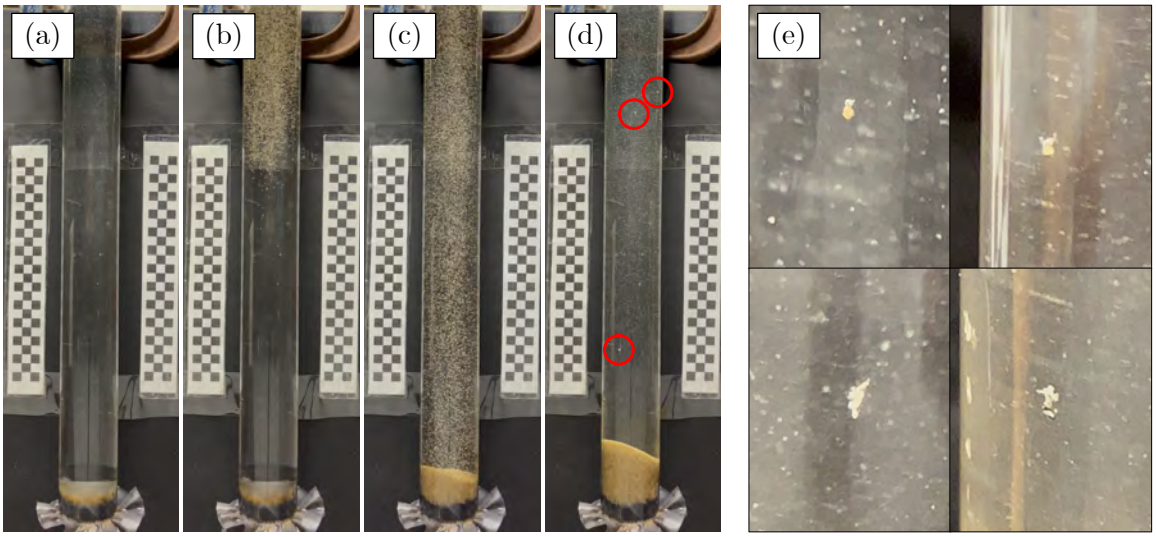

Figure 5: Step-by-step progression of a typical experiment (Exp. 7). The lower half of the tube is shown. (a) The tube immediately before sand has been added. (b) Sand makes its way down the tube, carrying plastic with it. (c) Sand begins accumulating on the bottom. (d) All sand has settled to the bottom. Conglomerates, which settle at slower rate, are circled in red. (e) Close-up in situ photos of individual conglomerates.

"clean" (no attachment with sand) buoyant pieces of plastic that are being transported downward by physical impact with sand or whether they are fully-formed negatively-buoyant conglomerates that are in the process of sinking regardless of further impact with sand. The formation of conglomerates does not rule out burial as a contributing factor to plastic deposition; we will discuss this further in Section 4.2.2.

4.2 Experimental parameters

Based on the form of Equation 8, the three experimental parameters varied in this study were: particle size, sand concentration (controlled by funnel diameter d_f), and sand quantity. The case in which $d_p = 215$ μm, $d_s = 568$ μm, $m_s = 100$ g, and $d_f = 3.94$ mm acted as a base case around which the parameters were varied. The base case was conducted a total of three times (Exp. 1,6,7 in Table 1) in order to obtain an estimate for the repeatability errors of the experiment. The error bars in the following figures are calculated as one standard deviation of the plastic deposition percentage value for the base case experiments.

4.2.1 Particle size

Varying particle size was the primary parameter motivating this study. Prior studies on plastic-sediment conglomerates used sediment particles *smaller* than the plastic fragments [10; 7]; we reverse this with sand *larger* than our plastic in an effort to further explore this parameter space, although two cases with $d_p/d_s > 1$ are also included.

Increasing the size of the plastic relative to the sand leads to greater plastic deposition on the bottom of the tube (see Figure 6). One physical explanation for this is that settling velocity is proportional to the square of particle diameter. Large sand grains move with higher velocities, meaning that the collision energy between sand and plastic is greater as well. It is possible that in the cases of $d_p/d_s < 1$, the collision between a large grain of sand and small plastic fragment is not suitable for forming a conglomerate. Existing conglomerates may also be ripped apart by drag forces from the water, which will also be elevated in cases with large sand. This phenomenon was visually observed in some experiments where a slowly settling conglomerate spontaneously breaks, sending the plastic back towards the top of the tube while the sand continues to settle.

Another contributing factor to the trend in Figure 6 could be the difference in surface roughness between the sand and plastic used. The sand is real sand that has been worn down by abrasion over time. The surface is relatively smooth and uniform; there is not much concavity. The plastic, on the other hand, was prepared from larger pieces of plastic (nurdles a few millimeters in diameter) that were ground down to the desired size ranges using a cryogrinder. The resulting plastic fragments are generally rougher than the sand. The plastic's surface is jagged and covered in small cavities. Thus, when the sand is small relative to the plastic ($d_p/d_s > 1$), the two can attach easily because sand becomes wedged in the cavities on the plastic's surface. When the sand is relatively large ($d_p/d_s > 1$), plastic can attach to the smooth surface of a sand grain, but it may be attached only at one contact point - a very weak connection.

These results seem to be consistent with previous work by Kriaa et al. (2024), which saw an even greater amount of plastic deposition ($\sim$15%) with higher diameter ratio ($d_p/d_s = 4.5$) [7]. However, the experiments conducted by Kriaa et al. (2024) used a turbidity current

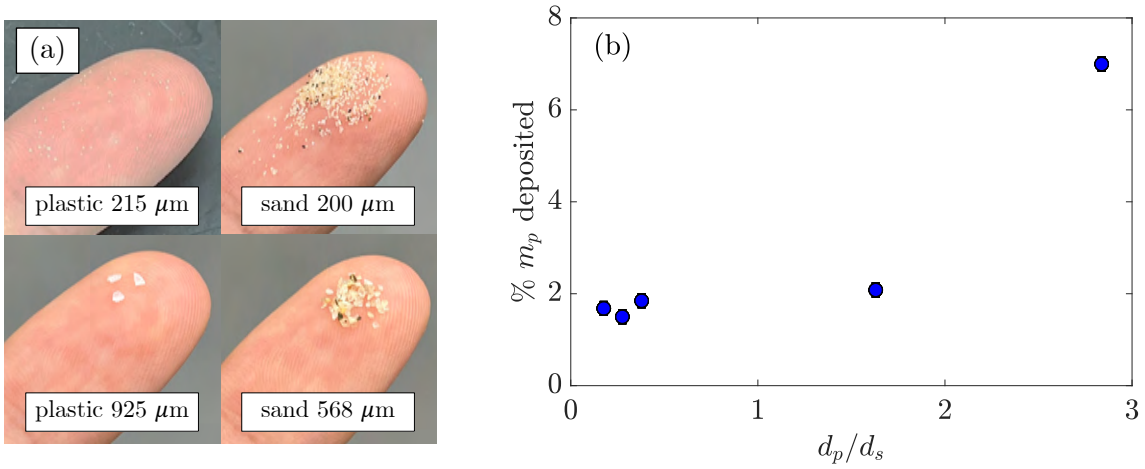

Figure 6: (a) Examples of different-sized particles used in the experiments, with a fingertip for scale. Not all sizes used are shown here. (b) Relationship between plastic deposition and ratio of average sand and plastic diameters. Percent plastic deposition is calculated as the mass of plastic found at the bottom of the tube divided by total input plastic mass.

rather than a vertical tube to explore the interaction of microplastics and sediment, so the two results are not directly comparable.

4.2.2 Sand concentration

Practically, we varied the sand concentration by varying the outlet size of the funnel used to pour in the sand (Figure 7a,b). Of the different experimental parameters in this study, we have the weakest understanding of how we expect the sand concentration to affect plastic deposition. Using a very rudimentary approach, we would expect more concentrated sand to cause more collisions with plastic and thus more conglomeration. Instead, the data in Figure 7c shows a clear linear trend of decreasing deposition with sand concentration. There could be several different reasons for this trend. Although there are more collisions and more chances to form conglomerates, there must also be more collisions between sand and conglomerates that may break the conglomerates apart. The process of conglomerate destruction is not well characterized in this study; we have neglected it when considering the model laid out in Section 2. Another potential explanation is that the Stokes number ($St = ut/l$, where u is particle speed and t is settling time) of the plastic particles has decreased. With more sand in the flow, it's possible that the sand moves in larger collections and induces larger eddies in the flow than in a low concentration case. Larger eddies indicate a large turbulent length scale l, which reduces the effective Stokes number of the plastic - meaning it is less likely to cross streamlines and collide with sand particles. In this explanation, there are actually fewer collisions occurring as concentration increases, so less conglomerates form.

An interesting takeaway from Figure 7c is that our results seem to contradict previous work demonstrating physical burial as the primary mechanism of plastic deposition [9]. Experiments conducted by Pohl et al. (2020) showed that long and stringy plastic fibers were

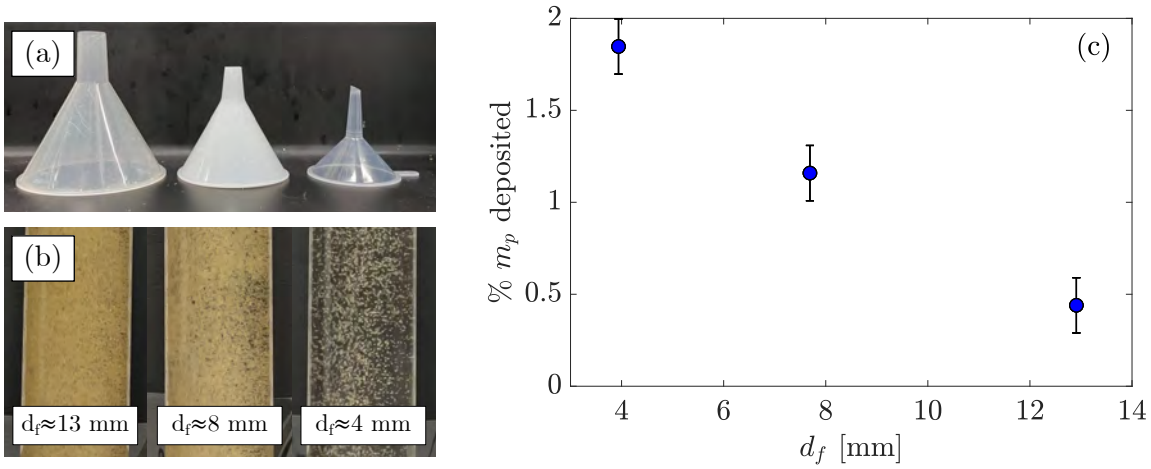

Figure 7: (a) Three different funnels used in the experiments. (b) Instantaneous snapshots of experiments showing sand concentration corresponding to each funnel. (c) Relationship between plastic deposition and funnel diameter. Percent plastic deposition is calculated as the mass of plastic found at the bottom of the tube divided by total input plastic mass.

deposited at a higher rate than more uniformly shaped fragments, suggesting that sinking sediment particles were physically pushing down the plastic and were able to catch on the fibers to a greater degree than the fragments. In our experiments, if this burial mechanism were at play, we would expect that increasing sand concentration would increase the amount of plastic deposition - the greater number of collisions would provide more opportunities to force the plastic downwards. However, our results show the opposite. The fact that deposition *decreases* with sand concentration reinforces our hypothesis that the mechanism of conglomeration can be more important than burial in the process of sediment-aided plastic deposition, particularly in the case of buoyant plastic as in the present study.

4.2.3 Sand quantity

It must be emphasized that the sand quantity is a different parameter from the sand concentration. Three different total masses of sand are used in the experiments (Figure 8a), but the sand concentration (set via funnel diameter) is kept constant. With a constant flow rate, changing the sand quantity is equivalent to changing the duration of the experiment.

Varying the sand quantity should have the most straightforward effect on plastic deposition: the experiment lasts longer, there are more opportunities for collision and more chances for conglomerates to form. From an analytical standpoint, this is shown in Equation 8. There is a linear relationship between the number of conglomerates formed and the number of sand particles N_s. Here we estimate N_s using the known density, mass, and approximate volume of the sand. The data in Figure 8b confirms this relationship with a monotonically increasing trend.

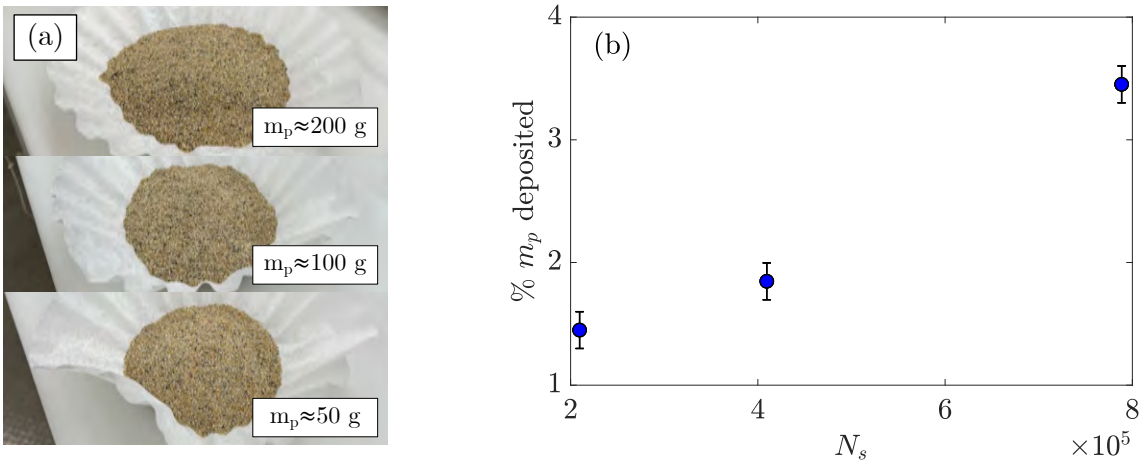

Figure 8: (a) Different sand quantities used in the experiments. (b) Relationship between plastic deposition and number of sand particles as estimated from the mass. Percent plastic deposition is calculated as the mass of plastic found at the bottom of the tube divided by total input plastic mass.

4.3 Estimation of P

As discussed in Section 2, using measurements of plastic deposition to estimate unknown coefficients is necessary for closure of a numerical model. Using Equation 8 and the input parameters, a value for the probability coefficient P can be calculated in each experiment (Figure 9).

In theory, P should reflect the fundamental interaction between one grain of sand and one plastic particle colliding - it should depend solely upon factors such as particle sizes, speed of collision, surface roughness, relative orientation of motion, particle spin, etc. Most of these parameters are not explored in this study because they would be too difficult to measure in our experimental setup. Among the parameters we *do* study here, particle size should influence P, while the concentration of sand and the input sand mass should not. As shown in Figure 9, P decreases with relative particle size. When plastic is large compared to sand, P is relatively small. The physical process that explains this relationship is not clear. It is possible that small sand grains simply deflect off of large plastic particles at a greater rate than when the sizes are reversed. P also decreases with sand concentration and input sand, although these trends are even less explainable using physical reasoning. The inherent challenge is that we attempt to make estimates of a small-scale parameter P that the interaction of individual sand and plastic particles, but we do so using data collected from the bulk interaction between many sand and plastic particles. As a result, these bulk parameters (concentration, input sand) show up in the data for P. Despite the apparent disagreement with theory, we still see very consistent results for the estimation of P. The value of P is $\mathcal{O}(10^{-4})$ across all experiments.

Looking beyond the immediate study presented here, P is a remarkably useful parameter because it informs a general numerical model which can then be applied to simulate any flow involving plastic and sand particles. As laid out in Section 2, P can be used to calculate

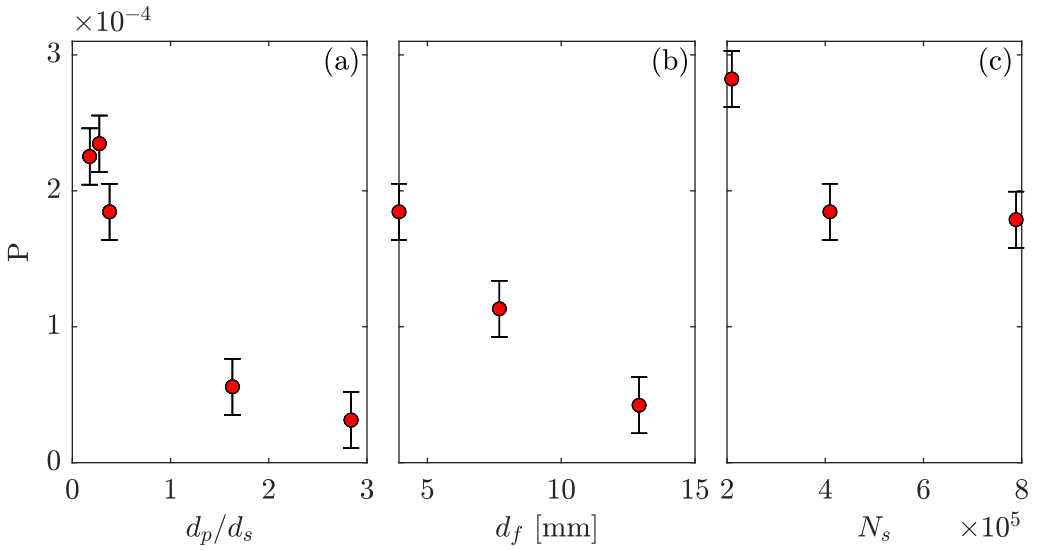

Figure 9: Estimates of P from each experiment, varying with the three independent parameters (a) particle size ratio, (b) funnel diameter, and (c) amount of sand.

the coefficient $\alpha = u\pi(r_s + r_p)^2 P$, which directly defines the conglomerate production rate term. A complementary extension to this study would involve running simulations with $P \sim 1 \times 10^{-4}$ and comparing to experimental data. The value of P could also be varied in order to explore how this parameter affects the behavior of particles in a simulation context.

4.4 Challenges and experimental error

In addition to the numerical data, another extremely valuable result is the experience and knowledge gained regarding the experiment itself. The vertical tube experiment presented here is the cumulative result of a summer-long iterative process that built upon many failed experiments. Initial tests with our particles (sand $d_s = 568$ μm, plastic $d_p = 215$ μm) were actually conducted as a turbidity current, although the sand proved to be too large to drive the flow in the available tank. The settling velocity of the sand was too high, so the sand would completely settle to the bottom of the tank before the turbidity current could propagate horizontally. At one point, the vertical tube experiment involved preloading sand at the bottom and plastic at the top, followed by flipping the entire tube upside down. This method proved to be unreliable due to large air bubbles and significant amounts of plastic sticking to the plug in the end of the tube.

The vertical tube experiment is still in active development, and there are remaining unaddressed experimental considerations worth mentioning. Some of the most prominent challenges and sources of error in conducting the experiments are listed here:

1. The tube is shaken slightly during extraction of plastic from the top, causing plastic along the sand's surface to dislodge and float away (Figure 10a). Similar to what was reported in Kriaa et al. (2024), even slight disturbances are capable of breaking

apart conglomerates, which are held together by very fragile bonds. Since most of the deposited plastic is embedded beneath layers of sand, this phenomenon is likely only a small contribution to the experimental error.

2. Plastic particles become trapped on the tube's side walls due to air bubbles and imperfections in the tube (Figure 10b). In theory this impacts the concentration of plastic in the tube, although it is likely a minimal effect. During preparation of the experiment, a long stick is used to agitate and remove bubbles on the sides which would interfere with the particles in the tube, but not all bubbles could be eliminated. and would obscure filming of the experiment. Completely removing this as a source of error could require leaving water in the tube to deaerate or finding a new tube of a different material.

3. Even without external disturbances, conglomerates break apart over time (Figure 10c). Because conglomerates have a smaller combined density than the sand alone, they sink slower and as a result end up on top of the bottom sand. There is no sand above the conglomerates to hold them in place, so if the fragile bonds holding sand and plastic particles break at any point during the overnight waiting period, the separated plastic will float back to the water surface. This sets forth an interesting question: Should these transient conglomerates be included in measurements of plastic deposition, and if so, how can those measurements be achieved? If we consider these experiments as a proxy for plastic deposition in the ocean, then it seems logical to only measure plastic that has been carried to the bottom and actually remains there in the long term. However, since we seek to estimate a probability of conglomerate formation, the transient conglomerates *should* be measured, as each one represents a successful collision between sand and plastic regardless of whether or not the two remain attached after the experiment has ended. Measuring the transient conglomerates is a challenge in and of itself. Some time must be given after the experiment ends for all the loose plastic to rise to the top so that it can be collected. During this time, it is inevitable that some conglomerates break apart. It is possible that there is an optimal window of time where most of the loose plastic has reached the top and most of the transient conglomerates are still intact; identifying this window would certainly require additional testing.

   It is worth noting that the case in Figure 10c (Exp. 4) is one specific size combination that led to a large number of conglomerates resting atop the sand. Most cases only had a few conglomerates atop the sand (see Figure 10a again for example), so it is unlikely that this was an issue in the majority of the experiments.

4. When not removed entirely, plastic from the top of the tube can contaminate measurements of bottom plastic (Figure 10d). The plastic remains on the water surface and is transported downwards with the water level during siphoning. This is plastic that did not reach the bottom as a sinking conglomerate, but it is still counted among the deposited plastic. As in the previous item, Figure 10d shows an extreme example; in most cases there was a minimal amount of top plastic left on the water surface post-siphoning. In one case where the plastic was large enough (Exp. 4), the plastic particles on the surface were counted individually before draining the bottom of the

tube. When compared to the total number of plastic particles recovered from the bottom, the top plastic only accounted for 11% by number. This estimate suggests that contamination by top plastic is not a major issue, although future work should aim to either reduce this error or improve quantification of the contamination.

5. The most consistent challenge throughout the development of the experimental apparatus and procedure was minimizing plastic loss. Reducing the amount of plastic lost due to error is essential for building confidence in our results, which center on accurate measurements of plastic deposition. Because plastic deposition is a relatively low proportion of input plastic mass (typically <5%), having significant plastic loss is unacceptable. Figure 11 shows how plastic loss improved with time, from as high as 20% to consistently below 5% in the last several experiments. This improvement can be attributed to changes in the setup and procedure, as well as the simple fact of having more practice handling the plastic with each new experiment.

5 Conclusion

In order to explore the processes involved in sediment-aided microplastic deposition, we conduct laboratory experiments in which sand was allowed to settle through plastic-laden water in a vertical tube. We identify conglomeration of individual sand and plastic particles as a mechanism by which plastic is transported to the bottom of the experimental setup. Motivated by the equations for a simple particle transport flow model, we vary the relative sizes of the plastic and sand, the concentration of sand, and the overall quantity of sand in the experiments. Increasing the plastic-to-sand size ratio yields greater deposition of plastic, likely due to smaller sand settling velocities. Higher concentrations of sand in the flow inhibit plastic deposition, indicating that conglomeration may be the dominant mechanism involved rather than physical burial. Increasing the sand quantity corresponds to a roughly linear increase in deposition, which is to be expected from theory. The experimental data is also used to estimate a universal probability coefficient for a numerical model, with all parameter cases giving a consistent result to one order of magnitude.

Due to the difficulty in obtaining high-quality measurements of plastic deposition, few experiments were conducted. Immediate future work on this topic should include running additional experiments to further map out the relationships between plastic deposition and the independent parameters. Other extensions of this project could examine the effect of surfactant, running complementary simulations, or could involve designing a related experiment to study the process of conglomerate destruction.

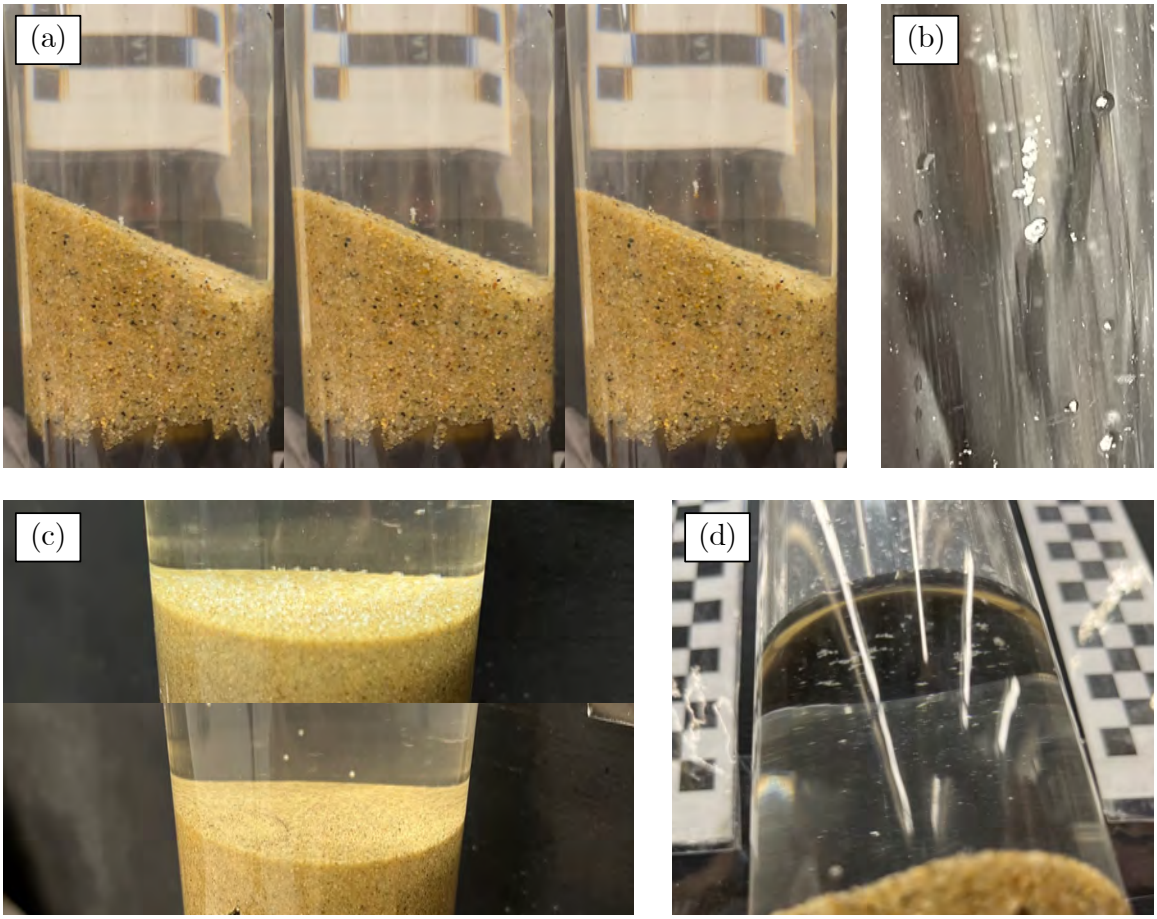

Figure 10: Challenges and sources of error in vertical tube experiments. (a) Conglomerates on the sand surface are dislodged by small motions during extraction of top plastic. The image shows one very large conglomerate as well as many other plastic particles floating away after a small shake to the tube. (b) Plastic attached to the side wall of the tube after draining all the water out. (c) Sand surface immediately after experiment completion and after experiment has been left overnight. The significant number of conglomerates present resting on the sand have broken apart, allowing the plastic to float back to the top of the tube. (d) Plastic on the water surface after the majority of the water has been siphoned from the tube. This plastic originated from the top of the tube and was carried down along with the water level. If collected with the rest of the bottom contents, this plastic contaminates the measurements of deposited plastic.

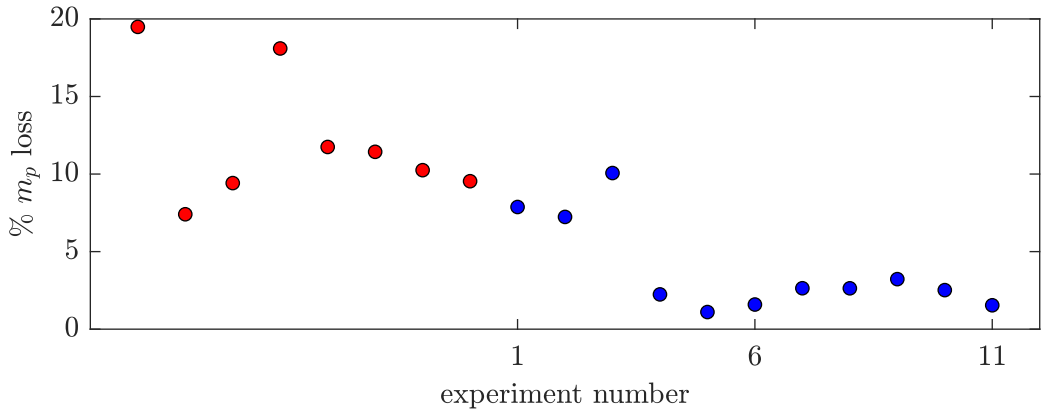

Figure 11: Percentage plastic loss, defined as the plastic mass *not* recovered during data collection divided by input plastic mass. Unlabelled data shown in red represents preliminary experiments conducted before the apparatus and procedure were finalized. Data in blue corresponds to the experiments listed in Table 1.

6 Acknowledgements

I would like to thank Claudia Cenedese, Jim McElwaine, and Bruce Sutherland, my advisors for this summer. Their guidance was invaluable in seeing this project through. Anders Jensen helped in design and construction of the experiment. I would also like to thank Basile Gallet and Edgar Knobloch for their engaging lectures, and Greg Chini and Bruce for ensuring the program ran smoothly while giving us such a wonderful summer experience.

References

[1] A. Andrady, *Microplastics in the marine environment*, Marine Pollution Bulletin, 62 (2011), pp. 1596–1605.

[2] R. Geyer et al., *Production, use, and fate of all plastics ever made*, Science Advances, 3 (2017).

[3] J. Jambeck et al., *Plastic waste inputs from land into the ocean*, Science, 347 (2015), pp. 768–771.

[4] I. Kane and M. Clare, *Dispersion, Accumulation, and the Ultimate Fate of Microplastics in Deep-Marine Environments: A Review and Future Directions*, Frontiers in Earth Science, 7 (2019).

[5] I. Kane et al., *Seafloor microplastic hotspots controlled by deep-sea circulation*, Science, 368 (2020), pp. 1140–1145.

[6] A. Koelmans et al., *All is not lost: deriving a top-down mass budget of plastic at sea*, Environmental Research Letters, 12 (2017).

[7] Q. Kriaa et al., *Transport and aggregation of microplastics in experimental turbidity currents*, 2023 WHOI GFD Proceedings Volume, (2024).

[8] Y. Li, *Potential Health Impact of Microplastics: A Review of Environmental Distribution, Human Exposure, and Toxic Effects*, Environment Health, 1 (2023).

[9] F. Pohl et al., *Transport and Burial of Microplastics in Deep-Marine Sediments by Turbidity Currents*, Environmental Science Technology, 54 (2020), pp. 4180–4189.

[10] B. Sutherland et al., *Suspended clay and surfactants enhance buoyant microplastic settling*, Communications Earth Environment, 4 (2023).

[11] E. van Sebille et al., *The physical oceanography of the transport of floating marine debris*, Environmental Research Letters, 15 (2020).

Numerical Experiments on the Stability of the Spicy Kolmogorov Flow

Ishwari Mulkalwar

August 20, 2024

Abstract

The density of seawater is controlled by two components that diffuse at different rates: heat in the ocean diffuses a hundred times faster than salt. This makes the ocean prone to double diffusive instabilities in which spice—the orthogonal variable to density—is an active contributor to diapycnal mixing. Stratified turbulence has also been shown to mix temperature and salinity differently in numerical and laboratory experiments as well as ocean observations. These effects influence our choice of mixing parameterizations but are generally omitted from both large-scale ocean models and small-scale idealized turbulence models. Here, we numerically investigate the effects of differing diffusivities in a two-dimensional turbulence model of the stratified Kolmogorov flow as seen in Balmforth & Young (2002), now stratified by both temperature and salinity. Linear stability analysis reveals that the flow supports two distinct instabilities: a monotonic mode resembling the classical shear instability of the unstratified flow, and a slower-growing oscillatory mode arising from stratification and differential diffusion. We demonstrate an equivalence between this model and the linear stability of flows stratified in a single scalar with an intermediate diffusivity between heat and salt, and propose an effective Prandtl number for the spicy flow based on scalar variance budgets. At low Reynolds numbers, numerical simulations confirm linear stability predictions through the emergence of finite-wavelength billows in the monotonic regime and long-wavelength oscillations in the oscillatory regime. For the monotonic mode, the density ratio plays an analogous role in setting scalar gradients and dissipation rates to the Prandtl number in the singly-stratified fluid, indicating that the leading-order effects of spice can be formulated under an effective Prandtl number in this weakly turbulent regime.

1 Background

Double diffusion, which occurs when the density of a fluid is controlled by two components diffusing at different rates, has been known for several decades now to be a source of turbulent mixing in the ocean. The density of seawater is most saliently controlled by temperature and salinity which have markedly different molecular diffusivities, with heat diffusing a hundred times faster than salt. As early as 1960, Melvin Stern argued that these two orders of magnitude between diffusivities allow the slow-diffusing component to "preserve" the density of a displaced water parcel, leading to interesting and perhaps unintuitive instabilities driven by molecular diffusion [18].

The earliest observations of these structures come from the laboratory, seen in finger-like intrusions of a denser fluid into an underlying lighter fluid in a temperature-stratified system. This behavior results from the salt-finger instability. In a stably stratified system with warm and salty water over cold and fresh water, imagine perturbing a parcel slightly downwards: the temperature of the parcel equilibrates faster with its colder and fresher surroundings than its salinity. The parcel is then saltier and heavier than its surroundings and keeps sinking under gravity, creating "salt-fingers" protruding into the fresher fluid. This process takes an already stable density configuration to one with an even lower center of mass, releasing potential energy. Counter-intuitively, diffusion thus acts towards *creating* density gradients.

This is the case when the slow diffuser is the destabilizing component (salty over fresh); the other kind of double-diffusive instability occurs when the fast-diffusing component is unstably stratified. When a parcel is disturbed downwards in a cold and fresh over warm and salty configuration, the parcel is fresher than its surroundings after its temperature equilibrates and thus is more buoyant and rises. As it is warmer than the water it is rising into, it overshoots its original position, until its higher salinity makes it sink again. This causes an oscillatory instability that keeps growing in amplitude, which is known as diffusive convection (also known as semiconvection in some contexts).

1.1 The density ratio and double-diffusive regimes

A useful measure of the stratification pattern is the density ratio R_ρ which depends on the local large-scale gradients in T and S. It is defined as

$$R_\rho = \frac{\alpha \overline{T_z}}{\beta \overline{S_z}}, \tag{1}$$

where α and β are the thermal expansion and haline contraction coefficients respectively, and ($\overline{T_z}$, $\overline{S_z}$) are the background vertical T and S gradients[1] (note that α and β are both defined to be positive values). The salt-fingering case happens when $\overline{S_z} > 0$ (destabilizing) and $\overline{T_z} > 0$ (stabilizing), i.e., for positive values of R_ρ. Positive values can also indicate diffusive convection, with $\overline{S_z} < 0$ (stabilizing) and $\overline{T_z} < 0$ (destabilizing). This ambiguity has led to another quantity, called the Turner angle[2], to be commonly used to characterize double diffusive regimes. In terms of the density ratio, the Turner angle is given by

$$R_\rho = -\tan(Tu + 45^\circ), \tag{2}$$

ranging from 0 to 2π. Figure 1 shows the double diffusive regimes described by the Turner angle. As the buoyancy is given by

$$b = g\alpha T - g\beta S, \tag{3}$$

[1] We can also define a horizontal density ratio based on horizontal T and S gradients, this is often used to quantify thermohaline compensation across fronts. Horizontal gradients lead to instabilities like interleaving currents which can drive double-diffusive mixing in large parts of the ocean, but that has not been the focus of this project.

[2] Named after J. Stewart Turner, the principal lecturer at the GFD school in 1972, where he demonstrated mixing experiments reportedly taught to him by G. I. Taylor.

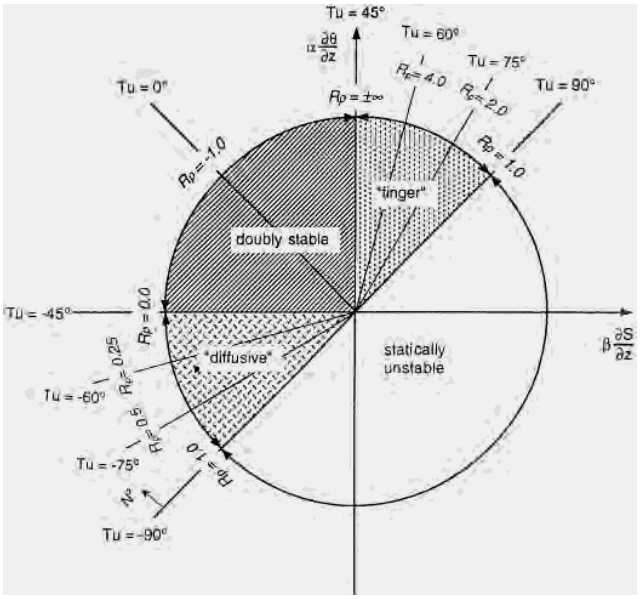

Figure 1: A sketch of the Turner angle with the density ratio showing different double diffusive regimes. Tu values between $-90°$ and $-45°$ are favorable to diffusive convection, and between $45°$ and $90°$ can lead to fingering instability. For Tu between $-45°$ and $45°$, the water column in stable in both T and S.

strongly double-diffusive regions that have values of R_ρ close to one, where both salinity and temperature gradients are equally strong, show significant density compensation [7]. (At very small scales, density gradients are destroyed by viscous effects which gives a density ratio of almost exactly one.) Negative values of R_ρ indicate either a top-heavy (unstable in both T and S) or a doubly stable (stable in both T and S) configuration. Global climatological Turner angle atlases show that significant parts of the thermocline in the three major ocean basins are susceptible to diffusive convection or salt fingering instabilities [21], with the rest having a doubly stable density profile.

1.2 Buoyancy–spice formulation

Strong T–S compensation in the ocean motivates the definition of an additional variable called "spice" that captures the uncompensated part of T–S variance. Using a linear combination of T and S, spice is defined orthogonal to buoyancy as

$$\gamma = g\alpha T + g\beta S. \tag{4}$$

Warm and salty water is called spicy, and cold and fresh water is minty. The advection-diffusion equations for temperature and salinity

$$\partial_t T + (\mathbf{u}\cdot\nabla)T = \kappa_T \nabla^2 T, \tag{5}$$

$$\partial_t S + (\mathbf{u}\cdot\nabla)S = \kappa_S \nabla^2 S \tag{6}$$

can be rewritten in terms of buoyancy and spice to give

$$\partial_t b + (\mathbf{u} \cdot \nabla) b = \frac{\kappa_T + \kappa_S}{2} \nabla^2 b + \frac{\kappa_T - \kappa_S}{2} \nabla^2 \gamma, \tag{7}$$

$$\partial_t \gamma + (\mathbf{u} \cdot \nabla) \gamma = \frac{\kappa_T + \kappa_S}{2} \nabla^2 \gamma + \frac{\kappa_T - \kappa_S}{2} \nabla^2 b. \tag{8}$$

When $\kappa_T = \kappa_S = \kappa_b$, equation 7 becomes the standard advection-diffusion buoyancy equation

$$\partial_t b + (\mathbf{u} \cdot \nabla) b = \kappa_b \nabla^2 b \,,$$

and spice is considered a passive scalar that does not affect the evolution of buoyancy. However, when $\kappa_T \neq \kappa_S$, the spice contribution to buoyancy is nonzero and thus spice actively stirred in a double diffusive fluid. Although the equations for the numerical simulations in this project have been written in T and S, the buoyancy and spice space provides more intuitive descriptions of the energetics, as will be described later.

1.3 The cascade of spice variance and mixing parameterizations

Double diffusion arises from differences in the molecular diffusivities of salt and heat, which are on the order of 10^{-9} and 10^{-7} $\mathrm{m}^2/\,\mathrm{s}$, respectively. Double-diffusive instabilities therefore occur on the microscale and the finescale and can contribute significantly to the local diapycnal buoyancy fluxes. In fact, in regions where internal wave-driven shear turbulence is not very strong, double diffusive turbulence can be the main driver of small-scale buoyancy mixing [13]. However, the role of these mechanisms at larger scales and the net effect this behavior has on the global ocean circulation remain unclear.

The temperature-salinity relationship is largely set at the surface mixed layer, where density-compensated T-S fronts (that is, fronts with small density gradients but large spice gradients in the horizontal) are a prevailing feature [7]. This compensated thermohaline variance that extends over isopycnal surfaces can then be acted upon by mesoscale eddies that stir along isopycnals, cascading spice gradients to smaller horizontal and vertical scales. Smith and Ferrari ([17]) showed that the passive stirring of spice by quasi-geostrophic eddies can effectively produce vertical gradients by creating thin tracer filaments, that could then be dissipated by a vertical turbulent diffusivity K_V, arresting the forward cascade of $T - S$ variance. However, instead of a constant K_V that assumes variance destruction by wave breaking-generated isotropic turbulence, it is also possible that thermohaline gradients are ultimately dissipated through the active process of double diffusive convection. Middleton et al. ([14]) estimated the dissipation rates associated with pure double diffusive turbulence acting on spice gradients set by large-scale stirring. They found that these rates agreed well with microstructure measurements made in the Chukchi Sea, Alaska, especially in regions where conventional shear-driven turbulence was considered subdominant. Double diffusive instabilities can thus be brought on by eddy-stirring rather than just background T-S gradients, highlighting the possibility that double diffusion may be far more widespread globally than what our conventional Turner angle maps predict.

This contributes to the challenges in estimating and parameterizing the vertical diffusivity and illustrates how little we understand about the exact mechanisms that lead to

diapycnal mixing in the ocean. Even the traditional pathway of mixing directly driven by internal wave shear is now believed to be an incomplete description—the forward cascade to small scales is suspected to occur through interaction with intermittent patches of turbulence characteristic of the LAST regime (layered anisotropic stratified turbulence) [5] [4]. The mixing efficiency Γ—a quantity that measures how much energy is expended in changing the background potential energy[3] via mixing, often modeled as the mixing parameterization in place of K_V—is extensively prescribed in large-scale ocean models as a constant value of 0.2. However, estimates of Γ vary quite widely between observations, laboratory studies and numerical experiments [10]. In the presence of double diffusive instabilities or differential restratification, the mixing efficiency can be negative, implying a kind of "un-mixing". Improving our understanding of the mixing processes at LAST scales, like whether spice is stirred actively or not in stratified turbulence, can help bridge this lack of consensus.

1.4 The doubly stable case

The doubly stable case with stabilizing mean gradients in both T and S is not expected to be subject to double diffusive instabilities, as there is no further potential energy to be released. However, double diffusive instabilities can still arise from T-S gradients being locally unstable or unresolved, or from the influence of horizontal temperature and salinity gradients leading to interleaving instability [19].

Even when double diffusion itself is not the source of turbulence, mechanical turbulence can still transport T and S at different rates because of their different molecular diffusivities. This is known as differential diffusion; it has been observed in the preferential transport of temperature over salinity ($K_T > K_S$) in several numerical and lab experiments, and some oceanic observations [9]. Jackson and Rehmann [11] showed that this differential transport is dependent on the buoyancy Reynolds number Re_b. Given by $Re_b \equiv \varepsilon/\nu N^2$, where ε is the turbulent kinetic energy dissipation rate, ν is the molecular viscosity and N is the buoyancy frequency, it is often used as a measure of the strength of isotropic turbulence. At large values of Re_b the scalars are irreversibly mixed by the flow before restratification can take place, and they get mixed at equal rates: $K_T = K_S$, which, along with other assumptions, leads to the widely used mixing efficiency value of 0.2. At lower values of Re_b (< 40, which is commonly seen in weakly turbulent parts of the ocean) significant differential diffusion is observed, causing the mixing efficiency to depend on the density ratio. Ocean model estimates of water mass transformations and upwelling rates are highly sensitive to the mixing efficiency parameterization [6], and hence understanding the functional dependencies of Γ on flow properties like the density ratio R_ρ is a central challenge.

[3] Introduced by Lorenz [12], background potential energy (BPE) is defined as the minimum potential energy of a stratified fluid that can be achieved by adiabatic rearrangement of the fluid parcels. Changes in BPE can only be brought upon by irreversible mixing [20], although this is not true in a double diffusive fluid: more on this later.

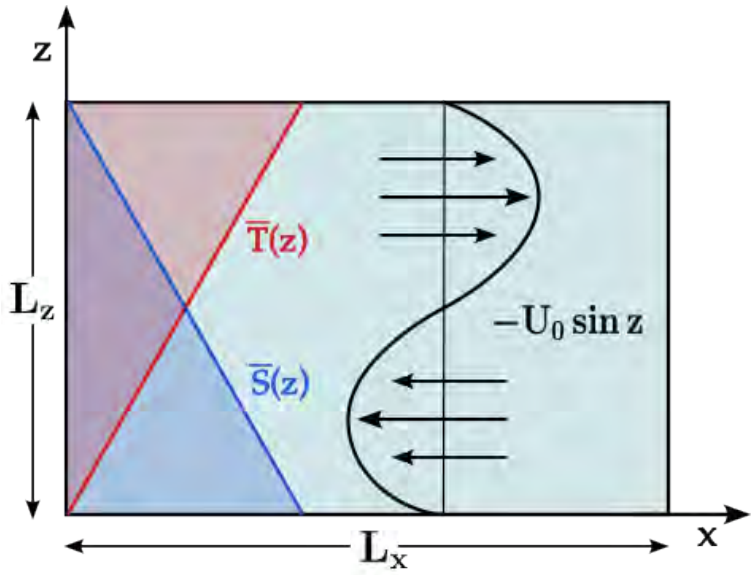

Figure 2: A schematic of the 2D Kolmogorov shear flow model, with stable mean gradients in T and S.

2 Aim

The Kolmogorov flow, a popular idealized model of shear-driven turbulence, is a two-dimensional shear flow with a unidirectional sinusoidal velocity profile that has to be maintained by an external forcing in a viscous fluid. This model admits a well-studied long-wave instability that is seeded by small-scale perturbations and cascades energy to large scales [16].

In a series of papers, Balmforth and Young[4] [1] [2] studied the stability and the evolution of the weakly stratified Kolmogorov flow. They noted that stratification was an arresting influence on the inverse cascade, limiting the large-scale instability—what they call the "viscous" instability—of the unstratified Kolmogorov flow to a finite wavenumber that resembled Kelvin-Helmholtz-like billows at equilibrium. In this project, we investigate the Kolmogorov flow that has been stably stratified in temperature *and* salinity, and numerically study the linear stability and the full nonlinear evolution of this two-component fluid system. We limit ourselves to the weakly stratified and weakly turbulent domain where the viscous (or monotonic) instability is active, and vary the diffusivity ratio $\tau = \kappa_S/\kappa_T$ and the density ratio R_ρ. How does the mixing of temperature and salinity depend on τ and R_ρ? Does double diffusion and/or differential diffusion affect the stability of the stratified shear flow? How actively are spice gradients stirred to smaller scales in stratified turbulence? These are some of the questions we seek to address in this study.

[4]This work actually began as Yuan-nan Young's GFD Summer Program project in 1999.

3 Formulation

3.1 Governing equations

Along with the temperature and salinity equations 5 and 6, we have the mass and momentum conservation equations for a 2-dimensional stratified flow in the (x, z) plane, with gravity along the negative z-direction, in a Boussinesq fluid:

$$\boldsymbol{\nabla} \cdot \mathbf{u} = 0, \tag{9}$$

$$\partial_t \mathbf{u} + (\mathbf{u} \cdot \boldsymbol{\nabla})\mathbf{u} = -\rho_0^{-1} \boldsymbol{\nabla} p + \nu \nabla^2 \mathbf{u} + g(\alpha T - \beta S)\hat{\mathbf{z}}. \tag{10}$$

Consider perturbations from a linear background profile in T and S:

$$T = \overline{T}_z z + T', \qquad S = \overline{S}_z z + S'. \tag{11}$$

Here, the mean gradients $\overline{T}_z$ and $\overline{S}_z$ are constant values. Absorb the mean temperature and salinity terms into the pressure, so the momentum equation is unchanged except that T' and S' now appear in the buoyancy. The temperature and salinity equations now become

$$\partial_t T' + (\mathbf{u} \cdot \boldsymbol{\nabla})T' = \kappa_T \nabla^2 T' - \overline{T}_z w, \tag{12}$$

$$\partial_t S' + (\mathbf{u} \cdot \boldsymbol{\nabla})S' = \kappa_S \nabla^2 S' - \overline{S}_z w. \tag{13}$$

Recall that $\overline{T}_z > 0$ and $\overline{S}_z < 0$ are stabilizing whereas $\overline{T}_z < 0$ and $\overline{S}_z > 0$ are destabilizing. We also have the perturbation equations in buoyancy and spice

$$\partial_t b' + (\mathbf{u} \cdot \boldsymbol{\nabla})b' = \frac{\kappa_T + \kappa_S}{2} \nabla^2 b' + \frac{\kappa_T - \kappa_S}{2} \nabla^2 \gamma' - N^2 w, \tag{14}$$

$$\partial_t \gamma' + (\mathbf{u} \cdot \boldsymbol{\nabla})\gamma' = \frac{\kappa_T + \kappa_S}{2} \nabla^2 \gamma' + \frac{\kappa_T - \kappa_S}{2} \nabla^2 b' - \overline{\gamma}_z w, \tag{15}$$

where

$$N^2 \equiv \overline{b}_z = g\alpha \overline{T}_z - g\beta \overline{S}_z, \qquad \overline{\gamma}_z = g\alpha \overline{T}_z + g\beta \overline{S}_z. \tag{16}$$

3.2 Non-dimensionalization

Since we will consider a flow forced to a particular mean velocity profile, we can non-dimensionalize the velocity by a typical scale U which varies on a typical length scale L. We then consider perturbations to temperature and salinity scaled by the background gradients, i.e., that $T' \sim |\overline{T}_z| L$ and $S' \sim |\overline{S}_z| L$. Choosing a pressure scale to balance the inertia, we then arrive at the dimensionless system

$$\partial_t \mathbf{u} + (\mathbf{u} \cdot \boldsymbol{\nabla})\mathbf{u} = -\boldsymbol{\nabla} p + Re^{-1} \nabla^2 \mathbf{u} + \frac{Ri}{R_\rho - 1}(R_\rho \mathrm{sgn}(\overline{T}_z) T' - \mathrm{sgn}(\overline{S}_z) S')\hat{\mathbf{z}}, \tag{17}$$

$$\begin{aligned} \partial_t T' + (\mathbf{u} \cdot \boldsymbol{\nabla})T' &= \frac{\kappa_T}{UL} \nabla^2 T' - \mathrm{sgn}(\overline{T}_z) w, \\ &= \frac{1}{PrRe} \nabla^2 T' - \mathrm{sgn}(\overline{T}_z) w, \end{aligned} \tag{18}$$

$$\begin{aligned} \partial_t S' + (\mathbf{u} \cdot \boldsymbol{\nabla})S' &= \frac{\kappa_S}{UL} \nabla^2 S' - \mathrm{sgn}(\overline{S}_z) w, \\ &= \frac{\tau}{PrRe} \nabla^2 S' - \mathrm{sgn}(\overline{S}_z) w, \end{aligned} \tag{19}$$

with the non-dimensional parameters

$$Re = \frac{UL}{\nu}, \qquad Ri = \frac{N^2 L^2}{U^2}, \qquad Pr = \frac{\nu}{\kappa_T}, \tag{20}$$

which are respectively the Reynolds number, the Richardson number, and the molecular Prandtl number for temperature, along with the previously defined density ratio R_ρ and diffusivity ratio τ. We also write down the non-dimensional equations for buoyancy and spice perturbation, where $b' \sim |N^2|L$ and $\gamma' \sim |\overline{\gamma_z}|L$, as we will need them to calculate the buoyancy variance:

$$\partial_t b' + \mathbf{u}\cdot\nabla b' = \frac{1}{Pe_b}\nabla^2 b' + \frac{A}{Pe_\gamma}\nabla^2\gamma' - \mathrm{sgn}(\overline{b_z})\, w, \tag{21}$$

$$\partial_t \gamma' + \mathbf{u}\cdot\nabla \gamma' = \frac{1}{APe_\gamma}\nabla^2 b' + \frac{1}{Pe_b}\nabla^2\gamma' - \mathrm{sgn}(\overline{\gamma_z})\, w, \tag{22}$$

where

$$Pe_b = \frac{UL}{(\kappa_T+\kappa_S)/2}, \qquad Pe_\gamma = \frac{UL}{(\kappa_T-\kappa_S)/2}, \qquad A = \left|\frac{\overline{\gamma}_z}{\overline{b}_z}\right|. \tag{23}$$

3.3 Kolmogorov forcing

The steady x-directional shear background flow of Balmforth and Young [1] (BY2002) is maintained by an external forcing (see figure 2 for a schematic). Adding in a forcing term $F(z)\hat{\mathbf{x}}$ to the non-dimensional momentum equation 17 and decomposing $\mathbf{u}$ as a steady $\overline{\mathbf{u}} = -\sin z\,\hat{\mathbf{x}}$ and a perturbation $\mathbf{u}'$, we get

$$\begin{aligned}\partial_t \mathbf{u}' - \sin z\partial_x\mathbf{u}' - w'\cos z\,\hat{\mathbf{x}} + (\mathbf{u}'\cdot\boldsymbol{\nabla})\mathbf{u}' = \\ -\boldsymbol{\nabla}p + Re^{-1}\left(\sin z\,\hat{\mathbf{x}} - \nabla^2\mathbf{u}'\right) + \frac{Ri}{R_\rho - 1}\left(R_\rho \mathrm{sgn}(\overline{T}_z)T' - \mathrm{sgn}(\overline{S}_z)S'\right)\hat{\mathbf{z}} + F\hat{\mathbf{x}}.\end{aligned} \tag{24}$$

To match with the form used in BY2002, we need the forcing to follow $F = -Re^{-1}\sin z$, i.e., the forcing needs to balance the viscous dissipation of the shear flow. The Reynolds number is thus the non-dimensional input parameter for this system. The velocity perturbation equation then becomes

$$\begin{aligned}\partial_t \mathbf{u}' - \sin z\partial_x\mathbf{u}' - w'\cos z\,\hat{\mathbf{x}} + (\mathbf{u}'\cdot\boldsymbol{\nabla})\mathbf{u}' = \\ -\boldsymbol{\nabla}p + Re^{-1}\nabla^2\mathbf{u}' + \frac{Ri}{R_\rho - 1}\left(R_\rho \mathrm{sgn}(\overline{T}_z)T' - \mathrm{sgn}(\overline{S}_z)S'\right)\hat{\mathbf{z}}.\end{aligned} \tag{25}$$

Although the sinusoidal background flow is just a source of constant velocity shear for generating turbulence, for small values of Re, we notice that in the horizontally averaged u-momentum equation

$$\partial_t\langle u\rangle + \partial_z\langle uw\rangle = Re^{-1}\partial_{zz}\langle u\rangle + F(z), \tag{26}$$

it is possible for the shear flow to be the steady solution, i.e., $\langle u\rangle = -\sin z$. This can happen for laminar flows with small values of Re, when the two terms on the right-hand side constitute the dominant balance, and the Reynolds stress term $\langle uw\rangle$ is negligible.

4 Results

We first perform a linear stability analysis on the non-dimensionalized system to compare the modes of instability of the doubly stratified system to results from Balmforth and Young. We then follow up with numerical simulations of the governing equations to test our predictions from linear stability and investigate the nonlinear effects of spice on flow evolution.

4.1 Linear stability

We linearize the perturbation equations in $\mathbf{u}'$, T' and S' (equations 25, 12, 13) around the basic state by dropping the nonlinear advection terms, and eliminating pressure from the w-momentum equation using the divergence of 25. We get three equations in w', T' and S'

$$\left(\partial_t + \overline{u}\partial_x\right)\nabla^2 w' - \overline{u}_{zz}\partial_x w' = Re^{-1}\nabla^4 w' + \frac{Ri}{R_\rho - 1}\left(R_\rho \,\mathrm{sgn}\left(\overline{T}_z\right)\,\partial_{xx}T' - \mathrm{sgn}\left(\overline{S}_z\right)\,\partial_{xx}S'\right), \tag{27}$$

$$\left(\partial_t + \overline{u}\partial_x\right)T' + \mathrm{sgn}\left(\overline{T}_z\right)\,w' - \frac{1}{Pr\,Re}\nabla^2 T' = 0, \tag{28}$$

$$\left(\partial_t + \overline{u}\partial_x\right)S' + \mathrm{sgn}\left(\overline{S}_z\right)\,w' - \frac{\tau}{Pr\,Re}\nabla^2 S' = 0. \tag{29}$$

Substituting normal modes of the form $[w', T', S'] = \exp\Big\{(ikx + \sigma t)[\hat{w}(z), \hat{T}(z), \hat{S}(z)]\Big\}$ with periodic boundary conditions on the amplitude functions at 0 and 2π, we get

$$\left(\sigma + ik\overline{u}\right)\nabla^2\hat{w} - ik\overline{u}_{zz}\hat{w} = Re^{-1}\nabla^4\hat{w} - k^2\left(\frac{R_\rho\,Ri}{R_\rho - 1}\mathrm{sgn}\left(\overline{T}_z\right)\hat{T} - \frac{Ri}{R_\rho - 1}\mathrm{sgn}\left(\overline{S}_z\right)\hat{S}\right), \tag{30}$$

$$\left(\sigma + ik\overline{u}\right)\hat{T} + \mathrm{sgn}\left(\overline{T}_z\right)\,\hat{w} - \frac{1}{Pr\,Re}\nabla^2\hat{T} = 0, \tag{31}$$

$$\left(\sigma + ik\overline{u}\right)\hat{S} + \mathrm{sgn}\left(\overline{S}_z\right)\,\hat{w} - \frac{\tau}{Pr\,Re}\nabla^2\hat{S} = 0, \tag{32}$$

where $\nabla^2 = d^2/dz^2 - k^2$.

For the nonstratified case ($Ri = 0$), this system is unstable to long-wave perturbations above a critical value of the Reynolds number, $Re_c = \sqrt{2}$ [16]. Weak stratification exerts a stabilizing effect on the longest length-scales and cordons off the linearly unstable region from extending to the smallest wavenumbers (BY2002). The critical threshold for stratification strength above which the instability is fully suppressed was found to be in excess of the $Ri = 1/4$ rule given by the famous Miles-Howard criterion for inviscid flows, indicating that the combined effect of viscosity and thermal diffusion destabilizes the sheared flow.

BY2002 also examines the low and high Péclet number cases for this flow, which is equivalent to the low and high Prandtl number cases as the Péclet number can be written as $Pe = PrRe$. They carried out numerical simulations to show that, for a fast diffusing

scalar (low Pr), the flow rolls up into billows of an intermediate wavelength that are stable for moderate Reynolds numbers. For a slow diffusing scalar (high Pr), the instability evolution is more complicated, possibly due to restratification of the scalar and formation of strong internal gradients that are harder to overturn. Our focus here is on understanding the behavior at intermediate-to-high Prandtl numbers, since heat has $Pr = 7$, and the equivalent for salt, the Schmidt number, is $Sc = 700$ in the ocean, and thus we closely examine the bifurcation behavior in the linear stability in this Prandtl range.

4.1.1 Two modes of instability

We solve the eigensystem in 30, 31, 32 using the spectral DE solver Dedalus [3]. We use 64 grid points in z to resolve one scale height and vary the horizontal wavenumbers between 0 and 1. The diffusivity ratio is set to be $\tau = 0.01$, and the temperature Prandtl number is set at $Pr = 7$.

Figure 3(a) shows the maximum growth rates in the $k - Re$ plane for the doubly stable flow (negative R_ρ) with weak stratification ($Ri = 0.05$). The marginal stability curves show two different regions of linear instability, both with critical Reynolds numbers greater than $\sqrt{2}$. From figure 3(b), we see that the region with the shorter wavelengths shows no oscillatory component, while the other region shows growing oscillations with a frequency very close to the non-dimensional buoyancy frequency $\sqrt{Ri}$. Hence, we will label the two instability modes as the **monotonic** mode and the **oscillatory** mode. The eigenfunctions for the fastest growing mode also have different vertical structures for the two regions, as shown in figure 3(c). The monotonic mode is symmetric in z with four nodes, or two full waves. The eigenfunction for the oscillatory region is similar to the neutrally stable region (i.e., region with neutral oscillations)—asymmetric in z with two nodes. Growth rates for the monotonic mode dominate the oscillatory mode, although the modes respond differently to changing the parameters of interest, R_ρ and Ri, as we discuss below.

4.1.2 Effect of the density ratio and stratification strength

Larger magnitudes of the density ratio indicate that the fast diffuser, temperature, contributes more to the stratification, while low magnitudes mean that the slow diffusing salinity dominates the buoyancy dynamics. Both instabilities are affected by the value of the density ratio, but the effect varies with the strength of the stratification.

In the $k - Re$ plane, when Ri exceeds 0.25, the critical Reynolds number for the monotonic instability is lower when $|R_\rho| \ll 1$, i.e., when slow diffusion is prevalent. For weaker stratification, the monotonic mode is not strongly affected by the density ratio, but shows a slight inverse trend, i.e, lower threshold Re values for higher $|R_\rho|$. The oscillatory mode, on the other hand, shows a more dramatic dependence on R_ρ. The instability extends to shorter waves, shows larger growth rates, and smaller threshold Re_c values with decreasing $|R_\rho|$. This holds across the range of Ri values that we tested ($10^{-4} - 0.5$), but the effect is most pronounced for low Ri, in contrast to the monotonic mode. Conversely, for $|R_\rho| \gg 1$, the oscillatory mode weakens and can become completely suppressed. Thus, slow, salinity-dominated diffusion has a destabilizing effect on both modes, although this is only explicit in the monotonic mode for $Ri > 0.25$ (Figure 5). Generally, increasing Ri pushes

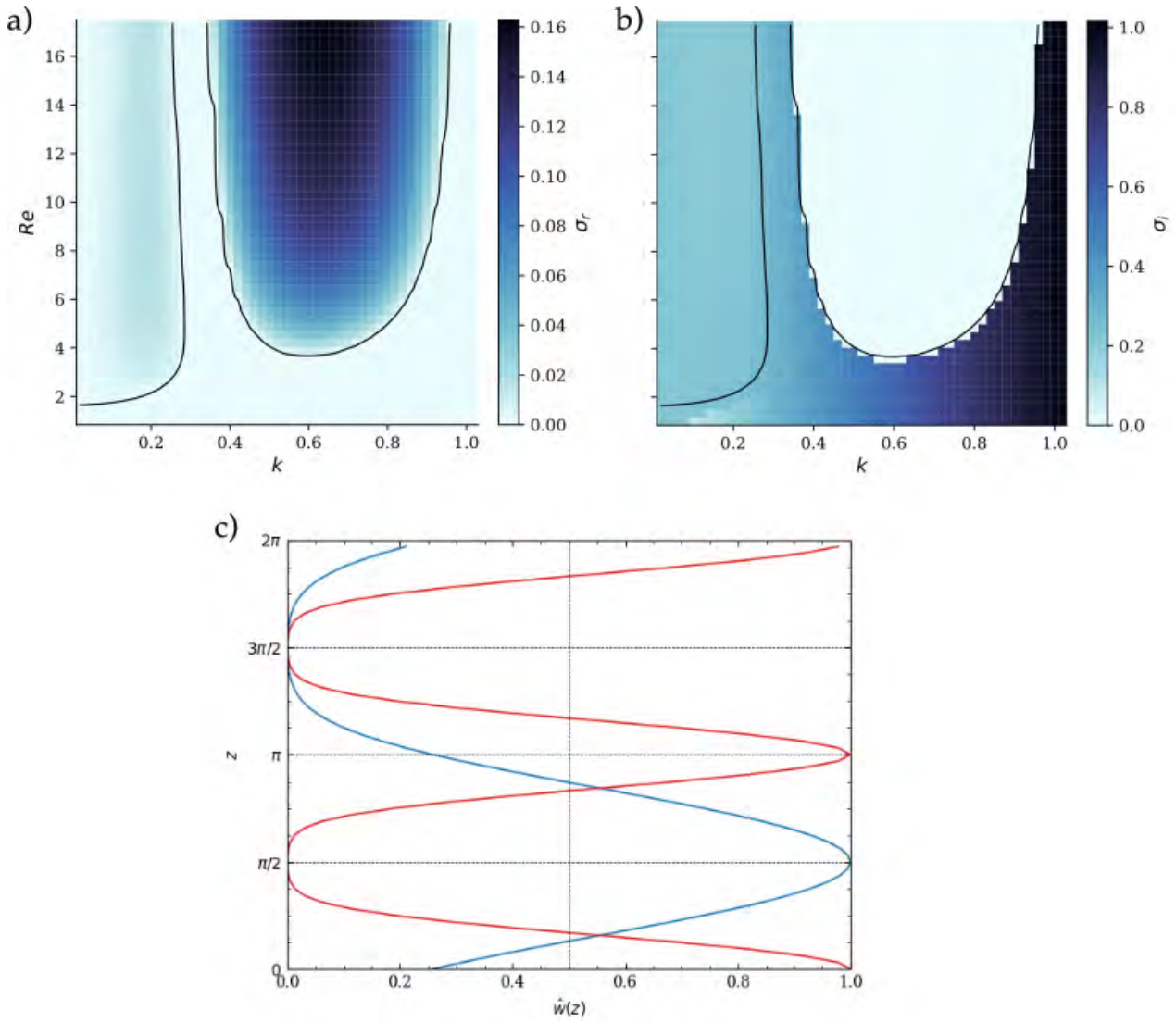

Figure 3: Linear stability results for $Ri = 0.05$, $R_\rho = -100$, $\tau = 0.01$, and $Pr = 7$. (a) Maximal values of the (real) growth rate for different (k, Re) pairs. Stability boundaries contoured in black. The region on the right with larger σ_r is the monotonic mode (what BY call the viscous mode), and the long-wave region on the left is the oscillatory mode. (b) Imaginary components of the growth rates in (a). (c) Vertical eigenfunctions $\hat{T}(z)$ of the fastest-growing modes for the monotonic instability in red, and the oscillatory instability in blue.

the wavelength with the maximal growth rate—we can call this k_{max}—to smaller values for both modes, for k ranging from 0 to 1. (For k larger than 1, we see some short-wave modes showing more complex behavior that we have not investigated in detail.) Increasing Ri also makes for slower growth rates for both modes, although the oscillatory mode can also disappear at very low values of Ri. This, along with the oscillation frequency being close to $\sqrt{Ri}$, indicates that the mode arises as a result of the stratified dynamics, although it is eventually suppressed at large Ri (¿ 0.5). Furthermore, the slow-diffusive low $|R_\rho|$

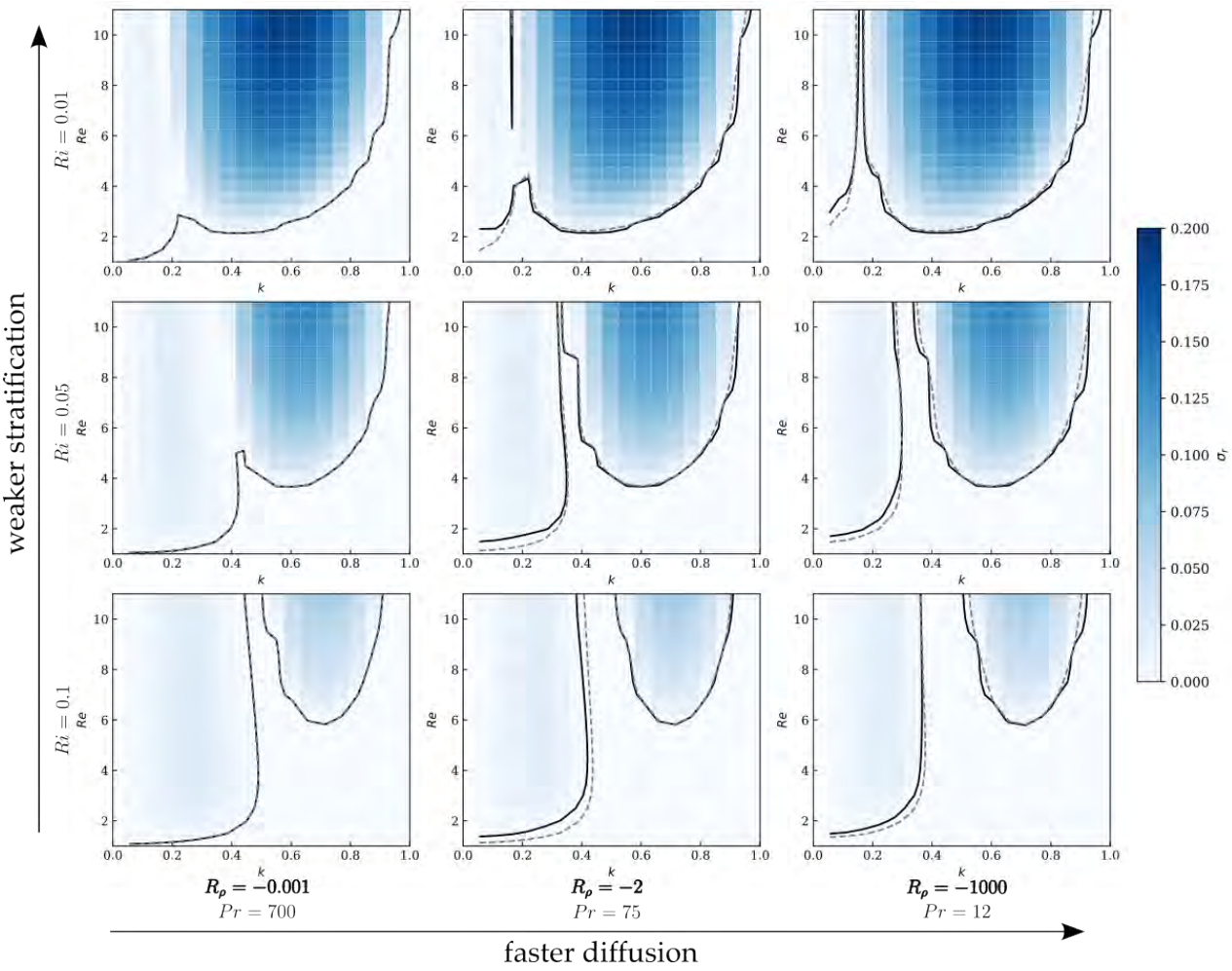

Figure 4: Effect of the density ratio and the stratification strength on the two modes, for $0 < k < 1$ and $1 < Re < 11$. Panels growth rates and stability boundaries contoured in black for density ratios at the bottom and Richardson number at the left of the figure. Dotted grey lines show stability boundaries for similar single diffusion cases, with Prandtl numbers indicated underneath density ratios.

scenario allows this instability to grow even at large Ri values, while high $|R_\rho|$ suppresses it for stratification strengths well below the Miles-Howard threshold. The monotonic mode is also in general hampered by the increasing stratification, but as discussed earlier, low $|R_\rho|$ allows the instability to grow up to $Ri = 0.5$ (we did not test beyond that), albeit with smaller growth rates.

These competing influences of Ri and R_ρ on the linear stability of the Kolmogorov flow are summarized in figure 4 and 5. We find that there are regions of overlap between the two modes of instability and that the monotonic mode always grows faster than the oscillatory mode when both are present in the parameter space.

The density ratio also controls the shape of the vertical eigenfunctions for buoyancy.

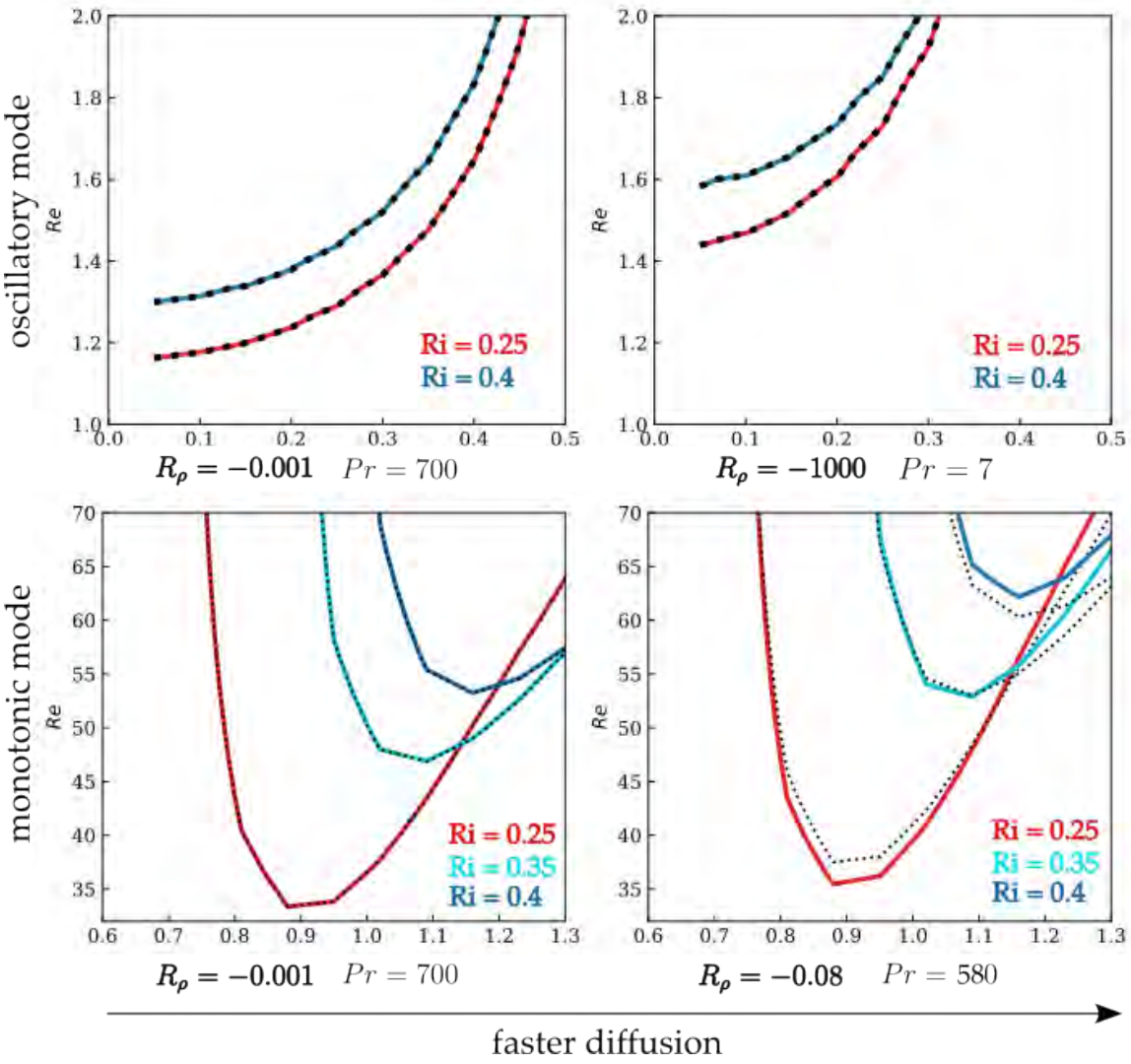

Figure 5: Stability boundaries in the (k, Re) plane for the oscillatory mode (top) and monotonic mode (bottom) for $Ri \geq 0.25$. Thick colored lines indicate stability curves for the double diffusive flow with given R_ρ at the bottom of each panel, dotted black lines indicate curves for the single diffusive case with given Pr.

The eigenmode for salinity shows sharper gradients than for temperature, consistent with the "internal boundary layer" structure noted by BY2002 for slow diffusers. Being a linear combination of T and S, the buoyancy eigenfunction correspondingly has sharp gradients for low $|R_\rho|$ values, when controlled by the slow diffuser, and smooth gradients for high $|R_\rho|$ values when it is controlled by the fast diffuser. Spice also shows a similar pattern, but for intermediate values of $|R_\rho|$ close to 1, there is no large-scale spice gradient, but local gradients can be quite sharp and persistent.

4.1.3 Comparison with single diffusion

In order to understand precisely how the spiciness affects the stability of this Kolmogorov flow, we need to compare to the linear stability results for a singly-stratified flow. We numerically solve the eigensystem for the single diffusion linear stability problem with parameters Re, Ri and Pr,

$$(\sigma + ik\overline{u})\,\nabla^2\hat{w} - ik\overline{u}_{zz}\hat{w} = Re^{-1}\nabla^4\hat{w} - k^2 Ri\,\mathrm{sgn}\left(\overline{T}_z\right)\hat{T}, \tag{33}$$

$$(\sigma + ik\overline{u})\,\hat{T} + \mathrm{sgn}\left(\overline{T}_z\right)\,\hat{w} - \frac{1}{Pr\,Re}\nabla^2\hat{T} = 0. \tag{34}$$

The single diffusion problem has been addressed before—BY2002 looks at a narrow region in the parameter space, covering only the monotonic mode, which they call the "viscous" instability. Their second paper [2], BY2005, mentions an additional mode that they call the "conductive" mode that seems to match the oscillatory mode we see in the doubly-stratified case above. However, they do not deliberate much on its oscillatory nature, focusing instead on the "negative-diffusion" and potential layer formation aspects of this mode. Their multiple scales theory for linear stability yields high Re cutoffs for both modes (Fig. 2 in the paper), which we have not seen in our computations for the either the single- or double-diffusion case, except for very low Prandtl numbers ($< 10^{-2}$). Additionally, their analysis is limited to $Pr \sim \mathcal{O}(1)$, which is not very applicable to our salt-stratified case with Pr (or Sc) $= 700$, especially since Prandtl is unmistakably a very influential parameter in controlling the behavior of these modes. A 2015 study [8] by Garaud et al. looked at the 3D Kolmogorov flow for low Péclet numbers in stellar interiors, but they also present linear stability results for 2D modes (Fig. 2 in the paper) that closely match the two modes we found in both the single- and double-diffusion cases. They also note that the growth rate for one of the modes has a non-zero imaginary part.

Now we briefly summarize our results for the linearized single-diffusion (SD) problem. As in the double-diffusion (DD) case, we find two main distinct unstable regions in parameter space. They are completely equivalent to the two DD modes; one of the modes is oscillatory with longer wavelengths and weaker growth rates, and the other is monotonic and grows much faster. The Prandtl number in the SD problem works analogously to the density ratio in the DD problem (when Pr and τ are kept constant) in controlling the relative strength and stability criteria for these modes. Indeed, we find that even at large Richardson number (~ 0.5), the oscillatory mode is marginally stable at lower Re_c for larger Pr (corresponding to $|R_\rho| \ll 1$). Conversely, it disappears below a Pr threshold of ~ 0.1—this was not observed in the DD case because the Prandtl number there ranged from 7 to $Pr/\tau = 700$. We also find a similar dependence on the Richardson number; the SD oscillatory mode appears only above a certain stratification strength, becomes more unstable with growing Ri up to $Ri \approx 0.25$, after which the stratification has more of a stabilizing effect on the mode. Similar to DD, the SD monotonic mode is not very strongly affected by Pr in the range $7 - 700$, except at high Ri, where large Pr leads to a more unstable mode.

Extending the parameter space to $Pr \ll 1, k > 1$ and large Re reveals new regions of instability. We find a long-wavelength monotonic mode for small Pr ($< 10^{-2}$) for

Richardson number up to 1, which is the instability described in [8] for high Ri and low Pe astrophysical flows. We also find two other unstable regions at $Re \sim \mathcal{O}(10^3)$ and $k > 1$ respectively. The equivalence of the SD and DD linear stability problem is such that it is possible to find these extra modes in the DD case by tweaking Pr, τ and R_ρ appropriately. For large Pr/small R_ρ, the stability behavior of the two-component flow with two diffusivities can be represented by a single-component fluid with an intermediate diffusivity. We now attempt to construct a form for this intermediate diffusivity, or an effective Prandtl number, for the spicy flow.

4.1.4 Budget terms

We define some quantitative measures of the flow dynamics to characterize the instability evolution. From the buoyancy perturbation equation 21, we get the following equation for the evolution of the buoyancy variance (see Appendix 7.1 for derivation details), where the angle brackets represent a volume average:

$$\frac{d\langle b'^2\rangle}{dt} = -\langle \chi_b \rangle - \langle \chi_{\gamma b} \rangle - 2\,\mathrm{sgn}(\overline{b_z})\langle w b' \rangle, \tag{35}$$

where we have the diffusive fluxes

$$\langle \chi_b \rangle = \frac{2}{Pe_b}\langle |\nabla b'|^2 \rangle, \qquad \langle \chi_{\gamma b} \rangle = \frac{2A}{Pe_\gamma}\langle \nabla\gamma' \cdot \nabla b' \rangle. \tag{36}$$

The term $\langle \chi_{\gamma b} \rangle$ is the extra double diffusive term that is absent in the single diffusion scalar variance equation which is given by

$$\frac{d\langle T'^2\rangle}{dt} = -\langle \chi_T \rangle - 2\,\mathrm{sgn}(\overline{T_z})\langle w T' \rangle. \tag{37}$$

Since $\langle \nabla\gamma' \cdot \nabla b' \rangle$ can be negative if $\nabla\gamma'$ and $\nabla b'$ are anti-correlated, this becomes a diffusive term that leads to an increase in scalar variance, i.e., creating up-gradient fluxes via diffusion. This behavior is sometimes called anti-diffusion, and is believed to be one of the mechanisms that leads to the staircase-like density profiles seen in many ocean observations.

In the single-diffusive fluid, diffusive mixing only leads to down-gradient fluxes and an increase in the background potential energy BPE (see footnote 3), which is considered irreversible. Available potential energy APE, defined as (total PE - BPE), is the part of the potential energy that can can drive fluid motion through its conversion to kinetic energy by the buoyancy flux. In double diffusion, however, energy can also be drawn from the BPE reservoir, making the conversion from APE to BPE bidirectional. Middleton and Taylor (2020) [15] discuss the possibility of parameterizing this up-gradient flux with an effective diffusivity that is in general a function of τ, R_ρ and the angle between $\nabla\gamma'$ and $\nabla b'$, with negative values of the diffusivity indicating a "reversible" BPE to APE transfer. Although it is not exactly the same as the effective Prandtl number we are interested in, this suggests that the effective Pr is unlikely to be represented by a simple sliding scale between the high salt Pr and low heat Pr values, but could be a more complex and multivariate function.

4.1.5 Effective Prandtl number from linear stability

The intermediate Prandtl number is likely a complex function of R_ρ, τ, Ri and other variables, and can be constructed in many different ways. However, motivated by our goal to understand double-differential mixing, we propose a construction based on scalar variance equations. Using 35 to define an effective Prandtl (or Péclet) for the fluxes would give the following definition in terms of R_ρ and τ

$$\frac{2}{Pe_{\text{eff}}}\langle|\nabla b'|^2\rangle = \frac{2}{Pe_b}\langle|\nabla b'|^2\rangle + \frac{2A}{Pe_\gamma}\langle\nabla\gamma'\cdot\nabla b'\rangle, \tag{38}$$

$$\implies Pe_{\text{eff}}^{-1} = {Pe_b}^{-1}\left(1+\frac{1-\tau}{1+\tau}\left|\frac{R_\rho+1}{R_\rho-1}\right|\frac{\langle\nabla\gamma'\cdot\nabla b'\rangle}{\langle|\nabla b'|^2\rangle}\right) \tag{39}$$

The term $\frac{\langle\nabla\gamma'\cdot\nabla b'\rangle}{\langle|\nabla b'|^2\rangle}$ captures the relative contribution of spice variance to total buoyancy dissipation. For the effective Péclet formulation to hold, we need the definition given in 39 to be largely independent of $\langle|\nabla b'|^2\rangle$. This is possible if we assume spice variations are correlated with buoyancy with a correlation coefficient $\hat{X}$, and have a deviation γ'',

$$\gamma' = \hat{X}b' + \gamma'', \tag{40}$$

so that we get

$$\frac{\langle\nabla\gamma'\cdot\nabla b'\rangle}{\langle|\nabla b'|^2\rangle} = \hat{X} + \frac{\langle\nabla\gamma''\cdot\nabla b'\rangle}{\langle|\nabla b'|^2\rangle}. \tag{41}$$

We can calculate the relative magnitudes of the two terms on the right hand side from the stable end states of the monotonic mode DNS results. If the second term dominates over the correlation coefficient, the effective Péclet in 39 may not hold. But assuming that term is small, this allows us to now write the following relations. From the non-dimensional scalar variance evolution equations, and the non-dimensional turbulent diffusivity closure $\langle wT'\rangle = -K_T\,\text{sgn}(\overline{T_z})$, at steady state we get:

$$\langle|\nabla T'|^2\rangle = -Pr_T Re\,\text{sgn}(\overline{T_z})\langle wT'\rangle = Pr_T Re\,\text{sgn}(\overline{T_z})^2 K_T, \tag{42}$$

$$\langle|\nabla S'|^2\rangle = -\frac{Pr_T Re}{\tau}\,\text{sgn}(\overline{S_z})\langle wS'\rangle = \frac{Pr_T Re}{\tau}\,\text{sgn}(\overline{S_z})^2 K_S, \tag{43}$$

$$\langle|\nabla b'|^2\rangle = -2Pr_{\text{eff}} Re\,\text{sgn}(\overline{b_z})\langle wb'\rangle = 2Pr_{\text{eff}} Re\,\text{sgn}(\overline{b_z})^2 K_b, \tag{44}$$

We can also write the buoyancy variance in terms of the temperature, salinity and spice variance, and then substitute 42–44:

$$\frac{\langle|\nabla b'|^2\rangle}{2} = \frac{R_\rho^2}{|1-R_\rho|^2}\langle|\nabla T'|^2\rangle + \frac{1}{|1-R_\rho|^2}\langle|\nabla S'|^2\rangle - \frac{|1+R_\rho|^2}{|1-R_\rho|^2}\frac{\langle|\nabla\gamma'|^2\rangle}{2}, \tag{45}$$

$$Pr_{\text{eff}}K_b = \frac{Pr_T\,K_S}{\tau}\left[\frac{\tau d^{-1}R_\rho^2+1}{|1-R_\rho|^2} - \frac{|1+R_\rho|^2}{|1-R_\rho|^2}\frac{\tau}{1-\tau}\left(\frac{\chi_\gamma}{\chi_S}\right)\right]. \tag{46}$$

Here, $d = K_S/K_T$ is the eddy diffusivity ratio, and $\chi_\gamma, \chi_S = \langle|\nabla\gamma'|^2\rangle/Pe_\gamma, \langle|\nabla S'|^2\rangle/Pe_S$. The ratio of the spice and salinity chi terms is assumed to be small, and thus second term

on the RHS in 46 becomes negligible. If we further assume $K_b = K_S$, our proposed effective Prandtl number simplifies to

$$Pr_{\text{eff}} = 7\frac{100 + d^{-1}|R_\rho|^2}{(1 + |R_\rho|)^2}. \tag{47}$$

To test our construction of the effective Prandtl number, we track how the critical Reynolds number changes with R_ρ and Pr for the doubly- and singly-stratified flow respectively, for the same Ri values. Figure 6 shows the difference between the single-diffusion and double-diffusion Re_c for the monotonic mode for $Ri = 0.3$. The zero contour (solid black line) in this figure maps the density ratio to its equivalent Prandtl number. We plot the effective Prandtl from 47 for $d = 1$ (magenta dashed) and $d = 1/150$ (green dashed) to show that the simplified formula captures the shape and trend of the observed curve fairly well, especially after including differential transport ($K_T > K_S$) in the form of d. We also calculate the effective Prandtl for density ratios in figures 4 and 5. With $d = 1$, $R_\rho = -0.001 \implies Pr_{\text{eff}} = 699$, $R_\rho = -1000 \implies Pr_{\text{eff}} = 6.98$, $R_\rho = -0.08 \implies Pr_{\text{eff}} = 600.1$, and $R_\rho = -2 \implies Pr_{\text{eff}} = 80.8$. We find that these values are not too far from the Prandtl numbers we have used to recreate the single diffusion stability boundaries in these figures.

4.2 Direct numerical simulations

Numerical simulations of the nonlinear perturbation equations 25, 12, 13, along with non-divergence and pressure gauge conditions[5] are carried out in the MPI-parallelized spectral solver Dedalus. Periodic boundary conditions are imposed in both directions. The computational domain is rectangular and fits one wavelength of the sinusoidal shear flow in the vertical and eight wavelengths in the horizontal (similar to BY2002), and the grid size is 512×64 points. The velocity and scalar fields are initialized with random and uncorrelated perturbations of very small size. The code uses a second-order semi-implicit BDF scheme in time and discretizes x and z with Fourier bases. The time step is chosen appropriately to ensure stable and convergent solutions.

4.2.1 Pure monotonic mode

Figure 7 shows the evolution of the flow with $Re = 3$, $Ri = 0.01$, and $R_\rho = -2$. Results from the previous section predict that this flow should be unstable only to the monotonic instability. The evolution of instability for this case compares well to the monotonic instability results of BY2002, with the vorticity pattern developing into meandering jets with embedded vortices at the center that grow into a finite wavelength at equilibrium, which is around one-fourth the domain length. Temperature, salinity and buoyancy form layers that then develop Kelvin-Helmholtz-like overturning vortices—called the "cat's eye" pattern in BY2002—which expand vertically until they reach the domain height. This results in rhomboid-shaped well-mixed vortices separated by diffusive interfaces, with the

[5]Pressure is only determined up to an arbitrary constant in the incompressible Navier Stokes equations, and thus a pressure gauge is needed to establish the exact value of the pressure. The non-divergence constraint on the mean Fourier mode also becomes degenerate because of the underdetermined pressure variable. Dedalus v3 handles this slightly indirectly by introducing a constant tau variable in the divergence equation to absorb the degeneracy, along with a pressure gauge.

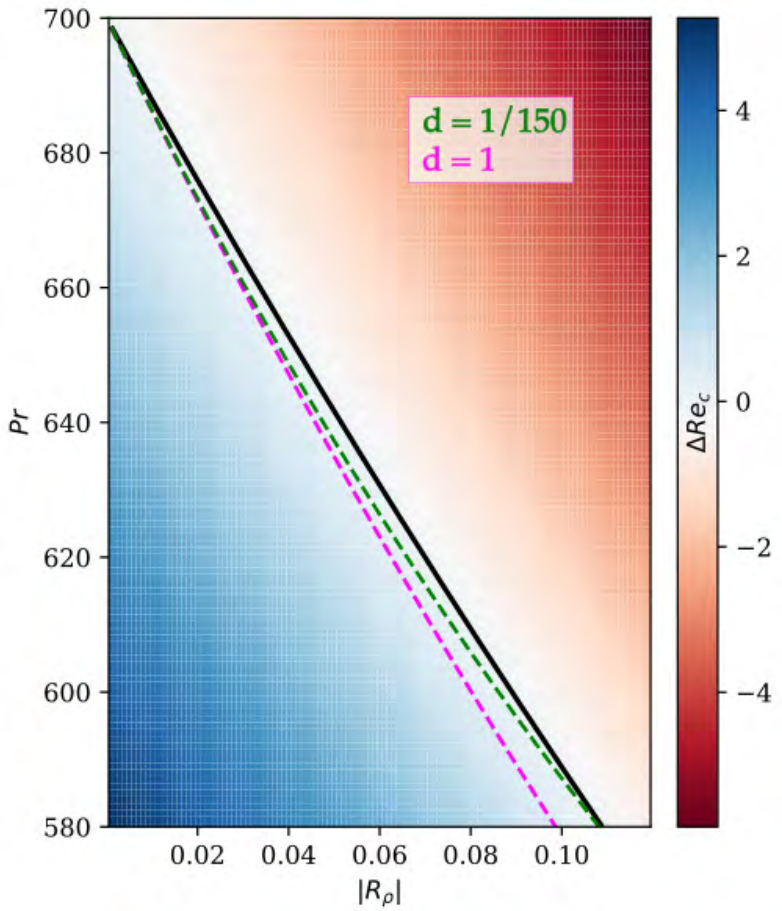

Figure 6: Effective Prandtl number curve for the monotonic mode at $Ri = 0.3$. For $k = 1$, Re_c(single diffusion) - Re_c(double diffusion) is plotted for $-0.12 < R_\rho < -0.001$ and $580 < Pr < 700$. Black curve shows the zero contour, dashed magenta (green) curve shows the predicted effective Prandtl number for $d = 1$ ($d = 1/150$).

interface gradients much sharper for salinity than temperature. These billows remain at a stable intermediate horizontal wavenumber and do not coarsen further, showing the clear arrest of the inverse cascade. For low Reynolds numbers, weak stratification and $|R_\rho| \sim \mathcal{O}(1)$ or higher, i.e., when the monotonic mode is dominant, linear stability predicts the existence of this instability quite well. We compare the end states for $R_\rho = -2$ and $R_\rho = -100$ in figure 8 and find that the smaller $|R_\rho|$ case significantly sharpens the buoyancy gradient, in line with our linear stability observation of the low $|R_\rho|$ case effectively behaving like a high effective Pr fluid. Noting the similarity of figure 8 with the single-diffusion $Pe = 400$ and $Pe = 100$ end states in Figure 14 of BY2002 (which have the same Re, Ri values) further confirms this.

Figure 9 shows the evolution of $\langle \chi_b \rangle$ and the TKE dissipation rate ε (dimensionless, so

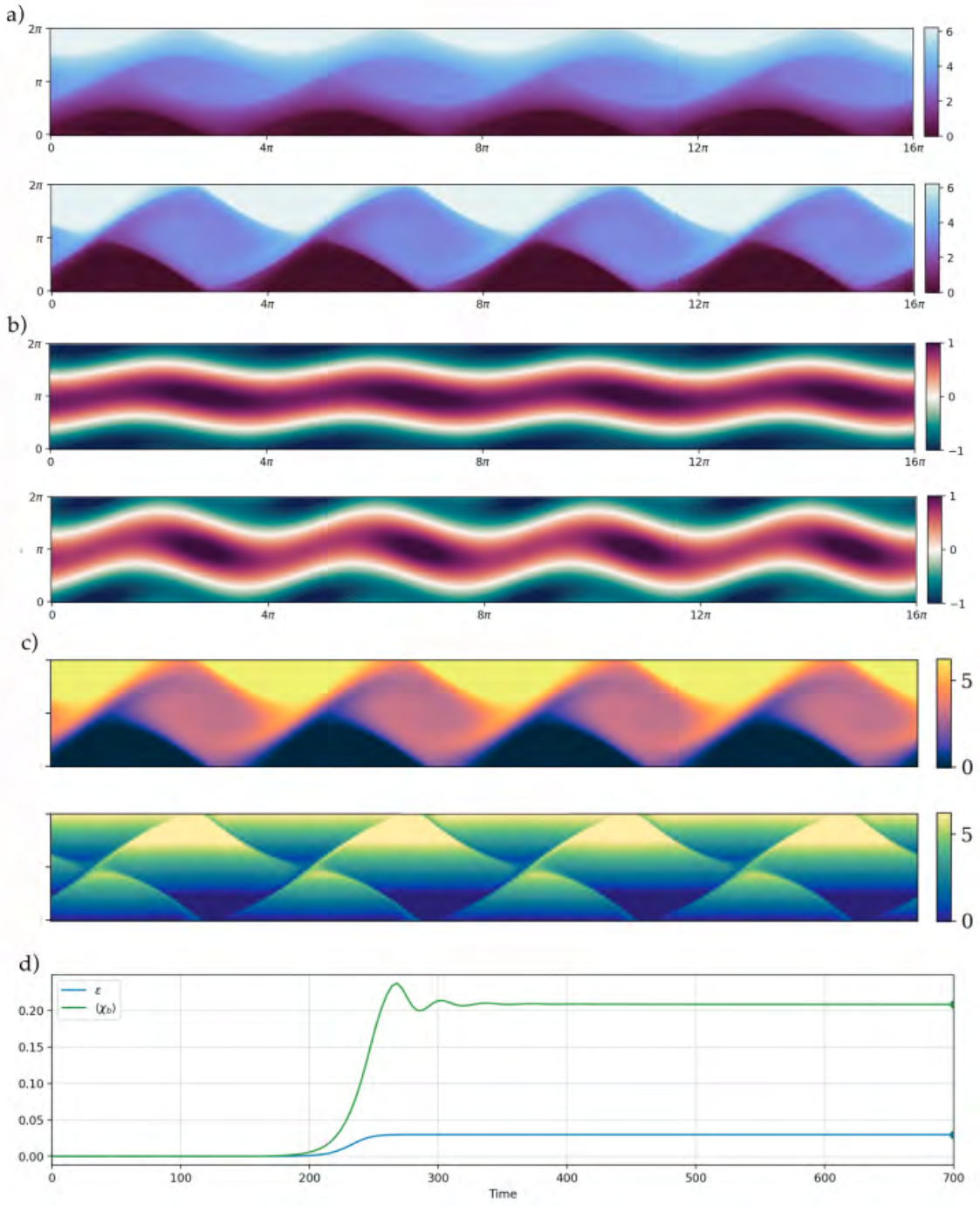

Figure 7: Snapshots of the (a) total buoyancy, and (b) total vorticity fields showing the development of the monotonic instability at times $t = 228$ (top) and $t = 356$ (bottom). (c) End states of the total temperature (top) and salinity (bottom) fields. (d) Evolution of the volume-averaged ε and χ_b terms.

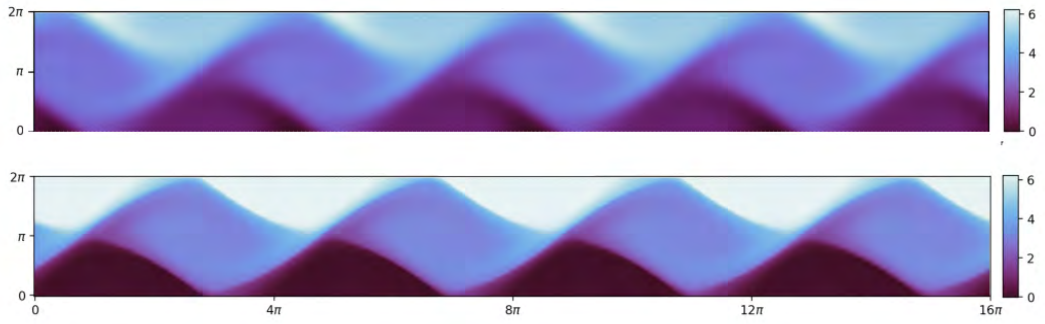

Figure 8: Final snapshots of the total buoyancy for $R_\rho = -100$ (top) and $R_\rho = -2$ (bottom).

given by $= \frac{1}{Re}\langle \frac{\partial u_i'}{\partial x_j}\frac{\partial u_i'}{\partial x_j}\rangle$) when we vary the density ratio for the runs. We find that low $|R_\rho|$ leads to larger values of $\langle \chi_b \rangle$ at equilibrium, since slow dissipation would be less effective in destroying buoyancy variance. We also see a slight increase in ε with decreasing $|R_\rho|$, about a 10% change as we go from $R_\rho = -100$ to $R_\rho = -2$. We compare this to single diffusion runs with the same (Re, Ri) values for different Pr, and observe a similar trend (figure 10) in $\langle \chi_T \rangle$ that it increases with Pr. The TKE dissipation also increases with Pr but seems to plateau for higher values, reflecting how the linearized monotonic mode is also not very sensitive to large Pr in this weak stratification scenario. We also note that the density ratio has an effect on the onset time of the instability, but we have not looked into this further.

4.2.2 Effective Prandtl number from the monotonic mode

We can also try to empirically extract the effective Pr. Like in the previous section, we compare $\Delta(\varepsilon_{DD} - \varepsilon_{SD})$ and $\Delta(\langle \chi_b \rangle_{DD} - \langle \chi_b \rangle_{SD})$ for different (R_ρ, Pr) pairs to extract their functional relationship. A next step for this project would be to compare the effective Prandtl number constructed earlier to one from the DNS end state budget terms.

4.2.3 Pure oscillatory mode

As we move into the linear instability region for the oscillatory mode in parameter space, we find growing oscillations seen as pulsations and nutations in the flow structures and in ε and $\langle \chi_b \rangle$. For smaller Reynolds numbers, these oscillations show a regular periodicity very close to the buoyancy frequency $\sqrt{Ri}$. As longer wavelengths are unstable to the oscillatory mode, we see more large-scale structures in this case.

In figure 11, we look at a case with parameters that are linearly unstable only to the oscillatory mode. Small initial perturbations start to oscillate and grow to a wave-like structure that is around half the domain length, so twice the wavelength of the monotonic mode. We also note the later onset of the instability, which might be due to the smaller growth rates of this mode compared to the monotonic mode. We were unable to determine if there is a stable end state for the oscillatory mode within the length of our runs.

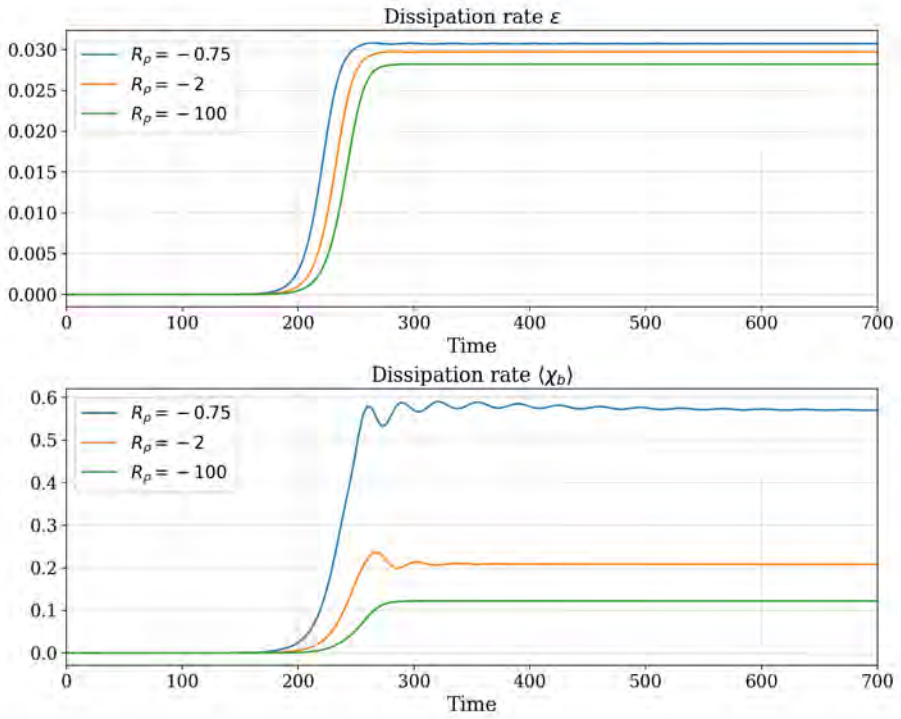

Figure 9: Dissipation rates for the monotonic mode with $Re = 3$, $Ri = 0.01$, $Pr = 7$ and $\tau = 0.01$. For three different R_ρ values, top (bottom) panel shows the evolution of ε (χ_b).

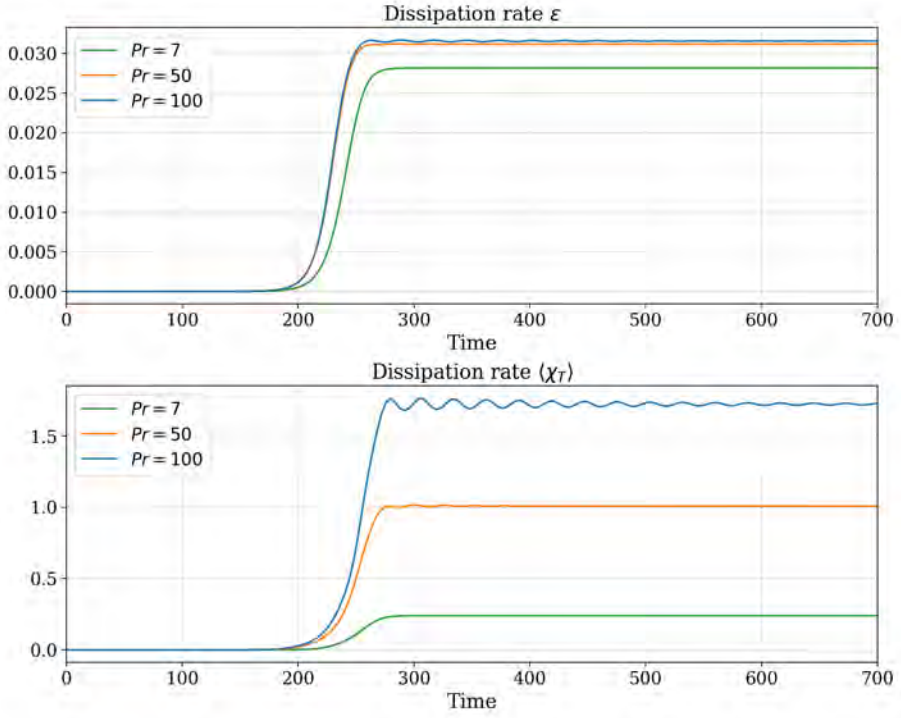

Figure 10: Same as Fig. 9 but for the single diffusion case with three different Pr values.

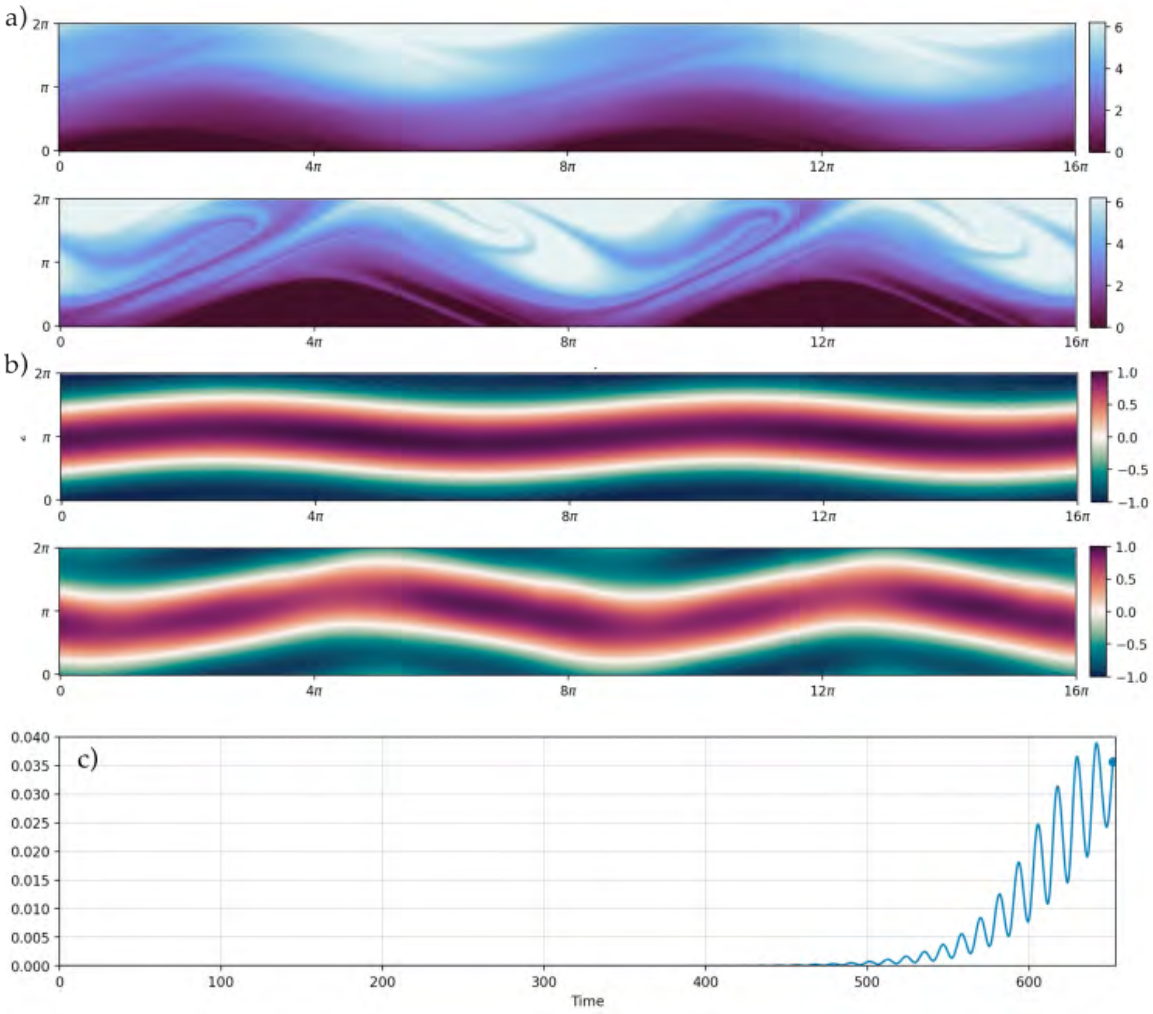

Figure 11: Snapshots of the (a) total buoyancy, and (b) total vorticity fields showing the development of the oscillatory instability at times $t = 584$ (top) and $t = 644$ (bottom). (c) Evolution of the volume-averaged ε term.

4.2.4 Combination modes

Lowering the stratification for the case above to a point where both instabilities are present, we find oscillations growing from the rolled-up end state of the monotonic instability. This could be due to the comparable growth rates for both modes at this Reynolds number, or this might be a secondary instability of the rolled-up state. The former might be the more likely case, as perturbing the density ratio to a larger value (so that monotonic mode is stronger) leads to slower-growing oscillations. Moreover, in these combination modes, oscillations sometimes set in at a much later time, and they can attain a steady amplitude or even decay. This could result from the monotonic mode dominating and suppressing the oscillatory mode when both are present (as noted by BY2005), or might be a different nonlinear effect introduced by the stratification. For higher Reynolds numbers, pure modes are rarely observed (atleast in the moderate Re range we tested). Figure 12 shows the development of instability for $Re = 6$, $Ri = 0.05$, and $R_\rho = -0.5$. Weak intermittent oscillations of the stable rolled-up state are seen for a while, until an energetic burst of cycling merges the vortices and rearranges the flow into a new long-wavelength state that is reminiscent of the structure seen for the pure oscillatory mode (in figure 11). Increasing Re further leads to combination modes with large aperiodic oscillations, with continuous rearrangement, merging and re-forming of the vortex billows. No steady state is observed, even for a short while. Although we do still see some of the expected behavior from linear stability results (oscillations suppressed for weak stratification and weak diffusion), the flow very quickly becomes inherently nonlinear and chaotic.

4.2.5 Layer formation

BY2005 investigated the oscillatory (or "conductive") instability as a source of layer formation. They noted the negative-diffusion behavior created within this instability, and observed buoyancy layers with coarsening vertical scales even in rather low Re simulations which were run for tall boxes with multiple scale heights. Given that a differentially diffusing fluid is also prone to negative diffusion (or restratification), it may be possible to observe layering in this setup too. Although we have not explored this question in much detail, we tried computations for boxes with equal length scales in x and z (figure 13). We see some markers of the monotonic mode in the evolution of this flow, in the formation of blob-like vortices of an intermediate size that pulsate and meander with the horizontal mean flow. We also see aperiodic oscillations and horizontal merging of vortices, trying to form larger-scale structures, and we see some interaction between vorticity layers that may point to some vertical merging as well. However, the flow remained chaotic for the entire length of time that we ran it for, and we did not observe any stable large-scale structures forming. This may be, as BY2005 claim, due to the monotonic mode dominating and suppressing layer formation, but it is hard to compare with the simulation end states in BY2005 as they have a different setup with a horizontal shear forcing.

5 Summary and Future Steps

We have investigated the stability of the two-dimensional spicy Kolmogorov flow by numerical exploration of the linear stability problem and the nonlinear flow evolution. Lin-

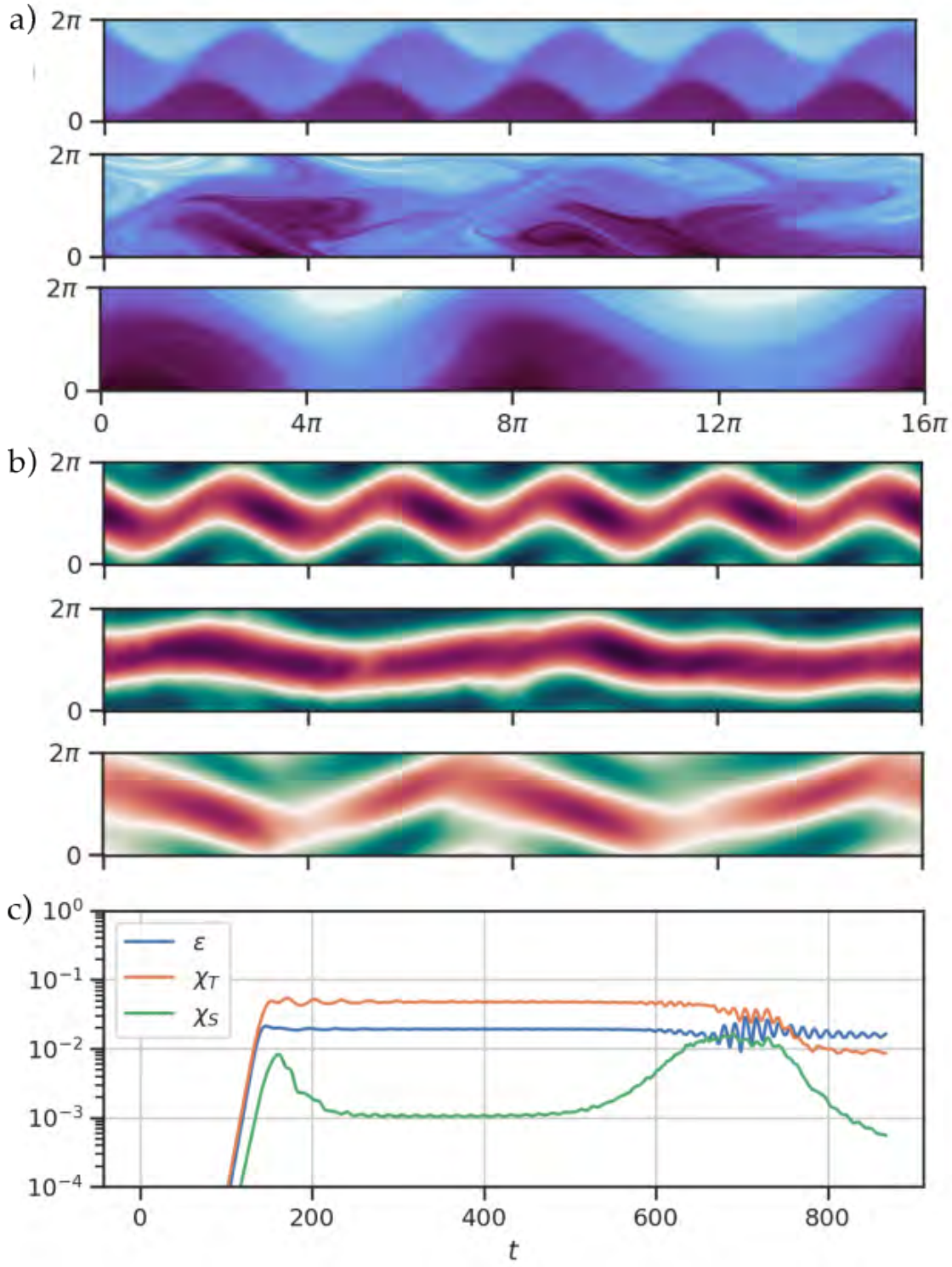

Figure 12: Evolution of the run with $Re = 6$, $Ri = 0.05$, and $R_\rho = -0.5$ for the (a) total buoyancy, and (b) total vorticity fields, for times $t = 350$ (top), $t = 700$ (middle), and $t = 850$ (bottom). (c) Dissipation rates of TKE and scalar variance with time.

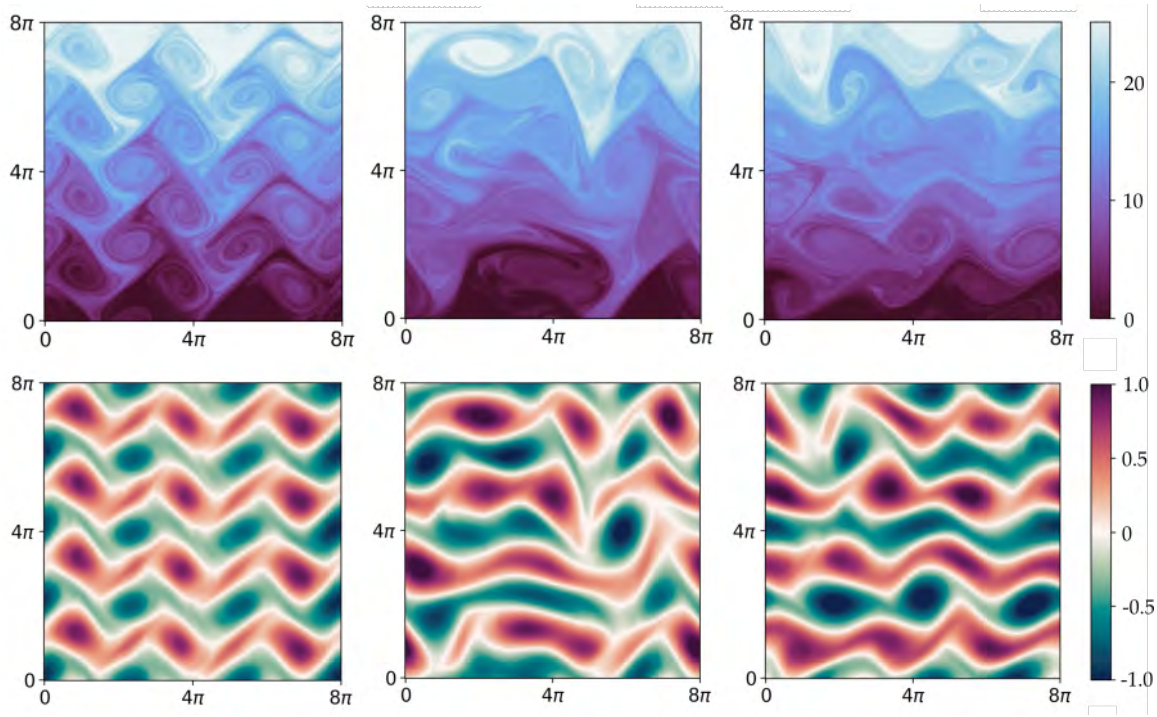

Figure 13: Evolution of the flow in a computational box with equal length scales in x and z. Snapshots of total buoyancy (top) and total vorticity (bottom) for times $t = 232$ (left), $t = 512$ (middle) and $t = 888$ (right), for the run with parameters $Re = 15$, $Ri = 0.01$, and $R_\rho = -2$.

ear stability analysis reveals two major regions of instability that we call the monotonic and the oscillatory mode. The oscillatory mode arises from the stratified dynamics and is destabilized further under weakly diffusing scalars, i.e., when salinity controls the buoyancy gradient. The monotonic mode dominates in weak stratification and fast diffusion (temperature-controlled) scenarios. For strong stratification, weak diffusion pushes both modes into instability well beyond the classical Miles-Howard threshold of $Ri = 1/4$ for inviscid shear stratified flows. The effect of changing the density ratio of the doubly-stratified flow is equivalent to changing the Prandtl number in the singly-stratified flow, and we use this to postulate an "effective Prandtl number" to capture the linear stability behavior of the two-component flow.

At low Reynolds number ($Re \leq 4$), linear stability predicts the nonlinear evolution of the flow fairly well. DNS for the monotonic mode shows intermediate-wavelength overturning billows, and the oscillatory mode shows longer-wavelength pulsating structures with a slower onset. The density ratio for the double-diffusive case affects the equilibrium values of the buoyancy fluxes in a similar way to the Prandtl number in the single-diffusive case. We can use this equivalence to construct an effective Prandtl number, or an effective diapycnal diffusivity K_V, for the weakly turbulent Kolmogorov flow. This will be especially enlightening in understanding how valid the widely-used $K_T = K_S$ assumption (which gives $\Gamma = 0.2$) is for smaller Re_b flows.

Here, we find that the strongly stratified Kolmogorov flow is unstable in both laminar (low Re, via the oscillatory mode) and turbulent (high Re, via the monotonic mode) flow regimes for small $|R_\rho|$. Slow diffusion can allow the creation of very small-scale density gradients that could become locally unstable and overturn, especially when viscous effects are weak (high Re). This results in locally well-mixed patches in a flow where vertical motion is otherwise restricted because of stratification. This is a pathway through which instability in high-Pr stratified turbulence often leads to the formation of layer-like structures in the scalar fields. Therefore, it is possible that the monotonic mode under strong stratification may lead to density layering, especially if double-diffusive effects are also present. Investigating whether layer formation occurs, and whether double-diffusive effects play a role in it beyond just changing the effective Pr, could be another interesting line of inquiry.

6 Acknowledgments

I want to thank my advisors for this project, Chris Howland and Leo Middleton, for proposing this very interesting and enjoyable project, and their constant guidance and support through my attempts at understanding what double-diffusion means. I would like to thank Colm-cille Caulfield for providing his invaluable insight and perspective on this problem throughout the summer. Edgar Knobloch, Basile Gallet and Greg Chini were fantastic principal lecturers and I deeply appreciate the opportunity to learn about multiscale turbulence from them. I want to acknowledge the efforts of Bruce Sutherland, Julie Hildebrandt, Janet Fields and Lanie Plueddemann in running a very-well organized program this summer. Lastly, a heartfelt thank you to all the other fellows for the joy of their company and friendship this summer!

7 Appendix

7.1 Scalar variance budget

We derive the evolution of the volume-averaged buoyancy variance $\langle b'^2 \rangle$ for the spicy flow as follows:

$$\frac{d\langle b'^2 \rangle}{dt} = \left\langle \frac{\partial b'^2}{\partial t} \right\rangle + \mathcal{L}, \tag{48}$$

where $\mathcal{L}$ contains the boundary terms from applying the Leibniz integral rule; $\mathcal{L} = 0$ as the boundaries of the box are fixed in time. Therefore

$$\frac{d\langle b'^2 \rangle}{dt} = \left\langle 2b' \partial_t b' \right\rangle, \tag{49}$$

and substituting 21,

$$\frac{d\langle b'^2\rangle}{dt} = \left\langle 2b'\left(-\mathbf{u}\cdot\nabla b' + \frac{1}{Pe_b}\nabla^2 b' + \frac{A}{Pe_\gamma}\nabla^2\gamma' - \operatorname{sgn}(\overline{b_z})\, w\right)\right\rangle, \tag{50}$$

$$= -\langle\nabla\cdot(\mathbf{u}b'^2)\rangle + \frac{2}{Pe_b}\langle\nabla\cdot(b'\nabla b')\rangle - \frac{2}{Pe_b}\langle|\nabla b'|^2\rangle + \frac{2A}{Pe_\gamma}\langle\nabla\cdot(b'\nabla\gamma')\rangle$$
$$- \frac{2A}{Pe_\gamma}\langle\nabla\gamma'\cdot\nabla b'\rangle - 2\operatorname{sgn}(\overline{b_z})\langle wb'\rangle, \tag{51}$$

$$= -\nabla\cdot\langle\mathbf{u}b'^2\rangle + \frac{1}{Pe_b}\nabla\cdot\nabla\langle b'^2\rangle + \frac{2A}{Pe_\gamma}\langle\nabla\cdot(b'\nabla\gamma')\rangle$$
$$- \langle\chi_b\rangle - \langle\chi_{\gamma b}\rangle - 2\operatorname{sgn}(\overline{b_z})\langle wb'\rangle, \tag{52}$$

where we have defined the the diffusive flux terms

$$\langle\chi_b\rangle = \frac{2}{Pe_b}\langle|\nabla b'|^2\rangle, \qquad \langle\chi_{\gamma b}\rangle = \frac{2A}{Pe_\gamma}\langle\nabla\gamma'\cdot\nabla b'\rangle. \tag{53}$$

Periodic boundary conditions make the divergences of the volume averages zero, and we get

$$\frac{d\langle b'^2\rangle}{dt} = -\langle\chi_b\rangle - \langle\chi_{\gamma b}\rangle - 2\operatorname{sgn}(\overline{b_z})\langle wb'\rangle. \tag{54}$$

References

[1] N. J. Balmforth and Y.-N. Young, *Stratified Kolmogorov flow*, Journal of Fluid Mechanics, 450 (2002), pp. 131–167.

[2] N. J. Balmforth and Y.-N. Young, *Stratified Kolmogorov flow. Part 2*, Journal of Fluid Mechanics, 528 (2005), pp. 23–42.

[3] K. J. Burns, G. M. Vasil, J. S. Oishi, D. Lecoanet, and B. P. Brown, *Dedalus: A flexible framework for numerical simulations with spectral methods*, Physical Review Research, 2 (2020), p. 023068.

[4] C. Caulfield, *Layering, Instabilities, and Mixing in Turbulent Stratified Flows*, Annual Review of Fluid Mechanics, 53 (2021), pp. 113–145.

[5] E. A. D'Asaro, *How do Internal Waves Create Turbulence and Mixing in the Ocean?*, July 2022.

[6] C. De Lavergne, G. Madec, J. Le Sommer, A. J. G. Nurser, and A. C. Naveira Garabato, *The Impact of a Variable Mixing Efficiency on the Abyssal Overturning*, Journal of Physical Oceanography, 46 (2016), pp. 663–681.

[7] R. Ferrari and K. L. Polzin, *Finescale Structure of the T–S Relation in the Eastern North Atlantic*, Journal of Physical Oceanography, 35 (2005), pp. 1437–1454.

[8] P. Garaud, B. Gallet, and T. Bischoff, *The stability of stratified spatially periodic shear flows at low Péclet number*, Physics of Fluids, 27 (2015), p. 084104.

[9] A. Gargett, *Differential diffusion: an oceanographic primer*, Progress in Oceanography, 56 (2003), pp. 559–570.

[10] M. Gregg, E. D'Asaro, J. Riley, and E. Kunze, *Mixing Efficiency in the Ocean*, Annual Review of Marine Science, 10 (2018), pp. 443–473.

[11] P. R. Jackson and C. R. Rehmann, *Experiments on Differential Scalar Mixing in Turbulence in a Sheared, Stratified Flow*, Journal of Physical Oceanography, 44 (2014), pp. 2661–2680.

[12] E. N. Lorenz, *Available potential energy and the maintenance of the general circulation*, Tellus, 7 (1955), pp. 157–167.

[13] L. Middleton, P. E. D. Davis, J. R. Taylor, and K. W. Nicholls, *Double Diffusion As a Driver of Turbulence in the Stratified Boundary Layer Beneath George VI Ice Shelf*, Geophysical Research Letters, 49 (2022), p. e2021GL096119.

[14] L. Middleton, E. C. Fine, J. A. MacKinnon, M. H. Alford, and J. R. Taylor, *Estimating Dissipation Rates Associated With Double Diffusion*, Geophysical Research Letters, 48 (2021), p. e2021GL092779.

[15] L. Middleton and J. R. Taylor, *A general criterion for the release of background potential energy through double diffusion*, Journal of Fluid Mechanics, 893 (2020), p. R3.

[16] G. I. Sivashinsky, *Weak turbulence in periodic flows*, Physica D: Nonlinear Phenomena, 17 (1985), pp. 243–255.

[17] K. S. Smith and R. Ferrari, *The Production and Dissipation of Compensated Thermohaline Variance by Mesoscale Stirring*, Journal of Physical Oceanography, 39 (2009), pp. 2477–2501.

[18] M. E. Stern, *The "Salt-Fountain" and Thermohaline Convection*, Tellus, 12 (1960), pp. 172–175.

[19] ——, *Initiation of a doubly diffusive convection in a stable halocline*, Journal of Marine Research, 61 (2003), pp. 211–233.

[20] K. B. Winters, P. N. Lombard, J. J. Riley, and E. A. D'Asaro, *Available potential energy and mixing in density-stratified fluids*, Journal of Fluid Mechanics, 289 (1995), pp. 115–128.

[21] Y. You, *A global ocean climatological atlas of the Turner angle: implications for double-diffusion and water-mass structure*, Deep Sea Research Part I: Oceanographic Research Papers, 49 (2002), pp. 2075–2093.

Mixing and Layering in Stratified Rotating Turbulent Flow

Cécile Le Dizes

August 20, 2024

1 Introduction

Layered density structures, commonly referred to as "staircases," are a common feature in stratified turbulent flows. These structures consist of vertically stacked well-mixed layers separated by sharp density gradients. They can have a significant impact on large-scale mixing and transport in geophysical and astrophysical systems (3), as they can significantly alter vertical fluxes of heat and momentum, as well as chemical mixing.

Persistent stepped profiles in temperature and salinity have been extensively documented in regions subject to double-diffusive instabilities, such as beneath the Mediterranean outflow in the Tyrrhenian Sea (6) and in the Arctic Ocean (10). In these cases, staircase formation is attributed to either salt fingering or diffusive convection. However, staircases have also been observed in systems where the stratification is stable to double-diffusive effects. For example, (15) documented stepped density profiles in Loch Ness, where stratification arises solely from temperature variations. Laboratory experiments have further demonstrated staircase formation in non-double-diffusive systems (11; 8), providing evidence that these structures can emerge from turbulent processes only.

In particular, (11) and (8) observed experimentally the spontaneous emergence of layers in a linearly stratified saltwater fluid stirred by the horizontal oscillation of vertical rods. Their design is similar to the one used in this project (see Figure 1), though without rotation. Their findings revealed distinct behaviours depending on the values of the Richardson number Ri and the Reynold Re, defined using external parameters. For weak stratification and strong stirring (small Ri and large Re), well-mixed regions initially form near the boundaries, where turbulent buoyancy fluxes are blocked by impermeable walls. These regions gradually extend into the interior, with a smooth transition. At higher Ri and over a wide range of Re, the density profile no longer remains smooth but develops a series of mixed layers separated by sharp interfaces. In cases with small Ri and small Re, (8) observed a different mechanism, which they named "boundary layering." Here, the mixed regions at the top and bottom boundaries erode the stratification, forming sharp interfaces. These interfaces, in turn, act as a barrier for buoyancy transport and additional mixed layers form. A summary of the experimental results from (8) is presented in Figure 2.

Staircases have also been observed in other experimental configurations (3; 16). Interestingly, the layering process appears consistent across a variety of setups, with layer thickness scaling as $3U/N$, where U is the characteristic velocity scale and N is the buoyancy frequency. This scaling law was also discussed by (2) and (4), using asymptotic analysis

for strongly stratified turbulence. They assumed that the strong stratification leads to an anisotropy of the turbulence, with horizontal scales larger than vertical scale.

The first theoretical models capturing the self-organization of stratified turbulence into staircases were proposed by (12) and (13). They showed that if the buoyancy flux depends on the local density gradient and decreases with increasing stratification beyond a certain threshold, the system becomes anti-diffusive and unstable to perturbations in the mean buoyancy. This mechanism explains the growth of localized layers, where converging buoyancy fluxes above regions of weakened stratification and diverging fluxes below drive the formation of layers. However, these models are limited by their ill-posed nature; smaller disturbances grow faster, leading to steepened interfaces and discontinuities in the absence of molecular diffusion. Building on these ideas, (1) developed a more comprehensive model that incorporates both the mean buoyancy field $b(z,t)$ and the turbulent kinetic energy density $e(z,t)$. Their model proposed an N-shaped law for the buoyancy flux, enabling layering instabilities at intermediate stratifications while arresting steepening at higher gradients. This equilibrium predicts finite-thickness interfaces, aligning with experimental observations. However, the relationship between buoyancy flux and stratification remains uncertain, and the model's simplified representation of turbulence and dissipation limits its general applicability (3).

Several questions still remain on the staircase formations. What mechanism selects the characteristic layer scale U/N? How are turbulent buoyancy flux and mean buoyancy gradient coupled? What distinguishes the layering and boundary layering regimes observed by (8)? To our knowledge, there have been no three-dimensional direct numerical simulations (DNS) reproducing the experiments of (11) and (8). In order to answer the previous questions, we revisit the Holford–Linden experiments in the laboratory and use DNS to access detailed turbulence statistics not directly measurable in experiments.

Stratified turbulence in geophysical and astrophysical applications is also influenced by rotation. This introduces additional complexity to staircase formation by incorporating Coriolis forces, which affect the anisotropy and coherence of turbulent motions (9). When stratification dominates ($f/N \ll 1$), horizontal layers with pancake vortices form (14). Conversely, when rotation dominates ($f/N \gg 1$), columnar vortices aligned with the rotation axis emerge. For intermediate regimes, vortex interactions fragment vertical coherence, producing layered structures with scales influenced more by f/N than U/N (7; 5). As rotation rates increase, the system transitions from pancake-like structures to robust vertical columns. These columns persist even under strong interactions, highlighting the stabilizing influence of rotation at high f/N. However, key questions remain: Can staircases still develop in rotating flows? If so, under what conditions do they emerge, and how do the Reynolds, Froude, and Rossby numbers influence their formation? What role does f/N play in setting the layer scale, and what processes govern their formation and stability over time?

In this study, we aim to investigate the formation and evolution of staircase structures in stratified, rotating turbulent flows. We begin by describing the experimental setup in section 2. Next, we detail in section 3 the numerical simulations conducted to complement the experiments, specifying the governing equations, boundary conditions, and forcing. The results for the non-rotating case are presented in §4, analyzing the mechanisms behind layering and identifying scaling laws. Finally, we examine the effects of rotation on staircase

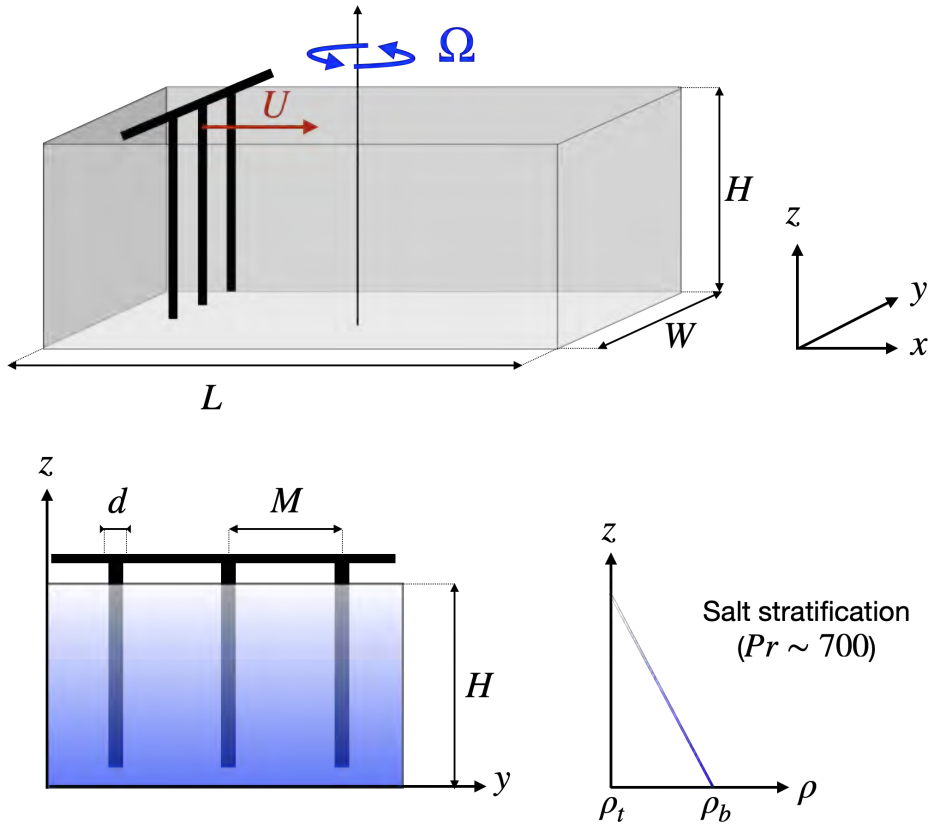

Figure 1: Experimental set-up

formation in §5, focusing on the role of f/N in shaping the observed patterns and comparing them to the non-rotating case.

2 The Experiments

2.1 The set-up

The experiments were conducted in a rectangular channel of length L, width W, and height H, mounted on a 2 m–diameter rotating platform (see Figure 1). The near-linear salt stratification is created using the double-bucket method. Fresh water is injected into a brine reservoir via a peristaltic pump, where it is mixed with the surrounding fluid by a stirring impeller. A second pump transfers the resulting mixture to the tank through a floating sponge to minimize mixing caused by surface waves. The flow rates of the pump are regulated to ensure a linear density gradient as the tank fills. To avoid temperatures variations, fresh water and brine were stored in large reservoirs at room temperature (18°C) before use. We estimate temperature variations to remain within $1.5°C$, such that density variations associated with temperature can be neglected. Buoyancy frequencies in the experiments ranged from $0.6s^{-1} < N < 1.8s^{-1}$.

The turbulence is generated by towing an array of vertical rods with width d and mesh

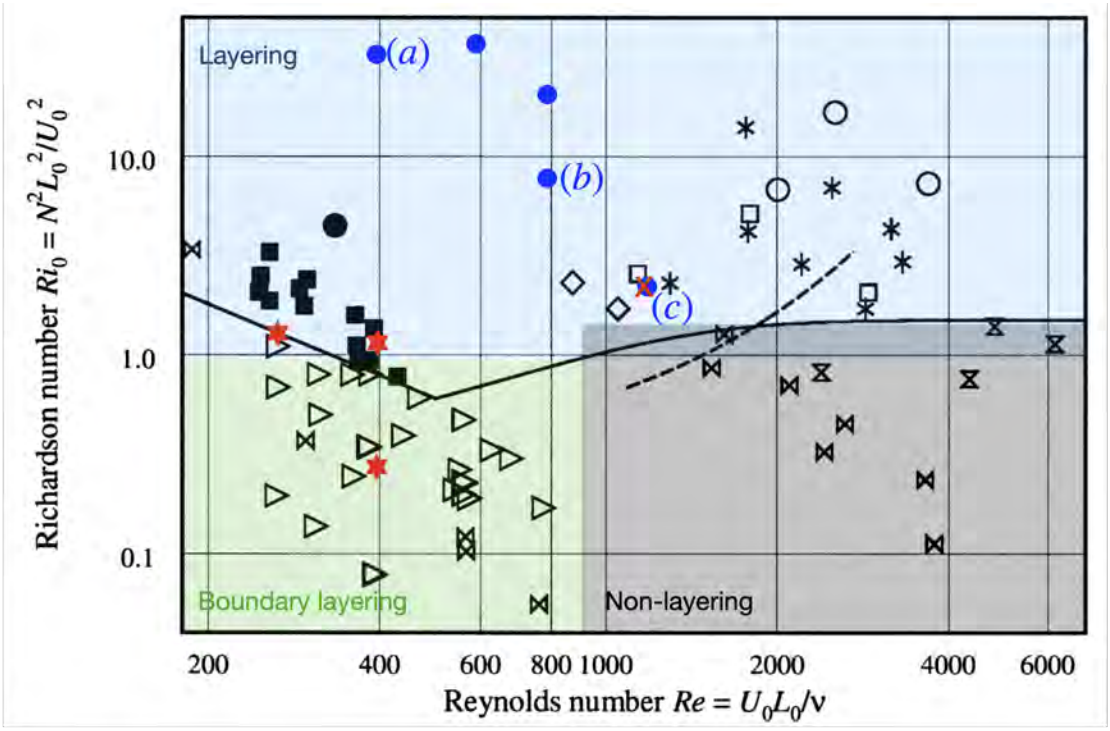

Holford & Linden (1999)

Symbol	d (cm)	M (cm)	S	n_{bars}	L
■	0.65	3.25	0.20	8	5–20 M
●	0.65	6.50	0.10	4	6 M
◇	2.50	6.40	0.39	4	8 M
□	2.50	12.80	0.20	2	4 M
○	2.80	25.60	0.11	1	2.5 M
*	3.15	15.60	0.20	8	25 M

⋈ ⧖ Non-layering experiments for experiments * and for the others

▷ Boundary layering

WHOI experiments (2024)

- $d = 2.5$ cm; $M = 11$ cm
- $d = 0.6$ cm; $M = 3$ cm
- Non-layering

Figure 2: Diagram adapted from (8). The shaded regions correspond to the different regimes identified by (8). The blue dots and red stars correspond to experiments run at the WHOI GFD laboratory during this project, with the experiments denoted (a-b-c) discussed in §4.1.

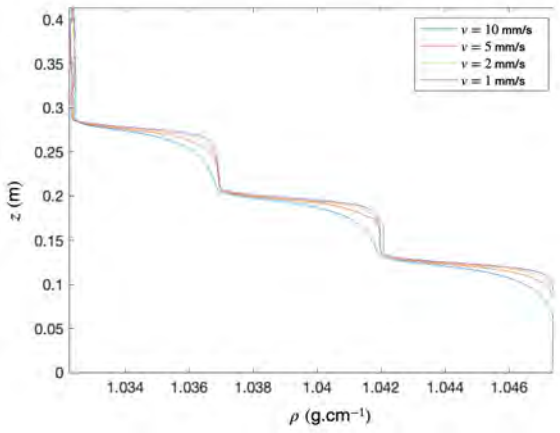

Figure 3: Measures of density profiles for different probe velocities

spacing M, at a constant speed U over the distance $L_{\text{stir}} \sim L - 2M$. The rods are suspended from a carriage driven by a computer-controlled DC motor, ensuring consistent motion and repeatability. The rake's velocity ramped linearly from 0 to U on a short distance of about $M/2$ and returned to 0 with controlled acceleration and deceleration.

Following (8), each run consisted of n sequences of 15 consecutive back-and-forth passes. After each sequence, the flow was allowed to decay for 150 s before the density profile was measured with a downward traverse of a conductivity probe. The probe was calibrated weekly to prevent drift. Since thin well-mixed layers rapidly formed at the top and bottom, the gradient in the central stratified region was used to determine the initial buoyancy frequency N_0. The effect of probe descent speed is shown in figure 3. At low speeds (v = 1-2 mm.s^{-1}), the probe resolved sharp density interfaces accurately. At higher speeds, entrainment of lighter fluid caused artificial smoothing of the gradients. All profiles were therefore measured at $v = 1$ mm.s^{-1}.

Additionally to the density measurements, shadow-graph imaging is used to monitor the evolving density field, highlighting regions with significant density curvature and providing independent measurements of layer scales along with insights into transient flow structures.

2.2 Rotating experiments

The rotating experiments were performed with the channel mounted on a 2 m–diameter turntable, whose rotation axis was aligned to within a few degrees of vertical. The angular velocity $\Omega = f/2$ of the rotating table was chosen in the range $0 \leq f \leq 2$ rad/s and held constant throughout each run.

The tank was set into rotation while empty and filled while rotating. In initial trials, we attempted to fill the tank from the bottom, in order to shorten the spin-up time. However, this method proved unsuitable: the bottom-filling device generated excessive mixing both during filling and throughout the experiment, which compromised the density stratification. We therefore reverted to filling from the top through a floating sponge, as in the non-rotating runs, which showed only minimal influence on the density profile.

To ensure that the fluid was in a state of solid-body rotation before the start of stirring,

the filling rate was reduced considerably, resulting in total filling times of 4 to 6 hours. However, this duration may still be insufficient to guarantee perfect solid-body rotation throughout the depth. This would necessitate additional verification, for example by tracking the motion of neutrally buoyant particles released at different depths during the filling process.

2.3 Dimensionless parameters

These experiments include a large number of control parameters, including five characteristic length scales (the dimensions of the tank W, L, H, the rod size d and mesh spacing M), the towing velocity U and the two frequencies N_0 and $f = 2\Omega$.

For definition of relevant dimensionless parameters of the turbulence, we need to use the turbulent velocity and horizontal integral length scales. Since we do not directly measure the turbulent field, these scales must be inferred indirectly. We consider the turbulence to be roughly uniform in the horizontal direction, with no significant mean flow over the length of a stirring sequence. Each tow of the rods creates structured wakes, but after many tows these patterns tend to mix and spread out evenly. With this in mind, we can describe the turbulence using a single velocity scale and a single length scale based on the external forcing. The forcing provides two possible horizontal length scales: the rod diameter d and the mesh spacing M. (8) found that in unstratified turbulence from biplanar grids, the main turbulent length scale is usually proportional to the mesh size, making M the most relevant scale for weakly stratified fluid. For higher stratification and low turbulence, the rod diameter d, which sets the scale of the wake, becomes more important. (8) argue that the best scaling for the layer depth was found using the length scale $L_0 = \sqrt{dM}$ and the velocity scale $U_0 = U\,(1 - d/M)$, which account for both the effects of the rod size and the mesh spacing. Both our and their experiments are reported in Figure 2 using these scalings.

For the present analysis, however, we use only the mesh spacing M and the towing velocity U as characteristic scales. This choice simplifies comparison with the DNS, which do not explicitly include the rod geometry. We then define the Reynold, Péclet, Richardson and Rossby numbers as :

$$Re = \frac{UM}{\nu} \;;\quad Pe = \frac{UM}{\kappa} \;;\quad Ri = \frac{N_0^2 M^2}{U^2} \;;\quad Ro = \frac{U}{fM} \tag{1}$$

We can equivalently define a Froude number as : $Fr = Ri^{-1/2}$.

Other geometric parameters of interest are the various aspect ratios between the tank dimensions and the rod length scales. These were varied by (8), who found no significant influence on layer formation. In our experiment, the tank dimensions were set to $L = 120$ cm, $W = 50$ cm and $H \approx 45$ cm.

All of the experiments conducted are listed in Table 1 and reported in the diagram of (8) (see Fig. 2). The black dots correspond to their experiments, while the red stars and the blue dots are the experiments run at the WHOI GFD laboratory during this project. The red stars correspond to the configuration (1) with an array of five small rods of width $d = 0.6$ separated by $M = 3$ cm, while the blue dots corresponds to the configuration (2) with two large rods ($d = 2.5$ and $M = 10.6$ cm). The smaller rods (1) are used to reach the boundary layering regime, as discussed in section 4.1.

Rods	N (s^{-1})	U (cm/s)	Re_0	Ri_0	Re	Ri	Case n°
(1)	1.2465	2	263.4	1.432	800	6.215	
(1)	1.77795	3	395	0.6902	1200	3.4083	
(1)	1.3846	3	395	1.1380	1200	5.6197	
(2)	0.8480	1	393.4	31.561	1060	80.796	(a)
(2)	0.82263	2	786.7	7.4255	2120	19.009	(b)
(2)	0.66425	3	1180	2.1518	3180	5.509	(c)
(2)	1.34044	1.5	590	36.2410	1590	89.7272	
(2)	1.32688	2	786.7	19.9752	2120	49.4555	

Table 1: Parameters used in the non-rotating experiments. The rod configurations correspond to : (1) $d = 0.6$ cm, $M = 3$ cm; (2) $d = 2.5$ cm, $M = 10.6$ cm. The value Re_0 and Ri_0 are the Reynolds and Richardson numbers computed using the length scale L_0 and velocity U_0 from (8).

3 The DNS

We simulate a three-dimensional, rotating, incompressible flow in Cartesian coordinates (x, y, z). The vertical coordinate z (unit vector $\mathbf{e_z}$) is aligned with both gravity ($\mathbf{g} = -g\mathbf{e_z}$) and the rotation axis ($\mathbf{\Omega} = \Omega\mathbf{e_z}$). The rods in the experiments move along the horizontal x-axis. The fluid is stably stratified with mean density ρ_0 and constant buoyancy frequency N. The computational domain is triply periodic, which eliminates boundary layers and free-surface effects. While this simplifies the numerical set-up, it also removes physical processes present in the experiments, limiting direct comparison. Capturing these effects numerically would require no-slip walls and a free surface. The domain size is set to $(L_x, L_y, L_z) = (4M, M, 2M)$, so only one rod spacing is represented explicitly in the y-direction.

The stirring effect of the rods is modelled using a vertically uniform, horizontal body force $\mathbf{F_h}$ that generates two counter-rotating vortices of scale M as illustrated in Figure 4. The vortex centres move back and forth in x. In a traverse from left to right, they are accelerating from 0 to U for $x \in [0, M]$, then moving at the constant speed U for $x \in [M, 3M]$ before decelerating and reversing direction. This forcing was implemented in PADDI by UCSC MS student Tiam Babadiyaghoubi.

We decompose the density field as $\rho(\boldsymbol{x}, t) = \bar{\rho}(z) + \rho'(\boldsymbol{x}, t)$, where $\bar{\rho}$ is the background density field such that $\frac{d\bar{\rho}}{dz} = -\rho_0 N^2/g$ and ρ' are the density perturbations. In the Boussinesq approximation, the governing equations are:

$$\boldsymbol{\nabla} \cdot \mathbf{u} = 0, \tag{2}$$

$$\frac{\partial \mathbf{u}}{\partial t} + \mathbf{u} \cdot \nabla \mathbf{u} + f\mathbf{e}_z \times \mathbf{u} = -\frac{1}{\rho_0}\boldsymbol{\nabla} p + \nu \nabla^2 \mathbf{u} + b\mathbf{e}_z + \frac{1}{\rho_0}\mathbf{F}_h, \tag{3}$$

$$\frac{\partial b}{\partial t} + \mathbf{u} \cdot \boldsymbol{\nabla} b + N^2 w = \kappa \nabla^2 b, \tag{4}$$

where $\mathbf{u} = (u, v, w)$ is the velocity field, p is the pressure, and $b = -g\rho'/\rho_0$ are the buoyancy perturbations. Buoyancy variations are assumed to arise solely from temperature, so the kinematic viscosity ν and diffusivity κ are constant.

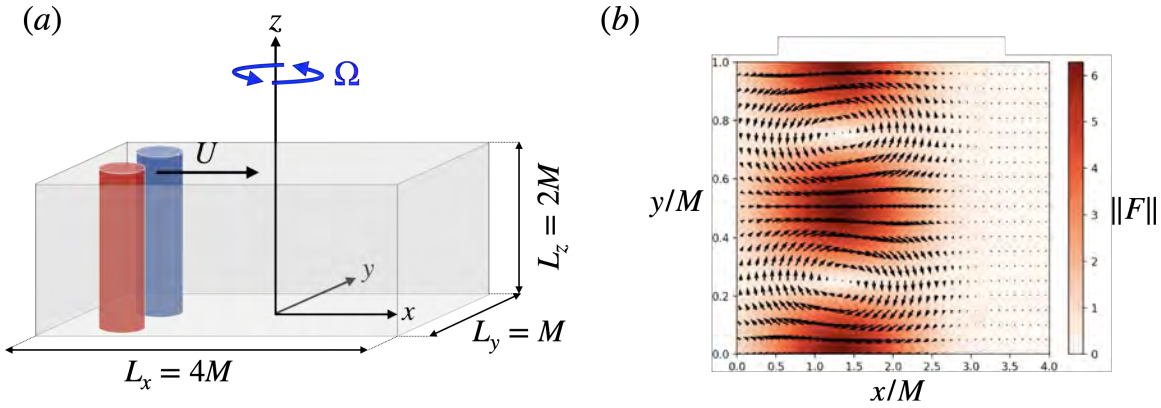

Figure 4: (a) Numerical set-up; (b) Snapshot of the forcing in an horizontal plane.

Since the rod geometry is not resolved and the domain is periodic, the only characteristic length scale is the mesh spacing M. We introduce the non-dimensional variables :

$$t_* = t\frac{U}{M};\ \ (x_*, y_*, z_*) = \frac{(x, y, z)}{M};\ \ \mathbf{u}_* = \frac{\mathbf{u}}{U};\ \ b_* = \frac{b}{N^2 M};\ \ p_* = \frac{p}{\rho_0 U^2};\ \ \mathbf{F}_{h*} = \mathbf{F}_h \frac{M}{\rho_0 U^2} \quad (5)$$

Using the dimensionless numbers defined in (1), we can rewrite the equations in the dimensionless form, getting rid of the * subscript for simplicity.

$$\boldsymbol{\nabla}.\mathbf{u} = 0, \quad (6)$$

$$\frac{\partial \mathbf{u}}{\partial t} + \mathbf{u}.\boldsymbol{\nabla}\boldsymbol{u} + \frac{\mathbf{e}_z \times \mathbf{u}}{Ro} = -\nabla p + \frac{1}{Re}\nabla^2 \mathbf{u} + Ri\ b\mathbf{e}_z + \mathbf{F}_h, \quad (7)$$

$$\frac{\partial b}{\partial t} + \mathbf{u}.\boldsymbol{\nabla} b + w = \frac{1}{Pe}\nabla^2 b. \quad (8)$$

For a fluid stratified in temperature, the Prandtl number $\nu/\kappa = \mathcal{O}(1)$, so we set $Pe = Re$. This choice is another critical difference between the experiments and the simulations, as salt tend to diffuse much slower than temperature ($Pr \approx 1000$ for salt-stratified experiments), which could influence the layer formation. In particular, strong temperature gradients that can arise in staircases are more easily smoothed out by diffusion than in salt-stratified staircases.

The equations are discretised over a $768 \times 192 \times 384$ grid for varying values of Ri and Re, listed in table 2. This choice of mesh size ensures that the turbulence and mixing are appropriately resolved since $Pr = 1$.

4 Staircase Formation in the Non-rotating Case

4.1 Laboratory experiments

In this first section, we focus on reproducing the experimental results of (8), examining three specific experiments (Fig. 5). The top panels show the evolution of the density profile from the initial to the final state, while the bottom panels show the time evolution of the vertical density-gradient profile.

Re	Ri	Ro	f/N	Total n° of passes
400	30	∞	0	30
400	100	∞	0	19
400	300	∞	0	25
800	60	∞	0	21
800	60	1	0.13	17
800	60	0.12	0.8	14

Table 2: Parameters used in the DNS.

For case (a), with $Re = 3200$ and $Ri = 5.5$, well-mixed layers form at the the top and bottom boundaries, where turbulent buoyancy fluxes are constrained by the impermeable boundaries. These mixed regions progressively expand toward the interior. However, the overall density profile remains smooth and monotonic, with no interior interfaces: it decreases from top to bottom without distinct steps. This case lies close to the non-layering threshold identified by (8) (see the regime diagram in Fig. 2), so the absence of layering is expected.

In case (b), with $Re = 2120$ and $Ri = 20$, mixed boundary layers again develop at the top and bottom, but here they are separated from the stratified interior by sharp gradients, visible as two pronounced peaks in the density-gradient profile. These 'interfaces' migrate toward mid-depth and eventually merge, yielding two mixed layers. However, no additional interior layers appear. This behaviour was reported by (11) but not discussed explicitly by (8). Although the parameters fall within the layering regime of (8), our tank's limited vertical extent likely allowed the boundary layers to meet before interior layers could develop. We, however, did not test this hypothesis further.

In case (c), with $Re = 1069$ and $Ri = 80$, quasi-homogeneous layers separated by thin interfaces form rapidly within the interior. The initial layer thickness is of order $3U/N_0$, where U is the rod speed and N_0 the initial buoyancy frequency. This is similar to what was observed in previous experiments (11; 8). Over time, the interior layering pattern evolves as the interfaces drift together and merge. Simultaneously, the edge layers advance inward, gradually eroding the interior layering structure. The experiment was stopped after 120 hours. The final state consists of four mixed layers separated by three strong interfaces. We expect that if the experiment was carried out for longer, the residual structure would have continued to evolve with interfaces merging or decaying, resulting in a fully homogeneous state.

To investigate the vicinity of the boundary layering regime, we also performed experiments with smaller rods ($d = 0.6$ cm, $M = 3$ cm), represented by red stars in Fig. 2. In this configuration, the layers were thinner and less distinct. The characteristic vertical scale in these cases was closer to U/N and typically smaller than the canonical $3U/N$, which made precise identification difficult. Layer formation was also slow, often taking more than 20 h, which made reaching the layering regime difficult within the timeframe of this project. As a result, this regime was not investigated further. However, the physical distinction between the 'boundary layering' and 'classical layering' regimes of (8) remains unclear and needs further investigations.

Layering proved more difficult to observe than anticipated; in particular, early attempts

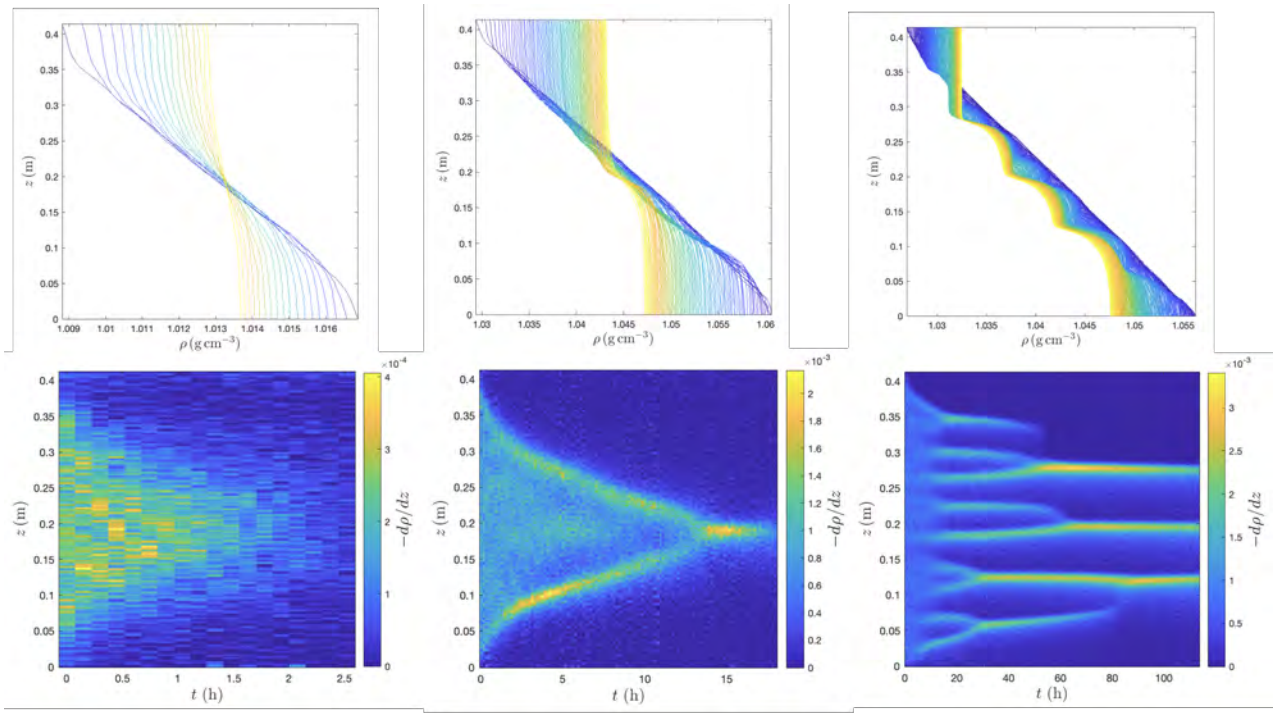

(*a*) $Re_M = 3200$; $Ri_M = 5.5$ (*b*) $Re_M = 2120$; $Ri_M = 20$ (*c*) $Re_M = 1069$; $Ri_M = 80$

Figure 5: Top panels : evolution of the density profile from the initial state (blue) to the end state (yellow). Bottom panels : time-evolution of the vertical density gradient profile (in g.cm^{-4}).

with a larger tank were unsuccessful and are not discussed here. Nevertheless, we were able to reproduce the non-rotating results of (8) and (11) and identify the main regimes of density layering. However, our experiments are still limited by the tank size, which accelerated boundary-layer merging and suppressed interior layering, and by the long timescales required for layer formation. A more systematic survey with longer runs, a larger aspect ratio, and denser sampling in (Re, Ri, U, N) is needed to better understand the layering process and clarify the transition between 'boundary-layering' and 'classical layering'.

4.2 Direct numerical simulations

We also attempted to reproduce layer formation numerically, using the setup described in §3. The formation of layers in numerical simulations was also challenging. Across all cases studied (Table 2), quasi-homogeneous layers appeared only for one parameter set ($Re = 800$, $Ri = 60$). In all other cases, the horizontally averaged density profile showed no stepped structure or sharp interfaces, despite lying in parameter regimes where layering was observed in the laboratory.

This discrepancy can be explained by several differences between the simulations and experiments. First, the numerical runtimes may have been too short for layers to emerge. Second, the simulations use a Prandtl number fixed to 1 for efficiency, whereas in the experiments it reaches values of about 700. This strongly influences the relative roles of viscous and thermal diffusion, potentially leading to distinct layering mechanisms. Another notable distinction is the absence in the simulations of physical walls, particularly the lower boundary, as well as the absence of a free surface. In the experiments, these boundaries play a crucial role in the formation of homogeneous layers at the top and bottom, which could be an important mechanism for the formation of interior layers.

The forcing mechanism also differs. In the experimental setup, the presence of a vertical bar introduces additional small-scale forcing that interacts with the stratification and promotes the formation of layers. This feature is not modeled in the simulations, where we introduce a forcing of horizontal scale corresponding to the mesh spacing M. Moreover, achieving Reynolds and Richardson numbers as high as those in the experiments remains a significant challenge in numerical simulations. The computational cost of resolving such high values is prohibitively expensive, limiting the parameter space that can be explored numerically.

Despite these limitations, we observed layering for the case ($Re = 800$, $Ri = 60$). In this run, the horizontally averaged buoyancy field exhibits a staircase-like pattern (Fig. 6). We observe regions of relatively weak gradient separated by thin interfaces of stronger gradient. The layers were not fully formed or homogenized, i.e., the gradient did not relax to zero by the end of the run (see Fig.6(b)). Here, the layer thickness is of order $6U/N \sim 0.8$, larger than the $\mathcal{O}(3U/N)$ reported in the laboratory experiments. This difference may be explained by the lower value of the Prandtl number.

To investigate the role of buoyancy flux in layer formation, we analyzed the time evolution of the horizontally averaged vertical buoyancy flux (Fig. 7). At first glance, low-flux regions tend to coincide with strong background density gradients, consistent with the Phillips–Posmentier flux–gradient feedback. However, the flux also exhibits pronounced temporal modulation driven by the rod motion: high-flux 'turbulent episodes' occur while

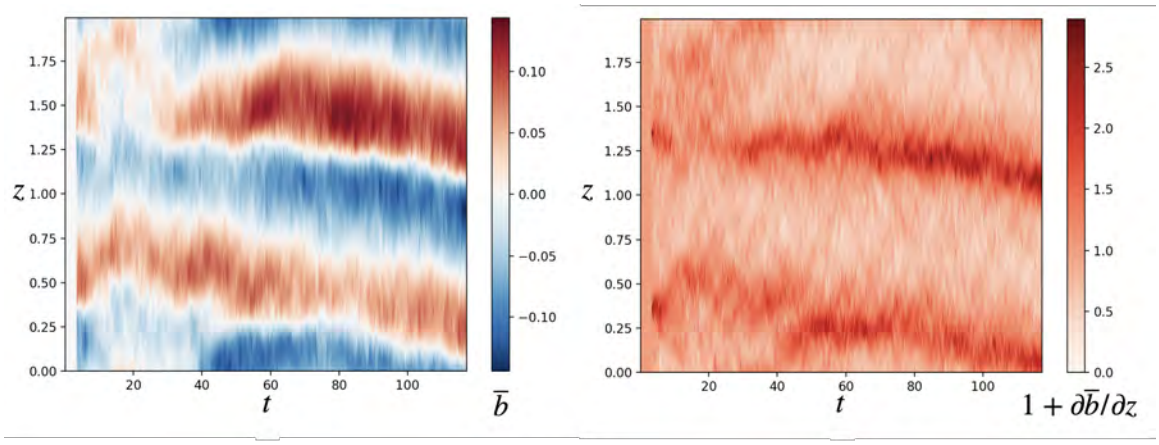

Figure 6: Evolution with time of the profiles of : (a) buoyancy, (b) buoyancy gradient for the case $Re = 800$, $Ri = 60$.

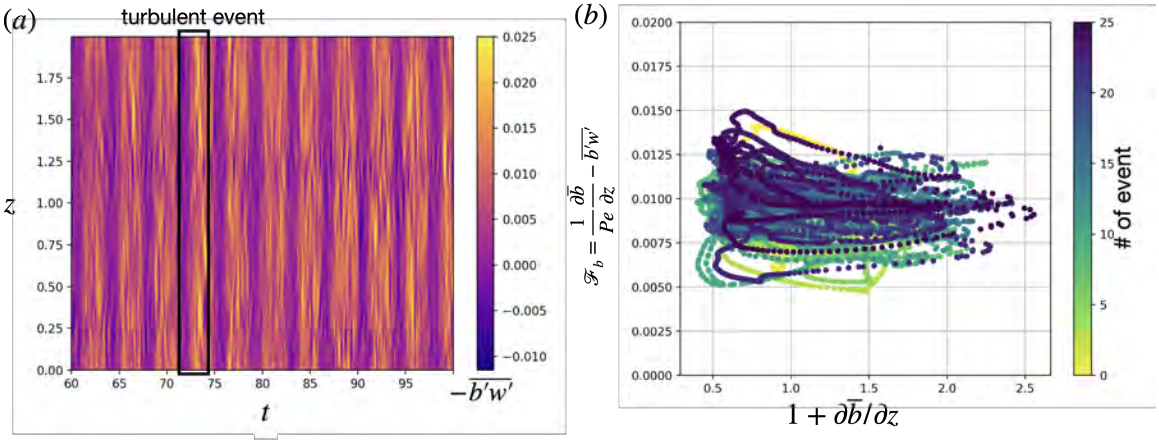

Figure 7: (a) Evolution with time of the horizontally averaged turbulent buoyancy flux. (b) Horizontally averaged buoyancy flux averaged over a turbulent event as a function of the total buoyancy gradient. Dots of a same color represent a single turbulent event at different vertical positions.

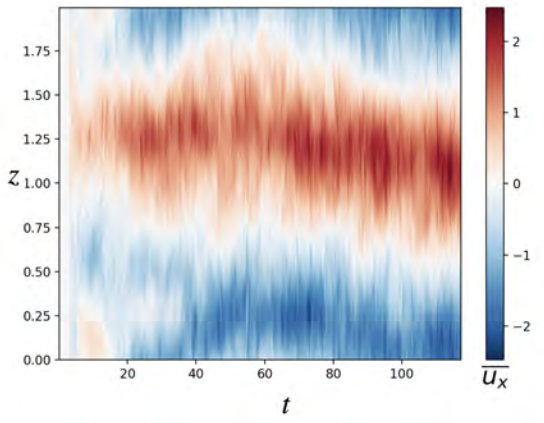

Figure 8: Vertical profile of the horizontally averaged velocity along the x-component as a function of time.

the rods are moving, whereas low-flux phases correspond to their deceleration and stop at the channel walls.

To refine our analysis, we consider the buoyancy flux averaged both spatially in the horizontal direction and temporally over a single stirring event, and we compare it to the total density gradient averaged over the same event and depth. This approach provides a more reliable comparison by filtering out low flux values. The resulting flux–gradient scatter is shown in Figure (7), where each color represents a distinct stirring event across different vertical positions. The results do not provide clear evidence of a systematic decrease in flux with increasing density gradient, as expected in the Phillips instability. However, a plateau, or even a slight decrease, is observed, compatible with the slow interface sharpening.

To gain further insight into layer-formation dynamics, we examine the horizontally averaged streamwise velocity (Fig. 8). The velocity field exhibited a vertically layered structure that is closely correlated with the observed density layers. The influence of this vertical structure on layer formation remains uncertain and raises new questions about how a mean flow with a distinct vertical structure might contribute to the layering process. This mean flow represents a fundamental difference from previous experiments, where the presence of horizontal boundaries suppressed such flows, making direct comparisons with the experiments difficult.

5 Influence of Rotation

5.1 Staircase formation in the experiments

In this section, we investigate the influence of rotation on staircase formation, with a particular focus on the role of the ratio f/N. We begin by considering the non-rotating case, where layering is observed, corresponding to a Richardson number $Ri \approx 50$ and a Reynolds number $Re \approx 2100$. These parameters are kept roughly constant across all experiments, while the angular velocity of the rotating table, f, is varied from 0 to 2 s^{-1} (see Table 3).

Figure 9 shows the temporal evolution of the density gradient for the different rotations

Rods	N (s^{-1})	f (s^{-1})	U (cm/s)	Re_0	Ri_0	Re	Ri	Ro
(2)	1.32688	0	2	786.7	19.9752	2120	49.4555	∞
(2)	1.26948	0.25	2	786.7	18.28425	2120	45.26904	0.755
(2)	1.39135	0.5	2	786.7	21.9636	2120	54.37856	0.3774
(2)	1.32724	0.75	2	786.7	19.9860	2120	49.4823	0.2516
(2)	1.32665	1	2	786.7	19.9682	2120	49.4382	0.1887
(2)	1.35153	2	2	786.7	20.7241	2120	51.3098	0.0943

Table 3: Parameters used in the rotating experiments.

rates. In the absence of rotation, the density gradient progressively develops a well-defined staircase structure. This structure consists of four well-mixed layers separated by three sharp interfaces, with the two intermediate layers measuring approximately 8 cm in height. Over time, the interfaces strengthen, reaching their maximum after approximately 6 hours. The top and bottom mixed layers then begin to erode these interfaces, with the top interface disappearing after 20 hours.

As the rotation rate increases, staircase formation is progressively delayed and eventually suppressed. For moderate values of $f/N = 0.2,\ 0.4,\ 0.5$, the density gradient still exhibits layering, but only two distinct interfaces form, instead of the three observed in the non-rotating case. Additionally, the time required for these interfaces to reach maximum strength increases significantly: 15 hours for $f/N = 0.2$, 20 hours for $f/N = 0.4$, and 30 hours for $/N = 0.5$. This suggests that rotation weakens the efficiency of layer formation by reducing the intensity of vertical mixing. Another observation is that the layer scale does not seem to be very affected by the rotation, but more data points would be needed to confirm this.

For higher values of $f/N = 0.75,\ 1.5$, no staircase forms. Instead, well-mixed layers develop at the top and bottom boundaries, progressively eroding the stratification in the interior. An additional observation is that the depth of these mixed layers at a given time decreases as rotation increases, indicating reduced mixing efficiency. In these cases, the vertical extent of the tank may be insufficient, preventing the interfaces from fully strengthening before the boundary layers reach the center of the tank. Future experiments with a taller tank would help determine whether interfaces would eventually emerge under strong rotational effects.

To better understand the differences between strongly rotating and non-rotating cases, we analyze the structure of the wake using the shadowgraph visualizations. Figure 10 presents snapshots of the flow at an early time (before layer formation) for the non-rotating case (left) and for the case $f/N = 1.5$ (right). The large vertical shadows correspond to the rods and the arrows to their direction. In the non-rotating case, turbulence initially appears homogeneous throughout the domain before interfaces develop. In contrast, under strong rotation, the flow structure differs dramatically. Rather than a homogeneous turbulent field, the density gradient reveals the presence of vertically invariant vortices that dominate the dynamics. Furthermore, turbulence becomes more localized, as the flow in the vortices remain relatively undisturbed. In particular, the suppression of vertical motion within these structures is evident, suggesting that vertical mixing is severely restricted. These vortices remain stable for a short time after the rods pass before gradually breaking down into

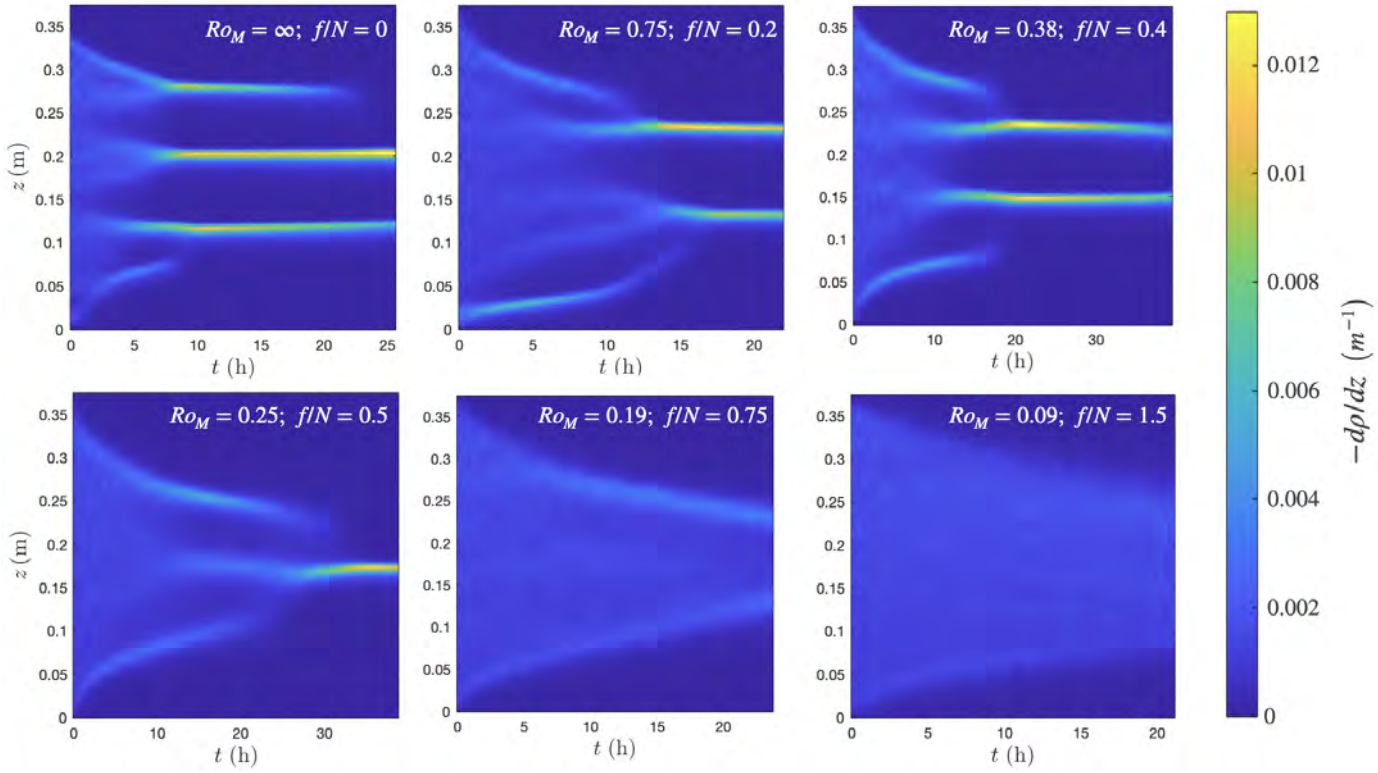

Figure 9: Time-evolution of the vertical density-gradient profiles, with rotation increasing from left to right and top to bottom.

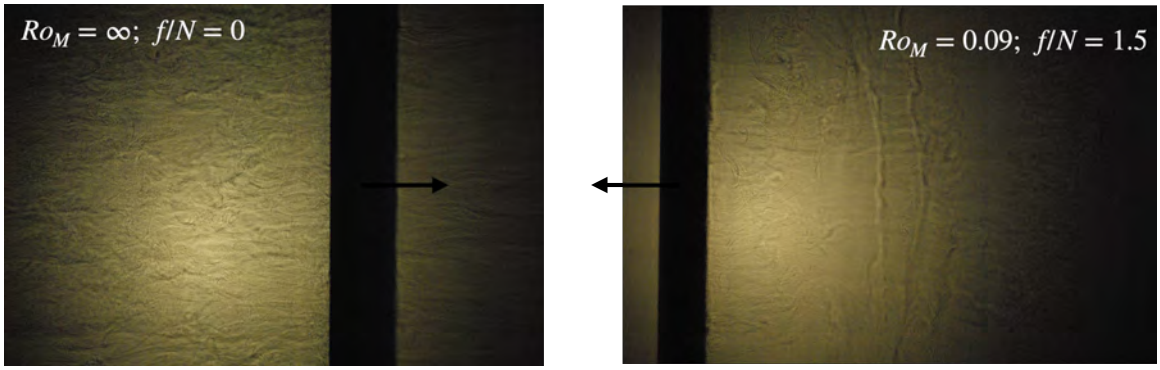

Figure 10: Shadowgraph visualisations of the turbulent flow past the rods in the beginning of the experiments The black shadows show the rods, and the arrows their direction. Both experiments were done with $Ri \approx 50$ and $Re \approx 2100$ at two different rotation rates: (left) $f/N = 0$, (right) $f/N = 1.5$.

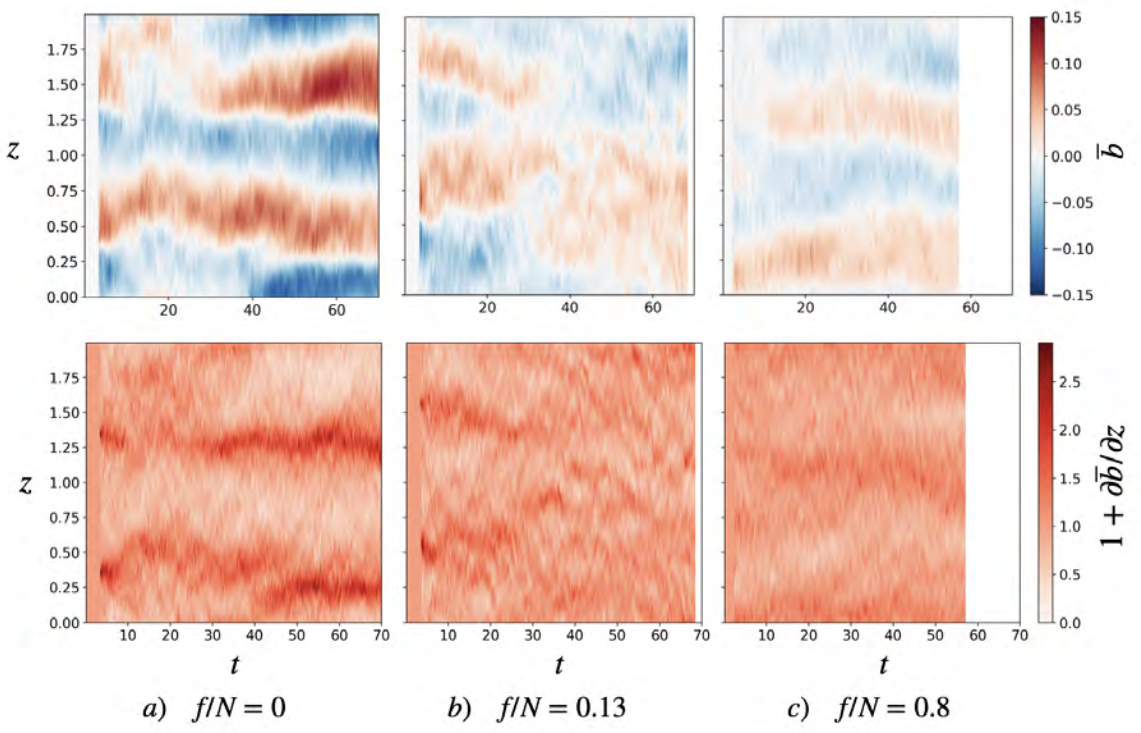

Figure 11: Top : Horizontally averaged buoyancy $\bar{b}$. Bottom : buoyancy gradient $1 + d\bar{b}/dz$ for different rotation rates.

turbulence. The persistence of these coherent vortices could play a crucial role in inhibiting staircase formation, and the reduced vertical mixing may explain the delayed formation of the density layers.

Another interesting question would be to vary the Rossby number, which measures how much the wake structure is influenced by the Coriolis effects, but keeping the ratio f/N fixed.

5.2 In the DNS

Similarly, we investigated the effect of rotation on layer formation in the DNS by varying the Coriolis frequency f while holding $Re = 800$ and $Ri = 60$ fixed. The Rossby number was varied from the non-rotating case $Ro = \infty$ to $Ro = 1$ and $Ro = 0.12$, corresponding to ratios $f/N = 0$, 0.13, and 0.8, respectively.

Figure 11 shows time–depth diagrams of the horizontally averaged buoyancy $\bar{b}$ and the total buoyancy gradient $1 + \partial_z \bar{b}$ for the three cases. In the moderately rotating case ((b) $f/N = 0.13$), the buoyancy profile shows no clear layering; the gradient exhibits temporal fluctuations but no persistent, sharp interfaces. In the strongly rotating case ((c) $f/N = 0.8$), a weakly layered structure appears in $\bar{b}$, but the amplitude is small and we do not observe interfaces that strengthen over time. For these cases (b) and (c), the simulations may not have been run long enough for layers to form; longer runs are needed to resolve

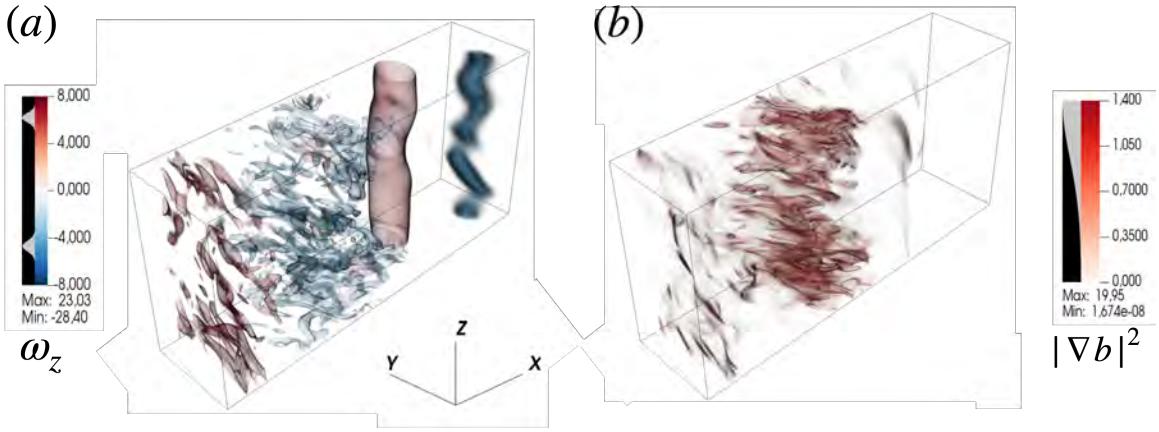

Figure 12: (a) Vertical vorticity ω_z. (b) Buoyancy gradient.

this question.

We also visualized the three-dimensional flow for the rotating case $f/N = 0.8$. Figure 12(a) shows the vertical vorticity, while Fig. 12(b) displays the local field $|\nabla b|^2$, the squared magnitude of the buoyancy gradient. When multiplied by the molecular diffusivity, $\kappa_b|\nabla b|^2$ gives the local irreversible sink of buoyancy variance, highlighting where diffusion consumes variance, i.e., regions of intense small-scale stirring. The rod wake consists of a quasi–vertically invariant cyclone that is stabilized by rotation (see Fig. 12(a)), whereas the anticyclones are more distorted and intermittent; enhanced values of $|\nabla b'|^2$ are collocated with the latter (Fig. 12(b)). This supports the interpretation that, under rotation, the presence of stabilized cyclones reduces the overall mixing in the tank and can delay or inhibit staircase formation.

6 Conclusion

This two-month project established the experimental and numerical framework for investigating the formation of density staircases in stratified and rotating turbulence. By combining laboratory experiments with direct numerical simulations, we aimed to explain how layering depends on stratification, forcing, and rotation and how these parameters influence the turbulence properties.

In the non-rotating case, we reproduced the main behaviours reported by (11) and (8). At high Re and low Ri, the density profile shows no layering: well-mixed boundary layers first develop at the top and bottom and progressively erode the interior stratification, and the profile remains smooth until it is fully homogenized. At high Ri, an interior staircase develops. At intermediate Ri and Re, no interior staircase forms, yet the profile is not smooth: sharp gradients separate the boundary layers from a stratified interior. Whether interior layers would emerge in this case within a taller tank remains an open question. Preliminary experiments in the boundary-layering regime at low Re and low Ri seem to produce layers thinner than the $3U/N$ scale observed by (11; 8). However, the parameter space is not yet sufficiently explored. Clarifying the transitions and layer scales will require

denser sampling in (Re, Ri), as well as longer runs in a taller tank. Possible improvements of the experimental set-up also include direct measurements of the turbulent field (using hot-wire or PIV).

In the DNS, staircase-like structure emerged in one case, but layers were not fully homogenized by the end of the integrations. The absence of rigid boundaries and a free surface limits direct comparison with the tank, and computational cost constrains the accessible parameter space. Wall-bounded DNS and longer integrations would enable closer quantitative comparison to the experiments.

In both the laboratory experiments and the DNS, layering was delayed or suppressed under rotation. We attribute this behaviour to the reduced mixing associated with vertically invariant vortices (stabilised cyclones), which confine small-scale mixing to anticyclones. However, a denser mapping of Rossby number and f/N, additional numerical experiments involving walls and a more detailed analysis of the flow structure are still required to clarify the role of rotation in inhibiting or delaying staircase formation.

7 Acknowledgements

I am deeply grateful to my three supervisors: Jim McElwaine and Claudia Cenedese, for designing and automating the experiments in the WHOI GFD lab and for making the lab a genuinely enjoyable place to work throughout the summer; and Pascale Garaud, for configuring the DNS simulations and for her guidance, which greatly deepened my understanding of the subject. I would also like to acknowledge the contributions of Dante Buhl, who helped update the PADDI version to include more versatile forcing, and Tiam Babadiyaghoubi, who created the forcing used in the simulations presented here. I also thank Bruce Sutherland and Greg Chini, this years GFD directors, and everyone who made the program possible. I am grateful to the visitors and the researchers at WHOI for their insightful discussions, in particular Jack Whitehead for his help and advice during the experiments. Finally, to the fellows who became friends, thank you for your support and for all the amazing memories that we made this summer.

References

[1] N. Balmforth, S. Llewellyn Smith, and W. Young, *Dynamics of interfaces and layers in a stratified turbulent fluid*, Journal of Fluid Mechanics, 355 (1998), pp. 329–358.

[2] P. Billant and J.-M. Chomaz, *Self-similarity of strongly stratified inviscid flows*, Physics of fluids, 13 (2001), pp. 1645–1651.

[3] C. Caulfield, *Layering, instabilities, and mixing in turbulent stratified flows*, Annual Review of Fluid Mechanics, 53 (2021), pp. 113–145.

[4] G. Chini, G. Michel, K. Julien, C. Rocha, and C. Caulfield, *Exploiting self-organized criticality in strongly stratified turbulence*, Journal of Fluid Mechanics, 933 (2022), p. A22.

[5] D. Dritschel and M. JuáRez, *The instability and breakdown of tall columnar vortices in a quasi-geostrophic fluid*, Journal of Fluid Mechanics, 328 (1996), pp. 129–160.

[6] S. Durante, K. Schroeder, L. Mazzei, S. Pierini, M. Borghini, and S. Sparnocchia, *Permanent thermohaline staircases in the tyrrhenian sea*, Geophysical Research Letters, 46 (2019), pp. 1562–1570.

[7] A. Fincham, T. Maxworthy, and G. Spedding, *Energy dissipation and vortex structure in freely decaying, stratified grid turbulence*, Dynamics of atmospheres and oceans, 23 (1996), pp. 155–169.

[8] J. Holford and P. Linden, *Turbulent mixing in a stratified fluid*, Dynamics of Atmospheres and Ocean, 30 (1999), pp. 173–198.

[9] E. Hopfinger and G. Van Heijst, *Vortices in rotating fluids*, Annual review of fluid mechanics, 25 (1993), pp. 241–289.

[10] Y. Ma and W. R. Peltier, *Thermohaline-turbulence instability and thermohaline staircase formation in the polar oceans*, Phys. Rev. Fluids, 7 (2022), p. 083801.

[11] Y. Park, J. Whitehead, and A. Gnanadeskian, *Turbulent mixing in stratified fluids: layer formation and energetics*, Journal of Fluid Mechanics, 279 (1994), pp. 279–311.

[12] O. Phillips, *Turbulence in a strongly stratified fluid—is it unstable?*, in Deep Sea Research and Oceanographic Abstracts, vol. 19, Elsevier, 1972, pp. 79–81.

[13] E. Posmentier, *The generation of salinity finestructure by vertical diffusion*, Journal of Physical Oceanography, 7 (1977), pp. 298–300.

[14] O. Praud, A. Fincham, and J. Sommeria, *Decaying grid turbulence in a strongly stratified fluid*, Journal of Fluid Mechanics, 522 (2005), pp. 1–33.

[15] J. Simpson and J. Woods, *Temperature microstructure in a fresh water thermocline*, Nature, 226 (1970), pp. 832–835.

[16] S. Thorpe, *Layers and internal waves in uniformly stratified fluids stirred by vertical grids*, Journal of Fluid Mechanics, 793 (2016), pp. 380–413.

Idealised Models of Moist Convection

Paul Edwin Curtis

August 21, 2024

1 Introduction

1.1 A brief review of atmospheric convection

Theories of atmospheric convection underpin our understanding of weather and climate (*e.g.*, [24]). In full, atmospheric convection is a remarkably complex phenomenon involving: complicated moist thermodynamics, planetary rotation, non-hydrostatic effects, interactions across many spatiotemporal scales, turbulence, radiation, cloud microphysics, air-sea interactions, orographical effects, and more (all *e.g.*, [30, 18, 1, 16, 19, 21, 22]). It is thus essential to have relatively simple, interpretable analytic models to link observed atmospheric phenomena to the underlying physics. Focusing primarily on the first three factors, this project aims to develop an analytical model of atmospheric convection which interweaves the effects of (i) moist thermodynamics, (ii) planetary rotation, and (iii) deep-reaching (non-hydrostatic) vertical convection. Our theory must therefore encompass several fundamental elements of atmospheric convection:

1. **Earth's atmosphere is stable to dry convection, but unstable to moist convection:** in essence, this lies in how temperature decreases with height. For dry adiabatic displacements, a simple calculation using the first law of thermodynamics and hydrostatic balance yields:

$$dU = \delta Q - \delta W \tag{1a}$$

$$c_v dT = \delta Q - P dv \tag{1b}$$

$$c_v dT = \delta Q - d(Pv) + v dP \tag{1c}$$

$$c_v dT = \delta Q - d(R_d T) + v dP \tag{1d}$$

$$(c_v + R_d) dT = \delta Q - v\rho g dz \tag{1e}$$

$$c_p dT = \delta Q - g dz \tag{1f}$$

$$(\text{as } \delta Q \to 0) \quad dT/dz = -g/c_p \approx -9.8 K/km \ \ (:= -\Gamma_d) \tag{1g}$$

   where $\Gamma_d \approx 9.8 K/km$ is the 'dry adiabatic lapse rate'. Typical observed 'environmental' (or 'ambient') lapse rates are $\approx 7 K/km$. That is, air parcels displaced to higher (lower) altitude along Γ_d will be less (more) buoyant than the environment, and will tend to return to their initial position. Hence the atmosphere is *stable* to dry convection. However, from simply observing phenomena such as thunderstorms and hurricanes, we know that convection does occur in the atmosphere. The condensation of water vapor[1] and subsequent latent heating of

[1] Or more broadly in planetary science, a condensate. For instance, in Titan's atmosphere methane (CH_4) plays the role of water. Moreover, for simplicity, in this work we will only consider the phase changes associated with the condensation of water vapor in Earth's atmosphere. In the real atmosphere, the picture is far more complicated due to the presence of multiple phases of water (see *e.g.*, [30]).

the atmosphere is absolutely fundamental to the physics of such systems, and therefore plays a primary role in theories of atmospheric convection.

Condensation of water vapor can only occur once the specific humidity of an air parcel (q) exceeds its saturation value (q_s). Thereupon water vapor will condense and latent heat is released, generating significant buoyancy which can lead to convection. To illustrate this, once condensation has initiated, the first law must be modified:

$$c_p dT = -gdz - L_v dq_s \tag{2}$$

where $L_v \approx 2.5 \times 10^6 J/kg$ is the latent heat of fusion of water. A similar calculation to before shows that a saturated air parcel evolves its temperature according to the 'saturated adiabatic lapse rate' Γ_m, which has the form:

$$\Gamma_m = \mathscr{C}(q_s, T)\Gamma_d \tag{3}$$

where $\mathscr{C}$ is a relatively complicated function of q_s and T. Crucially, however, $\mathscr{C} \approx 0.3 \Rightarrow \Gamma_m \approx 3K/km$ in the lower atmosphere, increasing to $\mathscr{C} \lesssim 1 \Rightarrow \Gamma_m \approx \Gamma_d$ at higher altitude. Hence, saturated parcels can be *unstable* with respect to the ambient environment when displaced vertically.

More strictly, latent heating through condensation only occurs for *upward* displacements of air parcels, manifesting a 'top-down' asymmetry. The first reason is that T generally decreases as a function of increasing altitude (Z). Since $q_s = q_s(T, ...)$, which in practice is determined with an approximated form of the Clausius-Clapeyron relation:

$$q_s \approx q_0 e^{\alpha T} \equiv q_0 e^{\alpha(b - \Gamma_d Z)} \tag{4}$$

(where T is the absolute temperature; b is the buoyancy; α is a parameter that controls the severity with which moisture falls of exponentially as a function of temperature; and q_0 is the specific humidity of the surface atmosphere) it is clear that q_s decreases sharply with altitude. Secondly, in the absence of condensation and diffusion, q is a materially conserved property of an air parcel. Hence, if an air parcel is unsaturated and quickly displaced downward into a warmer environment, q is conserved and $q - q_s$ simply becomes more negative. However, upward displacement into a cooler environment may eventually cause $q = q_s$, at which point water vapor condenses and convection may occur[2]. The key physics here is that latent heating and moist convection will only occur for large-scale upward displacements of air parcels[3]

2. **Convection in the atmosphere is non-hydrostatic.** The relatively large magnitude of L_v generates a significant buoyancy source. The resulting vertical convection (*e.g.*, that characteristic of a thunderstorm) is deep-reaching throughout the troposphere with large vertical velocities on the order $1 - 2m/s$. This represents an inherently non-hydrostatic phenomenon. A number of studies derive extensions of classical quasi-geostrophy with moist thermodynamics (*e.g.*, [17, 15, 28]), but these are necessarily hydrostatic theories, and consequently do not permit large-scale vertical convection.

[2] In the real atmosphere this is the 'lifting condensation level' (z_{LCL}). Yet, in general an air parcel may still be less buoyant than the environment at $z = z_{LCL}$, and hence sustained, deep-reaching convection can only occur once the parcel has been displaced along the moist adiabat to a high enough altitude to reach the level of neutral buoyancy. This is called the 'level of free convection': z_{LFC}. This level of detail is more than we will consider in this project.

[3] See [26] for an example where the opposite is true.

3. **Earth's rotation exerts a critical influence.** The Coriolis acceleration has a considerable effect on convection in the atmosphere, for instance, in the maintenance of tropical cyclones and midlatitude storm systems. Although several studies have incorporated moist thermodynamics into analytical models of convection (e.g., [3, 4, 23, 9, 32]), thus linking bullet points 1 and 2 above, all are in the absence of rotational effects.

Our principal research question is hence stated: **can we construct an analytical model of atmospheric convection which (i) incorporates the fundamental influence of moist thermodynamics; (ii) permits deep-reaching non-hydrostatic columnar convection; and (iii) the impact of planetary rotation?** Only rarely have these three essential ingredients been considered together either analytically (*e.g.*, [14]) or numerically (*e.g.*, [7]). The next subsection details the foundational analytical models of convection from which our research builds upon.

1.2 Introducing models of convection

1.2.1 Classical and moist Rayleigh-Bénard convection

How do we begin to model atmospheric convection? We begin with the Rayleigh-Bénard convection (RBC) problem (*e.g.*, [27]) of fluid flow between two solid plates aligned normal to gravity, each of a fixed temperature, where the bottom plate is warmer than the top plate. The relevant equations of motion are the Boussinesq equations (*e.g.*, [31]):

$$\frac{D\mathbf{u}}{Dt} = -\frac{1}{\rho_0}\nabla p + b\hat{\mathbf{z}} + \nu\nabla^2\mathbf{u} \tag{5a}$$

$$\frac{Db}{Dt} = \kappa_T\nabla^2\mathbf{u} \tag{5b}$$

$$\nabla\cdot\mathbf{u} = 0 \tag{5c}$$

Equation (5a) is the momentum equation; (5b) is the buoyancy equation; equation (5c) is the continuity equation. $\mathbf{u}(\mathbf{x},t) \equiv (u(\mathbf{x},t), v(\mathbf{x},t), w(\mathbf{x},t))$ is the velocity; $b(\mathbf{x},t) = -g\rho(\mathbf{x},t)/\rho_0$ is the buoyancy; $p(\mathbf{x})$ is the pressure perturbation; ν is the kinematic viscosity; κ_T is the thermal diffusivity; $D/Dt \equiv \partial/\partial t + \mathbf{u}\cdot\nabla$ is the material (or Lagrangian) derivative, where $\nabla := \partial_x\hat{\mathbf{x}} + \partial_y\hat{\mathbf{y}} + \partial_z\hat{\mathbf{z}}$; $\nabla^2 \equiv \nabla\cdot\nabla$ is the Laplacian operator; vectors written (e.g.,) $\hat{\mathbf{x}}$ denote unit vectors in the respective co-ordinate direction. Our co-ordinate system is orthogonal such that $\hat{\mathbf{z}}$ is oriented anti-parallel to gravity, and $\hat{\mathbf{x}}, \hat{\mathbf{y}}$ lie in the plane perpendicular to gravity: $\hat{\mathbf{x}}\times\hat{\mathbf{y}} = \hat{\mathbf{z}}$.

The relevant control parameter of the flow is the Rayleigh number

$$Ra = \frac{g\alpha\Delta T H^3}{\nu\kappa} \tag{6}$$

which is a measure of buoyancy forces to viscous dissipation. A standard linear stability analysis (*e.g.*, [27]) of equations (5a-5c) determines that for $Ra > 27\pi^4/4$ the system will transition from a motionless state characterised by the diffusion of heat, to a state of vigorous organised convection. The analytic simplicity of the Rayleigh-Bénard convection problem is our primary motivation for using it as a starting point. However, in light of the physics discussed in section 1.1, equations (5a-5c) are clearly insufficient to accurately describe the atmospheric problem.

One direction taken to make equations (5a-5c) more appropriate for the atmosphere is discussed in [32]: the 'Rainy'-Bénard convection (RyBC) model. The fundamental aim of the RyBC model is to study the influence of latent heating (through the condensation of water vapor) on convection.

Their model incorporates a simple scheme for moist thermodynamics into the system 5a-5c in the following way:

$$\frac{D\mathbf{u}}{Dt} = -\frac{1}{\rho_0}\nabla p + b\hat{\mathbf{z}} + \nu\nabla^2\mathbf{u} \tag{7a}$$

$$\frac{Db}{Dt} = \kappa_T\nabla^2\mathbf{u} + \gamma\frac{q-q_s}{\tau}\mathscr{H}(q-q_s) \tag{7b}$$

$$\frac{Dq}{Dt} = \kappa_q\nabla^2 q - \frac{q-q_s}{\tau}\mathscr{H}(q-q_s) \tag{7c}$$

$$\nabla\cdot\mathbf{u} = 0 \tag{7d}$$

Where equation (7c) describes the conservation of moisture in the system; γ is a constant which quantifies the relative strength of latent heating.

In this model, the key physics that convection should only occur when $q \geq q_s$ is enforced through the Heaviside step function, $\mathscr{H}(q-q_s)$, on the right hand sides of equations (7b-7c). Another key aspect (and simplification) of this model is that it is non-precipitating: *i.e.*, condensate is not solved for. This rapid condensation and rain-out is enforced through the *very* small timescale τ.

Ultimately, the main advantage of the model 7a-7d, and the primary motivation for its inclusion in our project is the simplicity with which latent heating is represented. However, this model omits the fundamental influences of (i) planetary rotation and (ii) non-hydrostatic effects.

1.2.2 Rapidly rotating non-hydrostatic Rayleigh-Bénard convection

To incorporate these latter effects into our theory of moist convection, we employ the (dry) rapidly rotating nonhydrostatic theory of [11] as a basis, which is detailed in this subsection. Therefore, our theory will necessarily deviate from more canonical models of rotating moist convection based on quasi-geostrophic (QG) theory (*e.g.*, [15]).

After rotation has been included, the (dry) equations (5a-5c) are non-dimensionalised using scales for the: velocity $\mathbf{u} = U\hat{\mathbf{u}}$; buoyancy $b = B\hat{b}$; pressure perturbation $p = P\hat{p}$; space $\mathbf{x} = L\hat{\mathbf{x}}$; and time $t = (L/U)\hat{t}$; where the velocity (U) and length (L) scales are as of yet unspecified. The resulting non-dimensional rotating Boussinesq equations read, after dropping the hats on non-dimensional quantities:

$$\frac{D\mathbf{u}}{Dt} + \frac{1}{Ro}\hat{\mathbf{z}}\times\mathbf{u} = -Eu\nabla p + \Gamma b\hat{\mathbf{z}} + \frac{1}{Re}\nabla^2\mathbf{u} \tag{8a}$$

$$\frac{Db}{Dt} = \frac{1}{Pe}\nabla^2 b \tag{8b}$$

$$\nabla\cdot\mathbf{u} = 0 \tag{8c}$$

where the non-dimensional: Rossby number, $Ro \equiv U/f_0L$; Euler number, $Eu \equiv P/\rho_0U^2$; Reynolds number, $Re \equiv UL/\nu$; buoyancy number, $\Gamma = BL/U^2$; and Péclet number, $Pe = UL/\kappa_T$ have been introduced.

How does strong rotation influence the nature of convection? [11] address this problem by reducing the system 8a-8c under the distinguished limit $Ro \to 0$. Although not a full restatement of their derivation, several key points are now detailed as they pertain to our research.

First, in the limit of rapid rotation, convection should be constrained to tall, thin vertical columnar structures through the Taylor-Proudman constraint. This *a-priori* scale separation between the horizontal and vertical length scales is exploited by introducing a vertical aspect ratio: $A_Z := H/L$ and corresponding "slow" vertical co-ordinate $Z := A_Z^{-1}z$. An analogous "slow" time

$T := A_T^{-1}t$ is introduced to capture the long-time modulation of the convection. This allows a multiscale re-formulation of the system 8a-8c, resulting in the re-scaled equations:

$$\left(D_t + \frac{1}{A_T}\partial_T + \frac{w}{A_Z}\partial_Z\right)\mathbf{u} + Ro^{-1}\hat{\mathbf{z}}\times\mathbf{u} = \\ -Eu\left(\nabla + \frac{\hat{\mathbf{z}}}{A_Z}\partial_Z\right)p + \Gamma b\hat{\mathbf{z}} + Re^{-1}\left(\nabla + \frac{\hat{\mathbf{z}}}{A_Z}\partial_Z\right)^2\mathbf{u} \tag{9a}$$

$$\left(D_t + \frac{1}{A_T}\partial_T + \frac{w}{A_Z}\partial_Z\right)b = Pe^{-1}\left(\nabla + \frac{\hat{\mathbf{z}}}{A_Z}\partial_Z\right)^2 b \tag{9b}$$

$$\nabla\cdot\mathbf{u} + \frac{1}{A_Z}\partial_Z w = 0 \tag{9c}$$

It is specifically the vertical scale separation which permits non-hydrostatic vertical convection.

Secondly, the fast/slow scale separation is further exploited by introducing an average over fast scales; for a general variable $\mathscr{V}(x,y,z,Z,t,T)$:

$$\overline{\mathscr{V}}(Z,T) := \lim_{\mathcal{T},\mathcal{V}\to\infty}\frac{1}{\mathcal{T}\cdot\mathcal{V}}\int_{\mathcal{T},\mathcal{V}}\mathscr{V}(x,y,z,Z,t,T)d\mathbf{x}dt; \qquad \mathbf{x},t\in\mathcal{V},\mathcal{T} \tag{10}$$

with which the re-scaled equations (9a-9c) are decomposed into mean:

$$\frac{1}{A_T}\partial_T\overline{\mathbf{u}} + \frac{1}{A_Z}\partial_Z(\overline{w}\overline{\mathbf{u}}) + Ro^{-1}\hat{\mathbf{z}}\times\overline{\mathbf{u}} = \left(-\frac{Eu}{A_Z}\partial_Z\overline{p} + \Gamma\overline{b}\right)\hat{\mathbf{z}} + \frac{1}{ReA_Z^2}\partial_Z^2\overline{\mathbf{u}} \tag{11a}$$

$$\frac{1}{A_T}\partial_T\overline{b} + \frac{1}{A_Z}\partial_Z(\overline{wb}) = \frac{1}{PeA_Z^2}\partial_Z^2\overline{b} \tag{11b}$$

$$\partial_Z\overline{w} = 0 \tag{11c}$$

and fluctuating (*i.e.*, $\mathscr{V}' \equiv \mathscr{V} - \overline{\mathscr{V}}$) components:

$$\left(D_t + \frac{1}{A_T}\partial_T + \frac{w}{A_Z}\partial_Z\right)\mathbf{u}' + \frac{w'}{A_Z}\partial_Z\overline{\mathbf{u}} - \frac{1}{A_Z}\partial_Z(\overline{w'\mathbf{u}'}) + \frac{1}{Ro}\mathbf{z}\times\mathbf{u}' \\ = -Eu\left(\nabla + \frac{\mathbf{z}}{A_Z}\partial_Z\right)p' + \Gamma b'\hat{\mathbf{z}} + \frac{1}{Re}\left(\nabla + \frac{\hat{\mathbf{z}}}{A_Z}\partial_Z\right)^2\mathbf{u}' \tag{12a}$$

$$\left(D_t + \frac{1}{A_T}\partial_T + \frac{w}{A_Z}\partial_Z\right)b' + \frac{w'}{A_Z}\partial_Z\overline{b} - \frac{1}{A_Z}\partial_Z(\overline{w'b'}) = \frac{1}{Pe}\left(\nabla + \frac{\hat{\mathbf{z}}}{A_Z}\partial_Z\right)^2 b' \tag{12b}$$

$$\nabla\cdot\mathbf{u}' + \frac{1}{A_Z}\partial_Z w' = 0 \tag{12c}$$

All barred variables depend only on the slow co-ordinates Z,T and all primed variables depend only on "fast" co-ordinates (i.e., parametric dependence on the slow co-ordinates).

Thirdly, in the distinguished limit of rapid rotation ($Ro\to 0$), the Rossby number is the formal small parameter[4]. Hence the mean and fluctuating variables in equations (11a-11c) and (12a-12c) are expanded in powers of Ro; as an example using the velocity:

$$\overline{\mathbf{u}} = \overline{\mathbf{u}}_0 + Ro\overline{\mathbf{u}}_1 + Ro^2\overline{\mathbf{u}}_2 + \mathscr{O}(Ro^3) \tag{13a}$$

[4] *n.b.*, in the rapidly rotating limit this is asymptotically equivalent to expanding in powers of $E^{1/3}$, where $E\equiv\nu/(f_0 l)$ is the Ekman number, and taking the limit $E\to 0$; see *e.g.*, [2].

$$\mathbf{u}' = \mathbf{u}'_0 + Ro\mathbf{u}'_1 + Ro^2\mathbf{u}'_2 + \mathscr{O}(Ro^3) \tag{13b}$$

Using this, the equations (11a-11c) and (12a-12c) are reduced under the distinguished limit $Ro \to 0$, as described fully in [11]. The resulting asymptotically reduced equations read (with the asymptotic ordering of terms introduced in the expansions (13a-13b) suppressed for clarity):

$$\partial_t \nabla_\perp^2 \phi + J(\psi, \nabla_\perp^2 \phi) + \partial_Z \psi = \frac{\widetilde{Ra}}{Pr} b' + \nabla_\perp^4 \phi \tag{14a}$$

$$\partial_t \nabla_\perp^2 \psi + J(\psi, \nabla_\perp^2 \psi) - \partial_Z \nabla_\perp^2 \phi = \nabla_\perp^4 \psi \tag{14b}$$

$$\partial_t b' + J(\psi, b') + \nabla_\perp^2 \phi \partial_Z \overline{b} = Pr^{-1} \nabla_\perp^2 b' \tag{14c}$$

$$\partial_T \overline{b} + \partial_Z (\overline{b' \nabla_\perp^2 \phi}) = Pr^{-1} \partial_Z^2 \overline{b} \tag{14d}$$

Equations (14a) and (14b) arise from the momentum equations (11a) and (12a), respectively; equations (14c) and (14d) arise from the buoyancy equations (11b) and (12b), respectively. In the above, the toroidal (ψ) and poloidal (ϕ) streamfunctions are defined via a Helmholtz decomposition: $\mathbf{u}' \coloneqq -\nabla \times \psi \hat{\mathbf{z}} - \nabla \times \nabla \times \phi \hat{\mathbf{z}}$ (where $w' = \nabla_\perp^2 \phi$ is the vertical velocity fluctuation). The horizontal Laplacian operator $\nabla_\perp^2 \coloneqq \partial_x^2 + \partial_y^2$ (consequently $\nabla_\perp^4 \coloneqq \nabla_\perp^2 \nabla_\perp^2 \equiv \partial_x^4 + 2\partial_x^2 \partial_y^2 + \partial_y^4$), and the horizontal Jacobian $J(f, g) \coloneqq \partial_x f \partial_y g - \partial_x g \partial_y f$ are introduced. Finally, a diffusive non-dimensionalisation is ultimately chosen for L and U, which introduces a 'scaled' Rayleigh Number, $\widetilde{Ra}$, the measure of supercriticality in the system.

The "fast" $z-$ dependence has been eliminated in the equations (14a-14d). This is a direct consequence of the Taylor-Proudman constraint under the asymptotic derivation, in which large scale non-hydrostatic vertical motions (i.e., those on the scale of Z) are balanced by small scale horizontal motions (i.e., those on the scale of x, y).

In addition to being significantly cheaper than direct numerical simulation of (8a-8c) at very low Ro, one major success of the reduced equations (14a-14d) is the ability to access different regimes of convection[5] based on the Rayleigh number, $\widetilde{Ra}$, and Prandtl number, Pr. *n.b.* the critical value of the Rayleigh Number for the onset of organized convection as it is defined in this system is $\widetilde{Ra}_c \approx 8.7$.

Numerical simulations of the reduced equations (14a-14d) are solved spectrally and output from two such simulations are shown in figure 1 (all simulation details are given in the caption). The system is solved with no-slip, and constant top and bottom buoyancy ($\overline{b}(Z=0) = 1$; $\overline{b}(Z=1) = 0$) boundary conditions. For $\widetilde{Ra} = 40$ and $Pr = 7$, figure 1.**a** (also figure 2) shows a developed state of convection characterised by laminar columnar structures. Then, for $\widetilde{Ra} = 80$ and $Pr = 1$, figure 1.**b** shows a flow which is still rotationally constrained, but has developed into a state representative of geostrophic turbulence. For instance, note the more vigorous convection indicated by the colourbars in figure 1.**b**.

1.3 Tying together moist thermodynamics, rotation, and non-hydrostatic convection: initial project aims

We can now re-cast our initial research question in context with the aforementioned models: **can the latent heating closure of [32] be consistently incorporated into the asymptotic reduction of [11]?** The primary aim is to thus write down a set of reduced equations extending (14a-14d) to include latent heating. With this model, we aim to answer questions such as: can we

[5] A full assessment of the convective regimes accessible from equations (14a-14d) is shown in figure 5 of [29].

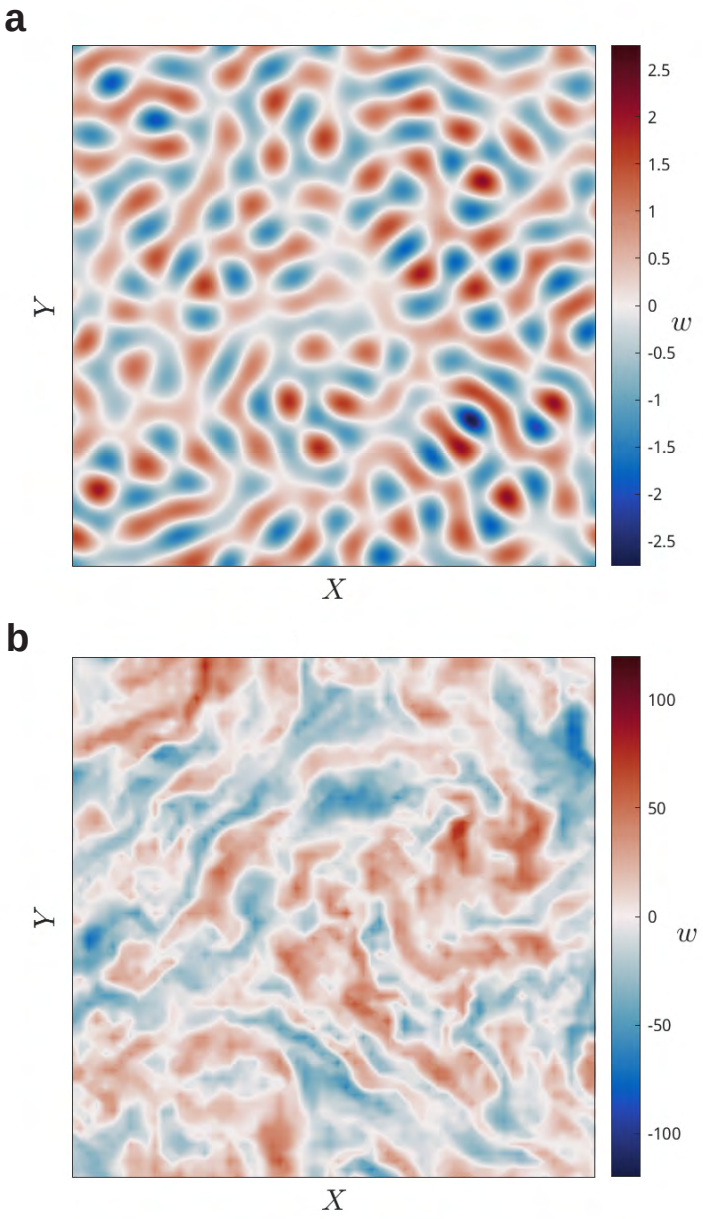

Figure 1: End of simulation vertical velocity (w') snapshots in the $Z-$ midplane from simulations of the reduced equations (14a-14d). Red colours correspond to regions of upwelling (i.e., out of the page); blue colours correspond to regions of downwelling (i.e., flow into the page). In **a**: $\widetilde{Ra} = 40$ and $Pr = 7$; in **b**: $\widetilde{Ra} = 80$ and $Pr = 1$. All simulations were performed using the Dedalus spectral code ([5]) in a doubly periodic (in the horizontal) domain with size $L_{x,y} = 10L_c; L_z = 1$, where L_c is the wavelength of the most unstable mode obtained from a linear stability analysis of equations (14a-14d) (cf. [29]); simulations are performed by resolving 64 Fourier coefficients in the horizontal, and 64 Chebyshev polynomials in the vertical. The simulations are time stepped using a fourth-order Runge-Kutta method, with initial timestep $dt = 5 \times 10^{-4}$; the Courant-Friederichs-Lewy condition is used to ensure good accuracy of the solution. Simulations are run towards a quasi-equilibrated state.

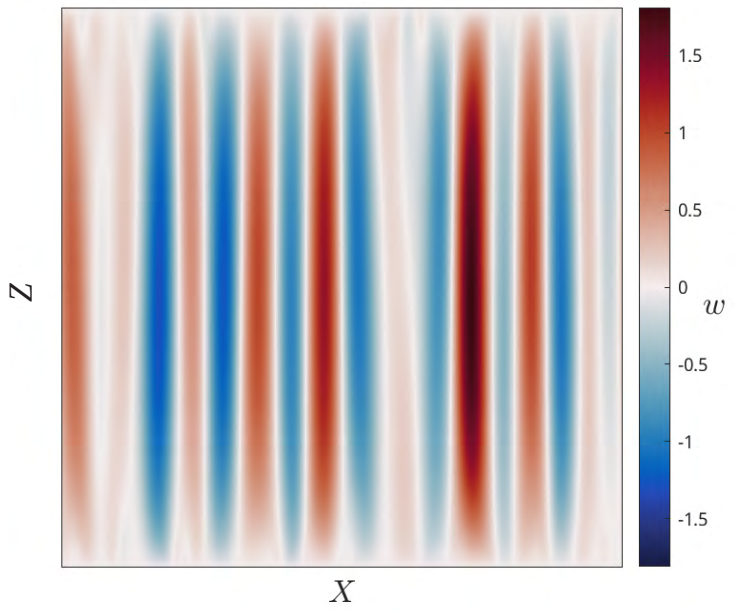

Figure 2: As in figure 1.**a** ($\widetilde{Ra} = 40$ and $Pr = 7$), but showing vertical velocity in the $y-$midplane to emphasize the columnar nature of the flow due to the Taylor-column constraint. All simulation details are given in the caption to figure 1.

understand the influence of both rotation and latent heating on the transition from a non-convecting to a convecting state? How does latent heating change the properties of the resulting convection compared to models which only incorporate dry thermodynamics? What observed properties of atmospheric convection can be explained by our model?

Despite the large degree of isomporphism between the systems 7a-7d and 8a-8c, and the apparent simplicity of the latent heating closure, using the RyBC system as a starting point for an asymptotic reduction closely following [11] turns out to be an *immensely* challenging problem. This is primarily due to two underlying factors:

1. The rapid condensation timescale parameter, τ, which is strictly the fastest timescale in the system.

2. The discontinuous nature of the forcing on the right hand sides of equations (7b and 7c). In general, this is a highly non-trivial problem (cf. differential inclusions; [8]).

Several approaches were taken to arrive at a set of reduced equations with latent heating, but issues arising from combinations of the aforementioned precluded progress. Appendices A and B provide a more comprehensive overview of these issues and the conclusions which motivated our revised approaches.

Instead, the rest of this report details our revised approach, providing an outline to circumvent many of the problems we faced with our first approach. Ultimately, we are able to write down a new set of rapidly rotating non-hydrostatic reduced equations incorporating latent heating. To start, the next section is specifically dedicated to a linear stability analysis of the RyBC system about the transition to organised convection. Understanding this provides a crucial insight to how

the asymptotic reduction starting from 7a-7d should ultimately be performed.

2 Towards a Set of Asymptotically Reduced Equations

The aim of this section is to delve into the RyBC system and investigate linear stability properties about the transition into organised convection. Although *also* challenging in and of itself, understanding this problem (in conjunction with material discussed in appendices A and B) provides critical insight into the behaviour of asymptotically reduced equations with the latent heating closure developed in [32]. Our approach first directly addresses the aforementioned issue regarding the rapid-condensation timescale by establishing a new system of equations with rapid-condensation 'hard-built' in, derived under the limit $\tau \to 0$. Then, by taking advantage of the properties of atmospheric convection, we demonstrate how the representation of latent heating in this system can be simplified for exponentially growing eigenmodes about the base diffusive state. The resulting (quasi-)linear system is amenable to a small-amplitude analysis which explicates the general structure of, and crucially the impact of rotation and latent heating on the fastest growing eigenmode. This information ultimately informs our development of a new set of rapidly rotating non-hydrostatic reduced equations incorporating latent heating, as described in the next section.

2.1 Transforming the RyBC equations

2.1.1 Taking the rapid-condensation limit: $\tau \to 0$

Our first aim is to take the limit $\tau \to 0$ of the system 7a-7d to effectively eliminate τ from the system. However, a useful (and simple) first stage is to re-cast the equations to more cleanly differentiate the dynamics in sub-saturated and saturated regions. We first define a 'super-saturation' parameter, s:

$$s = \frac{q - q_s}{\tau} \tag{15}$$

with which the buoyancy (7b) and moisture (7c) equations are re-written:

$$\frac{Db}{Dt} = \kappa \nabla^2 b + \gamma s \mathscr{H}(s) \tag{16a}$$

$$\frac{D}{Dt}(q_s + \tau s) = \kappa \nabla^2 (q_s + \tau s) - s\mathscr{H}(s) \tag{16b}$$

noting that $\mathscr{H}(s\tau) \equiv \mathscr{H}(s)$, and $\kappa_b = \kappa_q = \kappa$ for simplicity. Evaluating the material derivative on the left-hand side of equation (16b) generates:

$$\frac{Dq_s}{Dt} = \frac{D}{Dt}(q_0 \exp(\alpha b - \beta z)) = \alpha q_s \frac{Db}{Dt} - \beta q_s w \tag{17}$$

where $\beta = \alpha \Gamma_d$ is defined from equation (4). By directly substituting equation (16a) for Db/Dt and gathering terms, equation (17) can be re-written:

$$\tau \left[\frac{Ds}{Dt} - \kappa \nabla^2 s \right] = -(1 + \alpha q_s \gamma)[s\mathscr{H}(s) - S]; \qquad S = \frac{-\alpha q_s \kappa \nabla^2 b + \beta q_s w + \kappa \nabla^2 q_s}{1 + \alpha q_s \gamma} \tag{18}$$

hence yielding an evolution equation for the super-saturation parameter, s. Note that S is not a function of q, since $q_s = q_s(b, z)$.

To proceed, it is important to have an *a-priori* picture of the system behaviour under the limit $\tau \to 0$. To replicate the physics of atmospheric convection, the purpose of τ is to strongly restrict

q to minimal increases above saturation: *i.e.*, $q \gtrsim q_s$. For saturation, as $\tau \to 0$, we then expect $s = \mathscr{O}(1)$. More specifically we expect $s = S$ through equation (18). However, in the atmosphere q can drop well below q_s. Hence for sub-saturation, s may become arbitrarily negative as $\tau \to 0$. In the latter situation, moisture is advected as a passive tracer.

With this information, and further noting that S is $\mathscr{O}(\tau^0)$ (cf. equation (18)), we change variables: $s = S + \chi/\tau$, where χ is an $\mathscr{O}(\tau^0)$ parameter. Equation (18) becomes:

$$\tau^2\left(\frac{DS}{Dt} - \kappa\nabla^2 S\right) + \tau\left(\frac{D\chi}{Dt} - \kappa\nabla^2\chi\right) = -(1+\alpha\gamma q_s)\chi \qquad \text{For } S + \chi/\tau \geq 0 \tag{19a}$$

$$\tau\left(\frac{DS}{Dt} - \kappa\nabla^2 S\right) + \left(\frac{D\chi}{Dt} - \kappa\nabla^2\chi\right) = (1+\alpha\gamma q_s)S \qquad \text{For } S + \chi/\tau < 0 \tag{19b}$$

Then, taking the limit $\tau \to 0$ we obtain:

$$\chi = 0 \qquad \text{For } \chi \geq 0 \tag{20a}$$

$$\frac{D\chi}{Dt} - \kappa\nabla^2\chi = (1+\alpha\gamma q_s)S \qquad \text{For } \chi < 0 \tag{20b}$$

with corresponding buoyancy equations (cf. 16a):

$$\frac{Db}{Dt} = \gamma S + \kappa\nabla^2 b \qquad \text{For } \chi \geq 0 \tag{21a}$$

$$\frac{Db}{Dt} = \kappa\nabla^2 b \qquad \text{For } \chi < 0 \tag{21b}$$

where, on the right hand side of equation (21a), there is a buoyancy tendency through latent heating which is $\propto S$. Equations (20a-21b) describe the evolution of moisture and buoyancy in the rapid-condensation limit. Ultimately, the aim is to use these equations to understand the linear growth of the system as it transitions from a diffusing to convecting state. First, however, we take advantage of the physics of atmospheric convection to simplify their form.

2.1.2 Connecting latent heating and convective motions

We move to the case where both the buoyancy variations and the domain height are small. Equation (4) hence approximates to:

$$q_s \approx q_0(1 + \alpha b - \beta z) \tag{22}$$

and S simplifies to:

$$S = \frac{\beta q_0}{1 + \alpha\gamma q_0} w \tag{23}$$

critically this tells us that $S \propto w$ **only** in this approximation. As stated in [32], the base diffusive state of the RyBC system corresponds to $w = 0$ ($\forall \mathbf{x}$) and $b(z) = b_0 + Gz$ (here G quantifies the bulk vertical buoyancy stratification in the domain), where the domain is at the condensation threshold $q = q_s$ ($\forall \mathbf{x}$), and moisture simply diffuses through the top and bottom boundaries. We consider a small-amplitude analysis about the diffusive base state by introducing:

$$\begin{pmatrix} \chi(\mathbf{x},t) \\ b(\mathbf{x},t) \\ w(\mathbf{x},t) \end{pmatrix} = \begin{pmatrix} \widehat{\chi}(\mathbf{x}) \\ \widehat{b}(\mathbf{x}) \\ \widehat{w}(\mathbf{x}) \end{pmatrix} e^{\sigma t} \tag{24}$$

and dropping non-linear terms. Now, the question is to understand the linear evolution in regions of downwelling: $\widehat{w} < 0$; and upwelling: $\widehat{w} > 0$.

First, consider the case when $\widehat{w} < 0$ ($S < 0$; cf. equation (23)). Using expressions (23) and (24), equations (20b) and (21b) are transformed:

$$\sigma\widehat{\chi} - \kappa\nabla^2\widehat{\chi} = \beta q_0 \widehat{w} \tag{25a}$$

$$\sigma\widehat{b} + G\widehat{w} = \kappa\nabla^2\widehat{b} \tag{25b}$$

Equations (25a-25b) are a statement that downwelling regions correspond to passive advection of moisture without latent heating. To illustrate this, consider an exponentially growing eigenmode ($\sigma > 0$), and recall that $\beta q_0 \widehat{w} < 0$. Then, in evaluating equation (25a) for the maximum value of $\widehat{\chi}$ in the downwelling region, χ_{max}, the diffusive term becomes negative since $\nabla^2\widehat{\chi}|_{\chi=\chi_{max}} < 0$. Taken altogether, these enforce $\chi_{max} < 0$, and hence downwelling regions of the domain are *necessarily* sub-saturated. The second case is when $\widehat{w} > 0$. Using a similar argument, evaluating equation (25a) at the minimum value of χ in the upwelling region, χ_{min}, we have$\nabla^2\widehat{\chi}|_{\chi=\chi_{min}} > 0$. Hence, for $\sigma > 0$, $\chi_{min} > 0$, and upwelling regions of the domain *necessarily* correspond to saturated fluid. The buoyancy equation in this second scenario is 21a with S expressed using 23.

For exponentially growing eigenmodes, equations (25b) and 21a can therefore be combined into a single equation, where the latent heating term is expressible in the following way:

$$\sigma\hat{b} + G\hat{w} = \frac{\beta\gamma q_0}{1+\alpha\gamma q_0}\hat{w}\mathscr{H}(\hat{w}) + \kappa\nabla^2\hat{b} \tag{26}$$

Advantageously, this equation does not require *any* specification of the moisture field. Once the continuity and momentum equations (with rotation) are included, we have the 'quasi'-linear system:

$$\partial_t\mathbf{u} + f_0\hat{\mathbf{z}}\times\mathbf{u} = -\nabla\phi + b\hat{\mathbf{z}} + \nu\nabla^2\mathbf{u} \tag{27a}$$

$$\partial_t b = \kappa\nabla^2 b - (N^2 - \widetilde{\mu}\mathscr{H}(w))w \tag{27b}$$

$$\nabla\cdot\mathbf{u} = 0 \tag{27c}$$

where we've re-cast: $G = N^2$; $\widetilde{\mu} = \beta\gamma q_0/(1+\alpha\gamma q_0)$, and replaced $\sigma \to \partial_t$. This system is not quite linear since equation (27b) contains a term which is sign-dependent on w.

Equations (27a-27c) represent a significant milestone in this project. (i) From 2.1.1 these equations have rapid-condensation hard-built in; and (ii) for linear growth about the base diffusive state we do not need to keep track of the moisture field! From equations (27a-27c) we can far more easily investigate the influence of both rotation and the magnitude of latent heating on the structure of the fastest growing eigenmode. This last point is instrumental for an *apriori* understanding of the behaviour of asymptotically reduced equations with latent heating, *i.e.*, the ultimate goal of this project.

2.2 The fastest growing eigenmode of the quasi-linear system

2.2.1 Deriving the characteristic wavenumber polynomial

We are interested in the structure of the fastest growing eigenmode of the system 27a-27c, and how it varies with both rotation rate and latent heating. This first requires ascertaining the characteristic polynomial of the system (*e.g.*, [6]). Anticipating cylindrically symmetric solutions we perform a 2-dimensional/3-component analysis - hence from hereon all system variables will

be functions of x, z, t only. Some minor algebraic manipulation of equations (27a-27c) yields the system:

$$-f_0\partial_x v + \nabla^2\phi - \partial_z b = 0 \tag{28a}$$

$$\partial_t\zeta + f_0\partial_z v - \nu\nabla^2\zeta - \partial_x b = 0 \tag{28b}$$

$$\partial_t v + f_0 u - \nu\nabla^2 v = 0 \tag{28c}$$

$$\partial_t b - \kappa\nabla^2 b + (N^2 - \widetilde{\mu}\mathscr{H}(w))w = 0 \tag{28d}$$

$$\partial_x u + \partial_z w = 0 \tag{28e}$$

$$\zeta - \partial_x w + \partial_z u = 0 \tag{28f}$$

Where we have also introduced the vorticity defined through 28f.

Equations (28a-28f) are closed using stress-free boundary conditions. With that, the six problem variables are decomposed into spatially and temporally varying components:

$$\begin{pmatrix} \zeta(x,z,t) \\ u(x,z,t) \\ v(x,z,t) \\ w(x,z,t) \\ b(x,z,t) \\ \phi(x,z,t) \end{pmatrix} = \begin{pmatrix} \widehat{\zeta}(x)\sin(k_z z) \\ \widehat{u}(x)\cos(k_z z) \\ \widehat{v}(x)\cos(k_z z) \\ \widehat{w}(x)\sin(k_z z) \\ \widehat{b}(x)\sin(k_z z) \\ \widehat{\phi}(x)\cos(k_z z) \end{pmatrix} e^{\sigma t} \tag{29}$$

It is re-stressed that the linear stability of 27a-27c depends upon the sign of w. However, we readily identify that when $w < 0$, the prefactor on w in equation (28d) is simply N^2, and when $w \geq 0$, the pre-factor is $N^2 - \widetilde{\mu}$. Therefore, the following derivation is the same for both cases and we carry the Heaviside through. The ansatz 29 transforms the three diagnostic equations (28a), 28e, 28f):

$$k_z w = -\partial_x u \tag{30a}$$

$$k_z\zeta = -\nabla^2 u \tag{30b}$$

$$k_z b = \nabla^2\phi - f_0\partial_x v \tag{30c}$$

respectively; and the three prognostic equations (28b, 28c, 28d):

$$(\sigma - \nu\nabla^2)\nabla^2 u + f_0 k_z^2 v + k_z\partial_x b = 0 \tag{31a}$$

$$(\sigma - \nu\nabla^2)v + f_0 u = 0 \tag{31b}$$

$$k_z(\sigma - \kappa\nabla^2)b - (N^2 - \widetilde{\mu}\mathscr{H}(w))\partial_x u = 0 \tag{31c}$$

respectively, where equations (30a-30c) have been used in the manipulation. In matrix form equations (31a-31c) read:

$$\begin{bmatrix} (\sigma - \nu\nabla^2)\nabla^2 & f_0 k_z^2 & k_z\partial_x \\ f_0 & (\sigma - \nu\nabla^2) & 0 \\ -(N^2 - \widetilde{\mu}\mathscr{H}(w))\partial_x & 0 & k_z(\sigma - \kappa\nabla^2) \end{bmatrix} \begin{bmatrix} u \\ v \\ b \end{bmatrix} = \begin{bmatrix} 0 \\ 0 \\ 0 \end{bmatrix} \tag{32}$$

Evaluating the matrix determinant in equation (32) yields the eighth-order operator equation:

$$\boxed{[(\sigma - \nu\nabla^2)^2\nabla^2(\sigma - \kappa\nabla^2) - f_0^2 k_z^2(\sigma - \kappa\nabla^2) + (N^2 - \widetilde{\mu}\mathscr{H}(w))\partial_x^2(\sigma - \nu\nabla^2)]u = 0} \tag{33}$$

Our interest is in the marginal stability problem. Thus, setting $\sigma = 0$ in 33 and further non-dimensionalising by L_z, we obtain:

$$\left[\nabla^8 - \frac{f_0^2 L_z^4}{\nu^2}(k_z L_z)^2 \nabla^2 + \frac{(N^2 - \widetilde{\mu}) L_z^4}{\nu\kappa}\partial_x^2 \nabla^2\right] u = 0 \tag{34}$$

where we recognise the Taylor Number, T, Rayleigh Number, R (defined with $N^2 < 0$), and non-dimensionalised latent heating parameter, μ[6]:

$$T = \frac{f_0^2 L_z^4}{\nu^2}; \quad R = -\frac{N^2 L_z^4}{\nu\kappa}; \quad \mu = \frac{\widetilde{\mu} L_z^4}{\nu\kappa} \tag{35}$$

We now restrict our attention to the fundamental vertical mode, $k_z = \pi$, with domain height $L_z = 1$. Moreover we assume a periodic horizontal variation: $\partial_x \to ik_x$. Taken altogether, the Laplacian is rewritten: $\nabla^2 = -(k_x^2 + \pi^2)$, and the resulting characteristic polynomial (in k_x) obtained from equation (34), general for regions of upwelling *and* downwelling, reads:

$$\boxed{(k_x^2 + \pi^2)^4 + T\pi^2(k_x^2 + \pi^2) - (R + \mu\mathscr{H}(\hat{w}))k_x^2(k_x^2 + \pi^2) = 0} \tag{36}$$

where in taking the fundamental vertical mode: $\mathscr{H}(\widehat{w}(x)\sin(\pi z)) \equiv \mathscr{H}(\widehat{w}(x))$. Equation (36) is another milestone in our analysis. This may be compared to the (dry) rotating analysis of [6]; also that of [14] and [3], but those studies use differing formulations of moist thermodynamics to the present study.

Finally, we discuss an important balance in the characteristic polynomial 36 in the limit of rapid rotation. For $R = 0$, equation (36) can be factorised:

$$\alpha[\alpha^3 - \mu\mathscr{H}(\widehat{w})\alpha + (T + \mu\mathscr{H}(\widehat{w}))\pi^2] = 0 \tag{37}$$

where $\alpha := k_x^2 + \pi^2$ has been introduced. Considering upwellling regions, and inspecting the resulting cubic inside the parentheses in equation (37), for the system to feel the effects of rotation, all three terms need to balance. To illustrate this, consider the cubic discriminant:

$$\Delta = -4\mu^3 - 27(T + \mu)^2 \tag{38}$$

which, when one is close to threshold (*i.e.*, $\Delta \approx 0$), admits $\mu^3 \sim T^2 \Rightarrow \mu \sim T^{2/3} (\equiv E^{-4/3})$. It hence follows from equation (37) that $\alpha \sim T^{1/3} (\equiv E^{-2/3})$[7].

Crucially, this tells us that in the rapid rotation limit $T >> 1$, the critical heating rate for the onset of convection should scale with the Ekman number as $\mu_c \sim E^{-4/3}$. This is in accordance with our intuition that any latent heating needs to be significantly large to overcome the strongly stabilising influence of rapid rotation. More fundamentally, this scaling informs how our latent heating term should be balanced in the asymptotically reduced equations of [11] (see also [2]).

2.2.2 Non-rotating and rapidly rotating solutions to the characteristic polynomial

In the last part of this section we discuss solutions to the characteristic polynomial 36. As we proceed, we will anticipate plume-like solutions (*e.g.*, [14, 3, 33, 13]; cf. figure 3). Informing these solutions, we know that upwelling regions correspond to saturated fluid with non-zero latent

[6] In essence, μ takes on a very similar role to the Rayleigh Number.

[7] Note the balance $\alpha \sim T^{1/3}$ holds in downwelling regions from equation (37).

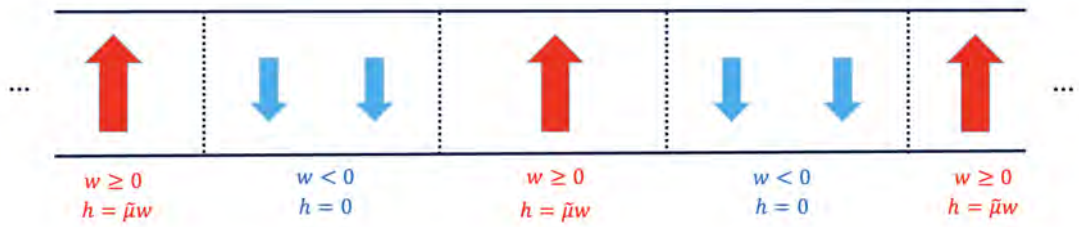

Figure 3: Schematic for periodic plume-like solutions. Here, h refers to latent heating: $h = w\mathscr{H}(w)$.

heating ($\mu \neq 0$), and downwelling regions correspond to un-saturated fluid without latent heating ($\mu = 0$). Moreover, any ascending plume must be balanced by adjacent downwlling regions as dictated by continuity.

First, we consider the non-rotating case: $T = 0$; moreover we set $R = 0$. Figure 4 presents solutions to equation (36) where we solve for a periodic 'chain' of plumes with upwelling half-width, a; furthermore, each adjacent plume has a half-spacing, L. The fastest growing mode is defined by the minimum value of the critical heating, which from figure 4 is an array of non-interacting plumes. Explicitly, as the plume half spacing, L, is increased, the critical heating rate decreases monotonically.

To further confirm this result, we perform direct numerical simulations (DNS) of the equations (27a-27c) initialised with noise. A simulation snapshot is shown in figure 5. Following the initial transient growth, it is clear that the fastest growing mode of the system is (in this example) two plumes which are isolated from each other and do not impact each other's growth. Broadly, this result is consistent with (*e.g.*,) [3].

We now consider the rotating case. Figure 6 shows results obtained by performing a similar analysis to the non-rotating case, but with different (non-zero) values of the Taylor Number, T. To complement this, numerical simulations of the 2-dimensional/3-component equations (27a-27c) are presented in figure 7.

In contrast to the non-rotating case, it becomes clear from these figures that the fastest growing mode in the rapidly rotating regime (*i.e.*, for sufficiently high T) is an array of tightly packed periodic plumes. As T is increased, a distinct minimum in the critical heating rate corresponding rate to a narrow plume half spacing is observed. The DNS results presented in figure 7 confirm this. This is a fundamental result which tells us that the fastest growing mode of the system 27a-27c changes qualitatively as rotation becomes more dominant.

3 Non-hydrostatic QG Equations with Latent Heating

3.1 Statement of the new reduced system

On the basis of the analysis presented above, and that discussed in appendix B, we propose a

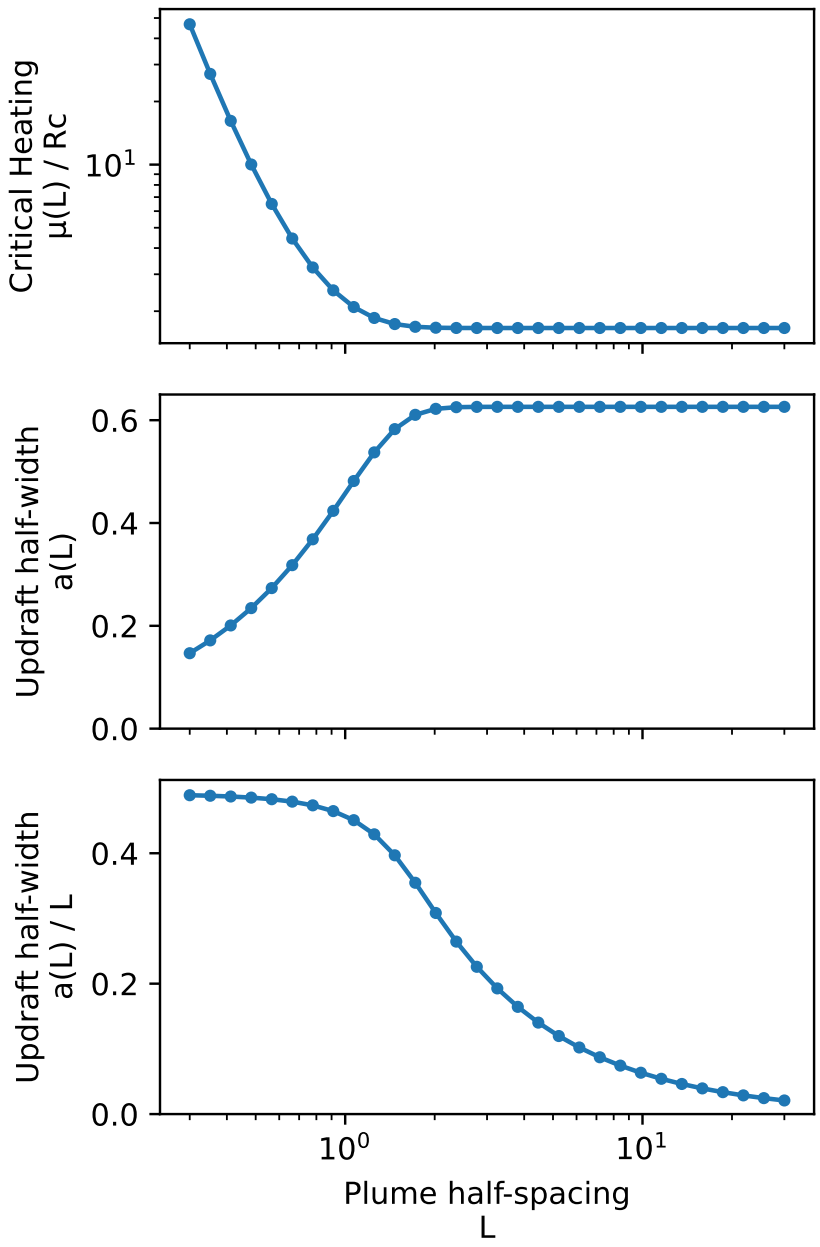

Figure 4: As a function of the plume half-spacing, L: **top:** critical heating rate, normalised by the critical Rayleigh number obtained from a classical Rayleigh-Bénard stability analysis ([27]); **middle:** updraft half width; **bottom:** updraft half-width normalised by the plume half-spacing. All panels correspond to the non-rotating case ($T = 0$). This figure confirms that the most unstable mode of the system is an array of non-interacting plumes.

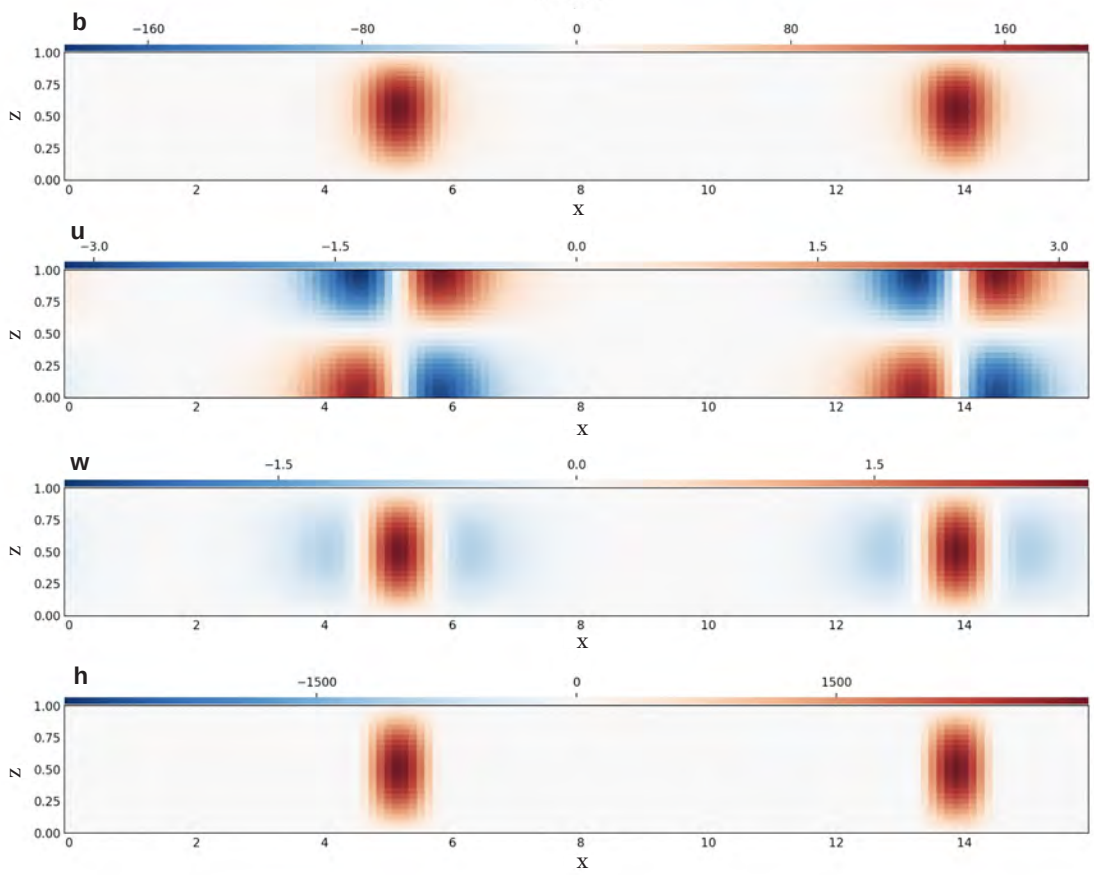

Figure 5: Results from direct numerical simulations of the Boussinesq equations with latent heating as described in equations (27a-27c) for the case where $T = 0$. Presented is the buoyancy (b), horizontal velocity (u), vertical velocity (w), and latent heating rate ($h = \mu w \mathscr{H}(w)$). In good agreement with the results presented in figure 4, we observe that the fastest growing mode of the system corresponds to non-interacting plumes. One should further note the asymmetry present in the vertical velocity, where updrafts (reds) are narrower, but stronger than adjacent downdrafts (blues)

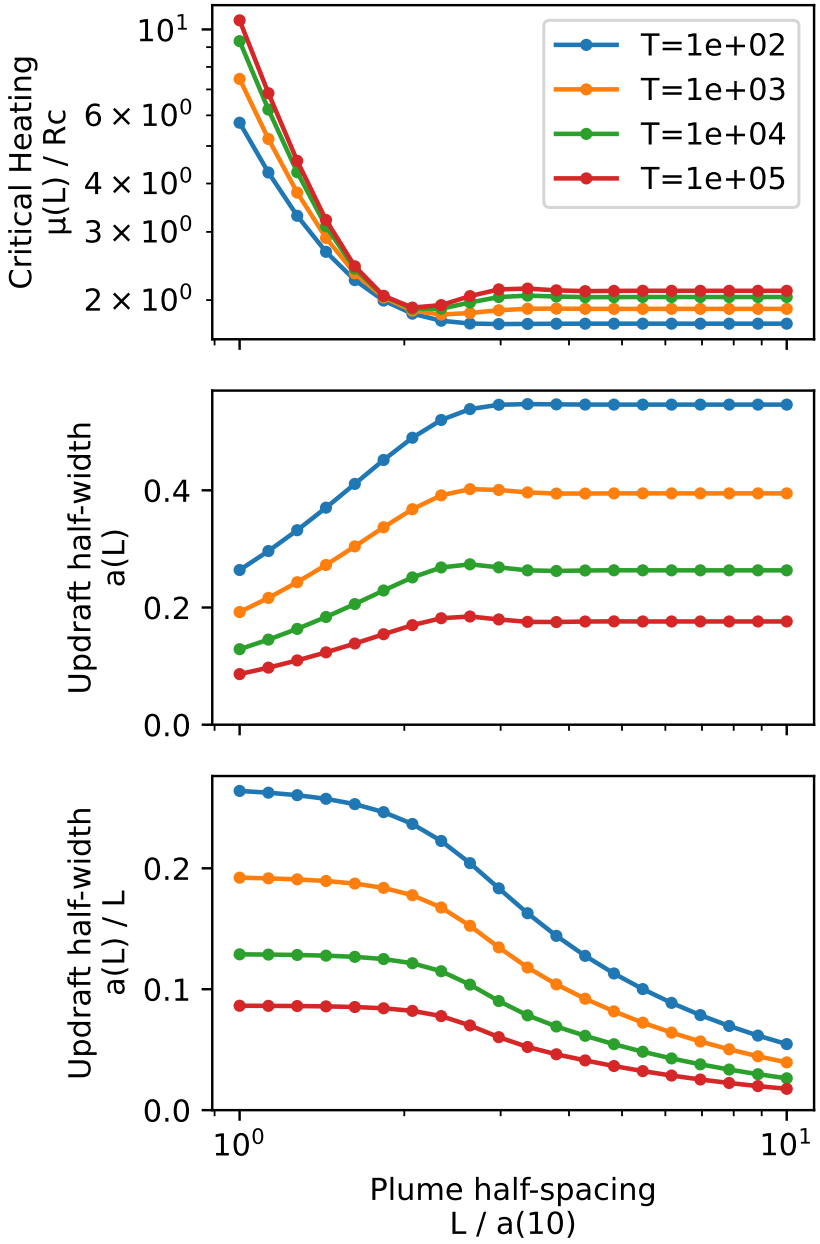

Figure 6: As in figure 4, but for different values of the Taylor number (T), as indicated by the legend in the top panel. In contrast to the non-rotating case, we see that for large T, the most unstable mode is now an array of closely packed plumes - cf. the distinct minimum in the top panel.

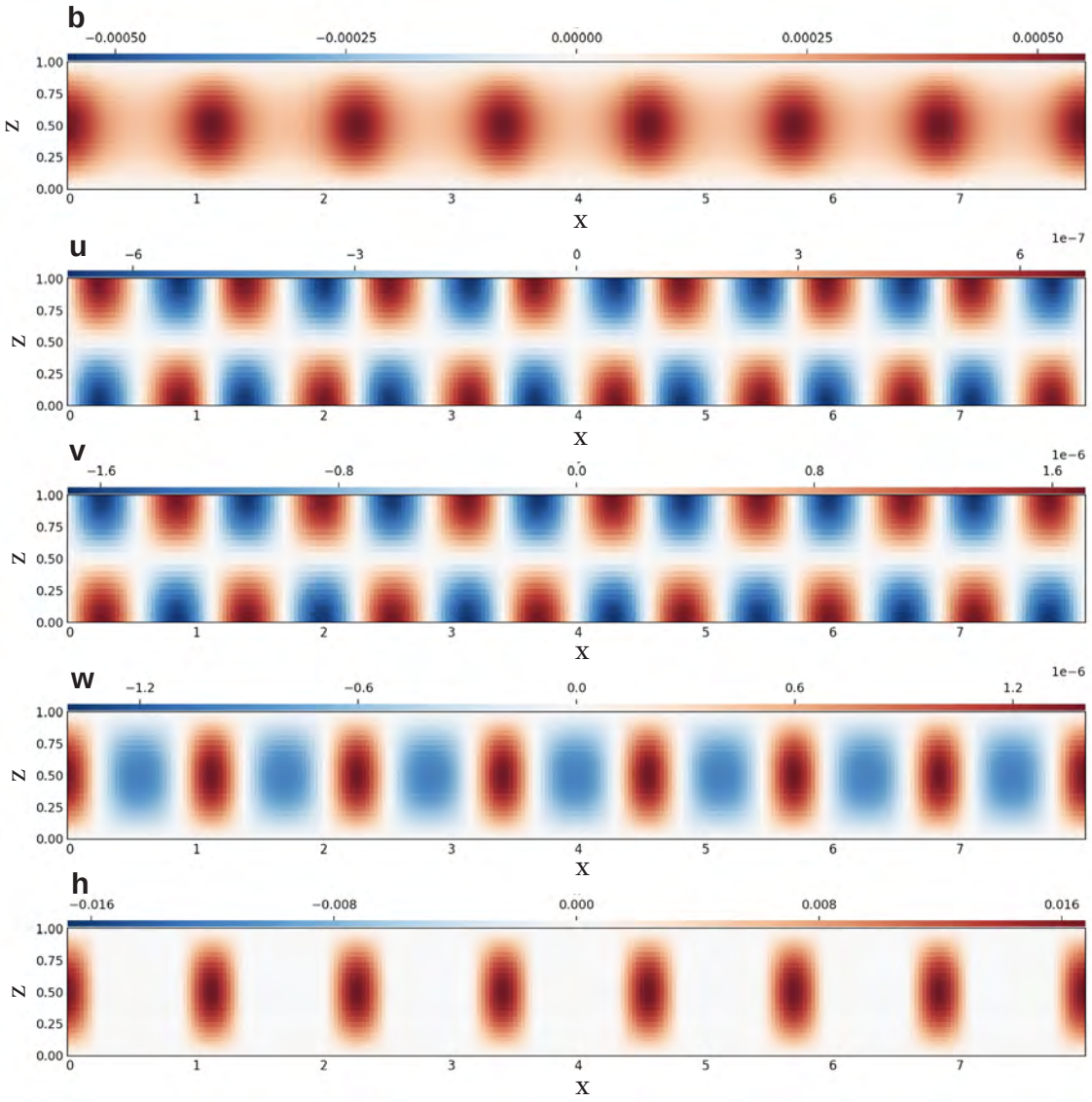

Figure 7: As in figure 5, but with rotation (i.e., 2-dimensional/3-component). In stark contrast to figure 5 the fastest growing mode of the system corresponds to an array of plumes, in agreement with the results of figure 6. Note the presence of the vertical velocity asymmetry described in the caption to figure 5.

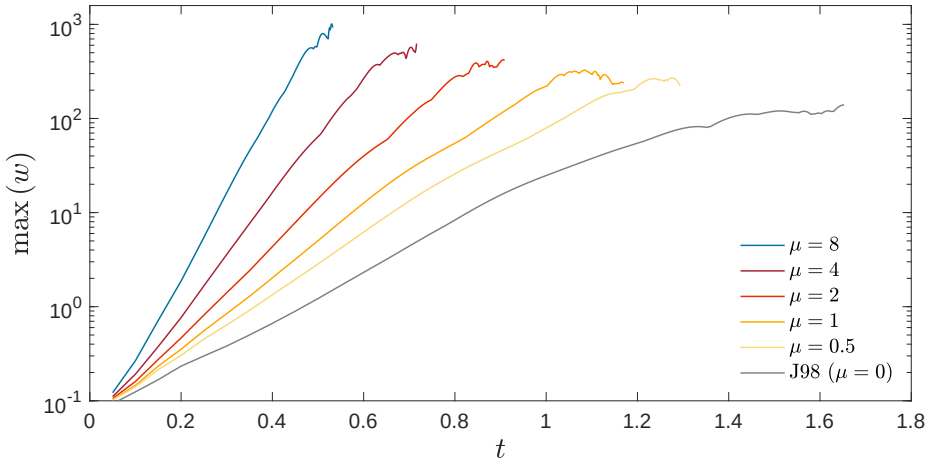

Figure 8: Time series of maximum vertical velocity w (evaluated over the whole domain) for different values of $\mu =$ constant. Here $\widetilde{Ra} = 80$ and $Pr = 1$. The case $\mu = 0$ corresponds to the original reduced equations described by [11] (J98). Note in particular the increase in growth rate as μ is increased. All simulation details are the same as those given in the caption to figure 1; however, due to computational expense and our focus here on the initial linear growth stage, these simulations were not run to a quasi-equilibrated state.

set of reduced equations, which read thus:

$$\partial_t \nabla^2\phi + J(\psi, \nabla^2\phi) + \partial_Z\psi = \frac{\widetilde{Ra}}{Pr} b' + \nabla^4_\perp \phi \tag{39a}$$

$$\partial_t \nabla^2_\perp \psi + J(\psi, \nabla^2_\perp \psi) - \partial_Z \nabla^2\phi = \nabla^4_\perp \psi \tag{39b}$$

$$\partial_t b' + J(\psi, b') + \nabla^2\phi \partial_Z \bar{b} = Pr^{-1}\nabla^2_\perp b' + \mu(Z)[\nabla^2\phi \mathscr{H}(\nabla^2\phi)]' \tag{39c}$$

$$\partial_T \bar{b} + \partial_Z(\overline{b'\nabla^2\phi}) = Pr^{-1}\partial^2_Z \bar{b} + \mu(Z)\overline{\nabla^2\phi \mathscr{H}(\nabla^2\phi)} \tag{39d}$$

Here the latent heating term has both a mean term: $\mu(Z)\overline{\nabla^2\phi\mathscr{H}(\nabla^2\phi)}$; and a fluctuating term: $\mu(Z)[\nabla^2\phi\mathscr{H}(\nabla^2\phi)]'$. In practice, we solve for 39a-39d using the substitution $\nabla^2\phi = w'$, as defined through the Helmholtz decomposition of the streamfunction.

The asymptotic validity of including these terms as written in equations (39c) and (39d) is discussed in the conclusions section and remains an open question of this project. For now, we will proceed with equations (39a-39d) fairly *ad-hoc*. In the next subsection we demonstrate that the system 39a-39d is a good starting point for a set of reduced equations.

3.2 Numerical simulations of the reduced equations (39a-39d)

We first briefly consider the case where μ is a constant in the $Z-$direction. Figure 8 shows time series of max (w') for simulations using different values of $\mu \in [0, 0.5, 1, 2, 4, 8]$; *n.b.* that the case $\mu = 0$ simply corresponds to the 'dry' reduced equations (14a-14d) and is referred to as 'J98' from hereon. All numerical simulation details are given in the caption to figure 1.

These simulations confirm that the linear growth rate scales with μ, as broadly expected from (*e.g.*,) figure 6. This is also in accordance with our intuition with atmospheric convection, that

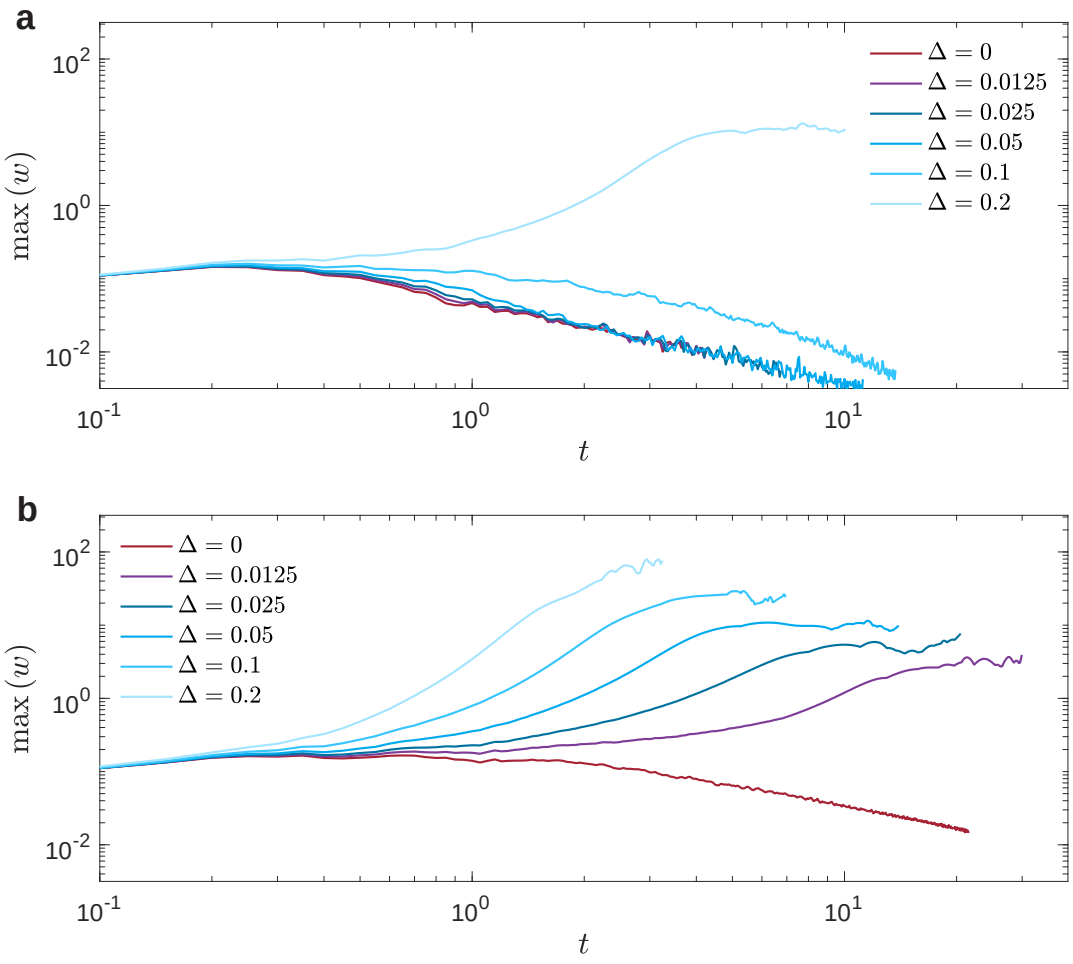

Figure 9: Time series of maximum vertical velocity w (evaluated over the whole domain) for different values of the scaled Rayleigh number, where in particular we consider $\widetilde{Ra} \cdot \Delta$ for $\widetilde{Ra} = 80$ and $Pr = 1$. In panel **a** we consider the case where $\mu = 0$, and hence the value of Δ corresponding to criticality as obtained by [29] is $\Delta_c \approx 0.11$, as broadly confirmed in this panel. In panel **b** we use an exponentially decaying form of $\mu(Z)$ (details given in the text), and find that the action of latent heating is to dramatically reduce the value of the critical Δ_c. See the caption to figure 8 for a description of the simulation procedure.

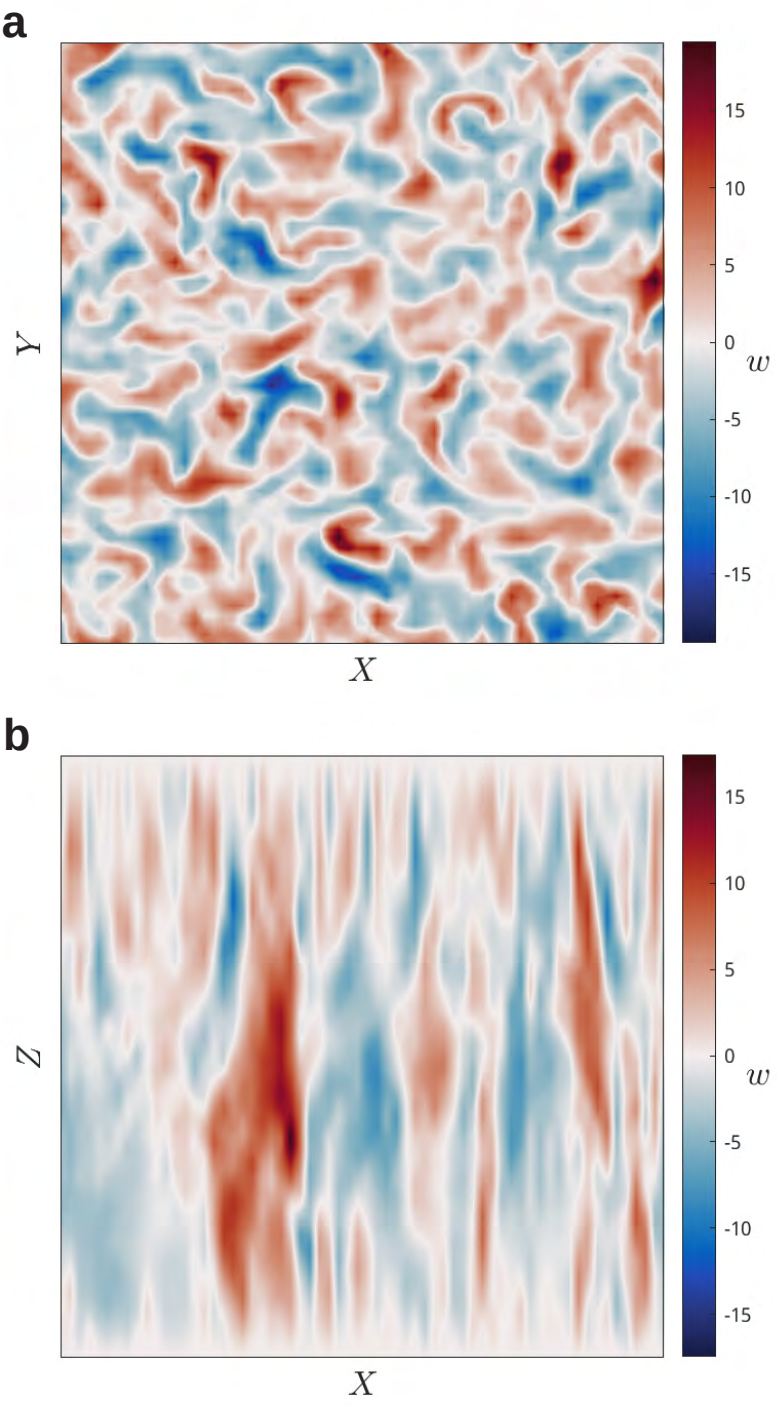

Figure 10: End of simulation vertical velocity (w') snapshots from simulations of the reduced equations (39a-39d) for $\widetilde{Ra} = 40$ and $Pr = 7$. In particular, one should compare panel **a** with figure 1.**a**, and panel **b** with figure 2, and observe that for the same values of $\widetilde{Ra}$ and Pr, latent heating has pushed the system towards a state of geostrophic turbulence. All simulations are quasi-equilibrated; other simulation details are the same as those given in the caption to figure 1.

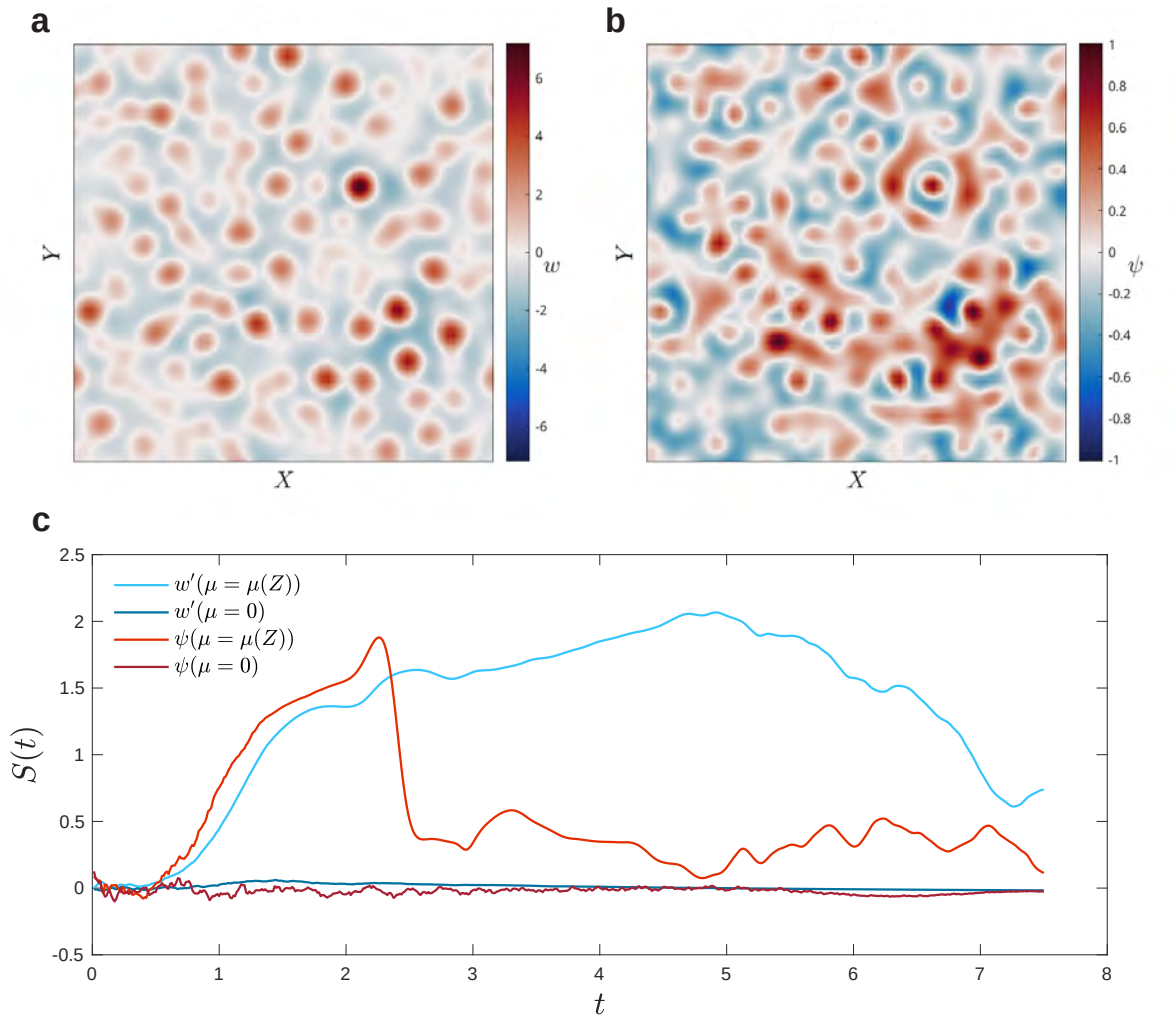

Figure 11: **a,b:** as in figure 10 but for snapshots earlier in the simulation to empahsize the asymmetries present in simulations of equations (39a-39d) (*e.g.*, one should compare panel **a** here with fig 1.**a**). To present a quantitative measure of the asymmetry introduced through the latent heating terms in equations (39a-39d), in **c** we compute the sknewness as a function of time, $S(t)$, for the midplane vertical velocity, w' (blues), and streamfunction, ψ (reds). **a-c:** Both simulations are performed with $\widetilde{Ra} = 40$ and $Pr = 7$; we compare the case with $\mu = 0$, and with an exponentially decaying profile, $\mu = \mu(Z)$, as indicated in the legend to panel **c**.

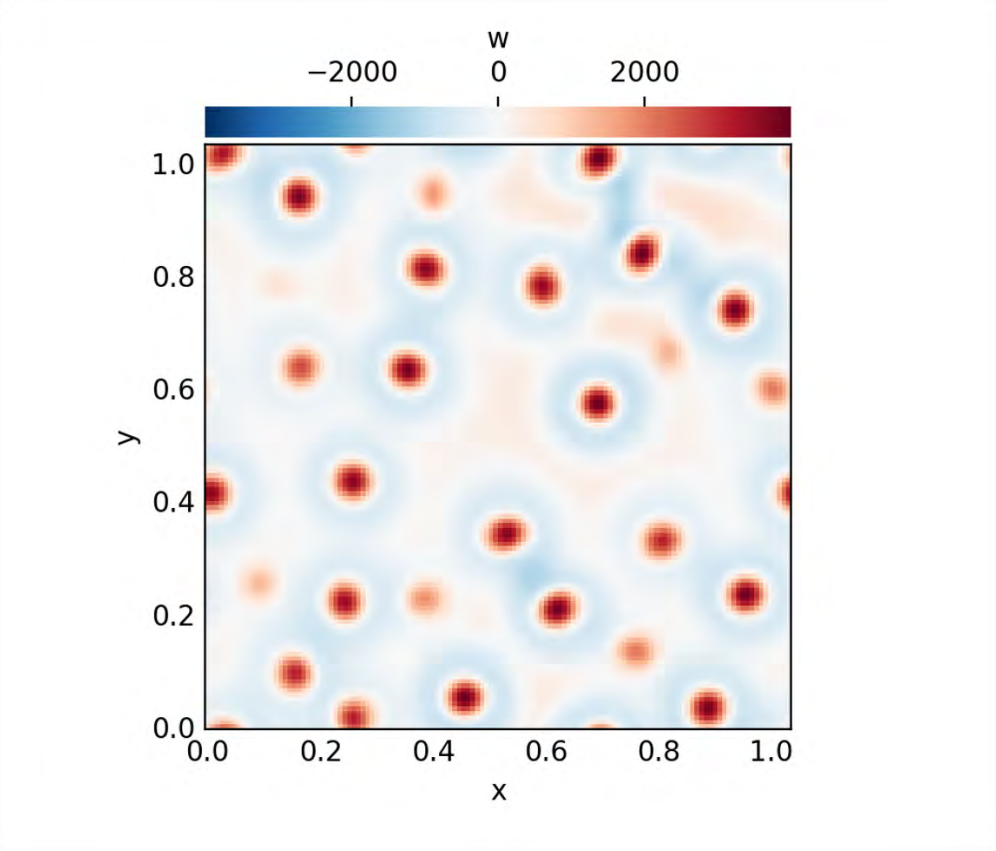

Figure 12: Direct numerical simulation of the Boussinesq equations with latent heating $h \propto w\mathscr{H}(w)$. The output is for early times in the simulation. Note the strong asymmetry in the vertical velocity, as also seen in simulations of the reduced equations in figure 11.

stronger latent heating should, in general, lead to stronger updrafts. In the remainder of our simulations and discussion of equations (39a-39d), we use an exponentially decaying profile of $\mu(Z)$:

$$\mu(Z) = -\gamma \partial_Z q_s \tag{40}$$

where q_s is determined through equation (4), and for Earth's atmosphere $\gamma = 0.2$, $\beta = 2$, and $\alpha = 3$ (all [32]). This form of $\mu(Z)$ has been chosen because it far more closely represents the atmospheric situation than a constant value (and arises directly in the analysis of appendix B).

The first investigation we perform seeks to answer the question "what impact does latent heating have on the criticality of the reduced equations?". To answer this, we construct figure 9.**b**, which broadly extends the analysis shown in figure 8, but now we use an exponentially decaying form of $\mu(Z)$, and importantly vary the Rayleigh number (see the description in the caption to figure 9) to assess the transition to organized convection in the system. We also construct figure 9.**a** to compare these results to simulations of the 'dry' equations (14a-14d). We choose a range of values of $\widetilde{Ra}$ which span sub-critical and critical values in the 'dry' equations: $(\widetilde{Ra} \cdot \Delta) \in [0, 1, 2, 4, 8, 16]$, for which the critical value $(\widetilde{Ra} \cdot \Delta)_c \approx 11$ is determined by (*e.g.*,) [29].

In the dry case, figure 9.**a** confirms that the system becomes convecting above this threshold value. Then in the 'moist' case, figure 9.**b** indicates that the system 39a-39d transitions to a convecting state at a much lower value of $\widetilde{Ra} \cdot \Delta$. Hence, a critical piece of atmospheric physics is seen in the system 39a-39d, that is, the presence of latent heating leads to organized convection in situations when 'dry' convection would not occur. To complement this, figures 10.**a** and 11.**a** show the structure of the vertical velocity field in the $Z-$midplane for the system 39a-39d with $\widetilde{Ra} = 40$, $Pr = 7$. Several important differences to the dry case are worth pointing out.

The first is that, due to the latent heating, for these parameter values the system transitions ultimately from a regime of laminar columnar convection (as shown in figure 1.**a**), into one which is characterised by geostrophic turbulence (10). Note for instance the more turbulent convective columns in figure 10.**b** as compared to figure 2. One hypothesis is that the latent heating term acts to increase the effective Rayleigh number of the system until the system transitions into a more turbulent state.

The second important difference is a transient anticylone/cyclone symmetry breaking in the system. Figure 11.**c** shows skewness as a function of time for the $Z-$midplane vertical velocity $w'(x, y, z_{mid})$ (and $Z-$midplane streamfunction, $\psi(x, y, z_{mid})$) where at each time instance the skewness computed over all horizontal gridpoints. During the initial growth of the system, the large positive skewness in $w'(x, y, z_{mid})$ indicates that there is a tendency towards stronger, but narrower updrafts, which are surrounded by broader, but weaker downwelling regions. This is clearly visible in figure 11.**a**. This pattern of updrafts and downdrafts clearly aligns with the picture obtained from linear stability, and will be a point of further investigation.

A similar positive skew is observed in the streamfunction ψ, which indicates a preference for either anticyclonic or cyclonic motion. Due to the computational expense of these experiments over the summer period, it is currently unclear whether this asymmetry persists through towards a statistically steady state. Nevertheless, even if this a transient phenomenon, it indicates a significant departure from the strong symmetry present in the original reduced equations (cf. (11.**c**)). Finally, we compare these results to direct numerical simulation of the 3D equations at high Rossby number(figure 12). Our simulations also show this asymmetry.

4 Discussion and Conclusions

The principal aim of this work is to develop a relatively simple theoretical model which unites

three elemental physical aspects of convection: moist thermodynamics; planetary rotation; and deep-reaching (non-hydrostatic) convection. This is an immensely rich and ongoing research problem, thus only the major conclusions of our work are detailed here.

We first attempted to formulate our model of atmospheric convection by performing an asymptotic reduction in the distinguished limit $Ro \to 0$ (following that detailed in [11]) using the RyBC model as our starting point. This approach for studying moist convection had hitherto not been performed.

Significant challenges in this approach quickly precipitated, primarily relating to the parametrisation of latent heating as a discontinuous function, and the formal ordering of the rapid condensation timescale. Partial differential equations with discontinuous forcing terms represent highly non-trivial problems, and such systems are not readily amenable to an asymptotic reduction (*e.g.*, [8]). Other models similar to RyBC (*e.g.*, [9], [28]) also employ discontinuous functions, hence similar starting points would have yielded the same conclusion. Whether there are other formulations of latent heating which (i) can be incorporated consistently into the dry Boussinesq equations and (ii) be more amenable to an asymptotic reduction remains an interesting question.

Instead, significant progress was made by understanding linear stability properties of the RyBC model in the limit $\tau \to 0$. Specifically, our interest was on the transition from a diffusive to a convective state. We ultimately showed that, for an exponentially growing eigenmode, regions of latent heating correspond to convective updrafts, and regions of zero latent heating correspond to downdrafts. This greatly simplifies the form of the latent heating closure, and remains rooted in the physics of atmospheric convection by establishing the clear role of convective updrafts and the top-down asymmetry.

Although the resulting 'quasi'-linear system 27a-27c is still discontinuous in a system variable, we were able to determine the physical structure of the fastest growing mode of the system. The analysis developed in 2.2 established the characterstic polynomial 36, broadly an extension to those discussed in other studies (*e.g.*, [6, 14, 3]). Most importantly, in the limit of rapid rotation ($T \gg 1$), the fastest growing eigenmode computed from this equation is characterised by relatively strong and narrow updrafts with adjacent, weaker, but broader, downwelling regions. Figure 6 shows that these plumes are tightly spaced. This represents a significant qualitative departure to the fastest growing eigenmode in the non-rotating case ($T = 0$) which is characterised by isolated plumes (*e.g.*, figure 4). All of these results were found to be robust via a direct numerical simulation of the quasi-linear equations (27a-27c).

Finally, in the rapidly rotating limit, the eigenmode equation (36) admits the scaling for the critical latent heating rate $\mu_c \sim T^{2/3} \equiv E^{-4/3}$, indicating that latent heating needs to be large. Physically, this makes sense: given the stablising effect of rotation through the Taylor-Proudman effect, any heat source should be significant to force convection in the system. This result in particular is crucial as we continue to scrutinise the form of our reduced equations with latent heating 39a-39d.

Using the aforementioned results, and the findings from appendices A-B, in section 3 we wrote down 'new' reduced equations with latent heating 39a-39d. Although *ad-hoc*, these equations exhibit many behaviours which align with our intuition of atmospheric convection. How exactly one should asymptotically balance the latent heating term remains an unsolved and interesting problem of this project.

4.1 Avenues for further work

With regards to the multiscale asymptotics analysis there are several avenues. An extension to the reduced equations is made by [10] in which they include slow modulation in the horizontal

directions, i.e., including slow variables: $X = A_X^{-1}x$; $Y = A_Y^{-1}y$. A recurring issue in our initial derivation of reduced equations was finding a horizontally invariant latent heating, which is not a physically interesting problem in the context of this study. Inclusion of slow modulation, and the corresponding re-definition of the fast scale average (defined through equation (10)) may provide an important insight.

This may also allow a study of the convective aggregation problem. One motivation would be to understand how, *e.g.*, the $\sim \mathscr{O}$(hours) and $\sim \mathscr{O}$(1km) scales for cumulus convective clouds which interact with the $\sim \mathscr{O}$(weeks) and $\sim \mathscr{O}$(100-1000km) scales typical of tropical cyclones and the intertropical convergence zone. Similar approaches have been used to explicate the dynamics of the tropical atmosphere on (fast) mesoscale and (slow) synoptic spatiotemporal scales (*e.g.*, [16]). As pointed out by [16], general circulation models do not accurately represent statistical interactions between tropical convection across spatiotemporal scales making this an important question for climate dynamics.

It is important to reconcile the asymptotic validity of the latent heating terms incorporated in equations (39a-39d). In their original derivation, equation (14c) enters at $\mathscr{O}(Ro)$ in the fluctuating buoyancy equation (12b), and equation 14d enters at $\mathscr{O}(Ro^2)$ in the mean buoyancy equation (11b). Hence, any additional terms need to respect this asymptotic ordering. Tangentially, whether equations (39a-39d) admit single-mode solutions is of great future interest.

With respect to numerical simulations, there are several ways in which one could envisage making the convection more appropriate for Earth's atmosphere. For instance, restoring to a profile of $\overline{b}$ which satisfies the nonlinear elliptic equation $\partial_z m = 0$, where $m = \overline{b} + \gamma \overline{q}_s$ is the moist static energy like variable in the system, would provide a closer analogy to tropical convection (*e.g.*, [20]).

Another avenue would be to consider different orientations of the Coriolis acceleration to access different regimes of Earth-like convection. Such analytic models were detailed in [12], but have not been performed numerically (to the knowledge of the author). These models allow for arbitrary orientation of the rotation vector relative to the horizontal plane, and with the inclusion of moist thermodynamics could aid in a description of, *e.g.*, midlatitude 'sloping convection' versus the upright convection characteristic of the tropics.

Acknowledgements

First, I want to thank Geoff Vallis for suggesting and guiding this incredibly rich problem, and for many insightful discussions throughout the summer. Next I want to thank Greg Chini (especially for his guidance in asymptotics), Keaton Burns (especially for his guidance of the work in section 2.2), and Basile Gallet (who graciously flew back from France in week 8, and guided the work detailed in section 2.1) who all helped significantly in guiding this project, and added different dimensions to the problem. Thanks goes to Adrian Fraser and Eric Hester for discussions and computational assistance early in the project. I also acknowledge Edgar Knobloch's inspiring lectures on asymptotically reduced models of convection at the start of the summer program, whose work with the late Keith Julien laid a very significant part of the groundwork for this project. A huge thanks to the organisers, Greg Chini, Bruce Sutherland, Janet Fields, Julie Hildebrandt, and Lanie Plueddemann for running the GFD program this summer. Lastly, thanks to the other fellows for making this a very memorable summer!

A Tribulations with Multiscale Asymptotics

A.1 The timescale ratio conundrum

The role of τ in the RyBC model is crucial; however, it creates significant challenges in performing the asymptotic reduction of [11], as exemplified below. Starting with the re-scaled and non-dimensionalised buoyancy equation (9b), including the latent heating term from the right hand side of equation (7b), and introducing the shorthand $\delta q \equiv q - q_s$, we have:

$$(D_t + A_T^{-1}\partial_T + wA_Z^{-1}\partial_Z)b = Pe^{-1}(\nabla + A_Z^{-1}\hat{\mathbf{z}}\partial_Z)^2 b + \gamma\left(\frac{L}{U\tau}\right)\delta q\mathscr{H}(\delta q) \tag{41}$$

where γ is non-dimensional (cf. [32]). To make progress, we consider the mean buoyancy equation and take the scalings of [11]: $A_Z^{-1} = \epsilon$; $A_T^{-1} = \epsilon^2$; $Pe \sim \mathscr{O}(1) \equiv \epsilon^0$. We will also take $\gamma \sim \mathscr{O}(1)$ and assume the mean component of the latent heating term is expressible as: $\overline{\delta q\mathscr{H}(\delta q)}$. This leaves free the scaling for the ratio of the advective to condensation timescales, for which we choose $(L/U\tau) = \epsilon^\alpha$. Some manipulation yields:

$$\epsilon^2\partial_T\bar{b} + \epsilon\partial_Z(\overline{wb}) = \epsilon^2\partial_Z^2\bar{b} + \epsilon^\alpha\overline{\delta q\mathscr{H}(\delta q)} \tag{42}$$

Then inserting explicit forms for the asymptotic expansions:

$$\epsilon^2\partial_T(\bar{b}_0 + \epsilon\bar{b}_1 + ...) + \epsilon\partial_Z(\overline{b_0'w_0'} + \epsilon(\overline{b_1'w_0'} + \overline{b_0'w_1'}) + ...) = \epsilon^2\partial_Z^2(\bar{b}_0 + \epsilon\bar{b}_1 + ...) + \epsilon^\alpha\overline{\delta q\mathscr{H}(\delta q)} \tag{43}$$

n.b. we have not made any decisions regarding the asymptotic expansion of $\overline{\delta q\mathscr{H}(\delta q)}$ - this separate and crucial issue is discussed in the next sub-appendix.

Continuing - *caveat emptor* - the leading order equation would read:

$$\partial_Z(\overline{b_0'w_0'}) = \epsilon^{\alpha-1}\overline{\delta q\mathscr{H}(\delta q)} \tag{44}$$

Then, it is fundamental that non-hydrostatic convection cannot occur unless $w_0' \neq 0$. In [10], where there is no term on the right hand side of equation (44), they enforce $b_0' = 0$. This result is ultimately critical for closing the system and arriving at the reduced equations (14a-14d). Hence, we also adopt this constraint for the case with latent heating. An exercise was performed relaxing this constraint, which led to the aforementioned closure issues and is thus not included in this report.

Enforcing the constraint $\overline{b_0'w_0'} = 0$ above implies $\alpha - 1 \geq 1 \Rightarrow \alpha \geq 2$. Then, to the next order in the mean buoyancy equation we have:

$$\partial_T\bar{b}_0 + \partial_Z(\overline{b_1'w_0'}) = \partial_Z^2\bar{b}_0 + \epsilon^{\alpha-2}\overline{\delta q\mathscr{H}(\delta q)} \tag{45}$$

If we take $\alpha = 2$, the above equation is exactly equation 12 of [10] with an additional latent heating term.

However, choosing $\alpha \geq 2$ fundamentally violates the underlying principle that the condensation timescale is the fastest timescale in the system! *A-priori* we would expect $L/(U\tau) >> 1$ and hence conclude that α should be negative, *i.e.*, at *least* $\alpha \leq -1$. In turn, this would require that the leading order relevant term in the expansion of $\overline{\delta q\mathscr{H}(\delta q)}$ were *at minimum* an order $\mathscr{O}(\epsilon^3)$ quantity. Ultimately, this would require solving for many higher order terms in the expansions of q and q_s, leading to a system which can't be closed.

A.2 The discontinuous latent heating term

The discontinuous manner in which latent heating is (necessarily) parametrised in the RyBC system raises two immediate questions: (i) how do we expand this term asymptotically, and (ii) what does it mean to formally take a fast-scale average?

To deal with the terms $\propto (q - q_s)\mathscr{H}(q - q_s)$, we use the asymptotic expansions:

$$q = \overline{q}_0 + \epsilon(\overline{q}_1 + q'_1) + \mathscr{O}(\epsilon^2) \tag{46}$$

$$q_s = \overline{q}_{s,0} + \epsilon(\overline{q}_{s,1} + q'_{s,1}) + \mathscr{O}(\epsilon^2) \tag{47}$$

where, through the isomporphism with b we have taken $q'_0 = q'_{s,0} = 0$. Then, writing out the discontinuous part of the latent heating term explicitly:

$$\mathscr{H}(q - q_s) = \mathscr{H}(\overline{q}_0 - \overline{q}_{0,s} + \epsilon(\overline{q}_1 - \overline{q}_{1,s} + q'_1 - q'_{1,s}) + \mathscr{O}(\epsilon^2)) \tag{48}$$

we could write down a Taylor expansion about the leading-order mean term to give:

$$\mathscr{H}(q - q_s) = \mathscr{H}(\overline{q}_0 - \overline{q}_{0,s}) + \epsilon(\overline{q}_1 - \overline{q}_{1,s} + q'_1 - q'_{1,s})\delta(\overline{q}_0 - \overline{q}_{0,s}) + \mathscr{O}(\epsilon^2) \tag{49}$$

Already this is an issue because the leading order term hints at a horizontally-uniform latent heating. *I.e.*, latent heating is only triggered once the mean component of the moisture field - *which here is equivalent to a domain average* - exceeds the mean saturated component. For instance there will be situations where small-scale fluctuations in moisture can cause local saturation. These are not encapsulated by the above formulation. Moreover, to order $\mathscr{O}(\epsilon)$ in the above expansion, there are higher order (than 0^{th}) mean terms which aren't required to be solved for in the original derivation of [11].

Secondly, if we now write out the latent heating term in full:

$$\begin{aligned}(q - q_s)\mathscr{H}(q - q_s) = \\ [\overline{q}_0 - \overline{q}_{0,s} + \epsilon(\overline{q}_1 - \overline{q}_{1,s} + q'_1 - q'_{1,s}) + \mathscr{O}(\epsilon^2)]\mathscr{H}(\overline{q}_0 - \overline{q}_{0,s}) \\ + \epsilon[\overline{q}_0 - \overline{q}_{0,s} + \epsilon(\overline{q}_1 - \overline{q}_{1,s} + q'_1 - q'_{1,s}) + \mathscr{O}(\epsilon^2)](\overline{q}_1 - \overline{q}_{1,s} + q'_1 - q'_{1,s})\delta(\overline{q}_0 - \overline{q}_{0,s}) \\ + \mathscr{O}(\epsilon^2)\end{aligned} \tag{50}$$

Then, what does the fast scale average look like for these terms? As an example using the leading-order mean component:

$$\overline{(q - q_s)\mathscr{H}(q - q_s)}_0 = \lim_{\mathcal{T},\mathcal{V}\to\infty} \frac{1}{\mathcal{T}\cdot\mathcal{V}} \int_{\mathcal{T},\mathcal{V}} (\overline{q}_0 - \overline{q}_{0,s})\mathscr{H}(\overline{q}_0 - \overline{q}_{0,s}) d\mathbf{x}dt; \qquad \mathbf{x}, t \in \mathcal{V}, \mathcal{T} \tag{51}$$

through equation (10). How to evaluate integrals such as the one above in the context of the physics of our problem remains an open mystery (cf. also [25]).

A.3 A 'generalised' condensation term

Both issues discussed above directly relate to the explicit form with which latent heating is parametrised in the RyBC model. Taking a step back, another approach could be to derive a set of reduced equations with a *general* condensation term: $\mathscr{P}$. Explicitly, the (dimensional) buoyancy and moisture equations would then be written:

$$\frac{Db}{Dt} = \kappa\nabla^2 b + \gamma\mathscr{P} \tag{52}$$

$$\frac{Dq}{Dt} = \kappa\nabla^2 q - \mathscr{P} \tag{53}$$

As a thought experiment, we won't yet make an appeal to rapid-condensation and assume that $\mathscr{P}$ can be 'nicely' decomposed into mean and fluctuating parts.

To understand how to carry this forward, it is critical that equations 14a and (14b) enter as a solveability condition in the $\mathscr{O}(Ro^2)$ fluctuating momentum equation; equation (14c) enters at $\mathscr{O}(Ro)$; equation (14d) enters at $\mathscr{O}(Ro^2)$. As such, any additional forcing terms in the reduced equations must respect this asymptotic ordering (cf. [12]). This eventually implies $\mathscr{P} = \epsilon^2\overline{\mathscr{P}} + \epsilon\mathscr{P}'$.

However, we do not have evolution equations for $\overline{\mathscr{P}}$ nor $\mathscr{P}'$. Rather, it is impossible to compute either quantity without first computing the full condensation field, $\mathscr{P}$. The necessary decomposition of $\mathscr{P}$ into mean and fluctuating components would thus require an arbitrary ϵ! Moreover, in principle $\mathscr{P}$ **must** be computed from the **full** q and q_s fields (*i.e.*, mean + fluctuations), thus *also* requiring reconstruction of the fields with arbitrary ϵ! There are considerable issues with this approach before we've even considered the rapid-condensation timescale and averaging.

B Treating τ as a Formal Small Parameter

B.1 Derivation of preliminary reduced equations with moisture in the limit $\tau \to 0$

The purpose of this subsection is to show how one might approach the asymptotic reduction of equations (7a-7d) with rotation following [11], but treating τ as a formal small parameter of the system. It is taken that both τ and Ro are formal small parameters, in such a way that $\tau << \epsilon = Ro << 1$. Given the critical role of τ, here we will consider the following 'dual' expansion to $q - q_s$, where it is assumed that the limit $\tau \to 0$ is taken before $\epsilon \to 0$.

$$q - q_s \sim \begin{cases} (\overline{q}_0 + \epsilon q_1 + ...) - (\overline{q}_{s,0} + \epsilon q_{s,1} + ...) & \text{when } q < q_s \\ (\overline{q}_0 + \tau q_\tau + ...) - (\overline{q}_{s,0} + \epsilon q_{s,1} + ...) & \text{when } q \geq q_s \end{cases} \tag{54}$$

Note that the leading order fluctuating terms q_0' and $q_{s,0}'$ would be determined to be 0.

Considering the expansion in expression 54, for $q < q_s$, the asymptotic reduction can be carried exactly as in [11] since q is decoupled from the buoyancy equation, and behaves as a passive tracer in the system.

Then, for $q > q_s$, one can show that the leading order mean and fluctuating q equations yield, after taking the limit $\tau \to 0$:

$$\epsilon^2\partial_T\overline{q}_0 + \epsilon^2\partial_Z^2(\overline{w_0'q_1'}) = \epsilon^2 Pe^{-1}\partial_Z^2\overline{q}_0 - \overline{q}_\tau \tag{55a}$$

$$\epsilon D_t^0 q_1' + \epsilon w_0'\partial_Z\overline{q}_0 - \epsilon Pe^{-1}\nabla^2 q_1' = -q_\tau' \tag{55b}$$

and hence find that the mean and fluctuating parts of q_τ can be written:

$$\overline{q}_\tau = -\epsilon^2[Pe^{-1}\partial_Z^2\overline{q} + \partial_T\overline{q}_s - \partial_Z(\overline{w_0'q_s'})] \tag{56a}$$

$$q_\tau' = -\epsilon[D_t q' + w'\partial_Z\overline{q}_s - Pe^{-1}\nabla^2 q'] \tag{56b}$$

where the asymptotic ordering of individual terms has been suppressed.

Critically $\overline{q}_\tau \sim \mathscr{O}(\epsilon^2)$ and $q_\tau' \sim \mathscr{O}(\epsilon)$. Then, in re-introducing the streamfunction formulation (e.g., $w' = \nabla_\perp^2\phi$), one *can* write a set of reduced equations of the following form:

$$\partial_t\nabla_\perp^2\phi + J(\psi, \nabla_\perp^2\phi) + \partial_Z\psi = \frac{\widetilde{Ra}}{Pr}b' + \nabla_\perp^4\phi \tag{57a}$$

$$\partial_t \nabla_\perp^2 \psi + J(\psi, \nabla_\perp^2 \psi) - \partial_Z \nabla_\perp^2 \phi = \nabla_\perp^4 \psi \tag{57b}$$

$$\partial_Z \overline{p} = \frac{\widetilde{Ra}}{\sigma} \overline{b} \tag{57c}$$

$$\partial_T \overline{b} - Pe^{-1} \partial_Z^2 \overline{b} + \partial_Z (\overline{b' \nabla_\perp^2 \phi}) = \begin{cases} 0 & \text{for } q < q_s \\ -\gamma [\partial_T \overline{q}_s - Pe^{-1} \partial_Z^2 \overline{q}_s + \partial_Z (\overline{q' \nabla_\perp^2 \phi})] & \text{for } q \geq q_s \end{cases} \tag{57d}$$

$$\partial_t b' + J(\psi, b') + \nabla_\perp^2 \phi \partial_Z \overline{b} - Pr^{-1} \nabla_\perp^2 b' = \begin{cases} 0 & \text{for } q < q_s \\ -\gamma [\partial_t q' + J(\psi, q') + \nabla_\perp^2 \phi \partial_Z \overline{q}_s - Pr^{-1} \nabla_\perp^2 q'] & \text{for } q \geq q_s \end{cases} \tag{57e}$$

$$\begin{cases} \partial_T \overline{q} - Pe^{-1} \partial_Z^2 \overline{q} + \partial_Z (\overline{q' \nabla_\perp^2 \phi}) = 0 & \text{for } q < q_s \\ \overline{q} = \overline{q}_s & \text{for } q \geq q_s \end{cases} \tag{57f}$$

$$\begin{cases} \partial_t q' + J(\psi, q') + \nabla_\perp^2 \phi \partial_Z \overline{q} - Pr^{-1} \nabla_\perp^2 q' = 0 & \text{for } q < q_s \\ \partial_t q' + J(\psi, q') + \nabla_\perp^2 \phi \partial_Z \overline{q}_s - Pr^{-1} \nabla_\perp^2 q' = 0 & \text{for } q \geq q_s \end{cases} \tag{57g}$$

Note that the last equation above is essentially a statement that one must keep track of the q' fields in order to evaluate the condition $q \geq q_s$ at each point in $(\mathbf{x}, t)$, which still requires reconstruction of the fields at arbitrary small *Ro*. Furthermore, equation (57f) leaves us with a situation in which there is a horizontally-uniform latent heating.

Nevertheless, the most important point to make is that equation (57e) contains a term on the right-hand side which goes as $-\gamma(\nabla_\perp^2 \phi) \partial_Z \overline{q}_s \equiv -\gamma w' \partial_Z \overline{q}_s$. This term is evocative of latent heating closures used in other studies [17]. In section 2 we take the $\tau \to 0$ limit of the RyBC equations which shows that under certain conditions, this term is actually the *only* term which one needs to include. In section 3 we hence argue the case for a set of reduced equations with this term. Hence, although somewhat unfruitful in of itself, the analysis described above greatly inspired the work outlined in the main report.

B.2 Moist static energy

A final interesting point is that one can use these equations to obtain evolution equations for moist static energy (MSE; *e.g.* [20]). For $q < q_s$: $57d + \gamma \times 57f$ yields:

$$\partial_T [\overline{b} + \gamma \overline{q}] - Pe^{-1} \partial_Z^2 [\overline{b} + \gamma \overline{q}] + \partial_Z (\overline{[b' + \gamma q'] \nabla_\perp^2 \phi}) = 0 \tag{58}$$

For $q \geq q_s$, equation (57d) can be re-arranged:

$$\partial_T [\overline{b} + \gamma \overline{q}_s] - Pe^{-1} \partial_Z^2 [\overline{b} + \gamma \overline{q}_s] + \partial_Z (\overline{[b' + \gamma q'] \nabla_\perp^2 \phi}) = 0 \tag{59}$$

Hence, we may combine both equations above through an MSE-like variable: $\Lambda = b + \gamma q$, which has mean, $\overline{\Lambda} = \overline{b} + \gamma \overline{q}$, and fluctuating $\Lambda' = b' + \gamma q'$ parts.

Introducing the slow differential operator $\mathscr{D}_T \equiv \partial_T - Pe^{-1} \partial_Z^2$, one obtains:

$$\boxed{\mathscr{D}_T \overline{\Lambda} = -\partial_Z (\overline{\Lambda' \nabla_\perp^2 \phi}) \quad \left(\equiv -\partial_Z (\overline{\Lambda' w'}) \right)} \tag{60}$$

and note that in the absence of diffusion (i.e., the RHS of the above $\to 0$), one would conserve the mean MSE on long scales. A similar manipulation of the fluctuating equations, and introducing the fast differential operator $\mathscr{D}_t \equiv \partial_t + J(\psi, ...) - Pe^{-1}\nabla_\perp^2$ yields:

$$\boxed{\mathscr{D}_t \Lambda' = -\nabla_\perp^2 \phi \partial_Z \overline{\Lambda} \ \left(\equiv -w' \partial_Z \overline{\Lambda} \right)} \tag{61}$$

and hence small-scale fluctuations in the MSE feed off gradients in the mean MSE through the small-scale vertical velocity fluctuations.

C Notes on the solution to the characteristic polynomial (33)

C.1 Dispersion relations

First re-stating the operator equation (33:

$$)[(\sigma - \nu\nabla^2)^2\nabla^2(\sigma - \kappa\nabla^2) - f_0^2 k_z^2(\sigma - \kappa\nabla^2) + (N^2 - \widetilde{\mu})\partial_x^2(\sigma - \nu\nabla^2)]u = 0$$

but now taking $\sigma \neq 0$, we may obtain dispersion relationships for σ in terms of k_x, k_z.

- **In the diffusion-free case:** $\kappa, \nu \to 0$, and where $N^2 = \mu = 0$.

$$\sigma^3\nabla^2 - f_0^2 k_z^2 \sigma = 0 \tag{62}$$

this gives us

$$\sigma^2 = -\frac{f_0^2 k_z^2}{k_x^2 + k_z^2} \tag{63}$$

$$\sigma_c = \frac{f_0 k_z}{|\mathbf{k}|} \tag{64}$$

where σ_c denotes the complex part of the growth rate. Equation (52) hence corresponds to inertial waves.

Including diffusion: Then, one could relax the constraint $\kappa, \nu \neq 0$, whilst maintaining $N^2 = \mu = 0$. In this situation the operator equation reduces to:

$$(\sigma - \nu\nabla^2)^2\nabla^2 = f_0^2 k_z^2 \tag{65}$$

and after some algebra leads to damped inertial waves:

$$\sigma = \underbrace{-\nu|\mathbf{k}|^2}_{\sigma_r} \pm i \underbrace{\frac{f_0 k_z}{|\mathbf{k}|}}_{\sigma_c} \Rightarrow \text{(e.g.,) } w \propto e^{-\nu|\mathbf{k}|^2} e^{\pm i \frac{f_0 k_z}{|\mathbf{k}|}} \tag{66}$$

since the real part of the growth rate, σ_r is < 0.

References

[1] A. Arakawa and W. H. Schubert. "Interaction of a Cumulus Cloud Ensemble with the Large-Scale Environment, Part 1". In: *Journal of the Atmospheric Sciences* 31 (1974), pp. 674–701.

[2] J. M. Aurnou, S. Horn, and K. Julien. "Connections between nonrotating, slowly rotating, and rapidly rotating turbulent convection transport scalings". In: *Physical Review Research* 2 (2020), p. 043115.

[3] C. S. Bretherton. "A Theory for Nonprecipitating Moist Convection between Two Parallel Plates. Part 1: Thermodynamics and Linear Solutions". In: *Journal of the Atmospheric Sciences* 44 (1987), pp. 1809–1827.

[4] C. S. Bretherton. "A Theory for Nonprecipitating Moist Convection between Two Parallel Plates. Part 2: Nonlinear Theory and Cloud Field Organization". In: *Journal of the Atmospheric Sciences* 45 (1988), pp. 2391–2415.

[5] K. J. Burns et al. "Dedalus: A flexible framework for numerical simulations with spectral methods". In: *Physical Review Research* 2 (2020), p. 023068.

[6] S. Chandrasekhar. "The instability of a layer of fluid heated below and subject to Coriolis forces". In: *Proceedings of the Royal Society A* 217 (1953), pp. 306–327.

[7] M.-H. Chien, O. Pauluis, and A. S. Almgren. "Hurricane-Like Vortices in Conditionally Unstable Moist Convection". In: *Journal of Advances in Modeling Earth Systems* 14 (2022), e2021MS002846.

[8] A. F. Filippov. *Differential Equations with Discontinuous Righthand Sides. Control Systems.* 1st ed. Springer Dordrecht, 1988.

[9] G. Hernandez-Duenas et al. "Minimal models for precipitating turbulent convection". In: *Journal of Fluid Mechanics* 717 (2013), pp. 576–611.

[10] K. Julien and E. Knobloch. "Reduced models for fluid flows with strong constraints". In: *Journal of Mathematical Physics* 48 (2007), p. 065405.

[11] K. Julien, E. Knobloch, and J. Werne. "A New Class of Equations for Rotationally Constrained Flows". In: *Theoretical and Computational Fluid Dynamics* 11 (1998), pp. 251–261.

[12] K. Julien et al. "Generalized quasi-geostrophy for spatially anisotropic rotationally constrained flows". In: *Journal of Fluid Mechanics* 555 (2006), pp. 233–274.

[13] M Kohl and P. A. O'Gorman. "The Diabatic Rossby Vortex: Growth Rate, Length Scale, and the Wave–Vortex Transition". In: *Journal of the Atmospheric Sciences* 79 (2022), pp. 2739–2755.

[14] H. L. Kuo. "Convection in Conditionally Unstable Atmosphere". In: *Tellus* 13 (1961), pp. 441–459.

[15] G. Lapeyre and I. M. Held. "The Role of Moisture in the Dynamics and Energetics of Turbulent Baroclinic Eddies". In: *Journal of Climate* 61 (2004), pp. 1693–1710.

[16] A. J. Majda. "New Multiscale Models and Self-Similarity in Tropical Convection". In: *Journal of the Atmospheric Sciences* 64 (2007), pp. 1393–1404.

[17] M. Mak. "On Moist Quasi-Geostrophic Baroclinic Instability". In: *Journal of the Atmospheric Sciences* 39 (1982), pp. 2028–2037.

[18] J. R. Malkus. "On the Maintenance of the Trade Winds". In: *Tellus A* 8 (1956), pp. 335–350.

[19] C. Muller et al. “Spontaneous Aggregation of Convective Storms”. In: *Annual Review of Fluid Mechanics* 54 (2022), pp. 133–157.

[20] J. D. Neelin and I. M. Held. “Modeling Tropical Convergence Based on the Moist Static Energy Budget”. In: *Monthly Weather Review* 115 (1987), pp. 3–12.

[21] J. D. Neelin, I. M. Held, and K. H. Cook. “Evaporation-Wind Feedback and Low-Frequency Variability in the Tropical Atmosphere”. In: *Journal of the Atmospheric Sciences* 44 (1987), pp. 2341–2348.

[22] Q. Nicolas and W. R. Boos. “A Theory for the Response of Tropical Moist Convection to Mechanical Orographic Forcing”. In: *Journal of the Atmospheric Sciences* 79 (2022), pp. 1759–1777.

[23] O. Pauluis and J. Schumacher. “Idealized moist Rayleigh-Bénard convection with piecewise linear equation of state”. In: *Communications in Mathematical Science* 5 (2010), pp. 295–319.

[24] J. P. Peixoto and A. H. Oort. *Physics of Climate*. American Institute of Physics, 1992.

[25] V. A. Plotnikov and T. S. Zverkova. “Method of partial averaging in the systems of standard form with discontinuous right-hand sides”. In: *Ukrainian Mathematical Journal* 45 (1993), pp. 156–159.

[26] D. A. Randall. “Conditional Instability of the First Kind Upside-Down”. In: *Journal of the Atmospheric Sciences* 37 (1980), pp. 125–130.

[27] Lord O.M. F.R.S. Rayleigh. “On convection currents in a horizontal layer of fluid, when the higher temperature is on the under side”. In: *The London, Edinburgh, and Dublin Philosophical Magazine and Journal of Science* 32 (1916), pp. 529–546.

[28] L. M. Smith and S. N. Stechmann. “Precipitating Quasigeostrophic Equations and Potential Vorticity Inversion with Phase Changes”. In: *Journal of the Atmospheric Sciences* 74 (2017), pp. 3285–3303.

[29] M. Sprague et al. “Numerical simulation of an asymptotically reduced system for rotationally constrained convection”. In: *Journal of Fluid Mechanics* 551 (2006), pp. 141–174.

[30] B. Stevens. “Atmospheric Moist Convection”. In: *Annual Review of Earth and Planetary Science* 33 (2005), pp. 605–643.

[31] G. K. Vallis. *Atmospheric and Oceanic Fluid Dynamics. Fundamentals and Large-Scale Circulation*. 2nd ed. Cambridge University Press, 2017.

[32] G. K. Vallis, D. G. Parker, and S. M. Tobias. “A simple system for moist convection: the Rainy-Bénard model”. In: *Journal of Fluid Mechanics* 862 (2019), pp. 162–199.

[33] P. Zurita-Gotor. “Updraft/Downdraft Constraints for Moist Baroclinic Modes and Their Implications for the Short-Wave Cutoff and Maximum Growth Rate”. In: *Journal of the Atmospheric Sciences* 62 (2005), pp. 4450–4458.

Fast Singular Limits of the Lagrangian-averaged Navier-Stokes-α Model

Lulabel Ruiz Seitz

August 21, 2024

1 Introduction

The Lagrangian-averaged Navier-Stokes-α, or LANS$-\alpha$, equations constitute a turbulence closure method based on mathematical regularization, and have been shown to be more successful than commonly used closure schemes in a number of contexts [9, 11, 12, 14]. In particular, the LANS$-\alpha$ model is more energetic at lower resolutions than large eddy simulations (LES) with other turbulence closure schemes at higher resolutions; it achieves at lower resolution what other methods require higher resolution to accomplish. Despite its successes in turbulence modeling, the LANS-α model's origins lie outside this field. Most directly, the LANS-α model emerged from the Gjaja-Holm Wave-Mean Flow Interaction (WMFI) equations, which were developed for entirely different purposes [14]. Once again appearing in an unexpected context, the LANS-α equations were subsequently found to answer a long-standing question related to the mathematical regularization of Navier-Stokes, with roots in Leray's work from 1934 [19].

Leray famously proved the existence of weak solutions to the Navier-Stokes equations, while recognizing the challenge of proving uniqueness for three-dimensional solutions [19]. Leray's key insight, now known as Leray regularization, involves smoothing the (nonlinear) advection term to form a regularized version of the equations. Leray accomplished this by using a sequence of mollifiers $\{\phi_\epsilon\}$ and replacing $\boldsymbol{v} \cdot \nabla \boldsymbol{v}$ with $(\phi_\epsilon * \boldsymbol{v}) \cdot \nabla \boldsymbol{v}$ [10]. Taking $\epsilon \to 0$ recovers the unregularized Navier-Stokes equations. The LANS-α equations employ this same regularization principle, but with a different operator than convolution with a mollifier: an inverse Helmholtz operator with smoothing parameter α, $(1 - \alpha^2\Delta)^{-1}$. This inverse Helmholtz operator is an approximation of the transformation between Lagrangian and Eulerian velocities and is the namesake of LANS-α. Although the Leray equations successfully regularize Navier-Stokes, they raised a key question: how to achieve such regularization while preserving important circulation properties. This open question was answered by the LANS-α equations, which extend Leray's approach by retaining a Kelvin circulation the-orem while maintaining well-posedness [24] and convergence to the original Navier-Stokes equations as $\alpha \to 0$.

Furthermore, the LANS-α equations embody the fundamental principle of LES: confining the inertial range of the energy cascade to exclude motions at unresolvably small spatial scales. Indeed, unlike many LES approaches that lack mathematical rigor, the LANS-α

model is particularly compelling due to its rigorous mathematical derivation and its deep connection to regularized Navier-Stokes [10].

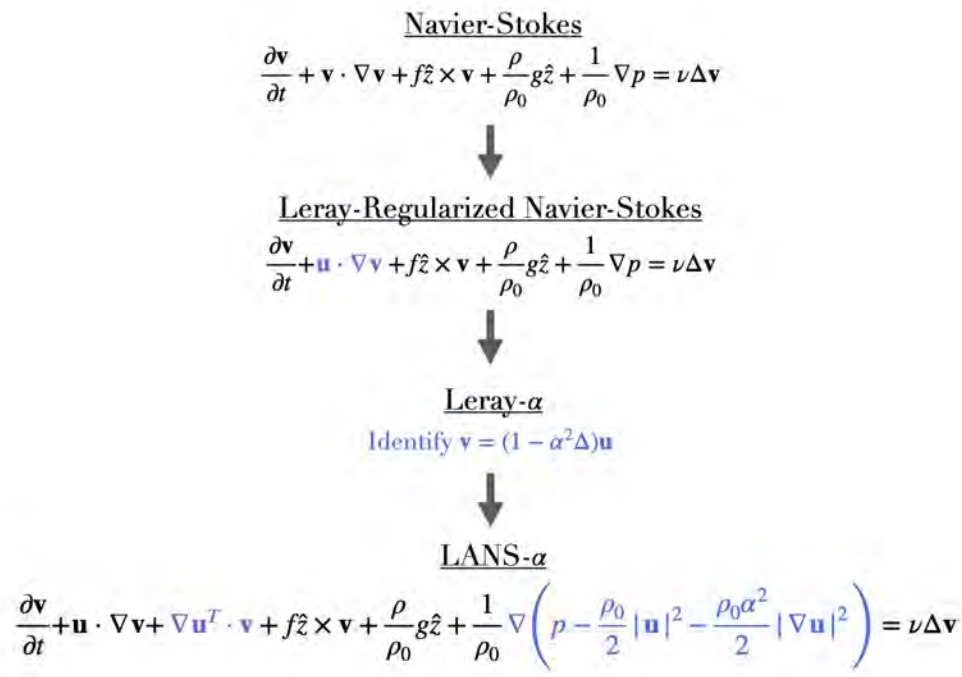

Figure 1: The hierarchy of equations: from the Navier-Stokes momentum equation to the LANS-α momentum equation. In blue, what differs from the previous equation is highlighted. From Navier-Stokes to Leray$-\alpha$ may be considered successive approximations, while the transition to LANS-α then adds necessary terms to obtain a Kelvin circulation theorem.

Despite its demonstrated success and theoretical foundations, the LANS-α model exhibits unusual numerical stability issues for certain values of the parameter α. Specifically, Hecht et al. (2008) found that simulations were unstable – the kinetic energy blew up – when $\alpha \geq 2\Delta x$, where Δx is the grid spacing [12]. This behavior is not unique; the mathematically similar Anstey and Zanna closure method has also faced numerical stability issues [1]. Although stability analyses have been conducted (c.f. [4], [12]), a clear resolution to these stability issues has remained elusive.

To this end, we compute fast singular limits of the LANS-α equations. The fast singular limit intended for "averaging over fast gravity waves" in geophysical flows was established by Embid and Majda in 1996 and further developed in 1998 [5, 6, 7]. This method not only determines the limiting slow dynamics, as in a singular limit, but also explicitly describes the impact of fast dynamics (i.e. waves) at that order. This approach yields a natural partition into slow and fast dynamics, unlike other asymptotic methods that only capture slow dynamics explicitly. It is often desirable to derive reduced, more computationally tractable equations that still model key dynamics of interest. By appropriately choosing a small parameter, one can employ multiscale asymptotics to obtain such reduced equations

representing "slow dynamics" while filtering out "fast dynamics." For example, the quasi-geostrophic equation represents the "slow dynamics" while wave effects filtered out during the reduction constitute fast dynamics.

The extent to which one can truly "filter out" fast dynamics was central to studies of the *slow manifold*. If there is a slow manifold – a subspace of the whole solution space on which only the balanced or dominant dynamics lie – is it true that dynamics off the manifold do not affect the evolution of those on the manifold? This concept was of much interest in the 1980s-1990s and sparked debate due to a fundamental disconnect: a slow manifold in the scientific sense, corresponding to the slow dynamic equations, is not necessarily a slow manifold in the mathematical sense of a center manifold. Even if there is a slow manifold in the mathematical sense, it does not necessarily serve as the desirable slow manifold in the scientific sense, on which, for instance, there would never be any gravity wave activity [16, 21, 22]. This framework has nonetheless provided valuable insights in many situations (c.f. [2], [20]).

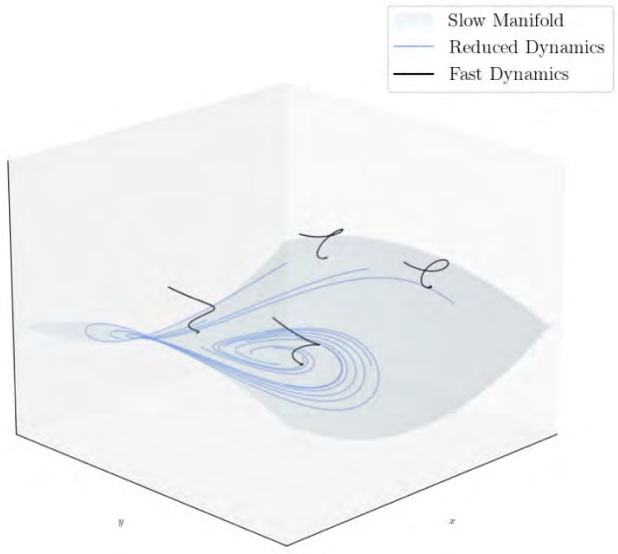

Figure 2: A schematic diagram of the (idealized) slow manifold: the slow manifold occupies a subset of the overall solution space, shown in light blue, and the reduced dynamics live on the slow manifold, shown in dark blue. Fast dynamics live off the manifold, shown in black. These dynamics are shown as oscillatory to represent that they are associated with different types of waves, and are shown as approaching the slow manifold to represent that the slow manifold may be thought of as an "attractor."

Whitehead and Wingate (2011) used the fast-slow decomposition that arises from a fast singular limit to assess the influence of fast dynamics on those lying on the slow manifold, and in doing so, addressing the validity of using the reduced equations and analyzing mean flow-wave interactions [29]. This investigation involved an analysis of the energy evolution of the system, in each of the three asymptotic limits for the Boussinesq equations (low Rossby only, low Froude only, and QG). It should be noted that not all of the three possible

slow manifolds should have no waves; in the low Rossby but finite Froude limit, for instance, the Froude-related operator is slow, so waves created due to stratification can be on the slow manifold. The energy analysis revealed that slow potential energy can convert to slow kinetic energy (remain slow) only in the QG limit. In the other cases, potential energy fed into the fluctuating components of the flow. However, when forcing the whole flow rather than just the slow or fast components, the fast dynamics significantly modulate energy transfer. Thus the fact that *leading order* fast dynamics cannot affect *leading order* slow dynamics gives an incomplete picture. These results concretely illustrate the potential of fast singular limits, especially when comparing multiple distinguished limits for the same system whenever they exist.

We similarly take advantage of the fast-slow decomposition, but in particular to approach the numerical instability issue. While slow dynamics for the LANS-α equations have been previously mathematically studied – in that the existence of attractors has been proven for the LANS-α equations [18] and the dimensions of these attractors studied [17] – the aim of prior work was not to study the evolution of fast and slow dynamics or to address the stability issue. In light of the kinetic energy blow-up, we hypothesize that the fast component of the energy is problematic: the fast dynamics drive the instability. By taking fast singular limits, we can better understand the properties of the LANS-α model and localize the origin of the stability issue, guiding the development of stable numerical implementations.

The structure of this report is as follows. In Section 2, we provide a full mathematical background for taking a fast singular limit in the context of geophysical fluids. A goal of this section is to provide a more robust exposition of this methodology, so that it may be readily applied to problems of interest by a reader who does not have prior experience with the method. This section also includes three fast singular limits calculated for unregularized Navier-Stokes, so that we can compare the $\alpha = 0$ results to the $\alpha \neq 0$ (LANS-α) results found in Section 3. Section 3 contains the three fast singular limits for LANS-α, which is the theoretical work underlying our results. Lastly, Section 4 describes the continued work following what is written in this report, including numerical simulations to complement the theoretical findings, and outlines possible future directions.

2 Background: Fast Singular Limits

In this section, we discuss the methodology of taking a fast singular limit and the significance of the resulting fast-slow decomposition, and apply this method to the (unregularized, $\alpha = 0$) Boussinesq equations. The rigorous mathematical formulation explicated in this section further illustrates why taking a fast singular limit is a particularly useful approach towards resolving the numerical instability associated with the LANS-α model.

2.1 Rotating, stably-stratified Boussinesq equations

To make the general framework for taking a fast singular limit established by [5] less abstract, we first write out the system it was originally designed to analyze. Note, however, that there are relatively relaxed requirements for applying this methodology such that it may be readily applied to other systems. The rotating, stably-stratified Boussinesq equations are given by

$$\frac{D^H \boldsymbol{v}_H}{Dt} + w\frac{\partial \boldsymbol{v}_H}{\partial z} + f\boldsymbol{v}_H^{\perp} + \frac{1}{\rho_0}\nabla_H p = \nu\Delta_H \boldsymbol{v}_H \tag{1}$$

$$\frac{D^H w}{Dt} + w\frac{\partial w}{\partial z} + \frac{1}{\rho_0}\frac{\partial p}{\partial z} + \frac{g}{\rho_0}\rho = \kappa\Delta_H \rho \tag{2}$$

$$\frac{D\rho}{Dt} = -w\frac{\partial \overline{\rho}}{\partial z} \tag{3}$$

$$\nabla_H \cdot \boldsymbol{v}_H + \frac{\partial w}{\partial z} = 0. \tag{4}$$

Here, the velocity field $\boldsymbol{v}$ is written in terms of its horizontal components and vertical component, $\boldsymbol{v} = (\boldsymbol{v}_H, w)$. The density ρ_{total} is decomposed into $\rho_{total} = \overline{\rho} + \rho$, where the mean $\overline{\rho} = \rho_0 - bz$ and $b > 0$ for stable stratification. The conservation of momentum has been split into an equation for the horizontal, Eq. (1), and the vertical, Eq. (2). In the momentum equations, ν and κ are constants. Conservation of mass is given by Eq. (3) and incompressibility by Eq. (4). The notation $\frac{D}{Dt}$ indicates the total derivative, $\frac{\partial}{\partial t} + \boldsymbol{v}\cdot\nabla$. The horizontal version $\frac{D^H}{Dt} \doteq \frac{\partial}{\partial t} + \boldsymbol{v}_H \cdot \nabla_H$, where ∇_H denotes the horizontal gradient. Similarly, $\nabla_H \cdot$ denotes the horizontal divergence. The symbol $\perp$ denotes $\boldsymbol{v}_H^{\perp} = (-v_2, v_1)$.

Now we non-dimensionalize Eqs. (1) to (4). Consider a characteristic velocity scale U, a characteristic length scale L, and a characteristic time scale $T = L/U$. We replace $\boldsymbol{x}$ with $\boldsymbol{x}/L$, t with t/T, and $\boldsymbol{v}$ by $\boldsymbol{v}/U$. We non-dimensionalize ρ using the buoyancy fluctuation scale bU/N, where $N = (gb/\rho_0)^{1/2}$ is the Brunt-Vaisala frequency. We replace p with $p/\overline{p}$. We now introduce the Rossby, Froude, Reynolds, Prandtl, and Euler numbers:

$$\mathrm{Ro} \doteq \frac{U}{fL}, \quad \mathrm{Fr} \doteq \frac{U}{NL}, \quad \mathrm{Re} \doteq \frac{UL}{\nu}, \quad \mathrm{Pr} \doteq \frac{\nu}{\kappa}, \text{ and } \mathrm{Eu} \doteq \frac{\overline{p}}{\rho_0 U^2}.$$

We then obtain the non-dimensional equations

$$\frac{D^H \boldsymbol{v}_H}{Dt} + w\frac{\partial \boldsymbol{v}_H}{\partial z} + \frac{1}{\mathrm{Ro}}\boldsymbol{v}_H^{\perp} + \mathrm{Eu}\nabla_H p = \frac{1}{\mathrm{Re}}\nabla_H \boldsymbol{v}_H \tag{5}$$

$$\frac{D^H w}{Dt} + w\frac{\partial w}{\partial z} + \mathrm{Eu}\frac{\partial p}{\partial z} + \Gamma\rho = \frac{1}{\mathrm{Re}}\frac{\partial w}{\partial z} \tag{6}$$

$$\frac{D\rho}{Dt} = -\frac{1}{\Gamma \mathrm{Fr}^2}w + \frac{1}{\mathrm{RePr}}\Delta\rho \tag{7}$$

$$\nabla_H \cdot \boldsymbol{v}_H + \frac{\partial w}{\partial z} = 0. \tag{8}$$

Here, $\Gamma \doteq \frac{bgL}{U^2}$. Note that we can solve for the pressure by taking the divergence, to find

$$\mathrm{Eu}\nabla p = \nabla\Delta^{-1}\left(\frac{1}{\mathrm{Ro}}(\hat{z}\times\boldsymbol{v}) - \nabla\cdot(\boldsymbol{v}\cdot\nabla\boldsymbol{v}) - \frac{1}{\mathrm{Fr}}\frac{\partial\rho}{\partial z}\right).$$

Substituting this back into Eqs. (5) to (8), we obtain

$$\frac{D^H \boldsymbol{v}_H}{Dt} + w\frac{\partial \boldsymbol{v}_H}{\partial z} + \frac{1}{\mathrm{Ro}}\boldsymbol{v}_H^{\perp} + \nabla_H\Delta^{-1}\left(\frac{1}{\mathrm{Ro}}\hat{z}\cdot(\nabla\times\boldsymbol{v}) - \nabla\cdot(\boldsymbol{v}\cdot\nabla\boldsymbol{v}) - \frac{1}{\mathrm{Fr}}\frac{\partial\rho}{\partial z}\right) \tag{9}$$

$$= \frac{1}{\mathrm{Re}}\nabla_H \boldsymbol{v}_H \tag{10}$$

$$\frac{D^H w}{Dt} + w\frac{\partial w}{\partial z} + \frac{\partial}{\partial z}\Delta^{-1}\left(\frac{1}{\mathrm{Ro}}\hat{z}\cdot(\nabla\times\boldsymbol{v}) - \nabla\cdot(\boldsymbol{v}\cdot\nabla\boldsymbol{v}) - \frac{1}{\mathrm{Fr}}\frac{\partial\rho}{\partial z}\right) + \Gamma\rho = \frac{1}{\mathrm{Re}}\frac{\partial w}{\partial z} \tag{11}$$

$$\frac{D\rho}{Dt} = -\frac{1}{\Gamma \mathrm{Fr}^2}w + \frac{1}{\mathrm{RePr}}\Delta\rho \tag{12}$$

$$\nabla_H \cdot \boldsymbol{v}_H + \frac{\partial w}{\partial z} = 0. \tag{13}$$

There are three distinguished limits of interest: low Rossby and finite Froude (rapid rotation but $O(1)$ stratification), low Froude and finite Rossby (strong stratification but $O(1)$ rotation), and simultaneously low Rossby and low Froude (quasi-geostrophy). In particular, when taking the quasi-geostrophic (QG) limit, one assigns $\epsilon \doteq \mathrm{Ro}$ where $\epsilon \ll 1$, so that rotation has a strong influence on the flow. One also uses geostrophic balance, which can be found from the leading order equations, so that $\mathrm{Eu} = \frac{1}{\mathrm{Ro}}$. One then assumes that $\mathrm{Fr} = \mathrm{BuRo}$ where Bu is the Burger number and is constant, so that the Froude number is small and proportional to the Rossby number. The scaling $\Gamma = \frac{1}{\mathrm{Fr}}$ is used so the buoyancy force is balanced in Eq. (6) and density changes due to buoyant convection in Eq. (7).

2.2 General mathematical framework

Before writing the equations for the three distinguished limits, we introduce the abstract operator form of the equations. This format is used to formally define the method for taking fast singular limits. We use $\boldsymbol{w}$ to denote the concatenation $\boldsymbol{w} = (\boldsymbol{v}, \rho)$. We can now express the problem in the abstract form

$$\frac{\partial \boldsymbol{w}}{\partial t} + \frac{1}{\epsilon}\mathcal{L}_F\boldsymbol{w} + \mathcal{L}_S\boldsymbol{w} + \mathcal{B}(\boldsymbol{w},\boldsymbol{w}) - \mathcal{D}\boldsymbol{w} = 0, \tag{14}$$

with $\boldsymbol{w}|_{t=0} = \boldsymbol{w}_0(\boldsymbol{x})$. Here, ϵ is the small parameter of interest, $\mathcal{L}_F$ is a fast operator, $\mathcal{L}_S$ is a slow operator, $\mathcal{B}$ is a bilinear form, and $\mathcal{D}$ is an operator associated with viscosity. In the above equation, 0 is really the zero vector, but we will denote it without boldface throughout since its dimension is clear from context. The small parameter $\epsilon \ll 1$ corresponds to a constant specific to the problem (e.g., the Rossby number), so Eq. (14) corresponds to the non-dimensionalized version of the equations of interest, e.g. Eqs. (5) to (8). Under various mathematical conditions described in [5], which the Boussinesq equations satisfy, Eq. (14) is well-posed. The solution to Eq. (14), which is based on the method of multiple scales, will be denoted $\boldsymbol{w}^\epsilon$ and depends on both the fast time scale $\tau = t/\epsilon$ and the slow time scale t. In particular, the solution can be expanded as

$$\boldsymbol{w}^\epsilon(\boldsymbol{x}, t, \tau) = \boldsymbol{w}^0(\boldsymbol{x}, t, \tau)|_{\tau=t/\epsilon} + \epsilon \boldsymbol{w}^1(\boldsymbol{x}, t, \tau)|_{\tau=t/\epsilon}. \tag{15}$$

For this to be asymptotically valid, the first order term cannot have secular growth, so we require $|\boldsymbol{w}^1(\boldsymbol{x}, t, \tau)| = o(\tau)$ uniformly on the interval of existence of solutions. Substituting the decomposition of the solution Eq. (15) into the abstract operator form Eq. (14), we obtain the $O(\epsilon^{-1})$ equation

$$\frac{\partial \boldsymbol{w}^0}{\partial \tau} + \mathcal{L}_F(\boldsymbol{w}^0) = 0. \tag{16}$$

By separation of variables, Eq. (16) has a solution of the form

$$\boldsymbol{w}^0(\boldsymbol{x}, t, \tau) = e^{-\tau \mathcal{L}_F} \overline{\boldsymbol{w}}(\boldsymbol{x}, t). \tag{17}$$

At next order, we obtain the $O(\epsilon^0)$ equation

$$\frac{\partial \boldsymbol{w}^1}{\partial \tau} + \mathcal{L}_F(\boldsymbol{w}^1) = -\left(\frac{\partial \boldsymbol{w}^0}{\partial \tau} + \mathcal{L}_S(\boldsymbol{w}^0) + \mathcal{B}(\boldsymbol{w}^0, \boldsymbol{w}^0) - \mathcal{D}(\boldsymbol{w}^0) \right). \tag{18}$$

Using Duhamel's principle and Eq. (17), we see that Eq. (18) has a solution of the form

$$\begin{aligned} e^{\tau \mathcal{L}_F} \boldsymbol{w}^1 = \boldsymbol{w}^1(\boldsymbol{x}, t, \tau)|_{\tau=0} - \tau \frac{\partial \overline{\boldsymbol{w}}}{\partial t}(\boldsymbol{x}, t) \\ - \int_0^\tau e^{s\mathcal{L}_F} (\mathcal{L}_S(e^{-s\mathcal{L}_F} \overline{\boldsymbol{w}}) + \mathcal{B}(e^{-s\mathcal{L}_F} \overline{\boldsymbol{w}}, e^{-s\mathcal{L}_F} \overline{\boldsymbol{w}}) - \mathcal{D}(e^{-s\mathcal{L}_F} \overline{\boldsymbol{w}})) ds. \end{aligned} \tag{19}$$

An easy condition to satisfy the sublinear growth condition is then for this integral to be zero, i.e. for

$$\begin{aligned} \frac{\partial \overline{\boldsymbol{w}}}{\partial t}(\boldsymbol{x}, t) &= -\lim_{\tau \to \infty} \frac{1}{\tau} \int_0^\tau e^{s\mathcal{L}_F} (\mathcal{L}_S(e^{-s\mathcal{L}_F} \overline{\boldsymbol{w}}) + \mathcal{B}(e^{-s\mathcal{L}_F} \overline{\boldsymbol{w}}, e^{-s\mathcal{L}_F} \overline{\boldsymbol{w}}) - \mathcal{D}(e^{-s\mathcal{L}_F} \overline{\boldsymbol{w}})) ds \\ \overline{\boldsymbol{w}}(\boldsymbol{x}, 0) &= \boldsymbol{w}_0(\boldsymbol{x}). \end{aligned} \tag{20}$$

The fact that Eq. (20) is satisfied is what is due to [26]. Then due to the identification Eq. (17), the principal term $\overline{w}(\boldsymbol{x}, t)$ has no fast oscillations.

Overall, to order ϵ,

$$\boldsymbol{w}^\epsilon(\boldsymbol{x}, t) = e^{-\frac{t}{\epsilon} \mathcal{L}_F} \overline{\boldsymbol{w}}(\boldsymbol{x}, t) + o(1), \tag{21}$$

valid as $\epsilon \to 0$. While $\overline{\boldsymbol{w}}$ has no oscillations, $e^{-\frac{t}{\epsilon} \mathcal{L}_F} \overline{\boldsymbol{w}}(\boldsymbol{x}, t)$ does. This motivates the fast-slow decomposition. Since $\mathcal{L}_F$ is required to be skew-Hermitian, by the Spectral Theorem,

we can decompose $\overline{\boldsymbol{w}}$ into a portion in the null space of $\mathcal{L}_F$ and a portion not in the null space of $\mathcal{L}_F$. Recall that $\mathcal{L}_F$ is interpreted as the operator yielding the fast dynamics – indeed, it is multiplied by $1/\epsilon$ in Eq. (14). Then this decomposition into one piece in Kernel $\mathcal{L}_F$ and one piece in Range $\mathcal{L}_F$ can be interpreted as

$$\overline{\boldsymbol{w}}(\boldsymbol{x},t) = \overline{\boldsymbol{w}}_F(\boldsymbol{x},t) + \overline{\boldsymbol{w}}_S(\boldsymbol{x},t), \tag{22}$$

where $\overline{\boldsymbol{w}}_F \in$ Range $\mathcal{L}_F$ is the fast portion and $\overline{\boldsymbol{w}}_S \in$ Kernel $\mathcal{L}_F$ is the slow portion. Substituting Eq. (22) into Eq. (21),

$$\boldsymbol{w}^\epsilon(\boldsymbol{x},t) = e^{-\frac{t}{\epsilon}\mathcal{L}_F}\overline{\boldsymbol{w}}_F(\boldsymbol{x},t) + \overline{\boldsymbol{w}}_S(\boldsymbol{x},t) + o(1). \tag{23}$$

Then $\overline{\boldsymbol{w}}_S$ has no fast oscillations. Now we can find equations whose solutions are $\overline{\boldsymbol{w}}_F$ and $\overline{\boldsymbol{w}}_S$, respectively. We can find an equation for the slow operator by projecting Eq. (14) onto the null space of the fast operator. However, we can actually simplify this by projecting only the $O(\epsilon^0)$ version of Eq. (14), which we have found so far to be

$$\frac{\partial \boldsymbol{w}^0}{\partial t} + \mathcal{L}_F(\boldsymbol{w}^1) + \mathcal{L}_S(\boldsymbol{w}^0) + \mathcal{B}(\boldsymbol{w}^0,\boldsymbol{w}^0) - \mathcal{D}(\boldsymbol{w}^0) = 0. \tag{24}$$

onto the null space of the fast operator. Letting P denote such a projection operator, then $\boldsymbol{w}_S$ may be alternatively represented as the solution to (i.e. it is identified with $\boldsymbol{w}^0$ in the following)

$$\frac{\partial \boldsymbol{w}^0}{\partial t} + P(\mathcal{L}_S(\boldsymbol{w}^0) + \mathcal{B}(\boldsymbol{w}^0,\boldsymbol{w}^0) - \mathcal{D}(\boldsymbol{w}^0)) = 0. \tag{25}$$

We will see that such a projection can be more readily found by using a Fourier transform in Section 3.

An equation for $\boldsymbol{w}_F$ can of course be found by projecting onto the range of $\mathcal{L}_F$; equivalently, by characterizing the orthogonal subspace to Kernel $\mathcal{L}_F$; or, equivalently, by subtracting the projection from the original. However, we will obtain a more useful interpretation if we keep in mind that for the fast dynamics, we are interested in wave effects. While the fast-slow decomposition is not necessarily into waves and mean-flow, the fast dynamics do involve waves. To that end, the method proposed by Embid and Majda is to expand $\overline{\boldsymbol{w}}$ in Eq. (20) in terms of the eigenfunctions of the fast operator $\mathcal{L}_F$. This method makes use of the theory of cancellation of oscillations due to [26]. The only terms that will then survive in the limit in Eq. (20) represent three-wave resonant interactions with frequency given by the eigenvalues of the fast operator. The central task for analyzing the fast dynamics is then finding the eigenvalues and eigenfunctions of the fast operator, and subsequently analyzing which three-wave resonance interactions can occur, and of those, which will appear in the equation for the fast dynamics and thus affect $\boldsymbol{w}_F$.

To see this explicitly, let $\boldsymbol{w}_{\boldsymbol{k}}^{(\beta)}(\boldsymbol{x}) = e^{i\boldsymbol{k}\cdot\boldsymbol{x}}\boldsymbol{r}_k^{(\beta)}$ denote an element of an orthonormal basis of periodic eigenfunctions for the fast operator $\mathcal{L}_F$, as in [30]. Here, $\boldsymbol{k} = (k,l,m)$ is the wavenumber (vector), β is a label which will be associate with the different modes that arise, and $\boldsymbol{r}_{\boldsymbol{k}}^{(\beta)} = (\boldsymbol{v}_{\boldsymbol{k}}^{(\beta)}, \rho_{\boldsymbol{k}}^{(\beta)})$. Denote the associated purely imaginary eigenvalues as $\lambda_{\boldsymbol{k}}^{(\beta)} = i\omega_{\boldsymbol{k}}^{(\beta)}$. Then we can rewrite $\overline{\boldsymbol{w}}$ in terms of these eigenfunctions,

$$\overline{\boldsymbol{w}}(\boldsymbol{x},t) = \sum_{\boldsymbol{k}}\sum_{\beta}\sigma_{\boldsymbol{k}}^{(\beta)}(t)e^{i\boldsymbol{k}\cdot\boldsymbol{x}}\boldsymbol{r}_{\boldsymbol{k}}^{(\beta)}. \tag{26}$$

Now, since

$$e^{-s\mathcal{L}_F}(e^{i\boldsymbol{x}\cdot\boldsymbol{k}}\cdot\boldsymbol{r}_{\boldsymbol{k}}^{(\beta)}) = e^{-is\omega_{\boldsymbol{k}}^{(\beta)}}e^{i\boldsymbol{k}\cdot\boldsymbol{x}}\boldsymbol{r}_{\boldsymbol{k}}^{(\beta)} = e^{i(\boldsymbol{k}\cdot\boldsymbol{x}-s\omega_{\boldsymbol{k}}^{(\beta)})}\boldsymbol{r}_{\boldsymbol{k}}^{(\beta)}, \tag{27}$$

upon writing the bilinear form in terms of the eigenfunctions, we will obtain in the integral in Eq. (20) terms of the form $e^{i(\boldsymbol{k}\cdot\boldsymbol{x}-(\omega_{\boldsymbol{k}'}^{(\beta')}+\omega_{\boldsymbol{k}''}^{(\beta'')}-\omega_{\boldsymbol{k}'+\boldsymbol{k}''}^{(\beta)})s)}$. A limit of the form $\lim_{\tau\to\infty}\frac{1}{\tau}\int_0^\tau e^{i\omega s}ds$ is one whenever $\omega = 0$ and zero otherwise, so only modes associated with wavenumbers such that $\omega_{\boldsymbol{k}'}^{(\beta')}+\omega_{\boldsymbol{k}''}^{(\beta'')}-\omega_{\boldsymbol{k}'+\boldsymbol{k}''}^{(\beta)}=0$ can possibly contribute to the dynamics. To make this concrete, denote the set of constituent wavenumbers and mode labels that result in a resonant interaction for a particular mode label β and wavenumber $\boldsymbol{k}$ as

$$R_{\beta,\boldsymbol{k}} \doteq \{(\boldsymbol{k}',\boldsymbol{k}'',\beta',\beta'') \,|\, \boldsymbol{k}'+\boldsymbol{k}''=\boldsymbol{k}, \quad \omega_{\boldsymbol{k}'}^{(\beta')}+\omega_{\boldsymbol{k}''}^{(\beta'')}=\omega_{\boldsymbol{k}}^{(\beta)}\} \tag{28}$$

(R for "resonant"). After substituting the representation Eq. (27) into the bilinear form, one finds its contributions are

$$\begin{aligned}\lim_{\tau\to\infty}\int_0^\tau e^{s\mathcal{L}_F}\mathcal{B}(e^{-s\mathcal{L}_F}\overline{\boldsymbol{w}}(\mathbf{x},t), e^{-s\mathcal{L}_F}\overline{\boldsymbol{w}}(\mathbf{x},t)) = \\ \sum_{\boldsymbol{k}\in\mathbb{Z}^3}\sum_{\beta}\left(\sum_{R_{\beta,\boldsymbol{k}}} B_{(\boldsymbol{k}',\boldsymbol{k}'',\boldsymbol{k})}^{(\beta',\beta'',\beta)}\sigma_{\boldsymbol{k}'}^{(\beta')}(t)\sigma_{\boldsymbol{k}''}^{(\beta'')}(t)\right)e^{i\boldsymbol{k}\cdot\boldsymbol{x}}\boldsymbol{r}_{\boldsymbol{k}}^{(\beta)},\end{aligned} \tag{29}$$

where the $B_{(\boldsymbol{k}',\boldsymbol{k}'',\boldsymbol{k})}^{(\beta',\beta'',\beta)}$ are interaction coefficients which can be computed based on the eigenvectors (c.f. [7], p.18). Similar formulas with other coefficients can be found for the contributions from $\mathcal{L}_S$ and $\mathcal{D}$. Thus, for there to be any dynamical contribution associated with a particular set of wavenumbers, there must be a triad interaction (determined by the eigenvalues), and at least one of the coefficients associated with the operators $\mathcal{B}$, $\mathcal{L}_S$, and $\mathcal{D}$ (determined by the eigenvectors and the matrix form of those operators) must be nonzero.

One can explicitly calculate the Fourier amplitudes $\sigma_{\boldsymbol{k}}^{(\beta)}$ as in Wingate et al. (2011) and thus actually calculate $\boldsymbol{w}_F(\boldsymbol{x},t)$ (for a finite range of possible $\boldsymbol{k}$) [30]. However, this is generally not computationally feasible; for instance, in Embid and Majda (1998), over 200 resonant interactions of a single type (as in, combinations of the possible labels β) were found for just $|k|,|m|,|l|\leq 30$, in the (simpler than QG) low Froude, finite Rossby case [7]. In any case, it is more interesting to analyze which types of wave interactions are present in the fast dynamics, in order to understand which wave interactions can and cannot affect the overall dynamics.

2.3 Summary of requirements and method

The requirements for applying this method of finding a fast singular limit can then be summarized:

1. There is a small parameter ϵ occurring in the non-dimensionalized version of the system of interest, such that the system may be written in the abstract operator form Eq. (14).

2. The fast operator $\mathcal{L}_F$ is skew-Hermitian.

3. While a timescale separation is assumed, no additional separation of spatial scales is assumed; in this case, it is not *guaranteed* that this method can be used to obtain a true fast-slow decomposition, as the theory of cancellation of oscillations may not apply [27]. While one can still get the slow equations in the same fashion, it is not necessarily the case that the leading order slow solution is truly "slow."

If the requirements are satisfied, the application of the method can be summarized:

1. An explicit formula for a projection operator onto the null space of the fast operator must be found.

2. The eigenvalues and eigenvectors of the fast operator must be found, and which resonant triads with frequency given by those eigenvalues can occur must be determined.

We then have a convenient representation of the slow dynamics, given by Eq. (25), while the fast dynamics can best be (mathematically) analyzed by considering which resonant triad interactions can occur according to the eigenfrequencies.

2.4 Fast singular limits of the rotating, stably-stratified Boussinesq equations

Now we return to the concrete system, Eqs. (5) to (8), see what the abstract operator form is, and discuss the slow/reduced equations and the analysis of the fast dynamics found in [7]. We start by writing Eqs. (10) to (13) in the abstract operator form Eq. (14). Clearly this depends on what ϵ is, which depends on the dynamical regime of interest. Following [29], we can first write the system in the form

$$\frac{\partial \boldsymbol{w}}{\partial t} + \frac{1}{\mathrm{Ro}}\mathcal{L}_{\mathrm{Ro}}\boldsymbol{w} + \frac{1}{\mathrm{Fr}}\mathcal{L}_{\mathrm{Fr}}\boldsymbol{w} + \mathcal{B}(\boldsymbol{w},\boldsymbol{w}) - \mathcal{D}\boldsymbol{w} = 0, \tag{30}$$

where

$$\begin{aligned}
\mathcal{L}_{\mathrm{Ro}}\boldsymbol{w} &\doteq \begin{pmatrix} \boldsymbol{v}_H^{\perp} + \nabla_H \Delta^{-1}(\hat{z}\cdot(\nabla\times\boldsymbol{v})) \\ \frac{\partial}{\partial z}\Delta^{-1}(\hat{z}\cdot(\nabla\times\boldsymbol{v})) \\ 0 \end{pmatrix}, \\
\mathcal{L}_{\mathrm{Fr}}\boldsymbol{w} &\doteq \begin{pmatrix} -\nabla_H\Delta^{-1}\left(\frac{\partial\rho}{\partial z}\right) \\ -\Delta^{-1}\frac{\partial^2\rho}{\partial z^2} + \rho \\ -w \end{pmatrix}, \\
\mathcal{B}(\boldsymbol{w},\boldsymbol{w}) &\doteq \begin{pmatrix} \boldsymbol{v}\cdot\nabla\boldsymbol{v} - \nabla\Delta^{-1}(\nabla\cdot(\boldsymbol{v}\cdot\nabla\boldsymbol{v}) \\ \boldsymbol{v}\cdot\nabla\rho \end{pmatrix}, \\
\mathcal{D}\boldsymbol{w} &\doteq \frac{1}{\mathrm{Re}}\begin{pmatrix} \Delta\boldsymbol{v} \\ \frac{1}{\mathrm{Pr}}\Delta\rho \end{pmatrix}.
\end{aligned} \tag{31}$$

Then, based on which of the three limiting cases we consider, we can decide which of the two linear operators is fast or slow. In the low Rossby, finite Froude regime, we decide $\mathrm{Ro} = \epsilon$, Fr, Pr, Re $= O(1)$ as $\epsilon \to 0$, and $\mathcal{L}_{\mathrm{Ro}}$ is identified as $\mathcal{L}_F$ while $\mathcal{L}_{\mathrm{Fr}}$ is identified as $\mathcal{L}_S$. For low Froude, finite Rossby scaling, we make the opposite identification. For the

simultaneously low Froude and Rossby (QG) limit, we have no slow operator and the sum of the two linear operators is identified as the fast operator. More specifically, we assign $\mathrm{Fr} = \epsilon$, and assume that the Rossby and Froude numbers scale in a constant ratio, the Burger number $\mathrm{Bu} = \mathrm{Fr}/\mathrm{Ro}$. It was known prior to this work that the slow solution (which has been referred to as the quasigeostrophic equation) satisfies conservation of potential vorticity. In this situation, we notice that even if there is no slow operator in the equation, the projection onto the slow subspace still applies and will yield the slow equation. This further motivates why we have been considering this projection to be onto the null space of the fast operator rather than the range of the slow operator. Additionally, using the projection provides another, perhaps more mathematical, route to deriving conservation of potential vorticity. Moreover, it also allows us to see the "fast portion" associated with QG scaling, which cannot be readily obtained through the classical derivation of QG.

To obtain the slow equations, we compute the projection in each case. These are written explicitly in [29], and the full details of how to compute the projection in the QG case is provided in the Appendix, Section 6.1. For concreteness, the projection in this case is given by

$$P_{\mathrm{QG}}\boldsymbol{w} = \begin{pmatrix} \boldsymbol{v}_H - \mathrm{Bu}^2\Delta_{\mathrm{QG}}^{-1}\frac{\partial^2 \boldsymbol{v}_H}{\partial z^2} - \Delta_{\mathrm{QG}}^{-1}\left(\nabla_H(\nabla_H\cdot\boldsymbol{v}_H) + \mathrm{Bu}\nabla_H^{\perp}\left(\frac{\partial\rho}{\partial z}\right)\right) \\ 0 \\ \rho - \mathrm{Bu}\Delta_{\mathrm{QG}}^{-1}\left(\frac{\partial}{\partial z}(\nabla_H\times\boldsymbol{v}_H)\right) - \Delta_{\mathrm{QG}}^{-1}\Delta_H\rho \end{pmatrix}, \tag{32}$$

where $\Delta_{\mathrm{QG}} = \Delta_H + \mathrm{Bu}^2\frac{\partial^2}{\partial z^2}$ and $\nabla_H^{\perp} = \left(-\frac{\partial}{\partial x_2}, \frac{\partial}{\partial x_1}\right)$. By substituting in $B(\boldsymbol{w},\boldsymbol{w}) - \mathcal{D}(\boldsymbol{w})$ in for the placeholder $\boldsymbol{w}$ in Eq. (32), the slow equations can be found as in [29], which can then be seen to reduce to conservation of potential vorticity (PV) (in the case of no diffusion). After some (involved) algebra (shown in the Appendix, Section 6.4), we indeed obtain

$$\frac{D}{Dt}\left(\omega_3 - \mathrm{Bu}\,\frac{\partial\rho}{\partial z}\right) = 0. \tag{33}$$

Here, ω_3 denotes the vertical component of the vorticity. In terms of the streamfunction ψ, $\omega_3 = \Delta_H\psi$. Equation (33) can be equivalently expressed in terms of the potential ϕ (which is the pressure), so that $q = \Delta_H\phi + \mathrm{Bu}^2\frac{\partial^2\phi}{\partial z^2}$ and q (the potential vorticity) is materially conserved. Thus, the projection method does yield the usual slow dynamics equation.

For completeness and to contrast with the $\alpha \neq 0$ versions of these limits, we write the limiting slow dynamics for the other two limits, as in [29]. We will again neglect the diffusion terms for simplicity. For low Rossby number and finite Froude number,

$$\begin{aligned} \frac{D^H}{Dt}\boldsymbol{v}_H + \nabla_H\Delta_H^{-1}(\nabla_H\cdot(\boldsymbol{v}_H\cdot\nabla_H\boldsymbol{v}_H)) &= 0 \\ \frac{D^H}{Dt}w + \frac{1}{\mathrm{Fr}}\langle\rho\rangle_z &= 0 \\ \frac{D}{Dt}\rho - \frac{1}{\mathrm{Fr}}w &= 0, \end{aligned} \tag{34}$$

where $\langle\cdot\rangle_z$ indicates a vertical average. Note that the vertical average comes from a different approach of finding the projection operator than the Fourier transform method used to obtain Eq. (32), since the form of the projection is not unique. It should be noted that

the Fourier transform method may not provide the most informative formulation of the projection in all cases, e.g. when the equation to find the vector spanning the nullspace is either algebraically intractable or only gives a trivial result.

For low Froude number and finite Rossby number,

$$\begin{aligned} \frac{D^H}{Dt}\boldsymbol{v}_H + \frac{1}{\mathrm{Ro}}(\hat{z}\times\boldsymbol{v}_H) + \nabla_H\Delta_H^{-1}\left(\frac{1}{\mathrm{Ro}}\omega - \nabla_H\cdot(\boldsymbol{v}_H\cdot\nabla_H\boldsymbol{v}_H)\right) &= 0 \\ \nabla_H\cdot\boldsymbol{v}_H &= 0 \\ \frac{\partial}{\partial t}\rho &= 0. \end{aligned} \tag{35}$$

The form of the projection in this limit is due to the fact the null space of the fast operator is characterized by $\nabla\cdot\boldsymbol{v}_H = 0$, $w = 0$, and $\rho = \rho(z)$ [7].

Now we summarize the limiting fast dynamics for each case. Let $|\cdot|$ denote the Euclidean norm. The subscript H denotes that only the first two components of the wavenumber are being considered, $\boldsymbol{k}_H \doteq (k,l)$. Throughout this section we will focus on the general case and assume that $|\boldsymbol{k}|, |\boldsymbol{k}_H| \neq 0$, though eigenvalues and eigenvectors can still be computed when this is not the case.

For the low Rossby, finite Froude limit,

$$\omega_{\boldsymbol{k}}^{(-1)} = -\frac{|m|}{|\boldsymbol{k}|}, \quad \omega_{\boldsymbol{k}}^{(0)} = 0 \text{ (double)}, \quad \omega_{\boldsymbol{k}}^{(1)} = \frac{|m|}{|\boldsymbol{k}|}. \tag{36}$$

Here, the eigenfrequencies without the absolute value also work, but then a desirable symmetry condition $\overline{\boldsymbol{r}_{\boldsymbol{k}}^{(1)}} = \boldsymbol{r}_{-\boldsymbol{k}}^{(-1)}$ that is used if one wants to actually compute $\boldsymbol{\sigma}_{\boldsymbol{k}}^{(\beta)}$ in Eq. (26) does not hold for the corresponding eigenvectors.

For the low Froude, finite Rossby case, the eigenfrequencies associated to a wavenumber $\boldsymbol{k}$ can be computed as

$$\omega_{\boldsymbol{k}}^{(-1)} = -\frac{|\boldsymbol{k}_H|}{|\boldsymbol{k}|}, \quad \omega_{\boldsymbol{k}}^{(0)} = 0 \text{ (double)}, \quad \omega_{\boldsymbol{k}}^{(1)} = \frac{|\boldsymbol{k}_H|}{|\boldsymbol{k}|}. \tag{37}$$

Lastly, for the QG case, the eigenfrequencies are

$$\omega_{\boldsymbol{k}}^{(-1)} = -\frac{(|\boldsymbol{k}_H|^2 + \mathrm{Bu}^2 m^2)^{1/2}}{|\boldsymbol{k}|}, \quad \omega_{\boldsymbol{k}}^{(0)} = 0 \text{ (double)}, \quad \omega_{\boldsymbol{k}}^{(1)} = \frac{(|\boldsymbol{k}_H|^2 + \mathrm{Bu}^2 m^2)^{1/2}}{|\boldsymbol{k}|}. \tag{38}$$

For each of the limits, we notice that there is a zero eigenfrequency with multiplicity two and two nonzero eigenfrequencies that are the same except for sign. The interpretation is that the zero eigenfrequencies correspond to a slow vortical mode, while the other two correspond to fast gravity waves (or inertial modes) [7].

Interestingly, we can observe that if one assembles the eigenfrequencies of the simpler cases into a vector $(\omega_{\boldsymbol{k}}^{\mathrm{Ro}}, \mathrm{Bu}\ \omega_{\boldsymbol{k}}^{\mathrm{Fr}})$, then (for each label, $\{-1,0,1\}$),

$$\omega_{\boldsymbol{k}}^{\mathrm{QG}} = |(\omega_{\boldsymbol{k}}^{\mathrm{Ro}}, \mathrm{Bu}\ \omega_{\boldsymbol{k}}^{\mathrm{Fr}})|.$$

This identification reflects the intuition that each of the simple limits is along each of two orthogonal axes, with the combined limit representing the hypotenuse connecting points

along them. Physically, the slow manifold can have waves generated by the slow operator. In the case of QG, there is no slow operator, so all of these waves are associated with the fast operator. Of the three limits considered here, only in the QG limit is the fast-slow decomposition truly a wave-mean flow decomposition.

3 Three Fast Singular Limits for the LANS-α Model

Before deriving the same three fast singular limits for the LANS-α model and comparing to the $\alpha = 0$ case, we introduce the governing equations in detail. The LANS$-\alpha$ equations are given by [15]:

$$\begin{aligned} \frac{\partial \boldsymbol{v}}{\partial t} + \boldsymbol{u}\cdot\nabla\boldsymbol{v} + \boldsymbol{v}\cdot\nabla\boldsymbol{u}^T + f\hat{\boldsymbol{z}}\times\boldsymbol{u} + \nabla\phi + \frac{\rho}{\rho_0}g\hat{\boldsymbol{z}} &= \nu\Delta\boldsymbol{v} \\ \frac{\partial \rho}{\partial t} + \boldsymbol{u}\cdot\nabla\rho - \boldsymbol{u}\cdot b\hat{\boldsymbol{z}} &= \kappa\Delta\rho \\ \nabla\cdot\boldsymbol{u} &= 0 \\ \boldsymbol{v} &= \boldsymbol{u} - \alpha^2\Delta\boldsymbol{u}, \end{aligned} \tag{39}$$

where ϕ is the modified pressure,

$$\phi = \frac{p}{\rho_0} - \frac{1}{2}|\boldsymbol{u}|^2 - \frac{\alpha^2}{2}|\nabla\boldsymbol{u}|^2,$$

and $\alpha \in \mathbb{R}$ is a parameter with units of length whose meaning will soon be elucidated. We do not split into horizontal and vertical equations in order to draw attention to the presence of the term $\boldsymbol{v}\cdot\nabla\boldsymbol{u}^T$, which is also written as $(\nabla\boldsymbol{u}^T)\cdot\boldsymbol{v}$ or $v_j\nabla u_j$. In the x-momentum equation, this term then contributes $v_1\partial_x u_1 + v_2\partial_x u_2 + v_3\partial_x u_3$, in the $y-$momentum equation, $v_1\partial_y u_1 + v_2\partial_y u_2 + v_3\partial_y u_3$, and in the z-momentum equation, $v_1\partial_z u_1 + v_2\partial_z u_2 + v_3\partial_z u_3$. Besides this and of course the presence of both $\boldsymbol{u}$ and $\boldsymbol{v}$, the main difference from Eqs. (1) to (3) is the modification to the pressure.

We will denote

$$\boldsymbol{v} = \mathcal{S}\boldsymbol{u}, \quad \mathcal{S} \doteq (1 - \alpha^2\Delta). \tag{40}$$

This operator $\mathcal{S}$ is the Helmholtz operator or filter, and is denoted with an $\mathcal{S}$ because of the interpretation of "smoothing" (in particular, its inverse is "smoothing"). Then $\boldsymbol{u} = \mathcal{S}^{-1}\boldsymbol{v}$ is the "smoothed" version of $\boldsymbol{v}$. We can immediately see from this that the incompressibility of $\boldsymbol{u}$ implies that of $\boldsymbol{v}$, and vice versa, since the order of the divergence and the Laplacian can be interchanged. Note also that $\mathcal{S}$ can be applied to scalar functions, with the interpretation that Δ is the scalar Laplacian rather than the vector Laplacian (which is just the scalar Laplacian, copied in each component).

The introduction of the smoothing parameter α partially reveals why this is called the LANS-α model, but why is it "Lagrangian-averaged"? From Eq. (40), we can see that if $\boldsymbol{u}$ can be interpreted as the Lagrangian average of $\boldsymbol{v}$, it would then make sense why this is "Lagrangian-averaged" Navier-Stokes. For this to be true, it must be the case that the Helmholtz operator, applied to a Lagrangian-averaged field, yields an Eulerian-averaged field, and vice versa with the inverse. This is true under certain approximations, i.e. $\mathcal{S}$ is an approximation to the true operator for which this (asymptotically) true.

This operator, the dynamical Helmholtz operator, is given by $(1-\tilde{\Delta})$ where $\tilde{\Delta} = \nabla \cdot \langle \boldsymbol{\xi}\boldsymbol{\xi} \rangle \cdot \nabla$ [13]. Here, $\boldsymbol{\xi}$ represents a displacement fluctuation of a particle trajectory $\boldsymbol{X}$, i.e.

$$\boldsymbol{\xi} \doteq \boldsymbol{X}^{\xi} - \langle \boldsymbol{X}^{\xi} \rangle$$

where $\langle \cdot \rangle$ denotes time-averaging over a fixed Lagrangian label. Accordingly, $\langle \boldsymbol{\xi}\boldsymbol{\xi} \rangle$ is the covariance of the displacement fluctuation. It can be seen that to $o(|\boldsymbol{\xi}|^2)$ that

$$(\nabla \cdot \langle \boldsymbol{\xi}\boldsymbol{\xi} \rangle \cdot \nabla) \langle \boldsymbol{U} \rangle^L,$$

where $\langle \boldsymbol{U} \rangle^L$ is a Lagrangian mean velocity, is the Stokes drift. Thus, the dynamical Helmholtz operator $(1-\tilde{\Delta})$ can indeed be interpreted as mapping Lagrangian-averaged fields to their Eulerian-averaged counterparts.

Of course, the LANS-α equations do not feature the dynamical Helmholtz operator; $\tilde{\Delta}$ is replaced with the much simpler $\alpha^2\Delta$. This is possible under the isotropy condition $\langle \xi^k \xi^l \rangle = \alpha^2 \delta^{kl}$, and α can be assumed to be constant so long as the statistics are homogeneous. Thus, by assuming statistically stationary and isotropic turbulence (in a sense), we can indeed interpret this model as Lagrangian-averaged Navier-Stokes and $\mathcal{S}$ to be a Lagrangian filter. This interpretation is in fact mathematically necessary. This is due to the interpretation as a Lagrangian average (which can be mathematically shown, up to $o(|\boldsymbol{\xi}|^2)$), the dynamical Helmholtz operator *commutes* with the advective time derivative $\frac{D}{Dt}$. We will see that this is a key property when deriving the slow dynamics equations. By making the necessary assumptions so that the dynamical Helmholtz operator reduces to the constant α Helmholtz operator $\mathcal{S}$ appearing in the LANS-α equations, we can then justify commuting this operator with the advective operator. We can see mathematically that the Helmholtz operator commutes with space and time derivatives in general, but without the interpretation of Lagrangian averaging, the general Helmholtz operator with constant α *cannot* be shown to commute with the advective operator. While one can imagine formulating a smoothed Navier-Stokes akin to the LANS-α model above by applying a number of different filters, this particular filter, with the given meaning of α, is especially advantageous due to its commutative properties with space and time derivatives *and* advection.

Another peculiarity of the LANS$-\alpha$ model is the presence of the additional nonlinear term $\boldsymbol{v} \cdot \nabla \boldsymbol{u}^T$. As mentioned in the introduction, the LANS-α model can be seen as an extension of the Leray-regularized Navier-Stokes, and this term is one of the differences. This term arises in order to formulate a regularized Navier-Stokes that also possess a Kelvin circulation theorem. For more details, one may see [9]. This is also where the remaining extra terms, which appear in the modified pressure, stem from.

Lastly, we can see that this system reduces to our original un-regularized system in the case of $\alpha = 0$. Clearly, $\boldsymbol{u} \cdot \nabla \boldsymbol{v}$ reduces to $\boldsymbol{v} \cdot \nabla \boldsymbol{v}$. The additional nonlinear term then cancels with the remaining term $\frac{1}{2}|\boldsymbol{v}|^2$ in the modified pressure, after applying the gradient on ϕ. From this, we can expect that the results found in the following sections must reduce to those of the previous sections in the case $\alpha = 0$.

We use the same non-dimensionalization as before. Omitting the primes, we then obtain the non-dimensionalized momentum equation

$$\frac{\partial \boldsymbol{v}}{\partial t} + \mathcal{S}^{-1}\boldsymbol{v} \cdot \nabla \boldsymbol{v} + \frac{1}{\mathrm{Ro}} \hat{z} \times \boldsymbol{v} + \nabla \left(\mathrm{Eu}\ p - \frac{1}{2}|\mathcal{S}^{-1}\boldsymbol{v}|^2 - \frac{L_\alpha^2}{2}|\nabla(\mathcal{S}^{-1}\boldsymbol{v})|^2 \right) + \Gamma \rho \hat{\mathbf{z}} = \frac{1}{\mathrm{Re}} \nabla \boldsymbol{v}. \quad (41)$$

Here, $\mathcal{S}$ is actually the non-dimensionalized $(1 - L_\alpha^2 \Delta)$, where $L_\alpha = \alpha/L$. The constant Γ is as before and we will use the scaling $\Gamma = \mathrm{Fr}^{-1}$. We further simplify Eq. (41) by eliminating the *modified pressure* in exactly the same way as before. After taking the divergence of Eq. (41), rearranging, and taking the gradient, we find

$$\begin{aligned} \nabla \left(\mathrm{Eu}\ \phi - \frac{1}{2} |\mathcal{S}^{-1} \boldsymbol{v}|^2 - \frac{L_\alpha^2}{2} |\nabla (\mathcal{S}^{-1} \boldsymbol{v})|^2 \right) = \\ \nabla \Delta^{-1} \left(\frac{1}{\mathrm{Ro}} \hat{z} \cdot \mathcal{S}^{-1} \boldsymbol{\omega} - \nabla \cdot (\mathcal{S}^{-1} \boldsymbol{v} \cdot \nabla \boldsymbol{v} + \boldsymbol{v} \cdot \nabla (\mathcal{S}^{-1} \boldsymbol{v})^T) - \frac{1}{\mathrm{Fr}} \rho \hat{\mathbf{z}} \right). \end{aligned} \tag{42}$$

The modified pressure then does not make any further impact on the difference between LANS-α and the original system; ϕ is a free variable in exactly the same sense p is. We will use Eq. (42) in Eq. (41) to determine the abstract operator equation for LANS-α.

3.1 Slow dynamics

We again write

$$\frac{\partial \boldsymbol{w}}{\partial t} + \frac{1}{\mathrm{Ro}} \mathcal{L}_{\mathrm{Ro}}^\alpha \boldsymbol{w} + \frac{1}{\mathrm{Fr}} \mathcal{L}_{\mathrm{Fr}}^\alpha \boldsymbol{w} + \mathcal{B}^\alpha (\boldsymbol{w}, \boldsymbol{w}) - \mathcal{D}^\alpha \boldsymbol{w} = 0,$$

where

$$\begin{aligned} \mathcal{L}_{\mathrm{Ro}}^\alpha \boldsymbol{w} &= \begin{pmatrix} \mathcal{S}^{-1} (\boldsymbol{v}_H^\perp + \nabla_H \Delta^{-1} (\hat{z} \cdot (\nabla \times \boldsymbol{v}))) \\ \mathcal{S}^{-1} (\frac{\partial}{\partial z} \Delta^{-1} (\hat{z} \cdot (\nabla \times \boldsymbol{v}))) \\ 0 \end{pmatrix}, \\ \mathcal{L}_{\mathrm{Fr}}^\alpha \boldsymbol{w} &= \begin{pmatrix} -\nabla_H \Delta^{-1} \left(\frac{\partial \rho}{\partial z} \right) \\ -\Delta^{-1} \left(\frac{\partial^2 \rho}{\partial z^2} \right) + \rho \\ -\mathcal{S}^{-1} w \end{pmatrix}, \\ \mathcal{B}^\alpha (\boldsymbol{w}, \boldsymbol{w}) &= \begin{pmatrix} (\mathcal{S}^{-1} \boldsymbol{v} \cdot \nabla) \boldsymbol{v} - \nabla \Delta^{-1} (\nabla \cdot ((\mathcal{S}^{-1} \boldsymbol{v} \cdot \nabla) \boldsymbol{v})) \\ (\mathcal{S}^{-1} \boldsymbol{v} \cdot \nabla) \rho \end{pmatrix}, \\ \mathcal{D}^\alpha \boldsymbol{w} &= \frac{1}{\mathrm{Re}} \begin{pmatrix} \Delta \boldsymbol{v} \\ \frac{1}{\mathrm{Pr}} \Delta \rho \end{pmatrix}. \end{aligned} \tag{43}$$

To write the operators in this form, we made use of the commutative properties of $\mathcal{S}$. Comparing to Eq. (31), we see that $\mathcal{L}_{\mathrm{Ro}}^\alpha = \mathcal{S}^{-1} \mathcal{L}_{\mathrm{Ro}}$, i.e. it is the "smoothed" version. In contrast, only the third component of $\mathcal{L}_{\mathrm{Fr}}$ features $\mathcal{S}^{-1}$, so it is not the case that $\mathcal{S}^{-1}$ is just applied to every term in the slow $\alpha = 0$ equations in order to get the $\alpha \neq 0$ slow equations.

3.1.1 Low Rossby, finite Froude

Because $\mathcal{L}_{\mathrm{Ro}}^\alpha = \mathcal{S}^{-1} \mathcal{L}_{\mathrm{Ro}}$, the projection in the low Rossby, finite Froude case is exactly the same for $\alpha = 0$ and $\alpha \neq 0$ cases. The slow dynamics equation will be slightly different though, since we substitute in $\mathcal{S}^{-1} w$ in the fourth slot rather than just w, and the bilinear

form involves the inverse Helmholtz operator. Neglecting diffusion, the slow equations are

$$\begin{aligned}\frac{D^{H,\alpha}}{Dt}\boldsymbol{v}_H + \nabla_H \Delta_H^{-1}(\nabla_H \cdot ((\mathcal{S}^{-1}\boldsymbol{v}_H)\cdot\nabla_H)\boldsymbol{v}_H)) &= 0\\ \frac{D^{H,\alpha}}{Dt}w + \frac{1}{\mathrm{Fr}}\langle\rho\rangle_z &= 0\\ \frac{D^{\alpha}}{Dt}\rho - \frac{1}{\mathrm{Fr}}\mathcal{S}^{-1}w &= 0,\end{aligned} \tag{44}$$

where $\frac{D^{H,\alpha}}{Dt}$ denotes horizontal advection but with respect to the smoothed velocity.

3.1.2 Low Froude, finite Rossby

Since only w is modified in $\mathcal{L}^{\alpha}_{\mathrm{Fr}}$ from $\mathcal{L}_{\mathrm{Fr}}$, and the equation for the null space in that component still reduces to $w = 0$, the projection also does not change. Since $\mathcal{L}^{\alpha}_{\mathrm{Ro}} = \mathcal{S}^{-1}\mathcal{L}_{\mathrm{Ro}}$ and the operator $\mathcal{S}^{-1}$ can be "factored out" of the bilinear form as well using the commuting property, the slow equations, neglecting diffusion, are nearly the same between the $\alpha = 0$ and $\alpha \neq 0$ cases in the low Froude, finite Rossby cases (but not quite because of the time derivative). The slow equations are

$$\begin{aligned}\frac{D^{H,\alpha}}{Dt}\boldsymbol{v}_H + \frac{1}{\mathrm{Ro}}\mathcal{S}^{-1}(\hat{z}\times\boldsymbol{v}_H) + \nabla_H\Delta_H^{-1}\left(\frac{1}{\mathrm{Ro}}\mathcal{S}^{-1}\omega - \nabla_H\cdot((\mathcal{S}^{-1}\boldsymbol{v}_H)\cdot\nabla_H)\boldsymbol{v}_H)\right) &= 0\\ \nabla_H\cdot\boldsymbol{v}_H &= 0\\ \frac{\partial}{\partial t}\rho &= 0.\end{aligned} \tag{45}$$

Notice the second equation could equivalently be formulated with $\mathcal{S}^{-1}$; this originally came from $w = 0$, so $\nabla_H\cdot\boldsymbol{v}_H = 0$ is true for incompressibility. From the projection it is perhaps "more directly" true that $\mathcal{S}^{-1}w = 0$ in this case, but in any case, they are equivalent.

3.1.3 Low Rossby and low Froude (QG)

For the QG case, we do need to actually compute the projection. This calculation may be found in the Appendix, Section 6.1. The projection is given by

$$P_{\mathrm{QG}_\alpha}\boldsymbol{w} = \begin{pmatrix}\boldsymbol{v}_H - \mathrm{Bu}^2\mathcal{S}^{-2}\Delta^{-1}_{\mathrm{QG}_\alpha}\frac{\partial^2\boldsymbol{v}_H}{\partial z^2} - \Delta^{-1}_{\mathrm{QG}_\alpha}\left(\nabla_H(\nabla_H\cdot\boldsymbol{v}_H) + \mathrm{Bu}\mathcal{S}^{-1}\nabla_H^{\perp}\left(\frac{\partial\rho}{\partial z}\right)\right)\\ 0\\ \rho - \mathrm{Bu}\mathcal{S}^{-1}\Delta^{-1}_{\mathrm{QG}_\alpha}\left(\frac{\partial}{\partial z}(\nabla_H\times\boldsymbol{v}_H)\right) - \Delta^{-1}_{\mathrm{QG}_\alpha}\Delta_H\rho\end{pmatrix} \tag{46}$$

where $\Delta_{\mathrm{QG}_\alpha} = \Delta_H + \mathrm{Bu}^2\mathcal{S}^{-2}\frac{\partial^2}{\partial z^2}$, and $\mathcal{S}^{-2}$ denotes $\mathcal{S}^{-1}$ applied twice. We can immediately see that when $\alpha = 0$, since $\mathcal{S} = \mathcal{S}^{-1} = I$, this correctly reduces to the known projection operator, Eq. (32).

From here, some involved algebra is required in order to obtain the QG-α equation; this is shown in its entirety in the Appendix, Section 6.5.2. The slow dynamics are found from the projection via

$$\frac{\partial\boldsymbol{w}^0}{\partial t} + P_{\mathrm{QG}_\alpha}(\mathcal{B}(\boldsymbol{w}^0,\boldsymbol{w}^0) - \mathcal{D}(\boldsymbol{w}^0)) = 0. \tag{47}$$

The slow dynamics equation, which we title QG-α, is then given by

$$\frac{D^\alpha}{Dt}\left(\Delta_H \mathcal{S}\phi + \mathrm{Bu}^2 \mathcal{S}^{-1}\frac{\partial^2}{\partial z^2}\phi\right) = 0, \tag{48}$$

where $\frac{D^\alpha}{Dt}$ denotes advection with respect to the smoothed velocity, and ϕ denotes the potential, so that the third component of the vorticity $\omega_3 = \mathcal{S}\Delta_H\phi$. In the original QG, this was the pressure, and in QG$-\alpha$, this is then the modified pressure. By using the commuting properties of $\mathcal{S}$, we can see that analogously to the $\alpha = 0$ case, the PV is just the $\Delta_{\mathrm{QG}_\alpha}$ operator applied to the potential ϕ. We can also rewrite Eq. (48) as

$$\frac{D^\alpha}{Dt}\left(\omega_3 - \mathrm{Bu}\ \mathcal{S}^{-1}\frac{\partial}{\partial z}\rho\right) = 0, \tag{49}$$

which is very similar to the PV conservation equation in the $\alpha = 0$ case, Eq. (33) (and indeed reduces appropriately). The key differences are that the density is now smoothed, and the vorticity has a different relationship to the (modified) pressure, now involving the Helmholtz operator.

3.2 Fast dynamics

In this section, we again focus on the general case and assume that $|\boldsymbol{k}|, |\boldsymbol{k}_H| \neq 0$.

3.2.1 Low Rossby, finite Froude

We obtain the matrix representation for the fast operator

$$\mathcal{L}_{\mathrm{Ro}}(ik) = \frac{1}{(1+L_\alpha|\boldsymbol{k}|^2)|\boldsymbol{k}|^2}\begin{bmatrix} -kl & -(l^2+m^2) & 0 & 0 \\ k^2+m^2 & kl & 0 & 0 \\ -lm & km & 0 & 0 \\ 0 & 0 & 0 & 0 \end{bmatrix}. \tag{50}$$

We then obtain the eigenvalues $\lambda^\beta = i\omega_{\boldsymbol{k}}^{(\beta)}$ where

$$\omega_{\boldsymbol{k}}^{(0)} = 0 \text{ (double)} \quad \text{and} \quad \omega_{\boldsymbol{k}}^{(\pm 1)} = \pm\frac{m}{|\boldsymbol{k}|(1+L_\alpha|\boldsymbol{k}|^2)}. \tag{51}$$

3.2.2 Low Froude, finite Rossby

In this case, we obtain the matrix representation for the fast operator

$$\mathcal{L}_{\mathrm{Fr}}(ik) = \begin{bmatrix} 0 & 0 & 0 & -\frac{km}{|\boldsymbol{k}|^2} \\ 0 & 0 & 0 & -\frac{km}{|\boldsymbol{k}|^2} \\ 0 & 0 & 0 & 1-\frac{m^2}{|\boldsymbol{k}|^2} \\ 0 & 0 & -\frac{1}{1+L_\alpha|\boldsymbol{k}|^2} & 0 \end{bmatrix}. \tag{52}$$

The eigenvalues are then given by

$$\omega_{\boldsymbol{k}}^{(0)} = 0 \text{ (double)} \quad \text{and} \quad \omega_{\boldsymbol{k}}^{(\pm 1)} = \pm\frac{|\boldsymbol{k}_H|}{(1+L_\alpha|\boldsymbol{k}|^2)^{1/2}|\boldsymbol{k}|}. \tag{53}$$

3.2.3 Low Rossby and low Froude (QG)

The matrix representation for the fast operator is given by $\frac{1}{Ro}\mathcal{L}_{\mathrm{Ro}}(i\boldsymbol{k}) + \frac{1}{\mathrm{Fr}}\mathcal{L}_{\mathrm{Fr}}(i\boldsymbol{k})$, written out explicitly in the Appendix, Eq. (57). Using this matrix representation, we find

$$\omega_{\boldsymbol{k}}^{(0)} = 0 \quad \text{(double)} \quad \text{and} \quad \omega_{\boldsymbol{k}}^{(\pm 1)} = \pm \frac{((1 + L_\alpha |\boldsymbol{k}|^2)|\boldsymbol{k}_H|^2 + \mathrm{Bu}^2 m^2)^{1/2}}{(1 + L_\alpha |\boldsymbol{k}|^2)|\boldsymbol{k}|}. \tag{54}$$

3.2.4 Discussion of fast dynamics: $\alpha = 0$ vs. $\alpha \neq 0$

The set of triads is described by

$$R^{\alpha}_{\beta,\boldsymbol{k}} = \{(\boldsymbol{k}', \boldsymbol{k}'', \beta', \beta'') \mid \boldsymbol{k}' + \boldsymbol{k}'' = \boldsymbol{k},\ \omega_{\boldsymbol{k}'}^{(\beta')} + \omega_{\boldsymbol{k}''}^{(\beta'')} = \omega_{\boldsymbol{k}}^{(\beta)}\}.$$

The superscript α indicates that the set of possible interactions now depends on α in the $\alpha \neq 0$ case, since the eigenvalues do. In Sections 3.2.1 to 3.2.3, we saw that in each of the three limiting cases, there are slow modes (zero eigenvalues) and fast modes. The the possible triad interactions can be grouped into six types : slow-slow-fast, slow-fast-fast, fast-fast-fast, slow-slow-slow, slow-fast-slow, and fast-fast-slow. In this list, slow-slow-fast should be read as "slow+slow→fast," so two slow frequencies add to make a fast frequency. The list has only six entries because permutations of the first two frequencies are considered the same (a slow frequency written first added to a fast frequency written second is not functionally different than adding them in the reverse order).

To analyze the fast dynamics, we are concerned with the first three types. The second three types represent an alternative way to compute the slow dynamics, which gives the same result as the projection method ([7], c.f. p.21). Importantly, it can be shown that the interaction coefficients corresponding to fast-fast-slow interactions are zero, so that the slow dynamics are decoupled from fast (at the orders considered) [7, 30]. Within the interactions that result in fast frequencies, we can be even more specific; for the low Froude, finite Rossby and QG cases in Sections 3.2.1 to 3.2.3, it is not possible to have slow-slow-fast interactions, and for the low Rossby, finite Froude case, it is only possible when the vertical wavenumbers are zero. In all three cases, slow-fast-fast and fast-fast-fast triads are possible when both $\alpha = 0$ and when $\alpha \neq 0$. Because of the relationship between the eigenvalues,

$$\omega_{\mathrm{QG}}^{(\pm 1)}(\boldsymbol{k}) = \pm |(\omega_{\mathrm{Fr}}^{(\pm 1)}(\boldsymbol{k}), \mathrm{Bu}\ \omega_{\mathrm{Ro}}^{(\pm 1)}(\boldsymbol{k}))|, \tag{55}$$

we focus on the QG case.

We first observe that the shift from $\alpha = 0$ to $\alpha \neq 0$ can significantly affect geometric properties of the hyperplanes corresponding to the eigenfrequencies: an example is shown in Figure 3. It is clear that the set of wavenumbers $\boldsymbol{k} \in \mathbb{Z}^3$ and corresponding $\boldsymbol{k}'$ and $\boldsymbol{k}''$ can be completely different for each value of α.

The slow-fast-fast interactions involve a higher dimensional equation in the $\alpha \neq 0$ case than the $\alpha = 0$ case, whose solutions have been described in a relatively simple geometric fashion. In the $\alpha = 0$ case, due to Eq. (38), [7] state that the $\boldsymbol{k}'$ that result in resonance interactions with $\boldsymbol{k}$ (if $\boldsymbol{k}''$ corresponds to the vortical mode, it plays no role except for that associated with $\boldsymbol{k} = \boldsymbol{k}' + \boldsymbol{k}''$) lie *within* a cone generated by rotating $\boldsymbol{k}$ about the vertical axis. This implies that the Burger number, which scales the vertical component of the

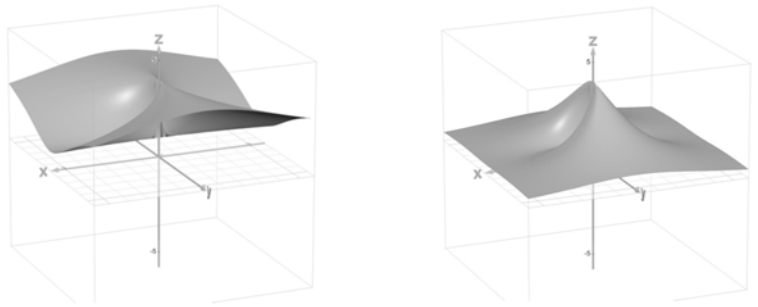

$\alpha = 0, \quad \text{Bu} = 4$ $\alpha = 0.1, \quad \text{Bu} = 4$

Figure 3: A plot of two instances of the QG dispersion relation, for $\alpha = 0$ vs. a small value of α, 0.1, and an arbitrarily selected value of the Burger number. Here, dimensions are suppressed in that $|\boldsymbol{k}_H|$ is represented on the x-axis, m is represented on the $y-$axis, and the output $\omega^{(1)}_{QG}(\boldsymbol{k})$ is represented on the z-axis. We can qualitatively see a large difference going from zero α to small nonzero α, and that geometric properties, such as convexity in certain regions, are altered.

wavenumber, then does not play a role in this geometric constraint. This should still hold in the $\alpha \neq 0$ case as the relative scaling between $|\boldsymbol{k}_H|^2$ and $|\boldsymbol{k}|$ versus that of m^2 is still the same. However, this geometric picture is more complicated in the presence of nonzero α because it introduces an additional scaling by $|\boldsymbol{k}|^2$ as well the non-dimensionalized α in Eq. (54).

The fast-fast-fast resonant interactions are of perhaps most interest for two reasons: they exclusively feature fast modes, and their defining relationship is much more algebraically involved. Unlike the other fast resonant interactions, the fast-fast-fast triads lack a geometric characterization of solutions even in the $\alpha = 0$ case. However, we do find a striking mathematical result: the algebraic argument in Sections 6.6.2 to 6.6.4 shows that any fast-fast-fast interactions that can occur in the $\alpha = 0$ case cannot occur in the $\alpha \neq 0$ case when $L_\alpha|\boldsymbol{k}'|^2 < 1$, and similarly for $\boldsymbol{k}''$ and $\boldsymbol{k} = \boldsymbol{k}' + \boldsymbol{k}''$. A numerical search shows that there are indeed fast-fast-fast triad interactions when this criterion is not met. It makes intuitive sense that there should be less resonant interactions possible in the LANS-α equations than the unregularized equations, but the crucial point is that this specifically depends on picking α below a threshold value.

The practical significance of this threshold is not immediately apparent. However, when implementing these equations numerically, there are general relationships that can be formed between the maximum resolvable wavenumber and the grid spacing. Recall that the numerical issues associated with α were only found for specific values of α with respect to the grid spacing. Rewriting our criterion, we have that there are no resonance interactions when

$$\frac{\alpha}{L}|\boldsymbol{k}| < 1. \tag{56}$$

In particular, this is true when

$$\frac{\alpha}{L}|\boldsymbol{k}_{\max}| < 1,$$

where $\boldsymbol{k}_{\max}$ is the maximum resolvable wavenumber. One may reasonably choose L to be the length of the domain. Suppose we have N gridpoints and a domain length of 2π, so that $L = 2\pi$ (for simplicity – other scalings of this also yield the same conclusion). Then replacing $|\boldsymbol{k}_{\max}|$ with the Nyquist wavenumber, we have

$$\frac{\alpha}{L}\frac{\pi}{\Delta x} < 1.$$

Substituting in L and re-arranging, we then find

$$\alpha < 2\Delta x,$$

which is the exact criterion for stability that was empirically found, as discussed in the introduction. This is of course not an exact explanation for this empirically determined bound, as there are other rules of thumb for what the maximum resolvable wavenumber is in terms of the grid spacing, depending on the setup of the simulation. The key point is the similarity between this mathematically-determined threshold for α, based on the fast dynamics, and the empirical observations of that threshold. The criterion on α relates directly to grid spacing, providing guidance for both our investigation of the instability and, eventually, how to choose α in future implementations of LANS-α.

4 Directions for Current and Future Work

This report presents the theoretical framework for our investigation of the LANS-α model. The continued work on this project involves numerical simulations to complement our findings.

These numerical simulations are implemented in Dedalus [3]. We use random forcing about a specific wavenumber, as described in [28]. We will compare the across different values of α, including $\alpha = 0$ and values previously associated with numerical instability. Our goal is to run simulations at a resolution of 256^3, computational resources allowing. Following Whitehead and Wingate (2011), a key focus of our analysis will be examining the evolution of slow versus fast energy for different values of α. If there are values of α for which the kinetic energy exhibits blow-up behavior, it will be useful to see whether only the fast component of the energy is driving this.

While our analysis of the slow and fast dynamics suggests that resonant interactions may be the source of instability, something else, such as near-resonance interactions, could also be responsible. In any case, the theoretical framework in this paper will still help to identify the origin of the numerical problems, particularly because we can separate out the slow dynamics. Beyond addressing numerical stability, these simulations will provide valuable insights into the broader behavior of the LANS-α model, as relatively few such simulations exist in the literature. For instance, we will be able to specifically see how α affects different flow features, such as potential vorticity evolution. We can also analyze the α criterion Eq. (56) in greater detail given our simulation setup.

The analysis of the slow and fast dynamics and energy evolution for the LANS-α model from our simulations will complete this project, but several immediately feasible future directions are apparent. One is a deeper analysis of the fast dynamics given what was presented here: a more robust exploration of how the geometry of solutions to the slow-fast-fast resonant equation changes going from $\alpha = 0$ to $\alpha \neq 0$. A more computational route would be to employ a large numerical search of solutions to the fast-fast-fast resonance equation, which may reveal underlying patterns. It would also be a straightforward extension of the simulations to experiment with forcing the dynamics at resonant frequencies. The results of this project will inform how to improve implementations of the LANS-α model, and developing publicly available, accessible versions using different numerical methods, such as spectral methods, would be valuable. Our simulation results may build on findings such as those in Hecht et al. (2008b), which suggest an alternate filter could address the numerical issues. In that case, it must be determined whether such modifications preserve the Lagrangian-averaging interpretation, and if not, evaluate the theoretical implications of losing this framework. This motivates the search for filters that improve computational performance while maintaining the model's desirable properties as possible. Lastly, LANS-α is a prime example of invertible-operator-based LES techniques, as in Geurts and Holm (2003), which are also promising turbulence closure models due to their mathematical basis [8]. This motivates implementing these techniques in novel situations, such as ocean biogeochemistry. Overall, LANS-α remains a rich model with many unexplored facets and far-reaching applications.

5 Acknowledgments

I would first like to thank my advisor on this project, Beth Wingate, not only for her guidance and support, but especially for our inspiring discussions about future mathematical possibilities. I would like to also thank the principal lecturers, Edgar Knobloch and Basile Gallet, for the rare privilege of learning about multiscale asymptotics from leading figures in the field. I thank the directors, Greg Chini and Bruce Sutherland, for making such a fantastic program possible this summer. I also greatly appreciate the Dedalus team, especially Keaton Burns, for their continued effort in making it possible for the GFD fellows to run these simulations which are often an integral part of the work (and also for teaching us softball). Lastly, I would like to thank the other 2024 GFD fellows for teaching me so much and the memorable times together.

6 Appendix

6.1 Obtaining the projection operator

6.2 Projection for QG, α=0

This section contains the full details of how to obtain the projection operator onto the null space of the fast operator, Eq. (32). We can find the following matrix for the fast operator in Fourier space:

$$A(\boldsymbol{k}) = \frac{1}{|\boldsymbol{k}|^2}\begin{bmatrix} -\frac{kl}{\mathrm{Ro}} & -\frac{l^2+m^2}{\mathrm{Ro}} & 0 & -\frac{km}{\mathrm{Fr}} \\ \frac{k^2+m^2}{\mathrm{Ro}} & \frac{kl}{\mathrm{Ro}} & 0 & -\frac{lm}{\mathrm{Fr}} \\ -\frac{lm}{\mathrm{Ro}} & \frac{km}{\mathrm{Ro}} & 0 & \frac{k^2+l^2}{\mathrm{Fr}} \\ 0 & 0 & -\frac{|\boldsymbol{k}|^2}{\mathrm{Fr}} & 0 \end{bmatrix}.$$

The null space is spanned by the unit vector

$$\frac{1}{\sqrt{k^2+l^2+\mathrm{Bu}^2m^2}}\begin{bmatrix} l \\ -k \\ 0 \\ \mathrm{Bu}\ m \end{bmatrix}$$

Then we can construct, where $\hat{\boldsymbol{w}}_k = (\hat{u}_k, \hat{v}_k, \hat{w}_k, \hat{\rho}_k)$,

$$P\hat{\boldsymbol{w}}_k = \frac{1}{k^2+l^2+\mathrm{Bu}^2m^2}\begin{pmatrix} l^2\hat{u}_k - kl\hat{v}_k + \mathrm{Bu}\ lm\hat{\rho}_k \\ k^2\hat{v}_k - kl\hat{u}_k - \mathrm{Bu}\ km\hat{\rho}_k \\ 0 \\ \mathrm{Bu}\ m\,(l\hat{u}_k - k\hat{v}_k + \mathrm{Bu}\ m\hat{\rho}_k) \end{pmatrix}$$

To transform back into physical space, we just need to add and subtract $(k^2+\mathrm{Bu}^2m^2)\hat{u}_k$ from the first component and $(l^2+F^2m^2)\hat{v}_k$ from the second. Next notice that in Fourier space, $\nabla_H(\nabla_H\cdot\boldsymbol{v}_H)$ is $(k^2\hat{u}_k + kl\hat{v}_k, lk\hat{u}_k + l^2\hat{v}_k, 0)^T$. This then covers what we added and what is left except for the terms involving the Burger number: $\mathrm{Bu}lm\hat{\rho}_k$ and $\mathrm{Bu}^2m^2\hat{u}_k$, and similarly in the other component. Transforming back into physical space then yields Eq. (32).

6.3 Projection for QG, $\alpha \neq$0

We take Fourier transform and find the the matrix for the fast operator:

$$A(\boldsymbol{k}) = \frac{1}{|\boldsymbol{k}|^2}\begin{bmatrix} -\frac{kl}{\mathrm{Ro}C} & -\frac{l^2+m^2}{\mathrm{Ro}C} & 0 & -\frac{km}{\mathrm{Fr}} \\ \frac{k^2+m^2}{\mathrm{Ro}C} & \frac{kl}{\mathrm{Ro}C} & 0 & -\frac{lm}{\mathrm{Fr}} \\ -\frac{lm}{\mathrm{Ro}C} & \frac{km}{\mathrm{Ro}C} & 0 & \frac{k^2+l^2}{\mathrm{Fr}} \\ 0 & 0 & -\frac{|\boldsymbol{k}|^2}{\mathrm{Fr}C} & 0 \end{bmatrix} \tag{57}$$

where $C \doteq 1 + L_\alpha|\boldsymbol{k}|^2$. The null space is spanned by the unit vector

$$\frac{1}{\sqrt{k^2+l^2+\left(\frac{\mathrm{Bu}}{C}\right)^2m^2}}\begin{bmatrix} l \\ -k \\ 0 \\ \frac{\mathrm{Bu}}{C}m \end{bmatrix}$$

Then we can construct, where $\hat{\boldsymbol{w}}_k = (\hat{u}_k, \hat{v}_k, \hat{w}_k, \hat{\rho}_k)$,

$$P\hat{\boldsymbol{w}}_k = \frac{1}{k^2 + l^2 + \left(\frac{\mathrm{Bu}}{C}\right)^2 m^2} \begin{pmatrix} l^2\hat{u}_k - kl\hat{v}_k + \frac{\mathrm{Bu}}{C} lm\hat{\rho}_k \\ k^2\hat{v}_k - kl\hat{u}_k - \frac{\mathrm{Bu}}{C} km\hat{\rho}_k \\ 0 \\ \frac{\mathrm{Bu}}{C} m\left(l\hat{u}_k - k\hat{v}_k + \frac{\mathrm{Bu}}{C} m\hat{\rho}_k\right) \end{pmatrix}$$

To transform back into physical space, we just need to add and subtract $(k^2 + \left(\frac{\mathrm{Bu}}{C}\right)^2 m^2)\hat{u}_k$ from the first component and $(l^2 + \left(\frac{\mathrm{Bu}}{C}\right)^2 m^2)\hat{v}_k$ from the second. With the cancellation with the denominator, we can get the $\boldsymbol{v}_H$ term (notice this does not have any $\mathcal{S}^{-1}$). Transforming back into physical space yields Eq. (46).

6.4 Slow dynamics equation from the projection, α=0

In this section, we see in detail how the projected equations simplify to the PV equation that was found in [7] for the $\alpha = 0$ case. An important note prior to performing this calculation is that the identity for the vector Laplacian,

$$\Delta \boldsymbol{v} = \nabla(\nabla \cdot \boldsymbol{v}) - \nabla \times \nabla \times \boldsymbol{v}$$

does not hold for the two-dimensional vector Laplacian. Indeed, when we define curl for a two-dimensional vector, it outputs a scalar, so this could not possibly work. Instead, we derive the following vector identity for the vector Laplacian in 2D:

$$\Delta_H \boldsymbol{v}_H = \nabla_H(\nabla_H \cdot \boldsymbol{v}_H) - \nabla_H^{\perp}(\nabla_H \times \boldsymbol{v}_H). \tag{58}$$

Here, $\nabla_H^{\perp}$ is the perpendicular gradient, $(-\frac{\partial}{\partial y}, \frac{\partial}{\partial x})$ (notice that when we have a streamfunction, $\boldsymbol{v}_H = \nabla_H^{\perp}\psi$).

Recall the projection is given by

$$P_{\mathrm{QG}}\boldsymbol{w} = \begin{pmatrix} \boldsymbol{v}_H - \mathrm{Bu}^2 \Delta_{\mathrm{QG}_\alpha}^{-1} \frac{\partial^2 \boldsymbol{v}_H}{\partial z^2} - \Delta_{\mathrm{QG}}^{-1}\left(\nabla_H(\nabla_H \cdot \boldsymbol{v}_H) + \mathrm{Bu}\nabla_H^{\perp}\left(\frac{\partial \rho}{\partial z}\right)\right) \\ 0 \\ \rho - \mathrm{Bu}\Delta_{\mathrm{QG}}^{-1}\left(\frac{\partial}{\partial z}(\nabla_H \times \boldsymbol{v}_H)\right) - \Delta_{\mathrm{QG}}^{-1}\Delta_H \rho \end{pmatrix} \tag{59}$$

where $\Delta_{\mathrm{QG}} = \Delta_H + \mathrm{Bu}^2 \frac{\partial^2}{\partial z^2}$ and $\nabla_H^{\perp} = \left(-\frac{\partial}{\partial x_2}, \frac{\partial}{\partial x_1}\right)$. Recall also that in place of $\boldsymbol{w}$ above, we must substitute $\mathcal{B}(\boldsymbol{w}, \boldsymbol{w}) - \mathcal{D}(\boldsymbol{w}))$ where these $\boldsymbol{w}$ are really $\boldsymbol{w}^0$. The bilinear form and diffusion operator were found to be

$$\mathcal{B}(\boldsymbol{w}, \boldsymbol{w}) = \begin{pmatrix} \boldsymbol{v} \cdot \nabla \boldsymbol{v} - \nabla \Delta^{-1}(\nabla \cdot (\boldsymbol{v} \cdot \nabla \boldsymbol{v}) \\ \boldsymbol{v} \cdot \nabla \rho \end{pmatrix} \quad \text{and} \quad \mathcal{D}\boldsymbol{w} = \frac{1}{\mathrm{Re}} \begin{pmatrix} \Delta \boldsymbol{v} \\ \frac{1}{\mathrm{Pr}} \Delta \rho \end{pmatrix}.$$

It does not add any difficulty to evaluate the projection on $\mathcal{D}\boldsymbol{w}$, but since we aim to derive the conservation of PV, we will consider the case with no diffusion.

Using the new identity Eq. (58), we calculate the result of substituting in the term $\nabla_H \Delta_H^{-1}(\nabla_H \cdot (\boldsymbol{v}_H \cdot \nabla_H)\boldsymbol{v}_H)$. We will be left with a term

$$\Delta_{QG}^{-1}(\nabla_H^{\perp}(\nabla_H \times \nabla_H \Delta_H^{-1}(\nabla_H \cdot (\boldsymbol{v}_H \cdot \nabla_H)\boldsymbol{v}_H))).$$

Notice that this is zero, because $\nabla_H \times$ a gradient is something of the form $\frac{\partial^2 v}{\partial y \partial z} - \frac{\partial^2 v}{\partial y \partial x}$, but u and v are going to be the same here because they come from the vector Laplacian, which is just the Laplacian in each component. Then we can conclude the contribution from that term is zero.

Then considering our equation, plugging in everything except what we know will yield a zero contribution from $\mathcal{B}(\cdot,\cdot)$, we have

$$-\mathrm{Bu}^2 \Delta_{QG}^{-1} \frac{\partial^2}{\partial z^2}((\boldsymbol{v}_H \cdot \nabla)\boldsymbol{v}_H) - \Delta_{QG}^{-1}(\nabla_H(\nabla_H \cdot \boldsymbol{v}_H \cdot \nabla_H \boldsymbol{v}_H)) = \\ -(\boldsymbol{v}_H \cdot \nabla_H)\boldsymbol{v}_H + \Delta_{QG}^{-1}(\nabla_H^{\perp}(\nabla_H \times ((\boldsymbol{v}_H \cdot \nabla_H)\boldsymbol{v}_H))).$$

The momentum equation then reduces to, from Eq. (25),

$$\frac{\partial \boldsymbol{v}_H}{\partial t} + \Delta_{\mathrm{QG}}^{-1}\left(\nabla_H^{\perp}(\nabla_H \times ((\boldsymbol{v}_H \cdot \nabla_H)\boldsymbol{v}_H)) - \mathrm{Bu}\nabla_H^{\perp}\left(\frac{\partial}{\partial z}(\boldsymbol{v}_H \cdot \nabla_H)\rho\right)\right) = 0.$$

Note that we can interpret the advection term applied to ρ as a matrix times a scalar function. We will want to take the curl of the momentum equation to get the PV conservation equation. First, we need to simplify the equation so there is no operator $\Delta_{\mathrm{QG}}^{-1}$. If we replace $\boldsymbol{v}_H$ in terms of the streamfunction ψ, so that $\frac{\partial \psi}{\partial z} = -\mathrm{Bu}^{-1}\rho$ (hydrostatic balance), we obtain

$$\frac{\partial \boldsymbol{v}_H}{\partial t} + \Delta_{\mathrm{QG}}^{-1}\left(\nabla_H^{\perp}(\nabla_H \times ((\boldsymbol{v}_H \cdot \nabla_H)\boldsymbol{v}_H)) + \mathrm{Bu}^2\nabla_H^{\perp}\left((\boldsymbol{v}_H \cdot \nabla_H)\frac{\partial^2}{\partial z^2}\psi\right)\right) = 0.$$

This was because

$$\partial_z \boldsymbol{v}_H = \partial_z \nabla_H^{\perp}\psi = \nabla_H^{\perp}\partial_z\psi = -\mathrm{Bu}^{-1}\nabla_H^{\perp}\rho,$$

and $\nabla_H \rho \cdot \nabla_H^{\perp}\rho = 0$. Since $\omega_3 = \Delta_H \psi$,

$$-\frac{\partial \boldsymbol{v}_H}{\partial t} = \Delta_{\mathrm{QG}}^{-1}\left(\nabla_H^{\perp}((\boldsymbol{v}_H \cdot \nabla_H)\Delta_H\psi) + \mathrm{Bu}^2\nabla_H^{\perp}\left((\boldsymbol{v}_H \cdot \nabla_H)\frac{\partial^2}{\partial z^2}\psi\right)\right) \\ = \Delta_{\mathrm{QG}}^{-1}\nabla_H^{\perp}((\boldsymbol{v}_H \cdot \nabla_H)q)$$

where q denotes potential vorticity, by definition. Since this approach to finding the slow dynamics equations, which can also be found in [23], may be considered, due to the explicit calculation of the projection, the more mathematically rigorous derivation of the slow dynamics equations than the classical derivation of QG, c.f. [25], it may seem odd to simply "apply" hydrostatic and geostrophic balance here. However, this can actually be seen formally as the leading order solution from the asymptotic expansion (so order $\frac{1}{\epsilon}$), e.g. [23] pp.155-157. This requires initial data to be in geostrophic balance. There is the the question of whether we can still use these balances in the case of the fast singular limit, in which there are fast gravity waves. We indeed can, *only* because the wave contributions (both slow and fast) can be shown to not affect these balances: see Lemma 8.3 and the proceeding text in [23]. A key fact is that expanded potential vorticity, $q^{\epsilon} = q + o(1)$, where $q \doteq \omega_3 - \mathrm{Bu}\,\frac{\partial \rho}{\partial z}$ is the familiar potential vorticity, has no leading order gravity wave fluctuations for small ϵ. This is shown mathematically in [23], though it was of course known before, i.e. that the waves do not carry PV.

Applying the operator Δ_{QG} to both sides, and substituting $\nabla_H^\perp \psi = \boldsymbol{v}_H$, we obtain

$$-\nabla_H^\perp \frac{\partial}{\partial t} q = \nabla_H^\perp (\boldsymbol{v}_H \cdot \nabla_H) q.$$

We cannot just take an inverse on both sides because that is not necessarily well-defined, but notice if we take the horizontal curl of both sides, we obtain a horizontal Laplacian rather than the perpendicular gradient. Then we can apply the inverse horizontal Laplacian operator to both sides, rearrange, and obtain exactly

$$\frac{D^H}{Dt} q = 0.$$

Notice we essentially used the same procedure as if we were deriving the conservation of PV from the momentum equation – as in, we took the horizontal curl – with the key difference being that we did so in a more convenient order, given the presence of the $\Delta_{\mathrm{QG}_\alpha}$ operator.

Now we will also check what we obtain for the density equation. To do so, we substitute in $(\boldsymbol{v}_H \cdot \nabla_H)\rho$ for ρ and $(\boldsymbol{v}_H \cdot \nabla_H)\boldsymbol{v}_H - \nabla_H \Delta_H^{-1}(\nabla_H \cdot (\boldsymbol{v}_H \cdot \nabla)\boldsymbol{v}_H)$ for $\boldsymbol{v}_H$, to obtain

$$\begin{aligned}&(\boldsymbol{v}_H \cdot \nabla_H)\rho \\ &\quad - \Delta_{QG}^{-1}\left(F\frac{\partial}{\partial z}(\nabla_H \times ((\boldsymbol{v}_H \cdot \nabla_H)\boldsymbol{v}_H - \nabla_H \Delta_H^{-1}(\nabla_H \cdot (\boldsymbol{v}_H \cdot \nabla)\boldsymbol{v}_H)) + \Delta_H (\boldsymbol{v}_H \cdot \nabla_H)\rho\right).\end{aligned}$$

Again the term with Δ_H^{-1} will end up contributing zero. We are left with

$$(\boldsymbol{v}_H \cdot \nabla_H)\rho - \Delta_{QG}^{-1}\left(F\frac{\partial}{\partial z}(\nabla_H \times ((\boldsymbol{v}_H \cdot \nabla_H)\boldsymbol{v}_H) + \Delta_H (\boldsymbol{v}_H \cdot \nabla_H)\rho\right),$$

or equivalently,

$$(\boldsymbol{v}_H \cdot \nabla_H)\rho - \Delta_{QG}^{-1}\left(F\frac{\partial}{\partial z}((\boldsymbol{v}_H \cdot \nabla_H)\omega_3) + \Delta_H (\boldsymbol{v}_H \cdot \nabla_H)\rho\right).$$

Notice that using $\omega_3 = \Delta_H \psi$ and $\frac{\partial \psi}{\partial z} = -\mathrm{Bu}^{-1}\rho$, $\omega_3 = \Delta_H \psi$. Then since $\rho = \mathrm{Bu}\frac{\partial \psi}{\partial x_3}$, we can equivalently write

$$(\boldsymbol{v}_H \cdot \nabla_H)\rho - \Delta_{QG}^{-1}\left(-\Delta_H \frac{\partial \psi}{\partial z} + \Delta_H \frac{\partial \psi}{\partial z}\right) = (\boldsymbol{v}_H \cdot \nabla_H)\rho$$

We then see that for density, we just have the mass continuity equation

$$\frac{D\rho}{Dt} = 0.$$

6.5 Slow dynamics equation from the projection, $\alpha \neq 0$

6.5.1 Vorticity identities

In this section, we establish the necessary vorticity identities for obtaining the (simplified) slow dynamics equation from the projection. From [13], the vorticity equation for the Leray-α model is

$$\frac{\partial \omega}{\partial t} + \mathcal{S}^{-1}\boldsymbol{v} \cdot \nabla \omega = \omega \cdot \nabla \mathcal{S}^{-1}\boldsymbol{v} + \nu \Delta \omega + [\nabla v_j \times \nabla \mathcal{S}^{-1} v^j]$$

whereas for the LANS$-\alpha$ model, we have

$$\frac{\partial \omega}{\partial t} + \mathcal{S}^{-1}\boldsymbol{v} \cdot \nabla \omega = \omega \cdot \nabla \mathcal{S}^{-1}\boldsymbol{v} + \nu \Delta \omega.$$

Here, the notation $\mathcal{S}^{-1}\boldsymbol{v} \cdot \nabla \omega$ means multiplying a row vector $\mathcal{S}^{-1}\boldsymbol{v}$ with the gradient matrix for ω. From these equations and the proof of Ertel's PV theorem in [23], we can now hypothesize that the projected equations for the LANS-α model will just be advection of PV *by the smoothed velocity* and the Leray-α model will be the same thing but with a source term resulting from the extra $[\nabla v_j \times \nabla \mathcal{S}^{-1} v^j]$. This is another reason why the LANS$-\alpha$ model is the more physical of the two; the added terms play a crucial role in formulating the generalized $\alpha \neq 0$ slow equations.

A useful note is that the extra term $[\nabla v_j \times \nabla \mathcal{S}^{-1} v^j]$ arises when we consider $\nabla \times ((\boldsymbol{u} \cdot \nabla)\boldsymbol{v})$. We can rewrite this as $\nabla \times ((\nabla \boldsymbol{v}) \cdot \boldsymbol{u})$, where the notation of the inner part means the Jacobian of $\boldsymbol{v}$ times the column vector $\boldsymbol{u}$ on the right. However, the term will cancel out when we instead consider $\nabla \times ((\nabla \boldsymbol{v}) \cdot \boldsymbol{u} + \boldsymbol{v} \cdot (\nabla \boldsymbol{u}))$. Note that the exact form of the terms will be different when we are considering the 2D curl (which results in a scalar) rather than the 3D curl.

Since we wil be interested in the horizontal velocities, we compute explicitly what we will get in 2D. We will use the notation $\boldsymbol{u}_H$ instead of $\mathcal{S}^{-1}\boldsymbol{v}_H$ for simplicity. We are interested in computing $\nabla_H \times ((\boldsymbol{u}_H \cdot \nabla_H)\boldsymbol{v}_H)$ and, for the LANS$-\alpha$ model, $\nabla_H \times ((\boldsymbol{v}_H \cdot \nabla_H)\boldsymbol{u}_H^T)$. We can equivalently write this quantities as $\nabla_H \times ((\nabla_H \boldsymbol{v}_H)\boldsymbol{u}_H) + \boldsymbol{v}_H(\nabla \boldsymbol{u}_H))$ where again the parentheses indicate this is a Jacobian matrix. We denote $\omega_3 \doteq \nabla_H \times \boldsymbol{v}_H$. An explicit calculation yields that

$$\begin{aligned}
\nabla_H \times ((\nabla_H \boldsymbol{v}_H)\boldsymbol{u}_H) &= \partial_x v_2 \partial_x u_1 + u_1 \partial_{xx} v_2 + \partial_y v_2 \partial_x u_2 + u_2 \partial_{xy} v_2 \\
&\quad - (\partial_x v_1 \partial_y u_1 + u_1 \partial_{xy} v_1 + \partial_y v_1 \partial_y u_2 + u_2 \partial_{yy} v_1) \\
\nabla_H \times (\boldsymbol{v}_H(\nabla_H \boldsymbol{u}_H)) &= \partial_y u_1 \partial_x v_1 + v_1 \partial_{xy} \partial u_1 + \partial_y u_2 \partial_x v_2 + v_2 \partial_{xy} u_2 \\
&\quad - (\partial_x u_1 \partial_y v_1 + v_1 \partial_{xy} u_1 + \partial_x u_2 \partial_y v_2 + v_2 \partial_{xy} u_2) \\
&= \partial_y u_1 \partial_x v_1 + \partial_y u_2 \partial_x v_2 - \partial_x u_1 \partial_y v_1 - \partial_x u_2 \partial_y v_2 \\
(\nabla_H \omega_3)\boldsymbol{u}_H &= u_1 \partial_{xx} v_2 - u_1 \partial_{xy} v_1 + u_2 \partial_{xy} v_2 - u_2 \partial_{yy} v_1.
\end{aligned}$$

Thus, upon using the incompressibility of $\boldsymbol{v}_H$ and $\boldsymbol{u}_H$,

$$\begin{aligned}
\nabla_H \times ((\nabla_H \boldsymbol{v}_H)\boldsymbol{u}_H) + \boldsymbol{v}_H(\nabla \boldsymbol{u}_H)) &= (\nabla_H \omega_3)\boldsymbol{u}_H \\
\nabla_H \times ((\nabla_H \boldsymbol{v}_H)\boldsymbol{u}_H) &= (\nabla_H \omega_3)\boldsymbol{u}_H + (\partial_x \boldsymbol{u}_H \cdot \nabla_H v_2 - \partial_y \boldsymbol{u}_H \cdot \nabla_H v_1).
\end{aligned}$$

Writing this in the notation we have been using,

$$\nabla_H \times ((\nabla_H \boldsymbol{v}_H)\boldsymbol{u}_H + \boldsymbol{v}_H(\nabla_H \boldsymbol{u}_H)) = (\mathcal{S}^{-1}\boldsymbol{v}_H \cdot \nabla_H)\omega_3 \tag{60}$$

and

$$\nabla_H \times ((\nabla_H \boldsymbol{v}_H)\boldsymbol{u}_H) = (\mathcal{S}^{-1}\boldsymbol{v}_H \cdot \nabla_H)\omega_3 + (\partial_x \mathcal{S}^{-1}\boldsymbol{v}_H \cdot \nabla_H v_2 - \partial_y \mathcal{S}^{-1}\boldsymbol{v}_H \cdot \nabla_H v_1). \tag{61}$$

To reduce the projected equations to the conservation of PV, we crucially needed to use hydrostatic and geostrophic balance, which, as discussed previously, can be seen to be

formally valid even in the case of a fast singular limit. The key equation to see that this generalizes in the $\alpha \neq 0$ case is Eq. (60). From this, a generalized Ertel's PV theorem can be proven, which is the theorem required to formally show leading order hydrostatic and geostrophic balance. Notice that this will not apply in the Leray$-\alpha$ case because instead Eq. (61) holds.

6.5.2 Derivation of 3D QG-α, conservation of PV

We will make use of the results of §6.4 and §6.5.1. To evaluate $P_{QG_\alpha}(\mathcal{B}(\boldsymbol{w},\boldsymbol{w}) - \mathcal{D}\boldsymbol{w})$, we need to substitute in for $\boldsymbol{v}_H$

$$(\mathcal{S}^{-1}\boldsymbol{v}_H \cdot \nabla_H)\boldsymbol{v}_H - \nabla_H \Delta_H^{-1}(\nabla_H \cdot ((\mathcal{S}^{-1}\boldsymbol{v}_H \cdot \nabla_H)\boldsymbol{v}_H)) - \frac{1}{\mathrm{Re}\Delta \boldsymbol{v}_H},$$

and for ρ,

$$(\mathcal{S}^{-1}\boldsymbol{v}_H \cdot \nabla_H)\rho - \frac{1}{\mathrm{Re}\,\mathrm{Pr}}\Delta\rho.$$

Here, $\mathcal{S}^{-1}$ indicates the two-dimensional version of the operator, and there is an H on the inverse Laplacian because it is actually a vector Laplacian. For now, we will ignore the diffusion terms.

Notice that for the same reason as the $\alpha = 0$ case, the contribution from the latter term in the sum, $\nabla_H \Delta_H^{-1}(\nabla_H \cdot ((\mathcal{S}^{-1}\boldsymbol{v}_H \cdot \nabla_H)\boldsymbol{v}_H))$, will be zero. At this stage, we have

$$\begin{aligned}
&P_{QG_\alpha}(\mathcal{B}(\boldsymbol{v},\boldsymbol{v}) - \mathcal{D}\boldsymbol{v}) \\
&\quad = \Delta_{\mathrm{QG}_\alpha}^{-1}\left(\nabla_H^\perp(\nabla_H \times ((\mathcal{S}^{-1}\boldsymbol{v}_H \cdot \nabla_H)\boldsymbol{v}_H)) - \mathrm{Bu}\mathcal{S}^{-1}\nabla_H^\perp\left(\frac{\partial}{\partial z}((\mathcal{S}^{-1}\boldsymbol{v}_H \cdot \nabla_H)\rho)\right)\right) \\
&\quad = \Delta_{\mathrm{QG}_\alpha}^{-1}\left(\nabla_H^\perp((\mathcal{S}^{-1}\boldsymbol{v}_H \cdot \nabla_H)\omega_3) - \mathrm{Bu}\mathcal{S}^{-1}\nabla_H^\perp\left(\frac{\partial}{\partial z}((\mathcal{S}^{-1}\boldsymbol{v}_H \cdot \nabla_H)\rho)\right)\right).
\end{aligned}$$

Using the commutativity of $\mathcal{S}^{-1}$ with the advection operator (under the interpretation of Lagrangian averaging, i.e. that this is a valid approximation to the dynamic Helmholtz operator), from which it follows due to the lack of time-dependence that there is commutativity with just the $\mathcal{S}^{-1}\boldsymbol{v}_H \cdot \nabla_H$) portion, we obtain

$$\begin{aligned}
&P_{QG_\alpha}(\mathcal{B}(\boldsymbol{v},\boldsymbol{v}) - \mathcal{D}\boldsymbol{v}) \\
&\qquad = \Delta_{\mathrm{QG}_\alpha}^{-1}\left(\nabla_H^\perp((\mathcal{S}^{-1}\boldsymbol{v}_H \cdot \nabla_H)\omega_3) - \mathrm{Bu}\nabla_H^\perp\left(\frac{\partial}{\partial z}(\mathcal{S}^{-1}\boldsymbol{v}_H \cdot \nabla_H)\mathcal{S}^{-1}\rho)\right)\right)
\end{aligned}$$

We apply hydrostatic balance, which in this case yields that $\omega_3 = \mathcal{S}\Delta_H\phi$ and $\rho = -\mathrm{Bu}\frac{\partial\phi}{\partial z}$. We can again commute the partial derivative with respect to z with the advective term due to the relationships with ϕ. We obtain

$$\begin{aligned}
&P_{QG_\alpha}(\mathcal{B}(\boldsymbol{v},\boldsymbol{v}) - \mathcal{D}\boldsymbol{v}) \\
&\quad = \Delta_{\mathrm{QG}_\alpha}^{-1}\left(\nabla_H^\perp((\mathcal{S}^{-1}\boldsymbol{v}_H \cdot \nabla_H)\mathcal{S}\Delta_H\phi) + \mathrm{Bu}^2\nabla_H^\perp\left((\mathcal{S}^{-1}\boldsymbol{v}_H \cdot \nabla_H)\mathcal{S}^{-1}\frac{\partial^2}{\partial z^2}\phi\right)\right)
\end{aligned}$$

Now assembling the first row (velocity portion) of the slow equation Eq. (47), we have

$$\frac{\partial \boldsymbol{v}_H}{\partial t} + \Delta_{\mathrm{QG}_\alpha}^{-1}\left(\nabla_H^\perp((\mathcal{S}^{-1}\boldsymbol{v}_H\cdot\nabla_H)\mathcal{S}\Delta_H\phi) + \mathrm{Bu}^2\nabla_H^\perp\left((\mathcal{S}^{-1}\boldsymbol{v}_H\cdot\nabla_H)\mathcal{S}^{-1}\frac{\partial^2}{\partial z^2}\phi\right)\right) = 0.$$

After applying $\Delta_{\mathrm{QG}_\alpha}$ to both sides, and substituting in $\boldsymbol{v}_H = \mathcal{S}\nabla_H^\perp\phi$, we obtain

$$\frac{\partial}{\partial t}\left(\Delta_H\nabla_H^\perp\mathcal{S}\phi + \mathrm{Bu}^2\mathcal{S}^{-2}\frac{\partial^2}{\partial z^2}\mathcal{S}\nabla_H^\perp\phi\right) + \nabla_H^\perp((\nabla_H^\perp\phi\cdot\nabla_H)\mathcal{S}\Delta_H\phi) + \mathrm{Bu}^2\nabla_H^\perp\left((\nabla_H^\perp\phi\cdot\nabla_H)\mathcal{S}^{-1}\frac{\partial^2}{\partial z^2}\phi\right) = 0.$$

After pulling out the $\nabla_H^\perp$ and either taking the horizontal curl of both sides in order to get a horizontal Laplacian and then applying the inverse horizontal Laplacian to both sides, or integrating each row and then putting together the results to see that the constant of integration must be zero, we obtain

$$\frac{D^{H,\alpha}}{Dt}\left(\Delta_H\mathcal{S}\phi + \mathrm{Bu}^2\mathcal{S}^{-1}\frac{\partial^2}{\partial z^2}\phi\right) = 0.$$

Above, this is advection with respect to the (horizontal) smoothed velocity (which is equal to $\nabla_H^\perp\phi$). If we use the commuting property again, We can see that again the PV is just the $\Delta_{\mathrm{QG}_\alpha}$ operator applied to the potential (which is the modified pressure) ϕ. We can also rewrite this as

$$\frac{D^{H,\alpha}}{Dt}\left(\omega_3 - \mathrm{Bu}\mathcal{S}^{-1}\frac{\partial}{\partial z}\rho\right) = 0,$$

which is very similar to the PV in the $\alpha = 0$ case (and indeed reduces appropriately) but the density is now smoothed and the vorticity has a different relationship to the pressure, now involving the Helmholtz operator.

6.6 Fast dynamics, $\alpha \neq 0$

6.6.1 More details for QG-α

Eigenvectors.

$$\boldsymbol{r}_{\boldsymbol{k}}^{(1)} = \frac{1}{\sqrt{2}|\boldsymbol{k}_H||\boldsymbol{k}|C}\begin{bmatrix} iCkm - \frac{\mathrm{Bu}\,lm}{\omega_{\boldsymbol{k}}^{(1)}} \\ iClm + \frac{\mathrm{Bu}\,km}{\omega_{\boldsymbol{k}}^{(1)}} \\ -iC|\boldsymbol{k}_H|^2 \\ \frac{|\boldsymbol{k}_H|^2}{\omega_{\boldsymbol{k}}^{(1)}} \end{bmatrix} \text{ and } \boldsymbol{r}_{\boldsymbol{k}}^{(-1)} = \frac{1}{\sqrt{2}|\boldsymbol{k}_H||\boldsymbol{k}|C}\begin{bmatrix} -iCkm - \frac{\mathrm{Bu}\,lm}{\omega_{\boldsymbol{k}}^{(1)}} \\ -iClm + \frac{\mathrm{Bu}\,km}{\omega_{\boldsymbol{k}}^{(1)}} \\ iC|\boldsymbol{k}_H|^2 \\ \frac{|\boldsymbol{k}_H|^2}{\omega_{\boldsymbol{k}}^{(1)}}. \end{bmatrix}$$

Notice most of the $C = (1 + L_\alpha |\boldsymbol{k}|^2)$ factor out and cancel, so we can obtain the more familiar form

$$\boldsymbol{r}_{\boldsymbol{k}}^{(1)} = \frac{1}{\sqrt{2}|\boldsymbol{k}_H||\boldsymbol{k}|} \begin{bmatrix} ikm - \frac{\text{Bu } lm|\boldsymbol{k}|}{(C|\boldsymbol{k}_H|^2 + \text{Bu}^2 m^2)^{1/2}} \\ ilm + \frac{\text{Bu } km|\boldsymbol{k}|}{(C|\boldsymbol{k}_H|^2 + \text{Bu}^2 m^2)^{1/2}} \\ -i|\boldsymbol{k}_H|^2 \\ \frac{|\boldsymbol{k}_H|^2|\boldsymbol{k}|}{(C|\boldsymbol{k}_H|^2 + \text{Bu}^2 m^2)^{1/2}} \end{bmatrix},$$

$$\boldsymbol{r}_{\boldsymbol{k}}^{(-1)} = \frac{1}{\sqrt{2}|\boldsymbol{k}_H||\boldsymbol{k}|} \begin{bmatrix} -ikm - \frac{\text{Bu } lm|\boldsymbol{k}|}{(C|\boldsymbol{k}_H|^2 + \text{Bu}^2 m^2)^{1/2}} \\ -ilm + \frac{\text{Bu } km|\boldsymbol{k}|}{(C|\boldsymbol{k}_H|^2 + \text{Bu}^2 m^2)^{1/2}} \\ i|\boldsymbol{k}_H|^2 \\ \frac{|\boldsymbol{k}_H|^2|\boldsymbol{k}|}{(C|\boldsymbol{k}_H|^2 + \text{Bu}^2 m^2)^{1/2}} \end{bmatrix}.$$

6.6.2 Triads: low Rossby only

We are interested in the set of possible three-wave resonant interactions. The eigenvalues of the fast operator are described by Eq. (51). The set of triads is described by

$$R_k^\alpha = \{(\boldsymbol{k}', \boldsymbol{k}'', \beta', \beta'', \beta) \mid \boldsymbol{k}' + \boldsymbol{k}'' = \boldsymbol{k},\ \omega_{\boldsymbol{k}'}^{(\beta')} + \omega_{\boldsymbol{k}''}^{(\beta'')} = \omega_{\boldsymbol{k}}^{(\beta)}\}.$$

The superscript α indicates that the set of possible interactions does depend on α in the $\alpha \neq 0$ case. Using Eq. (51), the relationship between the frequencies, under the assumption that $\boldsymbol{k}', \boldsymbol{k}'', \boldsymbol{k} \neq 0$ and $\boldsymbol{k}_H', \boldsymbol{k}_H'', \boldsymbol{k}_H \neq 0$, is given by

$$\frac{m_1}{|\boldsymbol{k}'|(1 + L_\alpha |\boldsymbol{k}'|^2)} + \frac{m_2}{|\boldsymbol{k}''|(1 + L_\alpha |\boldsymbol{k}''|^2)} = \frac{m}{|\boldsymbol{k}|(1 + L_\alpha |\boldsymbol{k}|^2)}$$

where m_1 is the third component of $\boldsymbol{k}'$, m_2 is the third component of $\boldsymbol{k}''$, m is third component of $\boldsymbol{k}$. We assume $m_1, m_2 \neq 0$, or else we obtain a trivial solution to this relationship. Now imposing also the condition $\boldsymbol{k}' + \boldsymbol{k}'' = \boldsymbol{k}$, we obtain

$$\frac{m_1}{|\boldsymbol{k}'|(1 + L_\alpha |\boldsymbol{k}'|^2)} + \frac{m_2}{|\boldsymbol{k}''|(1 + L_\alpha |\boldsymbol{k}''|^2)} = \frac{m_1 + m_2}{|\boldsymbol{k}' + \boldsymbol{k}''|(1 + L_\alpha |\boldsymbol{k}' + \boldsymbol{k}''|^2)}. \tag{62}$$

Notice in Eq. (62), for simplicity, we did not use the absolute value version of the eigenvalues; the below argument still goes through if we consider the absolute value version of the eigenvalues, since we would just solve for $|m_1 + m_2|$ and then substitute it in at each subsequent step. Moreover, we do not obtain the trivial case: the linearly dependent case is impossible (given they are not both zero).

We are in particular interested in how the solution set of Eq. (62) differs from the $\alpha = 0$ case, which has eigenvalues described by Eq. (36). By using a series expansion in Eq. (62), we can obtain the characterization:

$$\frac{m_1}{|\boldsymbol{k}'|} + \frac{m_2}{|\boldsymbol{k}''|} - \frac{m_1 + m_2}{|\boldsymbol{k}' + \boldsymbol{k}''|} \tag{63}$$

$$-(L_\alpha |\boldsymbol{k}'| m_1 + L_\alpha |\boldsymbol{k}''| m_2 - L_\alpha |\boldsymbol{k}' + \boldsymbol{k}''|(m_1 + m_2)) \tag{64}$$

$$+ L_\alpha^2 |\boldsymbol{k}'|^3 m_1 + L_\alpha^2 |\boldsymbol{k}''|^3 m_2 - L_\alpha^2 |\boldsymbol{k}' + \boldsymbol{k}''|^3 (m_1 + m_2) + ... = 0 \tag{65}$$

This expansion is valid / the series converges whenever $L_\alpha|\boldsymbol{k}'|^2 < 1$ (and similarly for $\boldsymbol{k}''$ and $\boldsymbol{k}$). Note also that we have treated each term as something like fg, where f and g are functions, series expanded g, and then multiplied by f, i.e. we only series expanded $\frac{1}{1+L_\alpha|\boldsymbol{k}'|^2}$. Then there is no technical point about some dependence of $|\boldsymbol{k}'|$ on m, etc.

We can at this point see issues with solvability (regardless of the exact value of L_α). We can break this up into a system of equations

$$\begin{aligned}
\frac{m_1}{|\boldsymbol{k}'|} + \frac{m_2}{|\boldsymbol{k}''|} - \frac{m_1+m_2}{|\boldsymbol{k}'+\boldsymbol{k}''|} &= 0 \\
L_\alpha|\boldsymbol{k}'|m_1 + L_\alpha|\boldsymbol{k}''|m_2 - L_\alpha|\boldsymbol{k}'+\boldsymbol{k}''|(m_1+m_2) &= 0 \\
L_\alpha^2|\boldsymbol{k}'|^3 m_1 + L_\alpha^2|\boldsymbol{k}''|^3 m_2 - L_\alpha^2|\boldsymbol{k}'+\boldsymbol{k}''|^3(m_1+m_2) &= 0 \\
&\vdots
\end{aligned}$$

and show that if the first equation holds, none of the others hold. Then the overall equation Eq. (65) cannot hold. This is just because zero + nonzero is nonzero, since the remaining equations cannot cancel each others' (nonzero) contributions due to the powers of $|\boldsymbol{k}'|$. For instance, the only way to satisfy $x + y = z$ and $x^2 + y^2 = z^2$ simultaneously, where $x, y, z > 0$, is for at least one of $x, y, z = 0$, which we cannot have by assumption here. It is not hard to show that in general $x^n + y^n = z^n$, $x^m + y^m = z^m$ where $x, y, z > 0$, $n, m \in \mathbb{N}$, $m > n$ do not have a simultaneous solution. First, one shows there is no $c > 0$ such that $x = cy$ and this holds, and then, towards a contradiction, one can see via substitution that $x^m + y^m = z^{m-n}(x^n + y^n)$ which by the linear independence implies $z^{m-n} = x^{m-n} = y^{m-n}$ but then those are all actually zero.

The first equation yields

$$m_1 + m_2 = |\boldsymbol{k}' + \boldsymbol{k}''| \left(\frac{m_1}{|\boldsymbol{k}'|} + \frac{m_2}{|\boldsymbol{k}''|} \right). \tag{66}$$

Now consider the next equation. The L_α cancel out and we need

$$\frac{|\boldsymbol{k}'|}{|\boldsymbol{k}'+\boldsymbol{k}''|} m_1 + \frac{|\boldsymbol{k}''|}{|\boldsymbol{k}'+\boldsymbol{k}''|} m_2 = m_1 + m_2, \tag{67}$$

but from assuming Eq. (66) holds,

$$\frac{|\boldsymbol{k}'|}{|\boldsymbol{k}'+\boldsymbol{k}''|} m_1 + \frac{|\boldsymbol{k}''|}{|\boldsymbol{k}'+\boldsymbol{k}''|} m_2 = \frac{|\boldsymbol{k}'+\boldsymbol{k}''|}{|\boldsymbol{k}'|} m_1 + \frac{|\boldsymbol{k}'+\boldsymbol{k}''|}{|\boldsymbol{k}''|} m_2.$$

Assuming m_1 and m_2 are linearly independent, we can compare the coefficients on each one, which implies $|\boldsymbol{k}'+\boldsymbol{k}''|^2 = |\boldsymbol{k}'|^2 = |\boldsymbol{k}''|^2$ which contradicts our assumption that $\boldsymbol{k}', \boldsymbol{k}'' \neq 0$.

If they are not linearly independent, i.e. $m_2 = Am_1$ for some $A \in \mathbb{R}$, then we solve the first equation to obtain that either $|m_1| = 0$ (which we cannot have, by assumption) or

$$A = \left(\frac{|\boldsymbol{k}''|}{|\boldsymbol{k}'|} \right) \frac{|\boldsymbol{k}'| - |\boldsymbol{k}'+\boldsymbol{k}''|}{|\boldsymbol{k}'+\boldsymbol{k}''| - |\boldsymbol{k}''|}.$$

From Eq. (67) though,

$$A = \frac{|\boldsymbol{k}'| - |\boldsymbol{k}' + \boldsymbol{k}''|}{|\boldsymbol{k}' + \boldsymbol{k}''| - |\boldsymbol{k}''|}.$$

Since A is a constant, then $|\boldsymbol{k}''| = |\boldsymbol{k}'|$, so $A = -1$, and this is another trivial solution. Higher order equations just yield

$$A = \frac{|\boldsymbol{k}'|^n - |\boldsymbol{k}' + \boldsymbol{k}''|^n}{|\boldsymbol{k}' + \boldsymbol{k}''|^n - |\boldsymbol{k}''|^n}$$

but since $|\boldsymbol{k}''| = |\boldsymbol{k}'|$, this is also -1 and there is no contradiction. In the absolute value case, however, we still obtain $A = -1$ but that is a contradiction because $|m_2|$ cannot be a negative number times $|m_1|$.

The next order equation: we need

$$\frac{|\boldsymbol{k}'|^3}{|\boldsymbol{k}' + \boldsymbol{k}''|^3} m_1 + \frac{|\boldsymbol{k}''|^3}{|\boldsymbol{k}' + \boldsymbol{k}''|^3} m_2 = m_1 + m_2.$$

Substituting the result from the first equation, Eq. (67),

$$\frac{|\boldsymbol{k}'|^3}{|\boldsymbol{k}' + \boldsymbol{k}''|^3} m_1 + \frac{|\boldsymbol{k}''|^3}{|\boldsymbol{k}' + \boldsymbol{k}''|^3} m_2 = \frac{|\boldsymbol{k}' + \boldsymbol{k}''|}{|\boldsymbol{k}'|} m_1 + \frac{|\boldsymbol{k}' + \boldsymbol{k}''|}{|\boldsymbol{k}''|} m_2.$$

Then we obtain $|\boldsymbol{k}' + \boldsymbol{k}''|^4 = |\boldsymbol{k}'|^4 = |\boldsymbol{k}''|^4$, which is the same contradiction again. We can see inductively that this will always be the case, and we actually cannot get any fast-fast-fast three-wave resonances, at least when we assume all the signs are the same.

Suppose we decide only the mode corresponding to $\boldsymbol{k}'$ is actually the negative one (as in the -1 mode; it is not necessarily negative because that depends on the sign of m, which we make no assumptions on). Then we have the system

$$\begin{aligned}
-\frac{m_1}{|\boldsymbol{k}'|} + \frac{m_2}{|\boldsymbol{k}''|} - \frac{m_1 + m_2}{|\boldsymbol{k}' + \boldsymbol{k}''|} &= 0 \\
-L_\alpha |\boldsymbol{k}'| m_1 + L_\alpha |\boldsymbol{k}''| m_2 - L_\alpha |\boldsymbol{k}' + \boldsymbol{k}''| (m_1 + m_2) &= 0 \\
-L_\alpha^2 |\boldsymbol{k}'|^3 m_1 + L_\alpha^2 |\boldsymbol{k}''|^3 m_2 - L_\alpha^2 |\boldsymbol{k}' + \boldsymbol{k}''|^3 (m_1 + m_2) &= 0 \\
&\vdots
\end{aligned}$$

If the first equation holds, we have

$$m_1 + m_2 = |\boldsymbol{k}' + \boldsymbol{k}''| \left(-\frac{m_1}{|\boldsymbol{k}'|} + \frac{m_2}{|\boldsymbol{k}''|} \right).$$

Then we need

$$-\frac{|\boldsymbol{k}'|}{|\boldsymbol{k}' + \boldsymbol{k}''|} m_1 + \frac{|\boldsymbol{k}''|}{|\boldsymbol{k}' + \boldsymbol{k}''|} m_2 = -\frac{|\boldsymbol{k}' + \boldsymbol{k}''|}{|\boldsymbol{k}'|} m_1 + \frac{|\boldsymbol{k}' + \boldsymbol{k}''|}{|\boldsymbol{k}''|} m_2$$

which is the exact same contradiction again. By symmetry, we can also conclude the result in the case that only the mode corresponding to $\boldsymbol{k}''$ is the negative one.

All that is left is to consider the case where the two sides of the equations are opposite modes. Without loss of generality, we consider the case $\omega^{(1)}(\boldsymbol{k}')+\omega^{(1)}(\boldsymbol{k}'')=\omega^{(-1)}(\boldsymbol{k}'+\boldsymbol{k}'')$. If the first equation holds in this case, we have

$$m_1+m_2=|\boldsymbol{k}'+\boldsymbol{k}''|\left(\frac{m_1}{|\boldsymbol{k}'|}+\frac{m_2}{|\boldsymbol{k}''|}\right).$$

Then we need

$$\frac{|\boldsymbol{k}'|}{|\boldsymbol{k}'+\boldsymbol{k}''|}m_1+\frac{|\boldsymbol{k}''|}{|\boldsymbol{k}'+\boldsymbol{k}''|}m_2=-\frac{|\boldsymbol{k}'+\boldsymbol{k}''|}{|\boldsymbol{k}'|}m_1-\frac{|\boldsymbol{k}'+\boldsymbol{k}''|}{|\boldsymbol{k}''|}m_2$$

which again yields the contradiction that $\boldsymbol{k}'=\boldsymbol{k}''=\boldsymbol{k}=\boldsymbol{0}$.

6.6.3 Triads: low Froude only

Now we complete the same analysis but for the low Froude, finite Rossby case. Based on the eigenvalues, Eq. (53), we are interested in the relationship

$$\frac{|\boldsymbol{k}'_H|}{|\boldsymbol{k}'|(1+L_\alpha|\boldsymbol{k}'|^2)^{1/2}}+\frac{|\boldsymbol{k}''_H|}{|\boldsymbol{k}''|(1+L_\alpha|\boldsymbol{k}''|^2)^{1/2}}=\frac{|\boldsymbol{k}'_H+\boldsymbol{k}''_H|}{|\boldsymbol{k}'+\boldsymbol{k}''|(1+L_\alpha|\boldsymbol{k}'+\boldsymbol{k}''|^2)^{1/2}}. \tag{68}$$

We cannot series expand in exactly the same way as in the low Rossby only case because of the square root. However, we can actually just get the same decoupling if we use the series expansion for $\frac{1}{\sqrt{1+x^2}}$. For the first term:

$$\frac{|\boldsymbol{k}'_H|}{|\boldsymbol{k}'|(1+L_\alpha|\boldsymbol{k}'|^2)^{1/2}}=\frac{|\boldsymbol{k}'_H|}{|\boldsymbol{k}'|}\left(1-\frac{L_\alpha|\boldsymbol{k}'|^2}{2}+\frac{3L_\alpha^2|\boldsymbol{k}'|^4}{8}-\frac{5L_\alpha^3|\boldsymbol{k}'|^6}{16}+...\right)$$

Note that the coefficients are $\binom{-1/2}{n}$. The only difference from the above analysis is the constant coefficients, which do not affect the analysis. We can immediately see that we get the same conclusion as before. To illustrate, for the first equation, we could solve for $|\boldsymbol{k}'_H+\boldsymbol{k}''_H|$,

$$|\boldsymbol{k}'_H+\boldsymbol{k}''_H|=|\boldsymbol{k}'+\boldsymbol{k}''|\left(\frac{|\boldsymbol{k}'_H|}{|\boldsymbol{k}'|}+\frac{|\boldsymbol{k}''_H|}{|\boldsymbol{k}''|}\right).$$

The next order equation reduces to

$$\frac{|\boldsymbol{k}'|}{|\boldsymbol{k}'+\boldsymbol{k}''|}|\boldsymbol{k}'_H|+\frac{|\boldsymbol{k}''|}{|\boldsymbol{k}'+\boldsymbol{k}''|}|\boldsymbol{k}''_H|=|\boldsymbol{k}'_H+\boldsymbol{k}''_H|.$$

Substituting,

$$\frac{|\boldsymbol{k}'|}{|\boldsymbol{k}'+\boldsymbol{k}''|}|\boldsymbol{k}'_H|+\frac{|\boldsymbol{k}''|}{|\boldsymbol{k}'+\boldsymbol{k}''|}|\boldsymbol{k}''_H|=\frac{|\boldsymbol{k}'+\boldsymbol{k}''|}{|\boldsymbol{k}'|}|\boldsymbol{k}'_H|+\frac{|\boldsymbol{k}'+\boldsymbol{k}''|}{|\boldsymbol{k}''|}|\boldsymbol{k}''_H|$$

and we have the same contradiction. Notice we will also reach the same contradiction upon assuming linear dependence.

6.6.4 Triads: simultaneously low Rossby and low Froude

Lastly, we complete the same analysis but for the low Froude and low Rossby case. Based on the eigenvalues, Eq. (54), we are interested in the relationship

$$\begin{aligned}\left(\frac{|\boldsymbol{k}'_H|^2}{|\boldsymbol{k}'|^2(1+L_\alpha|\boldsymbol{k}'|^2)}+\frac{\mathrm{Bu}^2m^2}{|\boldsymbol{k}'|^2(1+L_\alpha|\boldsymbol{k}'|^2)^2}\right)^{1/2}&\\ +\left(\frac{|\boldsymbol{k}''_H|^2}{|\boldsymbol{k}''|^2(1+L_\alpha|\boldsymbol{k}''|^2)}+\frac{\mathrm{Bu}^2m^2}{|\boldsymbol{k}''|^2(1+L_\alpha|\boldsymbol{k}''|^2)^2}\right)^{1/2}&\\ =\left(\frac{|\boldsymbol{k}'_H+\boldsymbol{k}''_H|^2}{|\boldsymbol{k}'+\boldsymbol{k}''|^2(1+L_\alpha|\boldsymbol{k}'+\boldsymbol{k}''|^2)}+\frac{\mathrm{Bu}^2m^2}{|\boldsymbol{k}'+\boldsymbol{k}''|^2(1+L_\alpha|\boldsymbol{k}'+\boldsymbol{k}''|^2)^2}\right)^{1/2}&.\end{aligned} \tag{69}$$

We assume that $|m_i|\neq 0$ and that $|\boldsymbol{k}'_H|\neq 0$ or else what we want to show follows from the previous cases, due to c55. We write each term in a more convenient form:

$$\frac{((1+L_\alpha|\boldsymbol{k}'|^2)|\boldsymbol{k}'_H|^2+\mathrm{Bu}^2m^2)^{1/2}}{|\boldsymbol{k}'|(1+L_\alpha|\boldsymbol{k}'|^2)}$$

Let

$$\omega'_0\doteq\frac{(|\boldsymbol{k}_H|^2+\mathrm{Bu}^2m_1^2)^{1/2}}{|\boldsymbol{k}'|}$$

We cannot really series expand in $|\boldsymbol{k}'|$ because unlike the other cases, we cannot express this as the product of a function involving only $|\boldsymbol{k}'|$ and no other variables dependent on k,m,l and another function. Expanding in $|\boldsymbol{k}'|$ would then necessarily involve doing a multivariable Taylor series. Instead, we expand in L_α. For each term, we obtain

$$\omega'_\alpha=\omega'_0\left(1+\frac{L_\alpha|\boldsymbol{k}'_H|^2}{2(\omega'_0)^2}\right)(1-L_\alpha^2|\boldsymbol{k}|^2+...)$$

so everything follows as before except we also need to address the terms involving $\frac{L_\alpha|\boldsymbol{k}'_H|^2}{2(\omega'_0)^2}$. However, it does not actually matter whether these terms have a zero or nonzero contribution so long as if they have a nonzero contribution, they cannot cancel out the nonzero contribution from the terms $\omega'_0L_\alpha^2|\boldsymbol{k}|^2,\omega'_0L_\alpha^2|\boldsymbol{k}|^4$, etc. To that end, we essentially need to show that

$$c_1x^n+c_2y^n-c_3z^n\neq\frac{d_1}{c_1}x^n+\frac{d_2}{c_2}y^n-\frac{d_3}{c_3}z^n$$

where in our case $n=1,2,3,...$, $x=|\boldsymbol{k}'|$, $y=|\boldsymbol{k}''|$, $z=|\boldsymbol{k}'+\boldsymbol{k}''|$, $c_1=(|\boldsymbol{k}'_H|^2+\mathrm{Bu}^2m_1^2)^{1/2}$ and analogously for c_2,c_3, and $d_1=|\boldsymbol{k}'_H|$ (and similarly for d_2,d_3). This is in fact true because otherwise m_i would be zero, which is not the case by assumption.

References

[1] S. D. Bachman, J. A. Anstey, and L. Zanna, *The relationship between a deformation-based eddy parameterization and the LANS-α turbulence model*, Ocean Modelling, 126 (2018), pp. 56–62.

[2] J. P. Boyd, *Eight definitions of the slow manifold: Seiches, pseudoseiches and exponential smallness*, Dynamics of Atmospheres and Oceans, 22 (1995), pp. 49–75.

[3] K. J. Burns, G. M. Vasil, J. S. Oishi, D. Lecoanet, and B. P. Brown, *Dedalus: A flexible framework for numerical simulations with spectral methods*, Physical Review Research, 2 (2020), p. 023068.

[4] J. Connors, *Convergence analysis and computational testing of the finite element discretization of the Navier–Stokes alpha model*, Numerical Methods for Partial Differential Equations, 26 (2010), pp. 1328–1350.

[5] P. F. Embid and A. J. Majda, *Averaging over fast gravity waves for geophysical flows with arbitary*, Communications in Partial Differential Equations, 21 (1996), pp. 619–658.

[6] ——, *Averaging over fast gravity waves for geophysical flows with unbalanced initial data*, Theoretical and computational fluid dynamics, 11 (1998), pp. 155–169.

[7] ——, *Low Froude number limiting dynamics for stably stratified flow with small or finite Rossby numbers*, Geophysical & Astrophysical Fluid Dynamics, 87 (1998), pp. 1–50.

[8] B. J. Geurts and D. D. Holm, *Regularization modeling for large-eddy simulation*, Physics of fluids, 15 (2003), pp. L13–L16.

[9] ——, *Leray and LANS-α modelling of turbulent mixing*, Journal of turbulence, (2006), p. N10.

[10] J.-L. Guermond, J. T. Oden, and S. Prudhomme, *An interpretation of the Navier–Stokes-alpha model as a frame-indifferent Leray regularization*, Physica D: Nonlinear Phenomena, 177 (2003), pp. 23–30.

[11] M. Hecht, D. Holm, M. Petersen, and B. Wingate, *The LANS-α and Leray turbulence parameterizations in primitive equation ocean modeling*, Journal of Physics A: Mathematical and Theoretical, 41 (2008), p. 344009.

[12] M. W. Hecht, D. D. Holm, M. R. Petersen, and B. A. Wingate, *Implementation of the LANS-α turbulence model in a primitive equation ocean model*, Journal of Computational Physics, 227 (2008), pp. 5691–5716.

[13] D. D. Holm, *Fluctuation effects on 3D Lagrangian mean and Eulerian mean fluid motion*, Physica D: Nonlinear Phenomena, 133 (1999), pp. 215–269.

[14] D. D. Holm, C. Jeffery, S. Kurien, D. Livescu, M. A. Taylor, and B. A. Wingate, *The LANS-α model for computing turbulence*, Los Alamos Sci, 29 (2005), pp. 152–171.

[15] D. D. Holm and E. S. Titi, *Computational models of turbulence: The LANS-α model and the role of global analysis*, SIAM News, 38 (2005), pp. 1–5.

[16] S. Jacobs, *Existence of a slow manifold in a model system of equations*, Journal of Atmospheric Sciences, 48 (1991), pp. 893–902.

[17] B.-S. Kim, *Attractor dimensions of three-dimensional Navier-Stokes-α model for fast rotating fluids on generic-period domains: Comparison with Navier-Stokes equations*, arXiv preprint arXiv:1808.09683, (2018).

[18] B.-S. Kim and B. Nicolaenko, *Existence and continuity of exponential attractors of the three dimensional Navier-Stokes-α equations for uniformly rotating geophysical fluids*, (2006).

[19] J. Leray, *Sur le mouvement d'un liquide visqueux emplissant l'espace*, Acta mathematica, 63 (1934), pp. 193–248.

[20] E. N. Lorenz, *On the existence of a slow manifold*, Journal of Atmospheric Sciences, 43 (1986), pp. 1547–1558.

[21] ——, *The slow manifold—what is it?*, Journal of Atmospheric Sciences, 49 (1992), pp. 2449–2451.

[22] E. N. Lorenz and V. Krishnamurthy, *On the nonexistence of a slow manifold*, Journal of Atmospheric Sciences, 44 (1987), pp. 2940–2950.

[23] A. Majda, *Introduction to PDEs and Waves for the Atmosphere and Ocean*, vol. 9, American Mathematical Society, 2003.

[24] J. E. Marsden and S. Shkoller, *Global well–posedness for the Lagrangian averaged Navier–Stokes (LANS–α) equations on bounded domains*, Philosophical Transactions of the Royal Society of London. Series A: Mathematical, Physical and Engineering Sciences, 359 (2001), pp. 1449–1468.

[25] J. Pedlosky, *Waves in the ocean and atmosphere: introduction to wave dynamics*, vol. 260, Springer, 2003.

[26] S. Schochet, *Fast singular limits of hyperbolic PDEs*, Journal of differential equations, 114 (1994), pp. 476–512.

[27] ——, *The mathematical theory of the incompressible limit in fluid dynamics*, in Handbook of mathematical fluid dynamics, vol. 4, Elsevier, 2007, pp. 123–157.

[28] L. M. Smith and F. Waleffe, *Generation of slow large scales in forced rotating stratified turbulence*, Journal of Fluid Mechanics, 451 (2002), pp. 145–168.

[29] J. P. Whitehead and B. A. Wingate, *The influence of fast waves and fluctuations on the evolution of the dynamics on the slow manifold*, Journal of Fluid Mechanics, 757 (2014), pp. 155–178.

[30] B. A. Wingate, P. Embid, M. Holmes-Cerfon, and M. A. Taylor, *Low Rossby limiting dynamics for stably stratified flow with finite Froude number*, Journal of fluid mechanics, 676 (2011), pp. 546–571.

Oceanic Internal Tides: Do They Get Phased at the Equator?

Camille Moisset

August 21, 2024

1 Introduction

Oceanic tides are an essential component of the global ocean circulation, with an important role in the exchanges between the different energy reservoirs [15, 4]. However, two different contributions need to be separated: the first is the barotropic tide, generated by astronomical forcing, which produces a large scale movement of water masses across the entire global ocean; the second is baroclinic tide (or internal tide) which are internal waves excited by the movement of the water masses over topography [6, 18]. These waves then propagate away from their sources as low vertical modes and interact with numerous other oceanic processes [7]. The dynamics of internal tides are incredibly rich involving complex generation mechanisms, their interactions with topography, but also wave-wave and wave-mean flow interactions, all through the stratified and rotating fluid that is the ocean [see 5, 12, 17, for reviews on different dynamical aspects]. Internal tides are a significant source for deep oceanic mixing through their non-linear dynamics that ultimately induce turbulent dissipation and diapycnal mixing.

The lunar semidiurnal internal tide, denoted M2, is the most energetic tidal mode excited in Earth oceans and, as such, a major actor of oceanic dynamics. It is excited at a fixed frequency $\omega_0 = 1.4 \times 10^{-4}$ rad.s^{-1} and propagates over long distances as low modes with a horizontal wavelength around 150 kilometers [14, 3]. The ultimate fate of the baroclinic tides remains uncertain but a significant number of processes are proposed, amongst them non-linear breaking, triadic interactions, scattering of the energy to higher modes, and interaction with currents and eddies. Likewise, the interaction between the internal tides and eddy fields could cause such incoherences in the tidal signal [16]. It is also possible that strong currents and shelf fronts influence the dynamics of the M2 internal tide [9].

Satellite altimetry provides a way to track the baroclinic tidal signal over the global ocean, as oscillations of the interior affect the surface of the ocean. But in the region of the Equatorial Pacific, such observations show that the M2 signal (for example propagating northward from its generation near the French Polynesia Islands) seems to disappear when the internal waves cross the Equator (see fig. 1 from [1]). Buijsman et al. [1] argue that it could be due to a loss of coherence of the M2 signal and they hinted that equatorial jets (see figure 1) could play a significant role: the vertical and meridional variations in the zonal currents and the stratification can scatter the energy to higher modes and modify the phase and group speed of internal waves resulting in their incoherences. In such type

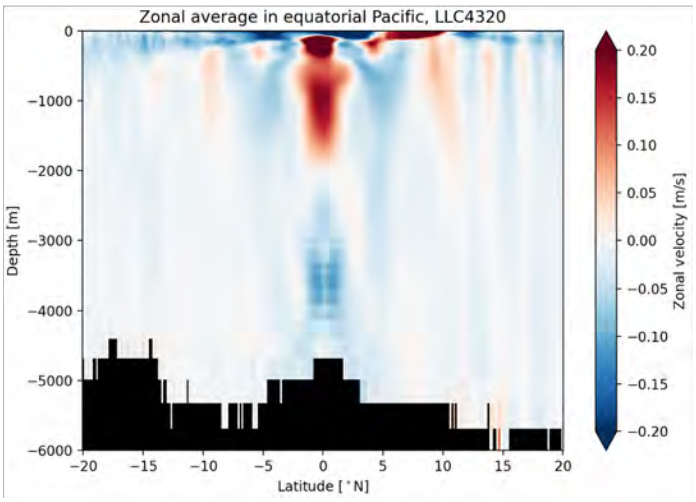

Figure 1: Vertical structure of the zonal equatorial current, computed using the LLC4320 configuration of the Massachusetts Institute of Technology general circulation model (MITgcm, [13])

of observations, the signal of the M2 internal tide is extracted using a harmonic fit to the excitation frequency of the tidal mode, meaning that incoherences could induce a significant loss of information.

We investigate whether the dynamics of the wave-mean flow interaction between the M2 internal wave and the equatorial jets could cause a loss of coherence in the M2 altimetry signal. To do so, we study the more general interaction between a vertical mode 1 internal tide wavepacket and a vertically sheared zonal jet. We follow the work of Kelly et al. [8, 10, 11] who proposed a model able to decompose the modal dynamics of the M2 internal tides. In particular, linear wave-mean flow interactions are retained but non-linear wave-wave interactions are neglected. Section 2 details the formalism of the vertical mode decomposition for internal tides, as well as the analytical framework used in our model. Simulations are realised using Dedalus [2], the numerical setup and parameters which are presented in section 3. Section 4 show the results for a simplified model in which the ocean is supposed to linearly stratified. This approximation allows for the exact comparison between the analytic calculations and the simulations. The conclusions and perspectives for future work are presented in section 5.

2 Analytical Framework

2.1 General equations

We use the tangent plane approximation to describe a patch of the Equatorial Pacific Ocean as a Cartesian box, where (x, y, z) represent longitude, latitude and depth respectively, with unit vectors $(\boldsymbol{e_x}, \boldsymbol{e_y}, \boldsymbol{e_z})$. We consider the fully non-linear Euler equations with the

Boussinesq approximation:

$$\partial_t \boldsymbol{u_T} + (\boldsymbol{u_T} \cdot \boldsymbol{\nabla})\boldsymbol{u_T} + \boldsymbol{f} \times \boldsymbol{u_T} = -\boldsymbol{\nabla} p + b_T \boldsymbol{e_z}, \tag{1a}$$

$$\partial_t b_T + \boldsymbol{u_T} \cdot \boldsymbol{\nabla} b_T = 0, \tag{1b}$$

$$\boldsymbol{\nabla} \cdot \boldsymbol{u_T} = 0, \tag{1c}$$

where $\boldsymbol{u_T} = (u_T, v_T, w_T) = (U + u, v, w)$ is the total velocity field (including currents and waves, with U the velocity of the current), $\boldsymbol{f} = 2\boldsymbol{\Omega_0} \sin\lambda$ the Coriolis parameter with $\boldsymbol{\Omega_0}$ the rotation vector and λ the latitude. $p = P/\rho_0$ is the reduced pressure where P is the dynamic pressure, the density has been decomposed as $\rho = \rho_0 + \overline{\rho}(z) + \rho(x, y, z, t)$ with ρ_0 a reference density, $\overline{\rho}$ the mean density profile and ρ the perturbation density. The squared buoyancy frequency is $\overline{N}^2 = -g\overline{\rho}'/\rho_0 = -\overline{b}'$, where g is gravity and the primes denote derivatives. The total buoyancy field is $b_T = B + \overline{b} + b$ with B the buoyancy perturbation corresponding to the zonal current, $\overline{b}$ that of the background stratification and b that of the waves.

At the Equator, in the f-plane approximation the traditional Coriolis parameter $\boldsymbol{f} = (0, 0, f)$ goes to zero so we use the β-plane approximation $f = \beta y$ (with constant $\beta = 2 \times 10^{-11}$ m^{-1}s^{-1}).

The mean flow U and its associated buoyancy B and pressure fields P_U verify the geostrophic and hydrostatic balance:

$$\beta y U = -\partial_y P_U, \tag{2a}$$

$$0 = -\partial_z P_U + B, \tag{2b}$$

which leads to

$$\partial_y B = -\beta y \partial_z U. \tag{3}$$

2.2 Base state

The base velocity considered is a zonal jet with separated meridional and vertical dependencies:

$$\boldsymbol{U} = (U(y, z), 0, 0) \quad \text{with} \quad U(y, z) = E(y)\tilde{U}(z), \tag{4}$$

where the meridional structure $E(y)$ is taken as a Gaussian:

$$E(y) = \exp\left(-\frac{y^2}{2\mathrm{W}^2}\right), \tag{5}$$

with the characteristic width of the jet denoted by W.
In what follows, $\tilde{U}(z)$ will be either a constant or a cosine function and $\overline{N}^2$ will be a constant. It is, however, possible to generalise to more complex and realistic jet configurations and background stratification.

Using (3), the associated base buoyancy is in hydrostatic and equatorial geostrophic balance:

$$B(y, z) = \beta\, \mathrm{W}^2 E(y)\tilde{U}'(z). \tag{6}$$

The background stratification includes the contribution of the equatorial jet ($\partial_z B$) and the far field stratification:

$$N^2(y,z) = \beta \mathrm{W}^2 E(y)\tilde{U}''(z) + \overline{N}^2(z)\,. \tag{7}$$

2.3 Equations for the perturbations

The base state (4-6) is subjected to perturbation by the internal tide. The total fields are given by:

$$(u_\mathrm{T}, v_\mathrm{T}, w_\mathrm{T}, p_\mathrm{T}, b_\mathrm{T}) = (U, 0, 0, P_U, B) + (u, v, w, p, b). \tag{8}$$

Substituting and neglecting non-linear wave-wave interaction terms in (1) yields the linearized system for the evolution of waves:

$$\partial_t u + E\tilde{U}\partial_x u + E'\tilde{U}v + E\tilde{U}'w - \beta y v = -\partial_x p, \tag{9a}$$

$$\partial_t v + E\tilde{U}\partial_x v + \beta y u = -\partial_y p, \tag{9b}$$

$$\alpha\left(\partial_t w + E\tilde{U}\partial_x w\right) = -\partial_z p + b, \tag{9c}$$

$$\partial_t b + E\tilde{U}\partial_x b + E'\tilde{U}'\beta\mathrm{W}^2 v + \beta\mathrm{W}^2 E\tilde{U}''w + \overline{N}^2 w = 0, \tag{9d}$$

$$\partial_x u + \partial_y v + \partial_z w = 0 \tag{9e}$$

where $\alpha \in \{0, 1\}$ allows to distinguish between the hydrostatic approximation ($\alpha = 0$) and non-hydrostatic case ($\alpha = 1$).

2.4 Vertical mode decomposition for internal tides

We will consider internal tides incident upon and interacting with equatorial jets. They are initialised far from the equator, where the equatorial currents are negligibly small. Here we describe the process of determining the internal structure of these waves.

2.4.1 General formalism

We derive the vertical structure of internal tides with no background flow ($U = 0$). Hydrostatic balance is also assumed by setting α to zero. The system (9) is linear and we expand the perturbations using the plane wave ansatz:

$$(u, v, w, p, b)(x, y, z, t) = (\hat{u}, \hat{v}, \hat{w}, \hat{p}, \hat{b})(z)e^{i(k_x x + k_y y - \omega t)}\,, \tag{10}$$

where k_x and k_y are the wavenumbers in the zonal and meridional directions, respectively and ω is the frequency. The system (9) becomes:

$$-i\omega\hat{u} - \beta y_0 \hat{v} = -ik_x\hat{p}, \tag{11a}$$

$$-i\omega v + \beta y_0 \hat{u} = -ik_y\hat{p}, \tag{11b}$$

$$0 = -\hat{p}' + \hat{b}, \tag{11c}$$

$$-i\omega\hat{b} + \overline{N}^2\hat{w} = 0, \tag{11d}$$

$$ik_x\hat{u} + ik_y\hat{v} + \hat{w}' = 0\,, \tag{11e}$$

in which y_0 is the initial latitude of the waves with $|y_0| \gg$W. The system (11) reduces to:

$$\hat{w}'' + k_h^2 \frac{\overline{N}^2(z)}{\omega^2 - (\beta y_0)^2} \hat{w} = 0\,, \tag{12}$$

where $k_h^2 = k_x^2 + k_y^2$.
The solution of (12) gives a sum of vertical modes $\hat{w} = \Sigma_n w_n \Phi_n(z)$ where the Φ_n satisfy the Sturm-Liouville problem:

$$\Phi_n'' + \frac{\overline{N}^2(z)}{c_n^2}\Phi_n = 0 \quad \text{with} \quad \Phi_n(0) = \Phi_n(-H) = 0, \tag{13}$$

with $c_n^2 = (\omega^2 - (\beta y_0)^2)/k_h^2$ as the eigenvalue and H the height of the domain. This gives the dispersion relation $\omega^2 = c_n^2 k_h^2 + (\beta y_0)^2$. The vertical modes, Φ_n, are orthogonal with respect to the weight function $\overline{N}^2(z)$. The normalisation is chosen so that $\max(|\Phi_n| = 1)$. Using (11) we can derive the corresponding expressions for horizontal velocity, pressure and buoyancy as a sum of vertical modes:

$$[\hat{u}, \hat{v}, \hat{p}](z) = \sum_{n=0}^{\infty} [u_n, v_n, p_n]\phi_n(z), \tag{14a}$$

$$\hat{b}(z) = \sum_{n=0}^{\infty} b_n \overline{N}^2(z)\Phi_n(z) \tag{14b}$$

where $\phi_n = \Phi_n'$.

2.4.2 Case $\overline{N}$ = constant

In the case where $\overline{N} = \overline{N_0} =$ constant, equation (13) reduces to that of a harmonic oscillator:

$$\Phi_n'' + m_n^2 \Phi_n = 0 \quad \text{with} \quad m_n^2 = \frac{\overline{N}_0^2}{\omega^2 - (\beta y_0)^2} k_h^2. \tag{15}$$

Combined with the boundary conditions (13), the vertical structure functions Φ_n can be expanded as a series of sine functions:

$$\Phi_n(z) = \sin(m_n z), \tag{16}$$

where $m_n = n\pi/H$, $n = 1, 2, ...$
Likewise,

$$\phi_n(z) = m_n \cos(m_n z). \tag{17}$$

Figure (2) shows the first three vertical structure functions for the case $\overline{N_0}^2 = 1 \times 10^{-4}$ s^{-2}, with H= 5000m.

From (15), the dispersion relation is given by

$$\omega^2 = \overline{N_0}^2 \left(\frac{k_h}{m_n}\right)^2 + (\beta y_0)^2. \tag{18}$$

Thus, specifying the frequency ω and mode number n of the initial waves gives the corresponding magnitude of the horizontal wavenumber k_h.

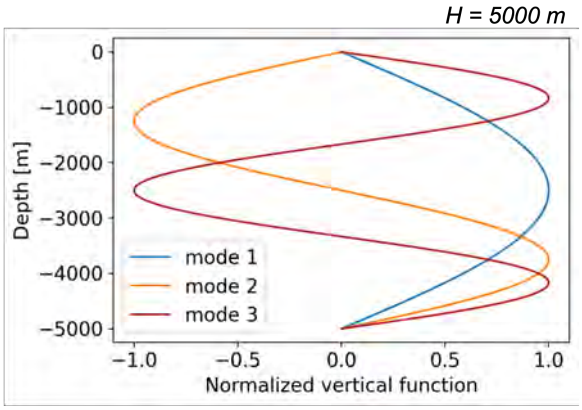

Figure 2: Three first vertical structure functions, Φ_n, for $\overline{N_0}^2 = 1 \times 10^{-4}$ s^{-2} and H= 5000m.

2.5 Ray-tracing theory

Ray tracing predicts the path of the wave energy, as it moves at the group velocity $\boldsymbol{c_g}$. For horizontal motion:

$$\boldsymbol{c_g} = \boldsymbol{\nabla_k}\,\omega = \left(\frac{\partial\omega}{\partial k_x}, \frac{\partial\omega}{\partial k_y}\right) \tag{19}$$

This is different from the phase velocity $\boldsymbol{c_p}$ that gives the velocity of the crests:

$$\boldsymbol{c_p} = \left(\frac{\omega}{|\boldsymbol{k}|}\right)\hat{\boldsymbol{k}} = \frac{\boldsymbol{k}}{|\boldsymbol{k}|^2}\omega, \tag{20}$$

In the long wave limit to be considered here, the group and phase velocity are in the same direction.

The addition of a mean flow $\boldsymbol{U} = U(y,z)\boldsymbol{e_x}$ will introduce a difference between the absolute frequency ω_0 and the intrinsic frequency ω_{int}, that are linked through:

$$\omega_0 = \omega_{\text{int}} + Uk_x, \tag{21}$$

where $\omega_0 = 1.4 \times 10^{-4}$ rad.s^{-1} is the excitation frequency of the M2 internal tide and ω_{int} the intrinsic frequency satisfies the dispersion relation for waves in stationary fluid. In all the expressions of sections 2.4.1 and 2.4.2 we replace $\omega \to \omega_{\text{int}}$.

In the absence of mean flow, (21) reduces to:

$$\omega_0 = \omega_{\text{int}}, \tag{22}$$

and ω_0 verifies the dispersion relation and all the results of sections 2.4.1 and 2.4.2.

As waves move inside the equatorial jet, it is necessary to separate:

- the absolute frequency ω_0, which is the frequency observed from the fixed frame: it is composed of the intrinsic frequency ω_{int} and a Doppler-shift that arise from the movement of the background fluid U;

- the intrinsic frequency ω_{int}, which is the frequency that corresponds to the frame moving with the mean-flow.

The separation between ω_0 and ω_{int} induced by the presence of the mean flow is inherited by the group velocity (19), such that:

$$c_{gx_0} = c_{gx_{\text{int}}} + U, \qquad c_{gy_0} = c_{gy_{\text{int}}} \tag{23}$$

where $(c_{gx_{\text{int}}}, c_{gy_{\text{int}}})$ are given by injecting the dispersion relation (18) in equation (19).

For ray tracing to be valid outside and inside of the jet, the vertical and horizontal scale of variations of the waves must be much shorter than the characteristic scale of background variations of N and U, respectively. The ray-tracing equations yield the evolution of the position of the wavepacket (x, y) and its direction (k_x, k_y):

$$\frac{\mathrm{d}x}{\mathrm{d}t} = \frac{\partial \omega_0}{\partial k_x} = c_{gx_{\text{int}}} + U, \qquad \frac{\mathrm{d}k_x}{dt} = -\frac{\partial \omega_0}{\partial x}, \tag{24a}$$

$$\frac{\mathrm{d}y}{\mathrm{d}t} = \frac{\partial \omega_0}{\partial k_y} = c_{gy_{\text{int}}}, \qquad \frac{\mathrm{d}k_y}{dt} = -\frac{\partial \omega_0}{\partial y}. \tag{24b}$$

For both cases (21) or (22), the dispersion relation yields:

$$\omega = \omega(k_x, k_y; y) = \omega_{\text{int}} + U k_x, \quad \omega_{\text{int}} = c_n^2 k_h^2 + (\beta y)^2. \tag{25}$$

which, combined with the right-equation of (24a) gives

$$k_x = k_{x_0} = \text{constant}. \tag{26}$$

The left hand equations of (24), gives the slope in the horizontal of the path:

$$\frac{\mathrm{d}x}{\mathrm{d}y} = \frac{c_{gx_{\text{int}}} + U}{c_{gy_{\text{int}}}} \tag{27}$$

Given the dispersion relation (25), k_y is implicitly a function of y, likewise $c_{gx} = \partial\omega_0/\partial k_x$ and $c_{gy} = \partial\omega_0/\partial k_y$ are implicitly functions of y.

If $U = E(y)$, independent of z, then (27) can be integrated to give the path starting at (x_0, y_0):

$$x(y) = \int_{y_0}^{y} \frac{c_{gx_{\text{int}}}(\tilde{y}) + E(\tilde{y})}{c_{gy_{\text{int}}}(\tilde{y})} \mathrm{d}\tilde{y} + x_0 \tag{28}$$

Ray tracing helps reveal how the β-plane and jet influence the dynamics of the wavepacket.

For example, ignoring the β-effect and supposing $U = E(y)$, (24b) yields

$$\frac{\mathrm{d}k_y}{dt} = -k_{x_0} E'(y). \tag{29}$$

Figure 3 shows how the results from this translate to wave dynamics. Variations of U change k_y affecting the wavelength and orientation of the wavepacket. If $E' > 0$, then k_y decreases. The wavepacket would contract and deviate away from northward (figure 3, bottom right). Ultimately, this could lead to total reflection. Conversely, if $E' < 0$ and k_y increases, the wavepacket would redirect more toward the north where $k_y \to \infty$ (figure 3, top panel) and this could encounter critical layers.

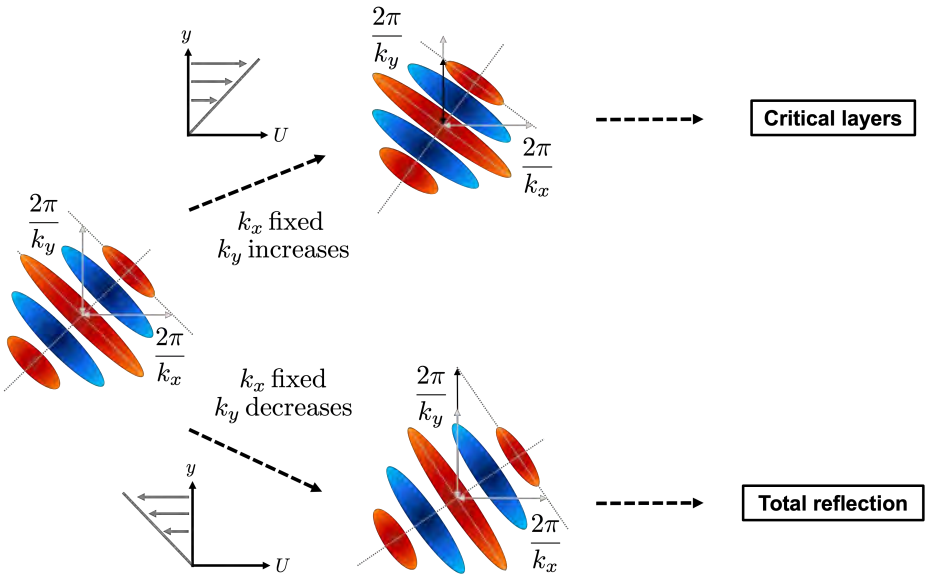

Figure 3: Schematics of the evolution of the wavepacket when interacting with a uniform jet ignoring the β effect. Initial situation is displayed in the center, with wavenumbers drawn in grey arrows. In the upper part, the wavepacket is incident upon a positive horizontal shear so that k_y increases while k_x stays fixed (black arrows), ultimately reacting to a critical layer where $k_y \to \infty$. In the lower part, the wavepacket is incident upon a negative horizontal shear and k_y decreases while k_x stays fixed (black arrows), ultimately leading to a total reflection of the wavepacket where $k_y \to 0$.

2.6 Modal wave equations

The modal wave equations are obtained by substituting the expansions (14) into the general equations (9). Multiplying (9a), (9b) and (9e) by ϕ_n, and (9c) and (9d) by Φ_n and integrating in the vertical, orthogonality allows us to extract the equations for the evolution of the amplitudes of each mode. Equation (9c) gives

$$0 = p_n + c_n^2 b_n \,, \tag{30}$$

and equation (9e) gives

$$\partial_x u_n + \partial_y v_n + w_n = 0. \tag{31}$$

These diagnostic equations are used to replace w_n and p_n in the remaining equations for horizontal velocity and buoyancy. From (9a):

$$\partial_t u_n + \sum_{m=0}^{\infty} \left(E \partial_x u_m C_{1_{mn}} + v_m E' C_{1_{mn}} + E'(y) w_m C_{2_{mn}} \right) - \beta y v_n - c_n^2 \partial_x b_n = 0, \tag{32}$$

where the interaction coefficients between the vertical structure of the modes and the vertical structure of the jet are given by

$$C_{1_{nm}} = \frac{\displaystyle\int_{-H}^{0} \tilde{U} \Phi_n' \Phi_m' \mathrm{d}z}{\displaystyle\int_{-H}^{0} (\Phi_n')^2 \mathrm{d}z} \quad \text{and} \quad C_{2_{nm}} = \frac{\displaystyle\int_{-H}^{0} \tilde{U}' \Phi_n' \Phi_m \mathrm{d}z}{\displaystyle\int_{-H}^{0} (\Phi_n')^2 \mathrm{d}z}. \tag{33}$$

From (9b), we find

$$\partial_t v_n + \sum_{m=0}^{\infty} \left(E \partial_x v_m C_{1_{mn}} \right) + \beta y u_n - c_n^2 \partial_y b_n = 0, \tag{34}$$

and from (9d),

$$\partial_t b_n + \sum_{m=0}^{\infty} \left[E \partial_x b_m C_{3_{nm}} + \beta W^2 E' v_m C_{4_{nm}} - \beta W^2 E (\partial_x u_m + \partial_y v_m) C_{5_{nm}} \right] - (\partial_x u_n + \partial_y v_n) = 0, \tag{35}$$

in which

$$C_{3_{nm}} = \frac{\displaystyle\int_{-H}^{0} \overline{N}^2 \tilde{U} \Phi_n \Phi_m \mathrm{d}z}{\displaystyle\int_{-H}^{0} \overline{N}^2 \Phi_n^2 \mathrm{d}z}, \quad C_{4_{nm}} = \frac{\displaystyle\int_{-H}^{0} \overline{N}^2 \tilde{U}' \Phi_n' \Phi_m \mathrm{d}z}{\displaystyle\int_{-H}^{0} \overline{N}^2 \Phi_n^2 \mathrm{d}z}, \quad \text{and} \quad C_{5_{nm}} = \frac{\displaystyle\int_{-H}^{0} \tilde{U}'' \Phi_n \Phi_m \mathrm{d}z}{\displaystyle\int_{-H}^{0} \overline{N}^2 \Phi_n^2 \mathrm{d}z}. \tag{36}$$

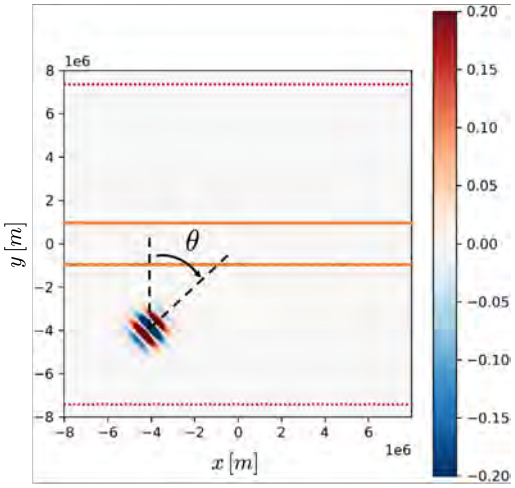

Figure 4: Initial condition in a typical simulation: the wavepacket is launched from the position (x_0, y_0) in the southern hemisphere at an angle θ from north. Jet limits at $y \pm 2\text{W}$ are shown by orange lines, sponge layers limits are shown by red dashed lines.

3 Numerical Methods

The equations for the mode amplitude evolution (32), (34) and (35) are solved using Dedalus [2]. The coefficients (33) and (36) are solved beforehand, using vertical modes Φ_n computed with the Galerkin method for a given stratification profile from (13), and a prescribed vertical profile $\tilde{U}$ for the jet.

The domain represents a patch of the Equatorial Pacific latitudinally centered on the equator. The domain is such that $x \in [-L_x; L_x]$ and $y \in [-L_y; L_y]$ where $(L_x, L_y) = (8000, 8000)\,\text{km}$ (figure (4)). It needs to be sufficiently large to allow the wavepacket to propagate toward the jet, interact with it and exit on the other size. The equator, specifically, is centered at $y = 0$. The equatorial jet uniformly spans the zonal direction. It is centered on the equator with an horizontal width of W=400 km. The domain is periodic in both x and y with zonally uniform sponge layers located near the north and south boundaries of the domain to prevent the waves crossing the top and bottom boundaries.

The resolution is set to $(N_x, N_y) = (512, 512)$ so that the wavelength of the internal tides are resolved by at least 16 grid points. The typical simulation duration is approximately 8.7 days: the number of iterations is fixed at 1500 with a timestep of $dt = 500\text{s}$ ensuring numerical stability of the CFL criterion. Viscosity is also added for numerical stability. It is fixed at $\nu = 1\ \text{m}^2\cdot\text{s}^{-1}$, though much larger than the viscosity of sea water, it is still small enough that dissipation of the waves is insignificant.

The dimensions of the domain are chosen to match the physics of the problem: the M2 internal tide has a forcing frequency of $\omega_0 = 1.4 \times 10^{-4}\ \text{rad.s}^{-1}$, with typical horizontal wavelengths having an order of magnitude $\sim$400 km ($k_h \sim 1.5 \times 10^{-5}\ \text{m}^{-1}$) and horizontal phase speeds $2\ \text{m}\cdot\text{s}^{-1}$. We are free to choose the orientation θ from north of initial horizontal

wavenumber vector $(k_x, k_y) = (k_h \sin\theta, k_h \cos\theta)$.

The model is tested here for a constant buoyancy frequency of $\overline{N}_0^2 = 1 \times 10^{-4}$ s^{-2}. Through the dispersion relation (18), for a mode 1 wave at $y_0 \ll -$W the resulting M2 horizontal wavelength is of order 600 km, a value on the larger side.

The wavepacket is initialized with inner oscillations of ω_0 fixed at the M2 forcing frequency (figure (4)). The effect of the rotation is included using $f = \beta y_0$. The envelope has a typical width of σ_x and σ_y with an amplitude fixed as $A_0 = 0.01 \times H$ with H the depth of the ocean previously used for computing the vertical modes. The wavepacket can be launched from different locations (x_0, y_0) and with various angles θ compared to the north.

The kinetic energy (KE), available potential energy (APE) and total energy (TE=KE+APE) of the different modes of the internal tides are computed numerically using the vertical mode decomposition:

$$\mathrm{KE}_n = \frac{1}{2}\int\int (u_n^2 + v_n^2)\mathrm{d}x\mathrm{d}y \int ({\Phi_n}^2)'\mathrm{d}z, \tag{37}$$

$$\mathrm{APE}_n = \frac{1}{2\overline{N}_0^2}\int\int b_n^2\mathrm{d}x\mathrm{d}y \int \overline{N}_0^2{\Phi_n}^2\mathrm{d}z. \tag{38}$$

The total energy budget is also computed:

$$\partial_t(KE + APE) = -uv\partial_y U - uw\partial_z U - \frac{1}{\overline{N}^2}bv\partial_y B - \frac{1}{\overline{N}^2}bw\partial_z B, \tag{39}$$

where the two first terms of the right hand side correspond to shear production and the two others to buoyancy production.

4 Results for the Model $\overline{\mathrm{N}}_0$ = Constant

4.1 No Equatorial jet

4.1.1 Trajectories and dynamics

The model is first tested without any equatorial jet, to check the propagation of the wavepacket and the influence of the rotation on its dynamics through the beta-plane approximation. In all that follows, the buoyancy frequency is kept constant, at $\overline{N_0}^2 = 1 \times 10^{-4}$ s^{-2}. In that case, (32), (34) and (35) reduce to decoupled equations for each mode:

$$\partial_t u_n - \beta y v_n - c_n^2 \partial_x b_n = 0, \tag{40a}$$

$$\partial_t v_n + \beta y u_n - c_n^2 \partial_y b_n = 0, \tag{40b}$$

$$\partial_t b_n - (\partial_x u_n + \partial_y v_n) = 0, \tag{40c}$$

where $c_n^2 = (\omega_0^2 - (\beta y)^2)/k_h^2$.

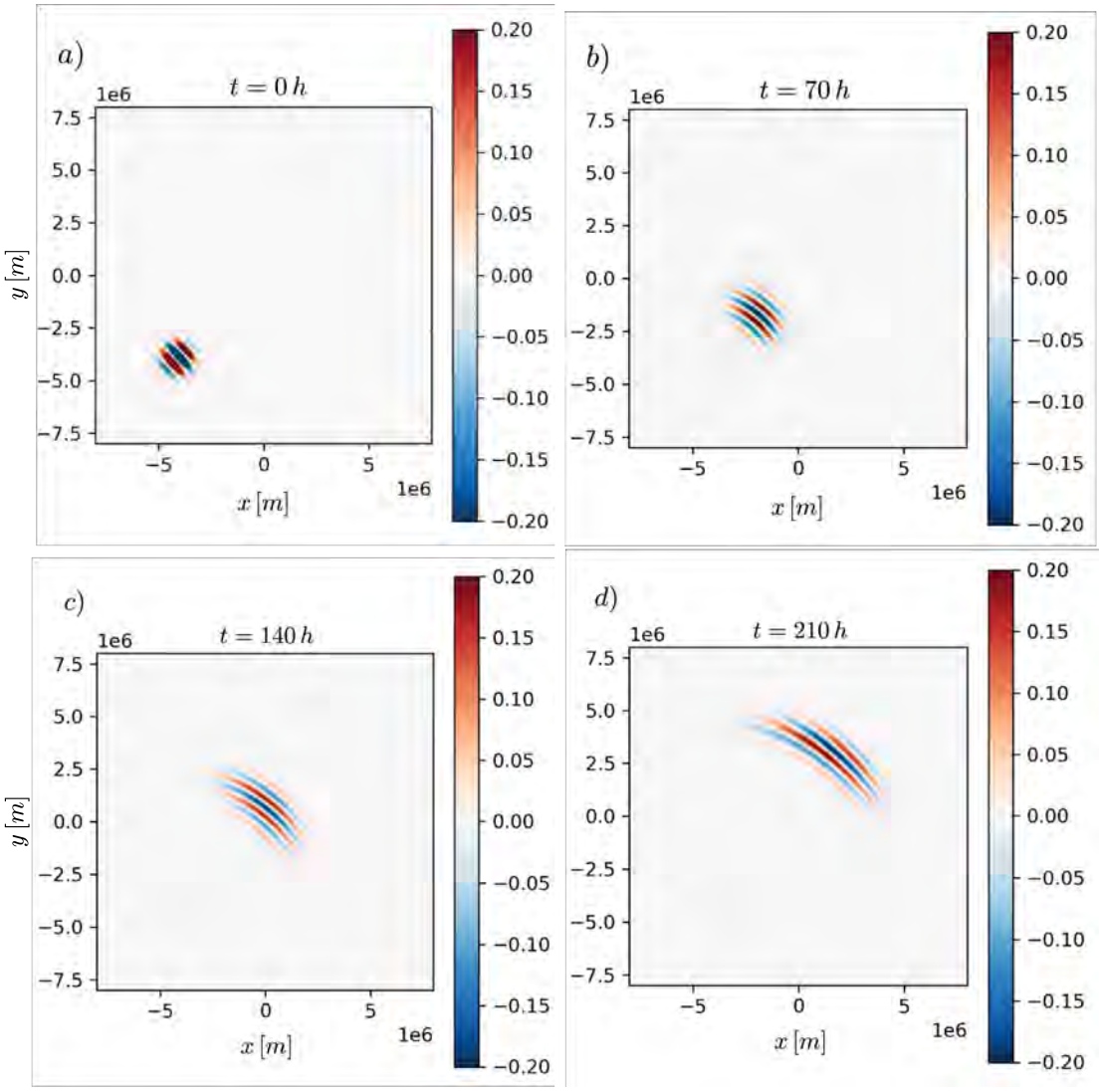

Figure 5: Zonal velocity ($\mathrm{m{\cdot}s^{-1}}$) of vertical mode 1 M2 internal tide. The wavepacket is launched from $(x_0, y_0) = (-0.5\,L_x, -0.5\,L_y)$ with $\theta = \pi/4$.

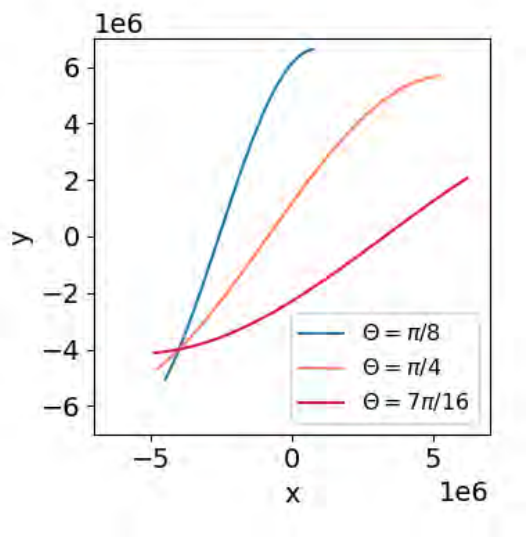

Figure 6: Trajectories computed using ray tracing for different angles of launch θ.

For a mode 1 wave ($n = 1$), c_1 is fixed. Setting $\omega_0 = 1.4 \times 10^{-4}$ rad.s^{-1} yields the initial wavenumber $k_{h0} = 7.2 \times 10^{-6}$ m^{-1}.

Figure (5) shows the evolution of a wavepacket, launched from $(x_0, y_0) = (-Lx/2, -Ly/2) = (-4000, -4000)$km with an angle of $\theta = \pi/4$ and $\sigma_x = \sigma_y = 500$ km. As such, the wavepacket is quasi-monochromatic, with $\sigma k_{h0} \gg 1$. As it crosses the domain, its trajectory is slightly deviated. It is also subjected to significant dispersion due to the limited number of wavelengths composing it. The measurements over time in simulations yield values around $c_p = 27\text{m}\cdot\text{s}^{-1}$ and $c_g = 9\text{m}\cdot\text{s}^{-1}$ for the mode 1.

4.1.2 Ray tracing

The ray-tracing analysis (see section 2.5 with $\omega_{\text{int}} = \omega_0$) can help disentangle the effect of the rotation over the wavepacket. In the β-plane approximation, the trajectory of the wavepacket can be computed using (28) with $E(y) = 0$:

$$x(y) = \frac{1}{\sqrt{C_1 \beta^2}} \operatorname{atan}\left(\frac{y}{\sqrt{C_2 - y^2}}\right), \tag{41}$$

with:

$$C_1 = \frac{\pi^2}{H^2 k_{x_0}^2 (\overline{N_0}^2 - \omega_0^2)}, \quad \text{and} \quad C_2 = \frac{1}{\beta^2}\left(\omega_0^2 - \frac{1}{C_1}\right) \tag{42}$$

This expression is valid provided:

$$y^2 < C_2 = \frac{\omega_0^2}{\beta^2} - \frac{1}{C_1 \beta^2} \tag{43}$$

The effect of the rotation and the influence of the initial angle of launch both directly influence the trajectory of the wavepacket through (41).

Figure (6) shows the expected trajectories for angles of $\theta = \pi/4$, $\theta = \pi/8$ and $\theta = 7\pi/16$. Rotation is responsible for the observed deviation of the trajectories. This effect also tends to disappear as the wavepacket approaches and crosses the Equator (where βy goes to zero).

Figure (7) shows the superposition of the computed trajectory with an initial angle of $\theta = 7\pi/16$ and the simulation. Both are in good agreement and illustrate how ray tracing succeeds in predicting the path of the wavepacket due to the rotation.

4.1.3 Energetics

In addition to the numerical computation (37), KE was computed analytically:

$$\mathrm{KE}_1 = \frac{\pi}{16}\mathrm{A}_0^2\sigma_x\sigma_y\left(\overline{N}^2 + 2\,\frac{m_1^2}{k_h^2}(\beta y)^2\right), \tag{44}$$

Equation (44) shows how rotation directly acts as a source term of kinetic energy for internal tides.

Figure (8) shows the total energy (TE; left panel), kinetic energy (KE; middle panel) and available potential energy (APE; right panel) of the first mode of the internal tide corresponding to the case in figure (5). As only the first mode is initialized and because there is no jet to create new modes, all the wave energy is present in the first mode. The steady decrease of total energy (figure (8), left panel) is explained by the dissipation added to guarantee numerical stability (fixed at $\nu = 1$ m·s^{-2}). Over the time of the simulation, the loss of energy due to viscosity is $\sim$1% initial energy. The kinetic energy (figure (8), middle panel) first decreases as the wavepacket approaches the Equator as a result of the term due to rotation in (44) tending to zero. Once the tide has crossed the Equator, the effect of rotation increases and KE increases again. APE (figure (8), right panel) changes as KE changes to keep the total energy nearly constant. In particular, at the Equator (here at $t \sim 90$h), equipartition of the energy between KE and APE is reached.

4.2 Vertically uniform equatorial jet

4.2.1 Jet configuration and M2 dynamics

The equatorial jet is added, centered on $y = 0$ with a characteristic width of W = 400 km and is uniform in the vertical:

$$U = U_0 \exp\left(-\frac{y^2}{2\mathrm{W}^2}\right). \tag{45}$$

The strength of the jet and its direction is fixed by the value taken for U_0 (positive eastward and negative westward).

Following (45), the equations (32), (34) and (35) become:

$$\partial_t u_n + EU_0\partial_x u_n + v_n E' U_0 - \beta y v_n - c_n^2\partial_x b_n = 0, \tag{46a}$$

$$\partial_t v_n + EU_0\partial_x v_n + \beta y u_n - c_n^2\partial_y b_n = 0, \tag{46b}$$

$$\partial_t b_n + EU_0\partial_x b_n - (\partial_x u_n + \partial_y v_n) = 0. \tag{46c}$$

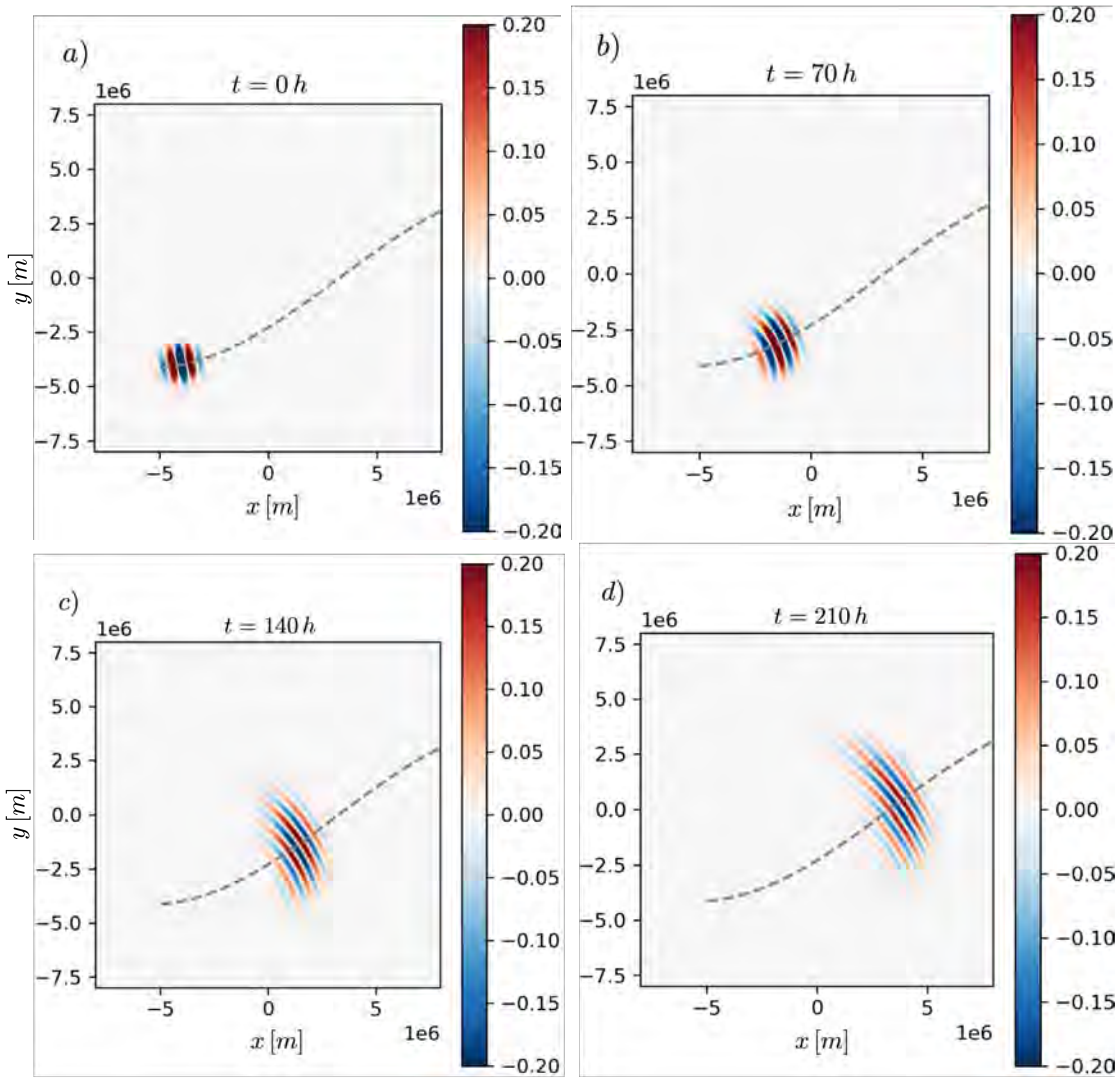

Figure 7: Colors: zonal velocity ($\mathrm{m{\cdot}s^{-1}}$) of vertical mode 1 M2 internal tide. The wavepacket is launched from $(x_0, y_0) = (-0.5\,L_x, -0.5\,L_y)$ with $\theta = 7\pi/16$. Grey dashed lines: trajectory computed using ray tracing.

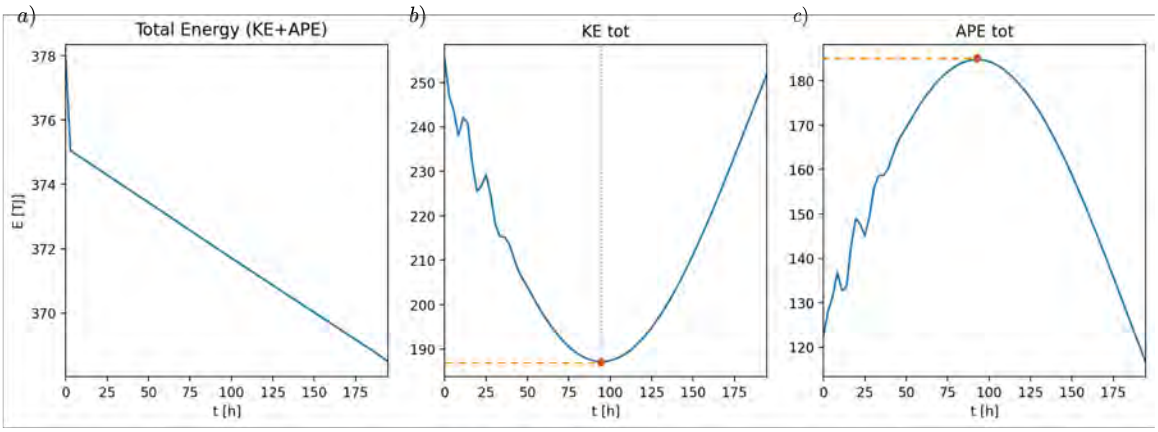

Figure 8: a) Total energy, b) kinetic energy, c) available potential energy; all computed for the simulation presented in figure (5).

Again the lack of vertical structure to U decouples the mode-mode interactions. The added terms show that the flow mostly contributes to the advection of the wave. Only the term $v_n E' U_0$ in (46a) contributes to the interaction between the perturbations and the mean flow gradient.

4.2.2 Ray tracing

The trajectories of the wavepacket can be predicted with ray tracing (see section 2.5, with $\omega_0 = \omega_{\text{int}} + Uk_x$). As the jet is located at the equator, where the rotation through the β-plane approximation is negligible, the Coriolis force is not included; $\omega_0 = \omega_{\text{int}}(k_x, k_y) + Uk_x$ with $\omega_{\text{int}}(k_x, k_y)$ the dispersion relation (18), which is then independent of y. Using (28), we find

$$x(y) = k_{x_0}\left(\frac{c_{gx_{\text{int}}}}{c_{gy_{\text{int}}}}y + \frac{1}{c_{gy_{\text{int}}}}\sqrt{\frac{\pi}{2}}\mathrm{W}\,\mathrm{erf}\left(\frac{y}{\sqrt{2}\mathrm{W}}\right)\right) \tag{47}$$

The trajectories for two jets of opposite direction (U_0=-5 m·s^{-1} and U_0=5m·s^{-1}) are shown in figure (9). These results are valid only inside the jet, where the effect of the rotation is negligible. Depending on the direction of the jet and its intensity, the trajectory of the wavepacket is diverted in the direction opposite (case U_0=-5) or toward ($U_0 = 5$) the direction propagation.

Figures (10) and (11) show two cases where the initial point of the wavepacket and its angle of launch ($(x_0, y_0) = (-7L_x/8, -L_y/2)$ and $\theta = 7\pi/16$) have been optimized to maximize the interactions with the jet. The jet is also stronger in both cases to enhance the effect. For a jet of $U_0 = -6$ m·s^{-1} (figure 10), the crests are strongly diverted in the direction of the current. When approaching this level, the increase in k_y (smaller meridional wavelength) means the simulation under-resolves the waves. Conversely, for $U_0 = 6$ m·s^{-1} (figure 11), the wavepacket largely reflects.

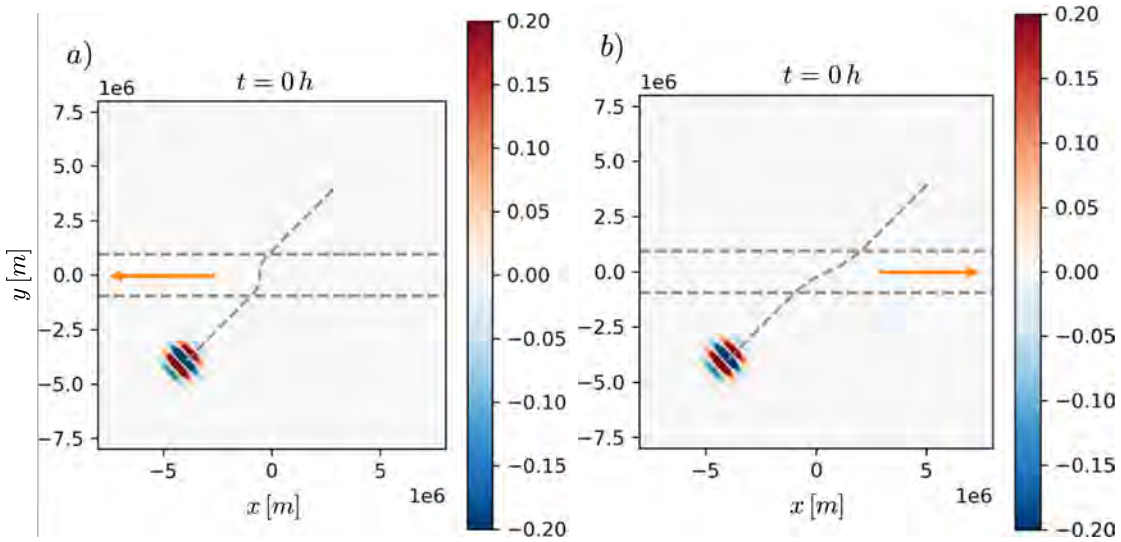

Figure 9: Zonal velocity ($\mathrm{m{\cdot}s^{-1}}$) of vertical mode 1 M2 internal tide. The wavepacket is launched from $(x_0, y_0) = (-0.5\,L_x, -0.5\,L_y)$ with $\theta = \pi/4$. Trajectory computed using ray tracing shown by oblique grey dashed lines. Jet limits are denoted by horizontal grey dashed lines. Jet is uniform on the vertical with maximum amplitude set at $\mathrm{U_0} = 5\mathrm{m{\cdot}s^{-1}}$, its direction varies according to the orange arrow: a) westward and b) eastward.

4.2.3 Energetics

Figure (12) shows the total energy (TE; left panel), kinetic energy (KE; middle panel) and available potential energy (APE; right panel) of the mode 1 wavepacket with no jet as in figure (8), also with a simulation computed with a westward jet having $\mathrm{U_0}$=-1 $\mathrm{m{\cdot}s^{-1}}$ (grey dashed profiles). Because in both cases the dynamics do not involve higher modes, the total wave energy is contained in mode 1.

The interaction between the jet and the wave causes the total energy of the wavepacket to rise significantly as it enters the jet (around $t \sim 60$h), but the process reverses before the wavepacket exits the jet (around $t \sim 160$h). This reversal of the energy transfer occurs after the wavepacket crosses the Equator at around $t \sim 95$ h.

As no evolution of the jet or feedback from the jet is included into the model, the total energy is not conserved (in addition to the effect of dissipation, as shown in figure (12a)). In such configuration, it is the wave action $\mathcal{A} = \mathrm{TE}/\omega_{\mathrm{int}}$ that is conserved, provided that there is a scale separation between the wave and the jet.

Outside of the jet, where $\omega_{\mathrm{int}} = \omega_0$, TE is given by:

$$\mathrm{TE} = \mathcal{A}\,\omega_0, \tag{48}$$

where ω_0 is fixed at the excitation frequency of the M2 internal tide and $\mathcal{A}$ is affected by the dissipation, causing the initial decrease observed in figure (12a).

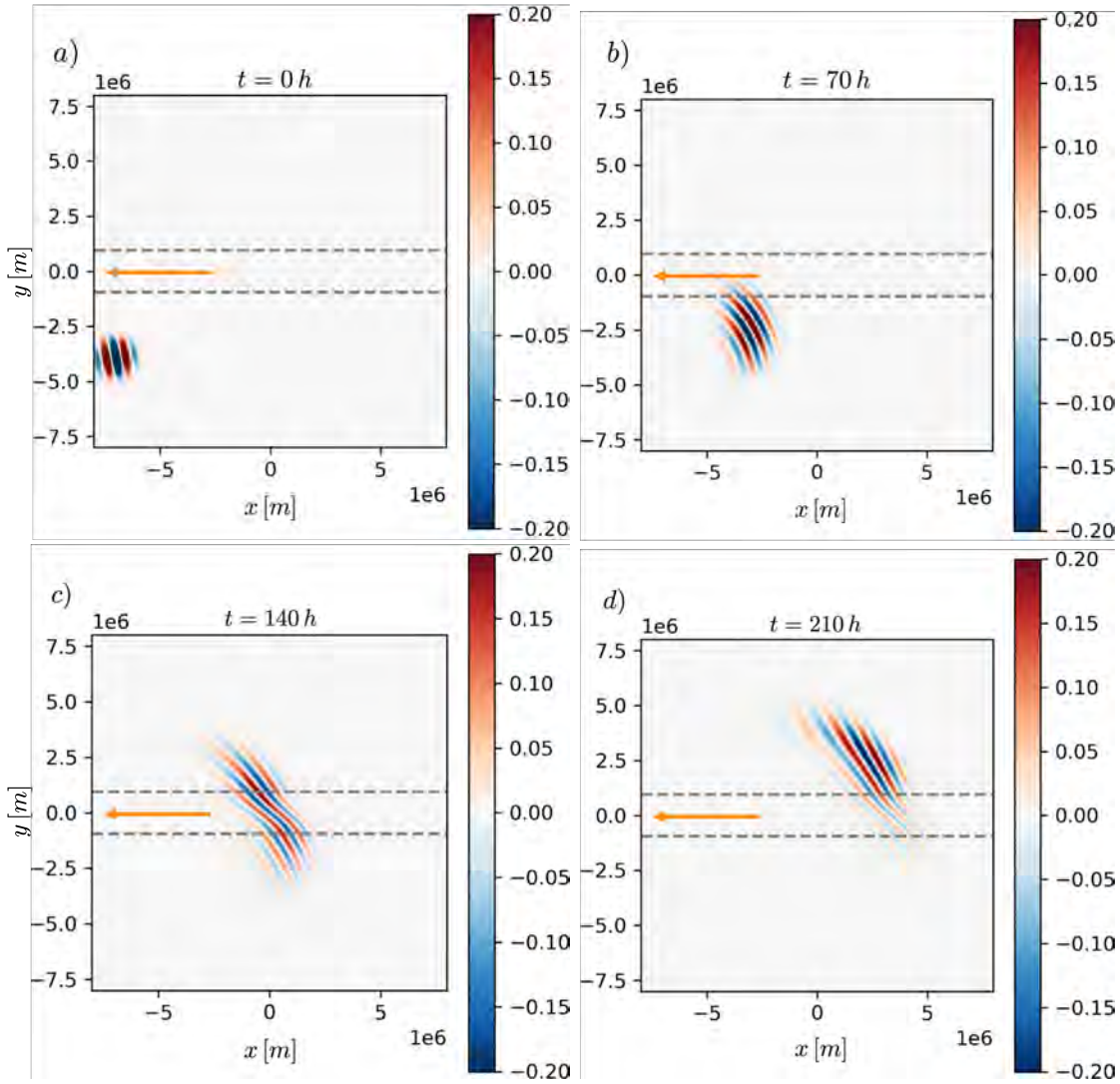

Figure 10: Zonal velocity ($\mathrm{m{\cdot}s^{-1}}$) of vertical mode 1 M2 internal tide. The wavepacket is launched from $(x_0, y_0) = (-0.9\,L_x, -0.5\,L_y)$ with $\theta = 7\pi/16$. Jet limits are denoted by horizontal grey dashed lines, its direction by the orange arrow. Jet is uniform on the vertical with $\mathrm{U_0} = -6\mathrm{m{\cdot}s^{-1}}$.

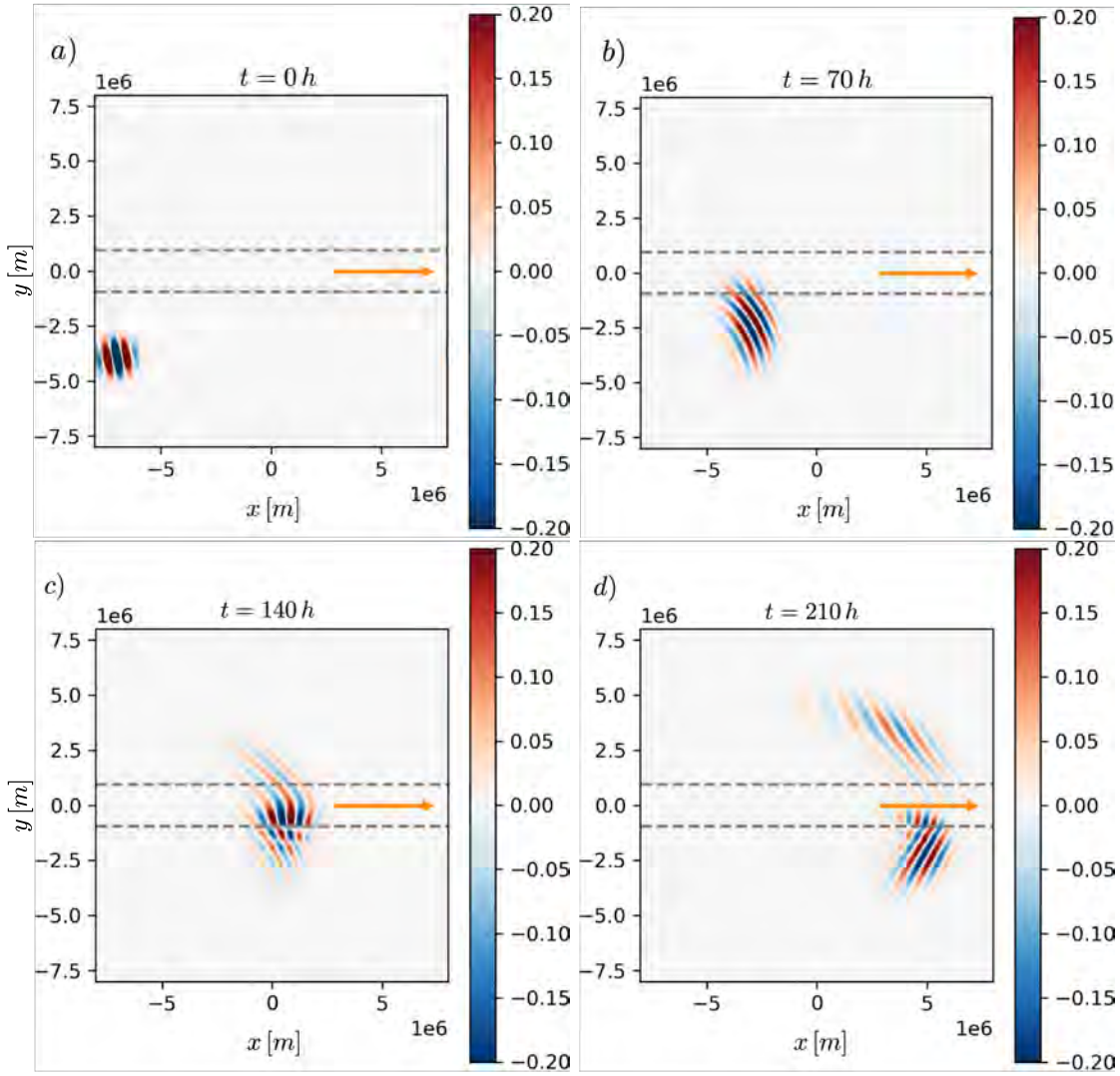

Figure 11: Zonal velocity ($\mathrm{m{\cdot}s^{-1}}$) of vertical mode 1 M2 internal tide. The wavepacket is launched from $(x_0, y_0) = (-0.9\,L_x, -0.5\,L_y)$ with $\theta = 7\pi/16$. Jet limits are denoted by horizontal grey dashed lines, its direction by the orange arrow. Jet is uniform on the vertical with $\mathrm{U_0} = 6\mathrm{m{\cdot}s^{-1}}$.

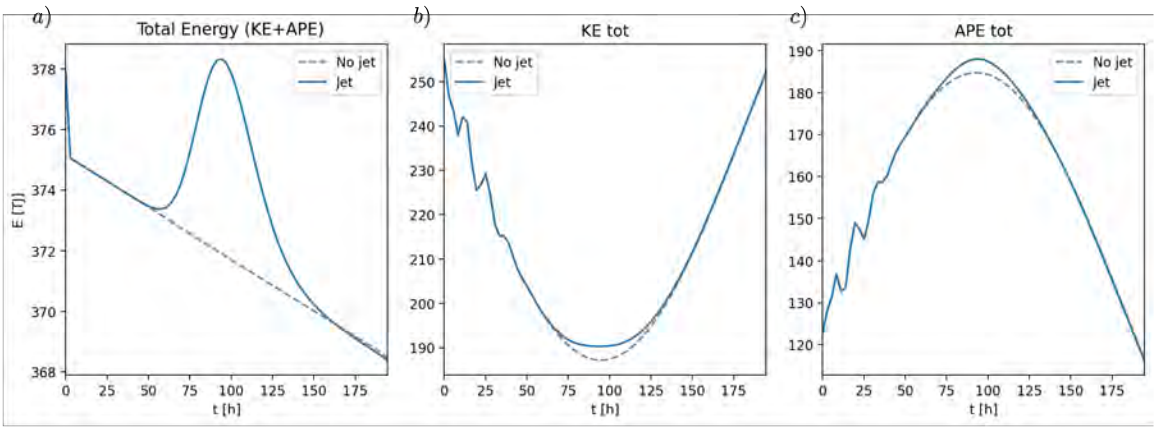

Figure 12: a) Total energy, b) kinetic energy, c) available potential energy. Blue profiles correspond to the case with no jet, grey dashed lines for the jet uniform on the vertical with amplitude U_0=-1 m·s^{-1}.

Inside the jet $\omega_{\text{int}} = \omega_0 - E(y)k_{x0}$. With $E(y) < 0$ as is the case in figure (12), ω_{int} increases to a maximum before decreasing back to ω_0 as the wavepacket exits the jet. As

$$\text{TE} = \mathcal{A}(\omega_0 - E(y)k_{x0}), \tag{49}$$

it means that, superimposed to the steady decrease caused by dissipation, TE first increases to a maximum due to wave/jet interactions before decreasing back to the value imposed by the dissipation when the wavepacket exits the jet.

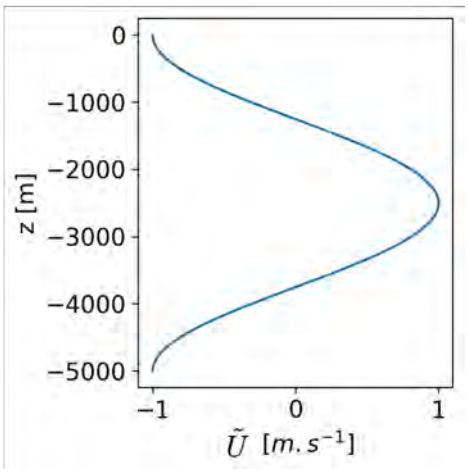

Figure 13: Vertical structure $\tilde{U}$ of the jet as described in (50).

4.3 Vertical mode 2 equatorial jet

4.3.1 Jet configuration and M2 dynamics

The horizontal structure of the equatorial jet is kept identical but its vertical structure corresponds to a vertical mode 2 ($n = 2$):

$$U(y,z) = U_0 \cos(m_n z) \exp\left(-\frac{y^2}{2\mathrm{W}^2}\right), \tag{50}$$

where $m_n = 2\pi/H$, $U_0 = -1$ m·s^{-1}, W = 400 km and $H = 5$ km.

The sheared vertical structure of the jet is displayed in figure (13) and represents an idealised equatorial jet: westward at the top and bottom of the ocean but eastward in the center of the ocean.

With the jet sheared in the vertical, the model is driven by the modal equations (32), (34), (35) with non-trivial interactions coefficients. Equations (33) and (36) also become non-trivial, representing the interactions between the vertical modes of the waves. In particular, for a jet with a vertical mode 2 structure, the coefficients have non-zero values for the wave modes $m = n - 2$ and $m = n + 2$, except for the case $n = 1$ which has also a non-zero interaction coefficient with itself ($m = n = 1$).

Despite this, the evolution of the vertical mode 1 M2 internal tide is qualitatively similar to the cases with no jet or with a vertically uniform jet. For example, the evolution shown in figure (14) should be compared with figure (7) that has no jet.

Higher modes are excited, but at much smaller amplitudes than mode 1. Figure (15) shows how, the mode 1 wavepacket, when propagating inside the jet, generates mode 3 with smaller amplitude less than 10% that of the mode 1 wave. This higher mode propagates inside the jet, in the same direction as the incident wave. It eventually decays, giving its energy back

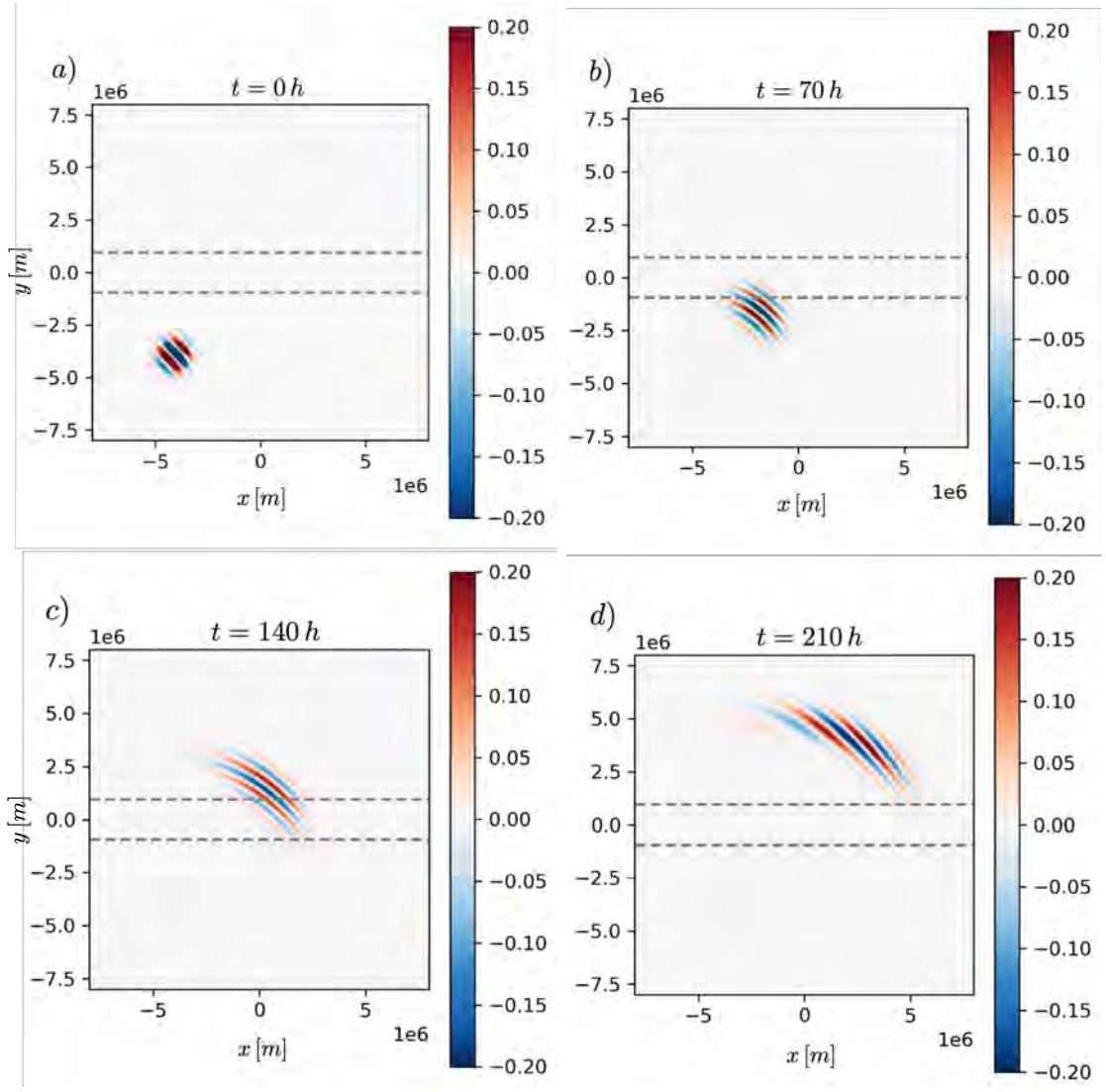

Figure 14: Zonal velocity ($\mathrm{m{\cdot}s^{-1}}$) of vertical mode 1 M2 internal tide. The wavepacket is launched from $(x_0, y_0) = (-0.5\,L_x, -0.5\,L_y)$ with $\theta = \pi/4$. Jet limits are denoted by horizontal grey dashed lines, with a structure as in (50).

to mode 1 as the mode 1 leaves the jet. Such behaviour is also observed with higher modes, modes 5, 7, 9,..., all created inside the jet with smaller and smaller amplitudes and vanishing as the mode 1 wavepacket leaves the jet.

For the case treated here (where N is constant) and near the equator where $\beta|y| \sim 0$, the phase and group speeds are inversely proportional to the mode number. As a result, the wavepacket envelope as well as the crests of higher modes are slower than those of the initial mode 1. For example, for $\theta = \pi/4$, the mode 1 velocities are $c_{p1} = 27\text{m}\cdot\text{s}^{-1}$ and $c_{g1} = 9\text{m}\cdot\text{s}^{-1}$, whereas the mode 3 has $c_{p3} = 9\text{m}\cdot\text{s}^{-1}$ and $c_{g3} = 3\text{m}\cdot\text{s}^{-1}$.

These higher modes also have smaller horizontal wavelengths (the wavenumbers grow with the mode number), which would cause then to be more susceptible to dissipation and encountering critical layers. Numerically it means that the number of modes solved for is limited (to 10 in our case) as well as the maximum velocity of the jet.

4.3.2 Energetics

Figure (16) shows the total energy of the wavepacket (left panel) for the case with the mode 2 jet, first for all the vertical modes (dark blue profile), then for the mode 1 only (light blue profile). The case with no jet has also been added (grey dashed line). Compared to the variation caused by the wave-mean flow interaction, the difference brought by the creation of the higher modes is small. However, looking at the middle panel figure (16) that represents the difference between the total energy of all the modes and that of mode 1, shows that this difference still accounts for more than 200 MJ and develops only when the M2 internal waves crosses the jet. In the right panel of figure (16), this difference in the total energy is mostly explained when also adding the total energies of mode 3 and mode 5. As such, it shows how the higher modes created inside the jet are the result of the scattering of the energy from mode 1 to the modes of higher order, made possible by the interaction with the jet's non-uniform vertical structure.

The difference between the total energy and the energy of the mode 1, due to the scattering of energy to higher modes, is observed to decay at later times, when the wavepacket exits the jet, it corresponds to the vanishing of the higher modes signal observed in figure (15). This scattered energy is returned to the mode 1, as observed for the energy of the wave-mean flow interaction in figure (12). Also, successive higher modes created receive less and less energy, as their amplitudes decrease with mode number.

The left panel of figure (17) shows the total energy of the mode three, which is the first to be created through wave-mean flow interactions and also the higher mode that receives the most energy. The comparison with the case without the jet is added in grey dashed lines to show how the creation is only possible with the addition of the vertically mode 2 jet. The middle panel of figure (17) presents only the kinetic energy of the mode 3. It demonstrates how the scattering of energy to the higher modes is realised through the growth of kinetic energy as it nearly accounts for the all of the mode's energy in comparison to the previous panel. The right panel of figure (17) shows the kinetic energy of all the higher

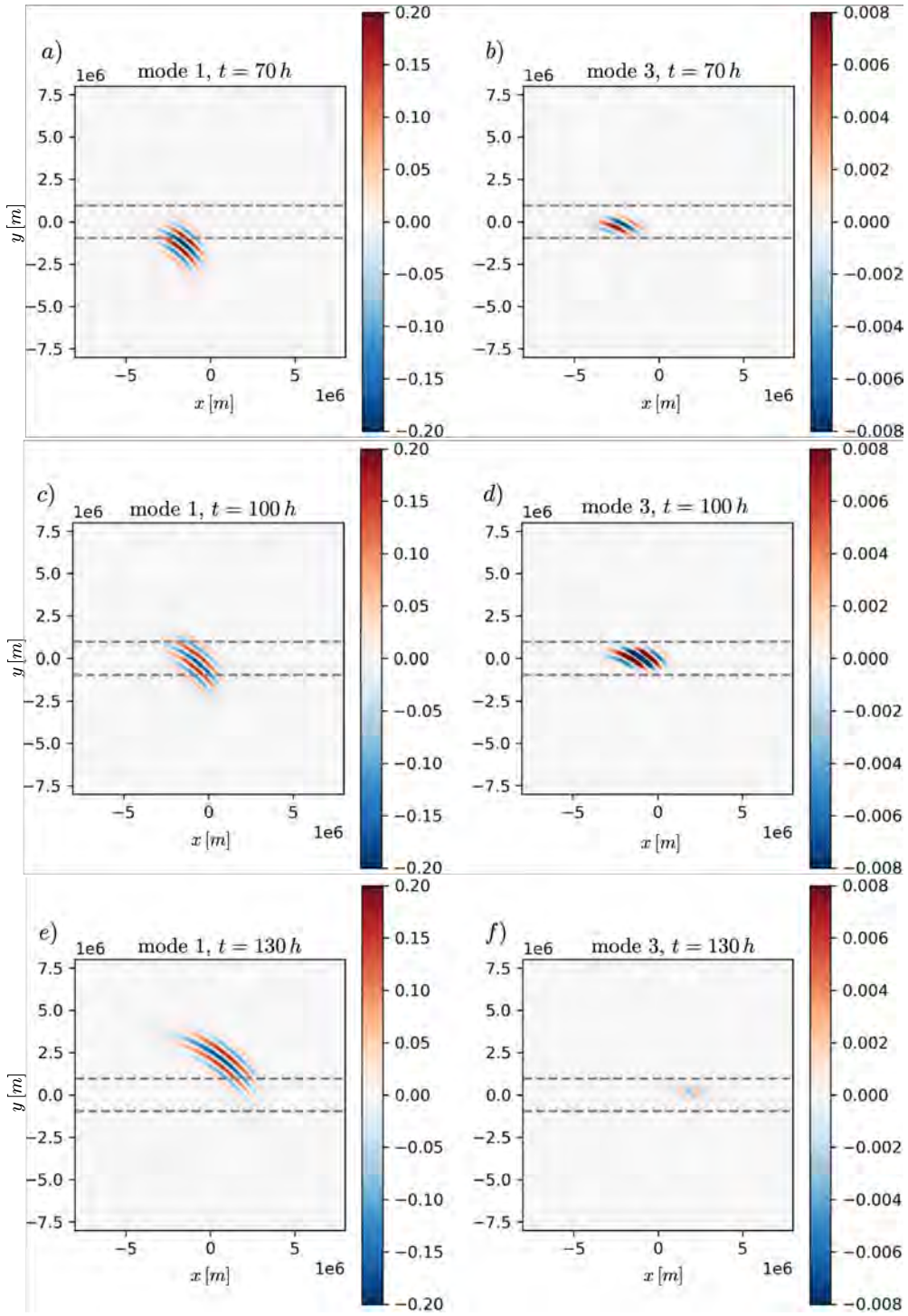

Figure 15: Zonal velocity ($\mathrm{m{\cdot}s^{-1}}$) of vertical mode 1 (panels a), c), e)) and mode 3 (panels b), d), f)) M2 internal tide. The wavepacket is launched from $(x_0, y_0) = (-0.5\,L_x, -0.5\,L_y)$ with $\theta = \pi/4$. Jet limits are denoted in grey dashed lines, with a structure as in (50).

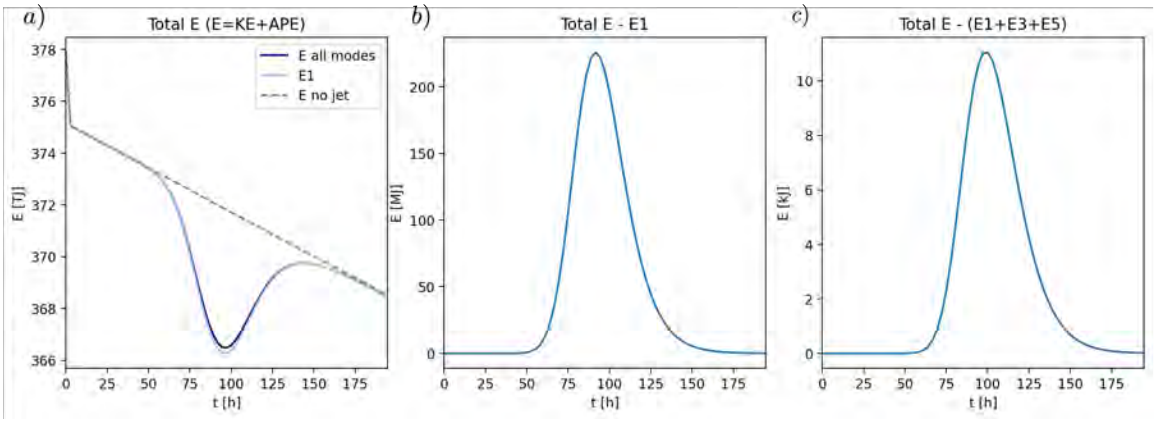

Figure 16: a) Total energy. Grey dashed profile corresponds to the case with no jet, light blue to the total energy of mode 1 with the sheared jet and darker blue to the total energy of all the modes combined, in the case of the sheared jet. b) difference between the total energy in the domain and the total energy of the mode 1. c) difference between the total energy in the domain and the total energy of the modes 1, 3 and 5 combined.

modes created (the maximum number of vertical modes solved for here is 10), normalised by their maximum value. It shows how the modes are created subsequently, mode 3 then mode 5, 7 and 9. The reverse transfer of energy toward mode 1 then occurs in the inverse order, mode 9 being the first to give all its energy back to mode 7 then mode 7 to mode 5 and so forth to mode 1. This effect is somewhat masked by the normalisation (right panel of figure (17)) as it shows that mode 9 seems to be the last to vanish. However, mode 9 represents so little energy compared to mode 3, that the tail of the distribution of mode 3 (around $t \sim 160$) still contains more of the total energy than what is distributed amongst the higher modes. The last mode to transfer its energy to mode 1 is then effectively mode 3.

Figure (18) shows the evolution of each term of the energy budget (39). The dominant terms are those of shear production (blue and orange profiles), related to the horizontal and vertical shear of the mean flow. Both shear contributions change sign after the wavepacket crosses the Equator. The part due to the vertical shear of the mean flow constitutes the biggest contribution to the energy budget as the shear is more intense being localised over the 5 km depth, as opposed to the 400 km of width the equatorial jet. The terms of buoyancy production do not contribute to the evolution of the total energy.

4.3.3 Possible incoherence?

Coming back to the motivating question, we want to check if the wave-mean flow interaction could explain the lack of observed M2 internal tide signal in the Equatorial Pacific [1].

We found the overall propagation of the tidal mode 1 negligibly changes with or without a sheared jet (figure (5) and (14)) and the processes related to the excitation of higher modes reverse when the wavepacket exits the jet (see section 4.3). To check if there are any differences due to the interaction with and without a jet, we assess wave incoherence, from

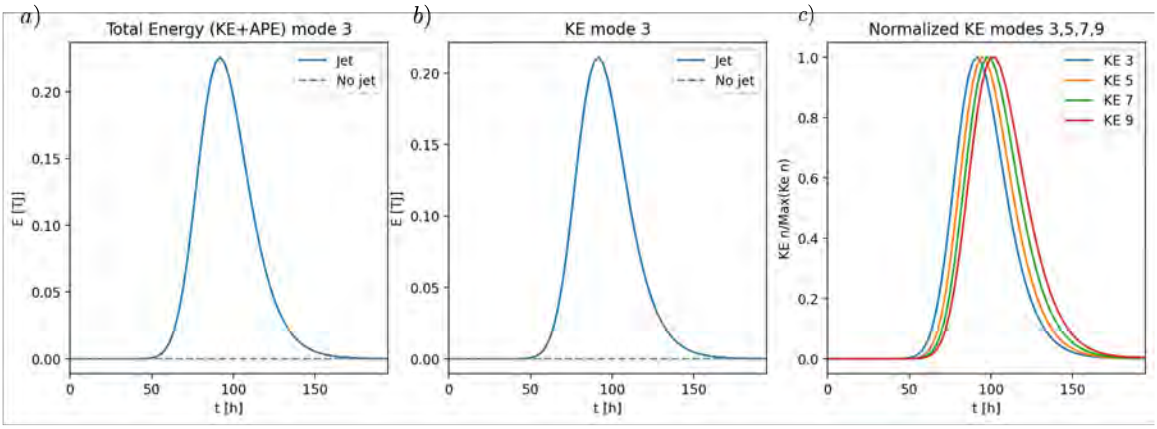

Figure 17: a) Total energy of mode 3. Grey dashed profile corresponds to the case with no jet and blue profile to the sheared jet case. b) kinetic energy of mode 3. c) kinetic energy of modes 3 (blue), 5 (orange), 7 (green) and 9 (red), normalized by their maximum values respectively.

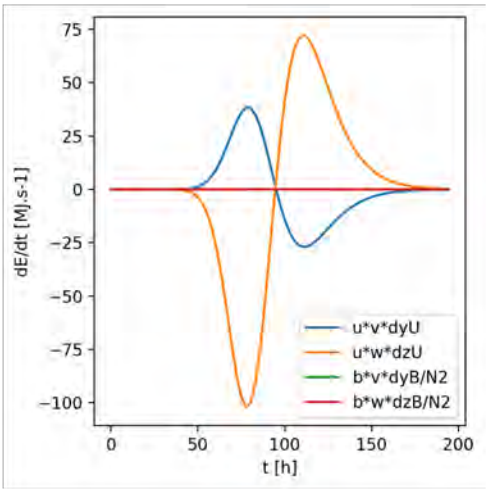

Figure 18: Variation of the different terms of the energy budget, as computed in (39).

the difference between the case with the mode 2 jet and the case with no jet.

Figure (19) shows how a difference in the dynamics is indeed created by the addition of the sheared jet. The difference only becomes significant when the wavepacket enters the jet and grows as long as both interact. The difference remains after the wavepacket is well north of the jet. This is unlike the dynamics and energy transfer observed for the creation of higher modes and it points toward the creation of lasting incoherence due to the wave-mean flow interaction.

Figure (20) is a schematic representation of our interpretation of such incoherence. As the mode 1 wavepacket enters the vertically sheared jet, energy is scattered toward higher modes. These modes propagate at a speed that is lower than that of mode 1 (both the group and phase speed are lower the higher the mode number). When the reverse transfer of energy occurs as the wavepacket propagates north of the Equator, the energy is transferred back to mode 1, but with a shift caused by the difference of phase speeds. The mode 1 wavepacket thus becomes phase shifted, creating incoherence in the internal tide signal. This incoherence is a possible explanation of the lack of internal tide signal detected north of the equator in the Equatorial Pacific [1].

5 Conclusion

We have investigated, by means of theory and numerical simulations within a idealised setup, the wave-mean flow interaction between a mode 1 M2 internal tide and a vertically uniform and sheared equatorial jet. The aim was to validate if such interactions could result in incoherence and hence explain the lack of M2 altimetry signal in the Equatorial Pacific.

We have identified different effects that can influence the dynamics of the M2 wavepacket. The β-effect deflects the path of the wavepacket but has negligible influence immediately at the Equator. A vertically uniform jet could, depending on its strength, lead to total reflection of the wavepacket or strong distortion of the crests. A vertically sheared jet, however, scatters energy to higher modes. These higher modes have smaller horizontal wavelength but also lower phase and group speed. The transfer of energy is reversed after the wavepacket crosses the Equator, the higher modes vanishing and all the energy going back into mode 1. It is the difference of propagation speed between the different modes that could explain the creation of incoherence in the signal, that would affect the altimetry observations [1].

Because of their smaller horizontal wavelength and lower phase and group speed, the higher modes excited by the jet are likely to be more sensitive to dissipation, but also to critical layers in a case where N is not constant. It could cause further deposition of energy inside the jet and hence modify its dynamics as well as that of the wavepacket. It is an effect that we will develop further in future work.

The theoretical tools developed here are readily adapted to realistic profiles of stratification and equatorial currents. In particular, future work will model stratification motivated

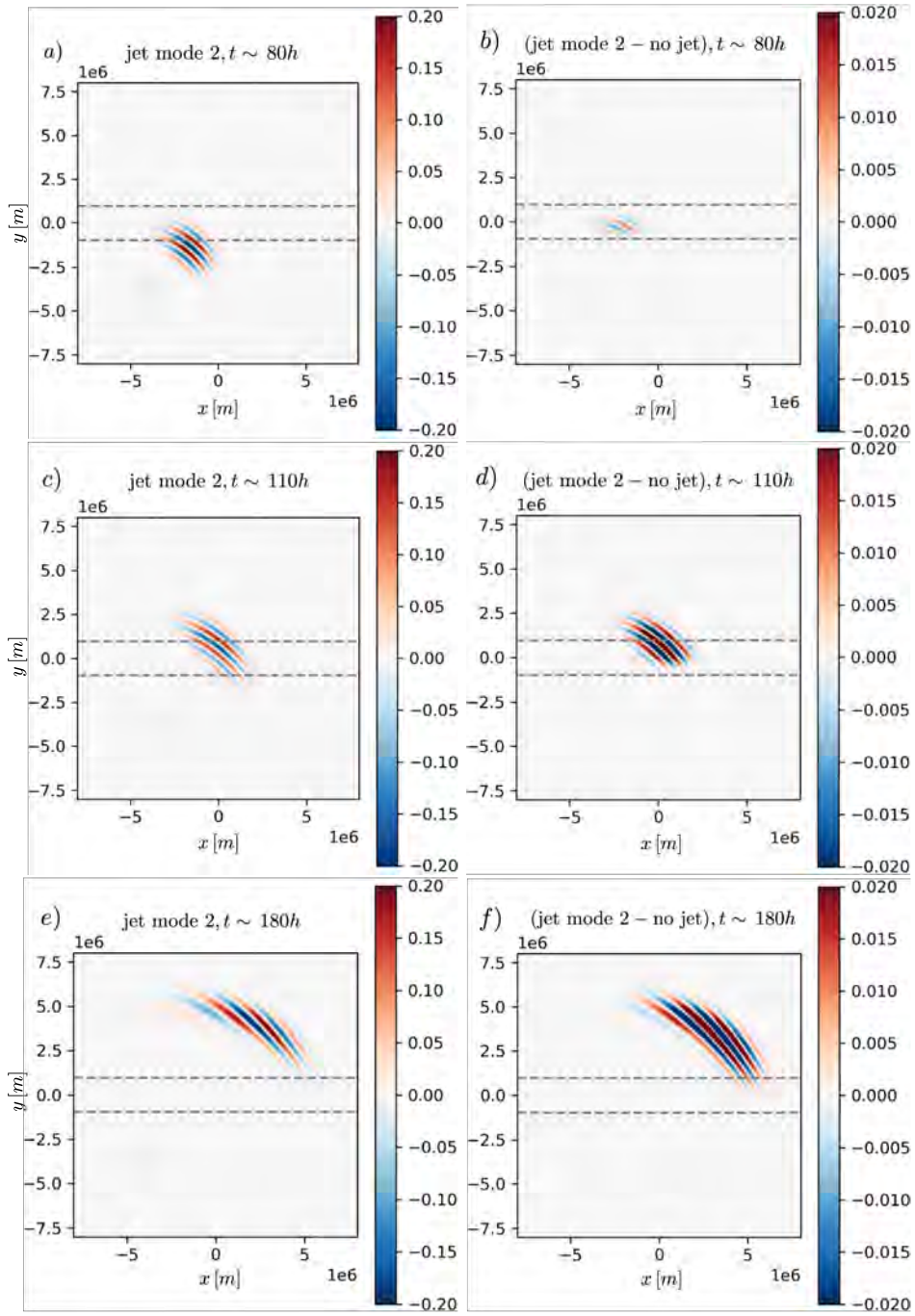

Figure 19: Zonal velocity ($\mathrm{m{\cdot}s^{-1}}$) of vertical mode 1 M2 internal tide with the sheared mode 2 jet (panels a), c), e)). Difference in the zonal velocity of vertical mode 1 M2 internal tide between the case with the sheared jet and the case with no jet (panels b), d), f)). The wavepacket is launched from $(x_0, y_0) = (-0.5\,L_x, -0.5\,L_y)$ with $\theta = \pi/4$. Jet limits are denoted in grey dashed lines, with a structure as in (50).

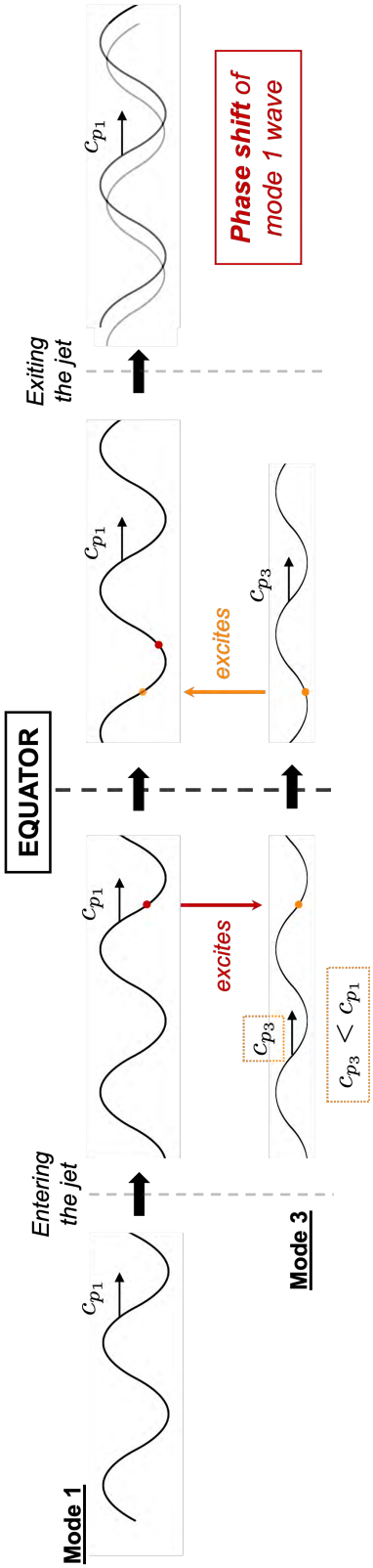

Figure 20: Scheme of the incoherence mechanisms due to wave-mean flow interaction and the creation of higher modes.

by observations and a zonal equatorial jet with strong westward near-surface flow and underlying countercurrents, as shown in figure (1).

6 Acknowledgements

I sincerely thank Bruce Sutherland and Lois Baker who supervised this project and from whom I learned a lot during this summer. They showed great patience and unwavering support at every step of the way, for which I am extremely grateful. I also want to deeply thank Keaton Burns and Eric Hester for the precious help they provided regarding Dedalus and how to build a numerical model from scratch. At last, I wish to profoundly thank everyone who was at Walsh Cottage this summer and who made this experience so wonderful and enriching.

References

[1] M. C. Buijsman, B. K. Arbic, J. G. Richman, J. F. Shriver, A. J. Wallcraft, and L. Zamudio, *Semidiurnal internal tide incoherence in the equatorial Pacific*, J. Geophys. Res.(Oceans), 122 (2017), pp. 5286–5305.

[2] K. J. Burns, G. M. Vasil, J. S. Oishi, D. Lecoanet, and B. P. Brown, *Dedalus: A flexible framework for numerical simulations with spectral methods*, Phys. Rev. Res., 2 (2020), p. 023068.

[3] C. de Lavergne, S. Falahat, G. Madec, F. Roquet, J. Nycander, and C. Vic, *Toward global maps of internal tide energy sinks*, Ocean Modell., 137 (2019), pp. 52–75.

[4] R. Ferrari and C. Wunsch, *Ocean Circulation Kinetic Energy: Reservoirs, Sources, and Sinks*, Annu. Rev. Fluid Mech., 41 (2009), pp. 253–282.

[5] C. Garrett and E. Kunze, *Internal Tide Generation in the Deep Ocean*, Annu. Rev. Fluid Mech., 39 (2007), pp. 57–87.

[6] T. Gerkema and J. T. F. Zimmerman, *An introduction to internal waves*, 2008.

[7] Jennifer A. MacKinnon and Zhongxiang Zhao and Caitlin B. Whalen and Amy F. Waterhouse and David S. Trossman and Oliver M. Sun and Louis C. St. Laurent and Harper L. Simmons and Kurt Polzin and Robert Pinkel and Andrew Pickering and Nancy J. Norton and Jonathan D. Nash and Ruth Musgrave and Lynne M. Merchant and Angelique V. Melet and Benjamin Mater and Sonya Legg and William G. Large and Eric Kunze and Jody M. Klymak and Markus Jochum and Steven R. Jayne and Robert W. Hallberg and Stephen M. Griffies and Steve Diggs and Gokhan Danabasoglu and Eric P. Chassignet and Maarten C. Buijsman and Frank O. Bryan and Bruce P. Briegleb and Andrew Barna and Brian K. Arbic and Joseph K. Ansong and Matthew H. Alford, *Climate Process Team on Internal Wave–Driven Ocean Mixing*, Bull. Amer. Meteor. Soc., 98 (2017), pp. 2429 – 2454.

[8] S. M. Kelly, *The Vertical Mode Decomposition of Surface and Internal Tides in the Presence of a Free Surface and Arbitrary Topography*, J. Phys. Oceanogr., 46 (2016), pp. 3777–3788.

[9] S. M. Kelly and P. F. J. Lermusiaux, *Internal-tide interactions with the Gulf Stream and Middle Atlantic Bight shelfbreak front*, J. Geophys. Res. (Oceans), 121 (2016), pp. 6271–6294.

[10] S. M. Kelly, P. F. J. Lermusiaux, T. F. Duda, and P. J. Haley, Jr., *A Coupled-Mode Shallow-Water Model for Tidal Analysis: Internal Tide Reflection and Refraction by the Gulf Stream*, J. Phys. Oceanogr., 46 (2016), pp. 3661–3679.

[11] S. M. Kelly, A. F. Waterhouse, and A. C. Savage, *Global Dynamics of the Stationary M_2 Mode-1 Internal Tide*, Geophys. Res. Lett., 48 (2021), p. e91692.

[12] K. G. Lamb, *Internal Wave Breaking and Dissipation Mechanisms on the Continental Slope/Shelf*, Annu. Rev. Fluid Mech., 46 (2014), pp. 231–254.

[13] J. Marshall, A. Adcroft, C. Hill, L. Perelman, and C. Heisey, *A finite-volume, incompressible navier stokes model for studies of the ocean on parallel computers*, J. Geophys. Res. (Oceans), 102 (1997), pp. 5753–5766.

[14] J. P. Martin, D. L. Rudnick, and R. Pinkel, *Spatially Broad Observations of Internal Waves in the Upper Ocean at the Hawaiian Ridge*, J. Phys. Oceanogr., 36 (2006), p. 1085.

[15] W. Munk and C. Wunsch, *Abyssal recipes II: energetics of tidal and wind mixing*, Deep-Sea Res. Part I, 45 (1998), pp. 1977–2010.

[16] L. Rainville and R. Pinkel, *Propagation of the low-modes internal waves through the ocean*, in AGU Spring Meeting Abstracts, vol. 2004, May 2004, pp. OS33B–05.

[17] S. Sarkar and A. Scotti, *From Topographic Internal Gravity Waves to Turbulence*, Annu. Rev. Fluid Mech., 49 (2017), pp. 195–220.

[18] B. R. Sutherland, *Internal Gravity Waves*, Cambridge University Press, 2010.

Interaction of Internal Gravity Waves with Magnetic Fields in Red Giant Stars

Cy Srisawas David

August 22, 2024

1 Introduction

Magnetic fields shape the dynamics in many stars and yield insights into stellar evolution [15, 10]. Though magnetic fields have largely been observed near the stellar surface [11], they may also exist in the convective cores of massive main sequence stars [5]. A deep magnetic field may persist even as a main-sequence star exhausts its supply of core hydrogen and moves onto the red giant branch (RGB) [14], leaving a stably stratified radiative interior surrounded by a convective outer envelope [20, 7].

While deep magnetic fields in RGB stars are inaccessible to direct measurement, their interaction with internal waves may be detectable in asteroseismological surface observations [22, 14]. Near-surface convective turbulence excites acoustic waves in the outer envelope [6], which tunnel into the core and propagate as internal gravity waves (IGWs) [2], which are restored by the buoyancy force. A cartoon of this process (adapted from [7]) is illustrated in figure 1(a). These IGWs can tunnel back out and convert to acoustic waves, setting up global mixed modes and producing periodic fluctuations in the brightness of the stellar surface [4]. Photometric observations of these deviations integrated over the stellar disk have been used by asteroseismologists to detect the lowest degree modes (higher degree modes are difficult to detect due to increasing geometric cancellation) [1]. Of particular importance are dipole modes, which are expected to couple strongly to IGWs in the core and thus effectively probe the deep interior [7].

However, roughly 20 percent of the RGB stars observed in the first 37 months of NASA's *Kepler* mission exhibit suppressed dipole modes [17, 22]. Curiously, the occurrence of dipole mode suppression is a strong function of stellar mass, and all the stars with suppressed dipole modes have masses at least 1.1 times the solar mass, the threshold above which core convection occurs while on the main sequence [22].

Convective dynamo magnetic fields in main-sequence cores may persist as these stars move onto the RGB due to the low magnetic diffusivity of stellar plasma ($\eta \sim 10^{-7}$–$10^{-3}\,\mathrm{m}^2/\mathrm{s}$ based on models of main sequence cores [9]). Ref. [7] thus proposed that a "magnetic greenhouse effect" from fossil magnetic fields could be responsible for trapping IGWs in RGB cores and stopping them from forming global dipole modes in the outer envelope.

Ref. [13] showed that a radially decaying background magnetic field can trap axisymmetric dipole modes in the core by converting downgoing IGWs to a class of magnetohydrodynamic (MHD) waves termed slow-magnetosonic (SM) waves. These incompressible

waves confusingly have the word "sonic" in their name, which originates from the fact that there are two (fast and slow) branches of mixed magnetosonic waves when the sound speed and Alfven speed are comparable [21]. In the limit of fast sound speed (relative to Alfven speed), the fast and slow branches diverge — the former turning into acoustic waves and the latter into the incompressible SM waves relevant here. Axisymmetric SM waves are confined to regions with high magnetic field strength [13], and are characterized by motion ($\boldsymbol{u}$) in the same plane as the wavenumber vector ($\boldsymbol{k}$) and background magnetic field ($\boldsymbol{B}_0$):

$$\boldsymbol{u} \cdot (\boldsymbol{k} \times \boldsymbol{B}_0) = 0. \tag{1}$$

In the axisymmetric case, the SM waves are decoupled from a second class of MHD waves: Alfven waves with

$$\boldsymbol{u} \times (\boldsymbol{k} \times \boldsymbol{B}_0) = \boldsymbol{0}. \tag{2}$$

These Alfven waves can only couple to the IGW and SM waves in the non-axisymmetric case, and develop much finer horizontal scales as the result of resonances with the background magnetic field [12, 19].

Though all three wave classes have been identified in eigenvalue problems [12, 19], analysis of their interaction is missing from the literature. In particular, it is unclear if downgoing IGWs or upgoing SM waves convert to resonant Alfven waves.

Here, we extend the analysis in [13] to non-axisymmetric modes. For wave frequencies much smaller than the background buoyancy frequency, the linear governing equations reduce to a generalized eigenvalue problem involving an internal singularity, which gives rise to a continuous spectrum of fine-scale resonant Alfven waves. By evolving the full linear equations, we show conversion between IGW and SM waves and the emergence of fine-scale features not seen in the axisymmetric case. Though the nature of these sharp features are unclear at present, they suggest that the mechanism of dipole mode suppression in RGB stars may be fundamentally different for non-axisymmetric versus axisymmetric modes.

2 Problem Set-up

We consider a Cartesian model of the stably stratified RGB core, with "latitude" $x \in [0, L]$, "azimuth" y, and "radius" $z \in [0, L/6]$. Figure 1(b) shows a diagram of the domain over x and z, roughly corresponding to the dashed region of the RGB core in figure 1(a).

Perturbations in velocity $\boldsymbol{u}$, pressure p, density ρ, and the magnetic field $\boldsymbol{b}$ are governed by the linearized magneto-Boussinesq equations [18]:

$$\rho_0 \partial_t \boldsymbol{u} + \boldsymbol{\nabla} p = -g\rho \boldsymbol{e}_z + \frac{1}{\mu_0} (\boldsymbol{\nabla} \times \boldsymbol{b}) \times \boldsymbol{B}_0 + \frac{1}{\mu_0} (\boldsymbol{\nabla} \times \boldsymbol{B}_0) \times \boldsymbol{b}, \tag{3a}$$

$$\boldsymbol{\nabla} \cdot \boldsymbol{u} = 0, \tag{3b}$$

$$\partial_t \boldsymbol{b} = \boldsymbol{\nabla} \times (\boldsymbol{u} \times \boldsymbol{B}_0) + \eta \nabla^2 \boldsymbol{b}, \tag{3c}$$

$$\boldsymbol{\nabla} \cdot \boldsymbol{b} = 0, \tag{3d}$$

$$\partial_t \rho = \frac{\rho_0 N^2}{g} \boldsymbol{e}_z \cdot \boldsymbol{u}, \tag{3e}$$

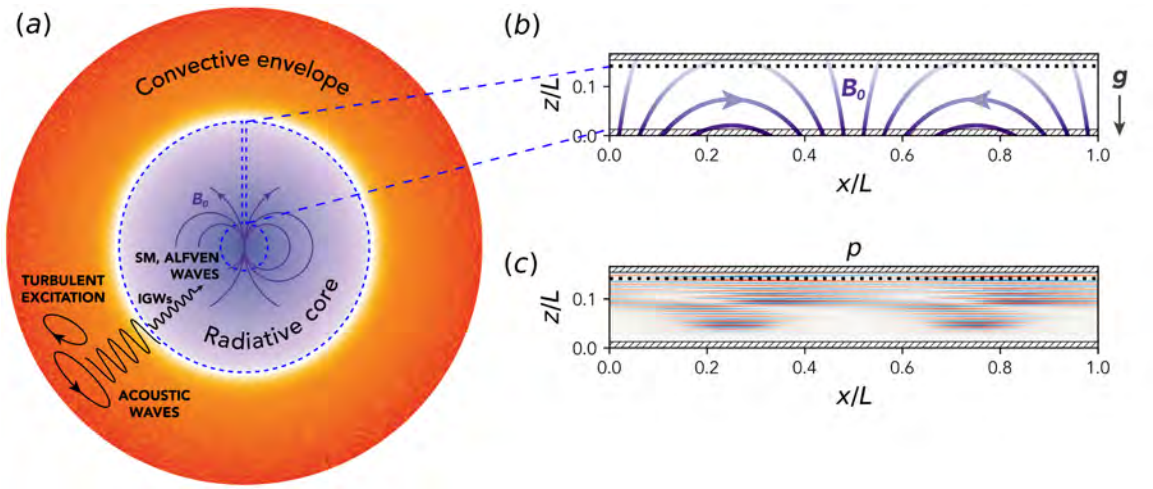

Figure 1: (a) Cartoon cross-section of an RGB star with convective outer envelope and stably-stratified core, adapted from [7]. Convective turbulence in the outer envelope excites acoustic waves which convert to internal gravity waves (IGWs) in the core. These IGWs may interact with slow magnetosonic (SM) and resonant Alfven waves supported by a remnant core magnetic field. (b) Idealized Cartesian model formed by "unwrapping" the region of the radiative core indicated with blue dashed lines in panel a, with x, y, z corresponding to latitude, azimuth, and radius, respectively. The field lines for the sinusoidal, vertically decaying background magnetic field $\boldsymbol{B}_0$ used in this study are plotted in purple. The opacity of the plotted field lines increases with $|\boldsymbol{B}_0|$. (c) The equilibrated numerical solution for the pressure perturbations driven by a sinusoidal wavemaker ($k_x = 2\pi/L$, $k_y = 4\pi/L$) located at the dotted line and damped at layers indicated by the hatched areas. A stretched-aspect version of the same plot is shown in figure 3(c). The true-aspect ratio version shown here emphasizes the scale separation between the vertical and horizontal oscillations.

where ρ_0 is the mean density, g is the gravitational acceleration, μ_0 is the magnetic permeability of free space, and η is the magnetic diffusivity. Rotation is neglected as the frequency of observed dipole modes ω is much faster than the rotational frequency Ω of the RGB stars ($\omega/\Omega \sim 20$ [22, 8]). Magnetic diffusion is retained to regularize sharp features associated with the hydromagnetic waves described in the next section, while viscous and radiative diffusion is neglected so that the propagation of IGWs is minimally affected.

We assume a uniform Brunt-Vaisala frequency N and a non-uniform background magnetic field chosen to mimic a dipole magnetic field in spherical geometry:

$$\boldsymbol{B}_0 = \mathcal{B} e^{-2\pi z/L} \left[\sin(2\pi x/L)\boldsymbol{e}_x + \cos(2\pi x/L)\boldsymbol{e}_z\right]. \tag{4}$$

Associated fieldlines are plotted in purple in figure 1(b). Importantly, this background magnetic field has no current (i.e., $\boldsymbol{J}_0 = \mu_0^{-1}(\boldsymbol{\nabla} \times \boldsymbol{B}_0)$), which ensures that $\boldsymbol{B}_0$ is stable to perturbations (see Appendix A.1.1 for a derivation of this result).

We consider "non-axisymmetric" dipole-like modes forced at the top of the domain ($z_0/L = 1/6 - 1/40$) with frequency ω and horizontal wavenumbers $k_x = 2\pi/L$, $k_y = 4\pi/L \neq 0$. We chose $k_y > k_x$ to yield clear separation in the behavior of IGWs with different parity, as will be shown in the following section. This facilitates analysis and is not expected to qualitatively change the physics.

The flow is controlled by three dimensionless ratios: the Froude number,

$$Fr = \frac{\text{wave inertia}}{\text{gravity}} = \frac{\omega}{N} \sim 10^{-1} \text{ in RGB core [22, 16]}, \tag{5}$$

the Lundquist number

$$S = \frac{\text{wave inertia}}{\text{magnetic diffusion}} = \frac{\omega L^2}{\eta} \sim 10^{18}\text{–}10^{22} \text{ in RGB core [22, 16, 9]}, \tag{6}$$

and the magneto-gravity ratio

$$\Gamma = \frac{\text{Lorentz force over IGW scales}}{\text{wave inertia}} = \frac{\mathcal{B}(\mu_0\rho_0)^{-1/2}N}{\omega^2 L}. \tag{7}$$

The value of Γ in RGB cores is not known *a priori*, and it is instead assumed that $\Gamma \lesssim 1$ in the forward modelling of RGB core waves [7]. This restriction ensures that the background magnetic field lines are not so stiff that they cannot be bent by the IGWs excited at the top of the domain.

The parameter values $Fr = 0.025$, $S = 10^8$, and $\Gamma = 0.073$ are employed in our numerical simulation and the following analysis. The linear equations (Appendix A, eqs. 17,18) are Fourier transformed in y and solved over the x-z plane using the Dedalus pseudospectral code [3] with 2048 and 512 complex Fourier modes in x and z, respectively. Linear damping layers at the top and bottom 7.5% of the domain prevent reflections.

3 Results and Asymptotic Analysis

The equilibrated pressure perturbation field in the initial value problem (IVP) described above is plotted in figure 1(c) (a stretched aspect-ratio version of this plot is included in figure 3c), and reveals the presence of multiple modes whose parity and structure vary with depth.

Since these modes are difficult to discern from direct analysis of the full linear equations (3), we make a multiple-scales asymptotic reduction that takes advantage of the scale separation between fast oscillations in the vertical direction and the slow variation of the background magnetic field. To estimate how this anisotropy scales with the input parameters, we consider the dispersion relation for pure IGWs:

$$\omega = \frac{N\sqrt{k_x^2 + k_y^2}}{k} \approx \frac{N\sqrt{k_x^2 + k_y^2}}{k_z} \quad \text{if} \quad k_z \gg \sqrt{k_x^2 + k_y^2}. \tag{8}$$

Then, we find that the ratio of vertical to horizontal lengths scale as

$$\frac{l_z}{L} \sim \frac{k_x}{k_z} \sim \frac{\omega}{N} = Fr. \tag{9}$$

Accordingly, we take $Fr = \epsilon$ as our small parameter with $\Gamma = O(1)$ and $S = O(\epsilon^{-2})$.

Employing a Wentzel–Kramers–Brillouin (WKB) approximation in the vertical direction yields (to leading order) a generalized eigenvalue problem in x with eigenvalue k_z^2 (k_z is the vertical wavenumber) and horizontal pressure eigenfunction p_0 (see Appendix A for details):

$$\frac{k_z^2}{N^2} p_0 + \hat{\boldsymbol{\nabla}} \cdot \left(\frac{\hat{\boldsymbol{\nabla}} p_0}{\omega^2 - v_{Az}^2 k_z^2} \right) = 0, \tag{10}$$

where $\hat{\boldsymbol{\nabla}} = \boldsymbol{e}_x \partial_x + \boldsymbol{e}_y i k_y$ is the transformed horizontal gradient operator and $v_{Az}(x,z) = \pm(\boldsymbol{B}_0 \cdot \boldsymbol{e}_z)/\sqrt{\mu_0 \rho_0}$, is the Alfven wave speed. Though (10) is an eigenvalue problem in x, there is a parametric dependence on z through v_{Az}, which decays slowly with height. Accordingly, the eigenfunctions p_0 and eigenvalues k_z vary slowly with z.

In (10), there is a singularity at $\omega^2 - v_{Az}^2 k_z^2 = 0$ that cannot be removed for $k_y \neq 0$ (i.e., for "non-axisymmetric" modes) and that appears again in the polarization relation for the "azimuthal" velocity eigenfunction:

$$v_0 = \frac{k_y \omega p_0}{\rho_0(\omega^2 - v_{Az}^2 k_z^2)}. \tag{11}$$

For $k_y \neq 0$, the "azimuthal" (y) flow is coupled to the "meridional" (x, z) flow and resonates with the background magnetic field at critical "latitudes" x_c where $\omega^2 - v_{Az}^2 k_z^2 = 0$. Since v_{Az} varies continuously with x, this condition may be satisfied for a continuous spectrum of real vertical wavenumbers

$$|k_z| \geq k_A(z) \equiv \omega \mathcal{B}^{-1} \sqrt{\mu_0 \rho_0} \exp(2\pi z/L) = (\Gamma Fr L)^{-1} \exp(2\pi z/L), \tag{12}$$

which varies with height. Figure 2(a) plots this continuous spectrum as a shaded gray region in the space of wavenumbers k_z and height z.

The non-resonant modes are found by solving the eigenvalue problem (10) in Dedalus using 256 complex Fourier modes in x for 1024 evenly-spaced values of $z \in [0, L/6]$. We find three propagating non-resonant waves with "dipolar" ($n_x = 1$) structure: an IGW-like wave with odd parity in pressure ('IGW-1'), an IGW-like wave with even parity in pressure ('IGW-0'), and a slow-magnetosonic-like wave [13] with even parity in pressure ('SM-0').

Figure 2(a) plots the dispersion curves for IGW-1, IGW-0, and SM-0 in solid blue, teal, and olive, respectively. The corresponding "azimuthal" velocity eigenfunctions v_0 at $z/L = 0.09$ are plotted in figure 2(b–d).

Though pure IGWs have negative group velocities for positive vertical wavenumber, magnetic effects can produce turning points at which the direction of energy propagation reverses. These effects are weak for the odd-parity IGW mode (IGW-1), which is anti-phase with the vertical component of the background magnetic field. Consequently, IGW-1 (figure 2a, solid blue curve) propagates down until it reaches the continuum of resonant Alfven waves at $z/L = 0.044$. In contrast, IGW-0 (solid teal curve), which is in-phase with $\boldsymbol{B}_0 \cdot \boldsymbol{e}_z$, reaches a turning point at $z/L = 0.085$ and is reflected as a slow-magnetosonic wave (SM-0), leaving a pair of evanescent tails for $z/L < 0.085$ (dotted teal curve). SM-0 (solid olive curve) propagates upwards from the turning point, refracting to higher wavenumbers until it reaches the Alfven wavenumber boundary, $k_z = k_A$ (12) at $z/L = 0.11$. Comparing figures 2(c) and (d) shows a horizontal sharpening as the wave approaches the resonant Alfven boundary in wavenumber space.

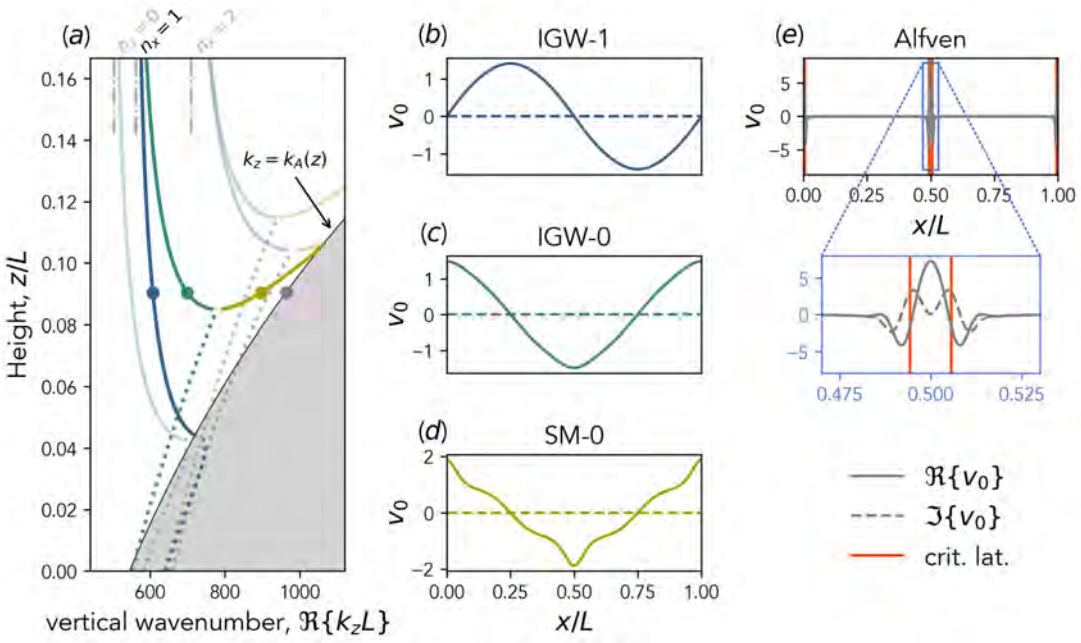

Figure 2: The wavenumbers and modes of the reduced dispersion relation (10). (a) The real part of the vertical wavenumber k_z versus height z for modes with $n_x = 0, 1, 2$ wavelengths in x. The values of k_z for pure (non-magnetic) IGWs corresponding to each n_x are plotted in gray dash-dotted lines. Even and odd parity IGW-like branches of the dispersion relation (IGW-0 and IGW-1) are plotted as blue and teal curves, respectively, while the even-parity SM branch (SM-0) is plotted in olive green. The continuum of resonant Alfven waves is plotted as a gray region bounded in wavenumber space by (12). (b-d) The horizontal structure of the IGW-1, IGW-0, and SM-0 modes, respectively, corresponding to the colored points in panel a. The real and imaginary parts of the Cartesianized "azimuthal" velocity eigenfunction v_0 are plotted as solid and dashed lines. (e) Resonant Alfven eigenfunction resolved by adding magnetic diffusion ($S = 10^8$) to the eigenvalue problem, corresponding to the gray point in panel a. An enlarged view shows peaks in v_0 at the critical "latitudes" (red lines) predicted by the ideal MHD theory.

Finally, the resonant Alfven modes may be resolved by regularizing the eigenvalue problem (10) with magnetic diffusion. Figure 2(e) shows an example found using Dedalus' sparse eigenvalue solver with $S = 10^8$ and 16384 complex Fourier modes. Vertical red lines illustrate the coincidence of peaks in v_0 with the critical latitudes predicted by setting $\omega^2 - v_{Az}^2 k_z^2 = 0$.

The theoretical results described above predict the locations (in z) of wave conversion and possible interaction with the resonant Alfven continuum, which we can test on the full, numerically integrated IVP. To do so, we obtain an amplitude equation (Appendix A, eq. 88) at the next order in ϵ and construct a WKB solution for the three $n_x = 1$ modes (IGW-1, IGW-0, SM-0) and their decaying evanescent tails. The overall (complex) amplitude, the phase shift between IGW-0 and SM-0 modes, and the complex amplitude of the evanescent modes are then fit to the equilibrated pressure field from the IVP at $x/L = 0.33$, while the amplitudes of IGW-0 and SM-0 are assumed to be equal at the turning point. Furthermore, the IGW-0 and IGW-1 amplitudes are held equal at the forcing height apart from a $\pi/2$

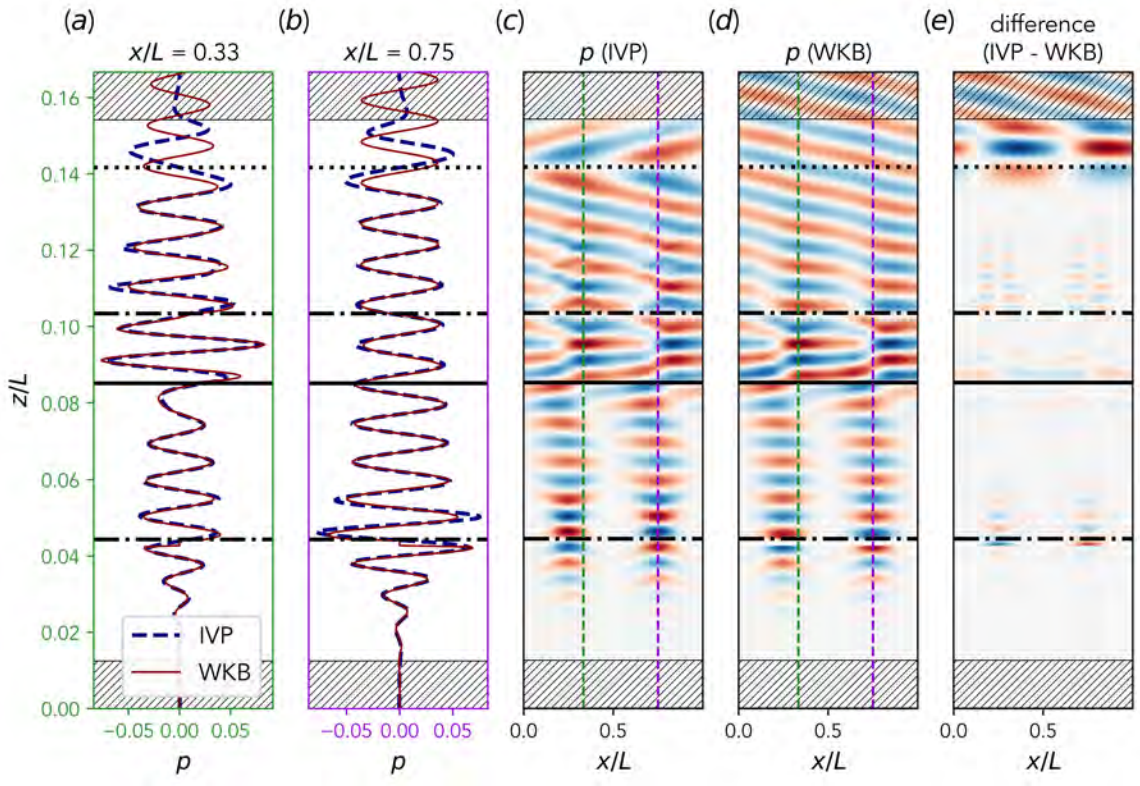

Figure 3: (a,b) Vertical profiles of the pressure perturbation field from the numerical IVP (dashed blue curve) and the WKB theory (solid red curve) at $x/L = 0.33$ and $x/L = 0.75$. The overall amplitude, the phase shift between IGW-0 and SM-0 modes, and the complex amplitudes of the evanescent modes in the WKB solution are fit to the IVP pressure field at $x/L = 0.33$, between $z/L = 0.03$ and $z/L = 0.1375$. The excellent agreement between IVP and WKB theory below the forcing height (dotted line) and outside of the numerical damping layers (hatched regions) is maintained at $x/L = 0.75$. The fit even persists across the turning point between IGW-0 and SM-0 branches (solid black line), where the WKB amplitude function diverges. (c,d) Snapshot of the equilibrated pressure perturbation field from the numerical IVP and plot of the WKB solution. Vertical dashed green and purple lines at $x/L = 0.33$ and $x/L = 0.75$ correspond to the vertical profiles in panels a and b, respectively. (e) The difference between IVP and WKB pressure perturbation fields, revealing the emergence of large-scale vertically-decaying features from the locations at which IGW-1 and SM-0 branches intersect the Alfven wavenumber boundary (dash-dotted lines).

phase shift.

Figure 3 compares the numerical IVP solution with WKB theory. Panel (a) shows a strong match between the vertical profiles of the IVP and WKB pressure fields at the fitting "latitude", $x/L = 0.33$. Large deviations occur only above the forcing height (dotted line) and within the damping layers (hatched regions), as expected. The robust agreement at $x/L = 0.33$ also holds e.g., at $x/L = 0.75$ (figure 3b) and indeed over the entire domain, as can be seen by comparing figure 3(c) and (d). The difference between IVP and WKB fields shown in figure 3(e) is small, but reveals large-scale, slowly-decaying features that appear at the locations in z where the IGW-1 and SM-0 modes reach the Alfven wavenumber

boundary (dash-dotted lines).

The difference between simulation and WKB theory is starker when comparing the "azimuthal" velocity component, v. Figure 4 plots v from the IVP and v computed from the WKB pressure solution using the polarization relation (11). The difference between IVP and WKB, plotted in figure 4(e), reveals large-scale features emerging from $z/L = 0.044$ and $z/L = 0.11$ (dash-dotted lines), where IGW-1 and SM-0 modes hit the Alfven wavenumber boundary. The odd-parity features emerging from $z/L = 0.044$ sharpen as they propagate upwards, leading to fine-scale features just below the forcing height (dotted line) in panel (e). In contrast, the even-parity features emerging from $z/L = 0.11$ remain at large scales up to the forcing height. The nature of both the odd- and even-parity features remains puzzling, since the Alfven modes resolved by regularizing the reduced eigenvalue problem are fine-scale, as in figure 2(e). Regardless, the results suggest that the Alfven continuum

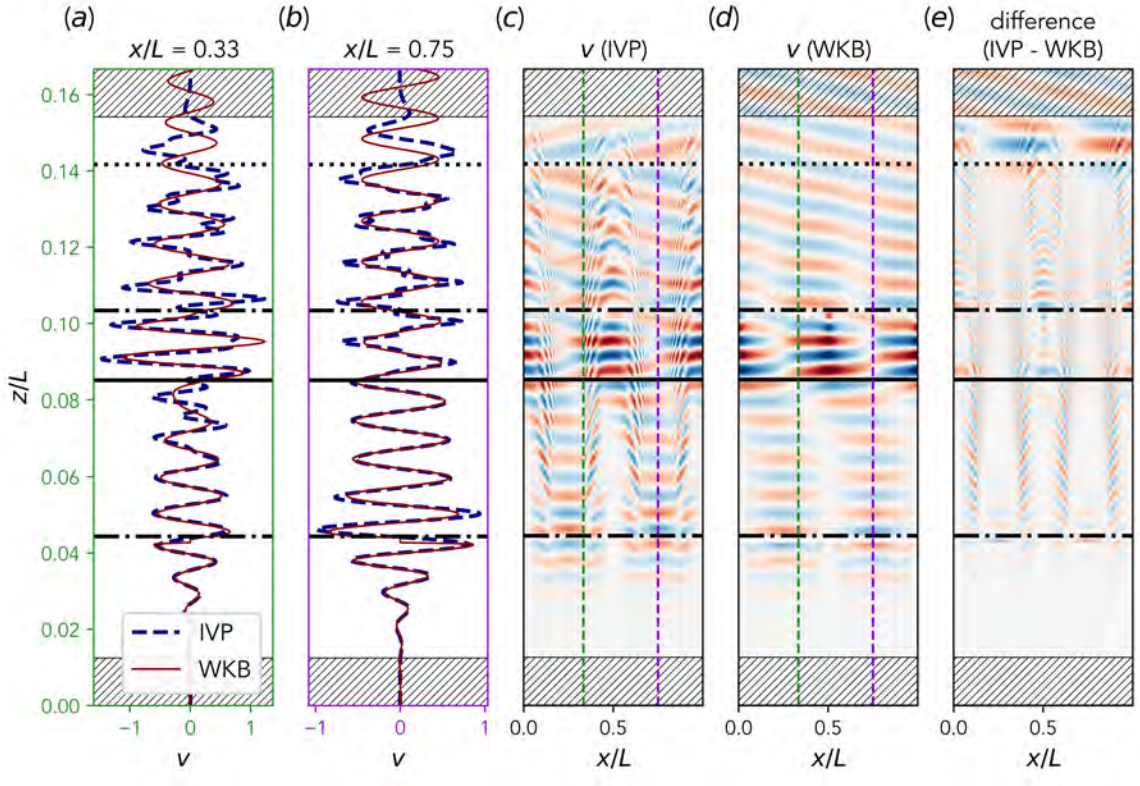

Figure 4: Redux of figure 3 showing the Cartesianized "azimuthal" velocity perturbation v instead of the pressure perturbation p. The WKB solution for v is computed directly from the WKB solution for p shown in figure 3 using the polarization relation (11). The WKB solution for v in panels (a-b) does not capture the sharp, high-wavenumber features in the numerical IVP solution. Plots of the field over x, z in panels (c-d) reveal structures in the simulation that are lacking from the WKB theory. Panel (e) plots the difference between IVP and WKB fields, revealing large-scale horizontal features emerging from the heights at which the IGW-1 and SM-0 branches hit the Alfven wavenumber boundary (dash-dotted lines). The odd-parity features emerging from $z/L = 0.044$ sharpen with height, while the even-parity features emerging from $z/L = 0.11$ remain large-scale as they propagate up to the forcing height (dotted line).

has some effect on the odd-parity mode, since the fine-scale features observed in the IVP are not present when $k_y = 0$ (cf. Ref. [13]).

4 Discussion

Deep magnetic fields likely play a role in the suppression of dipole modes in asteroseismological observations of many RGB stars. As shown by Ref. [13], axisymmetric dipole modes can be suppressed by the trapping of IGWs in the stably-stratified core via conversion to SM waves.

Non-axisymmetry introduces fundamentally different physics by coupling azimuthal and meridional motions. The associated effects on wave interactions are studied by numerically evolving the full linear equations and comparing the result to a WKB solution, which takes advantage of the scale separation induced by small *Fr*.

A reduced eigenvalue problem reveals a continuous spectrum of Alfven waves, which resonate with the background magnetic field at critical latitudes. For $k_y = 4\pi$, the Alfven spectrum has no apparent effect on the conversion between the even parity IGW and SM waves also found for $k_y = 0$ [13]. However, the turning point between odd-parity IGW and SM waves seen in the axisymmetric (reduced) eigenvalue problem vanishes in the non-axisymmetric case. Instead, the odd IGW branch in the reduced dispersion relation is cut off by the lower boundary of the continuous Alfven spectrum. In the numerical IVP, large-scale features with odd parity emerge from this point of intersection and give rise to fine-scale horizontal oscillations as they propagate upwards. Similarly large-scale features emerge from the height at which the even-parity SM wave intersects the Alfven wavenumber boundary. However, these even-parity features remain large-scale as they propagate upwards.

The nature of these odd- and even-parity features — presently unaccounted for by the WKB solution — could have major implications for the trapping of IGWs and the "magnetic greenhouse effect". The even-parity features are of particular import; while the odd-parity features would likely damp (viscously and ohmically) as they propagate upwards due to their fine scales, the even-parity features would experience little damping due to their large horizontal scales. If these even-parity features behave like SM waves and are similarly bounded by a magnetic cutoff height, then a slightly weaker magnetic field (lower Γ) could trap them within the core. However, if these features have altogether different character and are able to escape the magnetized core, the magnetic greenhouse effect would be greatly curtailed for nonaxisymmetric modes.

Meanwhile, asteroseismological observations of RGB stars show comparable suppression of both the axisymmetric and non-axisymmetric dipole modes [22]. Thus, the nature of these even-parity features could determine whether an alternate "trapping" mechanism for non-axisymmetric modes is needed to explain the data, which would have important implications for the inference of deep magnetic field strength from asteroseismology.

Determining the nature of the upgoing large-scale features and the role of the continuous Alfven spectrum is the subject of our ongoing work on this project.

Acknowledgements

I would like to thank Daniel Lecoanet for sharing this rich problem and for reorganizing his summer to guide me through this project. I am grateful to my second mentor Pascale Garaud for her constant support and skill at teaching asymptotic methods (even to an experimentalist like myself). I thank the program organizers Greg Chini, Bruce Suther-land, Janet Fields, Julie Hildebrandt, and Lanie Plueddemann for creating an unforgettable summer. To the fellows, I express my deepest gratitude for their unwavering support and friendship. Finally, I must give thanks to the Walsh cottage printer and its unintuitive user interface. Without it, Daniel and I might not have spoken and this project would not have happened.

Appendix A Multiple-scales asymptotic analysis

A.1 Governing equations

The full magnetohydrodynamic (MHD) equations

$$\rho\left(\partial_t \boldsymbol{u} + \boldsymbol{u}\cdot\boldsymbol{\nabla}\boldsymbol{u}\right) = -\boldsymbol{\nabla}p - \rho g \boldsymbol{e_z} + \frac{1}{\mu_0}(\boldsymbol{\nabla}\times\boldsymbol{B})\times\boldsymbol{B}, \tag{13a}$$

$$\partial_t \rho + \boldsymbol{\nabla}\cdot(\rho\boldsymbol{u}) = 0, \tag{13b}$$

$$\partial_t \boldsymbol{B} = \boldsymbol{\nabla}\times(\boldsymbol{u}\times\boldsymbol{B}) + \eta\nabla^2\boldsymbol{B}, \tag{13c}$$

$$\boldsymbol{\nabla}\cdot\boldsymbol{B} = 0, \tag{13d}$$

govern the evolution of velocity $\boldsymbol{u}$, pressure p, density ρ, and magnetic $\boldsymbol{B}$ fields in nonlinear, compressible flows.

To study linear, incompressible MHD waves, we first make the following substitutions

$$\boldsymbol{u}\to\delta\boldsymbol{u},\quad \boldsymbol{B}\to\boldsymbol{B}_0+\delta\boldsymbol{b},\quad \rho\to\rho_0+\delta\varrho(z)+\delta^2\rho(x,z,t),\quad p\to\delta^{-1}p_0+\underline{p}+\delta p,\quad g\to\delta^{-1}g, \tag{14}$$

where $\delta \ll 1$. At $O(\delta^{-1})$:

$$\partial_z P_0 = -\rho_0 g. \tag{15}$$

At $O(1)$:

$$\partial_z \overline{P} = -\overline{\rho} g, \tag{16a}$$

$$\boldsymbol{\nabla}\cdot\boldsymbol{B}_0 = 0. \tag{16b}$$

At $O(\delta)$:

$$\rho_0\partial_t\boldsymbol{u} + \boldsymbol{\nabla}p = -g\rho\boldsymbol{e}_z + \frac{1}{\mu_0}(\boldsymbol{\nabla}\times\boldsymbol{b})\times\boldsymbol{B}_0 + \frac{1}{\mu_0}(\boldsymbol{\nabla}\times\boldsymbol{B}_0)\times\boldsymbol{b} \tag{17a}$$

$$\boldsymbol{\nabla}\cdot\boldsymbol{u} = 0. \tag{17b}$$

$$\partial_t\boldsymbol{b} = \boldsymbol{\nabla}\times(\boldsymbol{u}\times\boldsymbol{B}_0) + \eta\nabla^2\boldsymbol{b}. \tag{17c}$$

$$\boldsymbol{\nabla}\cdot\boldsymbol{b} = 0. \tag{17d}$$

At $O(\delta^2)$:

$$\partial_t\rho = \frac{\rho_0 N^2}{g}\boldsymbol{e}_z\cdot\boldsymbol{u}, \tag{18}$$

where $N^2 = -g\rho_0^{-1}\partial_z\underline{\rho}$. The linear equations (17, 18) form a closed system for the perturbations and are known as the linearized magneto-Boussinesq equations [18].

A.1.1 Energy equation

Thus far we have not specified the background magnetic field $\boldsymbol{B}_0$. By deriving the perturbation energy equation, we show that $\boldsymbol{B}_0$ must satisfy $\boldsymbol{\nabla} \times \boldsymbol{B}_0 = 0$ to prevent instability. For this purpose, we neglect diffusion ($\eta = 0$) and take $\boldsymbol{u}\cdot$(17a)+p(17b)+$\rho g^2/(\rho_0 N^2)$(18):

$$\partial_t \left(\rho_0 \frac{|\boldsymbol{u}|^2}{2} + \frac{g^2}{\rho_0 N^2} \frac{\rho^2}{2} \right) + \boldsymbol{\nabla} \cdot (p\boldsymbol{u}) = -\frac{1}{\mu_0} (\boldsymbol{u} \times \boldsymbol{B}_0) \cdot (\boldsymbol{\nabla} \times \boldsymbol{b}) - \frac{1}{\mu_0} (\boldsymbol{u} \times \boldsymbol{b}) \cdot (\boldsymbol{\nabla} \times \boldsymbol{B}_0) \quad (19)$$

Now take $\boldsymbol{b}\cdot$(17c):

$$\partial_t \frac{|\boldsymbol{b}|^2}{2} = (\boldsymbol{u} \times \boldsymbol{B}_0) \cdot (\boldsymbol{\nabla} \times \boldsymbol{b}) + \boldsymbol{\nabla} \cdot [(\boldsymbol{u} \times \boldsymbol{B}_0) \times \boldsymbol{b}] \,. \quad (20)$$

Taking (19)+μ_0^{-1}(20) yields

$$\partial_t \left(\rho_0 \frac{|\boldsymbol{u}|^2}{2} + \frac{g^2}{\rho_0 N^2} \frac{\rho^2}{2} + \frac{|\boldsymbol{b}|^2}{2\mu_0} \right) + \boldsymbol{\nabla} \cdot \left[p\boldsymbol{u} + \frac{1}{\mu_0} \boldsymbol{b} \times (\boldsymbol{u} \times \boldsymbol{B}_0) \right] = -\frac{1}{\mu_0} (\boldsymbol{u} \times \boldsymbol{b}) \cdot (\boldsymbol{\nabla} \times \boldsymbol{B}_0). \quad (21)$$

By integrating (21) over the domain, we can see that the wave energy (in the perturbations) can grow if the right hand side does not vanish. That is, if the background magnetic field has current $\boldsymbol{J}_0 = \mu_0^{-1}(\boldsymbol{\nabla} \times \boldsymbol{B}_0)$, the perturbations can couple to the background such that they grow. To avoid instability, we set $\boldsymbol{J}_0 = \boldsymbol{0}$, yielding

$$\partial_t \left(\rho_0 \frac{|\boldsymbol{u}|^2}{2} + \frac{g^2}{\rho_0 N^2} \frac{\rho^2}{2} + \frac{|\boldsymbol{b}|^2}{2\mu_0} \right) + \boldsymbol{\nabla} \cdot \left[p\boldsymbol{u} + \frac{1}{\mu_0} \boldsymbol{b} \times (\boldsymbol{u} \times \boldsymbol{B}_0) \right] = 0. \quad (22)$$

A.2 Nondimensionalization

Let $\boldsymbol{u} = u\boldsymbol{e}_x + v\boldsymbol{e}_y + w\boldsymbol{e}_z$, and restrict the background magnetic field to $\boldsymbol{B}_0(x, z) = B_{0,x}(x, z)\boldsymbol{e}_x + B_{0,z}(x, z)\boldsymbol{e}_z$.

Nondimensionalize (16b),(17a), (17b), (17c), (17d), (18) using the wavelength of the forcing L, the driving frequency ω, the background magnetic field scale $\mathcal{B}$, the scale of the Brunt-Vaisala frequency $\mathcal{N}$, and the small vertical lengthscale $l_z = L\omega/\mathcal{N}$. We scale the independent variables as $(x, y) = (L\tilde{x}, L\tilde{y})$, $z = l_z\tilde{z} = L\tilde{\mathcal{Z}}$, $t = \omega^{-1}\tilde{t}$. The background fields are scaled as $\boldsymbol{B}_0 = \mathcal{B}\tilde{\boldsymbol{v}}_A(\tilde{x}, \tilde{\mathcal{Z}})$ and $N = \mathcal{N}\tilde{N}(\tilde{\mathcal{Z}})$. The perturbations are nondimensionalized as $\boldsymbol{u}_H = \mathcal{U}\tilde{\boldsymbol{u}}_H(\tilde{x}, \tilde{y}, \tilde{z}, \tilde{t})$, $w = \mathcal{U}(l_z/L)\tilde{w}(\tilde{x}, \tilde{y}, \tilde{z}, \tilde{t})$, $\boldsymbol{b}_H = \mathcal{U}\sqrt{\mu_0\rho_0}\tilde{\boldsymbol{b}}_H(\tilde{x}, \tilde{y}, \tilde{z}, \tilde{t})$, $b_z = \mathcal{U}(l_z/L)\sqrt{\mu_0\rho_0}\tilde{b}_z(\tilde{x}, \tilde{y}, \tilde{z}, \tilde{t})$, $\rho = \mathcal{U}(\rho_0\mathcal{N}/g)\tilde{\rho}(\tilde{x}, \tilde{y}, \tilde{z}, \tilde{t})$, and $p = \mathcal{U}\rho_0\omega L\tilde{p}(\tilde{x}, \tilde{y}, \tilde{z}, \tilde{t})$, where $\mathcal{U}$ is an arbitrary amplitude with the dimensions of velocity.

Since our scalings our anisotropic, we will break our equations into horizontal and vertical components. We will use the identities

$$[(\boldsymbol{\nabla} \times \boldsymbol{b}) \times \boldsymbol{B}_0]_H = B_{0z}(\partial_z \boldsymbol{b}_H - \boldsymbol{\nabla}_H b_z) + (\boldsymbol{\nabla}_H \times \boldsymbol{b}_H) \times B_{0x}\boldsymbol{e}_x, \quad (23)$$

$$[(\boldsymbol{\nabla} \times \boldsymbol{b}) \times \boldsymbol{B}_0] \cdot \boldsymbol{e}_z = B_{0x}(\partial_x b_z - \partial_z b_x) \quad (24)$$

which assume that $\boldsymbol{B}_0 \cdot \boldsymbol{e}_y = 0$.

Then after nondimensionalizing and dropping tildes, the linearized equations become

$$\boldsymbol{\nabla}_H \cdot \boldsymbol{u}_H + \partial_z w = 0 \quad (25a)$$

$$\partial_x v_{Ax} + \partial_{\mathcal{Z}} v_{Az} = 0 \tag{25b}$$

$$\boldsymbol{\nabla}_H \cdot \boldsymbol{b}_H + \partial_z b_z = 0 \tag{25c}$$

$$\partial_t \boldsymbol{u}_H + \boldsymbol{\nabla}_H p = \mathcal{M}_A v_{Az}(Fr^{-1}\partial_z \boldsymbol{b}_H - Fr\boldsymbol{\nabla}_H b_z) + \mathcal{M}_A(\boldsymbol{\nabla}_H \times \boldsymbol{b}_H) \times v_{Ax}\boldsymbol{e}_x \tag{25d}$$

$$Fr\partial_t w + Fr^{-1}\partial_z p = -Fr^{-1}\rho + \mathcal{M}_A v_{Ax}(Fr\partial_x b_z - Fr^{-1}\partial_z b_x) \tag{25e}$$

$$\partial_t \boldsymbol{b}_H = \mathcal{M}_A(Fr^{-1}v_{Az}\partial_z \boldsymbol{u}_H - Frw\partial_{\mathcal{Z}} v_{Ax}\boldsymbol{e}_x) + \mathcal{M}_A\left(\boldsymbol{v}_A \cdot \boldsymbol{\nabla}_H \boldsymbol{u}_H - \boldsymbol{u}_H \cdot \boldsymbol{\nabla}_H v_{Ax}\boldsymbol{e}_x\right) + S^{-1}\left(Fr^{-2}\partial_z^2 \boldsymbol{b}_H + \nabla_H^2 \boldsymbol{b}_H\right) \tag{25f}$$

$$Fr\partial_t b_z = \mathcal{M}_A(v_{Az}\partial_z w - u\partial_x v_{Az}) + \mathcal{M}_A Fr(v_{Ax}\partial_x w - w\partial_{\mathcal{Z}} v_{Az}) + FrS^{-1}\left(Fr^{-2}\partial_z^2 b_z + \nabla_H^2 b_z\right) \tag{25g}$$

$$\partial_t \rho = N^2(\mathcal{Z})w, \tag{25h}$$

where $\boldsymbol{\nabla}_H = \boldsymbol{\nabla} - \boldsymbol{e}_z\partial_z$, $\boldsymbol{v}_A = v_{Ax}\boldsymbol{e}_x + v_{Az}\boldsymbol{e}_z$, and

$$Fr = \frac{l_z}{L} = \frac{\omega}{\mathcal{N}}, \quad \mathcal{M}_A = \frac{\mathcal{B}(\mu_0\rho_0)^{-1/2}}{\omega L}, \quad S = \frac{\omega L^2}{\eta}. \tag{26}$$

We are interested in driving frequencies ω that are much faster than the Alfven frequency but much slower than the buoyancy frequency, i.e.,

$$\frac{\mathcal{B}}{L\sqrt{\mu_0\rho_0}} \ll \omega \ll \mathcal{N}, \tag{27}$$

which corresponds nondimensionally to $Fr \ll 1$, $\mathcal{M}_A \ll 1$. Another restriction is that the driving frequency should be greater than the magneto-gravity frequency [7], ω_{MG}:

$$\omega > \omega_{\mathrm{MG}} \equiv \left(\frac{\mathcal{B}^2\mathcal{N}^2}{L^2\mu_0\rho_0}\right)^{1/4}, \tag{28}$$

or

$$\Gamma \equiv \frac{\mathcal{M}_A}{Fr} = \left(\frac{\omega_{\mathrm{MG}}}{\omega}\right)^2 < 1 \tag{29}$$

Thus, we choose the distinguished limit $Fr \sim \mathcal{M}_A$ as $Fr \to 0$. Accordingly, let $Fr = \epsilon$ and $\mathcal{M}_A = \Gamma\epsilon$ with $\Gamma = O(1)$. Additionally, let $S^{-1} \ll Fr$ such that we can neglect diffusion in the following subsections. The dimensionless equations then become:

$$\boldsymbol{\nabla}_H \cdot \boldsymbol{u}_H + \partial_z w = 0 \tag{30a}$$

$$\partial_t \boldsymbol{u}_H + \boldsymbol{\nabla}_H p = \Gamma v_{Az}(\partial_z \boldsymbol{b}_H - \epsilon^2 \boldsymbol{\nabla}_H b_z) + \epsilon\Gamma(\boldsymbol{\nabla}_H \times \boldsymbol{b}_H) \times v_{Ax}\boldsymbol{e}_x \tag{30b}$$

$$\epsilon\partial_t w + \epsilon^{-1}\partial_z p = -\epsilon^{-1}\rho + \epsilon\Gamma v_{Ax}(\epsilon\partial_x b_z - \epsilon^{-1}\partial_z b_x) \tag{30c}$$

$$\partial_t \rho = N^2(\mathcal{Z})w, \tag{30d}$$

$$\partial_t \boldsymbol{b}_H = \Gamma(v_{Az}\partial_z \boldsymbol{u}_H - \epsilon^2 w\partial_{\mathcal{Z}} v_{Ax}\boldsymbol{e}_x) + \epsilon\Gamma\left(v_{Ax}\partial_x \boldsymbol{u}_H - u\partial_x v_{Ax}\boldsymbol{e}_x\right) \tag{30e}$$

$$\partial_t b_z = \Gamma(v_{Az}\partial_z w - u\partial_x v_{Az}) + \epsilon\Gamma(v_{Ax}\partial_x w - w\partial_{\mathcal{Z}} v_{Az}) \tag{30f}$$

A.3 Reduced system

We assume that the background magnetic field and buoyancy frequency vary with $\mathcal{Z} = \epsilon z$ and are 1-periodic in x, and we look for wave solutions with frequency ω and horizontal wavenumber k_y set by the driving.

Letting $\boldsymbol{q} = \begin{bmatrix} u & v & w & p & \rho & b_x & b_y & b_z \end{bmatrix}^T$, we make the expansion

$$\boldsymbol{q} = \Re\{\hat{\boldsymbol{q}}(x, \epsilon z) \exp(i\Theta(\epsilon z)/\epsilon) \exp(ik_y y - i\omega t)\}, \tag{31}$$

with

$$\hat{\boldsymbol{q}} = A(\epsilon z)\boldsymbol{q}_0(x, \epsilon z) + \epsilon \boldsymbol{q}_1(x, \epsilon z) + \epsilon^2 \boldsymbol{q}_2(x, \epsilon z) + ..., \tag{32}$$

where we have used a WKB ansatz in the z direction. The elements of $\boldsymbol{q}_0(x, \epsilon z)$ are eigenfunctions in x, the relative amplitudes of which vary with ϵz. An additional, *overall* dependence of the leading order solution on ϵz is captured by $A(\epsilon z)$. Thus, to construct the leading order solution, we need to determine $A(\epsilon z)$, $\boldsymbol{q}_0(x)$, $\Theta(\epsilon z)$. We require that $\boldsymbol{q}_0(x, \epsilon z)$ is periodic such that $\boldsymbol{q}_0(0, \epsilon z) = \boldsymbol{q}_0(1, \epsilon z)$, $\partial_x \boldsymbol{q}_0(0, \epsilon z) = \partial_x \boldsymbol{q}_0(1, \epsilon z)$.

A.3.1 Dispersion relation

The relevant leading order equations can be written in vector form as

$$\hat{\boldsymbol{\nabla}}_H \cdot \boldsymbol{u}_{0H} + i\Theta' w_0 = 0, \tag{33a}$$

$$-i\omega \boldsymbol{u}_{0H} + \hat{\boldsymbol{\nabla}}_H p_0 - i\Gamma v_{Az} \Theta' \boldsymbol{b}_{0H} = 0, \tag{33b}$$

$$\rho_0 + i\Theta' p_0 = 0, \tag{33c}$$

$$-i\omega\rho_0 - N^2 w_0 = 0, \tag{33d}$$

$$-i\omega \boldsymbol{b}_{0H} - i\Gamma\Theta' v_{Az} \boldsymbol{u}_{0H} = 0, \tag{33e}$$

where $\hat{\boldsymbol{\nabla}}_H = \boldsymbol{e}_x \partial_x + \boldsymbol{e}_y ik_y$. Note that in these equations and in the following sections, ρ_0 refers to the leading order (dimensionless) density perturbation, not the (dimensional) background density.

Note that the vertical component of the induction equation is not needed to close the system of equations, and b_{0z} is just determined diagnostically from $\boldsymbol{b}_{0H}$ via Gauss' law. Though the vertical velocity is of the same order as the vertical magnetic field component, w_0 is coupled to ρ_0 through the mass equation and does not drop out of the leading-order system.

We can combine the system (33) to yield a single equation for p_0. Taking $i\omega$(33c)+(33d) yields

$$-\omega\Theta' p_0 - N^2 w_0 = 0 \tag{34}$$

Then, take (33a)$+i\Theta' N^{-2}$(34):

$$\hat{\boldsymbol{\nabla}}_H \cdot \boldsymbol{u}_{0H} - \frac{i\omega\Theta'^2}{N^2} p_0 = 0. \tag{35}$$

Now, take $(\omega^2 - \Gamma^2 v_{Az}^2 \Theta'^2)^{-1}[i\omega(33\text{b}) - i\Gamma v_{Az}\Theta'(33\text{e})]$:

$$\boldsymbol{u}_{0H} + \frac{i\omega \hat{\boldsymbol{\nabla}}_H p_0}{\omega^2 - \Gamma^2 v_{Az}^2 \Theta'^2} = 0 \tag{36}$$

Lastly, taking $(i\omega)^{-1}(\hat{\boldsymbol{\nabla}}_H \cdot (36) - (35))$ yields

$$\frac{\Theta'^2}{N^2} p_0 + \hat{\boldsymbol{\nabla}}_H \cdot \left(\frac{\hat{\boldsymbol{\nabla}}_H p_0}{\omega^2 - \Gamma^2 v_{Az}^2 \Theta'^2} \right) = 0. \tag{37}$$

This is a generalized eigenvalue problem with eigenvalues $k_z^2 \equiv \Theta'^2$ and eigenfunctions p_0. For the purpose of implementation, it is useful to retain the equations for u_0 and v_0 as well:

$$\begin{bmatrix} \partial_x & ik_y & -i\omega N^{-2} k_z^2 \\ (\omega^2 - \Gamma^2 k_z^2 v_{Az}^2) & 0 & i\omega \partial_x \\ 0 & (\omega^2 - \Gamma^2 k_z^2 v_{Az}^2) & -\omega k_y \end{bmatrix} \begin{bmatrix} u_0 \\ v_0 \\ p_0 \end{bmatrix} = \mathbf{0} \tag{38}$$

Note that k_z is nondimensionalized by l_z^{-1} such that if the vertical group velocity is defined by

$$c_{gz} = \frac{\partial \omega}{\partial k_z}, \tag{39}$$

then c_{gz} is nondimensionalized by ωl_z in analogy with w.

Finally, it will be useful to find the adjoint of

$$\mathcal{L}_{\Theta'}[\,\cdot\,] = \frac{\Theta'^2}{N^2}(\cdot) + \hat{\boldsymbol{\nabla}}_H \cdot \left(\frac{\hat{\boldsymbol{\nabla}}_H (\cdot)}{\omega^2 - \Gamma^2 v_{Az}^2 \Theta'^2} \right), \tag{40}$$

which is the operator on the left-hand side of (37). We will use the properties

$$\int_0^1 g^* \hat{\boldsymbol{\nabla}}_H \cdot \boldsymbol{a} \mathrm{d}x = -\int_0^1 (\hat{\boldsymbol{\nabla}}_H g)^* \cdot \boldsymbol{a} \mathrm{d}x, \tag{41}$$

$$\int_0^1 c \hat{\boldsymbol{\nabla}}_H h \cdot (\hat{\boldsymbol{\nabla}}_H g)^* \mathrm{d}x = -\int_0^1 h \left[\hat{\boldsymbol{\nabla}}_H \cdot (c^* \hat{\boldsymbol{\nabla}}_H g) \right]^* \mathrm{d}x, \tag{42}$$

that hold for general vector $\boldsymbol{a}$ and scalar c, g, h fields that are periodic on $x \in [0, 1]$. We find that

$$\begin{aligned} \langle g, \mathcal{L}_{\Theta'}[h] \rangle &= \int_0^1 g^* \left[\frac{\Theta'^2}{N^2} h + \hat{\boldsymbol{\nabla}}_H \cdot \left(\frac{\hat{\boldsymbol{\nabla}}_H h}{\omega^2 - \Gamma^2 v_{Az}^2 \Theta'^2} \right) \right] \mathrm{d}x \\ &= \int_0^1 \left[\frac{\Theta'^2}{N^2} g^* h - \frac{\hat{\boldsymbol{\nabla}}_H h}{\omega^2 - \Gamma^2 v_{Az}^2 \Theta'^2} \cdot \left(\hat{\boldsymbol{\nabla}}_H g \right)^* \right] \mathrm{d}x \\ &= \int_0^1 \left[\frac{(\Theta'^2)^*}{N^2} g + \hat{\boldsymbol{\nabla}}_H \cdot \left(\frac{\hat{\boldsymbol{\nabla}}_H g}{\omega^2 - \Gamma^2 v_{Az}^2 (\Theta'^2)^*} \right) \right]^* h \mathrm{d}x \\ &= \langle \mathcal{L}_{\Theta'}^\dagger [g], h \rangle, \end{aligned} \tag{43}$$

where

$$\mathcal{L}^{\dagger}_{\Theta'}[\,\cdot\,] = \frac{(\Theta'^2)^*}{N^2}(\cdot) + \hat{\boldsymbol{\nabla}}_H \cdot \left(\frac{\hat{\boldsymbol{\nabla}}_H(\cdot)}{\omega^2 - \Gamma^2 v_{Az}^2 (\Theta'^2)^*} \right). \tag{44}$$

We can show that if $\mathcal{L}_{\Theta'}[p_0] = 0$, then $\mathcal{L}^{\dagger}_{\Theta'}[p_0^*] = 0$. Take the complex conjugate of (37):

$$\begin{aligned}
0 &= (\mathcal{L}_{\Theta'}[p_0])^* \\
&= \frac{(\Theta'^2)^*}{N^2} p_0^* + \left[\hat{\boldsymbol{\nabla}}_H \cdot \left(\frac{\hat{\boldsymbol{\nabla}}_H p_0}{\omega^2 - \Gamma^2 v_{Az}^2 \Theta'^2} \right) \right]^* \\
&= \frac{(\Theta'^2)^*}{N^2} p_0^* + \left[\partial_x \left(\frac{\partial_x p_0}{\omega^2 - \Gamma^2 v_{Az}^2 \Theta'^2} \right) + ik_y \left(\frac{ik_y p_0}{\omega^2 - \Gamma^2 v_{Az}^2 \Theta'^2} \right) \right]^* \\
&= \frac{(\Theta'^2)^*}{N^2} p_0^* + \partial_x \left(\frac{\partial_x p_0^*}{\omega^2 - \Gamma^2 v_{Az}^2 (\Theta'^2)^*} \right) - ik_y \left(\frac{-ik_y p_0^*}{\omega^2 - \Gamma^2 v_{Az}^2 (\Theta'^2)^*} \right) \\
&= \frac{(\Theta'^2)^*}{N^2} p_0^* + \hat{\boldsymbol{\nabla}}_H \cdot \left(\frac{\hat{\boldsymbol{\nabla}}_H p_0^*}{\omega^2 - \Gamma^2 v_{Az}^2 (\Theta'^2)^*} \right) \\
&= \mathcal{L}^{\dagger}_{\Theta'}[p_0^*]
\end{aligned} \tag{45}$$

Finally, we note that the operator $\mathcal{L}_{\Theta'}$ is self-adjoint ($\mathcal{L}^{\dagger}_{\Theta'} = \mathcal{L}_{\Theta'}$) if and only if $\Theta'^2 \in \mathbb{R}$.

A.3.2 Energy equation

The $O(1)$ equations yield the eigenfunctions p_0 and the vertical phase $\Theta(\mathcal{Z})$. For the remaining piece of the solution, $A(\mathcal{Z})$, we must proceed to the next order in ϵ. Before doing so, it is instructive to analyze the energy equation, which constrains the magnitude of the amplitude, $|A|$, but not its complex phase.

Nondimensionalizing (22) and dropping tildes yields

$$\partial_t E + \boldsymbol{\nabla}_H \cdot \boldsymbol{F} + \frac{1}{Fr} \partial_z F_z = 0, \tag{46}$$

where

$$E = \frac{1}{2}(\boldsymbol{u}_H \cdot \boldsymbol{u}_H + Fr^2 w^2) + \frac{\rho^2}{2N^2} + \frac{1}{2}(\boldsymbol{b}_H \cdot \boldsymbol{b}_H + Fr^2\, b_z^2), \tag{47}$$

$$\boldsymbol{F} = p(\boldsymbol{u}_H + Frw\boldsymbol{e}_z) + (\boldsymbol{b}_H + Frb_z\boldsymbol{e}_z) \times [(\boldsymbol{u}_H + Frw\boldsymbol{e}_z) \times \Gamma Fr \boldsymbol{v}_A], \tag{48}$$

and

$$F_z = \boldsymbol{F} \cdot \boldsymbol{e}_z = Fr\,[pw - \Gamma(\boldsymbol{b}_H \cdot \boldsymbol{u}_H) v_{Az} + \Gamma Fr b_x v_{Ax} w] \tag{49}$$

Integrate the (46) over x and y. The horizontal flux term will vanish (by periodicity), yielding

$$\partial_t \int_{-\pi/k_y}^{-\pi/k_y} \int_0^1 E \mathrm{d}x\mathrm{d}y + \frac{1}{Fr} \partial_z \int_{-\pi/k_y}^{-\pi/k_y} \int_0^1 F_z \mathrm{d}x\mathrm{d}y = 0. \tag{50}$$

Now, substitute the wave ansatz (31):

$$\frac{1}{2}\partial_t \int_0^1 \left(\frac{\hat{\boldsymbol{u}}_H \cdot \hat{\boldsymbol{u}}_H^*}{2} + \frac{\hat{\rho}\hat{\rho}^*}{2N^2} + \frac{\hat{\boldsymbol{b}}_H \cdot \hat{\boldsymbol{b}}_H^*}{2} \right) \mathrm{d}x + \frac{1}{2}\partial_z \int_0^1 \left[\Re\{\hat{p}^* \hat{w}\} - \Gamma v_{Az} \Re\{\hat{\boldsymbol{b}}_H \cdot \hat{\boldsymbol{u}}_H^*\} + \Gamma Fr v_{Ax} \Re\{\hat{B}_x \hat{w}^*\} \right] \mathrm{d}x = 0. \quad (51)$$

Now, let $Fr = \epsilon$ and let $\hat{\boldsymbol{q}} = \tilde{A}(\epsilon z, \epsilon t)\boldsymbol{q}_0(x, \epsilon z) + O(\epsilon)$. Further, define a slow time $\mathcal{T} = \epsilon t$. Then, at $O(\epsilon)$,

$$\partial_{\mathcal{T}} \left(\tilde{A}\tilde{A}^* \int_0^1 E_0 \mathrm{d}x \right) + \partial_{\mathcal{Z}} \left(\tilde{A}\tilde{A}^* \int_0^1 \Re\{F_0\} \mathrm{d}x \right) = 0, \quad (52)$$

where

$$E_0 = \frac{\boldsymbol{u}_{0H} \cdot \boldsymbol{u}_{0H}^*}{2} + \frac{\rho_0 \rho_0^*}{2N^2} + \frac{\boldsymbol{b}_{0H} \cdot \boldsymbol{b}_{0H}^*}{2} \quad (53)$$

and

$$F_0 = p_0^* w_0 - \Gamma v_{Az} \boldsymbol{b}_{0H} \cdot \boldsymbol{u}_{0H}^*. \quad (54)$$

Further, letting

$$\mathcal{E}_0 = \tilde{A}\tilde{A}^* \int_0^1 E_0 \mathrm{d}x \quad (55)$$

be the leading-order horizontally-averaged wave energy, we find that

$$\partial_{\mathcal{T}} \mathcal{E}_0 + c_{gz} \partial_{\mathcal{Z}} \mathcal{E}_0 = -\mathcal{E}_0 \partial_{\mathcal{Z}} c_{gz}. \quad (56)$$

Thus, energy is transported vertically at the group velocity

$$c_{gz} = \frac{\int_0^1 \Re\{F_0\} \mathrm{d}x}{\int_0^1 E_0 \mathrm{d}x}. \quad (57)$$

If the wave solution is equilibrated such that $\tilde{A} = A(\epsilon z)$, then (52) reduces to

$$\partial_{\mathcal{Z}} \left(AA^* \int_0^1 \Re\{F_0\} \mathrm{d}x \right) = 0 \quad (58)$$

Integrating with respect to $\mathcal{Z}$ yields

$$AA^* \int_0^1 \Re\{F_0\} \mathrm{d}x = |C|^2. \quad (59)$$

Next, we can use the polarization relations to simplify F_0. From (33), we find that

$$w_0 = -\frac{\omega \Theta'}{N^2} p_0 \quad (60a)$$

$$\boldsymbol{u}_{0H} = -\frac{i\omega \hat{\boldsymbol{\nabla}}_H p_0}{\omega^2 - \Gamma^2 v_{Az}^2 \Theta'^2}, \quad (60b)$$

and

$$\boldsymbol{b}_{0H} = -\frac{\Gamma v_{Az}\Theta'}{\omega}\boldsymbol{u}_{0H}. \tag{60c}$$

Then we can rewrite F_0 as

$$F_0 = -\frac{\omega\Theta'}{N^2}p_0^* p_0 + \Gamma^2 v_{Az}^2\Theta'\omega\frac{\partial_x p_0^*\partial_x p_0 + k_y^2 p_0^* p_0}{(\omega^2-\Gamma^2 v_{Az}^2\Theta'^2)^*(\omega^2-\Gamma^2 v_{Az}^2\Theta'^2)}, \tag{61}$$

or equivalently

$$F_0 = -\frac{\omega\Theta'}{N^2}|p_0|^2 + \Gamma^2 v_{Az}^2\Theta'\omega\frac{|\hat{\boldsymbol{\nabla}}_H p_0|^2}{|\omega^2-\Gamma^2 v_{Az}^2\Theta'^2|^2}. \tag{62}$$

Thus, (59) can be rearranged to give

$$|A|^2 = \frac{|C|^2}{\int_0^1\left(-\frac{\omega\Theta'}{N^2}|p_0|^2 + \Gamma^2 v_{Az}^2\Theta'\omega\frac{|\hat{\boldsymbol{\nabla}}_H p_0|^2}{|\omega^2-\Gamma^2 v_{Az}^2\Theta'^2|^2}\right)\mathrm{d}x} \tag{63}$$

where C is a constant. Note that so far we have only obtained the absolute value of the complex amplitude $|A|$, the full amplitude A including the complex phase will be derived in the following section.

A.3.3 Amplitude equation

The results from the energy equation will aid in the derivation of an amplitude equation from the $O(\epsilon)$ system:

$$\hat{\boldsymbol{\nabla}}_H\cdot\boldsymbol{u}_{1H} + i\Theta' w_1 = -\partial_{\mathcal{Z}}(Aw_0), \tag{64a}$$

$$-i\omega\boldsymbol{u}_{1H} + \hat{\boldsymbol{\nabla}}_H p_1 - i\,\Gamma v_{Az}\Theta'\boldsymbol{b}_{1H} = \Gamma v_{Az}\partial_{\mathcal{Z}}(A\boldsymbol{b}_{0H}) + \Gamma(\hat{\boldsymbol{\nabla}}_H\times A\boldsymbol{b}_{0H})\times v_{Ax}\boldsymbol{e}_x, \tag{64b}$$

$$\rho_1 + i\Theta' p_1 = -\partial_Z(Ap_0) - i\Theta'\Gamma A v_{Ax}b_{0x}, \tag{64c}$$

$$-i\omega\rho_1 - N^2 w_1 = 0, \tag{64d}$$

$$-i\omega\boldsymbol{b}_{1H} - i\Gamma\Theta' v_{Az}\boldsymbol{u}_{1H} = \Gamma\left[v_{Az}\partial_{\mathcal{Z}}(A\boldsymbol{u}_{0H}) + v_{Ax}\partial_x(A\boldsymbol{u}_{0H}) - Au_0\partial_x v_{Ax}\boldsymbol{e}_x\right]. \tag{64e}$$

Combining these equations following the procedure detailed in §A.3.1 yields

$$\begin{aligned}\frac{i\omega\Theta'^2}{N^2}p_1 + \hat{\boldsymbol{\nabla}}_H\cdot\left(\frac{i\omega\hat{\boldsymbol{\nabla}}_H p_1}{\omega^2-\Gamma^2\Theta'^2 v_{Az}^2}\right)\\ = \partial_{\mathcal{Z}}(Aw_0) - \frac{\omega\Theta'}{N^2}\partial_{\mathcal{Z}}(Ap_0) - \frac{i\omega\Theta'^2}{N^2}\Gamma A v_{Ax}b_{0x} + \hat{\boldsymbol{\nabla}}_H\cdot\left(\frac{i\omega\boldsymbol{s}}{\omega^2-\Gamma^2\Theta'^2 v_{Az}^2}\right),\end{aligned} \tag{65}$$

where

$$\begin{aligned}\boldsymbol{s} = \Gamma v_{Az}\partial_{\mathcal{Z}}(A\boldsymbol{b}_{0H}) + \Gamma(\hat{\boldsymbol{\nabla}}_H\times A\boldsymbol{b}_{0H})\times v_{Ax}\boldsymbol{e}_x\\ - \frac{\Gamma^2 v_{Az}\Theta'}{\omega}\left[v_{Az}\partial_{\mathcal{Z}}(A\boldsymbol{u}_{0H}) + v_{Ax}\partial_x(A\boldsymbol{u}_{0H}) - Au_0\partial_x v_{Ax}\boldsymbol{e}_x\right].\end{aligned} \tag{66}$$

We can express this as

$$\mathcal{L}_{\Theta'}[p_1] = f(A). \tag{67}$$

To obtain an equation for A, we can take the inner product of the equation above with any element $\tilde{p}_0$ of the cokernel of $\mathcal{L}_{\Theta'}$:

$$\begin{aligned} \langle \tilde{p}_0, \mathcal{L}_{\Theta'}[p_1] \rangle &= \langle \tilde{p}_0, f \rangle \\ \Rightarrow \langle \mathcal{L}^\dagger_{\Theta'}[\tilde{p}_0], p_1 \rangle &= \langle \tilde{p}_0, f \rangle \\ \Rightarrow \qquad 0 &= \langle \tilde{p}_0, f \rangle, \end{aligned} \tag{68}$$

since $\mathcal{L}^\dagger_{\Theta'}[\tilde{p}_0] = 0$ by definition.

Now, using $\tilde{p}_0$, define $\tilde{\boldsymbol{u}}_{0H}$, $\tilde{w}_0$, and $\tilde{\boldsymbol{b}}_{0H}$ such that

$$\hat{\boldsymbol{\nabla}}_H \cdot \tilde{\boldsymbol{u}}_{0H} + i(\Theta')^* \tilde{w}_0 = 0, \tag{69a}$$

$$-i\omega \tilde{\boldsymbol{u}}_{0H} + \hat{\boldsymbol{\nabla}}_H \tilde{p}_0 - i\ \Gamma v_{Az} (\Theta')^* \tilde{\boldsymbol{b}}_{0H} = 0, \tag{69b}$$

$$\omega (\Theta')^* \tilde{p}_0 + N^2 \tilde{w}_0 = 0, \tag{69c}$$

$$i\omega \tilde{\boldsymbol{b}}_{0H} + i\Gamma (\Theta')^* v_{Az} \tilde{\boldsymbol{u}}_{0H} = 0, \tag{69d}$$

The identities (69) will be useful for simplifying the solvability condition, $0 = \langle \tilde{p}_0, f \rangle$, which can be written out as

$$0 = \int_0^1 \left[\tilde{p}_0^* \partial_{\mathcal{Z}} (A w_0) - \tilde{p}_0^* \frac{\omega \Theta'}{N^2} \partial_{\mathcal{Z}} (A p_0) - \tilde{p}_0^* \frac{i\omega \Theta'^2}{N^2} \Gamma A v_{Ax} b_{0x} + \tilde{p}_0^* \hat{\boldsymbol{\nabla}}_H \cdot \left(\frac{i\omega \boldsymbol{s}}{\omega^2 - \Gamma^2 \Theta'^2 v_{Az}^2} \right) \right] \mathrm{d}x. \tag{70}$$

Using the identity (41) (integrating by parts) yields

$$0 = \int_0^1 \left[\tilde{p}_0^* \partial_{\mathcal{Z}} (A w_0) - \tilde{p}_0^* \frac{\omega \Theta'}{N^2} \partial_{\mathcal{Z}} (A p_0) - \tilde{p}_0^* \frac{i\omega \Theta'^2}{N^2} \Gamma A v_{Ax} b_{0x} - (\hat{\boldsymbol{\nabla}}_H \tilde{p}_0)^* \cdot \left(\frac{i\omega \boldsymbol{s}}{\omega^2 - \Gamma^2 \Theta'^2 v_{Az}^2} \right) \right] \mathrm{d}x. \tag{71}$$

Since $\tilde{\boldsymbol{u}}^*_{0H} = i\omega (\hat{\boldsymbol{\nabla}}_H \tilde{p}_0)^* / (\omega^2 - \Gamma^2 v_{Az}^2 \Theta'^2)$ and $\tilde{w}_0^* = -\tilde{p}_0^* \omega \Theta' / N^2$,

$$0 = \int_0^1 \left[\tilde{p}_0^* \partial_{\mathcal{Z}} (A w_0) + \tilde{w}_0^* \partial_{\mathcal{Z}} (A p_0) + \tilde{w}_0^* i \Theta' \Gamma A v_{Ax} b_{0x} - \tilde{\boldsymbol{u}}^*_{0H} \cdot \boldsymbol{s} \right] \mathrm{d}x \tag{72}$$

Now, we can simplify $\tilde{\boldsymbol{u}}^*_{0H} \cdot \boldsymbol{s}$ using the relations $\tilde{\boldsymbol{b}}^*_{0H} = -\Gamma v_{Az} \Theta' \tilde{\boldsymbol{u}}^*_{0H} / \omega$ and $\Gamma (\hat{\boldsymbol{\nabla}}_H \times A \boldsymbol{b}_{0H}) \times v_{Ax} \boldsymbol{e}_x = \Gamma v_{Ax} A (\partial_x b_{0y} - i k_y b_{0x}) \boldsymbol{e}_y$:

$$\begin{aligned} \tilde{\boldsymbol{u}}^*_{0H} \cdot \boldsymbol{s} &= \Gamma v_{Az} [\tilde{\boldsymbol{u}}^*_{0H} \cdot \partial_{\mathcal{Z}} (A \boldsymbol{b}_{0H}) - \frac{1}{\omega} \Gamma v_{Az} \Theta' \tilde{\boldsymbol{u}}^*_{0H} \cdot \partial_{\mathcal{Z}} (A \boldsymbol{u}_{0H})] \\ &\quad - \frac{1}{\omega} \Gamma^2 v_{Az} \Theta' \tilde{\boldsymbol{u}}^*_{0H} \cdot [v_{Ax} \partial_x (A \boldsymbol{u}_{0H}) - A u_0 \partial_x v_{Ax} \boldsymbol{e}_x] + \tilde{\boldsymbol{u}}^*_{0H} \cdot [\Gamma (\hat{\boldsymbol{\nabla}}_H \times A \boldsymbol{b}_{0H}) \times v_{Ax} \boldsymbol{e}_x] \\ &= \Gamma v_{Az} \left[\tilde{\boldsymbol{u}}^*_{0H} \cdot \partial_{\mathcal{Z}} (A \boldsymbol{b}_{0H}) + \tilde{\boldsymbol{b}}^*_{0H} \cdot \partial_{\mathcal{Z}} (A \boldsymbol{u}_{0H}) \right] + \Gamma \tilde{\boldsymbol{b}}^*_{0H} \cdot [v_{Ax} \partial_x (A \boldsymbol{u}_{0H}) - A u_0 \partial_x v_{Ax} \boldsymbol{e}_x] \\ &\qquad + \tilde{v}_0^* \Gamma v_{Ax} A (\partial_x b_{0y} - i k_y b_{0x}) \\ &= \Gamma v_{Az} \left[\tilde{\boldsymbol{u}}^*_{0H} \cdot \partial_{\mathcal{Z}} (A \boldsymbol{b}_{0H}) + \tilde{\boldsymbol{b}}^*_{0H} \cdot \partial_{\mathcal{Z}} (A \boldsymbol{u}_{0H}) \right] - \Gamma A \tilde{b}^*_{0x} u_0 \partial_x v_{Ax} \\ &\quad + \Gamma A v_{Ax} (\tilde{b}^*_{0y} \partial_x v_0 + \tilde{v}_0^* \partial_x b_{0y}) + \Gamma A v_{Ax} \tilde{b}^*_{0x} \partial_x u_0 - i \Gamma A v_{Ax} \tilde{v}_0^* k_y b_{0x}. \end{aligned} \tag{73}$$

From Gauss' law $\partial_x v_{Ax} = -\partial_{\mathcal{Z}} v_{Az}$, and thus

$$\tilde{\boldsymbol{u}}^*_{0H}\cdot\boldsymbol{s} = \Gamma v_{Az}\left[\tilde{\boldsymbol{u}}^*_{0H}\cdot\partial_{\mathcal{Z}}(A\boldsymbol{b}_{0H}) + \tilde{\boldsymbol{b}}^*_{0H}\cdot\partial_{\mathcal{Z}}(A\boldsymbol{u}_{0H})\right] + \Gamma A\tilde{b}^*_{0x}u_0\partial_{\mathcal{Z}}v_{Az} + \Gamma A v_{Ax}(\tilde{b}^*_{0y}\partial_x v_0 + \tilde{v}^*_0\partial_x b_{0y}) + \Gamma A v_{Ax}\tilde{b}^*_{0x}\partial_x u_0 - i\Gamma A v_{Ax}\tilde{v}^*_0 k_y b_{0x}. \quad (74)$$

Add and subtract $\Gamma A\tilde{b}^*_{0y}v_0\partial_x v_{Ax}$ and use $\partial_x v_{Ax} = -\partial_{\mathcal{Z}} v_{Az}$ again:

$$\begin{aligned}\tilde{\boldsymbol{u}}^*_{0H}\cdot\boldsymbol{s} &= \Gamma v_{Az}\left[\tilde{\boldsymbol{u}}^*_{0H}\cdot\partial_{\mathcal{Z}}(A\boldsymbol{b}_{0H}) + \tilde{\boldsymbol{b}}^*_{0H}\cdot\partial_{\mathcal{Z}}(A\boldsymbol{u}_{0H})\right] + \Gamma A\tilde{b}^*_{0x}u_0\partial_{\mathcal{Z}}v_{Az} - \Gamma A\tilde{b}^*_{0y}v_0\partial_x v_{Ax}\\ &\quad + \Gamma A v_{Ax}(\tilde{b}^*_{0y}\partial_x v_0 + \tilde{v}^*_0\partial_x b_{0y}) + \Gamma A\tilde{b}^*_{0y}v_0\partial_x v_{Ax} + \Gamma A v_{Ax}\tilde{b}^*_{0x}\partial_x u_0 - i\Gamma A v_{Ax}\tilde{v}^*_0 k_y b_{0x}\\ &= \Gamma v_{Az}\left[\tilde{\boldsymbol{u}}^*_{0H}\cdot\partial_{\mathcal{Z}}(A\boldsymbol{b}_{0H}) + \tilde{\boldsymbol{b}}^*_{0H}\cdot\partial_{\mathcal{Z}}(A\boldsymbol{u}_{0H})\right] + \Gamma A\tilde{\boldsymbol{b}}^*_{0H}\cdot\boldsymbol{u}_{0H}\partial_{\mathcal{Z}}v_{Az}\\ &\quad + \Gamma A v_{Ax}(\tilde{b}^*_{0y}\partial_x v_0 + \tilde{v}^*_0\partial_x b_{0y}) + \Gamma A\tilde{b}^*_{0y}v_0\partial_x v_{Ax} + \Gamma A v_{Ax}\tilde{b}^*_{0x}\partial_x u_0 - i\Gamma A v_{Ax}\tilde{v}^*_0 k_y b_{0x}.\end{aligned} \quad (75)$$

Then,

$$\begin{aligned}0 = \int_0^1 \Big\{ &\tilde{p}^*_0\partial_{\mathcal{Z}}(Aw_0) + \tilde{w}^*_0\partial_{\mathcal{Z}}(Ap_0) + \tilde{w}^*_0 i\Theta'\Gamma A v_{Ax}b_{0x}\\ &- \Gamma v_{Az}\left[\tilde{\boldsymbol{u}}^*_{0H}\cdot\partial_{\mathcal{Z}}(A\boldsymbol{b}_{0H}) + \tilde{\boldsymbol{b}}^*_{0H}\cdot\partial_{\mathcal{Z}}(A\boldsymbol{u}_{0H})\right] - \Gamma A\tilde{\boldsymbol{b}}^*_{0H}\cdot\boldsymbol{u}_{0H}\partial_{\mathcal{Z}}v_{Az}\\ &- \Gamma A v_{Ax}(\tilde{b}^*_{0y}\partial_x v_0 + \tilde{v}^*_0\partial_x b_{0y}) - \Gamma A\tilde{b}^*_{0y}v_0\partial_x v_{Ax} - \Gamma A v_{Ax}\tilde{b}^*_{0x}\partial_x u_0 + i\Gamma A v_{Ax}\tilde{v}^*_0 k_y b_{0x}\Big\}\mathrm{d}x\end{aligned} \quad (76)$$

Now, use $i\Theta'\tilde{w}^*_0 = \partial_x\tilde{u}^*_0 - ik_y\tilde{v}^*_0$:

$$\begin{aligned}0 = \int_0^1 \Big\{ &\tilde{p}^*_0\partial_{\mathcal{Z}}(Aw_0) + \tilde{w}^*_0\partial_{\mathcal{Z}}(Ap_0) + (\partial_x\tilde{u}^*_0 - ik_y\tilde{v}^*_0)\Gamma A v_{Ax}b_{0x}\\ &- \Gamma v_{Az}\left[\tilde{\boldsymbol{u}}^*_{0H}\cdot\partial_{\mathcal{Z}}(A\boldsymbol{b}_{0H}) + \tilde{\boldsymbol{b}}^*_{0H}\cdot\partial_{\mathcal{Z}}(A\boldsymbol{u}_{0H})\right] - \Gamma A\tilde{\boldsymbol{b}}^*_{0H}\cdot\boldsymbol{u}_{0H}\partial_{\mathcal{Z}}v_{Az}\\ &- \Gamma A v_{Ax}(\tilde{b}^*_{0y}\partial_x v_0 + \tilde{v}^*_0\partial_x b_{0y}) - \Gamma A\tilde{b}^*_{0y}v_0\partial_x v_{Ax} - \Gamma A v_{Ax}\tilde{b}^*_{0x}\partial_x u_0 + i\Gamma A v_{Ax}\tilde{v}^*_0 k_y b_{0x}\Big\}\mathrm{d}x\\ = \int_0^1 \Big\{ &\tilde{p}^*_0\partial_{\mathcal{Z}}(Aw_0) + \tilde{w}^*_0\partial_{\mathcal{Z}}(Ap_0) + \Gamma A v_{Ax}(b_{0x}\partial_x\tilde{u}^*_0 - \tilde{b}^*_{0x}\partial_x u_0)\\ &- \Gamma v_{Az}\left[\tilde{\boldsymbol{u}}^*_{0H}\cdot\partial_{\mathcal{Z}}(A\boldsymbol{b}_{0H}) + \tilde{\boldsymbol{b}}^*_{0H}\cdot\partial_{\mathcal{Z}}(A\boldsymbol{u}_{0H})\right] - \Gamma A\tilde{\boldsymbol{b}}^*_{0H}\cdot\boldsymbol{u}_{0H}\partial_{\mathcal{Z}}v_{Az}\\ &- \Gamma A v_{Ax}(\tilde{b}^*_{0y}\partial_x v_0 + \tilde{v}^*_0\partial_x b_{0y}) - \Gamma A\tilde{b}^*_{0y}v_0\partial_x v_{Ax}\Big\}\mathrm{d}x.\end{aligned} \quad (77)$$

Next, we shall put the amplitude equation in the form $\alpha(\mathcal{Z})\frac{\mathrm{d}A}{\mathrm{d}\mathcal{Z}} + \beta(\mathcal{Z})A(\mathcal{Z}) = 0$. We find

that

$$0 = \int_0^1 \Big\{ (\tilde{p}_0^* w_0 + \tilde{w}_0^* p_0)\frac{\mathrm{d}A}{\mathrm{d}\mathcal{Z}} + (\tilde{p}_0^* \partial_{\mathcal{Z}} w_0 + \tilde{w}_0^* \partial_{\mathcal{Z}} p_0)A + \Gamma v_{Ax}(b_{0x}\partial_x \tilde{u}_0^* - \tilde{b}_{0x}^* \partial_x u_0)A$$
$$- \Gamma v_{Az}\left(\tilde{\boldsymbol{u}}_{0H}^* \cdot \boldsymbol{b}_{0H} + \tilde{\boldsymbol{b}}_{0H}^* \cdot \boldsymbol{u}_{0H}\right)\frac{\mathrm{d}A}{\mathrm{d}\mathcal{Z}} - \Gamma v_{Az}\left(\tilde{\boldsymbol{u}}_{0H}^* \cdot \partial_{\mathcal{Z}}\boldsymbol{b}_{0H} + \tilde{\boldsymbol{b}}_{0H}^* \cdot \partial_{\mathcal{Z}}\boldsymbol{u}_{0H}\right)A$$
$$- \Gamma(\tilde{\boldsymbol{b}}_{0H}^* \cdot \boldsymbol{u}_{0H}\partial_{\mathcal{Z}} v_{Az})A - \Gamma v_{Ax}(\tilde{b}_{0y}^* \partial_x v_0 + \tilde{v}_0^* \partial_x b_{0y})A - \Gamma(\tilde{b}_{0y}^* v_0 \partial_x v_{Ax})A \Big\}\mathrm{d}x. \tag{78}$$

We will use the following identities to transform the terms in front of $\mathrm{d}A/\mathrm{d}\mathcal{Z}$:

$$\tilde{p}_0^* w_0 + \tilde{w}_0^* p_0 = \tilde{p}_0^* w_0 - \left(\frac{\omega\Theta'}{N^2}\tilde{p}_0^*\right)\left(-\frac{N^2}{\omega\Theta'}w_0\right) = 2\tilde{p}_0^* w_0, \tag{79a}$$

$$\tilde{\boldsymbol{b}}_{0H}^* \cdot \boldsymbol{u}_{0H} + \tilde{\boldsymbol{u}}_{0H}^* \cdot \boldsymbol{b}_{0H} = \tilde{\boldsymbol{b}}_{0H}^* \cdot \boldsymbol{u}_{0H} - \left(\frac{\omega}{\Gamma v_{Az}\Theta'}\tilde{\boldsymbol{b}}_{0H}^*\right)\cdot\left(-\frac{\Gamma v_{Az}\Theta'}{\omega}\boldsymbol{u}_{0H}\right) = 2\tilde{\boldsymbol{b}}_{0H}^* \cdot \boldsymbol{u}_{0H}. \tag{79b}$$

Then,

$$0 = \left[2\int_0^1 \left(\tilde{p}_0^* w_0 - \Gamma v_{Az}\tilde{\boldsymbol{b}}_{0H}^* \cdot \boldsymbol{u}_{0H}\right)\mathrm{d}x\right]\frac{\mathrm{d}A}{\mathrm{d}\mathcal{Z}}$$
$$+ \left[\int_0^1 \Big(\tilde{p}_0^* \partial_{\mathcal{Z}} w_0 + \tilde{w}_0^* \partial_{\mathcal{Z}} p_0 + \Gamma v_{Ax}(b_{0x}\partial_x \tilde{u}_0^* - \tilde{b}_{0x}^* \partial_x u_0) - \Gamma v_{Az}\left(\tilde{\boldsymbol{u}}_{0H}^* \cdot \partial_{\mathcal{Z}}\boldsymbol{b}_{0H} + \tilde{\boldsymbol{b}}_{0H}^* \cdot \partial_{\mathcal{Z}}\boldsymbol{u}_{0H}\right)$$
$$- \Gamma\tilde{\boldsymbol{b}}_{0H}^* \cdot \boldsymbol{u}_{0H}\partial_{\mathcal{Z}} v_{Az} - \Gamma v_{Ax}(\tilde{b}_{0y}^* \partial_x v_0 + \tilde{v}_0^* \partial_x b_{0y}) - \Gamma\tilde{b}_{0y}^* v_0 \partial_x v_{Ax}\Big)\mathrm{d}x\right]A \tag{80}$$

We can simplify the second term using the following identities:

$$\tilde{p}_0^* \partial_{\mathcal{Z}} w_0 + \tilde{w}_0^* \partial_{\mathcal{Z}} p_0 = \partial_{\mathcal{Z}}(\tilde{p}_0^* w_0) + (\tilde{w}_0^* \partial_{\mathcal{Z}} p_0 - w_0 \partial_{\mathcal{Z}}\tilde{p}_0^*), \tag{81a}$$

$$-\Gamma v_{Ax}(\tilde{b}_{0y}^* \partial_x v_0 + \tilde{v}_0^* \partial_x b_{0y}) - \Gamma\tilde{b}_{0y}^* v_0 \partial_x v_{Ax} = \Gamma v_{Ax}(v_0 \partial_x \tilde{b}_{0y}^* - \tilde{v}_0^* \partial_x b_{0y}) - \partial_x(\Gamma v_{Ax}\tilde{b}_{0y}^* v_0), \tag{81b}$$

$$- \Gamma v_{Az}(\tilde{\boldsymbol{u}}_{0H}^* \cdot \partial_{\mathcal{Z}}\boldsymbol{b}_{0H} + \tilde{\boldsymbol{b}}_{0H}^* \cdot \partial_{\mathcal{Z}}\boldsymbol{u}_{0H}) - \Gamma\tilde{\boldsymbol{b}}_{0H}^* \cdot \boldsymbol{u}_{0H}\partial_{\mathcal{Z}} v_{Az}$$
$$= -\Gamma\partial_{\mathcal{Z}}(v_{Az}\tilde{\boldsymbol{b}}_{0H}^* \cdot \boldsymbol{u}_{0H}) + \Gamma v_{Az}(\boldsymbol{u}_{0H} \cdot \partial_{\mathcal{Z}}\tilde{\boldsymbol{b}}_{0H}^* - \tilde{\boldsymbol{u}}_{0H}^* \cdot \partial_{\mathcal{Z}}\boldsymbol{b}_{0H}), \tag{81c}$$

so that

$$0 = \left[2\int_0^1 \left(\tilde{p}_0^* w_0 - \Gamma v_{Az}\tilde{\boldsymbol{b}}_{0H}^* \cdot \boldsymbol{u}_{0H}\right)\mathrm{d}x\right]\frac{\mathrm{d}A}{\mathrm{d}\mathcal{Z}} + \left[\int_0^1 \Big\{\partial_{\mathcal{Z}}\left(\tilde{p}_0^* w_0 - \Gamma v_{Az}\tilde{\boldsymbol{b}}_{0H}^* \cdot \boldsymbol{u}_{0H}\right)\right.$$
$$+ (\tilde{w}_0^* \partial_{\mathcal{Z}} p_0 - w_0 \partial_{\mathcal{Z}}\tilde{p}_0^*) + \Gamma v_{Az}(\boldsymbol{u}_{0H} \cdot \partial_{\mathcal{Z}}\tilde{\boldsymbol{b}}_{0H}^* - \tilde{\boldsymbol{u}}_{0H}^* \cdot \partial_{\mathcal{Z}}\boldsymbol{b}_{0H})$$
$$\left. + \Gamma v_{Ax}(b_{0x}\partial_x \tilde{u}_0^* - \tilde{b}_{0x}^* \partial_x u_0) + \Gamma v_{Ax}(v_0 \partial_x \tilde{b}_{0y}^* - \tilde{v}_0^* \partial_x b_{0y})\Big\}\mathrm{d}x\right]A, \tag{82}$$

where the term $-\partial_x(\Gamma v_{Ax}\tilde{b}^*_{0y}v_0)$ introduced using identity (81b) vanishes upon integration.

Now since $\mathcal{L}^\dagger_{\Theta'}[p^*_0]=0$, we can simplify (82) further by letting $\tilde{p}_0=p^*_0$. In this case, it follows from the polarization relations that

$$\tilde{w}^*_0=-\frac{\omega\Theta'}{N^2}\tilde{p}^*_0=-\frac{\omega\Theta'}{N^2}p_0=w_0, \tag{83a}$$

$$\tilde{u}^*_0=\frac{i\omega\partial_x\tilde{p}^*_0}{\omega^2-\Gamma^2v^2_{Az}\Theta'^2}=\frac{i\omega\partial_x p_0}{\omega^2-\Gamma^2v^2_{Az}\Theta'^2}=-u_0, \tag{83b}$$

$$\tilde{v}^*_0=\frac{i\omega(-ik_y\tilde{p}^*_0)}{\omega^2-\Gamma^2v^2_{Az}\Theta'^2}=-\frac{i\omega(ik_yp_0)}{\omega^2-\Gamma^2v^2_{Az}\Theta'^2}=v_0, \tag{83c}$$

$$\tilde{b}^*_{0x}=-\frac{\Gamma v_{Az}\Theta'}{\omega}\tilde{u}^*_0=\frac{\Gamma v_{Az}\Theta'}{\omega}u_0=-b_{0x}, \tag{83d}$$

$$\tilde{b}^*_{0y}=-\frac{\Gamma v_{Az}\Theta'}{\omega}\tilde{v}^*_0=-\frac{\Gamma v_{Az}\Theta'}{\omega}v_0=b_{0y}. \tag{83e}$$

The terms in the second integral in (82) simplify:

$$\tilde{w}^*_0\partial_{\mathcal{Z}}p_0-w_0\partial_{\mathcal{Z}}\tilde{p}^*_0=w_0\partial_{\mathcal{Z}}p_0-w_0\partial_{\mathcal{Z}}p_0=0, \tag{84a}$$

$$\begin{aligned}\boldsymbol{u}_{0H}\cdot\partial_{\mathcal{Z}}\tilde{\boldsymbol{b}}^*_{0H}-\tilde{\boldsymbol{u}}^*_{0H}\cdot\partial_{\mathcal{Z}}\boldsymbol{b}_{0H}&=\tilde{u}^*_0\partial_{\mathcal{Z}}b_{0x}+\tilde{v}^*_0\partial_{\mathcal{Z}}b_{0y}-u_0\partial_{\mathcal{Z}}\tilde{b}^*_{0x}-v_0\partial_{\mathcal{Z}}\tilde{b}^*_{0y}\\&=-u_0\partial_{\mathcal{Z}}b_{0x}+v_0\partial_{\mathcal{Z}}b_{0y}-u_0\partial_{\mathcal{Z}}(-b_{0x})-v_0\partial_{\mathcal{Z}}b_{0y}\\&=0,\end{aligned} \tag{84b}$$

$$b_{0x}\partial_x\tilde{u}^*_0-\tilde{b}^*_{0x}\partial_x u_0=-b_{0x}\partial_x u_0-b_{0x}\partial_x(-u_0)=0, \tag{84c}$$

$$v_0\partial_x\tilde{b}^*_{0y}-\tilde{v}^*_0\partial_x b_{0y}=v_0\partial_x b_{0y}-v_0\partial_x b_{0y}=0, \tag{84d}$$

leaving

$$0=\left[2\int_0^1\left(\tilde{p}^*_0w_0-\Gamma v_{Az}\tilde{\boldsymbol{b}}^*_{0H}\cdot\boldsymbol{u}_{0H}\right)\mathrm{d}x\right]\frac{\mathrm{d}A}{\mathrm{d}\mathcal{Z}}+\left[\int_0^1\partial_{\mathcal{Z}}\left(\tilde{p}^*_0w_0-\Gamma v_{Az}\tilde{\boldsymbol{b}}^*_{0H}\cdot\boldsymbol{u}_{0H}\mathrm{d}x\right)\right]A. \tag{85}$$

Alternatively, we may write this as

$$0=2\left(\int_0^1\mathcal{F}\mathrm{d}x\right)\frac{\mathrm{d}A}{\mathrm{d}\mathcal{Z}}+\partial_{\mathcal{Z}}\left(\int_0^1\mathcal{F}\mathrm{d}x\right)A, \tag{86}$$

where

$$\mathcal{F}=p_0w_0+\Gamma v_{Az}(b_{0x}u_0-b_{0y}v_0). \tag{87}$$

Then, the amplitude is given by

$$A(\mathcal{Z})=\left(\int_0^1\mathcal{F}\mathrm{d}x\right)^{-1/2} \tag{88}$$

up to a multiplicative constant.

References

[1] C. Aerts, *Probing the interior physics of stars through asteroseismology*, Reviews of Modern Physics, 93 (2021), p. 015001.

[2] T. R. Bedding, *Solar-like oscillations: An observational perspective*, in Asteroseismology, P. L. Pallé and C. Esteban, eds., Cambridge University Press, 1 ed., Jan. 2014, pp. 60–86.

[3] K. J. Burns, G. M. Vasil, J. S. Oishi, D. Lecoanet, and B. P. Brown, *Dedalus: A flexible framework for numerical simulations with spectral methods*, Physical Review Research, 2 (2020), p. 023068.

[4] W. J. Chaplin and A. Miglio, *Asteroseismology of Solar-Type and Red-Giant Stars*, Annual Review of Astronomy and Astrophysics, 51 (2013), pp. 353–392.

[5] P. Charbonneau and K. B. MacGregor, *Magnetic Fields in Massive Stars. I. Dynamo Models*, The Astrophysical Journal, 559 (2001), pp. 1094–1107.

[6] M.-A. Dupret, K. Belkacem, R. Samadi, J. Montalban, O. Moreira, A. Miglio, M. Godart, P. Ventura, H.-G. Ludwig, A. Grigahcène, M.-J. Goupil, A. Noels, and E. Caffau, *Theoretical amplitudes and lifetimes of non-radial solar-like oscillations in red giants*, Astronomy & Astrophysics, 506 (2009), pp. 57–67.

[7] J. Fuller, M. Cantiello, D. Stello, R. A. Garcia, and L. Bildsten, *Asteroseismology can reveal strong internal magnetic fields in red giant stars*, Science, 350 (2015), pp. 423–426.

[8] C. Gehan, B. Mosser, E. Michel, R. Samadi, and T. Kallinger, *Core rotation braking on the red giant branch for various mass ranges*, Astronomy & Astrophysics, 616 (2018), p. A24.

[9] A. Griffiths, P. Eggenberger, G. Meynet, F. Moyano, and M.-A. Aloy, *The magneto-rotational instability in massive stars*, Astronomy & Astrophysics, 665 (2022), p. A147.

[10] Z. Keszthelyi, G. Meynet, C. Georgy, G. A. Wade, V. Petit, and A. David-Uraz, *The effects of surface fossil magnetic fields on massive star evolution: I. Magnetic field evolution, mass-loss quenching, and magnetic braking*, Monthly Notices of the Royal Astronomical Society, 485 (2019), pp. 5843–5860.

[11] J. D. Landstreet, *Magnetic fields at the surfaces of stars*, The Astronomy and Astrophysics Review, 4 (1992), pp. 35–77.

[12] D. Lecoanet, D. M. Bowman, and T. Van Reeth, *Asteroseismic inference of the near-core magnetic field strength in the main-sequence B star HD 43317*, Monthly Notices of the Royal Astronomical Society: Letters, 512 (2022), pp. L16–L20.

[13] D. Lecoanet, G. M. Vasil, J. Fuller, M. Cantiello, and K. J. Burns, *Conversion of internal gravity waves into magnetic waves*, Monthly Notices of the Royal Astronomical Society, 466 (2017), pp. 2181–2193.

[14] G. Li, S. Deheuvels, J. Ballot, and F. Lignières, *Magnetic fields of 30 to 100 kG in the cores of red giant stars*, Nature, 610 (2022), pp. 43–46.

[15] A. Maeder and G. Meynet, *Stellar evolution with rotation and magnetic fields: III. The interplay of circulation and dynamo*, Astronomy & Astrophysics, 440 (2005), pp. 1041–1049.

[16] J. Montalban, A. Miglio, A. Noels, M.-A. Dupret, R. Scuflaire, and P. Ventura, *Testing convective-core overshooting using period spacings of dipole modes in red giants*, The Astrophysical Journal, 766 (2013), p. 118.

[17] B. Mosser, Y. Elsworth, S. Hekker, D. Huber, T. Kallinger, S. Mathur, K. Belkacem, M. J. Goupil, R. Samadi, C. Barban, T. R. Bedding, W. J. Chaplin, R. A. García, D. Stello, J. De Ridder, C. K. Middour, R. L. Morris, and E. V. Quintana, *Characterization of the power excess of solar-like oscillations in red giants with Kepler*, Astronomy & Astrophysics, 537 (2012), p. A30.

[18] M. R. E. Proctor and N. O. Weiss, *Magnetoconvection*, Reports on Progress in Physics, 45 (1982), pp. 1317–1379.

[19] N. Z. Rui and J. Fuller, *Gravity waves in strong magnetic fields*, Monthly Notices of the Royal Astronomical Society, 523 (2023), pp. 582–602.

[20] M. Salaris, S. Cassisi, and A. Weiss, *Red Giant Branch Stars: The Theoretical Framework*, Publications of the Astronomical Society of the Pacific, 114 (2002), pp. 375–402.

[21] F. H. Shu, *The Physics of Astrophysics. 2: Gas Dynamics*, A series of books in astronomy, Univ. Science Books, Mill Valley, Cal, 1992. Num Pages: 476.

[22] D. Stello, M. Cantiello, J. Fuller, D. Huber, R. A. García, T. R. Bedding, L. Bildsten, and V. S. Aguirre, *A prevalence of dynamo-generated magnetic fields in the cores of intermediate-mass stars*, Nature, 529 (2016), pp. 364–367.

A Little Goes a Long Way: Dismantling Weakly Nonlinear, Non-normal Dynamical Systems

Matthew McCormack

August 22, 2024

1 Introduction

Linear stability analysis is a fundamental tool in the analysis of nonlinear dynamical systems that determines the stability of a given solution to infinitesimal perturbations. In the presence of a linear instability, traditional weakly nonlinear theory may then be used to perturbatively examine non-trivial dynamics near the point of the instability into the nonlinear regime at finite amplitude, using the distance to the point of the linear instability in parameter space as a small parameter in an asymptotic expansion. This methodology has seen significant success in fluid dynamics and has been widely used in the sciences and engineering. However, in recent years, it has become apparent that transitions to non-trivial nonlinear solutions may be observed at parameter values far below those predicted by linear stability theory. This is perhaps most famously observed when studying the stability of the laminar profile in a variety of wall-bounded parallel shear flows, where the initial stages of the transition to turbulence are observed far beneath the threshold for a linear instability or even in cases where the laminar flow is linearly stable for all values of the Reynolds number [1, 9–12]. In these flows, the transition has been firmly associated with nonlinear dynamical systems theory, especially for spatially confined systems where the effects of spatio-temporal intermittency may be ignored [3]. In this framework, the initial stages of the transition can be understood in the context of the state-space structure of the system by studying the various bifurcations that occur as the Reynolds number (or some other relevant parameter) is varied. The near onset behaviour can be broadly characterised into two classes: supercritical and subcritical transitions.

In the case of a supercritical transition (see figure $1(a)$), the base state becomes linearly unstable at a critical parameter value and a branch (or branches) of stable solutions bifurcates directly from this bifurcation point, existing at parameter values above the threshold for a linear instability (as in a supercritical pitchfork bifurcation for example). This defines a precise point in parameter space where the transition takes place and no bistability or hysteresis is observed; that is, different behaviour is not observed depending on the initial conditions or the direction the transition point is approached in parameter space. Examples of such systems are classical Rayleigh-B´enard convection [5, 15] and co-rotating Taylor-Couette flow [6, 19], which are well suited to traditional weakly nonlinear theory since the distance to the transition point and thus, an appropriate small parameter, is well defined [7, 14, 17, 18, 22].

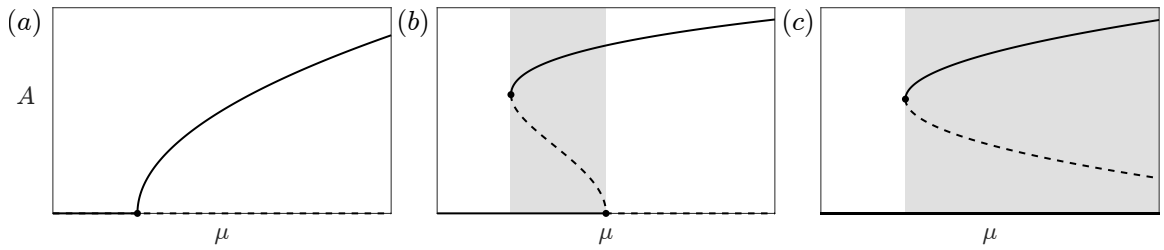

Figure 1: Sketches of various (a) supercritical and (b–c) subcritical transitions showing a general amplitude of the solution A as a function of a bifurcation parameter μ, with the base (laminar) solution at $A = 0$. Solid lines represent stable solutions, dashed lines represent unstable solutions, and markers denote bifurcation points. The subcritical region of parameter space where non-trivial solutions exist beneath the linear instability of the base state is shaded in grey.

In subcritical transitions, however, a different phenomenology is observed which may or may not result from a linear instability of the base state. For example in figure 1(b), the base state bifurcates subcritically, becoming unstable and producing a branch of unstable solutions of growing amplitude with decreasing parameter value μ. This branch then undergoes a saddle node bifurcation producing a branch of large amplitude stable solutions. Another example of a subcritical transition is shown in figure 1(c); in this case, the base state is linearly stable for all values of the parameter μ. Here, a saddle-node bifurcation produces a stable/unstable pair of solutions that are disconnected from the branch of the base state. In both examples, the transition may occur subcritically for parameter values in the grey-shaded region if the solution is given a sufficiently large perturbation in amplitude to push the state above the unstable branch. In these examples, the utility of applying traditional weakly nonlinear theory is severely limited. For the case sketched in figure 1(b), an expansion near the bifurcation point of the base state can be constructed, however, information about the saddle node bifurcation and large-amplitude stable solution is unlikely to be captured by such a local expansion, even if higher order terms are included due to the likelihood that these often occur far away from the bifurcation point [4]. Indeed, in the case sketched in figure (c) where no bifurcation of the base state occurs, it is not possible to consider such an expansion as no formal small parameter exists in the sense of the traditional weakly nonlinear theory.

Nevertheless, there is a need to construct a weakly nonlinear theory for these types of subcritical transitions, which are important in a wide variety of physical systems. Current methods often rely on a numerical treatment of the problem, ad-hoc modelling or projection of the equations onto an ad-hoc truncated basis. Clearly, it would be valuable to have a formal way of investigating these systems that arise directly from the equations of motion.

In this work, we restrict ourselves to a certain class of dynamical systems; namely, one for which the linearised operator about the base state is highly non-normal [20]. A bounded linear operator $\mathcal{L} : X \to Y$, where X and Y are inner product spaces, is non-normal if it does not commute with its adjoint operator $\mathcal{L}^\dagger$, *i.e.*, $\mathcal{L}^\dagger\mathcal{L} \neq \mathcal{L}\mathcal{L}^\dagger$. Here the adjoint operator

is a linear operator $\mathcal{L}^\dagger : Y \to X$, such that for all $x \in X$ and $y \in Y$,

$$\langle \mathcal{L}x, y\rangle_Y = \langle x, \mathcal{L}^\dagger y\rangle_X, \tag{1}$$

where $\langle \cdot, \cdot \rangle$ denotes the inner product on the corresponding space. If $\mathcal{L} = \mathcal{L}^\dagger$ and $X = Y$, the operator is called self-adjoint. Thus, trivially, a linear operator is necessarily normal if it is self-adjoint, although the converse need not be true. Self-adjoint operators enjoy a number of nice properties. Firstly, the spectrum of a self-adjoint operator is real, and the corresponding eigenfunctions/eigenvectors are orthogonal. This is important in the context of our linear stability analysis: if the linearised operator about the base solution $\mathcal{L}$ is self-adjoint (and thus normal), and the eigenvalues of $\mathcal{L}$ all have a negative real part, then infinitesimal perturbations to the base state will decay monotonically. However, if the linearised operator is not self-adjoint, the eigenfunctions/eigenvectors may not be orthogonal and perturbations to the base state may grow transiently before they decay back to the base state in the linearised dynamics [16]. In this sense, the non-normality of the linearised system is important to consider when assessing the stability of the base state to finite amplitude perturbations, since even small disturbances can experience strong transient growth due to the non-normality. In turn, strong transient growth may be sufficient to enable the solution to grow into a nonlinear regime where the trajectory may then grow or decay due to the nonlinear effects. In the context of our original nonlinear initial value problem, non-normality provides a mechanism that may have a significant effect on the geometry of the separatrix dividing the basins of attraction of various stable states and can promote subcritical transitions. It is well established that non-normality is often observed in linearised versions of the Navier-Stokes equations, and may play a significant role in subcritical transitions in various parallel shear flows.

Strong non-normality has recently been utilised by Ducimetière *et al.* [8] to perform weakly nonlinear analysis of linearly stable systems. In contrast to traditional weakly nonlinear theory, the small parameter used in their analysis is the inverse of the optimal gain in the linearised system. The solutions of the resulting amplitude equation agreed reasonably well with solutions to the full nonlinear system, and reasonable estimates for the critical forcing amplitudes needed to observe a transition to a non-trivial nonlinear state were obtained. Although this study is pioneering in the utilisation of a different small parameter to extend traditional weakly nonlinear theory to linearly stable non-normal systems, the work nevertheless left a number of questions unanswered. In particular, it is not clear whether the inverse optimal gain is truly a formal small parameter and, if so, what the associated limit process is. Additionally, some of the coefficients in the amplitude equation were observed to exhibit a different asymptotic scaling to the assumed scaling when the amplitude equation was being balanced, resulting in a formally inconsistent equation. Consequently, the resulting system has no variation on the slow time scale and the stability of solutions could not be formally assessed. Finally, the methodology tied itself closely to traditional weakly nonlinear theory by artificially perturbing operators to render them singular so that the Fredholm alternative could be invoked in the derivation of the amplitude equation [7, 8]. However, these operators are not singular due to the linear stability of the system.

In this work, we wish to extend the ideas of Ducimetière *et al.* [8] to develop a new methodology that emphasises formal asymptotic consistency. We begin in §2 by outlining

our approach in a general setting and then perform the asymptotic reduction for a model problem in §3, the results of which are outlined in §4. Conclusions are presented in §5.

2 General System

We consider a system described by a state vector $\tilde{\boldsymbol{q}} \in X$ which is first decomposed into an equilibrium (laminar) solution of interest $\boldsymbol{q}_0$ and the fluctuations about this state $\boldsymbol{q}$ as

$$\tilde{\boldsymbol{q}}(\boldsymbol{x}, t) = \boldsymbol{q}_0(\boldsymbol{x}) + \boldsymbol{q}(\boldsymbol{x}, t). \tag{2}$$

We then consider the following harmonically forced nonlinear dynamical system for the fluctuations

$$\partial_t \boldsymbol{q} = \mathcal{L}_\mu \boldsymbol{q} + \mathcal{N}(\boldsymbol{q}, \boldsymbol{q}) + \delta(\hat{\boldsymbol{f}} e^{i\omega t} + c.c.), \tag{3}$$

where $\mathcal{L}_\mu$ is a linear operator which depends on a parameter μ (the Reynolds number for example), $\mathcal{N}$ is a quadratic nonlinear operator, ω is the frequency of the forcing, and *c.c.* denotes complex conjugate. By imposing that $\|\hat{\boldsymbol{f}}\| = 1$, the amplitude of the forcing is modulated by the parameter δ. By construction, equation (3) admits the equilibrium solution $\boldsymbol{q}_0$ when $\boldsymbol{q} = \boldsymbol{0}$ with $\delta = 0$.

In this work, we are interested in the dynamics of equation (3) close to this equilibrium point at a parameter value μ when the linearisation of equation (3) about $\boldsymbol{q} = \boldsymbol{0}$ is stable in the unforced system ($\delta = 0$), and the operator $\mathcal{L}_\mu$ is highly non-normal. In this sense, we wish to understand the weakly non-linear dynamics sustained by a small harmonic forcing, where the dynamical response may indeed be much greater than the magnitude of the forcing due to the large non-normality of the system.

2.1 The linearised system and resolvent analysis

We first analyse the linearisation of equation (3) about the $\boldsymbol{q} = \boldsymbol{0}$ equilibrium point

$$\partial_t \boldsymbol{q} = \mathcal{L}_\mu \boldsymbol{q} + \delta(\hat{\boldsymbol{f}} e^{i\omega t} + c.c.). \tag{4}$$

We are considering choices of parameters μ for which the $\boldsymbol{q} = \boldsymbol{0}$ equilibrium point is linearly stable, *i.e.*, the spectrum of $\mathcal{L}_\mu$ lies on the left-hand side of the complex plane, and unforced frequencies are expected to decay as $t \to \infty$. Thus, we Fourier-decompose the response $\boldsymbol{q} = \hat{\boldsymbol{q}} e^{i\omega t} + c.c.$. Using this ansatz in equation (4), we can map the Fourier coefficient of the forcing $\hat{\boldsymbol{f}}$ onto the associated Fourier coefficient of the response through a linear operator $\mathcal{R}$ known as the Resolvent operator

$$\hat{\boldsymbol{q}} = (i\omega I - \mathcal{L}_\mu)^{-1} \delta \hat{\boldsymbol{f}} = \mathcal{R} \delta \hat{\boldsymbol{f}}, \tag{5}$$

where I is the identity. Doing so has transformed the linear differential equation into an algebraic problem, allowing us to understand the linear response of the system by analysing the linear operator $\mathcal{R}$. Since we are typically interested in finite-dimensional problems, (i.e., $X = \mathbb{R}^n$ say), either coming from systems of ordinary differential equations or spatially discretised partial differential equations, the operator $\mathcal{R}$ is a matrix and can be analysed using tools from linear algebra. It is common in this setting to consider the singular value

decomposition (or the Schmidt decomposition in the infinite dimensional case) of $\mathcal{R}(\omega)$ for a given frequency ω

$$\mathcal{R} = U\Sigma V^H, \tag{6}$$

where Σ is a diagonal matrix whose entries $\Sigma_{jj} = \sigma_j$ where $\sigma_1 \geq \sigma_2 \geq \cdots \geq 0$ are referred to as the singular values, U and V are unitary matrices whose jth columns are referred to as the jth left and right singular vectors, respectively, and $(\cdot)^H$ denotes the Hermitian (conjugate) transpose. Since U and V are unitary, their columns form an orthonormal basis with respect to the Hermitian inner product $\langle \boldsymbol{z}, \boldsymbol{w} \rangle = \sum_i z_i w_i^*$ for two complex vectors $\boldsymbol{z}$ and $\boldsymbol{w}$, where $(\cdot)^*$ denotes complex conjugation. The singular value decomposition naturally decomposes the resolvent operator into a set of forcing structures encoded in the columns of V and the associated response in the columns of U, where the associated singular values describe the magnitude of this transformation. By ordering the singular values, forcing structures can thus be ranked by the magnitude of their associated response. Furthermore, the largest singular value represents the maximum gain achievable by a given linear operator, and thus, the leading left and right singular vectors represent the optimal forcing for the system and the associated response, respectively.

2.2 Defining weak nonlinearity

We wish to construct a weakly nonlinear expansion of equation (3) about the stable equilibrium point $\boldsymbol{q} = \boldsymbol{0}$. In traditional weakly nonlinear theory, one uses the distance from a bifurcation point $\mu - \mu_c$ as a small parameter. However, since our system is linearly stable for the range of parameter values considered, no local bifurcation occurs, and thus, μ_c is not defined. Instead, we restrict ourselves to systems which possess strong non-normality. In such a system, we expect the leading singular value of the resolvent operator to be large, (*i.e.*, $\sigma_1 \gg 1$) since small disturbances should be amplified greatly due to the non-normality. To study the simplest conceivable scenario, we shall assume that as the control parameter $\mu \to \mu^*$ where μ^* is some value of the control parameter, the leading singular value $\sigma_1 \to \infty$, while the other singular values $\sigma_j = \mathcal{O}(1)$ for $j \neq 1$. In this sense, we might anticipate a limiting procedure whereby the gain $\sigma_1 \to \infty$ as the Reynolds number $\mathrm{Re} \to \infty$ in a Couette or pipe flow, for example. In this case, we may formally introduce an asymptotic small parameter $\varepsilon \equiv 1/\sigma_1$ which we shall use to order an asymptotic expansion.

Furthermore, we can use the linearised system to anticipate the relative size of the response associated with each of the singular values. Examining equation (5), we can expect that the optimal response of the system associated with the leading singular value is of order δ/ε, whereas sub-optimal responses associated with the remaining singular values is of order δ. We thus define the weakly nonlinear regime as one where $\delta/\varepsilon \ll 1$.

2.3 Weakly nonlinear expansion

We now return to our original forced nonlinear problem

$$\partial_t \boldsymbol{q} = \mathcal{L}_\mu \boldsymbol{q} + \mathcal{N}(\boldsymbol{q}, \boldsymbol{q}) + \delta(\hat{\boldsymbol{f}} e^{i\omega t} + c.c.), \tag{7}$$

and introduce a slow time $T \equiv \Delta t$ as part of a multiple time-scale asymptotic expansion, where Δ is a currently unspecified small parameter. Heuristically, in the weakly nonlinear

regime, we anticipate a harmonic response on the original fast time scale, with the fast-time averaged amplitude of the solution evolving on the slow time scale T. We thus take $\partial_t \mapsto \partial_t + \Delta\partial_T$, and make the following ansatz for the evolution of the state vector by Fourier-decomposing over the fast time:

$$\boldsymbol{q}(\boldsymbol{x}, t, T) = \sum_n \hat{\boldsymbol{q}}_n(\boldsymbol{x}, T) e^{in\omega t}, \quad n \in \mathbb{Z}. \tag{8}$$

Substituting this ansatz into equation (7) and taking the L^2 inner product with respect to each Fourier mode separates the problem into a system of differential equations. At each frequency n we have

$$\Delta\partial_T \hat{\boldsymbol{q}}_n + (in\omega I - \mathcal{L}_\mu)\hat{\boldsymbol{q}}_n = \left\{\mathcal{N}(\boldsymbol{q}, \boldsymbol{q})\right\}_n + \delta\hat{\boldsymbol{f}}\delta_{\pm 1, n}, \tag{9}$$

where $\{\cdot\}_n$ denotes projection onto the frequency n and $\delta_{i,j}$ denotes the Kronecker delta. Noting the presence of the inverse resolvent operator in the linear part of the equation, we perform a singular value decomposition for each n as $\mathcal{R}_n = (in\omega I - \mathcal{L})^{-1} = U_n \Sigma_n V_n^H$. We further introduce the notation that the leading singular value for each n is given as σ_n^+, with associated left and right singular vectors given by $\hat{\boldsymbol{U}}_n$ and $\hat{\boldsymbol{V}}_n$, respectively. The remaining sub-dominant singular values are denoted by $\sigma_n^{(j)}$, which have associated left and right singular vectors given by $\boldsymbol{u}_n^{(j)}$ and $\boldsymbol{v}_n^{(j)}$.

We proceed by projecting equation (9) onto the optimal forcing shape given by $\hat{\boldsymbol{V}}_n$ using the Hermitian inner product

$$\hat{\boldsymbol{V}}_n^H\left(\Delta\partial_T \hat{\boldsymbol{q}}_n + (in\omega I - \mathcal{L})\hat{\boldsymbol{q}}_n\right) = \hat{\boldsymbol{V}}_n^H\left(\left\{\mathcal{N}(\boldsymbol{q}, \boldsymbol{q})\right\}_n + \delta\hat{\boldsymbol{f}}\delta_{\pm 1, n}\right), \tag{10}$$

which extracts the optimal forcing profile from the applied harmonic forcing. We then expand $\hat{\boldsymbol{q}}_n$ in the orthonormal basis spanned by the left singular vectors associated with the response at each n as

$$\hat{\boldsymbol{q}}_n(T) = a_n(T)\hat{\boldsymbol{U}}_n + \sum_j b_n^{(j)}(T)\boldsymbol{u}_n^{(j)}. \tag{11}$$

The general philosophy here is that, due to the strong non-normality, the dominant response of the system ought to be encoded in the coefficients a_n while the projection of the solution onto the sub-dominant response vectors will be small. We would thus like to perform a Galerkin projection onto the dominant modes utilising the orthogonality of the basis. However, we would like to do so in a formally justified way by insisting on asymptotic consistency as $\varepsilon \to 0$.

The choice to expand the state vector $\hat{\boldsymbol{q}}_n(T)$ in the basis spanned by left singular vectors at each n is motivated by the great simplification of the linear term on the left-hand side of equation (10), where the orthogonality of the bases can be utilised. More precisely, we have

$$\begin{aligned}\hat{\boldsymbol{V}}_n^H(in\omega I - \mathcal{L})\hat{\boldsymbol{q}}_n &= (\sigma_n^+)^{-1}(\hat{\boldsymbol{V}}_n^H\hat{\boldsymbol{V}}_n)(\hat{\boldsymbol{U}}_n^H\hat{\boldsymbol{q}}_n) + \sum_j (\sigma_n^{(j)})^{-1}(\hat{\boldsymbol{V}}_n^H\boldsymbol{v}_n^{(j)})(\boldsymbol{u}_n^{(j)H}\hat{\boldsymbol{q}}_n) \\ &= (\sigma_n^+)^{-1}a_n;\end{aligned} \tag{12}$$

thus, the linear term only depends on the leading singular vector σ_n^+ and the amplitude associated with this mode a_n. Our system of equations is thus simplified to

$$\Delta\partial_T(\hat{\boldsymbol{V}}_n^H\hat{\boldsymbol{q}}_n) + (\sigma_n^+)^{-1}a_n = \hat{\boldsymbol{V}}_n^H\big(\{\mathcal{N}(\boldsymbol{q},\boldsymbol{q})\}_n\big) + \delta\big(\hat{\boldsymbol{V}}_n^H\hat{\boldsymbol{f}}\big)\delta_{\pm1,n}. \tag{13}$$

To achieve a formally justified asymptotic reduction of this system for a given problem, we must consider the scaling of each of the remaining terms with our defined small parameter ε for each n. For example, we may anticipate that the projection of the forcing term $\hat{\boldsymbol{V}}_n^H\hat{\boldsymbol{f}} \sim 1$, expecting otherwise only for pathological choices of forcing $\hat{\boldsymbol{f}}$. However, it is not clear how other terms scale for a general system, particularly the nonlinear terms, which include many interactions between three different basis sets for a general quadratic nonlinearity at each n. We thus hope to build intuition for this type of asymptotic reduction by considering simple model problems that capture essential features of fluid dynamics systems to which we ultimately aim to apply this new formalism.

3 A Model Problem

We consider the following two-dimensional harmonically forced ODE system which evolves the state $\boldsymbol{q} = (v,\eta)^T$ according to

$$\frac{\mathrm{d}}{\mathrm{d}t}\begin{pmatrix}v\\\eta\end{pmatrix} = \begin{pmatrix}-\lambda & 0\\ 1 & -b\lambda\end{pmatrix}\begin{pmatrix}v\\\eta\end{pmatrix} + \begin{pmatrix}\eta^2\\ -v\eta\end{pmatrix} + \delta(\hat{\boldsymbol{f}}e^{i\omega t} + c.c.). \tag{14}$$

The linear operator in this equation is inspired by the Orr–Sommerfeld-Squire system, *i.e.*, the Navier-Stokes equations for a parallel shear flow linearised about a basic flow which only varies in the wall-normal direction, and is known to be non-normal. In this context, v and η loosely correspond to the Fourier coefficients of the wall-normal velocity and vorticity perturbations, respectively, and the parameter λ can be interpreted as an inverse Reynolds number: $\lambda = 1/\mathrm{Re}$. This linear term is supplemented with a quadratic nonlinearity, chosen to replicate the unforced ODE system studied by Trefethen *et al.* [21]. This and a class of similar ODE systems, all containing variants of the same non-normal linear operator used here, have been widely employed to study non-normal growth and its role in the transition to turbulence in shear flows [2,13,21]. This system is thus well suited to testing our asymptotic reduction methodology. In the remainder of this work, we choose a sinusoidal forcing $\sin(\omega t)$ and thus, $\hat{\boldsymbol{f}} = -i(1/2,1/2)^T$.

3.1 Characterisation of the unforced system

Equation (14) with $\delta = 0$ admits three equilibrium solutions

$$\overline{\boldsymbol{q}}_0 = \begin{pmatrix}0\\0\end{pmatrix}, \quad \overline{\boldsymbol{q}}_\pm = \begin{pmatrix}(1\pm\sqrt{1-4b\lambda^2})^2/4\lambda\\ (1\pm\sqrt{1-4b\lambda^2})/2\end{pmatrix}. \tag{15}$$

Linearising about the "laminar" base state $\overline{\boldsymbol{q}}_0$ yields the following linear system

$$\frac{\mathrm{d}}{\mathrm{d}t}\begin{pmatrix}v\\\eta\end{pmatrix} = \begin{pmatrix}-\lambda & 0\\ 1 & -b\lambda\end{pmatrix}\begin{pmatrix}v\\\eta\end{pmatrix} = \mathcal{L}_\lambda\boldsymbol{q}. \tag{16}$$

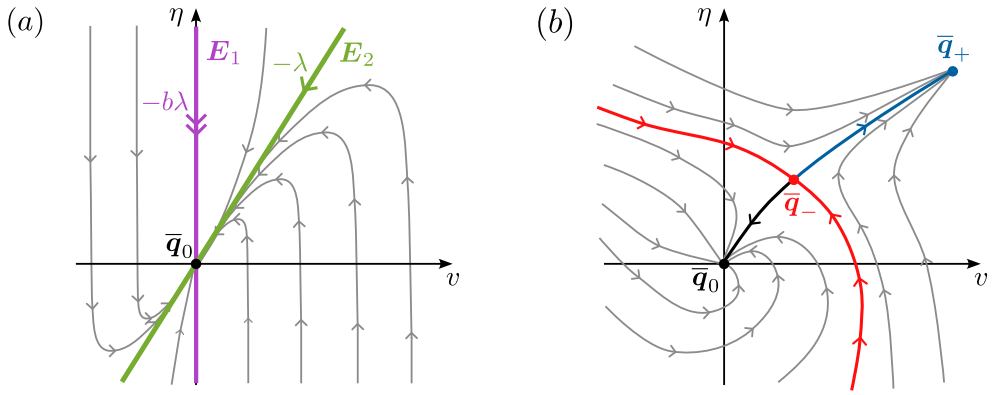

Figure 2: Sketch of the phase portraits with $b > 1$ for (a) the unforced linearised system showing the two stable eigendirections $\boldsymbol{E}_1$ (purple) and $\boldsymbol{E}_2$ (green), and (b) the unforced full nonlinear system showing the separatrix (red) defining the basin of attraction for the two stable equilibria $\overline{\boldsymbol{q}}_0$ and $\overline{\boldsymbol{q}}_+$, and the heteroclitic orbits between the fixed points (black/blue).

A simple calculation firstly shows that $\mathcal{L}_\lambda$ is indeed non-normal

$$\begin{aligned}\mathcal{L}_\lambda^\dagger \mathcal{L}_\lambda &= \begin{pmatrix} -\lambda & 1 \\ 0 & -b\lambda \end{pmatrix}\begin{pmatrix} -\lambda & 0 \\ 1 & -b\lambda \end{pmatrix} = \begin{pmatrix} 1+\lambda^2 & -b\lambda \\ -b\lambda & b^2\lambda^2 \end{pmatrix} \\ \neq \mathcal{L}_\lambda \mathcal{L}_\lambda^\dagger &= \begin{pmatrix} -\lambda & 0 \\ 1 & -b\lambda \end{pmatrix}\begin{pmatrix} -\lambda & 1 \\ 0 & -b\lambda \end{pmatrix} = \begin{pmatrix} \lambda^2 & -\lambda \\ -\lambda & 1+b^2\lambda^2 \end{pmatrix},\end{aligned}$$

and that the base state is linearly stable for all values of $\lambda > 0$. Further computation shows that $\mathcal{L}_\lambda$ has eigenvectors

$$\boldsymbol{E}_1 = \begin{pmatrix} 0 \\ 1 \end{pmatrix}, \quad \boldsymbol{E}_2 = \begin{pmatrix} 1 \\ \frac{1}{\lambda(b-1)} \end{pmatrix}, \tag{17}$$

which correspond to the eigenvalues $-b\lambda$ and $-\lambda$, respectively, and thus, the eigenvectors become more aligned as $\lambda \to 0$, (*i.e.* ,Re $\to \infty$), giving rise to large transient growth[1]. This transient growth can be observed in the sketch of the phase portrait of the linearised system in figure 2(a), where the norm of many trajectories grows initially before being attracted back to the stable equilibrium.

The introduction of the nonlinear terms introduces additional equilibrium states $\overline{\boldsymbol{q}}_\pm$. For the range of λ we shall consider, the equilibrium state $\overline{\boldsymbol{q}}_+$ is a stable equilibrium point, and the equilibrium $\overline{\boldsymbol{q}}_-$ is a saddle point which defines a separatrix between the two stable equilibria, sketched in the phase portrait in red in figure 2(b). Due to the simplicity of our system, we can compute a full phase portrait of the dynamics, which is shown in figure 2(b). In the following sections, we will refer to the solution $\overline{\boldsymbol{q}}_+$ as the fully nonlinear solution or state.

[1]Here we note that $\mathcal{L}$ is not diagonalisable for $b = 1$, however $\mathcal{L}$ is still non-normal and displays transient growth.

3.2 Singular values: do we really have a small parameter?

In the outline of our general method, we have assumed in §2.2 that we have a small parameter defined to be the inverse of the gain, *i.e.*, the leading singular value of the resolvent operator, $\varepsilon \equiv 1/\sigma_1$, where $\varepsilon \to 0$ as our control parameter μ approaches some particular value $\mu \to \mu^*$. Here, we investigate the behaviour of ε as $\lambda \to 0$ (Re $\to \infty$).

We begin by constructing the resolvent operator $\mathcal{R}(in\omega) = (in\omega I - \mathcal{L}_\lambda)^{-1}$, and calculate its two singular values $\sigma_n^\pm$ which are calculated as the square root of the eigenvalues of $\mathcal{R}^H\mathcal{R}$ as

$$\sigma_n^\pm = \sqrt{S_n \pm \sqrt{S_n^2 - Q_n}}. \tag{18}$$

For compactness of notation, we define the coefficients $S_n, Q_n \in \mathbb{R}$ as $2S_n = |\alpha_n|^2 + |\alpha_n|^2|\beta_n|^2 + |\beta_n|^2$ and $Q_n = |\alpha_n|^2|\beta_n|^2$, which themselves depend on $\alpha_n, \beta_n \in \mathbb{C}$, with $\alpha_n = (in\omega + \lambda)^{-1}$ and $\beta_n = (in\omega + b\lambda)^{-1}$.

We now examine the behaviour of $\sigma_1^\pm$ as $\lambda \to 0$. Assuming that $|\alpha_1|, |\beta_1| \gg 1$, we find that

$$\sigma_1^+ \approx \sqrt{\frac{1}{\omega^4 + (1+b^2)\omega^2\lambda^2 + b^2\lambda^4}}, \tag{19}$$

meaning the asymptotic behaviour of $\varepsilon \equiv 1/\sigma_1^+$ depends not only on the control parameter λ, but also the frequency of the harmonic forcing ω. The dependence of ω on σ_1^+ primarily depends on how ω compares to λ since $b = \mathcal{O}(1)$. Thus, we simplify the analysis by letting $\omega = \omega(\lambda)$. Letting $\omega \sim \lambda^\alpha$, we observe three different behaviours for the leading singular value depending on the value of α:

$$\begin{cases} \sigma_1^+ = \mathcal{O}(1), & \alpha = 0, \\ \sigma_1^+ = \mathcal{O}(\lambda^{-2\alpha}), & 0 < \alpha < 1, \\ \sigma_1^+ = \mathcal{O}(\lambda^{-2}), & \alpha \geq 1. \end{cases} \tag{20}$$

Thus, if we allow the frequency of the forcing $\omega \sim 1$, we do not have a well-defined small parameter. However, if we choose the exponent $\alpha > 0$, then $\varepsilon \to 0$ as $\lambda \to 0$, and we can construct an asymptotic expansion using ε as a small parameter.

A secondary assumption specified in §2.2, is that subdominant singular values of the resolvent operator are bounded in the same limiting process ($\lambda \to 0$). In this case we can examine the behaviour of σ_1^- by constructing a Puiseux series expansion for $S_1, Q_1 \gg 1$, which to leading order is

$$\sigma_1^- = \sqrt{\frac{Q_1}{2S_1}} + \mathcal{O}(S_1^{-5/2}Q_1^{3/2}), \tag{21}$$

which shows that $\sigma_1^- \to 1$ as $\lambda \to 0$, confirming that $\sigma_1^- = \mathcal{O}(1)$ as required.

Thus, we may now construct an asymptotic expansion for this problem as described in §2.3 provided that we choose the forcing frequency $\omega \sim \lambda^\alpha$ with $\alpha > 0$.

3.3 Singular vectors and nonlinear term

Our method relies on understanding the scaling of various terms involving the singular vectors of the resolvent operator, and we thus proceed by calculating them directly. The

right singular vectors of $\mathcal{R}(in\omega)$ are calculated as the right eigenvectors of $\mathcal{R}^H\mathcal{R}$, which in the notation of §3.2 are

$$\hat{\boldsymbol{V}}_n = C_n^+ \begin{pmatrix} \frac{1}{\alpha_n|\beta_n|^2}(S_n + \sqrt{S_n^2 - Q_n} - |\beta_n|^2) \\ 1 \end{pmatrix}, \tag{22}$$

$$\hat{\boldsymbol{v}}_n^{(2)} = C_n^- \begin{pmatrix} \frac{1}{\alpha_n|\beta_n|^2}(S_n - \sqrt{S_n^2 - Q_n} - |\beta_n|^2) \\ 1 \end{pmatrix}, \tag{23}$$

where the coefficients $C_n^\pm$ ensure that the singular vectors have unit norm, that is

$$C_n^\pm = \left(1 + \frac{1}{|\alpha_n|^2|\beta_n|^4}\left(S_n \pm \sqrt{S_n^2 - Q_n} - |\beta_n|^2\right)^2\right)^{-1/2}. \tag{24}$$

The corresponding left singular vectors can then be written as

$$\hat{\boldsymbol{U}}_n = \frac{1}{\sigma_1^+}\begin{pmatrix} \alpha_n & 0 \\ \alpha_n\beta_n & \beta_n \end{pmatrix}\hat{\boldsymbol{V}}_n, \tag{25}$$

$$\hat{\boldsymbol{u}}_n^{(2)} = \frac{1}{\sigma_1^-}\begin{pmatrix} \alpha_n & 0 \\ \alpha_n\beta_n & \beta_n \end{pmatrix}\hat{\boldsymbol{v}}_n^{(2)}. \tag{26}$$

In the context of our asymptotic reduction, we have expanded the Fourier coefficients of the state vector in terms of the left singular vectors, here as

$$\hat{\boldsymbol{q}}_n(T) = a_n(T)\hat{\boldsymbol{U}}_n + b_n^{(2)}(T)\hat{\boldsymbol{u}}_n^{(2)}. \tag{27}$$

Inserting this representation into our system of equations for each n yields

$$\Delta\partial_T(\hat{\boldsymbol{V}}_n^H\hat{\boldsymbol{q}}_n) + (\sigma_n^+)^{-1}a_n = \hat{\boldsymbol{V}}_n^H\left(\{\mathcal{N}(\boldsymbol{q},\boldsymbol{q})\}_n\right) + \delta(\hat{\boldsymbol{V}}_n^H\hat{\boldsymbol{f}})\delta_{\pm1,n}. \tag{28}$$

For our model problem, the nonlinear term is written as

$$\mathcal{N}(\boldsymbol{q},\boldsymbol{q}) = \begin{pmatrix} \eta^2 \\ -v\eta \end{pmatrix} = \begin{pmatrix} 0 & 1 \\ -1 & 0 \end{pmatrix}(\boldsymbol{e}_2\cdot\boldsymbol{q})\,\boldsymbol{q}, \tag{29}$$

where $\boldsymbol{e}_2 = (0,1)$. Thus, the projected nonlinear term has the form

$$\begin{aligned}\hat{\boldsymbol{V}}_n^H\{\mathcal{N}(\boldsymbol{q},\boldsymbol{q})\}_n = \hat{\boldsymbol{V}}_n^H\begin{pmatrix} 0 & 1 \\ -1 & 0 \end{pmatrix}\sum_k \Big(&a_{n-k}a_k(\boldsymbol{e}_2\cdot\hat{\boldsymbol{U}}_{n-k})\hat{\boldsymbol{U}}_k + a_k b_{n-k}^{(2)}(\boldsymbol{e}_2\cdot\boldsymbol{u}_{n-k}^{(2)})\hat{\boldsymbol{U}}_k \\ &+a_{n-k}b_k^{(2)}(\boldsymbol{e}_2\cdot\hat{\boldsymbol{U}}_{n-k})\boldsymbol{u}_k^{(2)} + b_{n-k}^{(2)}b_k^{(2)}(\boldsymbol{e}_2\cdot\boldsymbol{u}_{n-k}^{(2)})\boldsymbol{u}_k^{(2)}\Big).\end{aligned} \tag{30}$$

It is now crucial to determine which terms are asymptotically dominant as $\lambda \to 0$, in addition to determining the asymptotic fate of other terms such as the inner products $\hat{\boldsymbol{V}}_n^H\hat{\boldsymbol{U}}_n$ and $\hat{\boldsymbol{V}}_n^H\hat{\boldsymbol{u}}_n^{(2)}$ in equation (28). Notably, all of these terms contain a dependence on the forcing frequency ω. Here, we focus on two cases determined from the behaviour of the leading singular values (see equation (20)): namely $\omega \sim \lambda$, and $\omega \sim \lambda^\alpha$ for $0 < \alpha < 1$.

3.4 Asymptotic reduction when $\omega = \mathcal{O}(\lambda)$

We shall first consider the case when $\omega \sim \lambda$ since it is the simplest algebraically as the real and imaginary parts of α_n and β_n each scale in the same way for this case.

Recalling that our small parameter is defined as $\varepsilon \equiv 1/\sigma_1^+$, and examining the form of the leading singular value for each n (equation (18)), one observes that

$$\sigma_n^+ \sim 1/\varepsilon. \tag{31}$$

Further, one can examine the inner products that appear in the slow time derivative of equation (28), and see that

$$\hat{\boldsymbol{V}}_n^H \hat{\boldsymbol{U}}_n = \mathcal{O}(\varepsilon^{1/2}), \qquad \hat{\boldsymbol{V}}_n^H \boldsymbol{u}_n^{(2)} = \mathcal{O}(1). \tag{32}$$

Notably, we see that the projection onto the subdominant response vector $\boldsymbol{u}_n^{(2)}$ is asymptotically larger than the projection onto $\hat{\boldsymbol{U}}_n$. However, the coefficient $b_n^{(2)}$ is seen from the linear analysis to be of size ε smaller than the leading coefficient a_n and thus, the dominant term in the time derivative will be $a_n \hat{\boldsymbol{V}}_n^H \hat{\boldsymbol{U}}_n$.

We now turn our attention to the projection of the nonlinear terms. After lengthy evaluation of interactions of wavenumbers $n, k, \ell \in \mathbb{Z}$, we find the following scaling of the four nonlinear terms

$$\hat{\boldsymbol{V}}_n^H \begin{pmatrix} 0 & 1 \\ -1 & 0 \end{pmatrix} (\boldsymbol{e}_2 \cdot \hat{\boldsymbol{U}}_k)\hat{\boldsymbol{U}}_\ell \;\; = \mathcal{O}(1), \tag{33}$$

$$\hat{\boldsymbol{V}}_n^H \begin{pmatrix} 0 & 1 \\ -1 & 0 \end{pmatrix} (\boldsymbol{e}_2 \cdot \boldsymbol{u}_k^{(2)})\hat{\boldsymbol{U}}_\ell \;\; = \mathcal{O}(\varepsilon^{1/2}), \tag{34}$$

$$\hat{\boldsymbol{V}}_n^H \begin{pmatrix} 0 & 1 \\ -1 & 0 \end{pmatrix} (\boldsymbol{e}_2 \cdot \hat{\boldsymbol{U}}_k)\boldsymbol{u}_\ell^{(2)} \;\; = \mathcal{O}(\varepsilon^{1/2}), \tag{35}$$

$$\hat{\boldsymbol{V}}_n^H \begin{pmatrix} 0 & 1 \\ -1 & 0 \end{pmatrix} (\boldsymbol{e}_2 \cdot \boldsymbol{u}_k^{(2)})\boldsymbol{u}_\ell^{(2)} = \mathcal{O}(\varepsilon). \tag{36}$$

Consequently, as $\varepsilon \to 0$, only the nonlinear interactions between the leading singular vectors appear at leading order in equation (28). We additionally confirm that the projection of the forcing is

$$\hat{\boldsymbol{V}}_n^H \hat{\boldsymbol{f}} = \mathcal{O}(1). \tag{37}$$

Having found the scaling of each of the terms in equation (28), we must now find the choice of free parameters to make this equation balance non-trivially. The terms that may appear at leading order from the above analysis are

$$\Delta \partial_T a_n (\hat{\boldsymbol{V}}_n^H \hat{\boldsymbol{U}}_n) + (\sigma_n^+)^{-1} a_n = \hat{\boldsymbol{V}}_n^H \begin{pmatrix} 0 & 1 \\ -1 & 0 \end{pmatrix} \sum_k a_{n-k} a_k (\boldsymbol{e}_2 \cdot \hat{\boldsymbol{U}}_{n-k}) \hat{\boldsymbol{U}}_k + \delta \big(\hat{\boldsymbol{V}}_n^H \hat{\boldsymbol{f}} \big) \delta_{\pm 1, n} + \cdots, \tag{38}$$

which scales as

$$\Delta a_n \varepsilon^{1/2} + \varepsilon a_n - \sum_k a_{n-k} a_k = \mathcal{O}(\delta \delta_{\pm 1, n}). \tag{39}$$

3.4.1 Balancing the $\omega = \mathcal{O}(\lambda)$ amplitude equation

We first consider the scaling of the $n = 1$ equation

$$n = 1 : \qquad \Delta a_1 \varepsilon^{1/2} + \varepsilon a_1 - \sum_k a_{1-k} a_k = \mathcal{O}(\delta). \tag{40}$$

An asymptotic balance between the linear term εa_1 and δ sets $a_1 \sim \delta/\varepsilon$, as anticipated from the linear analysis (§2.2). Further, we consider a nonlinear interaction between the mean a_0 and the $n = 1$ mode a_1 at this order, thus introducing a feedback from the mean, which sets the amplitude of a_0 as $a_0\delta/\varepsilon \sim \delta$, giving $a_0 \sim \varepsilon$.

Turning our attention to the scaling of the $n = 0$ equation

$$n = 0 : \qquad \Delta a_0 \varepsilon^{1/2} + \varepsilon a_0 = \mathcal{O}\big(\sum_k a_{-k} a_k\big), \tag{41}$$

we may now set the amplitude of a_1 and δ. Since the amplitude of $a_0 \sim \varepsilon$, introducing a nontrivial nonlinearity in this equation due to a $k = 1$ nonlinear feedback sets the amplitude of a_1 through $a_1 a_{-1} \sim (\delta/\varepsilon)^2 \sim \varepsilon^2$, giving $\delta \sim \varepsilon^2$, and thus, $a_1 \sim \varepsilon$. We may now additionally see that Δ must be set as $\Delta \sim \varepsilon^{1/2}$ if it is to be included at leading order. However, we must now compare this to the fast time set by the forcing frequency ω to check if we indeed have time-scale separation. From equation (20), $\omega \sim \lambda \sim \varepsilon^{1/2}$, and thus the purported slow-time variation occurs on the same scale as the fast time variation, and thus, formally there is no time-scale separation.

Returning to the $n = 1$ equation, we may additionally anticipate a $k = 2$ interaction which sets $a_2 \sim \varepsilon$. If we do not include this interaction and assume that a_2 is asymptotically smaller than the other modes, we would see a violation of asymptotic consistency at the $n = 2$ equation, since a nonlinear interaction between $a_1 a_1$ would be asymptotically larger than the remaining terms. In a similar way, considering scaling of the equations at successively higher $n \neq \pm 1$,

$$n \neq \pm 1 : \qquad \varepsilon a_n = \mathcal{O}\big(\sum_k a_{n-k} a_k\big), \tag{42}$$

we see from the $k = 1$ nonlinear interaction, we must inductively set the amplitude $a_n \sim \varepsilon$. Otherwise, the nonlinear feedback would be asymptotically larger than any other term.

In conclusion, we find that the only asymptotically consistent choice of scaling of a_n, Δ and δ for $\omega = \mathcal{O}(\lambda)$ is:

- All amplitudes have the same asymptotic size $a_n = \mathcal{O}(\varepsilon)$ for $n \in \mathbb{Z}$,
- The forcing amplitude depends on ε as $\delta = \mathcal{O}(\varepsilon^2)$,
- The slow-time scale $\Delta = \mathcal{O}(\varepsilon^{1/2}) = \mathcal{O}(\omega)$ which implies that no time-scale separation exists.

We may now proceed to write down our system of amplitude equations. Setting $a_n \equiv \varepsilon A_n$ and $\delta \equiv \delta_F \varepsilon^2$, we obtain the following system of nonlinear algebraic equations for the amplitudes A_n as $\varepsilon \to 0$:

$$\gamma_n A_n + \sum_k \mu_{n,k} A_{n-k} A_k + \delta_F \nu_n \delta_{\pm 1,n} = 0, \tag{43}$$

where the coefficients,

$$\gamma_n = \frac{-1}{\varepsilon\sigma_n^+}, \quad \mu_{n,k} = \hat{\boldsymbol{V}}_n^H \begin{pmatrix} 0 & 1 \\ -1 & 0 \end{pmatrix} \sum_k (\boldsymbol{e}_2 \cdot \hat{\boldsymbol{U}}_{n-k}) \hat{\boldsymbol{U}}_k, \quad \nu_n = \hat{\boldsymbol{V}}_n^H \hat{\boldsymbol{f}}, \tag{44}$$

only depend on the *leading* singular values and vectors of the resolvent operator at each n, and crucially, are independent of ε as $\varepsilon \to 0$.

After obtaining the amplitudes, the full solution in terms of the original variables is reconstructed as

$$\boldsymbol{q} = \begin{pmatrix} v \\ \eta \end{pmatrix} = \sum_n \varepsilon A_n \hat{\boldsymbol{U}}_n e^{in\omega t}. \tag{45}$$

Although it is perhaps disappointing that we must retain the amplitude A_n associated with each frequency $\omega_n = n\omega$ to ensure asymptotic consistency, the nonlinearity in the original problem has been greatly simplified as we have shown that it depends only on the interaction between the leading singular vectors as $\varepsilon \to 0$. Further, in practice the amplitudes are seen to decay algebraically with n and good agreement with the exact solutions can typically be obtained with only a few modes. The lack of slow time in the amplitude system removes a formal notion of stability of the solutions in the context of the amplitude equations themselves, also found in Ref. [8]. Crucially, however, the attractor of the system may still be captured by the amplitude system, allowing the long-time behaviour of the system to be quantified. In this case, our asymptotic reduction restricts the obtained solutions to equilibria or periodic orbits.

3.5 Asymptotic reduction when $\boldsymbol{\omega = \mathcal{O}(\lambda^\alpha)}$ with $\boldsymbol{0 < \alpha < 1}$

We now turn our attention to the $0 < \alpha < 1$ case. This dependence on α introduces further complexity into the scaling of the various terms in equation (28), primarily because the real and imaginary parts of $\alpha_n = (in\omega + \lambda)^{-1}$ and $\beta_n = (in\omega + b\lambda)^{-1}$ scale differently. Regardless, it is possible to obtain the following results for the scaling of the various relevant terms with $\varepsilon \equiv 1/\sigma_1^+$. We note that we now must separately consider the scalings for $n = 0$ and $n \neq 0$. In particular, the leading singular value for each n now scales as

$$\sigma_n^+ \sim \begin{cases} \varepsilon^{-1}, & n \neq 0 \\ \varepsilon^{-1/\alpha}, & n = 0 \end{cases}, \tag{46}$$

the projection onto the leading singular vector is

$$\hat{\boldsymbol{V}}_n^H \hat{\boldsymbol{U}}_n \sim \begin{cases} \varepsilon^{1/2\alpha} + i\varepsilon^{1/2}, & n \neq 0 \\ \varepsilon^{1/2\alpha}, & n = 0 \end{cases}, \tag{47}$$

and the projection onto the subdominant singular vector is

$$\hat{\boldsymbol{V}}_n^H \boldsymbol{u}_n^{(2)} \sim \begin{cases} \varepsilon^{1/2\alpha - 1/2} + i, & n \neq 0 \\ 1, & n = 0 \end{cases}. \tag{48}$$

Similar to the $\omega = \mathcal{O}(\lambda)$ case, we see that the projection onto the subdominant response vector $\boldsymbol{u}_n^{(2)}$ is again asymptotically larger than the projection onto $\hat{\boldsymbol{V}}_n$. However, the $b_n^{(2)}$

coefficient is seen to be smaller than a_n by a factor of ε for $n \neq 0$ and $\varepsilon^{1/\alpha}$ for $n = 0$, and thus, the dominant time derivative term remains $a_n \hat{\boldsymbol{V}}_n^H \hat{\boldsymbol{U}}_n$ for all n.

For the projection of the nonlinear terms, the interaction of the leading singular vectors is seen to be asymptotically larger than the other interactions, and in this case for wavenumbers $n, k, \ell \in \mathbb{Z}$ scales as

$$\hat{\boldsymbol{V}}_n^H \begin{pmatrix} 0 & 1 \\ -1 & 0 \end{pmatrix} (\boldsymbol{e}_2 \cdot \hat{\boldsymbol{U}}_k) \hat{\boldsymbol{U}}_\ell \sim \begin{cases} 1, & n = k = \ell = 0 \\ 1 + i\varepsilon^{1/2\alpha + 1/2} & k + \ell = 0 \\ 1 + i\varepsilon^{1/2\alpha - 1/2}, & \text{otherwise} \end{cases} . \tag{49}$$

This results in two separate cases for the scaling of terms that can appear at leading order in equation (28)

$$n = 0 : \qquad \Delta a_0 \varepsilon^{1/2\alpha} + \varepsilon^{1/\alpha} a_0 = \mathcal{O}\big(\sum_k a_{-k} a_k\big), \tag{50}$$

$$n \neq 0 : \qquad \Delta a_n \varepsilon^{1/2\alpha} + \varepsilon a_n - \sum_k a_{n-k} a_k = \mathcal{O}(\delta \delta_{\pm 1, n}). \tag{51}$$

3.5.1 Balancing the $\omega = \mathcal{O}(\lambda^\alpha)$ amplitude equation

We first consider the $n = 1$ equation and again note that $a_1 \sim \delta/\varepsilon$ is needed to balance the linear and forcing terms. We then turn our attention to the $n = 0$ equation

$$n = 0 : \qquad \Delta a_0 \varepsilon^{1/2\alpha} + \varepsilon^{1/\alpha} a_0 = \mathcal{O}\big(\sum_k a_{-k} a_k\big), \tag{52}$$

observing that a nonlinear self-interaction of the mean mode appearing at the same order as the linear term must set $\varepsilon^{1/\alpha} a_0 \sim a_0 a_0$, and thus $a_0 \sim \varepsilon^{1/\alpha}$. We would additionally anticipate that the forced mode should modify the mean of the solution through a nonlinear interaction with the a_1 mode. Thus, we expect that $a_0 a_0 \sim a_{-1} a_1 \sim \delta^2/\varepsilon^2$, giving $\delta \sim \varepsilon^{1+1/\alpha}$, which subsequently sets the size of a_1 as $a_1 \sim \varepsilon^{1/\alpha}$. We may also now obtain the scaling of the slow time, since $\Delta a_0 \varepsilon^{1/2\alpha} \sim \varepsilon^{2/\alpha}$, giving $\Delta \sim \varepsilon^{1/2\alpha}$. Noting that $\omega \sim \lambda^\alpha \sim \varepsilon^{1/2}$, we now see that we have a well-defined slow time for $0 < \alpha < 1$ since then $\Delta \ll \omega$.

We have established that $a_0 \sim a_1 \sim \varepsilon^{1/\alpha}$, however, we must now quantify the size of the amplitudes for $|n| > 1$. Considering the $n = 2$ equation, we have

$$n = 2 : \qquad \Delta a_2 \varepsilon^{1/2\alpha} + \varepsilon a_2 = \mathcal{O}\big(\sum_k a_{2-k} a_k\big). \tag{53}$$

To maintain asymptotic consistency, we must set the size of a_2 by balancing the linear term εa_2 with the $k = 1$ interaction. This gives that $\varepsilon a_2 \sim a_1 a_1 \sim \varepsilon^{2/\alpha}$, and thus $a_2 \sim \varepsilon^{2/\alpha - 1}$. We note that the time derivative term here is now asymptotically smaller than the aforementioned terms at $n = 2$ as well as a $k = 0$ nonlinear interaction, and thus, proceeding in a different manner leads to asymptotic inconsistency. Similarly, now considering higher values of n, we have

$$n > 2 : \qquad \Delta a_n \varepsilon^{1/2\alpha} + \varepsilon a_n = \mathcal{O}\big(\sum_k a_{n-k} a_k\big). \tag{54}$$

Considering the $k = 1$ nonlinear interaction and balancing it with the linear term gives $\varepsilon a_n \sim a_{n-1}a_1$, meaning that $a_n \sim a_{n-1}\varepsilon^{1/\alpha-1}$, and since $0 < \alpha < 1$, we have that $1/\alpha - 1 > 0$. Thus, we may say inductively that $a_n \ll a_{n-1}$ for $n > 1$.

In conclusion, for $\omega \sim \lambda^\alpha$ with $0 < \lambda < 1$, the only asymptotically consistent choice of each a_n, Δ and δ are:

- The amplitudes for $n = \{0, \pm 1\}$ have the same asymptotic size $a_0 \sim a_{\pm 1} = \mathcal{O}(\varepsilon^{1/\alpha})$,
- The amplitudes for $|n| > 1$ are asymptotically smaller with $a_{\pm 1} \gg a_{\pm 2} \gg a_{\pm 3} \gg \cdots$ with the relation $a_{|n|} \sim a_{|n|-1}\varepsilon^{1/\alpha-1}$ for $|n| > 1$,
- The forcing amplitude depends on ε as $\delta = \mathcal{O}(\varepsilon^{1+1/\alpha})$,
- The slow time-scale $\Delta = \mathcal{O}(\varepsilon^{1/2\alpha}) \ll \omega = \mathcal{O}(\varepsilon^{1/2})$, meaning that we indeed have time scale separation.

Knowing the scaling of the various quantities, we may now proceed to write the amplitude equation. For $n = 1$, at leading order as $\varepsilon \to 0$ only contributions from the linear term and the forcing survive, enabling the amplitude a_1 to be solved for directly as

$$(\sigma_1^+)^{-1}a_1 = \delta(\hat{\boldsymbol{V}}_1^H \hat{\boldsymbol{f}}) \quad \Rightarrow a_1 = \delta\sigma_1^+(\hat{\boldsymbol{V}}_1^H \hat{\boldsymbol{f}}). \tag{55}$$

For the $n = 0$ equation, the linear response, slow time derivative terms, and nonlinear interactions for $k = \{0, \pm 1\}$ dominate as $\varepsilon \to 0$. Substituting the solved values for $a_{\pm 1}$ yields

$$\Delta\partial_T a_0(\hat{\boldsymbol{V}}_0^H \hat{\boldsymbol{U}}_0) + (\sigma_0^+)^{-1}a_0 = \mu_{0,0}a_0^2 + 2\mathfrak{Re}\{\mu_{0,1}\}|a_1|^2, \tag{56}$$

where again we use the notation

$$\mu_{n,k} = \hat{\boldsymbol{V}}_n^H \begin{pmatrix} 0 & 1 \\ -1 & 0 \end{pmatrix} \sum_k (\boldsymbol{e}_2 \cdot \hat{\boldsymbol{U}}_{n-k})\hat{\boldsymbol{U}}_k, \tag{57}$$

and $\mathfrak{Re}\{\cdot\}$ denotes the real part of the given quantity.

Rescaling the amplitude $a_0 = \varepsilon^{1/\alpha}A_0$, we may rewrite this equation more simply as

$$\dot{A}_0 = \eta A_0 + \nu A_0^2 + F, \tag{58}$$

where $\dot{(\cdot)}$ denotes the slow-time derivative, and the coefficients

$$\eta = \frac{-(\sigma_0^+)^{-1}}{\varepsilon^{1/2\alpha}(\hat{\boldsymbol{V}}_0^H \hat{\boldsymbol{U}}_0)}, \quad \nu = \frac{\mu_{0,0}\varepsilon^{1/2\alpha}}{(\hat{\boldsymbol{V}}_0^H \hat{\boldsymbol{U}}_{\boldsymbol{0}})}, \quad F = \frac{2\mathfrak{Re}\{\mu_{0,1}\}|a_1|^2}{\varepsilon^{3/2\alpha}(\hat{\boldsymbol{V}}_0^H \hat{\boldsymbol{U}}_0)}, \tag{59}$$

only depend on the *leading* singular values and vectors for $n = \{0, \pm 1\}$, and crucially remain $\mathcal{O}(1)$ as $\varepsilon \to 0$. Further, we have reduced our system to a single scalar amplitude equation while retaining time-scale separation. This reduction enables us to readily compute time-evolving solutions to the original system and to formally assess their stability. The solution in the original variables can then be reconstructed as

$$\boldsymbol{q} = \begin{pmatrix} v \\ \eta \end{pmatrix} \sim \varepsilon^{1/\alpha}A_0(T)\hat{\boldsymbol{U}}_0 + (\delta\sigma_1^+(\hat{\boldsymbol{V}}_1^H \hat{\boldsymbol{f}})\hat{\boldsymbol{U}}_1 e^{i\omega t} + c.c.). \tag{60}$$

4 Results for the Model Problem

4.1 System of amplitude equations when $\omega = \mathcal{O}(\lambda)$

In the regime when the forcing frequency $\omega = \mathcal{O}(\lambda)$, the long-time response of the system (equation (14)) asymptotically reduces to a system of nonlinear algebraic equations for amplitudes A_n with $n \in \mathbb{Z}$ (equation (43)) for large values of the inverse Reynolds number λ.. Although all of the amplitudes appear at the same asymptotic order and are nonlinearly coupled, we anticipate that there will be a decay in the amplitude of the solution with increased frequency. To this end, we investigate the spectral properties of the fully nonlinear solutions. A time-series, computed using the `ode15s` solver in `MATLAB` with a relative tolerance of 10^{-16}, is shown in figure 3(a), and the corresponding power spectral density of the time-series once it has reached the statistically steady state is shown in figure 3(b). We observe that the largest response of the system occurs at the frequency of the forcing which is shown in grey in figure 3(b), and even in this fully nonlinear state, the contribution to the solution at each harmonic of the forced frequency clearly decays with increased frequency. This scenario is typical across all of the parameter space tested (not shown), and thus, we anticipate that we will be able to truncate the system of nonlinear equations (equation (43)) at a finite frequency to a high level of accuracy. In the test cases we have considered, the system may be severely truncated, with only modes $|n| \lesssim 3$ being needed to obtain good agreement with the fully nonlinear solution.

With the understanding that we may truncate the nonlinear system of algebraic equations (43) while retaining a good numerical accuracy, we now seek to understand the solutions to this system. Generally, it is not possible to make statements about the solutions to this nonlinear algebraic system for an arbitrary choice of parameters. Thus, we investigate this system numerically for various specific choices of parameter values using the `fsolve` function in `MATLAB` with a relative tolerance of 10^{-14}. The solution branches found numer-

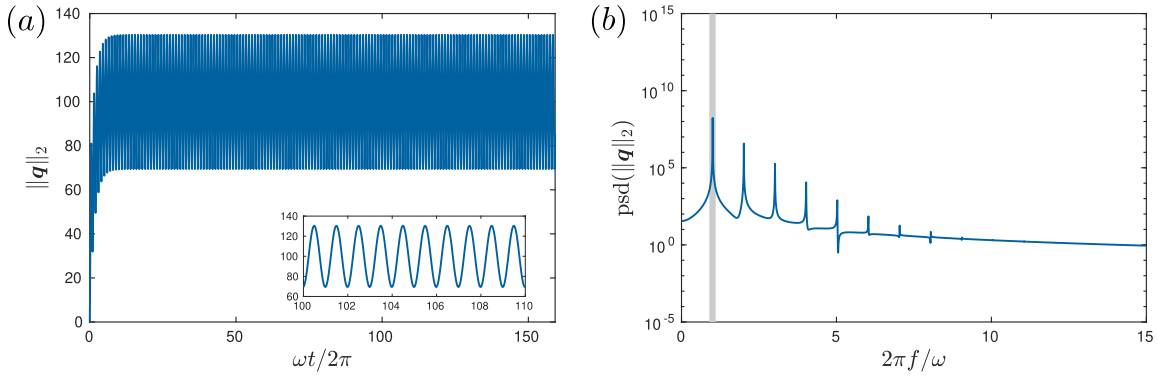

Figure 3: (a) Evolution of the state vector norm from the forced fully nonlinear system (Eq. (14)) with $\lambda = 10^{-2}$, $\omega = 10\lambda$, $\delta = 3$ from a $(0, 0)$ initial condition as a function of time normalised by the forcing period. The inset shows a smaller segment of the time series. (b) The power spectral density of the solution is shown as a function of the frequency normalised by the forcing period. The directly forced frequency is shown by the grey line. The spectral density clearly decays for higher harmonics in the fully nonlinear solution.

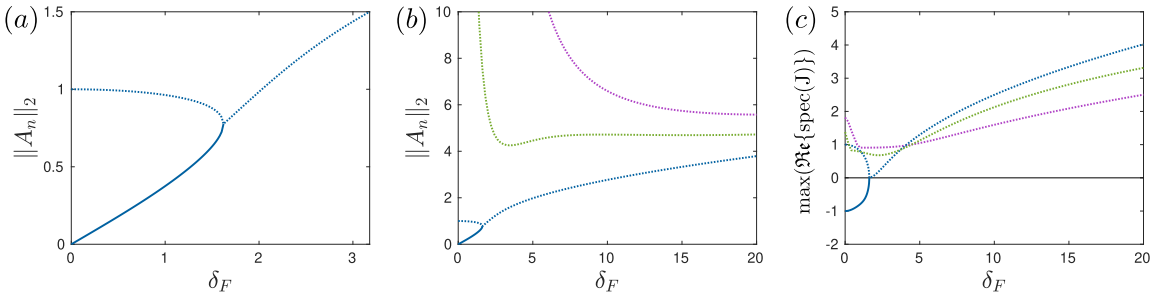

Figure 4: (a) Bifurcation diagram showing solutions of the system of amplitude equations (Eq. (43)) distinguished by the l^2 norm of the amplitude coefficients as a function of the forcing amplitude δ_F with $\lambda = 10^{-4}$, $\omega = \lambda$, $b = 1$. Solid lines denote stable solutions, and dotted lines represent saddle/unstable solutions. (b) Same bifurcation diagram for larger values of δ_F. (c) The real part of the leading eigenvalue of the Jacobian matrix J of equation (43) linearised about the corresponding solution.

ically for $\lambda = 10^{-4}$, $\omega = \lambda$, $b = 1$, and $0 \leq \delta_F \leq 10$ are shown in the bifurcation diagrams as a function of the forcing parameter δ_F in figure 4(a–b), and were obtained with a brute force search due to the simplicity of the system,. Although the stability of such solutions on the slow time scale may not be assessed formally (§3.4.1), we anticipate that we may be able to re-expand near the solution itself and thus consider the spectrum of the Jacobian of equation (43) to assess stability.

We observe in figure 4(a) that a stable branch of solutions (solid blue line), corresponding to a limit cycle in the original variables $\boldsymbol{q}$, emerges from the $\boldsymbol{q} = (0, 0)$ point as the forcing δ_F is increased from zero. Thus, the stable solution begins to move away from the origin, reaching a finite amplitude in response to the external forcing. Additionally, we observe a saddle point (dotted blue line) with one unstable direction, corresponding to an unstable periodic orbit (UPO) in the original variables, emerging from the saddle point in the unforced system in equation (14). As the forcing is increased, these two solutions approach each other, bifurcating at $\delta_{F,c} \approx 1.62$, which results in a single saddle point with broken symmetry in the A_n coefficients compared to the two solutions beneath the bifurcation point. At higher amplitudes and forcing values, a number of different solutions have been found (fig. 4(b)), and are all of saddle type, thus representing unstable periodic orbits in the original variables. At low values of δ_F, all of these solutions are observed to have large amplitudes in the A_n coefficients, and thus are not relevant in the context of our asymptotic reduction which assumes that $A_n = \mathcal{O}(1)$.

Consequently, as we increase the level of forcing in our system, starting from the "laminar solution", we see sustained stable periodic solutions which grow in amplitude in response to the harmonic forcing. As the strength of the forcing is increased, the limit cycle and UPO (beneath the bifurcation point in figure 4(a)) eventually collide, producing a UPO with broken symmetry above a critical point (at $\delta_{F,c} \approx 1.62$ at these parameter values) and no stable solutions exist in the amplitude system. Thus, we anticipate that in the full nonlinear system, solutions from all initial conditions above this critical threshold will transition, growing into the fully nonlinear state. Although it is likely that details of the

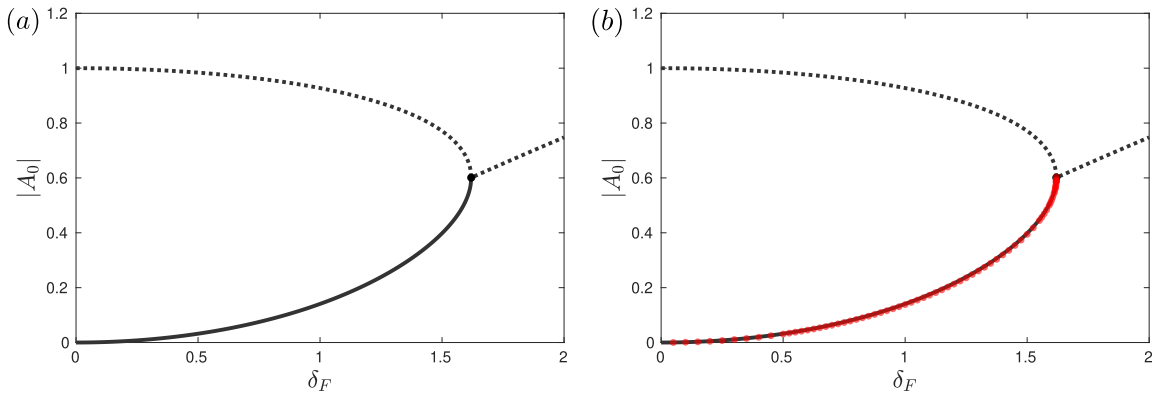

Figure 5: (a) Bifurcation diagram computed from the amplitude system (Eq. (43)) showing the magnitude of the mean amplitude A_0 as a function of the forcing amplitude δ_F with $\lambda = 10^{-4}$, $\omega = \lambda$, $b = 1$. Stable solutions are shown with solid lines, and unstable/saddle solutions are shown with dotted lines. The black marker shows the saddle-node bifurcation point. (b) Branch of stable solutions computed from the fully nonlinear system (Eq. (14)) shown by red markers on the same bifurcation diagram.

bifurcation scenario and the number of branches of UPOs may change with varied values of the system parameters, our tests indicate that the overall qualitative picture of the transition remains broadly similar.

We now turn our attention to comparing the solutions on the stable branch of the system of amplitude equations to the solutions of the full nonlinear system (equation (14)). We first compare the mean of the solution of the full nonlinear system to that of the amplitude equations through the magnitude of the mean amplitude A_0, shown in figure 5 for $\lambda = 10^{-4}$, $\omega = \lambda$, $b = 1$, observing excellent agreement. We additionally see excellent agreement in the forcing amplitude for which the stable branch loses stability. The bifurcation point for these parameter values in the amplitude system (equation (14)) occurs at $\delta_{F,c} \approx 1.61937$ and the corresponding critical forcing amplitude in the full nonlinear system is $\delta_{F,c} \approx 1.61965$, giving a relative error of order 10^{-4}. Thus, the amplitude equations can accurately predict the critical forcing value for which the forced "laminar" state exists, and hence, transitions to the fully nonlinear state.

To compare the temporal dynamics, we show a time-series with $\lambda = 10^{-5}$, $\omega = 3\lambda$, $b = 1$, $\delta_F = 5$ in figure 6. The full nonlinear system (equation (14)) is initialised from a $(0, 0)$ initial condition. The solution undergoes an initial transient before being attracted to a limit cycle solution shown in grey in figure 6. The components of $\boldsymbol{q} = (v, \eta)$ are shown in figure 6(a–b) normalised by the long-time average $\langle\cdot\rangle_t$ of $\|\boldsymbol{q}\|_2$, denoted as $\boldsymbol{q}^* = (v^*, \eta^*) = \boldsymbol{q}/\langle\|\boldsymbol{q}\|_2\rangle_t$. A phase portrait of the trajectory is shown in figure 6(c). This fully nonlinear solution in grey is compared to the limit cycle solution of the asymptotically reduced system (equation (43)) shown in red, where the solution in the original coordinates is reconstructed using equation (45). We observe excellent agreement between the two systems once the fully nonlinear solution has relaxed to the limit cycle, suggesting that the long-time behaviour of the asymptotically reduced system captures the true behaviour well, and thus, the attractor

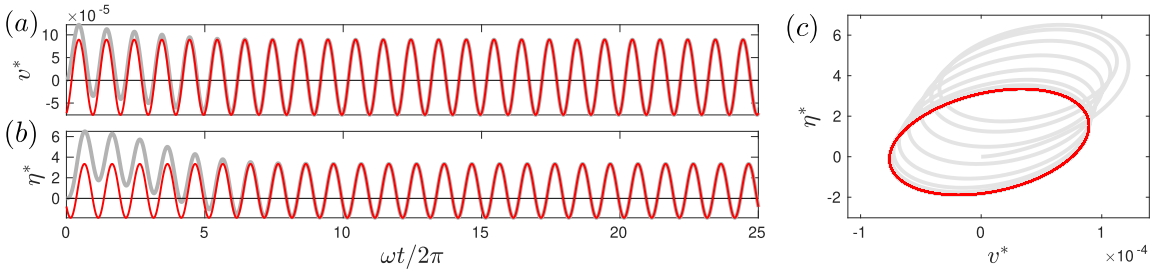

Figure 6: (a, b) Components of $\boldsymbol{q}^* = (v^*, \eta^*) = \boldsymbol{q}/\langle \|\boldsymbol{q}\|_2 \rangle_t$ as a function of time normalised by the forcing period for the fully nonlinear solution (grey) and the solution of the amplitude system (Eq. (43)) (red) for $\lambda = 10^{-5}$, $\omega = 3\lambda$, $b = 1$, $\delta_F = 5$. The black line shows the applied harmonic forcing as a function of time. (c) Phase portrait of the solutions showing the fully nonlinear solution relaxing to the limit cycle captured by the amplitude system.

of the system has been accurately obtained. These results are representative of our tests across a wide range of parameters beneath the critical forcing threshold that results in a transition to the fully nonlinear state of the original nonlinear system.

4.2 Amplitude equation when $\omega = \mathcal{O}(\lambda^\alpha)$ with $0 < \alpha < 1$

In the regime when the forcing frequency $\omega = \mathcal{O}(\lambda^\alpha)$ with $0 < \alpha < 1$, we obtained an asymptotically reduced differential equation (58) that determines the evolution of the mean amplitude of the solution A_0 as a function of the slow time T. The coefficients in this single, scalar amplitude equation only depend on the leading singular values and vectors for $n = \{0, \pm 1\}$; F may be interpreted as a proxy for the forcing, which is modulated by the nonlinear interaction of the mean and $n = 1$ singular vectors and does not evolve in time.

This amplitude equation is simpler than the system of nonlinear equations obtained in the case of $\omega = \mathcal{O}(\lambda)$ (equation (43)) and is amenable to an analytic treatment. To investigate the qualitative dynamics of this amplitude equation, we first note that the equilibrium solutions are given by

$$A_0^{\pm} = \frac{-\eta \pm \sqrt{\eta^2 - 4\nu F}}{2\nu}, \tag{61}$$

meaning that two equilibria exist when $\eta^2 > 4\nu F$ and no equilibria exist when $\eta^2 < 4\nu F$. Thus, at a critical value of the forcing F_c, we observe a saddle-node bifurcation occurring at

$$F_c = \frac{\eta^2}{4\nu}, \tag{62}$$

which can be directly related to the magnitude of the original applied forcing δ by manipulation of the coefficients in equation (59) and the expression for the coefficient a_1 given in equation (55). Expressing the forcing amplitude in terms of a rescaled order-one parameter δ_F as $\delta = \delta_F \varepsilon^{1+1/\alpha}$, the critical forcing for the saddle-node bifurcation may be written

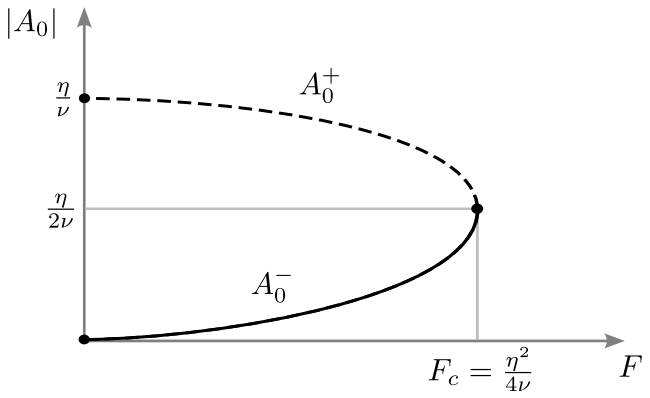

Figure 7: Sketch of bifurcation diagram for the amplitude equation (Eq. (58)) showing the saddle-node bifurcation occurring at a critical value of the forcing F_c. Solid lines denote stable solutions, and dashed lines denote unstable solutions.

explicitly from the amplitude equation as

$$\delta_{F,c} = \sqrt{\frac{-\mu_{0,0}\,\sigma_0^+}{8\,\varepsilon^{2-1/\alpha}\,(\sigma_1^+)^2\,\mathfrak{Re}\{\mu_{0,1}\}\,|\hat{\boldsymbol{V}}_1^H\,\hat{\boldsymbol{f}}|^2}}. \tag{63}$$

We may assess the linear stability of these two equilibrium points by perturbing the equilibrium solutions as $A_0 = A_0^{\pm} + A_0'$ and collecting terms at linear order:

$$\dot{A}_0' = \pm\sqrt{\eta^2 - 4\nu F}\,A_0' + \mathcal{O}({A_0'}^2). \tag{64}$$

Thus, when $F < F_c$, A_0^+ is linearly unstable and A_0^- is linearly stable. A sketch of the bifurcation diagram for this system is shown in figure 7.

Notably, we have obtained a different normal form than the weakly nonlinear analysis of Ducimetière *et al.* [8], where they obtained a perturbed subcritical pitchfork bifurcation, (*i.e.*, a pitchfork with a constant term related to the forcing that breaks the reflection symmetry of the amplitude). This leads to a somewhat similar bifurcation scenario featuring a saddle-node bifurcation, but this normal form additionally produces an unstable branch which plays no physical role in the transition (see figure 10(b) in [8]). This, combined with the asymptotic inconsistencies in [8] suggests that an incorrect normal form was obtained in this work which eliminated the most relevant nonlinearity, (*i.e.*, the quadratic term we observe here). This is further supported by the very large coefficient obtained for the cubic term (see table 2 and related discussion in [8]) which is 4 orders of magnitude larger than the coefficient of the time derivative term, for example.

Importantly, similarly to the results obtained numerically for the $\omega = \mathcal{O}(\lambda)$ system of equations (see fig. 4 and the accompanying discussion in §4.1), this bifurcation structure may be interpreted physically in the context of the model problem. When no forcing is applied to the system, the "laminar" solution $\boldsymbol{q} = \boldsymbol{0}$ is linearly stable, corresponding to a mean amplitude $A_0 = 0$, which is observed on the linearly stable A_0^- branch. As the forcing amplitude is increased, the mean of the linearly stable solution grows away from the

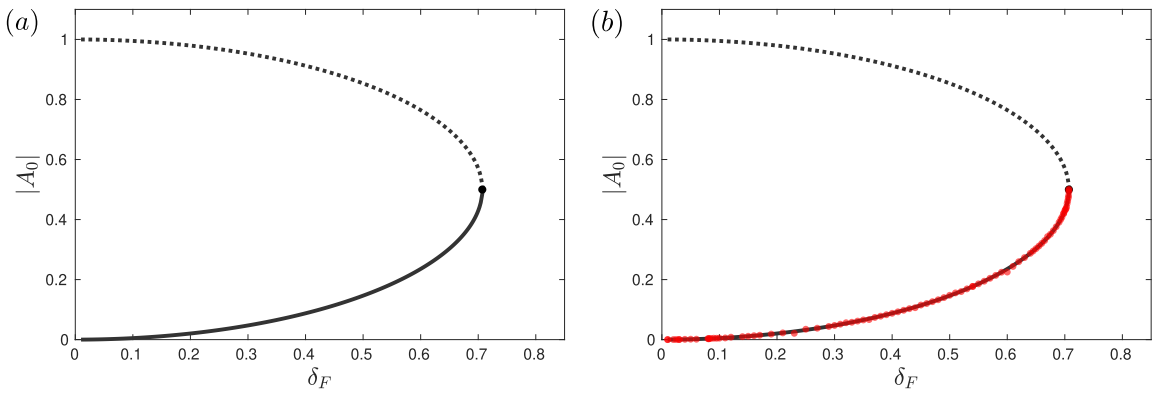

Figure 8: (a) Bifurcation diagram computed from the amplitude equation (Eq. (58)) with $\lambda = 10^{-4}$, $\omega = \lambda^{1/2}$, $b = 1$. Stable solutions are shown with solid lines, and unstable/saddle solutions are shown with dotted lines. The black marker shows the saddle-node bifurcation point. (b) Branch of stable solutions computed from the fully nonlinear system (Eq. (14)) shown in mean by red markers on the same bifurcation diagram.

$\boldsymbol{q} = \mathbf{0}$ point, following the A_0^- branch. However, if the "laminar" solution is perturbed with sufficient amplitude to push the initial condition above the linearly unstable A_0^+ branch, the solution from the amplitude equation grows without bound into the fully nonlinear regime. As the forcing is increased, an increasingly smaller amplitude is required to push the solution beyond this separatrix, until at the critical forcing amplitude F_c the two equilibria annihilate each other in the saddle-node bifurcation and trajectories from all initial conditions grow into the fully nonlinear regime. In the context of the forced fully nonlinear system, this corresponds to a saddle-node bifurcation of the limit cycle and unstable periodic orbit, leaving all trajectories in the phase portrait to be attracted to the upper branch fully nonlinear solution, as sketched in figure 2(b).

To quantitatively test this picture of the transition, we first compare the mean of the linearly stable A_0^- solution to that of the full numerical solution of equation (14) at $\lambda = 10^{-4}$, $\omega = \lambda^{1/2}$, $b = 1$ for a range of forcing values beneath the critical threshold $\delta_{F,c}$. In figure 8(a), we first show the bifurcation diagram computed from the predictions of the amplitude equation (58) for the given parameter values. In figure 8(b), we now overlay the mean of solutions from the full nonlinear system (equation (14)) using red markers. Excellent agreement with the model is evident. Furthermore, the critical forcing value for the saddle-node bifurcation point, which was calculated to be $\delta_{F,c} = 0.707072$ from the amplitude equation (using equation (63)) agrees nearly exactly with the value calculated from the full nonlinear system (equation (14)), $\delta_{F,c} = 0.70711$, giving a relative error of order 10^{-5}.

We now turn our attention from the equilibrium solutions of the amplitude equation to the transient slow-time dynamics, noting that the amplitude equation (equation (58)) is a Riccati equation with constant coefficients. Since this equation is separable, we may separate and directly integrate both sides of the equation with respect to time. Doing so

yields the following general solution to the problem

$$A_0(T) = \frac{\sqrt{4F\nu - \eta^2}\tan\left(\frac{1}{2}\sqrt{4F\nu - \eta^2}(T - C)\right) - \eta}{2\nu}, \tag{65}$$

where C is the constant of integration and is set by the initial condition $A_0(0)$ as

$$C = \frac{2}{\sqrt{4F\nu - \eta^2}} \arctan\left(\frac{2\nu A_0(0) + \eta}{\sqrt{4F\nu - \eta^2}}\right). \tag{66}$$

We reconstruct the full solution from the amplitude solution using equation (60) and compare it in figure 9 to the fully nonlinear solution using $\boldsymbol{q} = \boldsymbol{0}$ as the initial condition. In figure 9(a), we first show the evolution of the mean mode as a function of the original time variable (fast time t) normalised by the forcing period, revealing a clear monotonic evolution. In figures 9(b–d), we compare the evolution of the solution of the amplitude equation (58) to the solution from the full nonlinear system (14) over various time intervals. In the initial stages of the evolution (fig. 9(c)), the mean of both solutions grows in

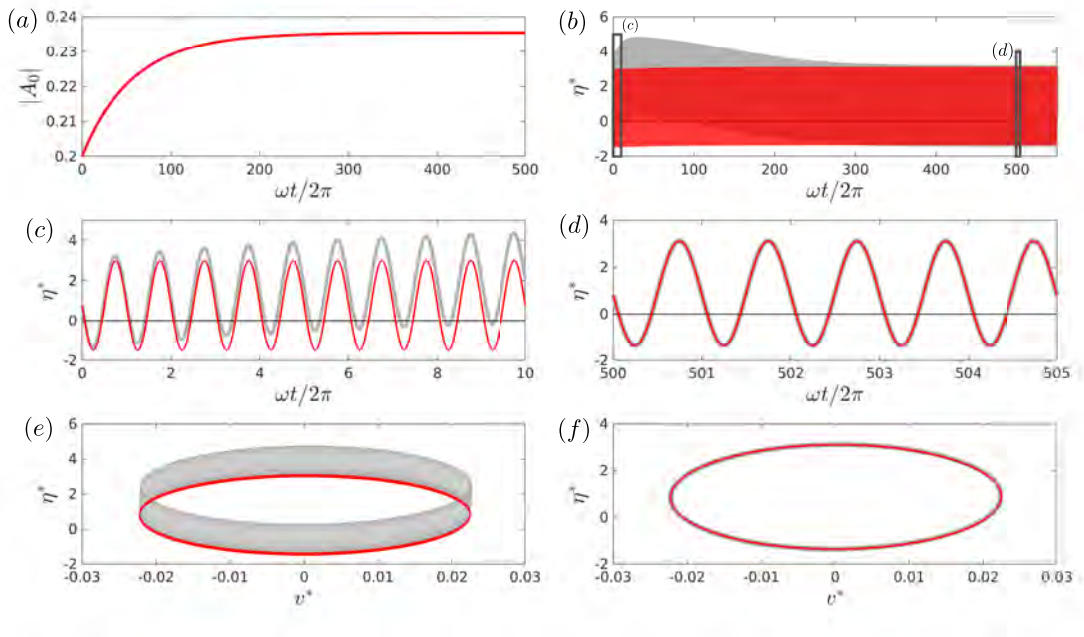

Figure 9: Comparison of the results from the fully nonlinear system (grey) and the solution from the amplitude equation (Eq. (58)) (red) with $\lambda = 10^{-4}$, $\omega = \lambda^{1/2}$, $b = 1$, $\delta_F = 0.6$. The initial condition is the same in both cases and is taken from a simulation of the fully nonlinear system at lower δ_F. (a) Evolution of the mean amplitude A_0 for the amplitude equation (Eq. (58)) as a function of time normalised by the forcing period. (b–d) $\eta^* = (\boldsymbol{q}\cdot\boldsymbol{e}_2)/\langle\|\boldsymbol{q}\|_2\rangle_t$ shown over the various time intervals indicated, with the applied harmonic forcing shown in black. (e, f) Phase portraits of the solutions constructed through the components of $\boldsymbol{q}^* = (v^*, \eta^*) = \boldsymbol{q}/\langle\|\boldsymbol{q}\|_2\rangle_t$ for (e) the full time series and (f) $\omega t/2\pi \geq 500$.

time. However, the fully nonlinear solution (grey) is seen to grow faster than that of the amplitude equation solution (red). The fully nonlinear solution reaches a maximal value at approximately 30 forcing periods before decaying back down to a stable periodic solution (see the grey solution envelope in fig. 9(b)). This behaviour falls outside of the scope of the 1-dimensional amplitude equation, which can only capture monotonic dynamics due to the asymptotic reduction. Indeed, the fully nonlinear solution in general appears to exhibit non-monotonic behaviour in this regime, and in fact, exhibits growth of the solution mean on the fast time scale for many initial conditions. Growth on the fast time scale falls outside of the scope of the present asymptotic reduction due to the ansatz made in equation (8), which assumed periodic response on the fast time scale.

Nevertheless, the long-time behaviour of the fully nonlinear solution is captured by the amplitude equation, as can be seen in the time series in figure 9(d), and the phase portrait showing trajectories of the statistically steady state in figure 9(f). This excellent agreement in the long-time behaviour of solutions has been observed over a wide range of parameter choices tested (not shown).

Although the initial "fast" transience is not captured well, the amplitude equation is still able to capture the dynamics of the full nonlinear solutions well if initialised appropriately. To illustrate this in figure 10, the initial condition of the amplitude equation is adjusted to that of the solution of the fully nonlinear system after 40 forcing periods (after the maxima of the time series at 30 forcing periods). The evolution of the amplitude equation from this contrived initial condition is shown in figure 10 for different parts of the time series in figures 10(a–b). We see good agreement between the slow-time evolution of the amplitude equation and the full nonlinear solution as it relaxes to the limit cycle which attracts trajectories as $t \to \infty$.

5 Conclusions

In this work, we have developed an asymptotically consistent, weakly nonlinear theory for systems that fall outside the scope of traditional weakly nonlinear analysis, where the base state of the system does not (necessarily) undergo a linear instability. This reduction is achieved under the assumption that the system is highly non-normal and subjected to harmonic forcing on a fast time scale. The former assumption is typical of the Navier-Stokes equations, as well as many other differential equations across science and engineering. Indeed, the method we have developed is well-suited for investigating systems such as parallel shear flows, where the transition to fully nonlinear states occurs subcritically through finite-amplitude perturbations of a linearly stable base state, and where the linearisation of the system about this base state is known to be highly non-normal. We have applied this methodology to a system of nonlinear ordinary differential equations (ODEs) inspired by the classical Orr–Sommerfeld-Squire system for parallel shear flows, noting that the asymptotic reduction depends on the prescribed relationship between the forcing frequency ω and the Reynolds number $\mathrm{Re} = \lambda^{-1}$. In particular, we discussed the asymptotic reduction of the system in two distinct regimes: $\omega = \mathcal{O}(\lambda)$ and $\omega = \mathcal{O}(\lambda^{\alpha})$ with $0 < \alpha < 1$, noting that the small parameter ε (the inverse maximum gain) is bounded from below for all values of Re if $\omega = \mathcal{O}(1)$.

For the $\omega = \mathcal{O}(\lambda)$ case, the nonlinear ODE reduces to a system of coupled nonlinear

equations for the solution amplitude at integer multiples of the forcing frequency A_n. Although formally each A_n appears at the same asymptotic order, we observe in practice that the amplitudes decay algebraically with increased n and that only a few amplitudes are needed to approximate the true solution with good accuracy. The resulting nonlinear system has been investigated for several test cases, yielding similar qualitative results across different choices of control parameters. As the forcing amplitude is increased, a limit cycle solution is born from the "laminar" $(0, 0)$ equilibrium point and is the only stable branch of solutions observed in the system. We investigate the dynamics of these solutions, observing excellent quantitative agreement between the asymptotically reduced solutions and the long-time behaviour of the full nonlinear solutions at a range of parameter values. Additionally, an unstable periodic orbit (UPO) is born from the saddle point in the unforced system, and this branch of solutions moves closer to the branch of limit cycles until they collide, bifurcating into a UPO with broken symmetry at a critical forcing value. For forcing amplitudes higher than this critical value, no stable solutions exist, and a transition to the full nonlinear state is anticipated. The critical forcing threshold compares excellently to the full nonlinear system, with a relative error of order 10^{-4}.

For the $\omega = \mathcal{O}(\lambda^\alpha)$ case with $0 < \alpha < 1$, we find that the full nonlinear system reduces to a scalar nonlinear ODE that retains dynamics on the slow time scale. This reduced equation can be solved analytically, and we show that the system undergoes a saddle-node bifurcation at a determined critical forcing amplitude. Similar to the $\omega = \mathcal{O}(\lambda)$ case, when

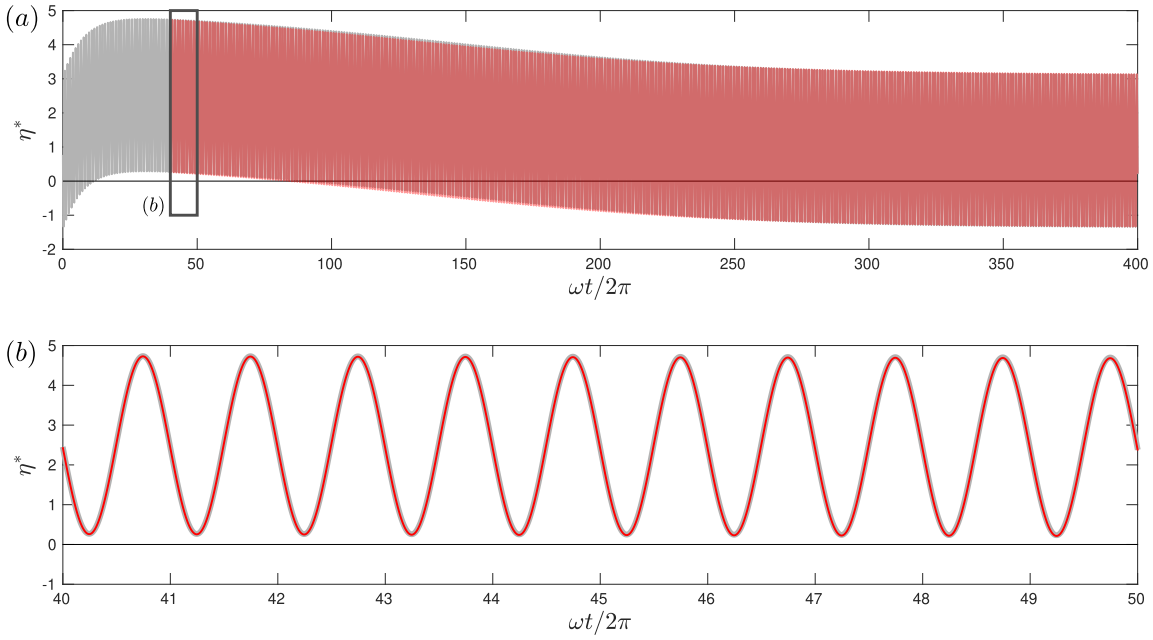

Figure 10: Evolution of $\eta^* = (\boldsymbol{q} \cdot \boldsymbol{e}_2)/\langle \|\boldsymbol{q}\|_2 \rangle_t$ shown for different time intervals from the fully nonlinear system (grey) and the amplitude equation (Eq. (58)) (red) with $\lambda = 10^{-4}$, $\omega = \lambda^{1/2}$, $b = 1$, $\delta_F = 0.6$. The initial condition for the amplitude equation has now been adjusted to match the fully nonlinear solution at $\omega t/2\pi = 40$. In both figures, the applied harmonic forcing is shown as a function of time by the black line.

the forcing amplitude is increased, a limit cycle is born from the "laminar" $(0, 0)$ equilibrium point, and a UPO is born from the saddle point in the unforced system. These solutions again collide at a critical forcing amplitude, but now annihilate each other in a saddle-node bifurcation. For forcing amplitudes above this bifurcation point, solutions grow without bound for all initial conditions and thus will grow into the fully nonlinear regime. The critical forcing amplitude, calculated explicitly from the amplitude equation, agrees with the value computed from the full nonlinear system to within a relative error of order 10^{-5}. In all cases, the attractor of the system is excellently captured by the amplitude equation. In many cases, where the full nonlinear system exhibits monotonic behaviour on the slow time scale, the temporal dynamics of the system are obtained with good accuracy. However, in some cases, we observe growth on the fast time scale, which is beyond the reach of the current method, necessarily constrained to monotonic slow-time dynamics.

In both cases, the general qualitative structure of the reduced systems can be interpreted physically within the context of the problem. As the forcing amplitude is increased, the stable "laminar" solution moves from its original point with increased amplitude due to the applied forcing. We note here that due to the large non-normality of the system, the amplitude of the response is orders of magnitude larger than that of the applied forcing. Similarly, an unstable periodic solution emerges from the saddle point, which defines the separatrix in the original unforced problem, and moves increasingly closer to the stable solution. Thus, as the forcing is increased, an ever smaller initial disturbance to the "laminar" solution is required to push the solution past the separatrix and drive a transition to the fully nonlinear state. As the forcing increases further, a critical threshold is reached where these stable and unstable solutions collide, bifurcating such that no stable solutions remain. Thus, above this critical forcing amplitude, the solutions from all initial conditions are attracted to the fully nonlinear state.

Although neither reduced system captures the fast-time growth observed in some full nonlinear solutions (which remains an open challenge), the scalar amplitude equation does capture slow time scale monotonic dynamics well, and both reduced systems display excellent agreement with the long-time behaviour of the full nonlinear system. Thus, this formalism may be useful in a wide range of potential applications where the long-time behaviour or slow-time scale dynamics (perhaps even with the amplitude of the forcing varying in slow-time) is of interest in highly non-normal dynamical systems. Additionally, the calculation of the critical forcing amplitude for the elimination of a stable "laminar" state is made significantly simpler in the reduced systems, and can even be written explicitly for the scalar amplitude equation. Although the asymptotic reduction for the particular nonlinear ODE we investigate here is modest, given the small size of the original system, we anticipate a significantly larger reduction in the number of degrees of freedom would be achieved for the case of a PDE satisfying the assumptions of our derivation. In particular, the dynamics would still reduce to a single or very small number of modes, leading to a far more significant reduction.

Critically, by emphasising asymptotic consistency in our method, we have obtained a different amplitude equation than the weakly nonlinear analysis of Ducimetière *et al.* [8] for a similar system. This suggests that asymptotic consistency is crucial to obtain the correct nonlinearities and thus, the correct normal form for the bifurcation. Here, the quadratic terms we obtain, which were eliminated by the method of [8], capture the behaviour of the

full system in the weakly nonlinear regime with excellent agreement, and are responsible for the nonlinear behaviour that destroys the stable laminar solution when the amplitude of the applied forcing is increased. In our approach, the cubic nonlinearity obtained by [8] is asymptotically smaller than the terms appearing in our amplitude equation. The correct role of the cubic term should be to stabilise the growth into the fully nonlinear regime and thereby capture the fully nonlinear (stable upper branch) solution $\overline{\boldsymbol{q}}_+$. Thus, for our model system, empirically we would expect the coefficient of the cubic term to behave as $\sim \varepsilon^{1/\alpha} \sim \lambda^2$. It is yet to be seen if this may be obtained formally by going to higher asymptotic order in our approach.

6 Acknowledgements

I would first like to thank my advisors, Greg Chini and Rich Kerswell, for their advice, guidance and enthusiasm, as well as for many interesting and fun scientific discussions throughout the programme. I would also like to thank Basile Gallet for the useful discussions near the end of the summer, which helped shape the results of this work. Thank you to Edgar Knobloch and Basile Gallet for the excellent principal lectures and to all of the GFD staff and visitors for making an enjoyable atmosphere in Walsh Cottage - a special thanks to Bruce Sutherland for allowing frequent invasion of his office space. Finally, I would like to thank the other fellows who made this summer fun and unforgettable.

References

[1] M. Avila, D. Barkley, and B. Hof, *Transition to turbulence in pipe flow*, Annu. Rev. Fluid Mech., 55 (2023), pp. 575–602.

[2] J. S. Baggett and L. N. Trefethen, *Low-dimensional models of subcritical transition to turbulence*, Physics of Fluids, 9 (1997), pp. 1043–1053.

[3] D. Barkley, *Theoretical perspective on the route to turbulence in a pipe*, Journal of Fluid Mechanics, 803 (2016), p. P1.

[4] P. Becherer, A. N. Morozov, and W. van Saarloos, *Probing a subcritical instability with an amplitude expansion: An exploration of how far one can get*, Physica D: Nonlinear Phenomena, 238 (2009), pp. 1827–1840.

[5] S. Chandrasekhar, *Hydrodynamic and hydromagnetic stability*, Int. Ser. Monogr. on Phys., (1961).

[6] P. Chossat and G. Iooss, *The Couette-Taylor Problem*, vol. 102, Springer Science & Business Media, 2012.

[7] M. C. Cross and P. C. Hohenberg, *Pattern formation outside of equilibrium*, Reviews of modern physics, 65 (1993), p. 851.

[8] Y.-M. Ducimetière, E. Boujo, and F. Gallaire, *Weak nonlinearity for strong non-normality*, Journal of Fluid Mechanics, 947 (2022), p. A43.

[9] B. Eckhardt, *Transition to turbulence in shear flows*, Physica A, 504 (2018), pp. 121–129.

[10] B. Eckhardt, T. Schneider, B. Hof, and J. Westerweel, *Turbulence transition in pipe flow*, Ann. Rev. Fluid Mech., 39 (2007), p. 447.

[11] G. Kawahara, M. Uhlmann, and L. van Veen, *The significance of simple invariant solutions in turbulent flows*, Annu. Rev. Fluid Mech., 44 (2012), pp. 203–225.

[12] R. R. Kerswell, *Recent progress in understanding the transition to turbulence*, Nonlinearity, 18 (2005), pp. R17–R44.

[13] C. Liu and D. F. Gayme, *Input-output inspired method for permissible perturbation amplitude of transitional wall-bounded shear flows*, Physical Review E, 102 (2020), p. 063108.

[14] W. V. R. Malkus and G. Veronis, *Finite amplitude cellular convection*, Journal of Fluid Mechanics, 4 (1958), p. 225–260.

[15] L. Rayleigh, *LIX. On convection currents in a horizontal layer of fluid, when the higher temperature is on the under side*, The London, Edinburgh, and Dublin Philosophical Magazine and Journal of Science, 32 (1916), pp. 529–546.

[16] P. J. Schmid, *Nonmodal stability theory*, Annu. Rev. Fluid Mech., 39 (2007), pp. 129–162.

[17] J. T. Stuart, *On the non-linear mechanics of hydrodynamic stability*, Journal of Fluid Mechanics, 4 (1958), pp. 1–21.

[18] ——, *On the non-linear mechanics of wave disturbances in stable and unstable parallel flows Part 1. The basic behaviour in plane Poiseuille flow*, Journal of Fluid Mechanics, 9 (1960), pp. 353–370.

[19] G. I. Taylor, *Viii. stability of a viscous liquid contained between two rotating cylinders*, Philosophical Transactions of the Royal Society of London. Series A, Containing Papers of a Mathematical or Physical Character, 223 (1923), pp. 289–343.

[20] L. N. Trefethen and M. Embree, *Spectra and pseudospectra: the behavior of nonnormal matrices and operators*, (2020).

[21] L. N. Trefethen, A. E. Trefethen, S. C. Reddy, and T. A. Driscoll, *Hydrodynamic stability without eigenvalues*, Science, 261 (1993), pp. 578–584.

[22] J. Watson, *On the non-linear mechanics of wave disturbances in stable and unstable parallel flows Part 2. the development of a solution for plane Poiseuille flow and for plane Couette flow*, Journal of Fluid Mechanics, 9 (1960), pp. 371–389.

REPORT DOCUMENTATION PAGE	1. Report No. WHOI-2025-14	2.	3. Recipient's Accession No.
4. Title and Subtitle 2024 Program of Study: Multiscale GFD			5. Report Date December 2025 6.
7. Author(s) Bruce Sutherland and Greg Chini			8. Performing Organization Rept. No. 10. Project/Task/Work Unit No.
9. Performing Organization Name and Address Woods Hole Oceanographic Institution			11. Contract(C) or Grant(G) No. (C) (G) OCE-1829864
12. Sponsoring Organization Name and Address National Science Foundation Program Manager Dr. Baris M. Uz 15 Eisenhower Avenue Alexandria, VA 22314			13. Type of Report & Period Covered Technical Report 14.

15. Supplementary Notes

This report should be cited as: Woods Hole Oceanographic Institution Technical Report, WHOI-2025-14 https://doi.org/10.1575/1912/72578

16. Abstract (Limit: 200 words)

The 2024 Geophysical Fluid Dynamics Summer Program ran from June 17 to August 23 under the direction of Greg Chini (University of New Hampshire) and Bruce Sutherland (University of Alberta). The theme of the opening lectures, given during the first two weeks, was Multiscale GFD. One of the principal lecturers was Basile Gallet (Université Paris-Saclay, CEA, CNRS). Keith Julien from the University of Colorado, Boulder, was slated to be the other principal lecturer. Tragically, however, he passed away unexpectedly in April 2024. We are extremely grateful to Edgar Knobloch (University of California, Berkeley) who, on short notice, agreed to be the other principal lecturer along with Greg Chini, who gave one of the principal lectures. Edgar opened the lectures with talks on weakly and strongly nonlinear theory for convection with and without rotation. He went on to describe fingering and parametric instabilities. Greg then described the application of the strongly-nonlinear multiscale approach to stably stratified turbulence. Basile gave lectures on turbulence with and without rotation, going on to discuss two dimensional turbulence above topography before describing multiscale methods used to model turbulent transport and near-inertial waves in the ocean. As is now an annual tradition at Walsh Cottage, Keaton Burns (MIT) delivered a "Dedalus tutorial" for the benefit of the fellows and staff.

17. Document Analysis

a. Descriptors: Geophysical fluid dynamics, Convective instabilities, Geostrophic turbulence

b. Identifiers/ Open-Ended Terms

c. COSATI Field/ Group

18. Availability Statement	19. Security Class (This Report)	21. No. of Pages
Approved for public release, distribution unlimited	20. Security Class (This Page)	22. Price